

POR-2037
(WT-2037)(EX)
VOLUME 1
EXTRACTED VERSION

OPERATION DOMINIC, FISH BOWL SERIES

Project Officer's Report—Project 8A.3

Close-In Thermal and X-ray Vulnerability Measurements—Shots Blue Gill and King Fish

F. D. Adams, Project Officer
Flight Dynamics Laboratory
Wright-Patterson AFB, OH

O. R. Anderson	F. E. Fahrenholz
M. Annis	G. G. Fryklund
L. E. Ashley	J. R. Taylor
M. P. Berardi	G. R. Vrablik
A. B. Cicero	B. C. Watson
C. M. Cobb	

American Science and Engineering, Inc.
Cambridge, MA

DTIC
ELECTE
JUN 02 1987
S D
D

6 April 1965

NOTICE:

This is an extracted version of POR-2037 (WT-2037), Volume 1, OPERATION DOMINIC; Fish Bowl Series, Project 8A.3.

Approved for public release; distribution is unlimited.
--

Extracted version prepared for
Director
DEFENSE NUCLEAR AGENCY
Washington, DC 20305-1000

1 September 1985

AD-A995 482

Destroy this report when it is no longer needed. Do not return to sender.

PLEASE NOTIFY THE DEFENSE NUCLEAR AGENCY,
ATTN: STTI, WASHINGTON, DC 20305-1000, IF YOUR
ADDRESS IS INCORRECT, IF YOU WISH IT DELETED
FROM THE DISTRIBUTION LIST, OR IF THE ADDRESSEE
IS NO LONGER EMPLOYED BY YOUR ORGANIZATION.



UNCLASSIFIED

SECURITY CLASSIFICATION OF THIS PAGE

REPORT DOCUMENTATION PAGE

1a. REPORT SECURITY CLASSIFICATION UNCLASSIFIED		1b. RESTRICTIVE MARKINGS	
2a. SECURITY CLASSIFICATION AUTHORITY		3. DISTRIBUTION/AVAILABILITY OF REPORT Approved for public release; distribution is unlimited.	
2b. DECLASSIFICATION/DOWNGRADING SCHEDULE			
4. PERFORMING ORGANIZATION REPORT NUMBER(S)		5. MONITORING ORGANIZATION REPORT NUMBER(S) POR-2037 (EX) (WT-2037) (EX) VOLUME 1	
6a. NAME OF PERFORMING ORGANIZATION 1-Flight Dynamics Lab. 2-American Science & Engineering, Inc.	6b. OFFICE SYMBOL (if applicable)	7a. NAME OF MONITORING ORGANIZATION Defense Atomic Support Agency	
6c. ADDRESS (City, State, and ZIP Code) 1-Wright Patterson AFB, Ohio 2-Cambridge, Massachusetts		7b. ADDRESS (City, State, and ZIP Code) Washington, DC	
8a. NAME OF FUNDING, SPONSORING ORGANIZATION	8b. OFFICE SYMBOL (if applicable)	9. PROCUREMENT INSTRUMENT IDENTIFICATION NUMBER	
8c. ADDRESS (City, State, and ZIP Code)		10. SOURCE OF FUNDING NUMBERS	
		PROGRAM ELEMENT NO	PROJECT NO
		TASK NO.	WORK UNIT ACCESSION NO.
11. TITLE (Include Security Classification) OPERATION DOMINIC, FISH BOWL SERIES, PROJECT OFFICER'S REPORT - PROJECT 8A.3 - Close-In Thermal and X-ray Vulnerability Measurements - Shots Blue Gill and King Fish, Extracted Version			
12. PERSONAL AUTHOR(S) F. D. Adams, O. R. Anderson, M. Annis, L. E. Ashley, M. P. Berardi, A. B. Cicero, (Continued)			
13a. TYPE OF REPORT	13b. TIME COVERED FROM TO	14. DATE OF REPORT (Year, Month, Day) 650406	15. PAGE COUNT 426
16. SUPPLEMENTARY NOTATION This report has had sensitive military information removed in order to provide an unclassified version for unlimited distribution. The work was performed by the Defense Nuclear Agency in support of the DoD Nuclear Test Personnel Review Program.			
17. COSATI CODES		18. SUBJECT TERMS (Continue on reverse if necessary and identify by block number)	
FIELD	GROUP	SUB-GROUP	
18	3	Dominic X-rays	
20	8	Fish Bowl Blue Gill	
		Thermal Radiation King Fish	
19. ABSTRACT (Continue on reverse if necessary and identify by block number) The objective of this project was to verify the existence of a nuclear-weapon-induced thermo-mechanical loading which could cause structural damage to a reentry vehicle. Three instrument carrying pods were exposed at ranges of 3300, 4600, and 6800 feet below the burst. Two pods were recovered in excellent condition; and one was damaged at water impact, but most of the instruments were readable. Impulse time-history measurements indicated that most of the impulse was received in about 0.25 msec. The average acceleration of the pod was at least 200 g's over this duration. All but a small part of the measured impulse can be attributed to the thermomechanical loading mechanism. The measured thermal source intensity decreased rapidly with lateral distance from the burst point. A high-intensity core was observed (from the pods) less than 100 meters in diameter.			
20. DISTRIBUTION STATEMENT OF ABSTRACT UNCLASSIFIED		21. ABSTRACT SECURITY CLASSIFICATION UNCLASSIFIED	
22a. NAME OF RESPONSIBLE INDIVIDUAL Mark D. Flohr		22b. TELEPHONE (Include Area Code) (2-2) 325-755	22c. OFFICE SYMBOL N/ISCM

UNCLASSIFIED

SECURITY CLASSIFICATION OF THIS PAGE

12. PERSONAL AUTHOR(S) (Continued).

C. M. Cobb, F. E. Fahrenholz, G. G. Fryklund, J. R. Taylor, G. R. Vrablik, and B. C. Watson

UNCLASSIFIED

SECURITY CLASSIFICATION OF THIS PAGE

FOREWORD

Classified material has been removed in order to make the information available on an unclassified, open publication basis, to any interested parties. The effort to declassify this report has been accomplished specifically to support the Department of Defense Nuclear Test Personnel Review (NTPR) Program. The objective is to facilitate studies of the low levels of radiation received by some individuals during the atmospheric nuclear test program by making as much information as possible available to all interested parties.

The material which has been deleted is either currently classified as Restricted Data or Formerly Restricted Data under the provisions of the Atomic Energy Act of 1954 (as amended), or is National Security Information, or has been determined to be critical military information which could reveal system or equipment vulnerabilities and is, therefore, not appropriate for open publication.

The Defense Nuclear Agency (DNA) believes that though all classified material has been deleted, the report accurately portrays the contents of the original. DNA also believes that the deleted material is of little or no significance to studies into the amounts, or types, of radiation received by any individuals during the atmospheric nuclear test program.

Accession For	
NTIS CRA&I	<input checked="" type="checkbox"/>
DIC TAB	<input type="checkbox"/>
Unannounced	<input type="checkbox"/>
Justification	
By	
Distribution	
Availability Codes	
Date	Avail and/or Special
A-1	



UNANNOUNCED

OPERATION DOMINIC

FISH BOWL SERIES

PROJECT OFFICERS REPORT—PROJECT 8A3

**CLOSE-IN THERMAL AND X-RAY VULNERABILITY
MEASUREMENTS—SHOTS BLUE GILL AND
KING FISH**

F. D. Adams, Project Officer

**Flight Dynamics Laboratory
Wright-Patterson AFB, Ohio**

O. R. Anderson	F. E. Fahrenholz
M. Annis	G. G. Fryklund
L. E. Ashley	J. R. Taylor
M. P. Berardi	G. R. Vrablik
A. B. Cicero	B. C. Watson
C. M. Cobb	

**American Science and Engineering, Inc.
Cambridge, Massachusetts**

This document is the author(s) report to the Director, Defense Atomic Support Agency, of the results of experimentation sponsored by that agency during nuclear weapons effects testing. The results and findings in this report are those of the author(s) and not necessarily those of the DOD. Accordingly, reference to this material must credit the author(s). This report is the property of the Department of Defense and, as such, may be reclassified or withdrawn from circulation as appropriate by the Defense Atomic Support Agency.

**DEPARTMENT OF DEFENSE
WASHINGTON, D.C. 20301**

ABSTRACT

The objective of the Project 8A.3 participation in Shot Blue Gill was to verify the existence of a nuclear-weapon-induced thermomechanical loading which could cause structural damage to a re-entry vehicle. Three instrument-carrying pods (designated B-1, B-2, B-3, respectively) were exposed at ranges of 3300, 4600, and 6800 ft. below a burst

Pods B-1 and B-3 were recovered in excellent condition; pod B-2 was damaged at water impact, but most of the instruments were readable.

Passive instrumentation measured total impulse loadings to the refrasil-phenolic coated pods of $(9.7 \pm 0.2) \times 10^3$, $(7.5 \pm 0.3) \times 10^3$, and $(3.7 \pm 0.7) \times 10^3$ dyne-sec/cm² at B-1, B-2, and B-3, respectively. Impulse time-history measurements indicated that most of the impulse was received in about 0.25 msec. The average acceleration of the B-1 pod was at least 200 g's over this duration. All but a small part of the measured impulse can be attributed to the thermomechanical loading mechanism.

The material ablation of refrasil-phenolic on all pods was very small with less than 0.1 gm/cm² being lost on pod B-1.

Intensity, spectral, and spatial measurements were made of the weapon radiative source with diagnostic instruments on all pods. An X-ray source one meter in effective diameter was measured by a pinhole camera. This X-ray source radiated at a temperature

of 0.62 to 1.23 kev with a time-integrated intensity of 2.8 to 7.6 cal/cm² at pod B-1. This X-ray flux contributed very little to the loadings.

The measured thermal source intensity decreased rapidly with lateral distance from the burst point: a high-intensity core was observed (from the pods) less than 100 meters in diameter. * A second, lower intensity source 900 meters in diameter was also measured. There is no conclusive evidence that the pods were ever immersed in the source.

The short-duration integrated thermal intensities, measured by instruments partially shielded by the refrasil-phenolic vapor, at the three pods were respectively, ≥ 25 cal/cm², ≥ 17 cal/cm², and 9 to 50 cal/cm². The measured time durations of the inputs were $> 2 \times 10^{-3}$ sec to the instrument at B-2 and 0.5 to 4×10^{-3} sec to the instrument at B-3. Direct measurements at B-3 indicated that a large fraction of the short-time thermal input to the instrument was in the visible or the near ultraviolet. The thermal intensities measured over long times were at least 165 cal/cm² at B-1 and 72 cal/cm² at B-3, not corrected for reflection of radiation at the surface. The duration at B-1 has not been determined; the lower bound on time at B-3 is 0.16 sec. The thermal intensity measurements were made at different depths within the refrasil-phenolic vapor and are not directly applicable at the pod surface. Attenuation of the thermal intensity in the region immediately adjacent to the pod surface, presumably due to the opacity of the vapor products, was not directly measured.

* Subsequent to the submission of this report, certain ambiguities have become apparent in the data relating to the size and importance of the small source. Later analysis of these data may, therefore, necessitate revision of the tentative results presented in the text.

Semi-conductor elements were permanently damaged at B-1; they survived intact at B-3. Other electronic elements (capacitors, resistors, relays, photocells) were not damaged.

The Project 8A.3 participation in Shot King Fish concerned structural vulnerability measurements near a high-altitude burst.

The King Fish instruments were adaptations of those used in Blue Gill.

The ablation of most materials was too small to be of direct structural significance; Avcoat 19 and Rad 58B suffered severe mechanical fragmentation. Impulse values at K-1 in units of 10^3 dyne-sec/cm² were: refracil-phenolic 1.2, teflon 1.0, Micarta 3.0, pyrolytic graphite <0.2, steel 1.0, beryllium <0.2, and aluminum 0.6. An apparent time history was measured for lead (impulses from 1.2×10^3 to 4.6×10^3), but no corroborative evidence of a long-duration energy input has been found. Simple structural elements in the form of circular membranes deformed in a manner predicted by theoretical models.

PREFACE

This document describes the participation of Project 8A.3 in Shots Blue Gill and King Fish. The program has been performed under the technical monitorship of the Flight Dynamics Laboratory, Wright-Patterson Air Force Base, Ohio. The Contractor was American Science and Engineering, Inc., under Defense Atomic Support Agency (DASA) Contract No. DA-49-146-XZ-136.

The emphasis during the data reduction has been on Shot Blue Gill. All instruments from this experiment have been examined to the extent that significant revisions in the raw data are not expected. The results based on these data must, however, be considered preliminary, since only limited analysis has been possible up to the present time.

The Shot King Fish data reduction is not quite complete, and significant information may still be within instruments which have not been examined in detail. The results on King Fish must, therefore, be considered tentative and subject to modification by further analysis.

This report represents the status as of January 15, 1964 and supersedes all previous technical publications on Project 8A.3.

The authors wish to acknowledge the assistance of the following personnel from the Air Force Flight Dynamics Laboratory: Maj. C. Akard, Lt. H. Davis, Mr. J. Dolan, Mr. L. Gilbert, Mr. F. Janik, Mr. J. Pumphrey and Capt. R. Walker. Messrs. A. DeCaprio and E. Williams of American Science and Engineering, Inc., have provided support throughout the design and field

phases of the program. Acknowledgement is also made of the contribution of Professor George Clark of the Massachusetts Institute of Technology to the theoretical foundation of the thermomechanical effect and the contribution of Professor John Zotos of Northeastern University to the metallurgical procedures used in the design and examination of passive thermal instruments.

CONTENTS

ABSTRACT -----	5
PREFACE -----	9
PART 1 SHOT BLUE GILL -----	19
CHAPTER 1 INTRODUCTION -----	19
1.1 Objectives-----	19
1.2 Background-----	21
1.3 Technical Discussion-----	24
1.3.1 Weapon Phenomenology-----	24
1.3.2 Material Response to X-Ray and Thermal Radiation-----	29
1.3.3 X-Ray and Thermal Blowoff Effects-----	37
CHAPTER 2 PROCEDURE AND INSTRUMENTATION -----	62
2.1 Planned Test Operations-----	62
2.2 Instrument Pod-----	65
2.3 Instrumentation-----	67
2.3.1 Indent Recorder Clusters-----	67
2.3.2 Spall Gage-----	79
2.3.3 Ablation-Condensation Gage-----	81
2.3.4 Thermal Pinhole Camera-----	83
2.3.5 Cut-Off Filter Spectral Gage-----	85
2.3.6 Reflective Coating Spectral Gage-----	87
2.3.7 Long-Time Thermal Gage-----	90
2.3.8 X-Ray Pinhole Camera-----	92
2.3.9 Photocell X-Ray Detector-----	94
2.3.10 Instrument Installation-----	96
CHAPTER 3 EXPERIMENTAL RESULTS -----	117
3.1 Operational Results-----	117
3.1.1 Aborted Shot Blue Gill-----	117
3.1.2 Blue Gill Prime-----	118
3.1.3 Blue Gill Double Prime-----	118
3.1.4 Blue Gill Triple Prime-----	118
3.2 Instrument Performance-----	123
3.2.1 Impulse Measurements-----	126
3.2.2 Spall Gages-----	149
3.2.3 Ablation Measurements-----	150
3.2.4 Thermal Pinhole Cameras-----	159
3.2.5 Cut-Off Filter Spectral Gage-----	163
3.2.6 Reflective Coating Spectral Gage-----	164

3.2.7 Long-Time Thermal Gages	167
3.2.8 X-Ray Pinhole Camera	169
3.2.9 Photocell X-Ray Detector	172
3.2.10 Further Sources of X-Ray Intensity Information	174
3.3 Preliminary X-Ray and Thermal Input Analyses	175
3.3.1 X-Ray Inputs	175
3.3.2 Short-Time Thermal Radiation Inputs	182
3.3.3 Long-Time Thermal Radiation Inputs	191
3.3.4 Spectrum of Thermal Radiation, Pod B-3	194
3.3.5 Thermal Source Size	195
CHAPTER 4 SUMMARY AND DISCUSSION	305
4.1 Input Measurements	306
4.1.1 X-Ray Inputs	306
4.1.2 Thermal Inputs	307
4.2 Response Measurements	312
4.2.1 Thermomechanical Response	312
4.2.2 Ablation Response	315
4.3 Applied Blue Gill Results	317
4.4 Conclusions	319
PART 2 SHOT KING FISH	327
CHAPTER 5 INTRODUCTION	327
5.1 Objectives	327
5.2 Technical Discussion	328
CHAPTER 6 PROCEDURE AND INSTRUMENTATION	332
6.1 Planned Test Operations	332
6.1.1 Pod Positioning	332
6.1.2 Beryllium Facility	333
6.1.3 Recovery and Radiation Protection	333
6.2 Instrumentation	333
6.2.1 Indent Recorder Clusters	334
6.2.2 Spall Gages	338
6.2.3 Ablation-Condensation Gage	339
6.2.4 Thermal/Debris Pinhole Camera	340
6.2.5 X-Ray Intensity Gage	341
6.2.6 Pinhole Closure Gage	343
6.2.7 Long-Time Thermal Gages	343
6.2.8 X-Ray Pinhole Camera	344
6.2.9 Membrane Structure Gages	345
6.2.10 Instrument Installation	346
CHAPTER 7 EXPERIMENTAL RESULTS	358
7.1 Operational Results	358
7.2 Instrument Performance	360
7.2.1 Indent Recorder Clusters	361

7.2.2 Spall Gages	368
7.2.3 Ablation-Condensation Gages	369
7.2.4 Debris/Thermal Pinhole Cameras	372
7.2.5 X-Ray Intensity Gages	374
7.2.6 Pinhole Closure Gage	375
7.2.7 Long-Time Thermal Gage	375
7.2.8 X-Ray Pinhole Camera	376
7.2.9 Membrane Structure Gages	378
7.2.10 Additional X-Ray Intensity Data	383
7.3 X-Ray Input Analysis	383

CHAPTER 8 SUMMARY AND DISCUSSION	420
----------------------------------	-----

TABLES

1.1 Time-Integrated Intensity Incident on Blue Gill Pods up to Five Milliseconds (Predicted)	52
1.2 Absorption Depths and Minimum Vaporization Energies	52
2.1 Nominal Indent Recorder Piston Parameters	98
2.2 Predicted Thermal Radiation Impulses	98
3.1 Summary of Control Piston Data	201
3.2 Summary of Impulse Data	202
3.3 Quality of Indents, Shot Blue Gill	207
3.4 Blue Gill Ablation Data	207
3.5 Condition of Top Filters in Cut-Off Filter Spectral Gages	209
3.6 Foil Melt Depths, Long-Time Thermal Gage	211
3.7 Fraction of X-Ray Yield Transmitted to Blue Gill Pods	213
3.8 Relative X-Ray Intensities Received at Blue Gill Pods	213
3.9 Bulk Thermal Properties of Exposed Materials, Analysis of Short-Time and X-Ray Inputs	214
3.10 Normalized Surface X-Ray Energy Deposition in Steel at B-2	214
3.11 Bounds on Integrated X-Ray Intensity Received at B-1,	215
3.12 Bulk Thermal Properties of Exposed Materials, Analysis of Long-Time Input	215
3.13 Bulk Thermal Properties of Exposed Materials, Analysis of Input Spectrum	216
3.14 Thermal Source Size Estimates	216
7.1 Summary of Impulse Data	387
7.2 Measured Weight Losses of King Fish Ablation Samples	389
7.3 Long-Time Thermal Gage Data, Pod K-1	390
7.4 King Fish Transmission	390

FIGURES

1.1 X-ray energy deposition versus range at end of X-ray pulse	53
1.2 Transmitted X-ray spectrum through cold air (X-ray source temperature = 3/2 kev)	54
1.3 Transmitted X-ray spectrum through cold air (X-ray source temperature = 1 kev)	55

1.4	Transmitted X-ray spectrum through cold air (X-ray source temperature = 1/2 kev) -----	56
1.5	Fraction of X-radiation energy transmitted versus mass per unit area of air -----	57
1.6	Isothermal core radius versus time -----	58
1.7	Time history of thermal radiation emission by core -----	59
1.8	Time history of thermal radiation intensity within core -----	60
1.9	Time history of thermal radiation intensity incident on Project 8A.3 pods -----	61
2.1	Thor and instrument pod planned operational sequence, Blue Gill -----	99
2.2	Pod experiment -----	100
2.3	Pod storage cell -----	101
2.4	Instrument pod -----	102
2.5	Indent recorder pistons, Blue Gill -----	103
2.6	Indent impulse recorder -----	104
2.7	Spall gage -----	105
2.8	Ablation-condensation gage -----	106
2.9	Thermal pinhole camera -----	107
2.10	Transmission of spectral cutoff filters -----	108
2.11	Cutoff filter spectral gage -----	109
2.12	Reflective coating spectral gage -----	110
2.13	Spectral cutoff characteristics of reflecting surfaces -----	111
2.14	Long-time thermal gage (flush) -----	112
2.15	Long-time thermal gage (recessed) -----	113
2.16	Nominal 12-inch-focal-length X-ray pinhole camera, Blue Gill -----	114
2.17	Photocell X-ray detector -----	115
2.18	Instrumentation array, Blue Gill -----	116
3.1	Blue Gill pod reentry -----	217
3.2	Blue Gill pod reentry (closeup) -----	218
3.3	Summary of data reduction, Blue Gill Pod 1 -----	219
3.4	Summary of data reduction, Blue Gill Pod 2 -----	220
3.5	Summary of data reduction, Blue Gill Pod 3 -----	221
3.6	Flow patterns on indent recorder cluster, Blue Gill Pod 1 -----	223
3.7	Gas flow patterns below backplate, Blue Gill Pod 1 -----	224
3.8	Possible back-pressure influences on piston measurements -----	225
3.9	Indications of cluster motion, Blue Gill Pod 1 -----	226
3.10	Schematic interaction of pod and indent recorder -----	227
3.11	Postshot condition of anvils, Blue Gill -----	228
3.12	Variation of total impulse with pod-to-R/V range -----	229
3.13	Integral of impulse versus impulse, Pod B-1 -----	230
3.14	Integral of impulse versus impulse, Pod B-2 -----	231
3.15	Integral of impulse versus impulse, Pod B-3 -----	232
3.16	Integral of impulse versus impulse, Pod B-1, A-pistons -----	233
3.17	Force time history, Pod B-1 -----	234
3.18	Uncorrected force time histories, A-pistons -----	235
3.19	Postshot condition of spall gage, Pod B-1 -----	236
3.20	Ablation of reffrasil-phenolic, A-piston sample -----	237
3.21	Ablation of reffrasil-phenolic, F-piston sample -----	238
3.22	Reffrasil-phenolic before exposure -----	239
3.23	Exposed reffrasil-phenolic, Pod B-1 -----	240

3.24	Postshot condition of ablation-condensation gages-----	241
3.25	Surface profiles of Blue Gill ablation samples (refrasil- phenolic and micarta) -----	242
3.26	Surface profiles of Blue Gill ablation samples, iron devcon -----	243
3.27	Surface profiles of Blue Gill ablation samples, lead -----	244
3.28	Surface profiles of Blue Gill ablation samples, silver, aluminum, and zinc -----	245
3.29	Location of metallurgical data in thermal instruments -----	246
3.30	Transformation depths in thermal pinhole camera, top slotted steel gage, 1-mm aperture, Pod B-1 -----	247
3.31	Transformation depths in thermal pinhole camera, top slotted steel gage, 3-mm aperture, Pod B-1 -----	248
3.32	Transformation depths in thermal pinhole camera, top unslotted steel gage, 3-mm aperture, Pod B-1 -----	249
3.33	Transformation depths in thermal pinhole camera, top slotted steel gage, 10-mm aperture, Pod B-1 -----	250
3.34	Transformation depths in thermal pinhole camera, top slotted steel gage, 1-mm aperture, Pod B-1 -----	251
3.35	Photomicrograph of solid transformation -----	252
3.36	Photomicrographs showing transformations on top flush steel gage -----	253
3.37	Transformation depths in thermal pinhole camera, top flush steel gage, Pod B-1 -----	254
3.38	Transformation depths in thermal pinhole camera, side flush steel gage, Pod B-1 -----	255
3.39	Transformation depths in thermal pinhole camera, top slotted steel gage, 10-mm aperture, Pod B-2 -----	256
3.40	Transformation depths in thermal pinhole camera, top slotted steel gage, 10-mm aperture, Pod B-3 -----	257
3.41	Transformation depths in thermal pinhole camera, top flush steel gage, Pod B-3 -----	258
3.42	Postshot condition of TiO ₂ filter -----	259
3.43	Surface of bismuth-tin detector in cutoff filter spectral gage -----	260
3.44	X-ray shine-through in reflective coating spectral gage -----	261
3.45	Transformation depths in reflective coating spectral gage, steel, no coating, 10-mm aperture, Pod B-1 -----	262
3.46	Photomicrograph of transformations in reflective coating spectral gage -----	263
3.47	Transformation depths in reflective coating spectral gage, Bi-Sn, no coating, 3-mm aperture, Pod B-1 -----	264
3.48	Transformation depths in reflective coating spectral gage, Bi-Sn, gold black, 3-mm aperture, Pod B-1 -----	265
3.49	Transformation depths in reflective coating spectral gage, Bi-Sn, no coating, 10-mm aperture, Pod B-1 -----	266
3.50	Transformation depths in reflective coating spectral gage, Bi-Sn, gold black, 10-mm aperture, Pod B-1 -----	267
3.51	Transformation depths in reflective coating spectral gage, Bi-Sn, no coating, flush, Pod B-1 -----	268
3.52	Transformation depths in reflective coating spectral gage, Bi-Sn, no coating, 3-mm aperture, Pod B-3 -----	269

3.53	Transformation depths in reflective coating spectral gage, Bi-Sn, gold black, 3-mm aperture, Pod B-3 -----	269
3.54	Transformation depths in reflective coating spectral gage, Bi-Sn, no coating, 10-mm aperture, Pod B-3-----	270
3.55	Transformation depths in reflective coating spectral gage, Bi-Sn, gold black, 10-mm aperture, Pod B-3-----	271
3.56	Transformation depths in reflective coating spectral gage, Bi-Sn, no coating, flush, Pod B-3 -----	272
3.57	Depth of melt in bismuth-tin detector -----	273
3.58	Response of long-time thermal gage-----	274
3.59	X-ray pinhole camera film plate, Blue Gill Pod 1 -----	275
3.60	X-ray pinhole camera images, Blue Gill Pod 1 -----	276
3.61	Contour map of X-ray pinhole camera image, Blue Gill Pod 1, 0.033-cm pinhole -----	277
3.62	Contour map of X-ray pinhole camera image, Blue Gill Pod 1, 0.010-cm pinhole -----	278
3.63	Cross section of images in X-ray pinhole camera, Blue Gill Pod 1-----	279
3.64	X-ray pinhole camera film plate, Blue Gill Pod 2 -----	280
3.65	X-ray pinhole camera images, Blue Gill Pod 2 -----	281
3.66	Cross section of crater in film plate on X-ray pinhole camera, Blue Gill Pod 2, lead -----	282
3.67	Photograph showing X-ray-illuminated areas on aluminum, Blue Gill Pod 1, Cluster 62 -----	283
3.68	X-ray effects on aluminum, Pod B-1, Cluster 62, Crescent 1 -----	284
3.69	X-ray effects on aluminum, Pod B-1, Cluster 62, Crescent 2 -----	285
3.70	Photomicrograph showing melt in aluminum, Pod B-1, Cluster 62 -----	286
3.71	X-ray-illuminated area on inner surface of aluminum guide sleeve, Pod B-1 -----	287
3.72	X-ray effects on aluminum guide sleeve, Pod B-1, Cluster 57 -----	288
3.73	Transmission spectra at B-1 -----	289
3.74	Transmission spectra at B-2 -----	290
3.75	Transmission spectra at B-3 -----	291
3.76	Normalized X-ray energy deposition in aluminum at B-1-----	292
3.77	Calculated X-ray output versus weapon temperature, Shot Blue Gill -----	293
3.78	Time-temperature profiles at 138- μ depth in 1019 steel -----	294
3.79	Calculated thermal radiation input to B-1 instrument, based on martensite formation at 138- μ depth, rectangular wave input -----	295
3.80	Time-temperature profiles at 105- μ depth in 1019 steel -----	296
3.81	Calculated thermal radiation input to B-1 instrument, based on martensite formation at 105- μ depth, rectangular wave input -----	297
3.82	Time-temperature profiles at 53- μ depth in 1019 steel -----	298
3.83	Calculated thermal radiation input to B-3 instrument, based on martensite formation at 53- μ depth, rectangular wave input -----	299

3.84	Calculated bounds on absorbed energy in Pod B-3 instruments, short-time input -----	300
3.85	Calculated bounds on incident energy, assuming input is visible radiation, short-time input, Pod B-3 -----	301
3.86	Calculated energies absorbed by long-time thermal gages, Pod B-1 -----	302
3.87	Calculated energies absorbed by long-time thermal gages, Pod B-3 -----	303
3.88	Thermal source/camera image geometry -----	304
4.1	Source size-R/V relation -----	320
4.2	Blue Gill thermal sources -----	321
4.3	Blue Gill fireball geometry -----	322
4.4	Comparison of estimated and measured impulses -----	323
4.5	Mechanism for fast absorption of energy in refrasil-phenolic -----	324
4.6	Damage ranges, Mark 3 R/V -----	325
4.7	Damage ranges, Mark 4 R/V -----	325
4.8	Damage regimes for reentry vehicles -----	326
6.1	Indent recorder pistons, Shot King Fish -----	347
6.2	Indent recorder piston beryllium window configuration -----	348
6.3	Indent recorder piston hatch configuration -----	349
6.4	Spall gage, metallic samples -----	350
6.5	Debris/thermal pinhole camera hatch configuration -----	351
6.6	X-ray intensity gage, film stack -----	352
6.7	X-ray intensity gage, particle suspension -----	353
6.8	Aperture closure gage -----	354
6.9	X-ray pinhole camera -----	355
6.10	Structural gage -----	356
6.11	Instrument array, King Fish Pod 1 -----	357
7.1	Status of King Fish data reduction -----	391
7.2	Postshot condition of Indent Recorder Cluster 80 -----	393
7.3	Integral of impulse versus impulse, Pod K-1, lead -----	394
7.4	Loading time data, King Fish Pod 1, lead -----	395
7.5	Postshot condition of spall gage, Pod K-1 -----	396
7.6	Ablation-condensation gage reentry material, Avcoat 19, King Fish -----	397
7.7	Surface profiles of King Fish ablation samples -----	398
7.8	Postshot condition of refrasil-phenolic, King Fish Pod 1 -----	399
7.9	Transformation depths in thermal pinhole camera, top-slotted steel gage, 10-mm aperture, without hatch, Pod K-1 -----	400
7.10	Transformation depths in thermal pinhole camera, top-slotted steel gage, 1-mm aperture, without hatch, Pod K-1 -----	401
7.11	Cross-sectioning orientation for thermal pinhole camera, 1020 steel detector, Pod K-1 -----	402
7.12	Orientation and location of pinhole camera with respect to Pod K-1 -----	403

7.13	11.5-inch-focal-length X-ray pinhole camera film stack -----	404
7.14	11.5-inch-focal-length X-ray pinhole camera images, 0.011- and 0.008-cm apertures, King Fish -----	405
7.15	11.5-inch-focal-length X-ray pinhole camera images, 0.012- and 0.035-cm apertures, King Fish -----	406
7.16	11.5-focal-length X-ray pinhole camera images, 0.033- and 0.012-cm apertures, King Fish -----	407
7.17	4-inch focal-length X-ray pinhole camera film stack -----	408
7.18	4-inch-focal-length X-ray pinhole camera images, King Fish -----	409
7.19	Structural gages, steel, King Fish -----	410
7.20	Structural gages, aluminum, King Fish -----	411
7.21	Deflected shapes of membrane structural gages -----	412
7.22	Deflection mode of membrane structural gage, 0.050-inch aluminum, King Fish -----	413
7.23	X-ray effects on aluminum, Cluster 80, Pod K-1 -----	414
7.24	X-ray-illuminated area on inner surface of aluminum guide sleeve, Pod K-1-----	415
7.25	X-ray effects on aluminum guide sleeve, Cluster 80, Pod K-1 -----	416
7.26	Transmission spectra at pod, Shot King Fish -----	417
7.27	Normalized X-ray energy deposition in aluminum at Pod K-1 -----	418
7.28	Calculated X-ray output versus weapon temperature, King Fish -----	419

Science and Engineering, Inc. (Project 8A.3) participation in Shot Blue Gill were to:

1. Investigate the thermomechanical effect of an intermediate-altitude nuclear burst. Specifically, the instrumentation was designed to:

- a. verify the existence of a thermomechanical loading;
- b. measure the total impulse associated with it;
- c. attempt to measure the time history of the impulse;
- d. measure the total impulse as a function of material properties; and
- e. investigate the effect of the vaporized material shielding the surface.

2. Investigate the following characteristics of the thermal source as viewed at the test vehicle surface:

- a. the spectrum;
- b. the integrated thermal flux;
- c. the variation of the flux with time; and
- d. the spatial distribution of the thermal source.

3. Investigate the (non-thermomechanical) effects of an intermediate-altitude burst on materials.

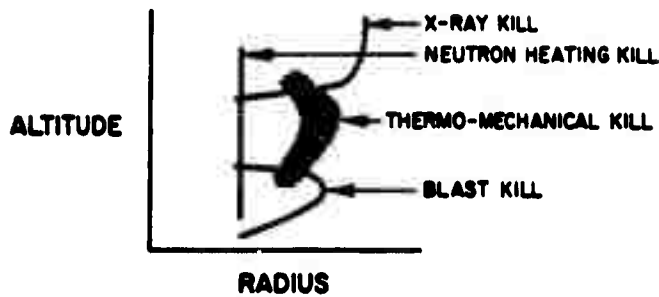
4. Perform sufficient measurements of the X-radiation to determine unambiguously the intensity and impulse due to X-rays alone. This objective was in the nature of a control experiment to demonstrate in an unequivocal manner that certain of the effects were indeed due to thermal radiation rather than X-radiation.

1.2 BACKGROUND

A nuclear burst may damage an ICBM at a significant range by one or more different mechanisms of which the most significant are:

1. blast—the impact of the aerodynamic shock (including the gust) formed when the explosion occurs within the atmosphere;
2. neutron heating—the sudden generation of destructive heat within the fissionable material in the warhead by nuclear reactions induced by the neutrons released by the burst;
3. ablation—the erosion of the surface materials of the R/V by vaporization and/or melting under thermal irradiation;
4. X-ray-induced loading—the impulsive loading of the missile structure by the pressure of the vapor generated at the R/V surface under irradiation by thermal X-rays from a weapon exploded in near-vacuum conditions; and
5. thermomechanical loading—the impulsive loading of the missile structure due to the pressure of the vapor generated at the missile surface when exposed to the short-time thermal radiation from an intermediate-altitude detonation.

With each mechanism can be associated a certain lethal radius within which an incoming R/V and/or warhead will be destroyed. The lethal radii depend on the character of the weapon, the structure of the warhead, and the altitude of the burst. Various studies have been carried out to evaluate the lethal radii, and shown below is a schematic representation of the way the lethal radii depend on altitude.



It is, of course, attractive to plan an antimissile interception of an enemy ICBM for a high altitude because of the opportunity for repeated interception attempts and because of safety considerations for ground installations and personnel. Thermal X-radiation from a nuclear detonation at high altitude has been analytically shown to constitute a potent source for destructive energy. The kill mechanism is blowoff pressure due to thermal X-radiation. This X-ray-induced pressure (and the resultant impulse) is, however, critically dependent on the altitude of interception, because a very small atmospheric density is sufficient to absorb the X-rays within a short distance of the burst.

At an intermediate altitude, the thermal X-rays are rapidly absorbed. Their energy generates an expanding fireball of hot atmospheric gases and bomb debris. This fireball may emit intense radiation in the ultraviolet and visible portions of the spectrum for a time which is short compared to the characteristic response time of a missile structure. Although this radiation does not penetrate the missile surface significantly (in contrast to the approximately 0.1-millimeter penetration of thermal X-radiation), calculations indicate that this radiation is capable of sufficient ablation to generate lethal blowoff pressures (or impulse) at significant ranges.

Three attempts have been made to measure X-ray-induced impulse prior to the Fish Bowl Series. One of these was in the Logan underground shot in 1958. The energy flux in this test was higher than the experiments were designed for. This fact, plus the severity of the tunnel environment, resulted in the acquisition of ambiguous data. The high-altitude tests carried out over the Pacific in Shot Teak of Operation Hardtack (1958) did not succeed in measuring X-ray impulses because of an X-ray shadow in the direction of the instrument pod. The underground test in Nevada (Shot Marshmallow of Operation Nougat) in July 1962 was successful. Extensive data is available concerning the effect of X-rays on materials, including pressure, time histories, impulses, and ablations.

Shot Teak, though only partially successful, gave at least suggestive evidence of the destructive potential of thermally induced blowoff pressure (thermomechanical effect). The instrument face of the Teak experimental pod suffered a permanent deformation conceivably caused by the explosive formation of vapor at the plastic-coated surface of the pod. Metallurgical examination of the exposed metal surfaces indicated that the pod had absorbed only 3 cal/cm^2 of X-rays and about 40 cal/cm^2 of short-time thermal radiation, suggesting that thermal radiation, rather than X-rays, was responsible for the observed deformation. The data, however, did not permit a decisive evaluation of the blow-off mechanism. Shot Orange of Operation Hardtack occurred in the intermediate-altitude regime (as defined above) and might have provided the desired information. Unfortunately, the instrument pod was not recovered.

The planned participation by the Flight Dynamics Laboratory (FDL) in Operation Willow involved shots at altitudes of 350,000, 125,000,

and 117,000 feet. The entire Willow program was cancelled in January 1960; the FDL effects effort for Willow is documented in Reference 2.

The present experiment was carried out, under the technical monitorship of the Flight Dynamics Laboratory of the Air Force Systems Command, by American Science and Engineering, Inc. (ASE) under Contract No. DA-49-146-XZ-136 with the Defense Atomic Support Agency. In this program, FDL/ASE had prime responsibility for instrument pods at nominal ranges of 2,500 feet and 6,000 feet from the burst center, and the Ballistic Research Laboratories had prime responsibility for the pod at 4,000 feet. In this document, no further differentiation is made of these responsibilities, since the operational procedure and instrumentation for all pods was virtually identical.

1.3 TECHNICAL DISCUSSION

1.3.1 Weapon Phenomenology. In a high-yield nuclear explosion, approximately 70% of the weapon yield is transmitted to the surrounding atmosphere in the form of thermal X-rays, which are emitted by the expanding bomb case (which has a temperature of approximately 1 kev) during the first fraction of a microsecond. At very low burst altitudes these soft X-rays have a short mean free path in the atmosphere. The resultant energy is deposited within a sphere of the order of meters in radius and which contains fully stripped air atoms. At very high altitudes where the X-ray mean free path is of the order of kilometers or greater, the energy deposition in the atmosphere is given by the familiar exponential-inverse square formula (see, for example, Reference 3).

In the intermediate-burst altitude range (i. e., 100,000 to 250,000 feet) the X-ray energy deposition in the atmosphere consists of a core of air containing fully stripped atoms surrounded by cooler air in which the energy variation over most of the range is given by the exponential-inverse square formula. Under Contract Number DA-19-020-ORD-5377 between the Picatinny Arsenal and American Science and Engineering, Inc., the X-ray energy deposition in the atmosphere has been studied (Reference 4). In addition, the subsequent energy transfer by radiation transport has been analyzed, and a technique has been formulated leading to predictions of the radiation transport phenomena after X-ray energy deposition in the atmosphere. The technique is suitable for hand computation and was utilized to compute the thermal radiation inputs to the Project 8A. 3 pods in the Fish Bowl experiment.

The sharp discontinuity results from the simplified physical model used in the subsequent analysis and is not real. The discontinuity marks the edge of an isothermal core. Outside of the isothermal core the X-ray transmission is assumed to be determined by the absorption characteristics of cold air. The transmitted spectra for three X-ray source temperatures are shown in Figures 1.2, 1.3 and 1.4 (atmospheric density at 165,000 feet is 10^{-6} gm/cm³). The fraction of the initial X-ray energy transmitted through air is presented in Figure 1.5.

The computation of the subsequent core expansion assumes that an isothermal core within the visible fireball exists at all times. The material and radiation within this high-temperature core are never in thermodynamic equilibrium at any stage of the calculation. The term "isothermal" refers to the kinetic temperature of the electrons in the continuum. The cooling and expansion rates of the isothermal core have been calculated, taking into account the following atomic processes: (1) electron recombination, (2) photo-ionization, (3) electron excitation, (4) bremsstrahlung, (5) free-free absorption, (6) electron ionization.

The quantum mechanical atomic cross sections for recombination and bremsstrahlung have been taken from References 5 and 6. The classical cross sections for ionization and excitation have been taken from References 7 and 8. The generalized energy transport equations are those which describe: (1) the spatial and time variation of the radiation density, (2) the spatial and time variation of the free electrons, and (3) the spatial and time variation of the ionized and excited atomic states. The

complex equations have been greatly simplified by assuming the presence of an isothermal core within the fireball and neglecting the hydrodynamic motion. It is felt that these simplifying assumptions do not detract greatly from the accuracy of the results. The greatest source of error is perhaps in the quantum mechanical estimates of atomic cross sections, many of which have never been measured experimentally. A detailed description of the analysis is contained in Reference 4.

Figure 1.6 displays the radius of the isothermal core as a function of time. The physical model utilized herein assumes

that the only thermal radiation that can leave the core and penetrate a target exterior to it are photons of energy between 0 and 6 ev (the latter energy corresponds to the cut-off in molecular oxygen). When the target is immersed in the core, photons of all frequencies are incident on the target. The assumptions utilized to enable one to compute core radius versus time begin to break down sometime after a few milliseconds. Thus, it was not possible to state unequivocally whether at 6,000 feet a pod will or will not see a late-time fireball environment. At about the time that this pod would enter the fireball, the fireball itself becomes rather tenuous.

Figure 1.7 shows the power output of the isothermal core for photon energies between 0 and 6 ev. Figure 1.8 shows the local radiation intensity over all frequencies incident on a flat target facing the burst point and immersed in the core. It has been assumed for simplicity that this intensity is uniform throughout the core. In the physical model utilized in this analysis the maximum spatial variation in radiation intensity on an immersed flat surface pointing toward the burst point is approximately 25%.

In a more exact computation, where the transition between the high temperature core and cooler air is smooth and occurs over a significant range, this assumption of uniformity of intensity is not justified and may indeed lead to large errors. Also, the assumption of uniformity of radiation intensity incident on a flat surface immersed in the core and facing away from the burst point would lead to large errors.

Figures 1.6, 1.7, and 1.8 have been utilized to determine inputs to targets (facing the burst) at different ranges. When

the target is outside of the core, the incident intensity $I(t)_{0-6 \text{ ev}}$ is given by

$$I(t)_{0-6 \text{ ev}} = \frac{P(t)_{0-6 \text{ ev}}}{4 \pi R_T^2} \quad (1.1)$$

where: $P(t)_{0-6 \text{ ev}}$ is the power output in the photon energy range 0 to 6 ev (given by Figure 1.7)

R_T is the target range

Figure 1.6 indicates the time at which the target is immersed in the core. Figure 1.8 can then be used to determine the time variation of input intensity $I(t)$. The photon intensity is assumed to be uniform throughout the core for a target facing the burst point.

Figure 1.9 shows the incident radiation intensity as a function of time on the three pods at their nominal locations. Table 1.1 summarizes the integrated thermal radiation inputs (integrated to 5 milliseconds) for the three pods. The incident radiation has been divided into two spectral regions: (1) 0 to 6 ev (IR, visible, and near ultraviolet) and (2) greater than 6 ev (essentially all vacuum ultraviolet). It is interesting to note from Table 1.1 that the innermost pod receives approximately 90% of its energy in the form of vacuum ultraviolet radiation, and about 10% of the energy in the range from 0 to 6 ev. The intermediate pod at 4,000 feet receives about 85% of its energy in the vacuum ultraviolet and about 15% of its energy between 0 and 6 ev. The outer pod receives none of its energy in the vacuum ultraviolet and, thus, all of it in the region from 0 to 6 ev.

1.3.2 Material Response to X-ray and Thermal Radiation.

The absorption of X-rays in materials is determined primarily by the intrinsic structure of the constituent atoms. Thus, the X-ray absorption coefficient is a function of the density and binding energies of the atomic electrons in the innermost electron shells and not of the inter-atomic forces or atomic vibration. Therefore, to a high degree of precision, the X-ray absorption is independent of material phase and temperature (as long as the temperature does not increase to the point where appreciable ionization of the atoms has taken place).

The response of metals to thermal inputs is qualitatively different from that of plastics. Metals behave relatively simply with heat conductivities and phase changes which are at least qualitatively understood. For plastics, the chemical reactions (either endothermic or exothermic), the phase changes, and heat conductivities are very complex and not easily predictable for the conditions of this test. The responses of metals and plastics to X-radiation and thermal radiation inputs are briefly discussed below.

Phase Transformation in Metals. In the solid metallic state, both short and long-range order prevails among the constituent atoms, and atomic motions are restrained by strong attractive forces. As the temperature of the metal rises with the addition of thermal energy, the vibrational energies of the atoms increase. At the melting temperature, the atomic vibrations overcome the attractive forces, and long-range order of the atoms within the metal disappears, while short range atomic order is retained. This phenomenon is the commonplace melting of a

metal. It is accompanied by the absorption of a finite amount of thermal energy to effect the phase change (latent heat of fusion). For a pure metal, the temperature during this phase transformation is essentially constant, since the dependence of the melting temperature upon pressure is small for pressures up to many atmospheres.

In the same fashion, the addition of thermal energy to a liquid metal causes an increase in the kinetic energy of the metal atoms, now relatively free to move. If vaporization is allowed to commence, the atomic vibrations in the liquid overcome the atomic attractive forces and short-range order disappears with the formation of a gas. Thermal energy required to effect this transformation of metal to gas is called the latent heat of vaporization. In the gaseous state, the distribution of atoms is completely unordered and changes continuously due to the random motion of the constituent atoms. In contrast to the phase change of melting, vaporization of a pure metal does not take place at a fixed temperature unless the pressure of the vaporized gas is fixed.

Thus, the commonplace phase changes, i. e., melting and vaporization, are associated with the destruction of long-range atomic order and short-range atomic order, respectively. There is, however, another class of phase changes in solid metals that is accompanied by a continuance of both long- and short-range atomic order. These phase changes are the so-called solid state transformations in which the metallic atoms slip from the initial geometrical array into a geometrical configuration that is more stable under the conditions present in the metal.

The martensite transformation in steel is an example of a solid state transformation in which the crystalline structure of the solid material is changed without a loss in either short-or long-range atomic order. The martensite transition is not instantaneous but involves a cooperative movement of atoms to produce a strain or a change in shape. Typically, one may heat a steel to a temperature at which martensite is formed, then cool the steel rapidly to room temperature. This procedure results in the formation and retention of martensite in the cooled steel. Although the martensite in steel is metastable at room temperature, it will often remain unchanged indefinitely. There is a finite latent heat associated with the martensite transformation, but it is typically negligible compared to the kinetic energies of the atoms in the crystal.

Phenomenological History of a Metal Exposed to High-Intensity X-Radiation. The X-ray energy deposition in a metal is a maximum at the exposed surface and decays exponentially away from the outer surface. Let us assume that the X-ray heating is an instantaneous volume heating effect so that heat conduction can be neglected in the initial phase. The irradiated metal may, therefore, consist of bands of vapor, vapor-liquid, liquid, liquid-solid and solid phases. The band of liquid-solid mixture may be of uniform temperature for a relatively pure metal. If the metal is an alloy, the liquid-solid band will display a finite temperature gradient.

After X-ray energy deposition the mechanism of thermal conduction transports energy toward the cooler interior of the material. With the advent of heat conduction, the liquid-solid

band will, in general, become narrower. For a relatively pure metal, the liquid-solid band vanishes with time and only bands of liquid and solid are present. In irradiated alloys the band of liquid-solid mixture will be of finite width, the magnitude of which is dependent on the liquidus and solidus temperatures and material properties. After X-ray energy deposition, the melt (or solidus) plane may move farther into the material, reaching a maximum depth, then receding and vanishing at the exposed plane.

Phenomenological History of a Metal Exposed to Thermal Radiation. Thermal radiation incident on the exposed surface of a metallic body is absorbed in the outermost atomic layers in a thickness typically of the order of 10^3 \AA . Some of the incident energy is utilized to raise the temperature of the surface layer, and the remainder is conducted into the interior. If the incident energy intensity is large enough relative to the thermal conductivity of the metal, the surface of the exposed metal attains the melting temperature and begins to melt. It is assumed herein that the solid state metal has a sufficient density of imperfections in its structure so that super-heating does not occur. Even under ideal laboratory conditions it is extremely difficult to super-heat a metal, so this assumption appears to be reasonable.

With continued absorption of thermal energy by the exposed surface, there is a widening of the band of melt and heating of the melt. In addition, vaporization may begin at the surface. For pure metals, which melt at a single temperature, there will be a definite boundary between the solid and the liquid portions

of the material. Thus, the melting temperature marks the position of the liquid-solid interface in the material when energy transport is carried out only by thermal conduction. On the other hand, such a sharp boundary need not exist when metallic alloys are heated by conduction. In these materials, there is a range of temperatures associated with melting (the extreme temperatures are called the solidus and liquidus). When such an irradiated metallic alloy undergoes melting by transient heat flow, there is generally a zone covering a range of temperature which contains a mixture of melt and solid.

After cessation of the energy input, the band of melt may thicken, then recede, and in time, complete resolidification occurs due to dissipation of energy by heat conduction into the interior of the metallic body. In the unmelted portion of the sample, a zone of material wider than the melt zone can often attain a maximum temperature sufficient to form a new solid phase. In the case of steel, this solid phase is martensite. After cooling to room temperature, such a zone in steel may consist of a uniform distribution of martensite, a non-uniform array of martensite, or a total absence of martensite depending on the cooling rates within the zone.

Thermal-Induced Decomposition of Plastics. The decomposition of plastics exposed to X-radiation and thermal radiation is accompanied by irreversible chemical reactions. These reactions result in the formation of molecules (and possibly atoms) of lower molecular weight than the primary plastic molecule. Based on experimental measurements of decomposing plastics exposed to a relatively low level thermal input intensity over

long periods of time, the chemical decomposition is, in general, a function of : (1) the detailed chemical composition and atomic structure of the plastic, (2) the input energy intensity and time history, and (3) the spectral distribution of the input radiation. There are few measurements of the chemical decomposition of plastics subjected to short-time high-intensity thermal radiation inputs. These few measurements seem to indicate that, for these input conditions, the chemical reaction may be qualitatively different. Specifically, for short bursts of either X-radiation or thermal radiation, the density, size, and distribution of impurities in the plastic materials may be of importance in the description of the plastic decomposition.

Thus, it is impossible to describe quantitatively the influence of impurities, cross-linking of the plastic molecule, and stability of the chemical structure on the decomposition of plastics under short, intense radiative inputs. One can only attempt to design simple experiments to achieve some understanding of the relative importance of these properties.

Use of Metallic Alloy Systems as Instruments. Since the metallic alloys retain transformations caused by intense thermal inputs, they can be used in various geometric configurations as passive detectors. As will be noted later in the sections describing instruments, geometry was used to achieve dynamic range. The metals themselves can also accept a large range of inputs. Because of the uncertain environment to be measured, a large dynamic range was a necessity.

Instrument design and data reduction procedures centered about the behavior of solutions to the one-dimensional, unsteady

heat conduction problem. For many situations, and certainly in the design of instruments, the bulk properties (e. g., specific heat, density, etc.) of the metal in a particular phase can be approximated as invariant with temperature. The validity of this assumption is discussed in Reference 9. The various solutions of the heat conduction equation that are used in this report are those presented by Carslaw and Jaeger (Reference 10). These are discussed in later sections of the report and in the appendices.

In heat conduction problems involving a change of phase with significant latent heat (Stefan-like problems) there exist no exact closed-form analytic solutions. The analytic solutions to the Stefan-like problems that are presently available fall into two classes. First, there are solutions resulting from a simplification of the boundary conditions in the mathematical formulation. For example, in calculating the thickness of the melt layer, the irradiated solid is often assumed to be initially at the melting temperature (Reference 10). Second, approximate analytic solutions may be derived using mathematical averaging techniques such as, for example, the heat-balance integral (Reference 11). For the general case where the solid initially is at a temperature below its melting point the heat balance integral technique often requires an iterative procedure of cross-interpolation in order to derive the answer. Nevertheless, the heat-balance integral technique appears to offer an excellent analytic tool by which certain heat conduction problems involving a change of phase may be studied.

Another tool available to the solution of Stefan-like problems

is the use of numerical solutions. Here, the degree of accuracy can be quite high, and solutions may also include both phase changes and changes in bulk properties with temperature. The numerical techniques published to date calculate the progression of the phase plane into the exposed material over chosen time intervals. This method introduces the basic non-linearity into the space field. If the technique utilizes a sizeable space mesh, then the computing time and resultant errors are both large. On the other hand, if the non-linearity is transferred into the time field and one calculates an elapsed time for the phase plane to progress one-mesh distance in the space array, then the non-linearity is removed from the many space points and inserted into the single time point. This method reduces computing time and increases the accuracy over that utilizing conventional numerical techniques.

The additional advantage of this new method of solving the Stefan problem, specifically in the case of simultaneous melting and vaporizing, is that one calculates time intervals during which equal amounts of material are vaporized. Thus, the blown-off vapor may be easily divided into distinct zones of material corresponding to the various material strata of equal thicknesses that have been vaporized. This technique enormously simplifies the hydrodynamic calculations, because it leads to realistic and physically meaningful zones in the vapor and ultimately to arrays of difference equations describing the fluid flow.

The described technique for the solution of the phase change problem has been developed to analyze some of the melt and vaporization data on the Blue Gill and King Fish pods. The

formulation of this basic technique has been started during the data reduction program. Some early results using this technique and the computing machine code are presented in later sections of this report and in appendixes.

1. 3. 3 X-Ray and Thermal Blowoff Effects. When vaporization occurs at a material surface, the vapor exerts a pressure on the surface. The magnitude of the pressure depends in a complicated way on the rate of vaporization, the temperature of the vapor, the degree of confinement of the vapor, and other factors. It can be said, however, that if a total thickness $M(\text{gm}/\text{cm}^2)$ of material is vaporized, and the vapor escapes into a vacuum with a final velocity V normal to the surface, then the net impulse delivered to the surface by the action of the pressure is MV according to the principle of conservation of momentum. If such an impulse were delivered to a missile or re-entry body in a sufficiently short time, then the impulsive load could cause a critical failure in the structure.

When X-rays impinge on a material, they deposit their energy beneath the surface with a density that decreases with depth below the surface according to the X-ray absorption characteristics of the material. If the total X-ray flux is sufficiently great, there will exist a depth above which the density of deposited energy exceeds the critical amount needed to heat and partially or completely vaporize the material. In this case, the vapor will be explosively formed and will escape outward, imparting a reaction impulse to the surface. Because of the brevity of the X-ray pulse and the explosive character of the blowoff, the delivery time of most of the reaction impulse is always short compared to the mechanical response time of structure, so that X-ray blowoff impulse, if sufficiently great, may cause permanent deformation or rupture of the structure. Indeed, the X-rays may induce an explosive blowoff sufficient to generate a

compressive wave which upon reflection from the interior free surface can cause tensile failure in a manner which is known as spalling.

It should be noted that the duration of the X-ray energy deposition process is usually so short that even in the case of good heat conductors (e. g. , copper) the heat conductivity of the material often does not substantially affect the result. Thus, the essential factors that determine the blowoff impulse due to an X-ray pulse are:

- (1) the total flux and spectrum of X-rays,
- (2) the X-ray absorption characteristics of the material,
and
- (3) the thermodynamic properties of the material and its decomposition products (in all phases).

A theory for the X-ray-induced impulse which takes into account all of the major changes in phase has been given in Reference 9 and applied to a variety of materials including plastics in Reference 12. A machine computation of the hydrodynamic behavior of the purely vapor phase has been performed. This computation, the so-called PUFF code, gives information on the pressure time-history. Certain features of the model used have been described in Reference 13.

In contrast to the phenomenology of the X-ray blowoff, the thermal radiation energy is deposited within a surface layer that is no thicker than a few thousand angstroms. Furthermore, the pulse duration is usually long enough so that in the case of exposed metals, a significant portion of the deposited energy may be lost from the surface by conduction into the interior. Thus, the amount of material ablated, and consequently the blowoff impulse, depend on:

- (1) the net flux and time history of the thermal radiation,

- (2) the reflectivity and emissivity of the surface,
- (3) the radiation transmission properties of the ablated vapor,
- (4) the thermodynamic properties of the material and its decomposition products, and
- (5) the bulk thermal properties of the exposed material.

Since the intensity of radiation inside a fireball greatly exceeds that outside of it, a body engulfed by the expanding fireball may suffer a greatly increased rate of ablation and a consequently greater blowoff pressure. Since the wavelength spectrum of the incident radiation in this case is predominantly in the vacuum ultraviolet region, the vapor escaping from an ablating surface may provide substantial shielding of the incident radiation, which would limit the ablation. The radiation that does reach the surface, however, is partially absorbed at the surface as is the longer wavelength radiation received outside the fireball. The same factors, therefore, govern the magnitude of the blowoff pressure.

In order to illustrate the essential physical processes that are involved in the phenomenon of radiation blowoff, we will now carry out several crude approximations.

Consider a pulse of monoenergetic X-rays incident on a surface. Call E the incident energy per unit area, λ the absorption length for the X-rays in the material, and Q_v the energy required to raise the unit mass of the material to the vaporization temperature (or to its decomposition temperature, in the case of plastics). Then the minimum value of E for vaporization is (see Reference 9)

$$E = \lambda Q_v \quad (1.2)$$

Table 1.2 lists absorption depths and minimum vaporization energies for several materials and quantum energy levels.

In the present experiment, the nearest test pod was at 3,280 feet from the burst. If the weapon had been unshielded, the total flux of X-rays for each pod could be derived from Figure 1.5, where account is taken of the spectral distribution of the X-rays and the mass absorption coefficients of the intervening air. In view of the fact that the weapon was shielded by the copper heat sink of the re-entry body, only the X-rays emitted by the exploding bomb material at relatively late times when it expands out from behind the shield were expected to strike the pod. (This expectation was not borne out by the pinhole camera pictures.) The expected total X-ray flux was, therefore, substantially smaller than the unshielded case. This smaller X-ray flux was not expected to be enough to cause sufficient vaporization to produce severe blowoff impulse even in the case of plastic re-entry coating material.

The justification for the view that absorption of thermal visible radiation in metals or graphite is essentially a surface phenomenon, rather than a bulk phenomenon as in the case of X-rays, lies in the very small depth of penetration of visible light. Typical penetration depths in metals are less than one-tenth of a wavelength; in graphitic carbon, of the order of one wavelength. To vaporize a layer 5000 \AA thick on the surface of graphite would require about 1 cal/cm^2 which is small compared to the expected total flux of thermal visible radiation even at the most distant pod. Therefore, the question of whether vaporization occurs is almost entirely one of whether the rate of energy absorption

is great enough to overcome the loss of heat from the surface layer by conduction.

Above a certain rate of energy absorption the ablation may be treated as a quasi-steady problem, and this has been done in all that follows.

The effect of re-radiation from the surface may be estimated by computing the rate of blackbody radiation at the vaporization temperature T_v of the material. The values of σT_v^4 for aluminum and graphite are 80 and 360 cal/cm²-sec, respectively (σ is the Stefan-Boltzmann constant). Since the emissivities of hot aluminum and graphite surfaces are not unity, these values should be reduced by an appropriate factor to obtain a more realistic estimate of the rate of re-radiation. In any case, these values are small compared to the incident intensities which can produce significant blowoff pressure. Re-radiation from the pod surface can, therefore, be neglected in all cases.

In order to predict thermomechanical loadings, it is essential that one have a physical model which correctly describes the processes which occur during the ablation of the surface. In Reference 1 a model was devised which postulated that the thermomechanical effect was due merely to vapor products of the surface material. It might be, however, that the mechanism of ablation is not so simply described, and that indeed the material is ablated in the form of a mixture of liquid and vapor depending on the nature of the material. In the following paragraphs, we repeat the crude calculation that was utilized to estimate the expected thermomechanical loads to the pod. Following this, a more general treatment is presented which serves to illustrate the parameters which must be measured if the thermomechanical effect is to be estimated for situations other than the present one.

To crudely approximate the expected impulse to the pods, it was estimated that Q calories per unit area would be absorbed by a graphite surface in a time sufficiently short that essentially all of the absorbed energy would go into latent heat of vaporization H_v . The total mass M of ablated material would then be

$$M = \frac{Q}{H_v} \quad (1.3)$$

If the final velocity of the vapor is set equal to the velocity of sound V_c at the vaporization temperature, then the net impulse would be

$$MV_c = \frac{QV_c}{H_v} \quad (1.4)$$

Assuming 1000 cal/cm^2 incident on graphite, a pulse duration of less than 10 msec satisfies the conditions that the heat conductivity may be neglected. The latent heat of vaporization is about 14,000 cal/gm, and the velocity of sound at the vaporization temperature of carbon is $2 \times 10^5 \text{ cm/sec}$. Thus, the net impulse per unit area would be $10^4 \text{ dyne-sec/cm}^2$. This impulse was judged to be sufficient to cause significant loads on the pod structure. The pod was therefore designed to withstand approximately four times this load.

The present experiment was designed to measure sufficient parameters concerning the nature of the input radiation and the response of materials to this input radiation to allow further calculations of thermomechanical loading under different conditions. The following equations, which describe the anticipated processes somewhat more generally than they are described in ASE-260 (Reference 14), furnish the framework in which the measurements may perhaps be understood and extrapolated to other situations.

No particular assumption is made on the nature of the ablation products; that is to say, it is not assumed that the ablation product is pure vapor. The possibility that a certain (unknown) fraction of the ablation product might be liquid or solid is allowed. Re-radiation from the vapor surface is not taken into account. Conservation of energy at the surface of the material is described by

$$Q_a(t) = (H_w + H_k) m(t) + Q_c(t) \quad (1.5)$$

where: $Q_a(t)$ is the energy absorbed at the surface up to the time t (ergs/cm²)

$H_w + H_k$ is the heat of ablation at the surface (ergs/gm)

H_w is the wasted heat of ablation which is not redelivered to the gas or to the ablated vapor as it expands. In ASE-260 (Reference 14) $H_w = \frac{1}{A} L_{i,0}$ (where $L_{i,0}$ is the molar internal heat of vaporization at temperature zero, and A is the atomic weight)

H_k is that part of the heat of ablation which can contribute to the impulse. In ASE-260 (Reference 14), $H_k = C_g (T - T_0) + RT + (L_{i,T} - L_{i,0}) \frac{m(t)}{A}$ (where C_g is the molar specific heat at constant volume, T is the temperature of the vapor, T_0 is the initial temperature, and L_{i,T_0} is the internal heat of vaporization at the temperature T_0)

$m(t)$ is the material vaporized up to the time t (gm/cm²)

$Q_c(t)$ is the portion of the absorbed energy which has been conducted into the interior by the time t

Conservation of energy in the ablated material is described by

$$e_k(t) = Q_v(t) + H_k m(t) \quad (1.6)$$

where: $e_k(t)$ is the kinetic energy of the ablation products at a point far away from the surface up to the time t (ergs/cm²)

$Q_v(t)$ is the energy absorbed in the vapor which contributes to the impulse

Combining the two equations above,

$$e_k(t) = Q_a(t) + Q_v(t) - H_w m(t) - Q_c(t) \quad (1.7)$$

If all of the ablated products come off at the same velocity, it would follow that the impulse to the time t would be given by $\sqrt{2me_k}$. However, it is not felt that this is a good a priori assumption. We, therefore, allow the possibility of a mixture of phases moving at different velocities in the blowoff. Assuming quasi-steady conditions, the force per unit area at the time t is given by

$$F(t) = \frac{dj(t)}{dt} = V(t) \frac{dm(t)}{dt} \quad (1.8)$$

where $j(t)$ is the impulse delivered up to the time t

$\bar{V}(t)$ is the average velocity of the ablation products at the particular time t

$\bar{V}(t)$ is given by

$$\bar{V}(t) = \frac{1}{m(t)} \int_0^{m(t)} V(t) dm(t) \quad (1.9)$$

The quantity $e_k(t)$, on the other hand, is related to the mean square velocity rather than the mean velocity.

$$e_k(t) = \frac{1}{2} m(t) \overline{V^2} \quad (1.10)$$

where:

$\overline{V^2}$ (t) is defined by the equation

$$\overline{V^2} (t) = \frac{1}{m(t)} \int_0^{m(t)} V^2 (t) d m (t) \quad (1.11)$$

In general, the data taken during the present experiment must conform to Equations 1.5, 1.6, and 1.8. The instrumentation was designed to measure in more or less detail:

- Q_a (t) the absorbed energy as a function of time
- m (t) where t is the total time of the ablation
- Q_c (t) is a directly derivable quantity
- j (t) is the impulse up to the time t

To illustrate the application of the above equations, a two-phase (vapor and liquid) system will now be assumed. The vapor and the liquid are assumed to ablate at different velocities. In this case

$$e_k = \frac{1}{2} m_v V_v^2 + \frac{1}{2} m_l V_l^2 \quad (1.12)$$

- where: m_v is the mass of the vapor ablated
- V_v is the velocity of the vapor
- m_l is the mass of the liquid ablated
- V_l is the velocity of the liquid

also,

$$j = m_v V_v + m_l V_l \quad (1.13)$$

and

$$m_v + m_l = m \quad (1.14)$$

where m is the total (and measured) mass ablated.

If
$$\frac{m_l}{m_v} = \mu, \quad \frac{V_l}{V_v} = \lambda \quad (1.15)$$

then j may be written as

$$j = \frac{1 + \mu\lambda}{\sqrt{(1 + \mu)(1 + \mu\lambda^2)}} \sqrt{2 m e_k} \quad (1.16)$$

Certain numerical results may be given based on Equations 1.5 through 1.16. Assume that the material is a metal which melts and which has H_W for the vapor phase of 1,800 cal/gm, H_K for the vapor phase of 300 cal/gm, H_W for the liquid phase of 150 cal/gm, and H_K for the liquid phase of 0. We assume conduction is negligible and the ablation products are transparent ($Q_v = 0$ $Q_c = 0$). Three cases will now be illustrated:

1. Most of the material ablates as liquid at low velocity.

$$\begin{aligned} Q_a &= 1000 \text{ cal/cm}^2 \\ \mu &= 10 \\ \lambda &= 0.1 \\ m &= 2.96 \text{ g/cm}^2 \end{aligned}$$

i. e., about 90% of the ablated material is liquid which comes off with 10% of the vapor velocity. In this case, it can be shown from the above equations that

$$j = 2.0 \times 10^5 \text{ dyne-sec/cm}^2$$

2. All of the material ablates as vapor.

$$\begin{aligned} Q_a &= 1000 \text{ cal/cm}^2 \\ \mu &= 0 \\ \lambda &= 0 \\ m &= 0.476 \end{aligned}$$

In this case,

$$j = 7.6 \times 10^4 \text{ dyne-sec/cm}^2$$

3. Suppose that the mass ablated were the same as in case 2 above, i.e., 0.476 gm/cm^2 , but $\mu = 10$ and $\lambda = 0.1$. That is, we observe the same ablation, but it is about 90% liquid and 10% vapor. From the above equations, it follows that

$$Q_a = 156 \text{ cal/cm}^2$$

i.e., the energy absorbed is far less; and

$$j = 3.2 \times 10^4 \text{ dyne-sec/cm}^2$$

i.e., a smaller impulse.

It is clear that a measurement of one of the quantities—impulse, mass ablated, or energy absorbed—alone, is not sufficient to describe the physical processes occurring. However, the simultaneous measurement of all of these quantities is useful in determining the mechanisms of ablation and blowoff.

The three illustrative cases that have been discussed contain the assumption of negligible heat conduction loss into the interior of the material. For relatively long thermal pulses incident on highly conducting metals (e.g., silver) this assumption may not be valid. Recourse may be made to the heat-integral technique or numerical analysis to include the heat conduction loss. However, a simpler technique has been utilized and affords crude estimates of this effect. Let the calculated depth of ablation, ignoring heat conduction losses, be denoted by m . Let the effective thickness of the thermal boundary layer associated with the heat conduction losses be denoted by m_c . The latter

thickness is crudely given by

$$m_c \approx \rho \sqrt{H t} \quad (1.17)$$

The depth of ablation (ignoring heat conduction) is given by an expression of the form of Equation 1.3.

If $m \gg m_c$ then heat conduction losses are negligible. If $m \ll m_c$ then thermal conduction losses are of significant importance, and the actual depth of ablation may be smaller than that given by Equation 1.3, or zero. In the preliminary analysis contained herein, the thermal impulse (including heat conduction losses) has been calculated in the following manner. First, heat conduction losses have been ignored and the impulse calculated using Equation 1.16. Second, the computed impulse has been crudely corrected by a multiplicative factor that includes the ratio of m to m_c .

$$\text{correction factor} = \frac{m}{m + \rho \sqrt{H t}} \quad (1.18)$$

A more detailed analysis using, for example, the heat-integral technique or numerical methods will afford more accurate estimates of the effects of heat conduction losses.

Materials Selected for Experiment.

Prior to the experiment, the thickness of the effective vapor layer was not known. Thus, the experiment was designed to allow for the possibility that various materials might react differently to the thermal input. Although this did not turn out to be the case, the materials used in Shot Blue Gill as basic experimental materials are listed below with brief qualitative reasons for their selection.

Lead. Its low heat of vaporization coupled with its relatively high density should result in a higher impulse being developed by lead for a given thermal flux than by other materials. This high

sensitivity also ensures that a reading can be achieved with a low input.

Pyrolytic Graphite. Pyrolytic graphite was included in the experiment for several reasons. First, carbon itself is a primary component of many of the plastics which are of interest in weapon effects studies. Knowledge of the behavior of carbon under the thermal loadings is fundamental to the study of the complex plastics. Second, pyrolytic graphite, which is formed by atomic deposition in layers, has thermal properties that are strongly anisotropic. Normal to the layers, its thermal conductivity is very low, comparable to many insulators, while in the direction of the grain the thermal conductivity of pyrolytic graphite is comparable to that of copper. This extreme variation of one fundamental property of a material, which in all other respects is identical, makes pyrolytic graphite a unique research tool in the study of the thermomechanical effect. Third, pyrolytic graphite has been of some interest as a re-entry nose cone material and any data obtained can be of direct value to weapon effects studies.

Copper. Copper is of interest because of its high thermal conductivity. Since its conductivity is about the same as pyrolytic graphite in edgewise orientation, a good opportunity is provided to study the effects of other physical properties on response.

Zinc. Zinc has a high first ionization potential and, based on the hypothesized model of the thermomechanical effect, should have a large radiation window at the low end of the energy spectrum. This may provide some insight into the effect of the vapor on the thermomechanical effect.

Aluminum. Aluminum has a lower first ionization potential than zinc and is expected to have a smaller radiation window. Comparison with the zinc results should provide data on this effect.

Aluminum is also of interest because it is a structural material and because of its reflectivity properties.

Silver. High reflectivity is the property of silver which is of particular interest in a thermomechanical experiment.

Steel. While its properties are primarily those of iron, steel, of course, is not a pure element. It is, however, a basic structural material. The main reason for using steel as a sample material in this experiment was an experimental one, i. e., its use would ensure the return of at least some piston samples. The steel samples were not bonded to the piston heads as were the other samples, but were integral extensions of these heads. It was felt that the advantages of ensuring that some exposed piston samples would return more than offset the analysis complications brought on by the alloying elements in the steel.

Refrasil-Phenolic. For reasons which will be discussed more fully later on, the backplates of the pods were coated with refrasil-phenolic. It was anticipated that the vaporization of the refrasil-phenolic backplate coating could be the dominant reaction in the region of the backplate. To evaluate this possibility quantitatively, an array of instruments had to be included which had as its sample a material which was identical to the backplate. In addition, refrasil-phenolic is a typical re-entry material.

Black-Phenolic. Black phenolic was included as a representative sample of cross-linked polymers which tend to be endothermic in their thermal reactions. It is expected that the reaction of these plastics will be characterized by the production of complex degradation products of rather large molecules.

Teflon. Teflon is a representative sample of non-cross-linked polymers, which tend to be exothermic in their reactions.

These plastics were expected to decompose completely under the thermal loading.

Iron-Devcon. Iron-devcon was one of the plastic materials studied in Shot Teak of Operation Hardtack. The Blue Gill experiment provided an excellent opportunity to confirm and extend the understanding of the Teak data.

Micarta. Micarta was also used in the Shot Teak experiment so that it was of interest in the Blue Gill experiment for the same reason mentioned above for iron-devcon. In addition, micarta is a high-temperature material with many characteristics similar to those of re-entry materials.

TABLE 1.1

TIME-INTEGRATED INTENSITY INCIDENT ON
BLUE GILL PODS UP TO FIVE MILLISECONDS
(PREDICTED)

<u>Pod Range</u>	<u>Time-Integrated Intensity</u>			<u>Fraction of Energy</u>
				<u>Incident in 10^{-3} sec.</u>
	<u>$0 < h\nu < 6 \text{ ev}$</u>	<u>$h\nu > 6 \text{ ev}$</u>	<u>All Energies</u>	
feet	cal/cm ²	cal/cm ²	cal/cm ²	
2,500				
4,000				
<u>6,000</u>				

TABLE 1.2

ABSORPTION DEPTHS AND MINIMUM
VAPORIZATION ENERGIES

Material	Q_v	X-Ray Energy	λ	E_{\min}
	cal/gm	kev	gm/cm ²	cal/cm ²
Carbon	2000	1	10^{-2}	20
		10	10^{-1}	200
Aluminum	500	1	10^{-3}	0.50
		3	10^{-3}	0.50
		10	3×10^{-2}	15.0
Refrasil	200	1	10^{-2}	2
		10	10^{-1}	20

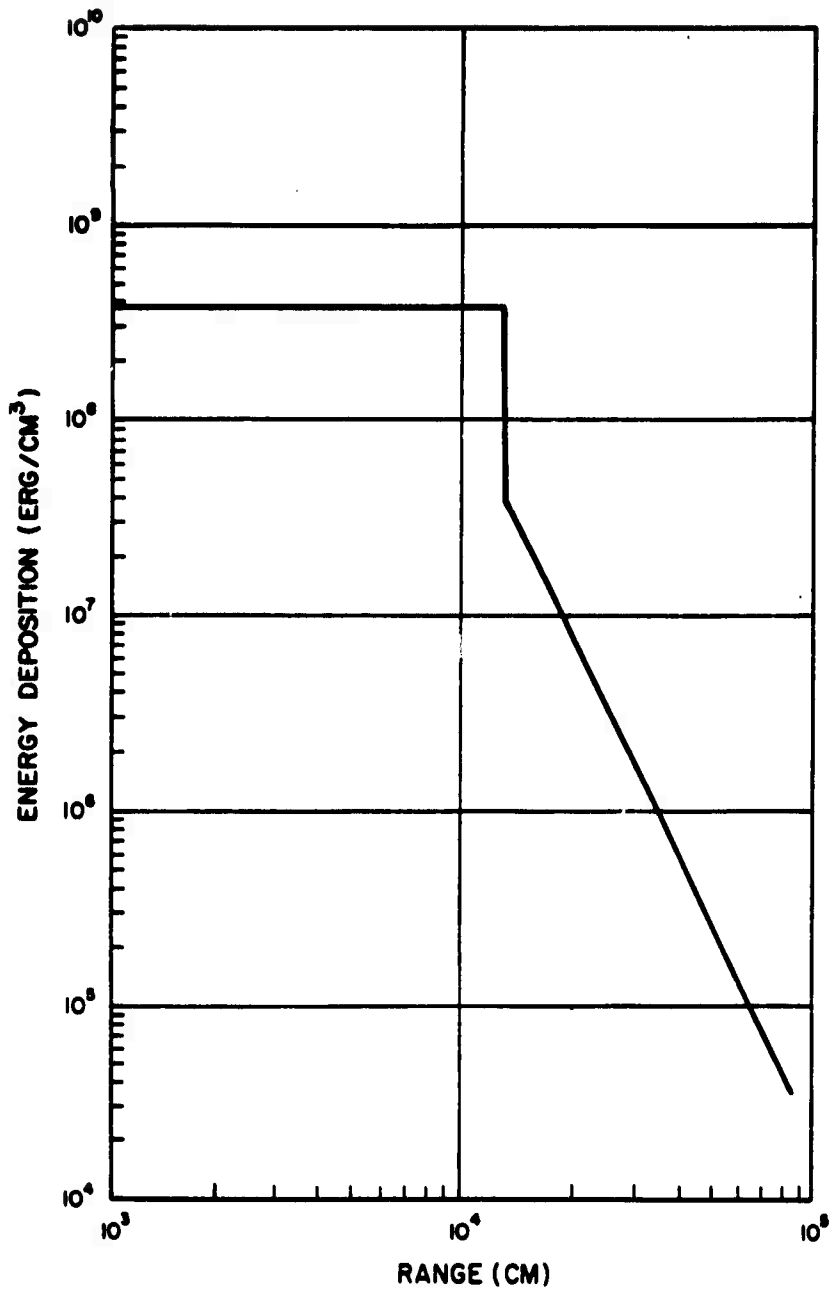


Figure 1.1 X-ray energy deposition versus range at end of X-ray pulse.

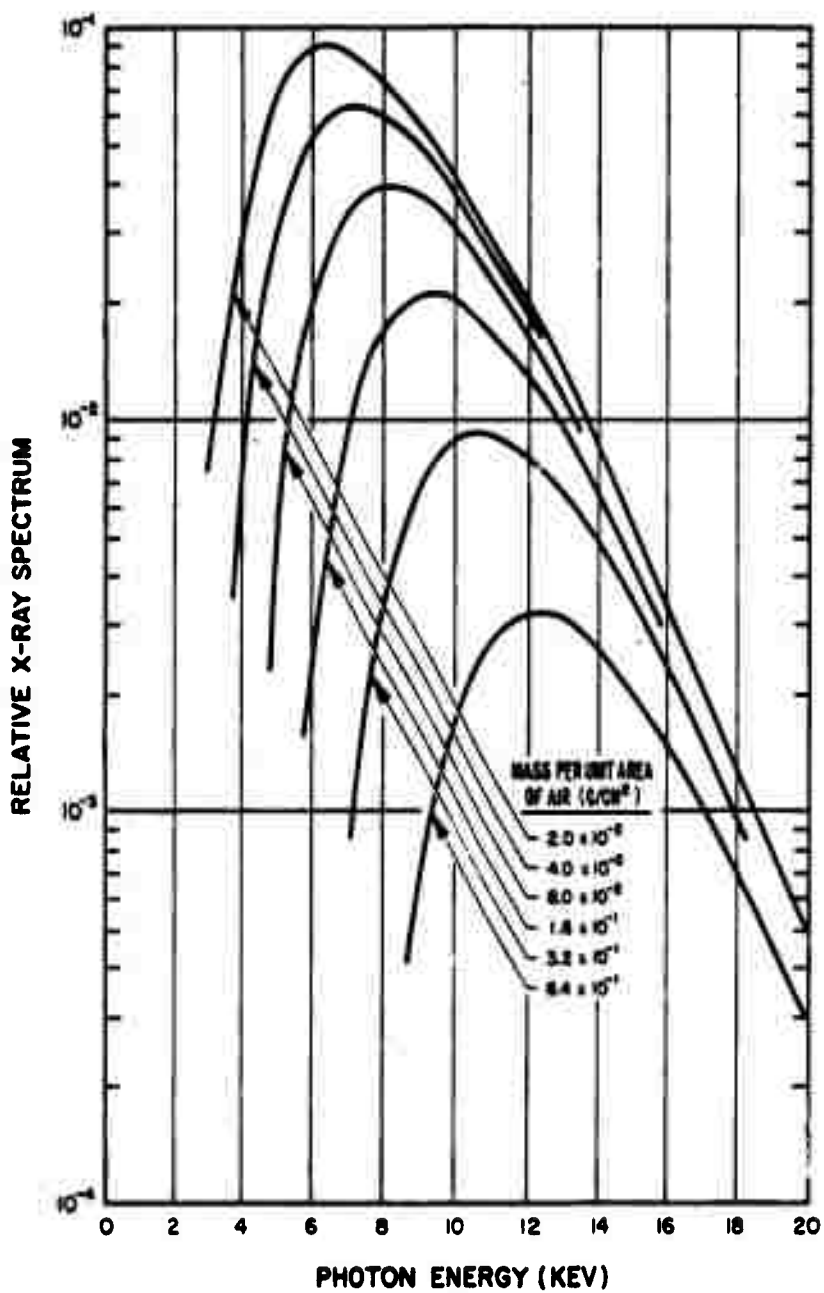


Figure 1.2 Transmitted X-ray spectrum through cold air (X-ray source temperature = 3/2 kev).

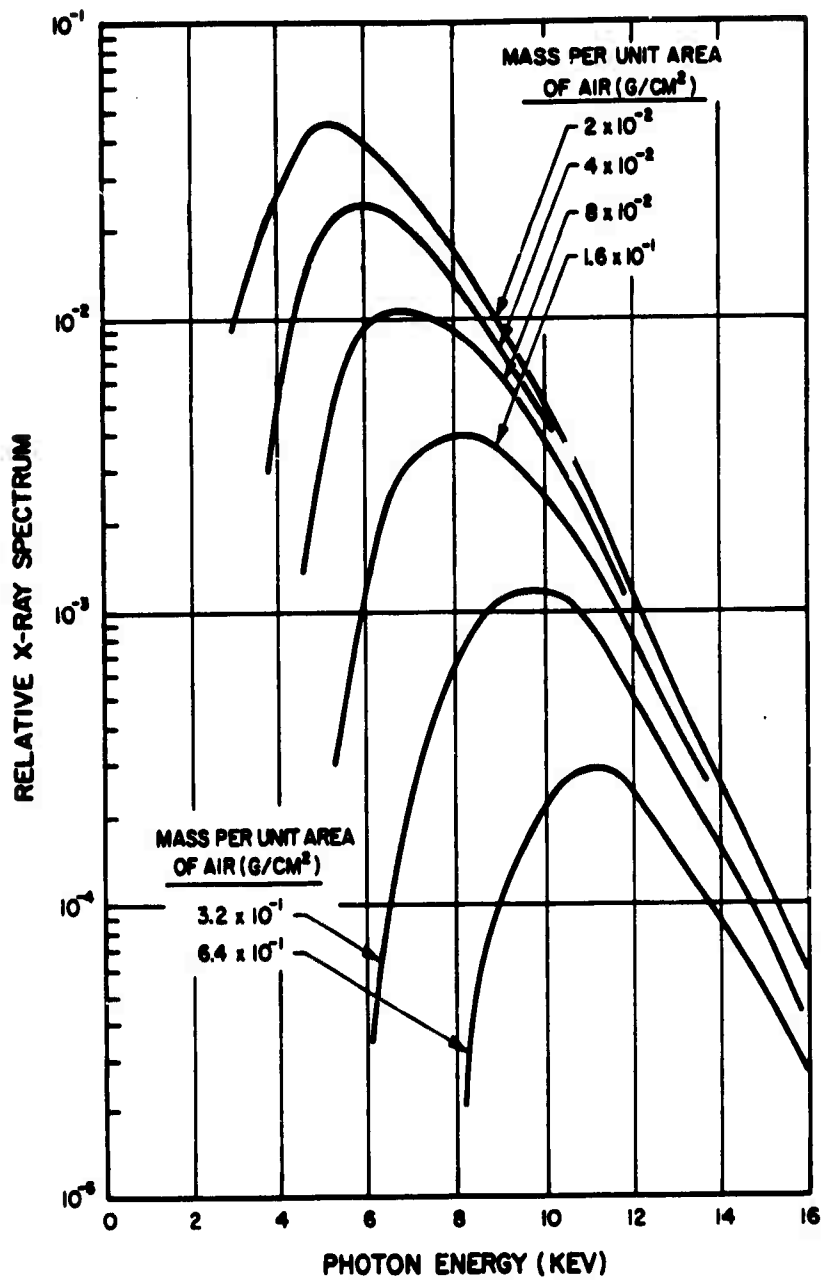


Figure 1.3 Transmitted X-ray spectrum through cold air (X-ray source temperature = 1 kev).

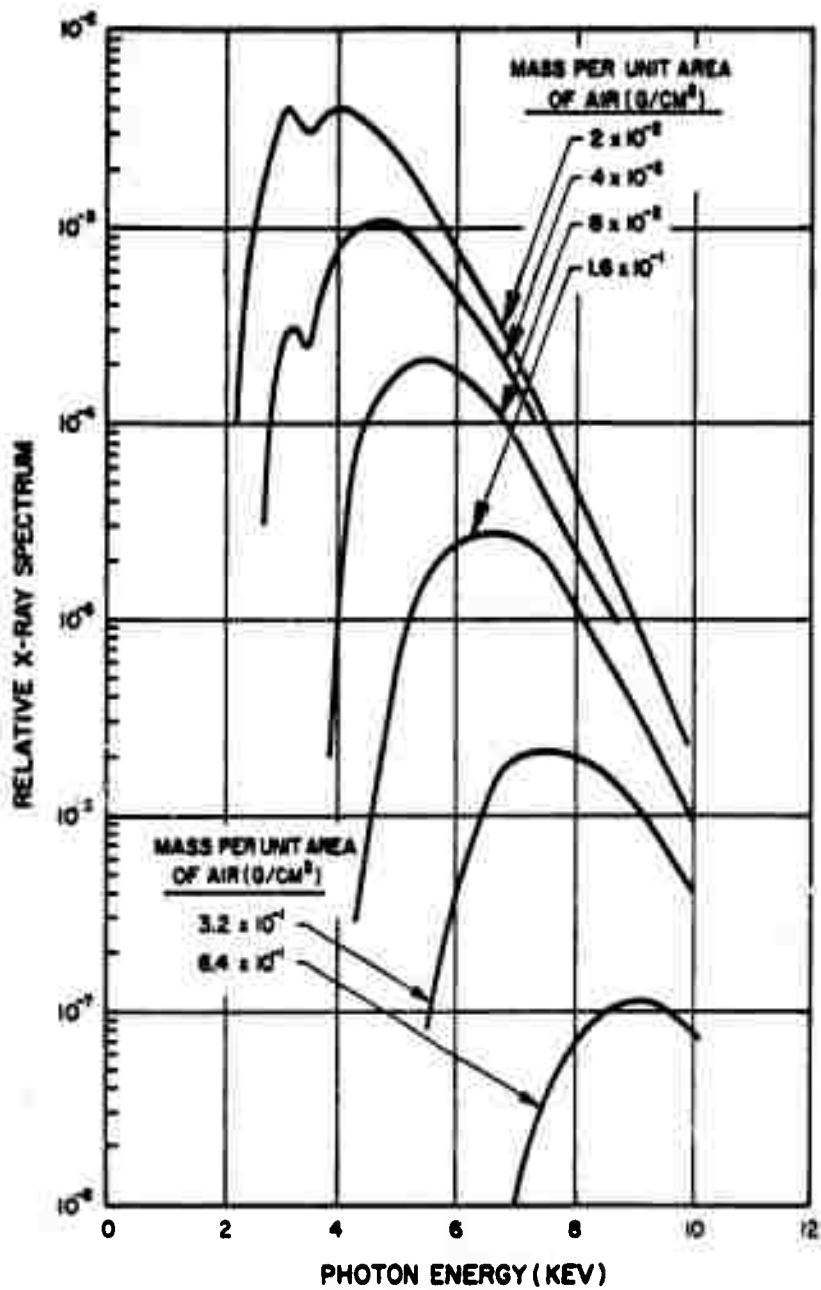


Figure 1.4 Transmitted X-ray spectrum through cold air (X-ray source temperature = 1/2 kev).

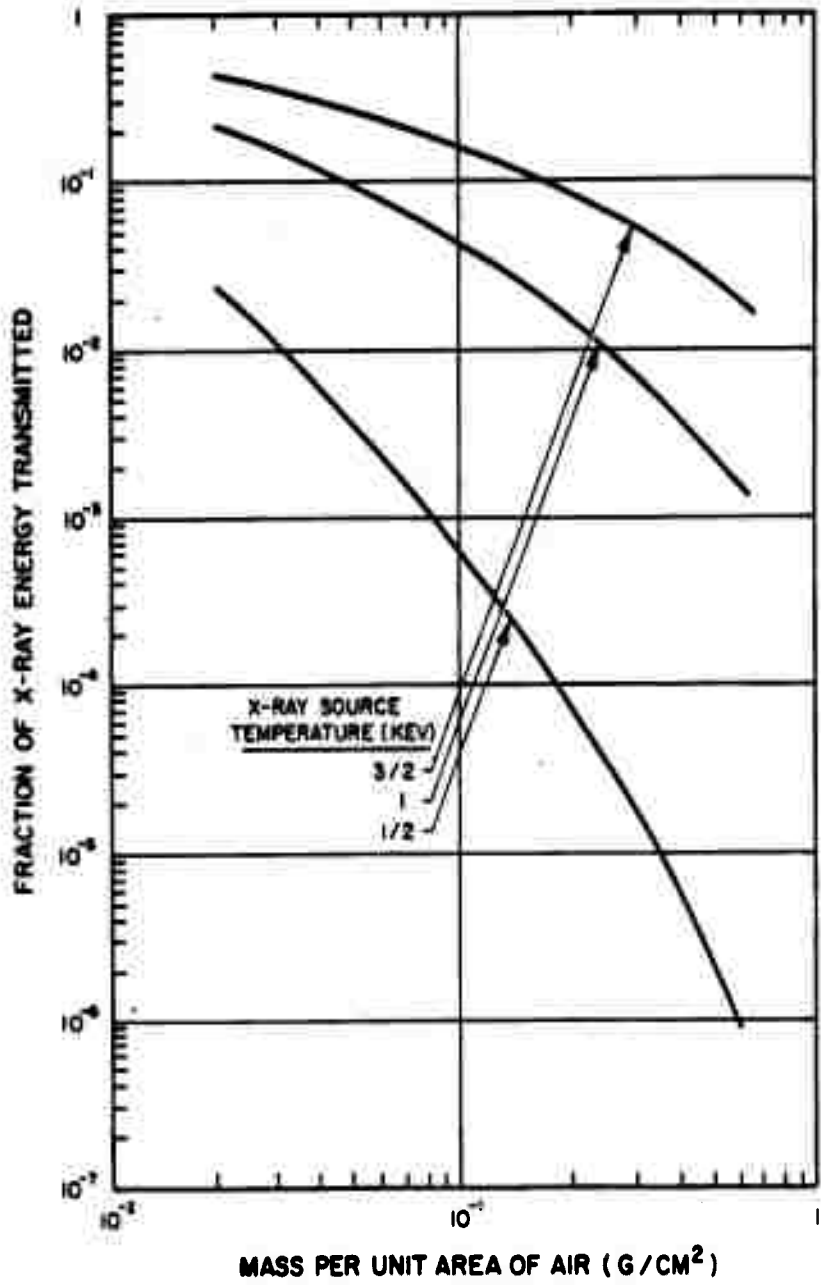


Figure 1.5 Fraction of X-radiation energy transmitted versus mass per unit area of air.

CHAPTER 2

PROCEDURE AND INSTRUMENTATION

2.1 PLANNED TEST OPERATIONS

The Project 8A.3 thermal instrumentation was mounted in three parasitic pods and carried aloft by a THOR IRBM. These pods were attached symmetrically about the rear section of the Thor booster with the pod noses pointed aft. The planned trajectory was a high loft with an apogee of just over 700 kilometers, and a predicted impact point 35 kilometers downrange (see Fig. 2.1). The pods were released from the Thor simultaneously shortly after all engines were cut off. To achieve separation at burst time, an incremental rearward velocity was given each pod by explosively released springs. After pod ejection, the warhead was separated from the Thor so that the booster would not be engulfed by the nuclear fireball at burst time.

During free flight, each pod was stabilized in a nose downward orientation by an inertia-reaction wheel which was designed to limit orientation misalignment to less than seven degrees from the vertical. At burst time, the pods were to be at nominal ranges of 2,500, 4,000, and 6,000 feet below the detonation. The Douglas Aircraft Company predicted that the accuracy of these ranges would be within plus or minus 20 percent of the nominal values.

To facilitate a soft water-entry and pod location after the burst, each unit was equipped with a deceleration and

recovery package. This package contained a two-stage parachute, flotation balloon, sea dye dispenser, flashing lamp, and Sarah radio beacon. Operations of the deceleration equipment and location aids are illustrated in Figure 2.2

Pod recovery was to be effected by helicopters and/or seagoing tugs. Three modes of retrieval were available to the recovery task force. The first mode was to utilize only helicopters which would retrieve and deliver the pods to the Johnston Island project recovery area. This mode was to be used if daylight conditions prevailed. The seagoing tugs were to act as backups should the helicopters fail to effect retrieval.

The second mode of recovery was to utilize only ships. This mode could be used under day or night conditions. After location, pod retrieval was to be effected by the seagoing tugs. These vessels would then transport the pods to the Johnston Island harbor entrance where they would be transferred to an LCM landing craft. The LCM would in turn transport the pods to the seaplane landing ramp where a truck-mounted crane would unload and deliver them to the project recovery area.

A third mode available to the recovery task force was to utilize both the ships and helicopters. Seagoing tugs were to make a night retrieval of the pods and begin transporting them toward Johnston Island. At dawn the pods were to be put back in the water for the helicopters to retrieve and complete the delivery.

Project 8A. 3 personnel were available, in an advisory capacity, to the commander of the recovery task force and the captain of each seagoing tug. These people

also made first-hand observations of any spurious inputs received by the pod due to handling. Such observations were valuable in resolving ambiguities during data reduction.

It was expected that the pods would be sufficiently radioactive so that personnel safety might be a problem. To facilitate work on the radioactive pods and to provide safe storage, three hot cells were constructed adjacent to the pod landing pad. The construction of these hot cells is illustrated in Figure 2.3. The lead and concrete thickness was specified on the basis of the calculations outlined in Appendix A. The rotating cover plate had a four-inch thickness of lead, in order to reduce the radiation level by a factor of about 4,000. The cumulative dose to personnel during the instrument removal period was, therefore, small. The cover was constructed with a rectangular port over which could be placed a lead-filled dolly. This lead dolly in turn had a viewing port and two tool access ports through which operations could be performed. The viewing port had 8- by 4- by 4-inch-thick lead glass brick. Special long-shafted drills and screwdrivers were fabricated to work through the tool access ports. These bits could be passed through lead bushings to decrease the radiation exposure to the operator. The entire cover was mounted on casters so that it could rotate on a steel plate turntable which formed the rim of the hot cell pit. The dolly in turn was movable in a radial direction on the cover. These two modes of motion, therefore, enabled work to be performed and observations to be made over the entire rear bulkhead of the pod.

Although the radiation level of all pods was predicted to be too high for safe instrument removal without use of the hot cells, it was recognized that one or more of the pods could be far less radioactive than expected. For such a case, it was planned to remove at least part of the instrumentation before the pod was put in the hot cells. This would speed up instrument removal operations.

Handling of the pods within the hot cell area was by a tractor crane with a 100-foot boom. The 100-foot distance plus a 10-foot dirt wall in front of the crane was designed to give more than adequate protection to the crane operator while handling the radioactive pods.

All personnel working on the pods were provided adequate radiation safety equipment to ensure against over-exposure to the nuclear radiation. This equipment included film badges, dosimeters, radiation counters, and safety clothing.

2.2 INSTRUMENT POD

As noted previously, the Project 8A.3 instruments were mounted in the aft section of a parasitic pod, three of which were carried aloft by a Thor Missile. These pods were an adaptation of a General Dynamics/Astronautics (GD/A) design originally intended for use as an instrument carrier for experiments over ICBM trajectories, with the Atlas missile. Figure 2.4 presents a simplified cross-sectional view of the pod showing the location of major components and instruments.

The original pod was basically a shell of refrasil-phenolic with only sufficient internal structure to support auxiliary systems and payload. Substantial structural modifications were incorporated into the basic shell by GD/A on the basis of load

criteria set forth by Project 8A.3. An example of such a criterion resulting from early calculations corresponded to a static load on the rear bulkhead of 500 psi lasting for a millisecond. A similar criterion for the cylinder and flare was 500-psi uniform load or an unsymmetrical load of 500 psi on one side and 300 psi on the other, whichever was worse. For dynamic tests performed with high explosives for GD/A by the Stanford Research Institute, the rear bulkhead load was translated into 3.5×10^4 dyne-sec/cm². The duration of one millisecond, which is relatively long for HE, was achieved with the use of a thick foam rubber pad between the HE and the bulkhead.

The final structure of the pods was characterized by heavy concentric aluminum barrels running the entire length of the pod, except for the nose. For the two pods closest to the burst, the flare was reinforced by a partial liner of aluminum. The aluminum rear bulkhead varied in thickness from 0.44 inch at the center to 0.20 inch at the edge. Every bulkhead was covered with refrasil-phenolic of the same composition as the ablative re-entry shield, except that a parallel laminate was used instead of the oblique lay of the heat shield. The covering of the bulkhead was performed by CTL, Division of Studebaker-Packard Corporation, under subcontract to American Science and Engineering, Inc. There were two reasons for the use of this covering: (1) it is a proven protective heat shield for re-entry conditions, and (2) it provided an environment for the instrumentation which closely duplicated the situation where the data are to be eventually applied. The refrasil-phenolic coating was expected to vaporize to a significant degree, and all instruments were, therefore, expected to be immersed in this vapor. The vapor would substantially modify the energy fluxes to the surface. This basic limitation must always be borne in mind when the measurements are used to describe the source. A further discussion of this point is given in Section 2.3.1.

2.3 INSTRUMENTATION

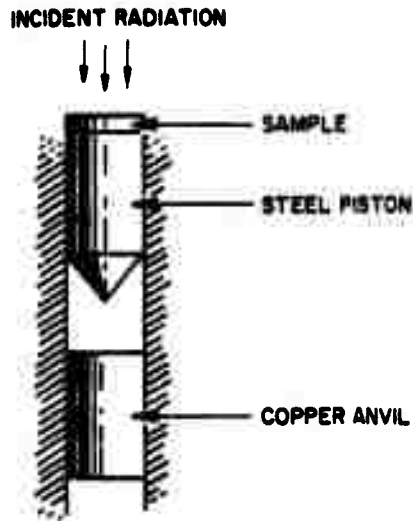
Prior to the Blue Gill event, the environment of a nuclear burst in this altitude regime was analytically anticipated to be very severe. Because of this severity and because of the large uncertainties in the analysis, rugged instrumentation with a large dynamic range was required.

The thermomechanical experiment mounted on the rear bulkhead of the Blue Gill pods was made up of sub-experiments which comprise nine different kinds of instruments. For each of these types of instruments, data to be derived are described in this section. Some of this information is qualitative in nature, such as whether a given mechanical input was caused by thermal radiation or by X-radiation. Most of the information is quantitative in nature, although the complete reduction to quantitative data may be very involved.

In addition to the principle of operation of the instruments and the type of information to be obtained, this section presents a physical description of each instrument.

2.3.1 Indent Recorder Clusters. The instrument used to measure thermomechanical loading was the indent recorder. The indent recorder, as the name implies, responds to a thermo-mechanical impulse and records data in the form of intelligible permanent deformations or indents. Design variables combine with inherent sensitivity to yield a passive, mechanical instrument which can measure impulse with precision over a large dynamic range.

A single indent recorder channel consists basically of a steel piston and copper anvil as shown in the sketch below.



Radiation incident on the sample produces a thermomechanical impulse which drives the piston and causes it to strike the anvil. The resultant collision is a very inelastic one in which the conical piston point creates a geometrically similar deformation in the soft copper anvil.

A laboratory investigation, reported in Ref. 12, established that the piston energy of motion is directly proportional to the volume of deformation. Thus, the derivation of input impulse follows from a measurement of the indent size. Although the investigation of Ref. 12 accurately characterizes the collision process, it is not necessarily applicable to any real instrument. That is, the overall performance of a particular instrument design may be somewhat different due to piston-anvil mass ratios, friction, losses associated with escape from positioning devices, etc. A direct calibration was therefore undertaken as a natural part of the total effort to achieve a high level of instrument performance. The laboratory calibration of the actual indent recorder configurations used in the Blue Gill experiment is presented in Appendix D.

The fundamental parameters which govern indent recorder performance are revealed by the equation

$$s = \iint a dt dt = \frac{A}{m} \iint \frac{F(t)}{A} dt dt = \frac{A}{m} \int j(t) dt \quad (2.1)$$

where:

- s is distance traveled by piston
- m is mass of piston (assumed constant)
- A is piston head area (assumed constant)
- a is acceleration
- t is time
- j(t) is the impulse function defined by

$$j(t) = \frac{1}{A} \int F(t) dt = \frac{m}{A} v(t) \quad (2.2)$$

where $F(t)$ is the force on the piston in the direction of motion. Equation 2.1 merely states that the distance traveled by a body as a function of time is a unique function of its acceleration. It is clear from Eq. 2.1 that the response time of the piston is directly proportional to piston mass and piston-anvil spacing and inversely proportional to piston head area. Response time is furthermore an inverse function of the impulse to be measured. Control over the design variables of piston mass, head area, and spacing to the anvil thus means that response time is ultimately definable a priori only to the extent that impulse is predictable. Response time is an important factor, because it characterizes the ability of a group of indent recorders to resolve the force-time history of the input pulse.

Impulse is a function of these same design variables as

shown by Eq. 2.2. In combination with the energy-to-deformation relationship which determines indent size, these variables ultimately define instrument sensitivity and dynamic range.

The types of pistons employed in the indent recorders for Shot Blue Gill are illustrated in Figure 2.5. Their general characteristics and applications in the experiment are given below.

The Type A piston has the highest head-area-to-mass ratio of any of the piston designs and, as such, is the most sensitive. The Type A piston is used with a striker. (The reasons for the use of this configuration are discussed later in this section.) Type A pistons are used to measure the very early phases of the impulse time history, since they respond in extremely short times. Owing to their inherent sensitivity, they are effectively total-integrating pistons for those material samples wherein a low impulse loading is anticipated.

The Type C piston has a lower head-area-to-mass ratio than the Type A piston. As such, it is slower responding and also somewhat less sensitive. In time history measurements, it is designed to obtain data in the middle-time regions of the pulse. In total impulse measurements, it is used for materials for which an appreciable impulse loading is anticipated.

The Type D piston has the same head area as the Type C piston, but a higher mass. Its lower head-area-to-mass ratio makes it slower responding and slightly less sensitive. It is a total-integrating piston which in time history measurements should provide a measure of almost the total impulse developed by the thermal loading. Materials for which a fairly high impulse is anticipated are used on Type D pistons.

The Type E piston has a slightly smaller mass than the Type D piston, but a much smaller head area. It has the smallest head-area-to-mass ratio of the piston designs and as such is the slowest responding and least sensitive. It constitutes a practical limit in the design of pistons slow enough to approach a total integration of the impulse while maintaining enough sensitivity to provide a reading. It can only be used for those materials for which high values of impulse are expected.

Before describing the remaining piston types, which are special purpose, it is worth noting the wide variety of materials included in the experiment. In a majority of cases, pure elements were employed, in order to permit the study of basic parameters involved in the thermomechanical effect. Certain other materials of interest were also included, however, as may be seen from the table below which lists the piston sample materials. These samples were bonded to the piston (see Appendix B).

<u>Material</u>	<u>Piston Types</u>		
	<u>Pod B-1</u>	<u>Pod B-2</u>	<u>Pod B-3</u>
Refrasil-Phenolic	A, C, D, E, F	A, C, D, E, F,	A, C, D, E, F
Lead	A, C, D, E, F	A, C, D, E, F	A, C, D, E, F
Pyrolytic Graphite (grain perpendicular)	A	A	A
Pyrolytic Graphite (grain parallel)	A	A	A
Micarta	A	A	C
1095 Steel	A	C	C
Phenolic	D	A	D
Aluminum	C	C	A
Copper	C	C	A
Zinc	D	D	C
Silver	D	D	D
Iron-Devcon	E	E	F
Teflon	E	E	E

The results of the Blue Gill experiment, which are described and discussed in Section 3.2.1, indicated ex post facto that the dominating influence in the piston response to the thermomechanical loading was the pressure field resulting from the vaporization of the reffrasil-phenolic backplate coating rather than the response of the individual materials themselves. This phenomenon was recognized as a possibility, but by no means a certainty, prior to the experiment. It turned out, therefore, that no study of material property characteristics on the thermomechanical effect could be made. Nevertheless, it is valuable to document the reasons for including the various materials in a thermomechanical investigation. The materials employed in the experiment are listed in Section 1.3.3 with brief descriptions of their significant properties. In addition to the specific properties mentioned for the elements, it should be noted that these elements encompass a wide range in atomic number.

The Type E piston with collar (see Fig. 2.5) is employed to measure the maximum velocity of the pod backplate as it deflects under the thermal loading. The thin piston head passes through the backplate as the other pistons do, but the collar comes up to a point just below the backplate bottom surface. As the backplate deflects, it strikes the collar and drives the piston at a velocity corresponding to the maximum deflection velocity achieved by the backplate. One Type E piston with collar was installed in each pod.

The Type F piston, as can be seen in Figure 2.5 is, with its striker, longer than the other recording pistons of the group. It is designed so that when installed, its head extends about one inch above the upper surface of the pod backplate. Theory predicts that the impulse imparted to a surface by the thermo-

mechanical effect is a function of the momentum imparted by the vapor as it leaves the surface and the static pressure developed about the surface by the vapor. The Type F piston is employed to differentiate between these two types of loading. The area of the underside of the piston head is only slightly less than that of the upper surface. Therefore, the Type F piston is insensitive to the pressure field into which it extends and can sense only the impulse imparted to it by the momentum transfer of the vapor leaving the surface of the sample material.

The Type G pistons are the controls employed in the experiment and are similar in most respects to the other pistons. These pistons have no samples. The Type G-2 piston, when installed, terminates about one inch below the backplate bottom surface. Since there is no viewing hole in the backplate, this piston is thus blind to direct radiation from the detonation. The Type G-2 piston is, however, exposed to the pressure in the region behind the backplate and can respond if this pressure is large enough. This pressure could be important to the interpretation of data from other pistons. The Type G-1 piston, on the other hand, is mounted in a barrel which, being plugged at the top, makes this piston completely blind to both the detonation and the pressure under the backplate. The purpose of the Type G-1 pistons is to serve as controls which can indicate whether or not the indent recorder cluster (which holds seven other channels) functioned properly. The anvil beneath a G-1 piston (isolated from inputs), would, under normal operation, withdraw (due to re-entry) from the reach of the piston early enough to avoid an indent. Care must be taken in interpreting the data provided by the control recorders, however, as the responses of the various elements involved are very complex. Lack of any reading on a control

anvil, for example, implies proper functioning of the recorder cluster, but does not attest to it absolutely. Conversely, a reading on a control anvil provides only an indication of some possible malfunction. These control data must be analyzed in conjunction with all the other data obtained in the experiment to permit proper conclusions to be reached.

The important piston characteristics of the indent recorder configurations for the Blue Gill experiment are listed in Table 2.1. The actual values varied somewhat from the design values given because of differences in the densities of the sample materials and manufacturing tolerances. The parameter sm_p/A_h is tabulated to provide an indication of response time (see Eq. 2.1). For a constant impulse, these values indicate the actual relative response times which are seen to span almost three orders of magnitude.

The first three piston designs listed in Table 2.1 are Type A pistons, which have very fast response characteristics. As piston response times become very short, they approach the time required for the piston to make the indent in the anvil. During this latter time period, the piston is simultaneously absorbing energy from the thermal loading and transmitting energy to the anvil as it creates the indent. A large uncertainty would appear in the data if this indent-forming or energy-transfer time remained comparable to the integration time. The Type A piston, therefore, attempts to avoid this basic problem by incorporating a striker between the piston and the anvil (see Type A and Type F pistons in Figure 2.5). The piston in this configuration has a flat surface at its end instead of a point. In operation, the piston transfers its momentum to the striker and the striker in turn makes the indent in the anvil. The collision between piston and striker is

very elastic, and collision time is extremely short. This collision time is small compared to the piston response time, and therefore, the integration time is clearly defined. Since no further energy is supplied to the striker after its collision with the piston, the time the striker takes to reach the anvil and form the indent is independent of the integration process.

Estimates of total thermal impulse for the materials included in the experiment are presented in Table 2.2. They are based on the analytical model presented in Chapter 1. This analysis of the thermomechanical impulse includes the assumption that the latent heats of the irradiated materials are known. For irradiated metals the conventional latent heats of vaporization and fusion have been utilized. In the case of irradiated plastics the effective latent heat is probably a function of the input radiation intensity and time history and the non-steady chemical decomposition of the plastic material. In Reference 12 the modes of decomposition of typical plastics exposed to short-time, high-intensity bursts of X-radiation have been analytically studied. The various steps in the chemical decomposition of the typical plastics have been postulated and effective latent heats computed. These latent heats have been utilized to compute the thermomechanical impulses to plastics presented in Table 2.2.

A detailed representation of the indent recorder clusters used in the experiment is presented in Figure 2.6. The piston configurations shown are the fast-response, striker types. The indent recorders are held in a cluster of seven active recorders and one control recorder. Except for the control and pressure-insensitive types, all of the pistons are mounted so that the top surface of the sample is flush with the top surface of the back-

plate. The control, which is blind to the thermal input, but identical to the active recorders in all other respects, was included to provide a check on possible false data, as mentioned previously.

Prior to recorder operation, the piston and anvil must be held in position. Two systems were employed in the instrument a strong holding device to secure these parts during the high accelerations and vibrations of powered flight, and a weak holding device to maintain piston and anvil positions during the coast portion of the flight to burst time.

The strong holding was accomplished by a locking pin on each part as shown in Figure 2.6. Locking pin release was effected by a motor-driven cam. This motor consists of a pair of bellows connected in series (see Figure 2.6). One is vented to the atmosphere and the other is evacuated. The motor operates on the decrease in ambient pressure as the vehicle ascends. This decrease permits the air stored in the vented bellows to leak out. As the pressure drops in the vented bellows, the evacuated bellows, which is essentially a compressed spring, expands and moves the cam. The rate at which air leaves the vented bellows through a porous plug provides operation timing control. The bellows motor system was designed to arm the instrument about 400 seconds following missile lift-off. This time is well past the powered-flight portion of the trajectory but early enough to provide a long time margin before burst (over 500 seconds). Locking pins were retracted by individual springs on each pin as shown in Figure 2.6.

A number of advantages attend the use of the bellows motor for arming indent recorder clusters. First, the bellows motor

requires no external power source for its operation. A long delay in missile launch, therefore, has no detrimental effects on the operation of the bellows motor, as it might, for example, in a battery-powered system. Second, the arming action in the bellows motor system is quite gentle, thereby avoiding the possibility of damage to the instrument and reducing the probability of spurious data. Third, since each bellows motor operates as an independent unit, coupled failure is impossible. Finally, the complete arming operation of each cluster may be check-tested in the field with a simple bell-jar vacuum system.

The soft holding device maintains piston and anvil positions against small disturbances which may occur during the coast portion of the missile flight. It is a small ball plunger with matching detent as shown in Figure 2.6. The holding force of the ball plunger is adjustable, and at the settings employed, little energy is expended in the escape of the detent. The ball plungers for the Shot Blue Gill experiment were set to hold approximately three times the weight of the pistons and approximately two times the weight of the anvils, i. e., 3-g and 2-g settings, respectively. At burst time, the pods were to have been just starting to re-enter the atmosphere. The deceleration at that point was to be approximately 1 g. The higher g settings employed were an attempt to ensure that the pistons and anvils would remain in proper position should an error in pod positioning or burst timing have occurred causing an acceleration field of greater than 1 g. Anvil settings were made less than those of the pistons, however, so that a zero reading would be preserved, i. e., if the thermomechanical impulse to a certain material was indeed unrecordable, subsequent re-entry deceleration would then retract the anvil early enough to avoid a spurious input from the piston.

After the piston or striker has struck the anvil and created an indent, it is essential that the anvil be retracted in such a way that no further collisions occur. The momentum imparted to the anvil by the piston and the g forces exerted on the anvil as the pod decelerates during re-entry bring about this retraction. The retracted anvil falls into the anvil catcher located at the bottom of the barrel as shown in Figure 2.6. The anvil is prevented from re-entering the barrel by several simple passive design features. First, the inside diameter of the anvil catcher is larger than that of the barrel, thereby forming a step at the lower end of the barrel. Second, a key in the barrel and matching keyway in the anvil disengage when the anvil leaves the barrel and enters the catcher. Third, a conical point, located off-center at the bottom of the anvil catcher, tends to make the retracted anvil cock at an angle. The possibility of the anvil becoming aligned enough to re-enter the barrel in spite of the step, the key and keyway combination, and the cocking action is remote.

A vibration mount isolates the indent recorder cluster from vibrations in the axial direction. This mount is pictured in Figure 2.6. Additional axial isolation against the shock of the impulse loading on the pod is provided by a spring mounting at the base of the cluster, as also shown in Figure 2.6. This spring mount permits almost one inch of travel to the instrument to delay interaction with pod motion. The upper end of the indent recorder is held in lateral and rotational position by a guide sleeve attached to the backplate. Free axial motion is ensured by teflon buttons on the periphery of the cluster, which provide low-friction bearing surfaces.

Each indent recorder was installed on the pods by means of a bridge structure mounted between the inner and outer structural

cylinders of the pods. The base of the indent recorder was attached to the bridge as indicated in Figure 2.6. The mounting bridge was made strong enough to hold the indent recorder inside the pod in the event the loading on the pods was sufficient to blow off the backplate. As an added safety factor against the possible loss of the indent recorders, a stainless steel cable from each instrument was attached to the inner cylinder of the pod in which it was mounted (Figure 2.6). These lanyards, with a breaking strength of about 1,000 pounds, provided formidable insurance against the loss of any indent recorders from the pods.

2.3.2 Spall Gage. As mentioned previously, the measurement of a force-time history assists one to differentiate between the thermomechanical and the X-ray effect. The indent recorder, however, cannot resolve pulse durations less than a few tenths of a millisecond. To detect the presence of a significant force pulse of shorter duration, a spall gage was incorporated into the instrument array. The spall gage is sensitive only to forces of duration less than about 10 microseconds. The existence of a reading on this gage, therefore, gives the qualitative information that an extremely short time impulse (less than about 10 microseconds) must have existed. The gage reading can also be interpreted to give an approximate value for the intensity and time duration of this impulse. A very short duration impulse would reasonably be expected only from a flux of X-radiation above a threshold of a few calories/cm². Further verification of the presence of X-rays is provided by the X-ray pinhole camera (see Section 2.3.8).

Detailed Description of Spall Gage. The spall gage owes its performance to the fact that a compressive stress pulse at a free surface reflects as a tensile stress pulse. After reflection, the net stress at points just inside the free surface is the algebraic sum of

the remaining compressive stress of the outgoing pulse and the tensile stress of the reflected ingoing pulse. If this sum becomes a net tension which exceeds the breaking strength of the material, a fracture is formed. The presence of this fracture provides immediate qualitative information that a pressure pulse existed at the exposed surface which had a duration of the order of the shock transit time through the material. The position of the fracture is a function of the size and shape of the original stress pulse.

The spall gage used in the Blue Gill pod experiment is shown in Figure 2.7. The basic unit is a Lucite (methylmethacrylate) cylinder which has a 0.001-inch-thick lead disk cemented with Canada Balsam onto the surface exposed to the energy flux. Lucite was used because of its relatively low tensile strength and because internal fractures are readily visible. Lead was used for the exposed element because of its low ablation threshold and concomitant low reading threshold. The Lucite cylinder is supported circumferentially in a block of styrofoam of 22-pounds/cubic foot density and rests on a pad of the same material. Four such cylinders were contained in each spall gage. Each of the cylinders had a shoulder at the lower end which acted as a restraint to prevent motion through the hole in the foam supporting block. The foamed block supporting the cylinders was shaped to fit closely into a rugged aluminum holder which has become known as a box car. This box car body is used also by the gages described in Sections 2.3.5, 2.3.6, and 2.3.7. These instruments were held by a single bolt to the rear bulkhead; rotation was prevented by a roll pin. A compressed spring was installed between the bolt head and the bulkhead to prevent the instrument from being unseated by acceleration or vibration forces, while permitting the bulkhead to flex under load without fracturing the bolt.

A large dynamic range was assured the spall gage by having different-sized entrance apertures in the mica cover enclosing the box car gage. The complete gage contained four cylinders placed beneath apertures of 1 mm, 3 mm, 6.35 mm, and 3 mm. With the smallest aperture, the pulse front would be expected to be very nearly spherical. With larger apertures, the shape becomes more complicated. In any case, the pulse expands outward through the cylinder at a speed of about 2,700 meters/second (Reference 15). Upon reaching a free surface, the pressure pulse is reflected as a tensile pulse having about the same speed.

A useful reading of the gage does not require the exact solution of the interference pattern. Instead, the duration of the pressure pulse can be estimated to an order of magnitude by measuring the perpendicular distance of any spall cracks from the free surface and dividing this distance by the velocity of the pulse, thus,

$$\Delta t = \frac{d}{2.7 \times 10^5} = 3.7 \times 10^{-6} d \text{ seconds}$$

where Δt is the estimated length of the pressure pulse in seconds, and d is the perpendicular distance of a spall crack from the wall of the spall gage in centimeters. The instrument is, therefore, potentially effective for pulses having durations up to several microseconds.

2.3.3 Ablation-Condensation Gage. The ablation-condensation gage is the primary instrument for the measurement of the ablation of a variety of materials. The sample materials are so placed with respect to a collection chamber that it is also possible to collect a sample of the condensation products from each sample material. A control run for this gage was provided by the aborted

Blue Gill event (see Appendix C).

Detailed Description of Ablation-Condensation Gage. Figure 2.8 shows a schematic representation of the ablation-condensation gage. The gage consists of an aluminum or stainless steel gage body which is fastened to the aluminum backplate by means of a spring and jam nut. The spring will, as mentioned before, allow the aluminum bulkhead to flex under the gage without shearing the fastener or without severely damaging the gage body. The inner wall of the gage is lined with a 3-mil-thick sheet of an alloy of 96% platinum, 4% rhodium. This liner is used to collect vaporized material, condensed in the chamber, and can be removed from the gage body. An aluminum end cap also equipped with a liner of 3-mil sheet platinum-rhodium serves as the end of the chamber.

The sample is screwed to the top of the gage body. Additional holding is accomplished by a stainless steel retainer ring. A micarta cover is glued to the stainless steel retainer ring to serve as a heat shield.

Eighteen such gages were used on each Blue Gill pod. The sample materials and entrance apertures of these gages are listed in the table below.

<u>Sample Material</u>	<u>Entrance Aperture (dia in mm)</u>
Refrasil-Phenolic	1, 3, 5
Micarta	5
Iron-Devcon	5
Black Phenolic	5
Teflon	5
Pyrolytic Graphite (grain parallel to surface)	5
Pyrolytic Graphite (grain perpendicular to surface)	5

<u>Sample Material (Continued)</u>	<u>Entrance Aperture (dia in mm)</u>
Aluminum	5
Copper	1, 5
Lead	5
Silver	5
1090 Steel	1, 3, 5
Zinc	5

The configuration of these instruments is such that the sample is flush with the micarta heat shield ring. They have, therefore, an effective viewing angle of 2π steradians.

2.3.4 Thermal Pinhole Camera. The principal functions of the thermal pinhole camera are to measure the intensity of the thermal radiation received at the surface of the pod and to measure the spatial characteristics of the thermal source.

The aperture of the camera forms an image of the source on a heat-sensitive material. Absorbed thermal radiation at any point of this image can be deduced from the irreversible solid state changes which occur in the material.

Detailed Description of Thermal Pinhole Camera. The instrument is shown in Figure 2.9 . It is composed of an aluminum body, a micarta heat shield, and heat-sensitive detectors. The apertures (pinholes) which control the acceptance angle are in the micarta heat shield which covers the whole exposed portion of the aluminum turret . The top of the aperture is 1 cm above the detector surface. Each thermal pinhole camera contains four apertures; three on the side, spaced equidistantly (120 degrees) around the periphery of the cylindrical turret and one on the top.

A few detectors are used in the shape of circular studs, 1 cm in diameter, which fit nearly flush with the periphery of

the heat shield, but the majority of the detectors are used behind apertures. These detectors are in the shape of slabs approximately $1/8$ inch in thickness and having a length and width of $3/4$ inch and $5/8$ inch, respectively, with one end rounded. They fit into slotted sections of the aluminum body and are held in place by roll pins. Two types of slab detectors are used. In one, the surface of the detector is smooth; in the other, the surface of the detector contains two slots, each $1/16$ inch wide and $1/16$ inch deep. The spacing between the closest edges of the slots is equal to the aperture diameter plus two millimeters. The slots were designed to separate the desired thermal intensity measurement from another possible phenomenon. This other phenomenon would occur if the hot vapor surrounding the pod entered the gage via the aperture. This hot vapor might condense on the detector, liberating heat and causing a spurious reading. Since this vapor could easily enter the slot, while the thermal radiation could not geometrically enter the corner of the slot near the aperture, the slots offer a method of separating the two effects.

The complete instrument is fastened to the backplate by a bolt threaded into it. A steel spring between the bolt head and bulkhead has the same design function as in the box car configuration and the ablation-condensation gage.

Seven such thermal pinhole cameras were placed on each pod backplate. They differed primarily in aperture geometry and hence in potential source intensity at the detector. The fields of view of the 1-mm, 3-mm, and 1-cm pinholes and flush surface are 0.0025π , 0.022π , 0.21π , and 2π steradians, respectively.

In six of the seven cameras, the side apertures were oriented in planes perpendicular to the base of the instrument. In one camera, the side apertures were oriented at 45 degrees

to the base plane of the instrument. The types of aperture and detector used in the seven instruments are summarized in the table below.

<u>Type of Aperture and Diameter of Aperture (in cm)</u>	<u>Sample Type</u>
Single hole, $d = 0.1$	Slotted
Single hole, $d = 0.3$	Slotted
Single hole, $d = 1.0$	Slotted
Single hole, inclined at an angle of 45° to in- strument base, $d = 0.1$	Plain
Two parallel rows of 0.1 diameter pinholes, five pinholes in each row	Slotted
Single hole, $d = 0.3$	Plain
Sample flush with surface of micarta heat shield, $d = 1.0$	Round stud- plain surface

2.3.5 Cut-Off Filter Spectral Gage. This gage and the following one are designed to give identical information using slightly different techniques.

The present gage utilizes a variety of cut-off filters to allow only a portion of the energy spectrum to impinge on the detector material. By observing the intensity transmitted through several of these filters, it is possible to derive information concerning the spectral distribution of the radiation from the source. Dynamic range is achieved as in the thermal pinhole cameras by using different-size apertures.

Detailed Description of the Cut-Off Filter Spectral Gage.
Each pod contained four cut-off filter spectral gages differing only

in the materials used for filters. The four filter materials are:

Fused Quartz, Si O_2

Titanium Dioxide, Ti O_2

Magnesium Fluoride, Mg F_2

Aluminum Oxide, Al_2O_3

The relative transmission properties of these four filters are shown in Figure 2.10 (References 18, 19, and 20). Magnesium fluoride passes radiation in the regions from 1 to 10 μ . Aluminum oxide is useful for the region from 0.2 to 7 μ , exhibiting a cut-off in the infrared at 7 μ and a cut-off of 0.2 μ in the region of the ultraviolet. Fused quartz has nearly the same short wavelength cut-off (0.19 μ), but cuts off in the infrared at 5 μ . Titanium dioxide has a short wavelength cut-off at about 0.4 μ and a cut-off in the infrared at about 7 μ .

The materials used as detectors are 1020 steel and bismuth-tin alloy. The techniques for inverting the metallographic data in these detectors into thermal intensity are the same as for the thermal pinhole camera (see also Section 1.3.2). The range of sensitivity in terms of absorbed radiation energy from the short-time thermal radiation is approximately 2 to 10 cal/cm^2 for 1020 steel and approximately 0.5 to 1.5 cal/cm^2 for the bismuth-tin alloy. The absorbed intensity as derived from the metallographic examination and analysis must be corrected for reflection characteristics at the detector surface. This value must then be further corrected for the transmission characteristics of the filter in its pass band to obtain an intensity value for the energy incident on the filter.

Figure 2.11 illustrates the mechanical design of the typical cut-off filter spectral detector used in the pods. The basic elements of the gage are an aperture, two identical filters in line, and the sensitive detector. Two filters are used to help ensure

that at least one survives the environment. If a single filter only were used, its loss would introduce a serious ambiguity in interpretation of the data because of the possible uncertainty concerning the filter condition throughout the input. The filters and detectors are held in a micarta block which slips into the aluminum body of a box car gage. Apertures are cut in the external micarta protective cover of the box car gage.

The aperture diameters and the detectors used with each aperture are listed in the sequence shown in Figure 2.18 proceeding from left to right as follows:

<u>Aperture Diameter, mm</u>	<u>Detector Material</u>
1	1020 Steel
3	1020 Steel
8	1020 Steel
3	Bi-Sn

The two detector materials provide a dynamic range of about 20 in intensity. Additional range is provided by geometry through the 1-mm, 3-mm, and 8-mm apertures which have fields of view of $.0025 \pi$, $.022 \pi$, and $.144 \pi$ steradians, respectively.

2.3.6 Reflective Coating Spectral Gage. This instrument operates in a manner similar to the cut-off filter spectral gage. The only difference is that the discrimination between wavelengths is given by reflective coatings of known properties. The reflective coatings have cut-off characteristics analogous to those of the filters mentioned above. The field of view and dynamic range of this instrument are similar to those of the cut-off filter spectral gage.

Detailed Description of Reflective Coating Spectral Gage.

The basic element of the reflective coating spectral gage is the

arrangement of an aperture and a flat plate of heat-sensitive material. Figure 2.12 shows the standard model of the gage. The detector plates rest on plastic supports. The detectors are separated from each other by micarta spacers which prevent flux directed onto one detector from affecting any other. The detectors, supports, and spacers are contained in a standard aluminum box car body. The micarta heat shield contains the apertures.

Six different combinations of materials and reflective coatings are used in this instrument. Each combination is used in a separate instrument. The reflective surfaces used are aluminum, silver, bismuth-tin alloy, and 1020 steel. Aluminum and silver are vacuum evaporated onto the polished surfaces of the steel. Surfaces coated with gold black, which has nearly zero reflectivity, are also used for comparison. The base materials, 1020 steel and bismuth-tin, are used both as reflective surfaces and as thermal intensity detecting elements in a manner similar to the cut-off filter spectral gages.

The reflection properties of the various surfaces, i. e. , aluminum, silver, low carbon steel and bismuth-tin, are shown in Figure 2.13 (References 15 and 21). The values for bismuth-tin were obtained by adding the reflectivities of bismuth and tin on a proportional basis. Assuming that bismuth-tin eutectic crystals behaved as a mechanical mixture, the reflectivity values $[\rho(\lambda)]$ for bismuth-3% tin were calculated by

$$\rho_{\text{alloy}}(\lambda) = x\rho_{\text{Bi}} + y\rho_{\text{Sn}} \quad (2.3)$$

where x and y are the volume fraction on an atom basis of bismuth and tin, respectively. Aluminum is highly reflecting throughout the

infrared, visible, and ultraviolet spectrum from 0.2 to 10 μ except for a sharp decrease in value from 95 per cent to 85 per cent at about 0.9 μ . Silver, which has a high reflectance throughout most of the spectral region including the infrared (approximately 98 per cent) exhibits a sharp cut-off at 0.32 μ . The reflection properties of low carbon steel and bismuth-tin are quite similar. These materials have reflectivities which are substantial in the infrared around 10 μ and decrease monotonically through the visible to a low value in the ultraviolet at 0.2 μ . The reflectivity of 1020 steel ranges from 95 per cent at 10 μ down to 22 per cent at 0.2 μ . That for bismuth-tin varies from 82 per cent at 10 μ to 20 per cent at 0.25 μ . The reflectivity of gold black is nearly zero over most of the spectral range of interest.

Six gages were mounted on each pod. Five have similar aperture arrangements consisting of 1-mm, 3-mm, 1-cm, and 3-mm holes. The sixth gage has an aperture arrangement which differs in the last hole size. Instead of 3-mm aperture, the hole size is increased to 1 cm and the detecting material extended and brought up through this hole and made flush with the surface of the micarta heat shield.

The complete arrangement of holes and sample materials for the six gages is shown below:

<u>Sample Material</u>	<u>Aperture Diameter</u>
Bi-Sn	1 mm 3 mm 1 cm 1 cm flush
Bi-Sn (Blackened)	1 mm 3 mm 1 cm 3 mm
1020 Steel	1 mm 3 mm 1 cm 3 mm
1020 Steel (Blackened)	1 mm 3 mm 1 cm 3 mm
1020 Steel (Aluminum Coated)	1 mm 3 mm 1 cm 3 mm
1020 Steel (Silver Coated)	1 mm 3 mm 1 cm 3 mm

The dynamic range provided by the detector material sensitivity

is about 20. The pinhole and flush surface geometries can provide an additional dynamic range of about 800, since the fields of view are the same as those of the thermal pinhole camera.

2.3.7 Long-Time Thermal Gage. The intrinsic character of the burst at the Blue Gill altitude led to the expectation that there would be significant long-time thermal radiation (up to perhaps a tenth of a second). On the basis of our present physical model for the thermo-mechanical effect this energy input would not, in general, result in large structural loadings. Over such a long time, the induced structural loadings, if any, would be static. In addition, the high velocity of the pod removes it from the thermal influence of the fireball in times of approximately tenths of a second. In order to verify this expectation and to perhaps gain a better understanding of the complete burst phenomenology, however, instrumentation was designed to measure the thermal radiation emitted by the weapon over this long period. This instrumentation was to measure not only the time history of the long-time thermal, but also certain spectral characteristics of this long-time thermal radiation, utilizing techniques described for previous gages.

Detailed Description of the Long-Time Thermal Gage.

The long-time thermal gage utilizes a relatively massive heat sink containing foils which will change in phase while the heat sink remains largely undisturbed throughout and after the thermal pulse. The foils are very thin so that they have negligible heat capacity and conduction by themselves and will, therefore, closely reflect the true maximum temperature distribution experienced by the heat sink. This temperature distribution will be indicated by the position of phase changes in the foils. Phase transformations in the heat sinks will, of course, give additional information.

Dynamic range for this instrument is achieved by using two

geometries and two heat sink materials. The geometric technique is apparent from a comparison of Figures 2.14 and 2.15. The version which has the heat sink flush with the top surface of the gage body has essentially a 2π steradian field of view. The other version has the heat sink recessed below the surface and has a field of view a factor of 10 less than the more sensitive instrument. The heat sink materials were 1020 steel and OFHC copper, which have heat conductivities different by a factor of almost 10.

Both materials were used with both geometries, resulting in a total of four long-time thermal instruments per pod. The steel instruments can withstand a surface temperature nearly 400°C greater than the copper heat sinks without melting, which further improves the dynamic range.

The heat sinks are housed in the standard aluminum box car body. Heat conduction to the gage body is reduced through micarta spacers placed between the heat sink and the box car body. The entire gage is covered with a micarta heat shield which also forms the apertures.

The heat sink consists of two rectangular metal slabs held upright on a rectangular metal base. The rectangular slabs have flat smooth surfaces and are joined together with machine screws. Only one slab is attached directly to the base with screws. Pure metal and plastic strips 0.001 inch thick and 0.25 inch wide are placed between the slabs as temperature indicators. The strips are partially held in place by making a right-angled bend at the bottom of each strip and clamping the bent section between the base and the slab. The inner walls of the heat sink slabs are each protected from contact with the melting foils by a 0.001-inch-thick foil of platinum. These platinum protective sheaths facilitate disassembly after exposure. The heat sink and foil geometries are essentially the same in the two

versions, except in the vertical dimension.

The foils were chosen to provide a range of melting temperatures. The following table lists the foils and their melting temperatures along with the other characteristics of the four gages mounted on each Blue Gill pod.

COPPER HEAT SINK

<u>Foil</u>	<u>Melting Temperature ($^{\circ}$C)</u>	<u>Geometry</u>	
		<u>Flush</u>	<u>Recessed</u>
Polystyrene	80	No Filter	Quartz Filter
Tin	231.9	"	No Filter
Lead	327.4	"	Quartz Filter
Aluminum	660	"	No Filter

1020 STEEL HEAT SINK

<u>Foil</u>	<u>Melting Temperature ($^{\circ}$C)</u>	<u>Geometry</u>	
		<u>Flush</u>	<u>Recessed</u>
Polystyrene	80	No Filter	Quartz Filter
Tin	231.9	"	No Filter
Lead	327.4	"	Quartz Filter
Gold	1063	"	No Filter

The copper heat sinks melt at 1083° C, while the 1020 steel begins to melt at 1500° C. The spectral sensitivity of the recessed gage is rendered uniform by having a gold black deposit approximately 0.6 micron thick over the exposed surface. The foils were made to fit flush with the top surface of the heat sink. A longitudinal scratch was inscribed on each foil to accentuate the position of the melt line.

2.3.8 X-Ray Pinhole Camera. At the Blue Gill burst altitude, the characteristic X-ray penetration length is much shorter than the range to the closest instrument pod. The initial X-ray flux is, therefore, drastically attenuated by the intervening atmosphere. At the range of the closest pod, the un-

attenuated X-ray flux from a 1-kev weapon would have been approximately 100 cal/cm^2 , the peak in the spectrum occurring at about 6 kev. A further reduction in flux was undoubtedly caused by the heat shield on the weapon which, for the planned trajectory, was to be oriented in a downward direction. Since the unshielded flux was considered sufficient to cause substantial ablation, measurements of the X-rays characteristic at the pods were considered a vital feature of the experiment. The spall gage described in Section 2.3.2 was to provide information on the structural implications of the X-radiation. Two other instruments were included to record the characteristics of the X-ray source at the pod. The instrument of this section has a threshold on the order of 1 cal/cm^2 ; Section 2.3.9 describes an instrument which will record a flux several orders of magnitude less. These two instruments together represent a dynamic range of about four orders of magnitude.

The X-ray pinhole camera photographs the source in its own radiation. Furthermore, the nature of the detectors used as film should allow some spectral information to be derived by observing solidus lines or other phase changes in these materials. In addition, very precise orientation information can be obtained using the images and the known geometry of the instrument. One of the most interesting bits of information, which it was thought likely might be observable, was whether or not the source might extend beyond the heat shield.

Detailed Description of the X-ray Pinhole Camera.

Figure 2.16 illustrates the principle features of the instrument. The body is of aluminum with an internal diameter of 3.75 inches and an effective focal length of about 12 inches. The pinholes are formed in gold foil and three pinhole diameters are provided,

0.004, 0.013, and 0.040 inch. These can provide two orders of magnitude dynamic range in image intensity. The smallest pinhole when projected to the source subtends about 10 per cent of the expected source size. This value indicates the expected resolving capability of the instrument. The twelve holes around the periphery are positioned unsymmetrically to preclude any ambiguity in associating an image with its pinhole. The foil is backed up by a micarta disk with small clearance holes at the pinhole locations. This disk was intended to inhibit washout of the images by the following thermal radiation, which was expected to readily vaporize the gold foil.

The film plate was made up of three materials. The main disk was of 1020 steel with 25 machined holes. Alternate holes were filled with lead. Behind the steel disk was a stack of 50 one-half-mil gold covered mylar tapes which looked through the remaining holes in the disk. This array of films provides a wide range of sensitivity. The lead would be most sensitive at low fluxes because of its low ablation threshold. The mylar tape and steel are less sensitive at low fluxes. With sufficiently high fluxes, however, they can give much more information through phase transformation in the case of steel and because of the formation of distinct images on the mylar tape.

The X-ray pinhole camera is limited in the pod misorientation that it can accept. Above about 17 degrees, the X-ray beam could not enter the camera because of the collimating effect of the aperture in the rear bulkhead.

2.3.9 Photocell X-Ray Detector. This instrument utilizes techniques which are somewhat different in principle from the other instruments installed on the pod. It is basically an electronic one, although it does not require that any active electronic

elements operate during and after burst.

The instrument is so designed that burst-induced damage to semi-conductor or tube elements will not endanger the acquisition of the data. The information is both measured and stored by small latching relays. In the present form, there are five of these relays. The data must, of course, suffer in accuracy to some extent because of the relative coarseness afforded by the limited number of relays. The form of the stored information is such that it may readily be telemetered to the ground, although this feature was not utilized in the experiment. This feature of the instrument would enable it to be used in connection with a weapons test program where the information could not easily be physically recovered (for example, in a deep-space testing program). In the present embodiment, the instrument is about two orders of magnitude more sensitive than the X-ray pinhole camera discussed above.

Detailed Description of the Photocell X-Ray Detector.

The sensitive element of this X-ray detector is a Sylvania 131 long-persistence phosphor. The light flash resulting from the energy released by the prompt X-radiation in the phosphor has a decay time of 50 μ sec. The response of the phototube which views the light flash is stored on the magnetic latching relays. Figure 2.17 is a circuit diagram of the instrument. Batteries B_1 , B_2 and B_3 are connected in parallel. This ensures a life of about 200 hours. However, the power connection is external, and the unit may be shut off when necessary. The diodes CR_1 , CR_2 , and CR_3 ensure that only the battery with the highest voltage is being used.

The high-voltage power supply biases the phototube

and stores a charge Q_1 on capacitor C_1 through R_1 . R_1 ensures that excessive current is not drawn in building up the charge on C_1 . The phototube has a resistance which is proportional to light intensity. While light is emitted by the phosphor, a certain amount of the charge Q_1 charges C_2 through the resistance of the phototube. This produces a voltage V_2 equal to Q_2/C_2 which discharges through relays K_1 to K_5 .

The magnetic latching relays are connected in series. The coil of each relay is shunted with a resistor such that K_1 switches at V_0 , K_2 switches at $2V_0$, K_3 at $4V_0$ and so on. These resistors are individually chosen, and the units are calibrated for the voltage required on C_2 to trigger each relay. The number of relays switched tells how large the voltage on C_2 is, and the charge Q_2 can be calculated. From a knowledge of the phototube and phosphor characteristics, the energy of the deposited X-rays can then be determined.

2.3.10 Instrument Installation. Figure 2.18 illustrates the placement of the instruments on the bulkhead of the pod. The indent recorders, X-ray pinhole cameras, and photocell X-ray detector, which require a large depth, were placed between the aluminum cylinders. The thermal diagnostic gages require considerably less depth and so were placed in the flare region. This flare region was filled with 4 lb/ft³ density Eccofoam for added buoyancy.

As has been mentioned previously, the thermal diagnostic instruments were held in place on the backplate by spring-loaded fasteners which could withstand backplate flexure (burst-induced or vibratory loads).

Most of the features of the mounting of the indent recorder

cluster are described in Section 2.3.1. In the installation, the bridge on which each cluster was mounted was put into place before the cluster mounting hole was drilled. This hole was spotted to be concentric with the alignment can by means of a hole-spotting jig which was substituted for the indent recorder cluster in the alignment can; the rear bulkhead was mounted temporarily on the bulkhead with a hole-spotting jig in each of the six alignment cans. After the holes were located, the bridges were removed, drilled, and replaced.

The X-ray pinhole camera was mounted from two brackets cantilevered out from the inner cylinder. Its longitudinal axis was aligned within less than 5 mils in 4 inches to be perpendicular to the steel ring which forms the end of the inner cylinder and which was used as a reference surface for the X-ray camera. Further security was provided the camera by a lanyard similar to those used with the indent recorder.

The photocell X-ray detector was fastened with relatively small screws into the inner surface of the rear bulkhead. It was then also secured with a lanyard to the pod structure. Hopefully, under loads severe enough to remove the rear bulkhead, the lanyard would have torn the gage loose from the light screws so that it would have remained with the pod.

TABLE 2.1

NOMINAL INDENT RECORDER PISTON PARAMETERS

Piston Type	Head Area A_h (cm ²)	Piston Mass m_p (gms)	Piston Travel s (cm)	$\frac{sm_p}{A_h}$ dyne sec ² /cm ²	Response Time Description
A-1	3.16	25	0.05	0.4	Fastest Response
A-2	3.16	25	0.15	1.2	Fast Response
A-3	3.16	25	0.55	4.4	Fast Response
C-1	0.51	19	0.25	9.5	Medium Response
C-2	0.51	19	1.00	38	Medium Response
D-1	0.51	45	1.00	90	Slow Response
E-1	0.19	36	1.00	212	Slowest Response
F-1	3.16	28	0.05	0.5	Fastest Pressure- Insensitive Type
F-2	3.16	28	0.15	1.3	Medium Pressure- Insensitive Type
F-3	3.16	28	0.55	4.9	Slowest Pressure- Insensitive Type
G-1	0.51	20	1.00	39	Doubly Blind
G-2	0.51	30	1.00	60	Control Singly Blind Control

TABLE 2.2

PREDICTED THERMAL RADIATION IMPULSES

(Vapor cloud around surface is assumed to be completely transparent)

Thermal Impulse (dyne-sec/cm²)

Material	Range = 2,500 ft.	Range = 4,000 ft.	Range = 6,000 ft.
Lead	5×10^5	3×10^5	1×10^4
Pyrolytic Graphite	6×10^4	3×10^4	1×10^3
Copper	2×10^5	8×10^4	1×10^3
Zinc	4×10^5	2×10^5	7×10^3
Aluminum	1×10^5	6×10^4	1×10^3
Silver	3×10^5	1×10^5	6×10^3
Steel	2×10^5	9×10^4	3×10^3
Refrasil-Phenolic	6×10^4	3×10^4	1×10^3
Black Phenolic	6×10^4	3×10^4	1×10^3
Teflon	1×10^6	7×10^5	5×10^4
Iron Devcon	3×10^6	9×10^5	2×10^4
Micarta	6×10^4	3×10^4	1×10^3

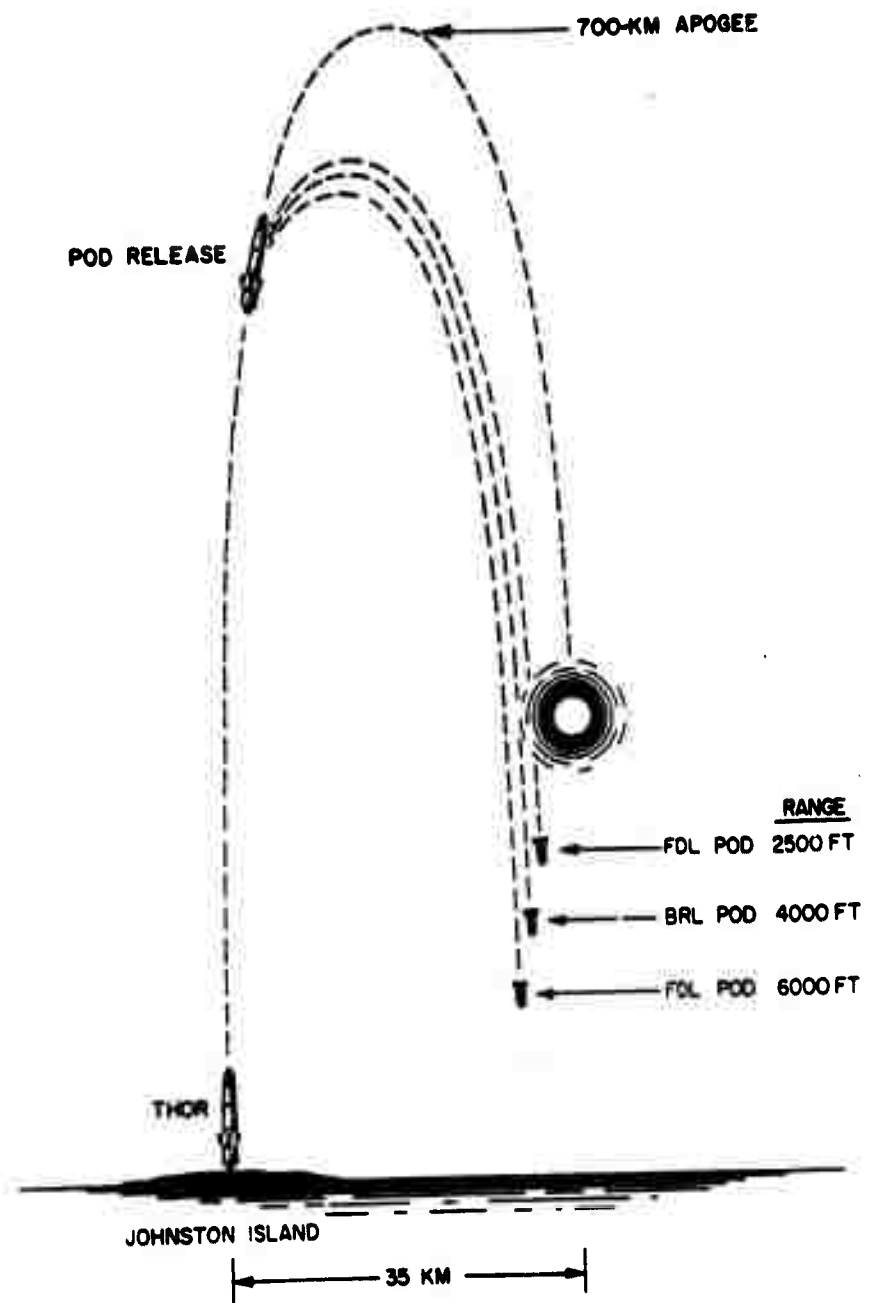


Figure 2.1 Thor and instrument pod planned operational sequence, Blue Gill.

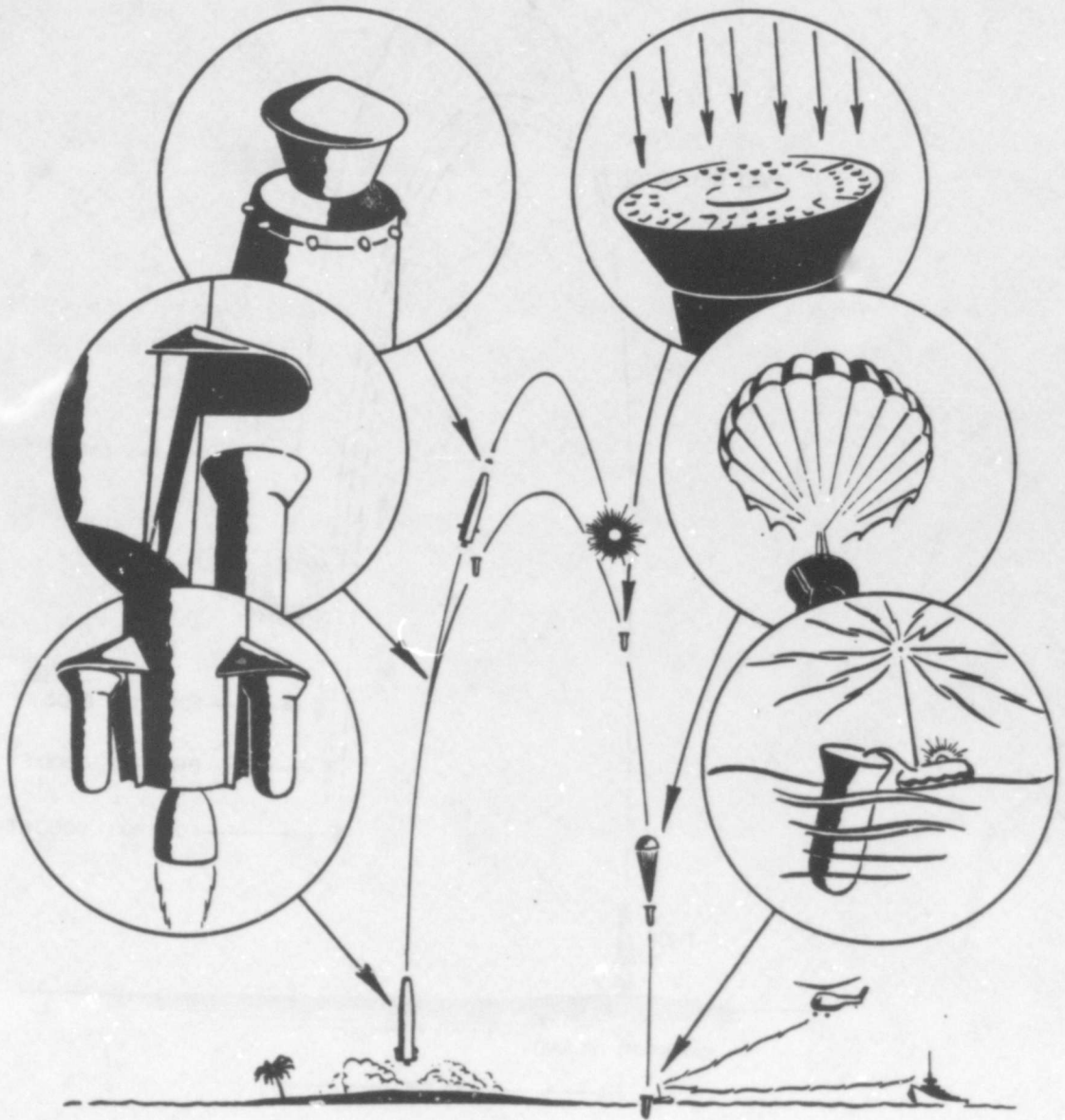


Figure 2.2 Pod experiment.

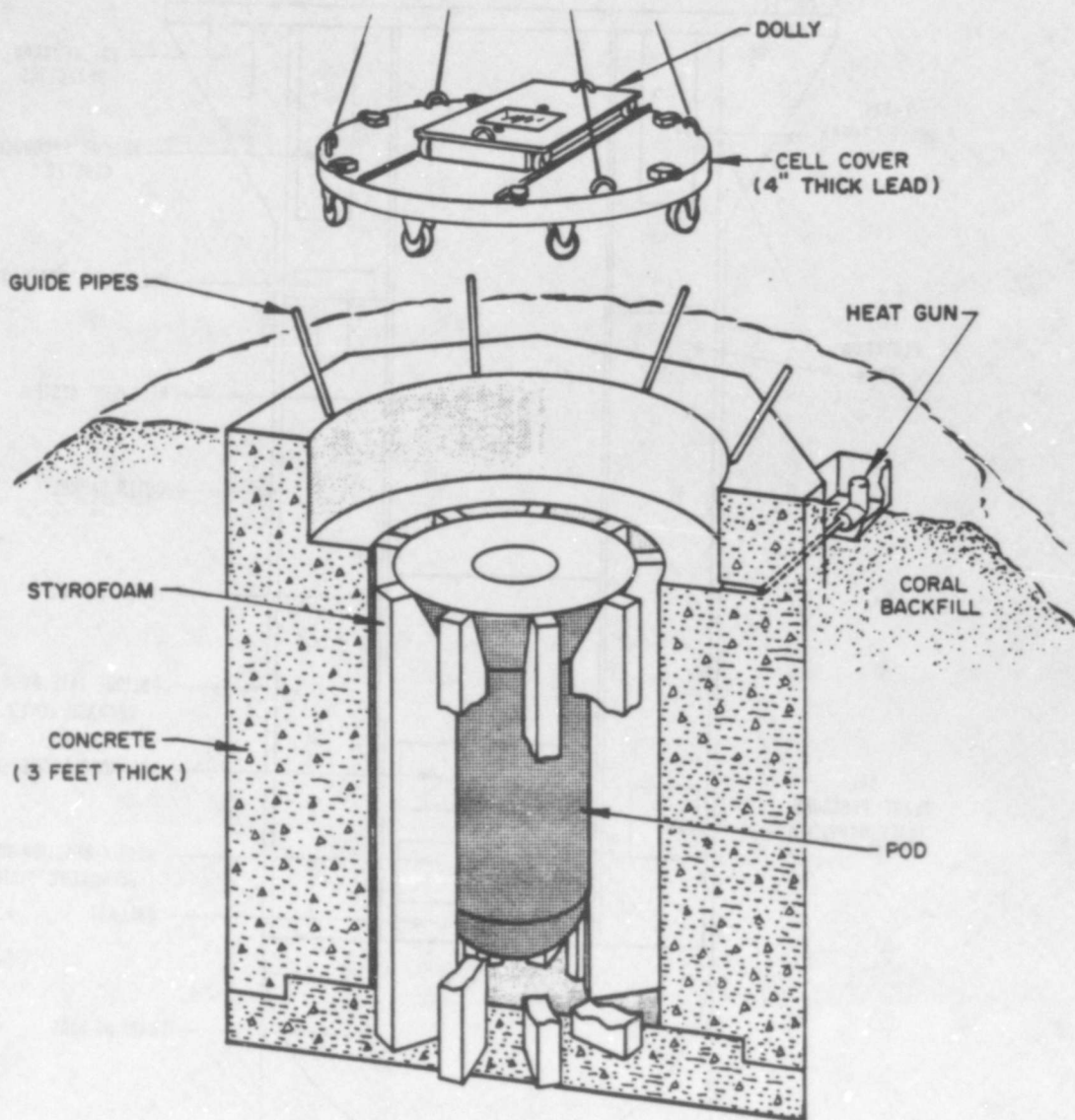


Figure 2.3 Pod storage cell.

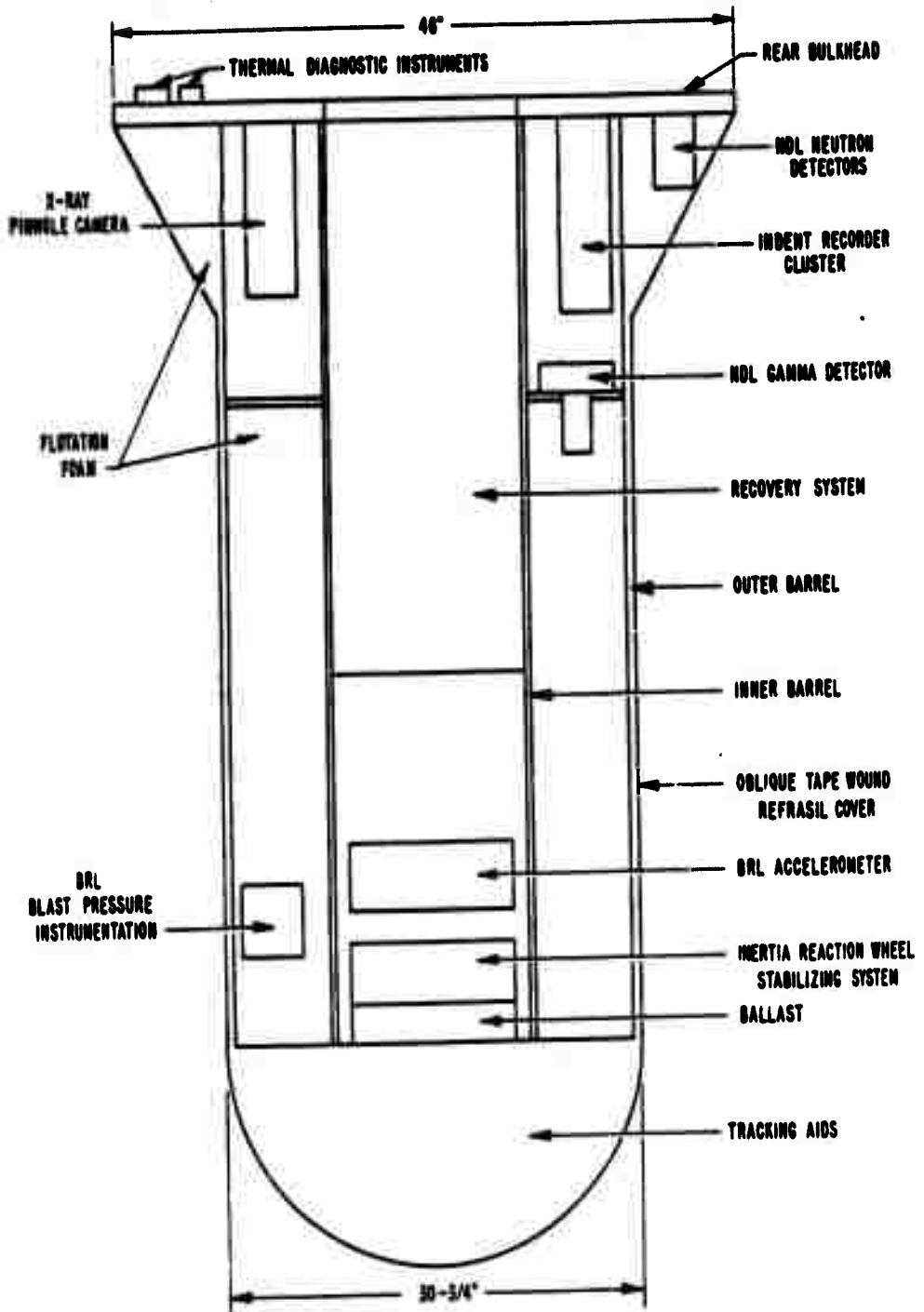


Figure 2.4 Instrument pod:

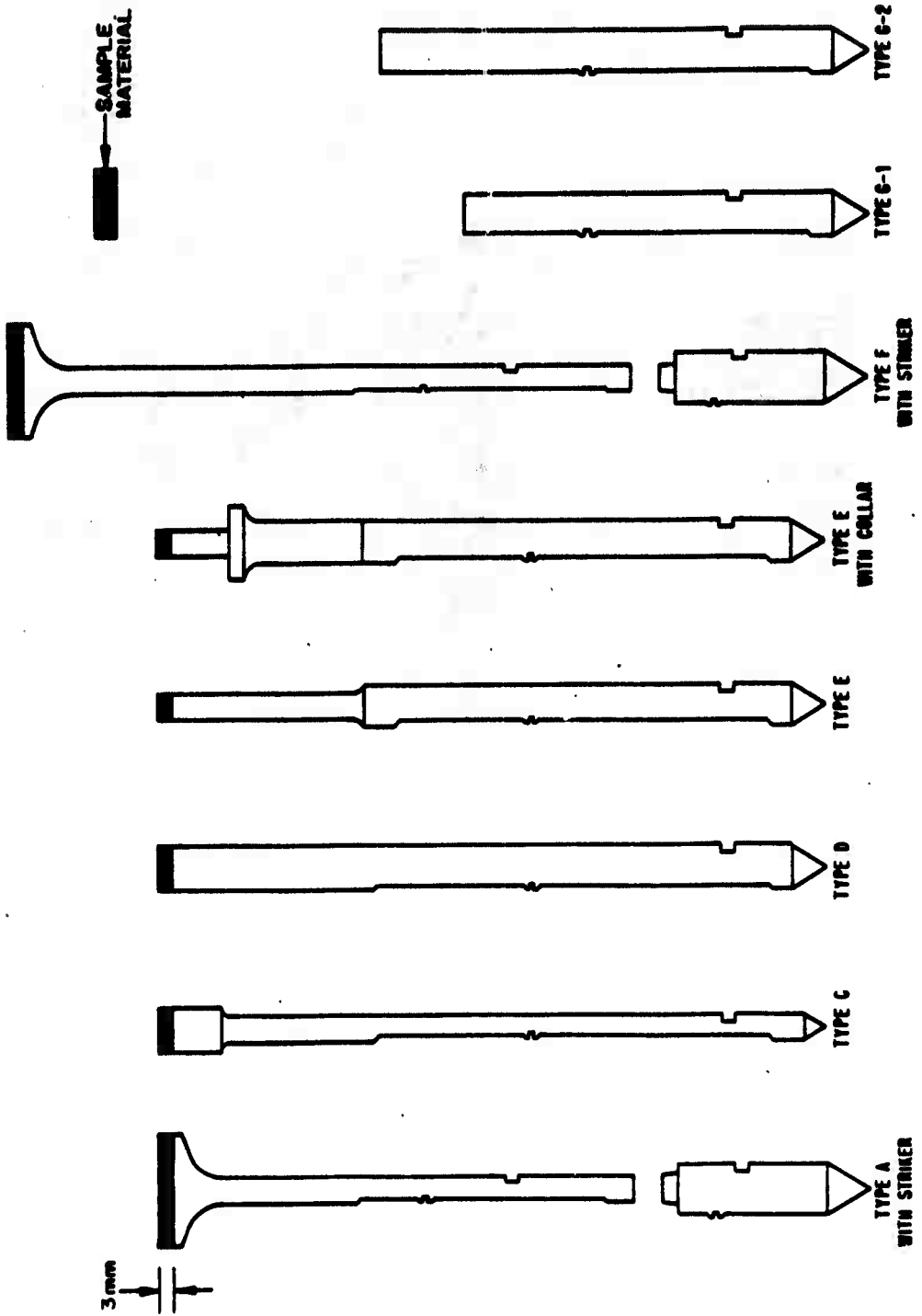
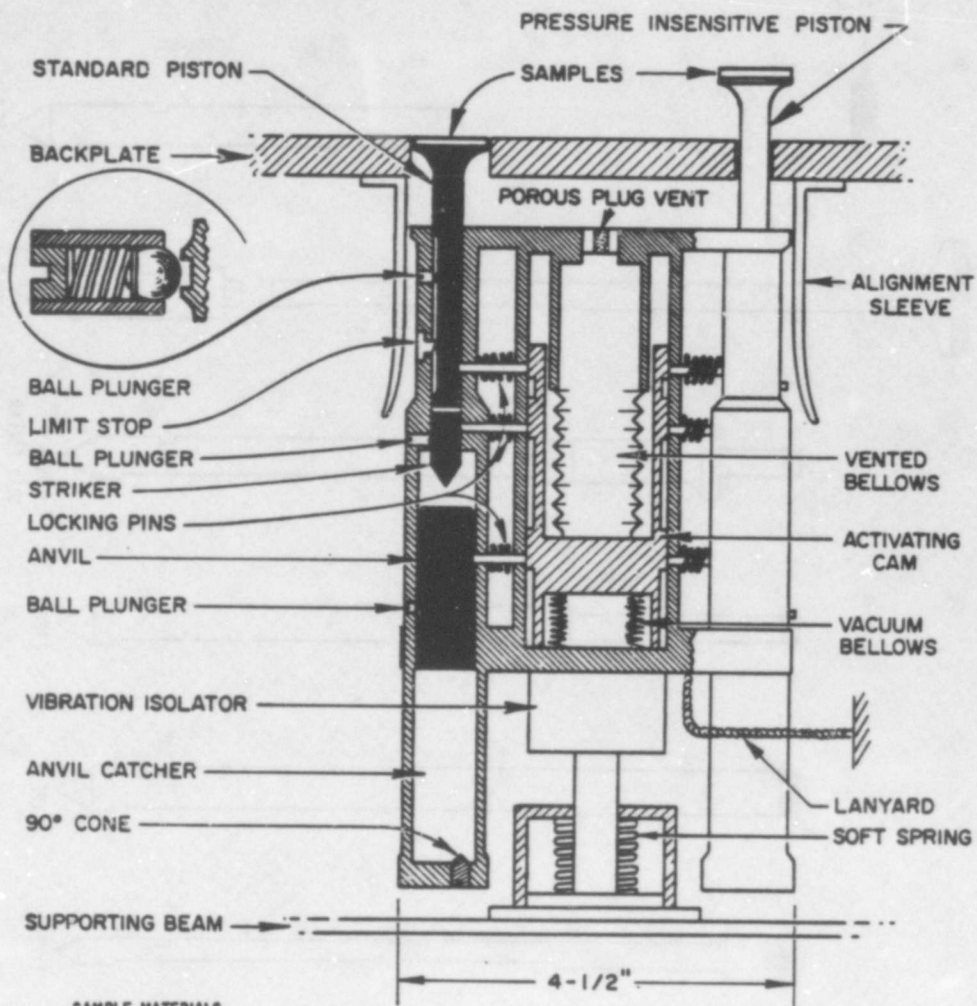


Figure 2.5 Indent recorder pistons, Blue Gill.

48 DATA CHANNELS PER POD



SAMPLE MATERIALS

PYROLYTIC GRAPHITE (PERPENDICULAR AND PARALLEL), ALUMINUM, STEEL, COPPER, ZINC, SILVER, LEAD, REFRASIL, PHENOLIC, MICARTA, TEFLON, IRON-DEVCON.

Figure 2.6 Indent impulse recorder.

4 DATA CHANNELS PER POD

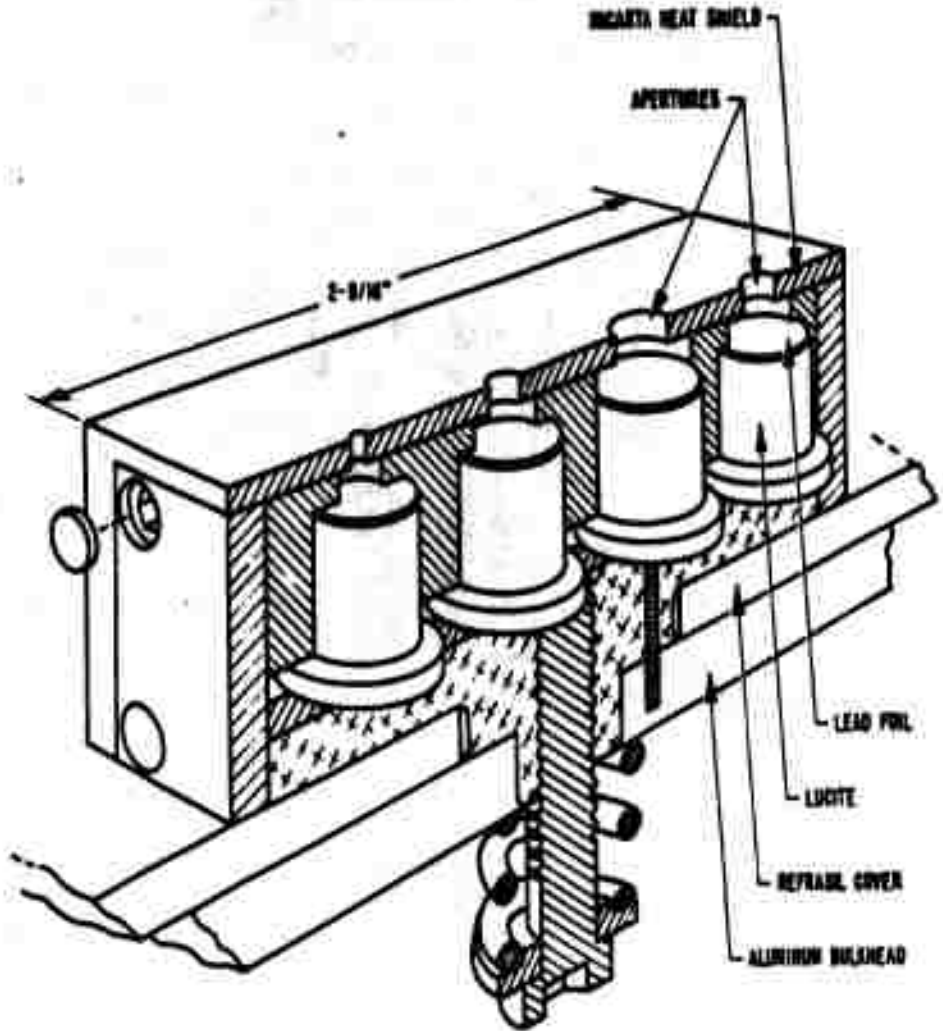


Figure 2.7 Spall gage.

18 DATA CHANNELS PER POD

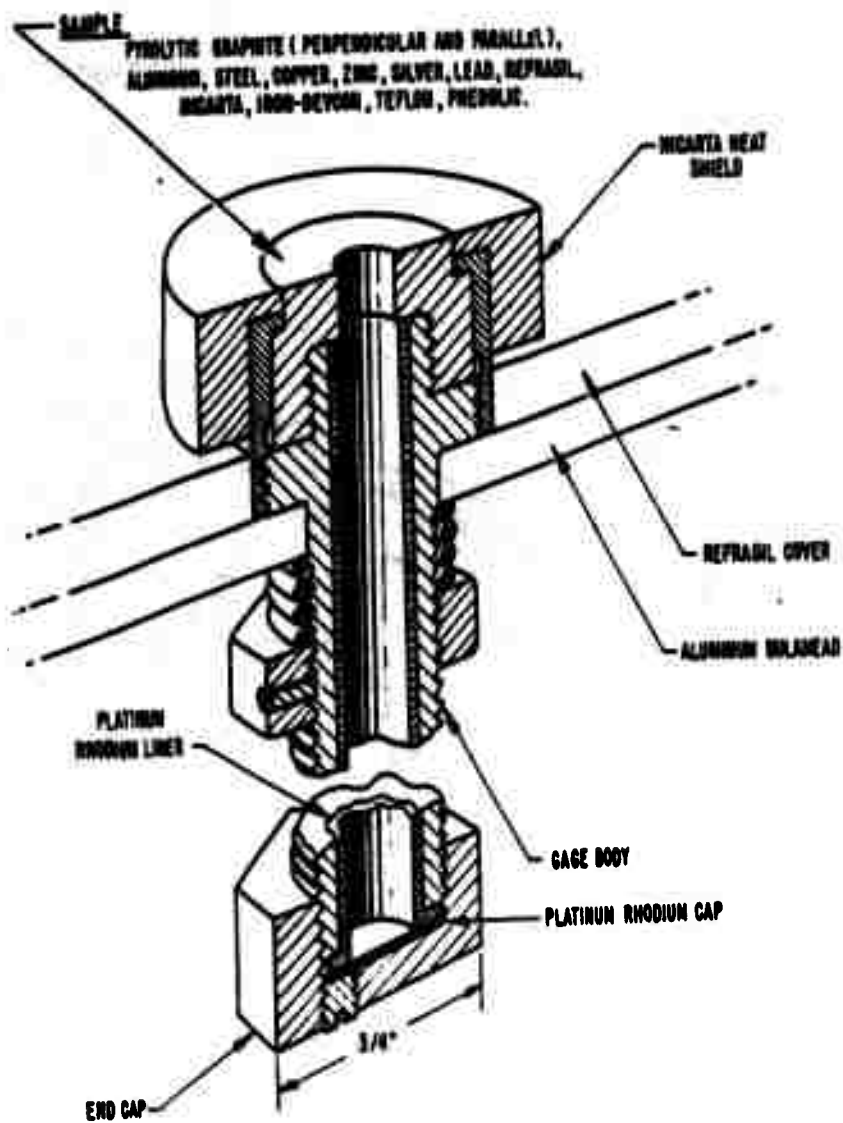


Figure 2.8 Ablation-condensation gage.

28 DATA CHANNELS PER POD

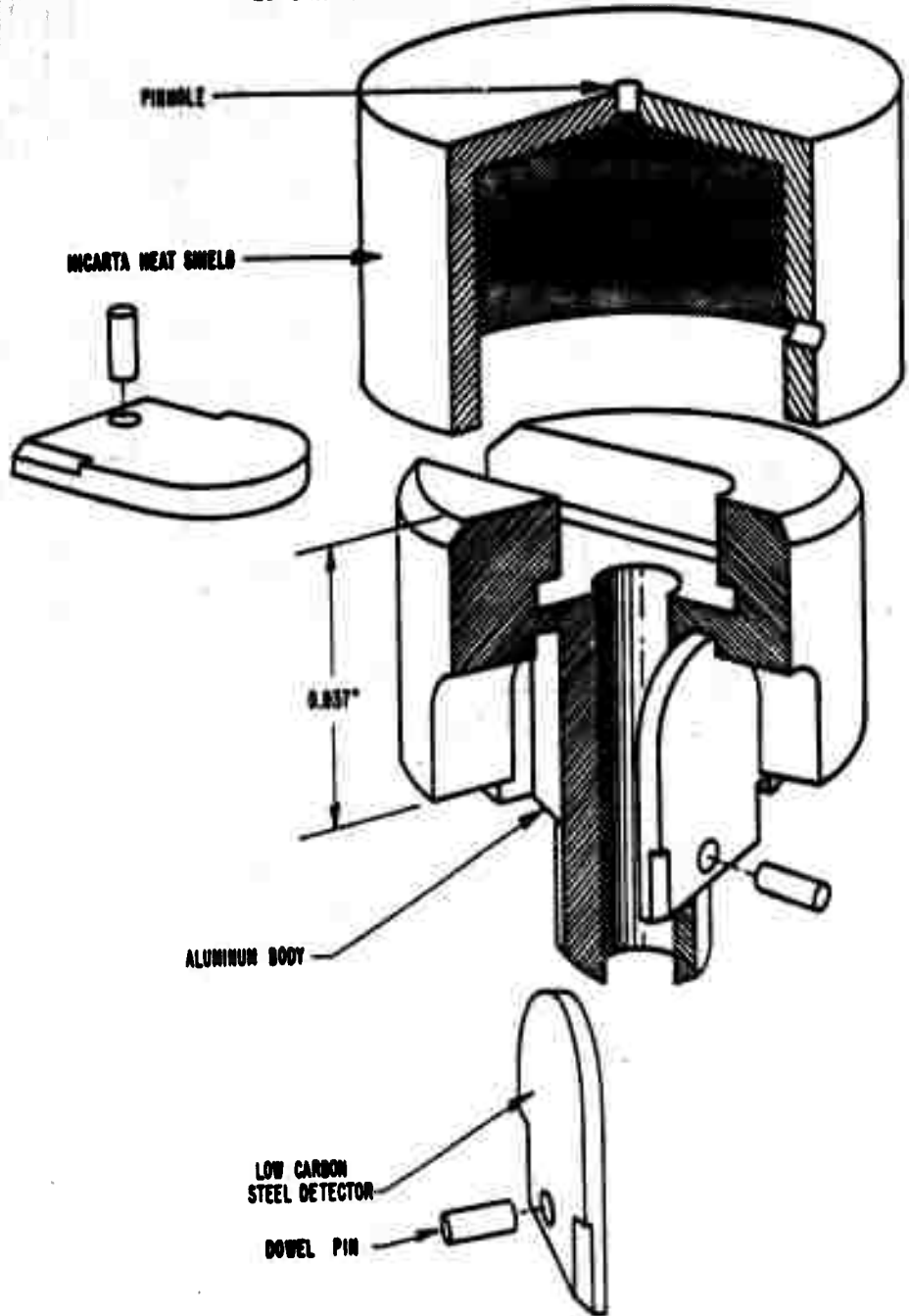


Figure 2.9 Thermal pinhole camera.

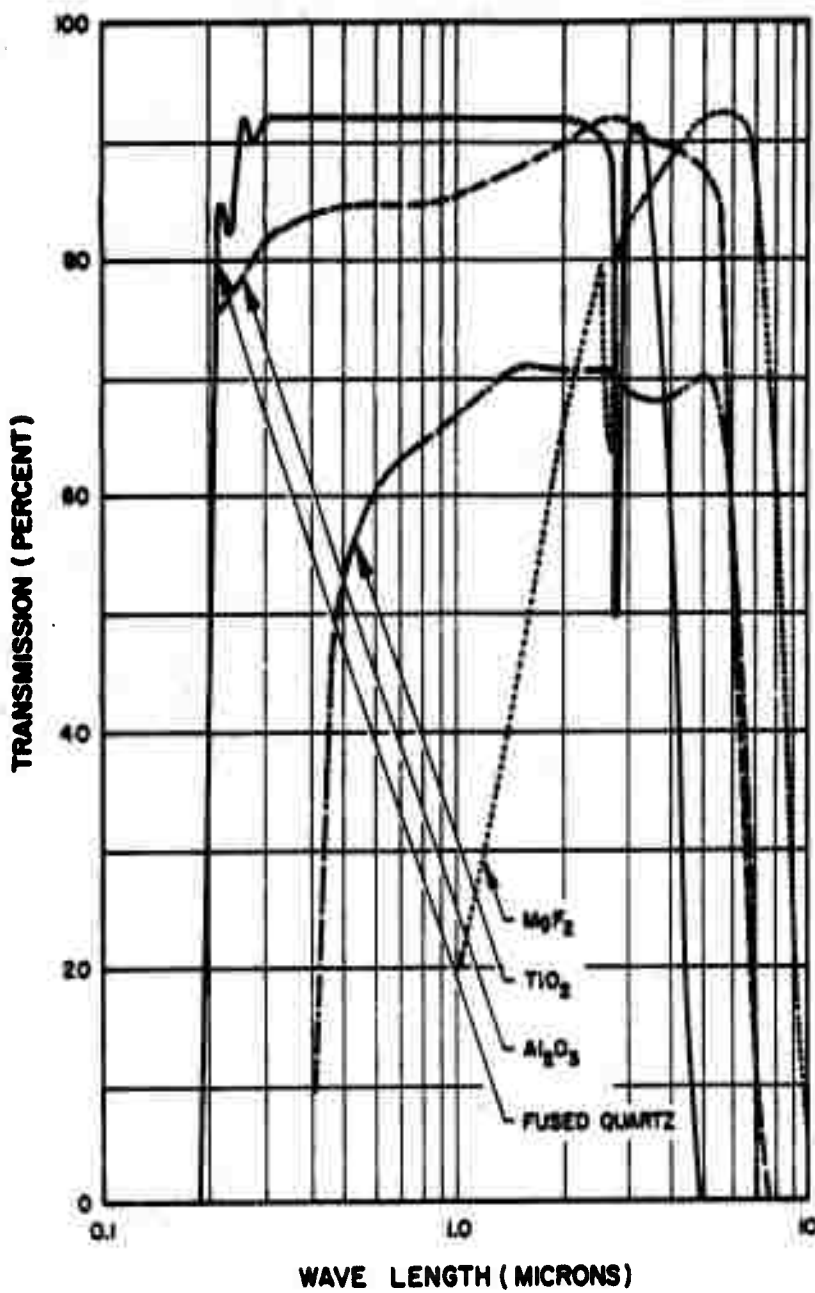


Figure 2.10 Transmission of spectral cutoff filters.

16 DATA CHANNELS PER POD

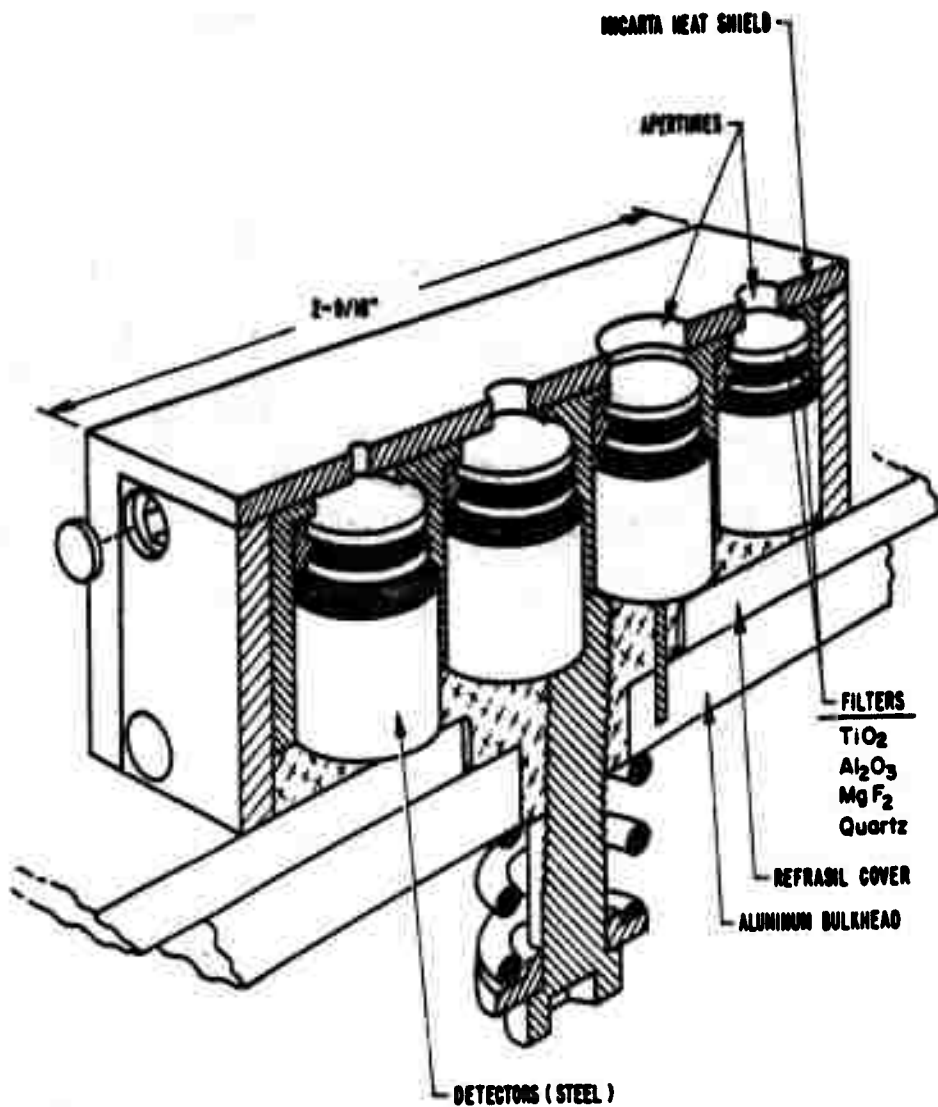


Figure 2.11 Cutoff filter spectral gage.

24 DATA CHANNELS PER POD

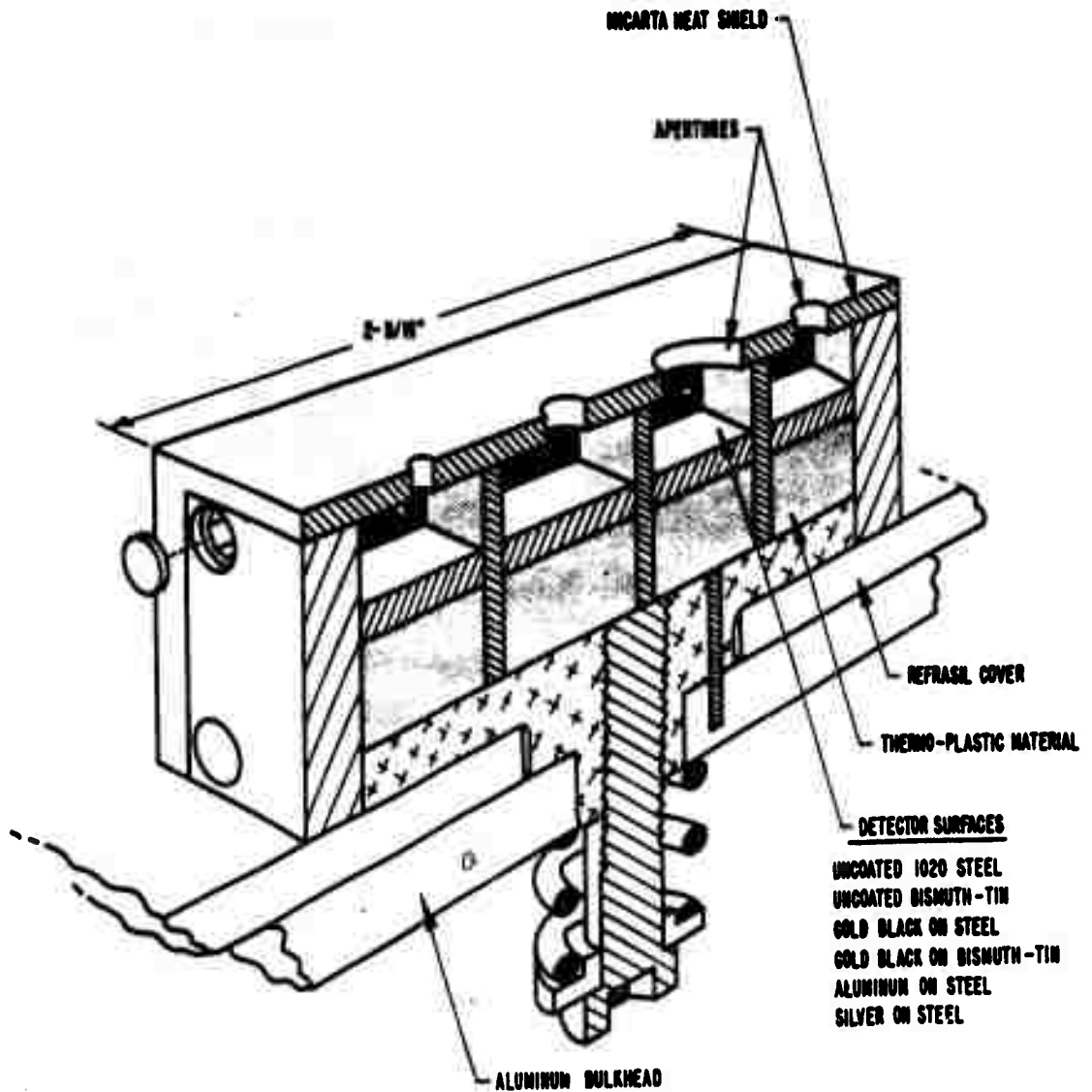


Figure 2.12 Reflective coating spectral gage.

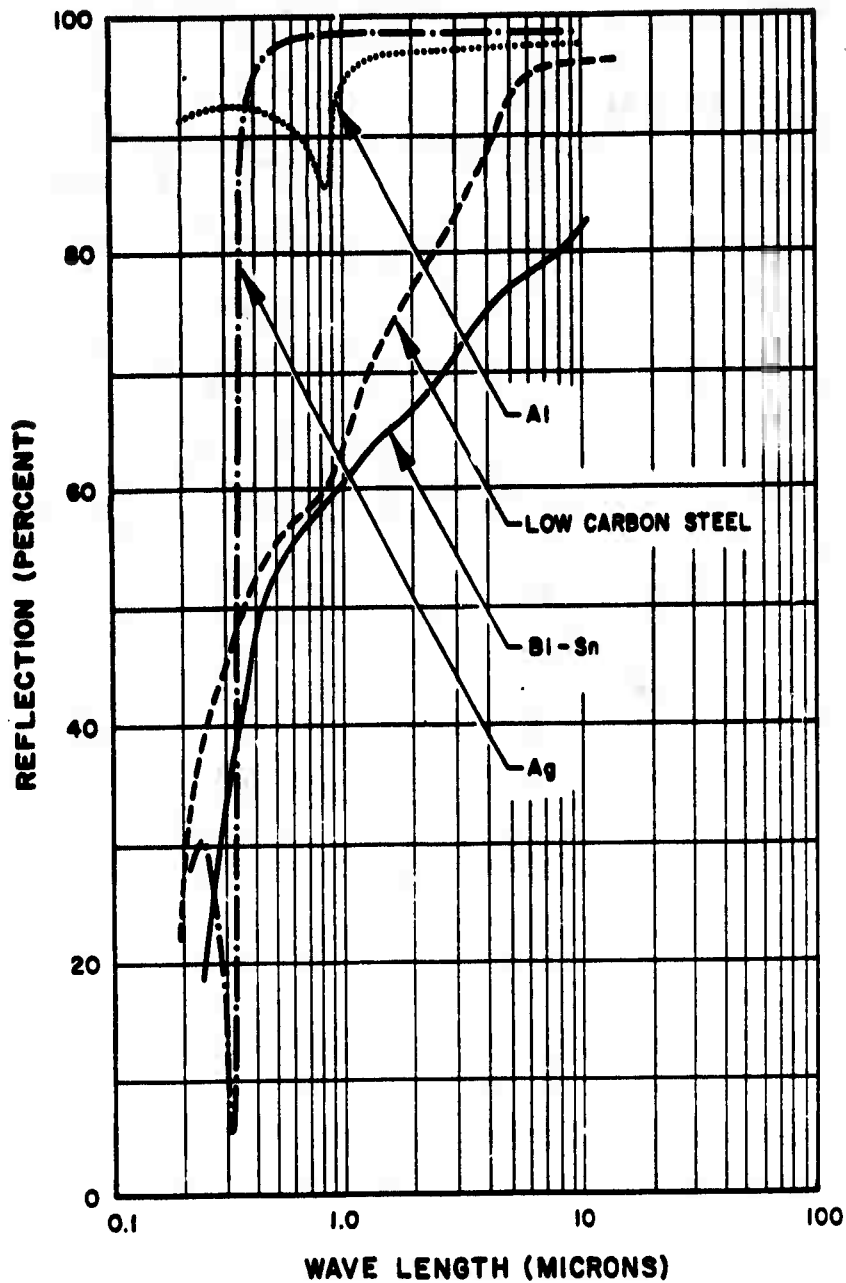


Figure 2.13 Spectral cutoff characteristics of reflecting surfaces.

8 DATA CHANNELS PER POD

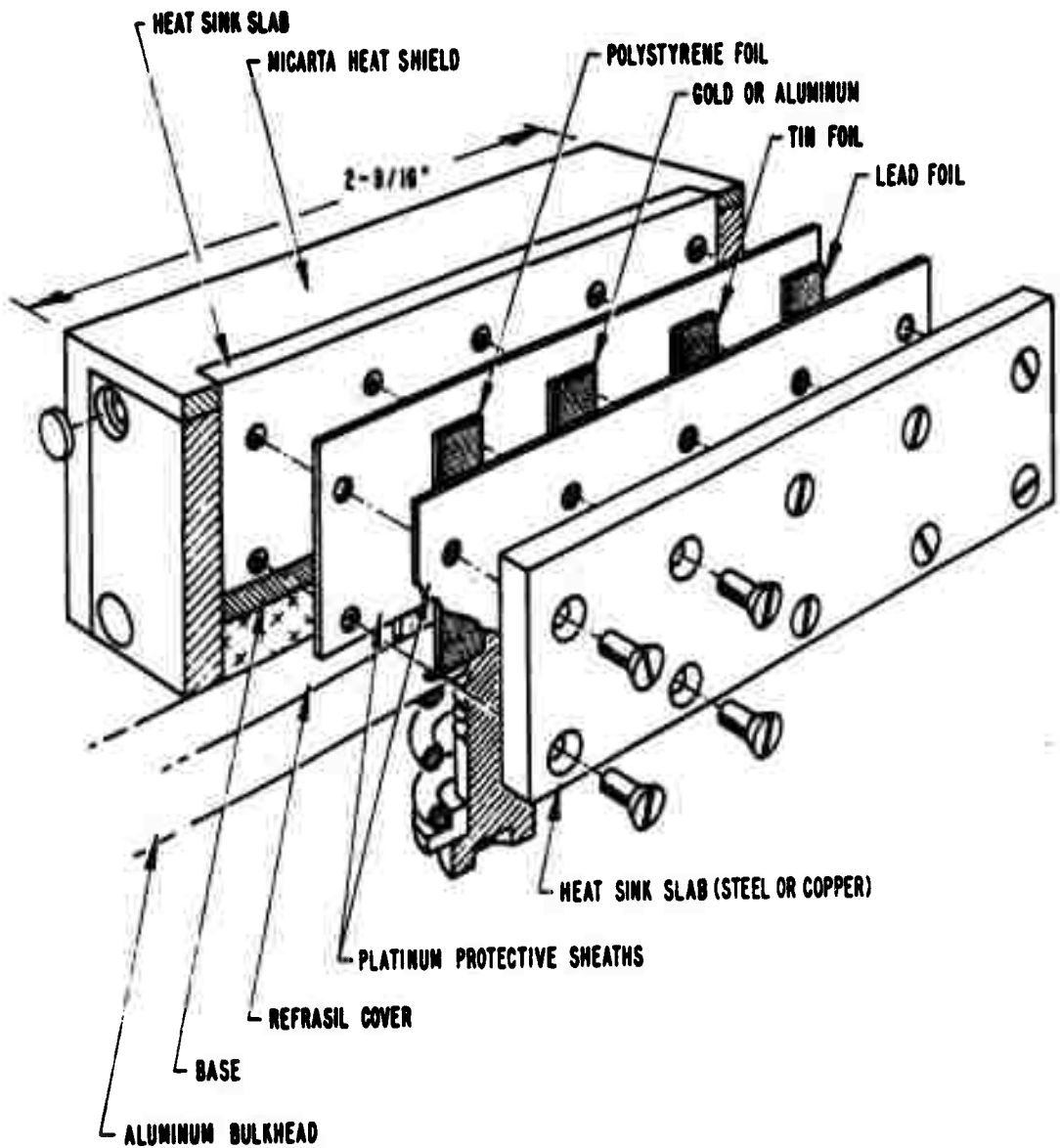


Figure 2.14 Long-time thermal gage (flush).

8 DATA CHANNELS PER POD

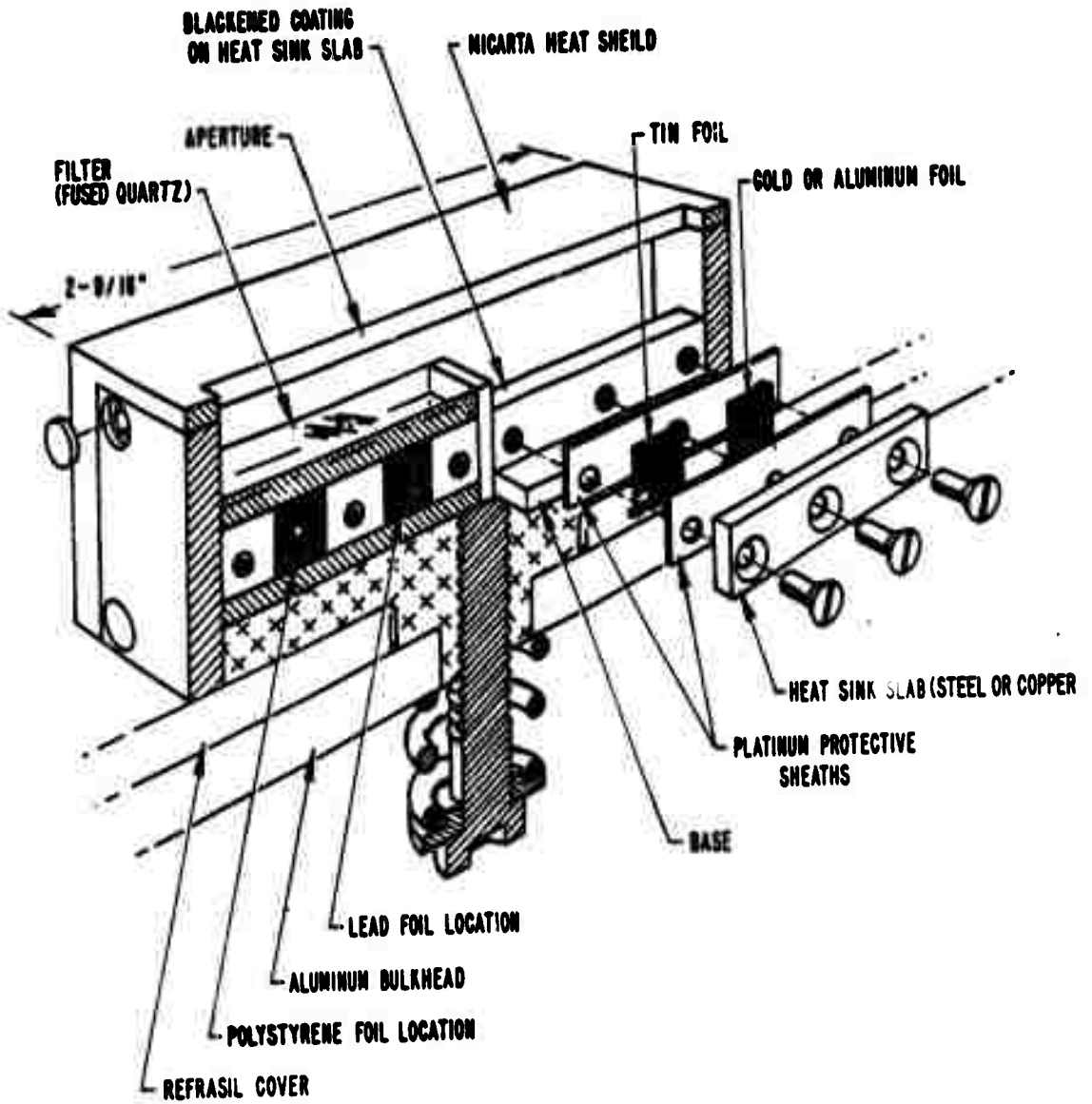


Figure 2.15 Long-time thermal gage (recessed).

13 DATA CHANNELS PER POD

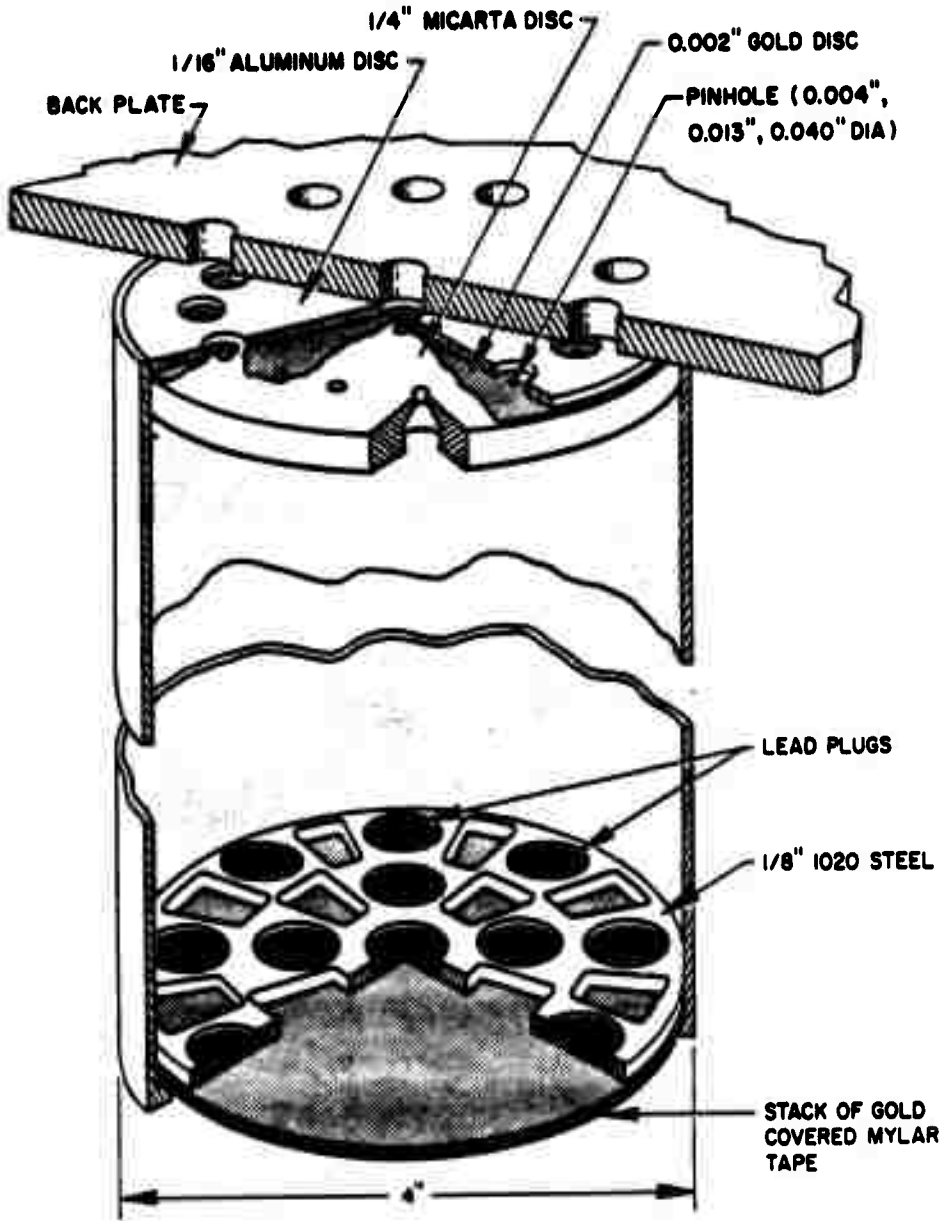


Figure 2.16 Nominal 12-inch-focal-length X-ray pinhole camera, Blue Gill.

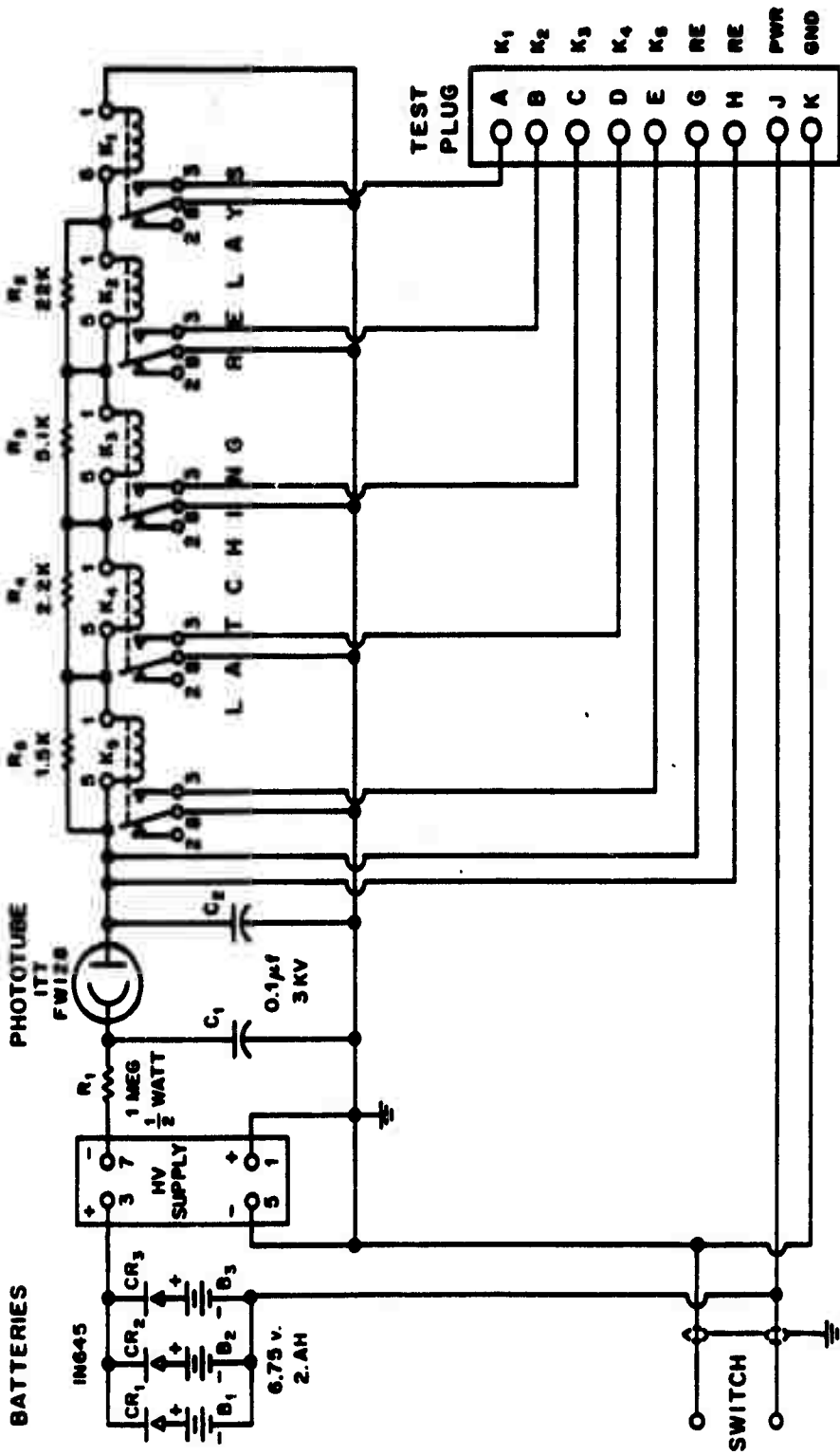
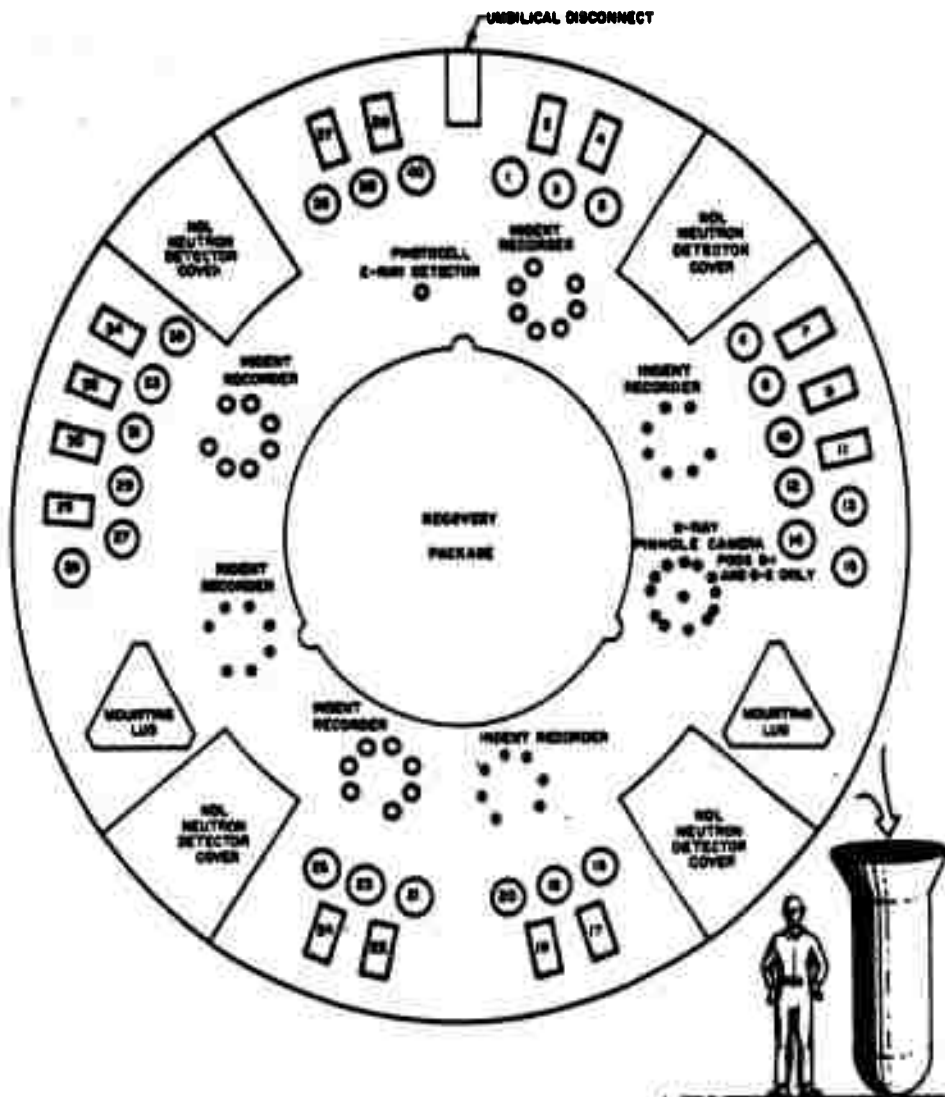


Figure 2.17 Photocell X-ray detector.



THERMAL PINHOLE CAMERA (TURRET GAGE) _____ 1,13,15,20,21,26,40
 CUT-OFF FILTER SPECTRAL GAGE (BOXCAR GAGE) _____ 17,19,22,24
 REFLECTIVE COATING SPECTRAL GAGE (BOXCAR GAGE) _____ 7,9,11,30,32,34
 SPALL DETECTOR (BOXCAR GAGE) _____ 20
 LONGTIME THERMAL DETECTOR - RECESSED (BOXCAR GAGE) _____ 37,39
 ABLATION CONDENSATION GAGE _____ 3,5,6,8,10,12,14,19,23,25,27,29,31,33,35,38,30
 LONGTIME THERMAL DETECTOR - FLUSH (BOXCAR GAGE) _____ 2,4

Figure 2.18 Instrumentation array, Blue Gill.

CHAPTER 3

EXPERIMENTAL RESULTS

3.1 OPERATIONAL RESULTS

3.1.1 Aborted Shot Blue Gill. An attempt to fire Shot Blue Gill occurred on 3 June 1962. The warhead was destroyed shortly before detonation. One pod completed its planned trajectory and re-entered successfully. Two pods apparently re-entered while still attached to the booster. They were separated, probably by aerodynamic forces, late in re-entry. All pods were recovered. This shot provided a record of the performance of pod and instruments where all the environments were encountered except the nuclear detonation. The before and after condition of the pods and instruments are described in Appendix C. The following conclusions were drawn from an inspection of the results of this test:

1. In pod B-2, which separated and re-entered as designed, over 80 per cent of the indent recorder channels recorded low-level data consistent with the beginning of re-entry, thereby confirming the innate sensitivity of the indent recorder technique. The condition of the indent recorders in pods B-1 and B-3 (planned ranges 2,500 feet and 4,000 feet) was consistent with proper performance.

2. The condition of all thermal diagnostic and material ablation instruments was such that data could have been extracted therefrom in the planned manner. From examination of the pods

it was apparent that sea-salt deposition and corrosion would complicate examination and interpretation of actual exposed instrumentation.

3.1.2 Blue Gill Prime. The launch attempt for the Blue Gill Prime event occurred at about 2315 hours on 25 July 1962. The vehicle was destroyed on the launch pad. Recovery or salvage of the Project 8A.3 pod instruments was not attempted.

3.1.3 Blue Gill Double Prime. At 2115 hours on 15 October 1962, a third Thor was launched for a Blue Gill attempt. The missile functioned correctly for approximately 85 seconds and then became erratic. The warhead was destroyed as the Thor reached an apogee of only about 100,000 feet. All pods were recovered, although two, B-2 and B-3, sustained severe damage. The pods were apparently torn loose from the Thor upon warhead destruction. Two of the recovery systems failed to function. Partial operation of the third system was obtained. Except for recovering two X-ray pinhole cameras, no attempt was made to salvage the Project 8A.3 instrumentation.

3.1.4 Blue Gill Triple Prime. A successful Blue Gill detonation occurred at 2400 hours on 25 October 1962. Preliminary tracking data indicated nominal trajectories for both the warhead and pods. The specific measurements of yield are not yet available

All three pods were recovered.

Pod B-1 was the first pod found; the sighting occurred two hours after the burst. The flashing light system was operating although the SARAH beacon failed to function. The Destroyer Leader USS McCain retrieved pod B-1 and returned it to the Johnston Island harbor entrance. Here it was transferred to a

LCM landing craft and hauled to the Johnston Island seaplane ramp. A mobile crane was then used to transport the pod to the recovery area and place it in a hot cell.

Pods B-2 and B-3 were not located until after dawn. The flashing lamp and SARAH beacon systems failed on both pods. The sea-dye dispenser functioned and aided search aircraft in locating each pod. A helicopter retrieved and returned pod B-2 to the Johnston Island recovery area. Pod B-3 could not be picked up by helicopter in the normal manner due to a malfunction in the parachute ejection system. The USS McCain aided in retrieving this pod by cutting the parachute lines and putting a modified cargo net around the pod. A helicopter then returned pod B-3 to the recovery area.

All pods were radioactive. The approximate surface activity levels eight hours after the event were as follows:

Pod B-1.....	14 roentgen/hour
Pod B-2.....	5 roentgen/hour
Pod B-3.....	3 roentgen/hour

These levels are in reasonable agreement with the predictions made in Appendix A. All activity was probably neutron-induced gamma and beta radiation. No alpha activity could be detected.

External appearances indicate that pods B-1 and B-3 re-entered normally and that the parachute deployment systems functioned as planned. These pods and instrumentation were recovered in excellent condition. Pod B-2 suffered severe damage to the rear bulkhead which probably occurred at water impact. Either bad orientation during re-entry or a recovery system malfunction could account for a failure of the parachute apparatus to deploy and slow the pod before it entered the water. The

backplate of B-2 was badly bent on one side, and most of the pod flare was missing. Approximately two-thirds of the surface-mounted instruments were lost or destroyed; however, all internally mounted instruments were recovered. The undamaged instruments provided most of the data desired from this pod.

Sandia Corporation had tracking transponders in the R/V and pod B-2. Cubic Corporation was responsible for tracking all three pods but not the warhead. The Z-coordinate and resultant ranges from R/V to pods at burst time as summarized in Cubic Corporation messages dated 18 April 1963 and 19 April 1963 (Confidential) are as follows:

<u>Item</u>	<u>R/V-to-Pod Range (ft)</u>
R/V	
Pod B-1	3,280
Pod B-2	4,603
Pod B-3	6,760

The above slant range for pod B-2 matches that quoted in Reference 22. Because of the need for accurate vehicle deceleration information at burst time in the reduction of indent recorder data (see Appendix D), the data from Reference 22 were examined critically in the immediate pre-detonation region. It appears that the data for the last five seconds before detonation were an extrapolation which gave a constant acceleration to the pod of 28 ft/sec^2 . This value is not consistent with the drag value of the pod at this altitude and velocity. Because of this inconsistency, American Science performed a trajectory computation (vertical component only) starting early enough in the trajectory of Reference 22 to be nearly in a drag-free field.

The value of $W/C_D A = 145$ was used for the pod and

$W/C_D A = 100$ for the R/V (based on personal communication with personnel at General Dynamics/Aeronautics and Field Command, DASA). A tropical atmosphere based on measurements at Johnston Island was used, which was provided by Dr. K. Champion of Air Force Cambridge Research Laboratories (Project 9.1).

According to this computation, the vertical separation between R/V and pod B-2 was 4,730 feet (compared to a value of 4,555 feet from Reference 22).

Other

evidence of pod positioning is provided by photographs of pod re-entry obtained by Project 8A.3. The photograph of Figures 3.1 and 3.2 was taken at 7 seconds after burst. The vertical separation distances at this time, as derived from this and subsequent frames, are [

The corresponding

vertical separation distances extrapolated back to burst time were calculated to be 1,360 feet and 2,090 feet. These burst-time values are consistent (well within the measurement accuracy from the photographs) with the vertical separation distances obtainable from the above table.

In summary, the various positioning data appear reasonably consistent. The only significant inconsistency appears when the tracking data are used to obtain pod deceleration at burst time. A more realistically extrapolated trajectory, based on computations using pod drag and a measured local atmosphere, was used instead in reduction of indent recorder data.

In the interpretation of all data from the Blue Gill instruments, the orientation of the pods with respect to the line between the pods and the burst must be taken into consideration. This orientation is the only one derived and used in this report. The orientations with respect to the Johnston Island coordinate system can be derived from the orientation angles presented herein and the rectilinear coordinates of the burst and pods.

In pods B-1 and B-2, the best sources of orientation information are the stippled or ablated areas illuminated by X-rays. These illuminated areas occur on many instruments and in many other fortuitous locations. Those on the thermal pinhole cameras were used as approximate guides to locate the illuminated areas on the X-ray pinhole camera film plates (see Section 3.2.8). More precise measurements were then made from the images on these plates. The camera axis itself was aligned with respect to a reference surface on the pod to within 0.005 inch in 4 inches. The largest uncertainty originates from locating the image center with respect to the pinhole center. The tabulation below encompasses the estimated uncertainty due to the various sources (including machining tolerances). The angle θ is the angle between the normal to the backplate and the direction to the burst. The azimuth angle ϕ is measured clockwise from the umbilical disconnect on the backplate. The latter angle is given without a range, but it may be considered accurate within several degrees.

<u>Pod</u>	<u>θ</u>	<u>ϕ</u>
B-1	12.1° to 13.1°	305°
B-2	7.5° to 8.7°	114°

The only sources of orientation information on pod B-3 were circular areas below apertures in reflective coating spectral

gages with bismuth-tin detectors. These areas have a different appearance than the surround and possess fairly sharp boundaries. Measurement of the offset from the aperture yields values of $\theta = 3^\circ$ and $\phi = 250^\circ$. These measurements must be considered less accurate than those on pods B-1 and B-2.

In this report all descriptions of instruments concern those from Blue Gill Triple Prime, although this term is not used any further. In Section 3.2.3 reference is made to certain control measurements made from instruments used in the aborted Shot Blue Gill of 3 June 1962. These measurements are always referred to in this manner so no confusion should result.

3.2 INSTRUMENT PERFORMANCE

Pod B-1 was recovered essentially intact. All instruments were in position and mechanically undamaged. Some samples on indent recorder pistons were missing. The pod itself and the instrument bulkhead were very homogeneously blackened except for the grey rearward streaming of molten material from screw-hole plugs on the flared portion which is characteristic of re-entry heating of fiberglass-phenolic.

Protruding instruments on the bulkhead were severely charred. Box car gage and thermal pinhole camera heat-protective covers remained in place, but many had expanded outward into a domed shape.

The removal of the bulkhead from the pod was performed in the hot cell utilizing full shielding, except that in the later stages the leaded glass window was eliminated. Most screw-hole plugs and many screws had to be removed by drilling.

Pod B-2 was found in a severely damaged condition.

The entire flare area had been torn loose and was missing. The bulkhead in the outer area was severely deformed inward toward the pod. All the box car type gages except one on the outermost ring were missing. This one instrument (a long-time thermal gage) was severely damaged, and the detecting element was missing. Only three of the seven thermal pinhole cameras remained on the bulkhead, and their heat-protective covers were missing. Most of the ablation-condensation gages remained on the bulkhead, although many were damaged. All instruments within the inner ring (indent recorder clusters, X-ray pinhole camera, and photocell X-ray detector) were in place, but several instruments were moderately deformed. Because of the damage it sustained, this pod was not placed in a hot cell. The radioactivity was allowed to decay two days before instrument removal was initiated.

Pod B-3 was received in a condition very similar to Pod B-1 except that a few instruments close to the edge of the bulkhead had been rotated from their original position, and pistons which protruded above the bulkhead were bent. This damage was apparently caused by contact with the landing net. Again the blackening was homogeneous with no obvious shadows. Pod B-3 was placed in a hot cell, and because of its relatively low radiation level, work on it was facilitated by rolling back the cover dolly to expose the entire port in the cover plate.

Only cursory examination of the instruments was made at the test site. Indent recorders were examined and approximate indent diameters measured. Photographs were made of every device, both before and after exposure to the detonation. In addition, significant aspects of the pod and of the operation were photographed.

The field examination of completely passive instruments such as the thermal gages, ablation gages, and pinhole cameras was limited to a superficial examination of their physical appearance. Devices subject to change with time and environment were taken apart, cleaned, oiled, and stored in a controlled atmosphere. Detailed examination at the test site was avoided because of the possibility of irreplaceable loss of vital information.

The sections which follow summarize the laboratory examination of the instruments and of other aspects of the pod which are pertinent to the objectives of the program.

Figures 3.3, 3.4, and 3.5 summarize the data reduction on the three pods. The instruments are briefly described on the figure, and the quality of the data is noted on the callouts. The notation "Improper Operation" on many of the instruments signifies that the instrument did not work as designed, but the information thereon may still be useful (e.g., ablation-condensation gages). In other cases this notation signifies an instrument failure through excessive corrosion (aluminum detector in long-time thermal gage) or through inadvertent use of a poor detector material (e.g., steel reflective coating spectral gages). The "Redundant Channel" notation signifies a detector which has not been examined because it would provide no information not already available from identical or more sensitive detectors. The "Effect Observed" notation is used with a detector which has a reading that cannot be evaluated as to quality since its meaning is not independent of other instruments (e.g., control indent recorder pistons). It is also used with some detectors which show an external effect but have not been cross-sectioned to extract quantitative information.

3.2.1 Impulse Measurements. After the event, all of the indent recorders were removed from the pods without difficulty. Immediate inspection of the instruments revealed some of the character of their burst-induced environment. The top of the cluster, the guide sleeve, and the under surface of the backplate (around piston holes) were blackened in a pattern which was clearly the result of a flow of vapor around the piston and into the pod. The top of the cluster also displayed rings of spattered, resolidified melt around many of the pistons. This deposit was piston sample material and apparently had been blown into the pod after being melted.

It was noted in the field that many of the piston samples were missing, although some of these were eventually found loose in the pods. It must be concluded that most piston samples did not survive the experiment environment. The tally of installed and recovered samples is given by the table below.

<u>Material</u>	<u>Recovered Samples</u>		
	<u>Number Installed</u>	<u>Number Remaining</u>	
		<u>Pod B-1</u>	<u>Pod B-3</u>
Refrasil-phenolic	10	6	9
Pyrolytic Graphite (grain parallel)	2	1	2
Pyrolytic Graphite (grain perpendicular)	2	0	0
Lead	10	0	5
Iron-Devcon	2	0	2
Teflon	2	0	1
Phenolic	2	0	1
Micarta, Aluminum, Copper, Zinc, Silver	2 each	None	None

It should be pointed out that out of only five samples recovered from pod B-2 (all loose inside the pod), three were refracil-phenolic, one was pyrolytic graphite (grain parallel), and one was lead.

All of the recovered lead samples were more than half melted and in some cases perhaps entirely melted. All of these had lost much material, which had apparently been swept away while in the melted state. The refracil-phenolic samples, which were flat laminated in the same way as the bulkhead cover, were charred but otherwise in good condition. The graphite samples were also in good condition, while the plastic samples appeared to be slightly deformed. Steel does not appear in the above list, as the sample was an integral part of the piston. The steel melted on the directly exposed surface. It is interesting to note that, in general, the number of samples recovered increases with increasing sample diameter. Since bonding area increases as the square of diameter while side load increases only as diameter, this is precisely what should be expected.

The statistics in the above table, aside from being a possible measure of adhesive quality, seem to bear qualitative information on the nature of the environment. That is, samples with relatively good thermal conductivity generally did not survive. This is pointedly clear in the case of pyrolytic graphite where none of the perpendicular grain (high conductivity normal to the exposed surface) samples were recovered. This could mean that a high thermal input, when rapidly conducted into the material, leads to failure of the adhesive junction. Metals, however, did not appear to behave in this manner. On many of the pistons with metal samples, traces of resolidified sample melt were found. One explanation for this behavior is that the glue line insulated the sample long enough to permit it to be completely melted and swept away before failure of the glue

joint. If this occurred, vapor blow-in must have existed for at least a time consistent with that required to melt a large fraction of the sample. The observations of sample melt should be at least qualitatively compatible with the data from instruments which measured thermal intensity.

Indent Recorder Performance. Careful examination did not uncover any evidence of bellows motor malfunction or non-retraction of locking pins. Of the anvils in pods B-1 and B-3, only one showed any evidence of improper retraction. In pod B-2, which was severely damaged, twelve of the forty-eight anvils were found to be normally retracted. Thirty-six of the anvils had been jarred back up into the barrels, presumably at water impact. Of these, however, only five were able to pass by the preventive key stop and get high enough into the barrel to permit possible restriking by the piston.

One anvil catcher of the pod B-2 indent recorder clusters had broken off, and the anvil was retrieved from within the pod. There was no indent on the face of this anvil, a condition which was consistent with its proper performance since it accompanied a control piston. In addition, the bottom of the anvil contained a retraction indent made by the 90-degree cone in the catcher bottom (see Figure 2.6). This combination of the absence of a data indent and the presence of a retraction indent is strong evidence that the indent recorder clusters in pod B-2 did function properly and that any apparent malfunctions were caused by the damage inflicted to the pod at water impact.

From the standpoint of mechanical operation all of the indent recorders appear to have functioned properly in the experiment. Supporting evidence for this conclusion came directly from the data obtained by the indent recorders. In addition,

an analysis of indent recorder motions (Appendix F) showed that in general the indent recorders were dynamically isolated during the time in which the data were recorded.

The first of the data sources supporting the validity of the indent recorder results is the control pistons. Two types were used in the experiment. One was the so-called singly blind piston, whose head was below the backplate so that it could not see the burst (Type G-2 piston). The head of this piston was open to the space beneath the backplate, however, so that it could sense any large pressure buildup in that region. The second type of control piston, the so-called doubly blind piston (Type G-1 piston), was sealed within a barrel of the indent recorder so that it could see neither the burst nor any pressure beneath the backplate. In all other respects, these control pistons were similar to the sample-carrying pistons used in the experiment.

As shown in the data of Table 3.1, eight out of the nine doubly blind pistons made no indents in their anvils. This is strong evidence of proper mechanical functioning of the indent recorder. In the case of the singly blind pistons (Type G-2), only three out of nine did not make readings in their anvils. It now seems most likely that the loading which caused some of the singly blind pistons to read was a combination of the collision of the piston head with the underside of the backplate and the pressure buildup beneath the backplate. It appears certain that a significant amount of pressure did develop beneath the backplate. Reasons for this conclusion are described later in this section. This pressure would, of course, tend to make the singly blind piston record a loading. The results of the dynamic analysis (Appendix F), in addition, imply that the singly blind

pistons did hit the undersides of the backplates as is confirmed by observation on some of the backplate regions above these pistons. The rebound of the piston would also cause it to record a loading. While these two effects cannot be determined quantitatively, they at least explain the occurrence of singly blind piston readings.

Moreover, there is nothing apparent in the singly blind control piston data to discredit the operation of the indent recorder, while the doubly blind control piston data strongly support the conclusion that the indent recorder operated mechanically in the manner intended.

Other evidence in support of the proper mechanical operation of the indent recorder comes from the data obtained by redundant sample-carrying pistons. These data are presented in Table 3.2, which is discussed later in this section.* In most cases, as can be seen in the table, redundant pairs agree quite closely. The slower responding pistons were to have been capable of measuring higher values of thermomechanical impulse than the faster responding ones in case the pulse were of sensible duration. In general, a definite correlation exists between the response speed and impulse measured.

While it is believed that the indent recorder functioned as designed, the readings made by certain classes of pistons are not considered to be solely the result of the thermomechanical loading on the heads of the pistons. It appears that significant amounts of blowoff gases on the backplate flowed through the clearance area surrounding the piston heads in the backplate. Since the A and C type pistons have heads which are larger

*The redundant pairs are designated in the table by a bracket in the piston number column.

than their shanks, any pressure under the backplate or merely locally under the piston heads would result in a reduction in the loading otherwise sensed by the piston. The reading in such a case would be that of the net loading on the piston head—the difference between the true thermomechanical loading on the surface facing the burst and some pressure loading on the underside. This reading would correspond to an apparent thermomechanical loading which is lower than the correct value.

There is much evidence that vapor from above the backplate flowed around the piston heads into the region below. Deposits on the tops of the indent recorder clusters (see Figure 3.6a) are in patterns which suggest high-speed, directed flow. The steel piston shown in Figure 3.6b implies the same high-speed gas flow. The resolidified flow lines of the molten steel indicate a strong sweeping action by the inward flow. Further evidence of this type of flow is presented in Figure 3.7a which illustrates gas flow patterns on the backplate undersurface about the top of the pinhole camera. The gas in this case flowed through the holes in the backplate (provided to expose the pinholes to the burst) and was deflected by the top of the camera to produce the patterns shown in Figure 3.7a. These patterns imply a significant amount of fairly energetic gas flow through the holes.

Some interesting evidence of long-duration gas flow beneath the backplate is pictured in Figure 3.7b. A distinct gradient in the deposition on the shank of a D-piston, over a length corresponding to its normal travel into the barrel, is visible in the figure. A correlation is evident between the relative exposure time within the cavity (under the backplate) and the density of the deposit — i. e., the upper portion of the region of interest, which entered the barrel last, has the heaviest deposition.

Such a result indicates a flow of gas into the cavity at times as late as those corresponding to the D-piston reading.

The two possible ways in which the pistons could have been affected by this gas flow are illustrated in Figure 3.8. Figure 3.8a depicts a local effect in which the gas expands along the underside of the piston and exerts a pressure on it in a manner somewhat akin to the flow through an expanding nozzle. This local pressure influence could reduce the readings of the A and C pistons by a factor of 2 or 3. Another possible effect is shown schematically in Figure 3.8b. As indicated, the volume bounded by the top of the cluster, the guide sleeve, and the lower surface of the backplate could have contained gas at significant pressure in spite of the flow out through the opening between the top of the cluster frame and the guide sleeve.

As noted previously, the singly blind control pistons were intended to provide a measure of the pressures within the chamber between the top of the cluster and the backplate. Unfortunately, this pressure effect cannot be evaluated, because as discussed above, the readings made by the singly blind pistons may be the sum of a pressure loading and rebound from the underside of the backplate. On pods B-1 and B-3, where the control data are apt to be more reliable, there is a trend toward higher impulse data from B-3 to B-1. Beyond this qualitative indication, however, the data is inconclusive.

As described previously, each indent recorder cluster was spring mounted to provide isolation from pod motion. During weapon-induced pod acceleration, the cluster can move within the guide sleeve toward the backplate. Indications of the actual cluster motions during the event were fortuitously provided by marks left on the inside surfaces of the guide sleeves by the teflon buttons used

as bearing surfaces within the guide sleeves. Two of these marks are pictured in Figure 3.9. When compared in relation to cluster type, it is found that the greatest displacement occurred for the cluster with the smallest piston-head clearance area (E type pistons), and the least displacement occurred for those with the largest piston-head clearance areas (A type pistons). This result is apparent on both the B-1 and B-2 pods; the motions on the B-3 pod are too small to permit any comparison. Teflon traces for a predominantly E-piston cluster and an A-piston cluster are shown in Figure 3.9. The traces understandably imply that the greater pressure above the cluster with the greater inlet area (piston-head clearance area) results in a relatively smaller cluster motion toward the backplate. In the case of the smaller inlet area, a lower pressure permits greater displacement of the cluster. The fact that a difference in inlet area into the volume above the cluster can have a significant effect on cluster motion strongly suggests that an appreciable pressure existed within the cavity.

It is likely that both local and volume pressure effects influenced piston response. It is possible, for example, that the fast-responding A type pistons produce readings before any appreciable buildup of pressure occurs within the cavity. Such readings would be influenced only by the local pressure effect. In the case of slower pistons, such as C-1 and C-2, however, the additional time may allow them to sense a volume pressure effect.

An experiment performed between the atmosphere and a vacuum chamber could probably determine the extent to which the pressure effects discussed above truly influenced the A- and C-piston readings. Such an experiment has not been attempted so that, at present, the A- and C-piston data must be regarded

as questionable. These data do represent lower bounds to the thermomechanical loadings, however, since any backpressure could only reduce the load levels from that which would otherwise be sensed by the pistons.

The response of E type pistons (the very slow responding type) show two possible sources of error. The first of these concerns the volume pressure effect discussed above (Figure 3.8b). The E-piston has a small-diameter head and a shank of larger diameter. The shoulder between these two diameters is located just at the top of the indent recorder cluster. Any pressure above the cluster top would therefore result in a force on this shoulder. The additional loading due to pressure acting on the shoulder would result in a larger indent than would otherwise occur under the action of the thermomechanical loading alone. If such a reading is converted to impulse per unit area on the basis of piston head area alone, it will be too large. Examination of the data presented in Table 3.2 reveals a number of such high values which imply that this effect could have occurred.

The other possible influence on the E-piston data concerns the relative motions of pod, cluster (indent recorder barrel or housing), piston, and anvil under the actions of the bomb loading (relative positions are shown in Figure 3.10). The dynamic analysis performed to describe these motions (Appendix F) showed that, if the impulse loading were confined to the head of the E-piston, the top of the anvil would strike the barrel before being struck by the piston. Such a collision would invalidate any indent data made by a subsequent piston-anvil collision. The situation is further aggravated by the fact that the E-piston (with only head loading) responds so slowly that it could engage the limit stop within the barrel before reaching the anvil. Such

behavior should result in a very low reading, if any. An examination of Table 3.2 reveals data which may stem from this behavior.

There seems to be adequate proof that the E-piston data are not valid readings of thermomechanically induced impulse. If the pressure under the backplate significantly increased the load on the piston, it might speed piston response sufficiently for it to read before any collisions with the indent recorder housing. Without a quantitative definition of the volume pressure effect, however, such a reading cannot be related to the true thermomechanical loading. In view of these considerations, the E-piston data have been excluded from further treatment in this report.

The pistons whose readings are unaffected by any of the adverse influences discussed above and, therefore, represent the best thermomechanical impulse data of the experiment are the D type pistons (see Figure 2.5). Piston shank and head have the same cross-sectional area, which makes this piston insensitive to any pressure which developed under the backplate. The readings made by the D-piston thus result from weapon inputs alone. It is of interest to note that the dynamic analysis (Appendix F) indicated that the D-piston response was fast enough to produce piston-anvil collisions before the anvil or piston could collide with the housing.* This result further supports the validity of the D-piston data.

Indent Recorder Data. A total of 144 indent recorder channels were employed for the Shot Blue Gill impulse experiment. All of the anvils were recovered. A measure of the performance of the indent recorder with regard to clarity of data can be obtained from an inspection of the indents. For the purposes of this

* The same was true for A-, C-, and F-pistons, as well.

appraisal, the data can be grouped into four quality categories defined as follows:

Perfect Indents. The indent has little distortion with the largest difference between diameter readings (four readings taken at 45-degree spacings) being 0.0005 inch or less. A "no indent" reading is included in the Perfect Indent category.

Double Indents. As the name implies, these anvils have a second indent (sometimes even a third). The initial indent is readily discernible from any subsequent indents both from size and distortion patterns. It is interesting to note that similar double indents occurred in the post-event indent recorder calibration.

Slightly Distorted Indents. Indent distortion is apparent, but the largest difference in diameter readings is not more than 0.0015 inch. These are usable data, since in most cases this difference is a very small percentage of the indent diameter.

Severely Distorted Indents. These are indents which have gross defects so that the data cannot be readily used. Some of these defects consisted of a very high degree of ellipticity, indications that the piston point was somewhat flat, and very irregular edges of the indent.

The breakdown of the Blue Gill indent data into the above categories is given in Table 3.3. The first three categories refer to data from which impulse is immediately derivable. These amount to 91 per cent of the Blue Gill anvils.

An interesting point has arisen with regard to the operation of the indent recorder which is worth describing before the discussion proceeds to consideration of the indent data. In addition to its function as an impulse-measuring device, the indent recorder can also provide some measure of the loading

experienced by the pod as a result of the burst. This is fortunate since no other data on pod loading or acceleration are available.

The mechanical relationship between piston, anvil, recorder housing (cluster), and pod are depicted schematically in Figure 3.10. For certain times after a perturbation, the piston and anvil act as essentially seismic masses with respect to the pod and recorder housing. The recorder housing has about one inch of travel before the spring bottoms out or the cluster strikes the rear bulkhead.

During examination of the anvils, it was noted that many of them had a circular mark on the top face. This was an indication that they had struck the top of the chamber. Further examination revealed a pattern to the occurrence of markings. Those anvils used with non-striker-type pistons were consistently marked, while anvils used with striker-type pistons were, in general, not marked. Examples of marked and unmarked anvil faces are shown in Figure 3.11.

This information was used in conjunction with the dynamic analysis, and the studies are discussed in some detail in Appendix F. The results of these studies show that the loads applied to the pods by the burst are predicted quite reasonably by the loads measured by the D-pistons, assuming no input loads on the front of the pods. In the case of pod B-1, the load experienced by the pod should be less than that indicated by the D-piston by about 10%. In the case of pods B-2 and B-3, the loads experienced by the pods appear to correlate well with the D-piston readings without any adjustment.

The indents in the anvils, of course, represent impulse levels measured by the pistons. The technique used in this program to relate the indent volume to the impulse sensed by the piston was direct laboratory calibration of the indent recorders. The calibration

technique employed in this data reduction operation is discussed in detail in Appendix D.

The indent recorder data obtained in Shot Blue Gill is presented in Table 3.2. Included are the diameters of the indents made in the anvils and the corresponding impulse values. The uncertainty quoted for each measurement is a $\pm\sigma$ value which results from scatter in the calibration. * This point is discussed fully in Appendix D. The indent diameters and corresponding impulse values are listed in Table 3.2 as a function of the particular piston (whose pertinent characteristics are also included). Precise values of quantities such as piston mass and piston-to-anvil spacing have been omitted, since they do not deviate significantly from the nominal values presented previously in Table 2.1. However, the actual values of the quantity $\frac{A_p}{A_h}$ which characterizes piston response and is of significance in studies described later in this section, have been included in Table 3.2. Pistons which were located in indent recorder clusters in which the control pistons made indents are identified in the table.

No correction has been made in the impulse data of Shot Blue Gill to account for any acoustical mismatch between the sample and the piston. The long duration of the loading pulse relative to the time required for stresswave transmission through the sample makes such a correction unnecessary.

The total impulse (measured by the D-pistons) is shown in Figure 3.12 as a function of range from the burst. The data line length indicates the standard deviation of the mean. The threshold level of the D-piston, at which the piston just breaks

* The quantity σ is the root-mean-squared deviation from the mean of the calibration data.

free of the ball plunger, is shown for comparison.

Time History Studies. The impulse data obtained in Shot Blue Gill (tabulated in Table 3.2) are plotted in the form necessary for time history studies in Figure 3.13, 3.14, and 3.15. Details of the time history analysis, including the significance of this arrangement of the impulse data, are contained in Appendix E. The impulse range of each data point in Figures 3.13, 3.14, and 3.15 represents the standard deviation based on the indent recorder calibration data (Appendix D).

The data shown in Figures 3.13 through 3.15 show that there is no consistent and distinct difference between the impulses recorded by the refrasil-phenolic pistons and pistons with other material samples. The explanation of this result is that the pressure of the vaporized refrasil-phenolic on the backplate dominated the loadings on the pistons. The effects of blowoff from particular sample materials can account for some of the differences in the readings, but this appears to be greatly overshadowed by the influence of the refrasil-phenolic vapor. The Blue Gill impulse experiment, in effect, turned out to be a one-material study — that of the response of refrasil-phenolic to the weapon input.

Further proof of the pressure-type loading which existed during the Blue Gill experiment is given by the results of the F-piston, shown in Table 3.2. These pistons are essentially the same as the A-pistons but protruded above the backplate. A preliminary time-history analysis has been done for these pistons as well as for the A-pistons. The F-pistons read very much less than the A-pistons during the same time period. Furthermore, the F-piston readings are not inconsistent with the D-pistons if there was essentially pressure equilibrium around the piston with the

force on the piston being that due to the area of the shank. In addition, the small readings of the F-pistons unequivocally rule out the possibility that X-rays contributed substantially to the total impulse at B-1.

The implications of this result in the Blue Gill experiment with regard to future thermomechanical effects studies are fairly obvious. In any such material studies, an adequate amount of the same material must surround the sample to eliminate any influence from other materials used in the experiment. There is, as yet, no quantitative definition of an adequate surround size. The criterion of an adequate surround may mean that the entire test vehicle must be coated with the sample material.

A consequence of the fact that all the pistons in the Shot Blue Gill experiment appear to have measured the impulse to reffrasil-phenolic is that all the data can be utilized in the determination of the time history of the thermomechanical loading. Therefore, in all subsequent references to the data with regard to the time history studies, no distinction will be made for materials.

The breakdown of the data in Figures 3.13, 3.14 and 3.15 with regard to the types of piston used for the measurements, is as follows:

The lowest values of impulse were measured by the A type pistons, which possessed the lowest values of $\frac{sm}{A_h}$, and thus were the fastest responding type of piston. The A-piston data fall within the range of $\frac{sm}{A_h}$ from the lowest values shown up to about five or six, with A-1 pistons representing the lowest values, A-3 the highest values, and A-2 in between (see Table

2. 1). The next data to be found, according to ascending values of $\frac{sm}{A_h}$, are the C-1 pistons which occupy the range of about eight to ten. These are the C-pistons with the smaller piston-to-anvil spacing. These pistons should have responded somewhat more slowly than the A-pistons and thus been able to measure more impulse than the A-pistons if the loading pulse duration extended beyond A-piston response times. The next data points, which fall in the $\frac{sm}{A_h}$ range of about 35 to 40, are the C-pistons with large piston-to-anvil spacings. The increased spacing means a longer time to respond than the C-1 pistons and, thus, the capacity to measure additional impulse if the loading pulse lasts longer than the C-1 piston response time. Finally, at the top of the $\frac{sm}{A_h}$ scale are the D-pistons which are characterized by values of about 90. As the slowest responding, the D-pistons should measure the largest values of impulse of all the pistons.

The fact that the slower responding pistons did indeed measure progressively higher values of impulse is most evident in the pod B-1 data. Except for the D-piston data, this trend is less evident for pod B-2 data and almost non-existent for pod B-3 data. The abrupt increase in impulse level between the C-2 and the D-piston data, which is characteristic of the data of all the pods, strongly suggests an additional influence on piston response. This indication supports the idea that pressure existed on the undersides of the heads of the A- and C-pistons and thus affected the measurements.

It should be mentioned that the A-3, C-1 and C-2, as well as the D-pistons, were originally thought of as total-impulse pistons. That is, their response times, based on the hypothesized

pulse, were relatively long. The possibility of a longer pulse was recognized, but compromises in the design had to be made between totality and sensitivity to ensure that some data would be obtained if inputs were low. The measurement of total impulse due to thermomechanical loading for a given material can be defined with certainty only through the use of a number of pistons with a large range of time responses to provide for wide ranges of load intensity and duration. This is tantamount to requiring a time history for each material.

If the data from all classes of pistons used in the experiment were considered to be reasonably accurate representations of the actual thermomechanical impulse, it would be a simple matter to compute the time history of the loading according to the relationships developed in Appendix E. The analysis of force time history is quite sensitive to the basic data (the impulse integral vs. impulse curve), however, so that inaccuracies in these basic data tend to distort the resulting time history. The strong possibility of pressure under the heads of the A and C-pistons therefore makes the direct application of the time history analysis to the entire group of impulse data premature.

Evidence has already been presented to the effect that pressure existed on the underside of the A and C type piston heads. It is worthwhile, however, to point out further that the time necessary for refrasil-phenolic vapor to travel from the surface of the backplate to a point beneath the piston heads is small compared to the fastest A-piston response time. On an A-piston, for example, this distance is in the neighborhood of 1.5 cm. With gas moving at a velocity of 4.5×10^4 cm/sec (sonic speed of CO_2 vapor at 1000°K), the time required to cover this distance is only 30 microseconds. This is small compared to the several

hundred microseconds that elapse before the fastest A-piston reaches its striker. Furthermore, the actual time for this gas motion is probably much less for two reasons. One is that the gas might be at higher temperature, and the other is that the expansion of gas around the piston head probably results in supersonic flow.

One fact is clear. A force time history based on data which corresponds to net impulse would represent only a portion of the actual thermomechanical loading. Such information is valuable, however. At the very least, such a force time history can be regarded as a lower bound and, in the absence of better time history definition, a first approximation to the thermomechanical pulse.

Calculation of this lower bound time history has been carried out based on the impulse data of the A type pistons. Since the pressure effects on the A- and C-pistons are not known quantitatively, there is no way of knowing exactly how the impulse to each type of piston was affected. Because of differences in geometry, it is quite likely that the A-pistons measured one fraction of the loading they would have sensed in the absence of the back-pressure effect, while the C-pistons measured another fraction. These measurements, in effect, would belong to two different pulses, and to combine these two types of data in one time-history calculation would not be correct. The A-piston data were selected for this study since these pistons were the fastest responding and could better define the earlier portions of the pulse.

The impulse integral vs. impulse data upon which this time history calculation was based for the B-1 pod is presented in

Figure 3.16. The curve drawn through the data in Figure 3.16 approximates the path of the mean of the data. A smooth curve is drawn based on the belief that no discontinuities occur in the regions between the data. It is drawn from the origin to the first data point with the following assumptions:

$$\left. \begin{aligned} sm_p/A_h &= 0 \\ j(t) &= 0 \\ d \left(\frac{sm_p}{A_h} \right) \\ \frac{d [j(t)]}{dt} &= 0 \end{aligned} \right\} \text{ at } t = 0$$

These assumptions can be shown to exclude only one functional form, that is, the form which represents infinite force at zero time.

The force time history was developed from the curve in Figure 3.16 according to the method described in Appendix E. The results of this analysis are presented in Figure 3.17, labeled "MEASURED". In connection with this figure it should be noted that one sea-level atmosphere (about 10^6 dyne/cm²) on the pod backplate—and no external pressure elsewhere—corresponds to a rigid-body pod acceleration of 21 g's.

A method of correcting this force time history to account for the back-pressure effects on the pistons and thus obtain a better estimate of the true thermomechanical pulse has been developed. The basis for this technique stems from the fact that hot vapor travels the distances involved so rapidly (as has been demonstrated above) that the underside pulse is virtually in phase with the above-piston pulse. It is also based on the assumption that the pressure distribution on the underside of the piston does not change — i. e., the mean value

varies in direct proportion to the pressure above the piston. This is certainly a reasonable supposition if the flow is supersonic. Thus, the net force measured by the piston varies in proportion to the force that would have been measured with zero back pressure. In equation form, this may be written for the A-piston, which has a head area 16 times that of the shank, as:

$$\begin{aligned}
 p_n &\approx k \left[\frac{1}{16} p_a + \frac{15}{16} (p_a - p_b) \right] \\
 &\approx k \left(p_a - \frac{15}{16} p_b \right) \approx k (p_a - p_b)
 \end{aligned}
 \tag{3.1}$$

where:

- p_n is the net pressure measured by the piston
- p_a is mean pressure on the underside of the piston head
- k is a constant of proportionality

The assumption that the net forces measured by the A-pistons are directly proportional to the actual forces applied to the upper surface of the piston means that a force time history based on the A-piston data has the same shape as the actual thermomechanical pulse. A measure of the thermomechanical force time history is thus obtained by correcting the level of the forces (but preserving the shape) so that the area under the curve represents the measured value of total impulse. The values of total impulse are taken as those measured by the D-pistons, which were unaffected by any pressure under the backplate and were sufficiently slow in their response to have measured the total impulse developed by the thermomechanical loading.

Such an analysis was performed for the B-1 pod data, and the results are shown in Figure 3.17. The corrected curve was

obtained by multiplying the uncorrected force time history by the factor k necessary to yield the total impulse measured by the D-pistons in pod B-1. The numerical value of k is approximately 2.5. According to the above equation, this value of k implies that p_b is about 60 per cent of p_a . This is a reasonable level for p_b and compatible with the experimental evidence presented earlier on gas flow through the backplate. It is interesting to note that, on the basis of the estimated thermomechanical force time history, the D-piston records at approximately 9 milliseconds. This time history is appropriate to such an estimate since, as mentioned above, the D-piston experiences no back-pressure effect. The corrected curve of Figure 3.17 has been transposed back to Figure 3.13 to show its relation to the data points.

It should be pointed out that the earliest datum of Figure 3.17 corresponds to a time of approximately 0.25 msec. Prior to this time, only the impulse, or integral of the force time variation, is known. In Figure 3.16, this datum can be seen to be at an impulse (uncorrected data) of about 2.4×10^3 dyne-sec/cm². If the pressure were constant over earlier times, it would have to be about ten sea-level atmospheres in order to yield the appropriate measured impulse, as indicated in Figure 3.17. In the estimated thermomechanical pulse, the corresponding constant pressure would be in the neighborhood of 25 atmospheres, and the adjusted impulse would be about 6×10^3 dyne-sec/cm². Since the force per unit area is below the average at 0.25 msec, the maximum pressure must be greater than 25 atmospheres.

Lower bound time histories for all three pods are presented in Figure 3.18. The impulses which are developed prior to the first data point are indicated for each curve. The B-2 and B-3

curves of Figure 3. 18 were derived in the same manner as that of B-1. It is obvious from these plots that the thermomechanical pulse shape may well be the same at all three pod stations. From Figures 3. 14 and 3. 15 it is possible to see that the A-piston data ($sm_p/A_h < 6$) become more vertical on pods B-2 and B-3; this is because the lower impulse level means longer integration times for the pistons. These longer integration times imply that the earliest reading pistons see more of the total pulse and, hence, are able to discern less of its shape.

A sense of pulse shape is given by the data in the following table:

Uncorrected Impulse Levels Developed to Indicated Times (units of 10^3 dyne-sec/cm ²)		
<u>Pod</u>	<u>t = 0.5 msec</u>	<u>t = 1.0 msec</u>
B-1	2.8	3.2
B-2	1.7	2.0
B-3	1.1	1.2

Over 80% of the impulse is seen to occur at very early times.

A point which should be noted is that the contact times of the piston-striker collisions may not be negligibly small compared to the earliest reading A-pistons. These times are at least tens of microseconds and may be 50 to 100 microseconds. Such times can represent significant uncertainties in the early data region shown in Figures 3. 17 and 3. 18.

It should be noted also that straightforward application of the time history analysis to the Blue Gill data in Figures 3. 13, 3. 14 and 3. 15 predicts force time histories which include a second pulse at very late times (> 10 msec.). Thus far, no other data found on the pods support the existence of a second pulse. The interpretation

presented herein appears the more reasonable because of the strong evidence of blow-in described previously. It is conceivable, of course, that data from other projects may support the possibility of the second pulse.

Backplate Contour Measurements. The high level of impulse (as indicated by the D-piston data) to the pod suggested the possibility of measurable permanent deformation of the aluminum backplate. A rough indication of the energy available to cause such damage is given by

$$E = \frac{J^2}{2m} \approx 2.3 \times 10^7 \frac{\text{ergs}}{\text{cm}^2}$$

where the impulse J and mass m are both per unit area. The mass considered here is the thin outer rim and includes the contribution of the refrasil-phenolic cover. An estimate of the energy necessary to strain the aluminum backplate to the yield point is given by

$$E = \sigma t \epsilon = 7.5 \times 10^6 \frac{\text{ergs}}{\text{cm}^2}$$

where σ is the yield stress, t is the thickness at the rim, and the strain ϵ is taken as σ divided by Young's modulus. This energy must, of course, be exceeded to produce permanent set in the material. A comparison of the energy available with that required indicates that permanent deformation might be expected. However, the situation is more marginal than this comparison indicates, because the strength of the refrasil-phenolic cover and of the supporting flare below the backplate is not accounted for, and the impulse at the backplate rim may have been less due to three-dimensional effects about the edge.

A series of measurements was made in an attempt to determine the post-experiment shape of the pod backplates. These were measurements of surface position taken on the bottom (uncovered)

or top (through specially drilled holes in the refrasil-phenolic cover) side of the aluminum backplate. They were made chiefly in the vicinity of the rim where the backplate is most likely to be deformed, since it is thinnest in this area and is supported locally in an unclamped fashion (by the pod flare). Data surveys of this type were made on the B-1, B-3, and K-1 pod backplates and on one backplate that was not used.

Unfortunately, the backplate contour data are not very conclusive. The B-1 backplate, which experienced the greatest impulse, showed some differences from the unused and B-3 backplates; these latter two were very similar to each other. These apparent differences occurred in areas where they would be predicted due to thermomechanical loading. The most distinctive such area was where the umbilical cable cluster entered the pod. This cluster was thick so that it did not fit well into its cutout in the flare and, therefore, provided slight local support for the rim. The data indicate a slight peak in the contour which could be the result of the plate locally forming about the hump created by the cable cluster. There are no hold-down bolts in the immediate vicinity which could cause this effect.

Another area, which gave measurements indicative of deformation, was one of the large bays between NDL instrument covers (see Figure 2.18); these covers provided increased local protection. The bay was, therefore, a relatively weak area between strong areas. The rim region in this bay exhibited a very slight downward curvature.

These are the only indications of deformation on pod B-1 worthy of mention. The King Fish pod 1 backplate did not show any evidence of deformation.

3.2.2 Spall Gages. The spall gages in pods B-1 and B-3 were recovered essentially intact. The gage in pod B-2 was

lost. The gage in pod B-3 was unaffected beyond the removal of the lead foil covering over the cylinders. In B-1, there was evidence of softening and minor ablation of the plastic in addition to the complete removal of the lead. All plastic cylinders remained clear with the exception of that under the largest aperture. Figure 3.19 is a photograph of the disassembled gage and of this cylinder. Within the cylinder are several unidentified black inclusions. Also prominent is an apparent fracture which can be seen in the photograph. This fracture occurs over less than one-half the cross-sectional area.

3.2.3 Ablation Measurements. It was noted in Section 3.2.1 that the Blue Gill experiment took place in an environment of the vapor emanating from the refrasil-phenolic of the pod backplate. This conclusion was based on the fact that the indent recorder data exhibited no consistent variations which could be attributed to the material exposed on the piston heads. Furthermore, the energy penetrating to the surface of the pod was substantially less than would be expected on any simple theoretical basis, as will be shown in later sections. In addition, some instruments exhibited spatial variations in intensity which can only be explained on the basis of opaque vapor. These factors indicate strongly that the entire backplate was immersed in a rather opaque environment characteristic of the vaporization of refrasil-phenolic. The ablation measurements for refrasil-phenolic, which are presented in this section, therefore are the only values which represent valid ablation data. The other materials reacted to radiation transmitted by the refrasil-phenolic vapor layer. The response of another material in its own environment may be entirely different.

In accordance with the above remarks, the Blue Gill ablation data, presented in Table 3.4, primarily concern refrasil-phenolic. Data for other non-metals are included only to illustrate that their

behavior was not drastically different. The various sources of ablation data are discussed in some detail below.

Piston Sample Dimensions.

Although the ablation of reffrasil-phenolic was small in terms of weight change, it was nevertheless large enough dimensionally to be readily observable and measurable. Such measurements constitute a reasonable basis for estimates of ablation.

An A- and an F-piston sample from pod B-1 were cross-sectioned and polished for examination by a metallograph. This examination revealed a distinct and well-defined layer of charred material beneath which the reffrasil-phenolic appeared to be essentially unaffected. The depth of this charred layer was measured along with the location of the present surface. These measurements are depicted graphically in Figures 3.20 and 3.21. It is likely that edge effects, which were apparent in the surface data, were also responsible for an unclear charred layer depth near the edges; this area was not included in the measurements. Away from the edges it is obvious that the data are quite uniform and can be taken to indicate the area of one-dimensional behavior.

The estimates of ablation in Table 3.4 are based on the mean of the data on surface position* and charred material depth. The lower bound figures are based on the surface data only. That is, the ablation is assumed to be the product of the original density and the distance from the original surface to the post-test (present) surface, which implies that the density of the remaining material (including the charred layer) is unchanged from its original value. The upper bound figures in the table are based, on the other hand, on the assumption that the density of the charred layer is zero. In this case the material

* Surface data were used only where charred depth data also existed.

lost is the product of the original density and the distance from the original surface to the bottom of the charred layer. The appearance of the material in the charred layer, as expected, suggests that the true value is near the lower bound. The uncertainties quoted in Table 3.4 are the standard deviation (standard error) of the mean of the data. These uncertainties include the effects of possible variations in the position of the original sample surface, material density (measured from the weights and volumes of 10 unexposed samples), and size of the exposed area. The uncertainty in original surface position and exposed area were derived from measurements of typical unexposed samples and consideration of manufacturing tolerances.

Piston Sample Weights.

In anticipation of their use for ablation measurements, all piston samples were weighed prior to the experiment. A selection of samples recovered in good condition permitted ablation estimates to be based on their changes in weight. The data are given in Table 3.4 wherein each entry corresponds to one piston sample.

The range of an individual datum is the result of two sources of uncertainty. One is the possible variation in exposed area (a few percent) permitted by manufacturing tolerances. The other concerns the post-experiment weight measurement. In the process of separating a sample from the recovered piston, a slight weight loss nearly always occurred according to the pre-disassembly and total post-disassembly weight measurements. Since this weight loss came from either the piston or the sample, it must naturally increase the uncertainty in the weight change of the sample. This uncertainty was about ± 1 milligram in the individual weight measurements, which is unimportant relative to the values in the table.

No estimate is given of the errors that might exist as a result

of the absorption of atmospheric moisture and sea salts. A comparison with the piston sample dimension data (pod B-1), where such absorption is not involved, indicates that the uncertainty due to absorption certainly does not overshadow the data. In this regard it should also be mentioned that the data from the aborted shot (June 3, 1962) represent upper bounds on sea salt and moisture absorption. That is, from visual examination it appears that material ablation due to re-entry heating was very small, and there was, of course, no weapon input. Therefore, any positive change in weight would presumably be due to the retention of sea salts and/or moisture. Unfortunately, it is obvious that the aborted shot samples absorbed some of the oil with which the pistons were coated to prevent corrosion. Therefore, weight gains may be due to the absorption of oil as well as (or instead of) sea salts and moisture.

Ablation-Condensation Gage.

The primary instrument designed to measure ablation was the ablation-condensation gage. All of the gages in pods B-1 and B-3 were recovered in good condition; in pod B-2, only a very few gages were either missing or damaged to the point of being unreadable.

The measured weight changes per unit area of exposed surface for the refrasil-phenolic, micarta, black phenolic, iron devcon, teflon, and parallel pyrographite samples are listed in Table 3.4. The data from pod B-2 of the aborted Shot Blue Gill are included for reference (see Appendix C). For all samples, the data corresponds to the difference between the average of several post-test weighings and one pre-test weighing. The differences between the original measurements and those taken after the event are not sufficient in themselves to allow precise deductions about ablation for two reasons. First, edge chipping and delamination of the plastic samples introduce significant errors. Second, mass losses were small, and a substantial

fraction of the change in a sample weight may be caused by factors other than the input. Considerable analysis and re-enactment of their history would be necessary to determine precisely these uncertainties. This sort of program has not yet been undertaken; Appendix G describes some first effort in this direction. In any data analysis program a more comprehensive study would have to be undertaken on selected materials to correct the apparent weight losses for spurious inputs.

The major uncertainties are the effects of ambient moisture and the immersion in sea water during recovery. The effects of sea water immersion are water and salt absorption for the composite materials (and corrosion for the metals). Less important uncertainties are the effects of the atmospheric gases on heated samples during the re-entry of the pods. For the refracil-phenolic and micarta the estimated uncertainty is $\pm 15 \text{ mg/cm}^2$.

As noted before, composite samples other than refracil-phenolic are included for comparative purposes. Their ablations are not drastically different from that of refracil-phenolic. Their data may possess reasonable validity because the vapor they would create would probably be reasonably close to that of refracil-phenolic, particularly since the silica of the latter may not have participated heavily in the ablation process (see below for further discussion). The data for pyrolytic graphite are listed only for the parallel orientation where the values are probably accurate to $\pm 1 \text{ mg/cm}^2$ because of the inherent stability of the material (see Appendix G). An uncertainty of $\pm 1 \text{ mg/cm}^2$ also applies to teflon, as it has very small absorption properties. For black phenolic the estimated uncertainty is $\pm 20 \text{ mg/cm}^2$. As shown in Appendix G, the iron-devcon is relatively resistant to moisture absorption, so that its estimated uncertainty is probably about $\pm 10 \text{ mg/cm}^2$. As noted previously, a laboratory program would be required to decrease these uncertainties and to correct the data for spurious inputs.

Estimates of ablation were also made from volume measurements; these disagreed markedly, however, with those from weight measurements for the composites (refrasil-phenolic, micarta, black phenolic). This disagreement is ascribed to the fact that some of these materials swelled slightly, and in addition, the char volume is of somewhat lower density than the unaffected material.

Table 3.4 also includes data on refrasil-phenolic ablation obtained by cutting out and weighing identically shaped plugs from closely adjacent exposed and shielded sections of the pod backplate. These data are labelled "plugs". The purpose of the plugs was to provide a direct comparison between identical materials where both samples had experienced identical environments except for exposure to the burst. The estimated weighing and measuring uncertainty in the measured plug weight losses is $\pm 1 \text{ mg/cm}^2$. In the case of pod B-3 this uncertainty does not reflect the probable error in the weight losses because of the prior history of the backplate. This backplate was re-used from pod B-2 of the aborted shot so that prior to final use it had already received a very light char which had been locally removed by sanding. In this aborted shot it had also been immersed in sea water, which probably accounts for much of the weight increase listed for the aborted shot samples in Table 3.4. The comparatively large scatter and low ablation values are undoubtedly a result of this prior history.

Although the uncertainties are in general a large percentage of the weight loss, it is interesting to note that there is very consistently and closely a 2 to 1 ratio in the weight loss from pod B-1 to B-3 (except for the refrasil-phenolic plugs and pyrographite).

Appearance of the Samples. All of the samples were examined on disassembly of the gages at the test site. Their appearance at this time was already the result of exposure to the test environment, immersion for several hours in sea water, and partial air drying for

several days. External surfaces appeared to be covered with a slight salt deposit, and many of the metallic materials showed some corrosion. Immediately after this initial examination, the samples were cleansed by 1.) soaking in a one-percent solution of Oakite 202 for ten minutes, 2.) soaking in tap water for twenty minutes, 3.) rinsing in reagent grade acetone, and 4.) drying in an air oven at 100°C for sixty minutes. On cooling, the samples were sealed in bags with dessicant packs. The cleaning procedure visibly removed the salt deposits but did not otherwise change the appearance of the samples.

Refrasil-phenolic, micarta, linen-filled black phenolic, and iron-devcon charred; teflon remained white although deeply fissured on pods B-1 and B-2. In all gages with refrasil-phenolic samples, the appearance of the refrasil-phenolic was consistent with that on the pistons which had retained their samples. Although charred, the samples were in good mechanical condition. The iron-devcon samples presented a rusty appearance in addition to the char. The perpendicular orientation pyrographite lost material primarily through edge chipping rather than through ablation in pod B-1; on B-2 the sample was severely fractured (probably at water impact); in B-3 any weight loss would be immeasurable since machining marks on the face were still crisp and distinct. In B-1 the parallel sample was in excellent mechanical condition, but the surface was stippled into a shallow cratered pattern; in B-3 the surface had a similar appearance, but the effect was so shallow that machining marks were still visible.

Microscopic examination of the refrasil-phenolic samples showed that most of the samples from the B-1 pod have twenty percent or more of the surface area covered with re-solidified molten glass. The major exception to this is the surface of the 5-mm refrasil-phenolic sample on pod B-1 which had little glass on the surface and suffered a noticeably different ablation.

Because of the generally small mass losses, the initial alternation in the composition of the unused reffrasil-phenolic with depth may account for many of the apparent differences in ablation listed in Table 3.4 . Samples whose surface layers were primarily glass cloth probably ablated at much different rates than those same materials whose exposed surfaces were primarily plastic. The backplate itself probably responded much like the samples where the top surface was mostly exposed glass. This response is illustrated by Figures 3.22 and 3.23 which show the before and after close-up appearance of the backplate. Large mass losses which encompassed the removal of several complete alternating layers of plastic and glass cloth would have cancelled out such differences in initial ablation rates, but large losses of this type did not occur.

The metal samples generally showed indications of melting. The photographs of Figure 3.24 illustrate the appearance of samples of two metals, lead and steel. On all pods, the lead suffered considerable melting and resolidification as can be seen in the figure. In pod B-3 the hole in the lead sample was plugged by the molten sample material. Melting of the steel samples (Figure 3.24) on pod B-1 is evidenced by superficial roughening of the surface; on pods B-2 and B-3 the surface is almost unaffected. The appearance of melting and resolidification was present also with aluminum and silver on pod B-1 except to a much lesser degree than with lead. There was a distinct decreasing progression of the effect on aluminum and silver from pod B-1 to pods B-2 and B-3. The aluminum samples on pod B-3 showed no surface melting effects. In fact, machining marks could still be discerned on the pod B-3 samples. The variation was similar in the case of copper, except that the apparent resolidification was not as distinctive. Zinc in all cases apparently lost material largely due to corrosion.

Surface profiles of many of the samples are presented in Figures 3.25, 3.26, 3.27, and 3.28. Except for the edge chipping and delamination, the composite and graphite samples ablated fairly uniformly. The metal samples which melted were not uniform because of the mass motion of the liquid metal toward the aperture of the collection chamber.

Condensed Products. Detailed analysis of the condensates has not been performed. Such an analysis can be justified only on a selective basis in a data analysis program where such information can conceivably be used in a description of the decomposition process.

The platinum-rhodium liners and end caps were removed from all the gages at the test site a few days after the event and their appearance recorded. Rusting of the internal surfaces of the stainless steel gage body had occurred in almost all cases. This rusting and the salt deposited from evaporated sea water made visual identification of condensed products difficult.

Except on the cases of lead, aluminum, and teflon, large deposits were not seen on the liners. In the case of lead, there was a large lump of resolidified melt in the bottom of the chamber. The deposit in the case of aluminum, probably an oxide, had a fluffy white appearance. The deposit in the case of teflon was black. A large number of liners had faint white deposits covering the bottom portion of the liner for a height of one-half inch to one inch. Many of these deposits were slightly red in color and were assumed to represent salt deposits contaminated with rust. In the same way, many had faint black deposits which could be deposited carbon or platinum black. A cursory attempt was made to examine the balance between weight loss of the sample and weight gain of the liners. In general, there was no inconsistency. In the case of the lead the comparison was surprisingly close in that the weight

gain of the liner was within less than 10% of the weight loss of the sample.

Many of the platinum-rhodium liners on the B-1 pod had elliptically shaped etched patterns due to X-rays illuminating the liner through the aperture. Some of the liners on pod B-2 have faint elliptical areas suggesting this same behavior. No quantitative use has been made of these patterns.

3.2.4 Thermal Pinhole Cameras. The thermal pinhole cameras offered little to external observation. On the three instruments recovered with pod B-2 and on the entire array of seven on pod B-3, there were no discernible external effects on the detector elements. All detectors on these gages were of low carbon (nominal 1020) steel. In pod B-1, where all seven gages were also recovered, the most obvious effect was found on the gage with flush detector elements. The top detector in this gage was pockmarked in a manner similar to the steel ablation-condensation samples, while the side elements were relatively unaffected except by rust. None of the other side elements were visibly affected. The top elements in the instruments on pod B-1 had stippled circular areas on their surfaces, which appeared to be of the same approximate size as their apertures but which were displaced laterally. This displacement was consistent with other orientation indications on the backplates. These stippled areas represent resolidified melt.

In order to determine the intensities incident on the three pods, the detectors were examined using standard metallurgical laboratory techniques. Appendix H describes in detail the techniques used to extract the data. These detectors were situated behind apertures of 1, 3; and 10-mm diameter at a focal length of 1 cm measured from the top of the micarta cover to the detector surface.

Sections in the plane of the burst through the gage surface were examined metallurgically. Figure 3.29 illustrates the orientation and location of metallurgical data on the sections examined. Two types of detectors were used in the thermal pinhole cameras; slotted and unslotted. The purpose of the slots was to detect, by means of transformations in the steel, any effects produced by indirect thermal heating from hot gases entering the aperture. Since part of the slot was shielded from direct exposure to X-ray and thermal radiation from the burst, any transformation along the shielded portion of the slot would have been from exposure to indirect thermal inputs. On none of the gages examined were any transitions observed in the slots.

A microscopic examination of a metallurgically prepared cross section confirmed that these exposed surfaces melted and also revealed a solid-state transformation of pearlite to martensite below the melt layer. Figures 3.30, 3.31, 3.32, and 3.33 are graphical representations of the complete set of data abstracted from the 1-mm, 3-mm and 10-mm aperture instruments on pod B-1. The data include the depths of material removed, resolidified melt, and pearlite-to-martensite (P-M) transition from the original unaffected surface of the detectors. The data presented in Figure 3.34 were abstracted from two affected portions of another gage. This detector was located behind ten 1-mm apertures (two rows of five). Melt was observed at all ten expected locations on the surface of this detector.

Side detectors on the pod B-1 pinhole cameras were also examined. Detectors behind 1- and 10-mm apertures in the direction of the burst and one behind a 10-mm aperture oriented away from the burst were sectioned and examined. These had no evidence of any transformations.

The four 10-mm detectors on pod B-1 which were flush with the surface of the micarta cover were cross sectioned and examined. One was on the top of the thermal camera, while the other three were on the side. One of the side detectors was almost in the burst azimuth; another was facing away from the burst; the third gage was facing a direction about at right angles to the burst azimuth. A microscopic examination of the latter showed a solid transformation on only the top corner of the detector. Figure 3.35 is a photo-micrograph of this transformation. A microscopic examination of the gage facing away from the burst showed no transformation in the steel. The surface of the top flush detector was very rough in appearance. A section through the center of this detector revealed layers of resolidified melt and a solid state transformation. Figure 3.36 shows cross-sectional photomicrographs of the exposed surface. Figure 3.37 shows a detailed graphical representation of the data abstracted from this instrument. These measurements were made from an arbitrary reference surface, because the entire detector surface was exposed and the original surface completely obliterated. A macroscopic examination of the side flush gage facing the burst showed no signs of surface melting. A cross-sectional view through the center confirmed this observation. However, a solid state transformation was evident. The depth of transition decreased from a maximum at the top of the detector (farthest away from the backplate) to zero at approximately 1 mm from the bottom of the detector (nearest the backplate). Figure 3.38 presents a detailed graphical representation of these data.

A visual examination of the steel detectors in thermal pinhole cameras on pods B-2 and B-3 showed no signs of melt. However, some of these had rusted significantly. It is possible

that this rust may have removed some resolidified material at the surface.

A cross-sectional examination of the top detectors behind 1-, 3, and 10-mm apertures on pod B-2 and pod B-3 did not reveal any evidence of melt. A solid state transformation however was found in the detectors beneath the 10-mm apertures on both pod B-2 and pod B-3. The other thermal cameras on these pods showed no observable transformations beneath the surface. Depth measurements of the solid state transformation in the detector on pod B-2 are presented graphically in Figure 3.39. The surface of this gage did not rust. Figures 3.40 and 3.41 show a graphical representation of the data abstracted from the 10-mm recessed and flush detectors on pod B-3. The removed material could be the result of salt water corrosion. None of the side steel detectors examined from thermal pinhole cameras on pod B-2 or pod B-3 showed any evidence of melt or solid state transformations.

The following table summarizes the instruments which have been examined and which possessed data and also gives the figure number where these data are presented.

<u>Pod</u>	<u>Aperture Size (mm)</u>	<u>Figure No.</u>
B-1	1	3.30, 3.34
B-1	3	3.31, 3.32
B-1	10	3.33
B-1	Top Flush Detector	3.37
B-1	Side Flush Detector	3.38
B-2	10	3.39
B-3	10	3.40
B-3	Top Flush Detector	3.41

3. 2. 5 Cut-Off Filter Spectral Gage. None of these gages remained on pod B-2. All were intact on pods B-1 and B-3. The filters were examined in considerable detail, since their condition can provide qualitative explanations for the response or lack of response of the detectors. Table 3. 5 presents the results of this examination. At this time the fracturing observed is thought to be due primarily to thermal shock. This is borne out by the fact that Al_2O_3 was substantially less affected than fused quartz, presumably because the former has much greater thermal shock resistance than the latter with roughly comparable transmissibility. The table treats only the first filter; except as noted, the second filter was unaffected. A TiO_2 filter is shown in Figure 3. 42.

Spectral information was sought from detectors of low carbon steel and bismuth-tin alloy behind filters by metallurgical examination (see Appendix H for a detailed discussion). The steel detectors have a nominal 1020 steel composition while the bismuth-tin material (3 per cent tin by weight) is a eutectic-forming alloy.

No steel detectors on any of the pods showed any evidence of melt from a macroscopic examination. In several cases this was verified by a microscopic examination. This examination also showed no evidence of a solid state transformation at or beneath the surface.

A macroscopic examination of the bismuth-tin detectors in both pods showed evidence of eutectic melt at the surface. The eutectic in this alloy melts at 139°C . Appendix I describes the phase transformations in this and other materials used in the experiments. Figure 3. 43 is a photomicrograph of the surface of a bismuth-tin alloy behind a fused quartz filter (3-mm-diameter aperture) on pod B-1. In this detector the surfaces of some of the eutectic are raised, presumably due to melting, surface tension effects, and resolidification

accompanied by a permanent density change. The raised and curved surfaces associated with the resolidified eutectic alloy are readily seen using slant lighting; Figure 3.43 represents an attempt to show this effect. A microscopic examination of the cross-section of one of these bismuth alloy detectors revealed no visible depth of eutectic melt. This can be explained in part by the fact that when the eutectic melts and resolidifies it has approximately the same structural appearance as the unaffected eutectic in the alloy. There was no evidence of the matrix material having melted.

On pod B-3 the TiO_2 filters beneath the 3- and 10-mm apertures showed signs of melting, i. e., black material with some flow lines and curved surfaces. Titanium dioxide melts at a temperature of 1833°C . The TiO_2 filter beneath the 1-mm aperture shows a small transformed region which is brownish in color. This has been assumed to be the solid state transformation occurring in TiO_2 at a temperature of 642°C .

3.2.6 Reflective Coating Spectral Gage, While no instruments were recovered on pod B-2, all appeared to be undamaged on pods B-1 and B-3. In pod B-1 the flush bismuth-tin detector element and the bismuth-tin detector element beneath the 1-cm aperture melted very heavily and resolidified in an irregular shape. The bismuth-tin elements which were gold-blackened showed no particular difference from those that were not coated. All steel detector elements were similar in appearance except for some variation in the degree of rust. The areas illuminated by X-rays in the pod B-1 instruments were stippled in a manner typical of other exposed steel detectors. No meaningful differences in melt appearance could be noted among the detectors with different coatings.

In pod B-3 the flush bismuth-tin element again gave the

molten/resolidified appearance, but in a relatively smooth symmetrical pattern. Below the 1-cm aperture the bismuth-tin element had melted in a circular pattern. The gold-blackened bismuth-tin again showed no apparent differences from the uncoated detector. As noted in Section 3.1.4 the bismuth-tin detector element within the 1-mm aperture displayed an area which differed slightly from its surround. This area was used to derive approximate orientation information for pod B-3. The steel detector elements were examined and appeared unaffected except for some rusting.

A macroscopic surface examination of the steel detectors revealed that the reflective silver coatings on pod B-1 melted in a striped pattern corresponding to the laminated structure of the micarta heat shield. The melt was probably produced from heating by X-ray shine-through in the micarta cover. Figure 3.44 presents photographs of these detectors with the striped melt pattern. The X-ray shine-through is further verified by the fact that plastic spacers and the aluminum side walls produced shadows on the gage surface. These shadows are clearly seen in the lower photograph of Figure 3.44 .

The steel detectors were intended to be of nominal 1020 steel composition. However, a microscopic examination of these gages revealed a grain structure near the recording surface comparable to a much lower carbon content steel. The region of interest showed a deficiency (in size and quantity) of pearlitic grains and increased the difficulty of recording the depths of the solid state transformations experienced by these gages. Figure 3.45 shows a graphical representation of the data from a steel detector (pod B-1) with no reflective coating (10-mm diameter aperture). Figure 3.46 presents a photomicrograph of a typical

section of this gage. This detector exhibited the best data of those examined from these instruments. The method for determining the transformation depths in this gage consisted of measuring the depth to a completely transformed pearlite to martensite grain (from the original surface) and the depth to the first observed untransformed pearlite grain vertically beneath the transformed grain. The true transformation depth must be somewhere between these two bounds. In many instances the pearlite grains were so small that they could not be distinguished from impurities within the alloy. There were only six partially transformed pearlite grains through the entire affected region of this sample. Data could not be abstracted from any of the other steel gages with this technique, since the pearlite grains were not distinguishable.

A macroscopic examination of the bismuth-tin alloys (3 percent by weight tin) disclosed evidence of surface melt in all these gages from both pods. The depth of melt was measured from a metallurgical cross-section through the center of the irradiated region. The depth measurements were made from the back surface of the detector, since most of the top surface had melted. Figure 3.29 is an illustration describing the orientation and location metallurgical data on the sections examined. Figures 3.47, 3.48, 3.49, 3.50, 3.51, 3.52, 3.53, 3.54, 3.55, and 3.56 show graphical representations of the depth-of-melt data abstracted from these gages: Figure 3.57 is a photomicrograph of a section through a flush bismuth-tin detector from pod B-1. The bismuth-tin detectors behind 1-mm apertures on pod B-3 appeared to have eutectic melt at the surface but no matrix melt. These detectors were not metallurgically sectioned, since the depth of eutectic melt alone is difficult to detect from a cross-sectional view. The eutectic melts at 139°C under equilibrium conditions (see Appendix I).

3.2.7 Long-Time Thermal Gages. All of the long-time thermal gages on pods B-1 and B-3 were recovered in good condition. The detector element was missing from the single gage recovered on pod B-2. The gages from pods B-1 and B-3 were partially disassembled and cleaned in the field. Disassembly was limited to removal of the heat sinks from the gages and did not include opening the heat sinks themselves.

The heat sink surfaces exposed to the burst were examined before the gages were opened. Since these surfaces were polished to within several microns beforehand, it was not difficult to recognize changes in them. It was obvious, for example, that none of the steel and copper heat sink surfaces melted on pod B-3. On pod B-1 the exposed surfaces of both the copper and steel heat sinks melted in the flush geometry gages. In the recessed geometry configuration, however, both steel and copper melted from direct exposure but not when shielded by a quartz filter. The appearance of the surfaces was similar to comparable ablation-condensation gages.

Subsequent to opening, representative portions of the long-time thermal steel heat sinks (flush, recessed, recessed filtered) were cross-sectioned and polished for metallurgical examination. The observed melt and P-M transformation depths agreed well with the data from the thermal pinhole camera. That is, the flush and recessed geometry data were essentially the same as that obtained from the flush and 3-mm aperture pinhole camera detectors, respectively. This agreement increases confidence in the foil melt depth measurements.

The steel beneath the quartz filter in the recessed gages revealed no martensitic layer. All of the quartz filters were covered with a faint black coating. This coating is believed

to be a soot deposition from the blowoff of either the micarta box-car body or the refrasil-phenolic backplate of the pod. The pod B-1 filters were more heavily coated than those of pod B-3. It is recognized that this coating could have significantly attenuated the thermal input.

The heat sinks had to be opened with considerable care since the foils were quite delicate and corrosion and melting tended to cause mating surfaces to adhere. In addition, the platinum protective sheaths sometimes work-hardened into awkward configurations from the bending which could not always be avoided in the opening procedure. Typical examples of foils in opened gages are shown by the photomicrographs of Figure 3.58. These photographs clearly show that melting was reasonably uniform. Bearing in mind that the foils are about 0.25 in. wide, it can be seen that the melt depths are appreciable. It can further be seen (Fig. 3.58) that the tin foil melted to a greater depth than the lead foil within the same gage which is consistent with the difference in melting point.

Unfortunately, the aluminum and polystyrene foils did not yield usable data. The aluminum foils were so severely corroded that no melt line could be found. The polystyrene foils had responded in an easily visible manner. In the heated condition, they had flowed into a greater width near the exposed end, and the scribe line (and surface scratches) became less distinct at about the same depth. These changes were relatively gradual. It was obvious that the polystyrene had flowed through a combination of temperature and the unknown pressure exerted on them by the fastening screws and thermal expansion of the heat sinks. Information on the polystyrene foils is therefore not included in this report.

Good data were obtained from the lead, tin, and gold foils. The melt depth measurements are presented in Table 3.6. The tin and gold foils possessed more distinct and uniform melt lines than did the lead. The measurement uncertainty (reading resolution) of the data is within ± 0.001 in. The true inaccuracy of the melt depth measurements, however, is more a function of the error in the estimated position of the original surface, especially in the cases where the heat sink surface melted. In these worst cases it is believed that the data could be in error by as much as several thousandths of an inch.

In summary, the long-time thermal gage apparently functioned as designed. In particular, the lead, tin and gold foil melt depth data yield an internally consistent set of measurements. The thermal inputs derived from these measurements are presented and discussed in detail in Section 3.2.10.

3.2.8 X-Ray Pinhole Camera. The X-ray cameras in Blue Gill were recovered in excellent mechanical condition. The orientations of the two pods were such that only a small fraction of the pinholes illuminated the film plates in each camera. In the case of Blue Gill pod B-1 only two images were found—both in lead. Their locations are shown in Figure 3.59. The orientation of the pod (Section 3.1.4) was derived from the location of these images. According to these images, a third image fell on the steel. This one was not visible, however, because the steel was deeply corroded in this area. An attempt to locate this image was made by metallurgical sectioning and polishing, but this proved to be inconclusive.

The two images which were found on B-1 were associated with pinholes of 0.033- and 0.010-cm diameter. Both images are significantly larger than their pinholes. They are in the form of

craters with considerable lead splash around their edges. Figures 3.60 A and 3.60 B illustrate various aspects of the images associated with these pinholes. The relative aperture size is indicated on the photographs. Contour maps of these images are shown in Figures 3.61 and 3.62. Typical contours through the centers of the images are presented in Figure 3.63. These data were obtained by measuring the vertical position of the stage of a metallographic microscope as it was focused on successive positions on the crater surface during a series of traverses. The depth of field at the high magnifications used is only several microns, which is a measure of the uncertainty in the data. The outer limit of a discolored area surrounding the images is indicated in Figures 3.61 and 3.62.

The extent of melt and discoloration, may, with further analysis, yield information of the spatial variation of intensity. Much of the roughness within the craters is probably haphazard re-solidified melt rather than a reflection of source details.

In the case of a finite size pinhole, a dimension at the source location is related to a dimension on the image very closely by the relation

$$D = \frac{R}{f} (i - d)$$

where:

- D is a dimension at the source location
- R is the range to the source from the pinholes
- f is the focal length of the camera
- i is a dimension on the image
- d is the pinhole diameter

The one-meter scales shown on Figure 3.63 result from the above relation, using the range to the burst from pod B-1 as 3,280 feet. It

may be seen that the two images are very consistent in dimension and that one meter is a reasonable characteristic dimension of the source. The edge of the source corresponds, of course, to the reading threshold of the detector, which in this case is about 0.05 cal/cm^2 . The X-ray source is certainly not larger than the five-foot diameter of the copper heat shield of the R/V, since a source of this size would produce an image 1/3 greater than observed. Moreover, there is no evidence to indicate that there was a high intensity halo which might be expected if the source were visible beyond the heat shield.

In the pod B-2 camera, two craters were found in lead in the locations shown in Figure 3.64. Both correspond to pinholes of 0.100-cm diameter. An aperture of this size is such that a point in the film plane when projected through the aperture would see everything within a source 4.6 meters in diameter. Moreover, from Figure 3.65 it can be seen that the crater diameter is very close to the diameter of the aperture. It seems clear, therefore, that true images were not formed in the lead in pod B-2. Other pinholes illuminated steel, but no image was observed because of severe rust. Unfortunately, no image in either camera fell on the mylar, which conceivably would have yielded spatial and/or spectral variations of the source.

A macroscopic examination of the crater on one of the lead samples on pod B-2 confirmed that the surface material melted and splashed. Four parallel sections through the crater were metallographically examined. The measurements through these four sections are shown in Figure 3.66. The examination revealed that some material was removed but that no remaining re-solidified melt layer was discernible. Either the melt layer thickness was very small and irregular and consequently could not be seen after polishing and etching operations, or the structure of the re-solidified melt was the

same as the matrix material making the two indistinguishable.

3.2.9 Photocell X-Ray Detector. All photocell X-ray detectors were removed from the pods in a straightforward manner. The instruments in pods B-1 and B-3 were in excellent mechanical condition. The two instruments in pod B-2 were severely deformed by being crushed between the inner and outer cylinders of the pod. An interrogation with an ohmmeter was made to derive the following relay positions.

<u>Pod</u>	<u>Instrument No.</u>	<u>K₁</u>	<u>K₂</u>	<u>K₃</u>	<u>K₄</u>	<u>K₅</u>
B-1	1200-6	closed	closed	closed	closed	open
B-2	1200-8	open	closed	open	closed	open
B-2	1200-4 (blind)	closed	closed	closed	closed	closed
B-3	1200-7	open	open	open	open	open

These positions were verified by visual inspection of the gages after disassembly.

The behavior of the relays in Instrument No. 1200-8 is consistent with the high lateral g-loads that the instrument experienced at water impact, since the relays were installed in alternating orientations. Both detectors carried by pod B-2 show evidence of extensive mechanical damage: Instrument No. 1200-4 (behind a thick aluminum shield) and Instrument No. 1200-8 (behind a carbon filter) both show indentations in the container, broken photomultiplier tubes, cracked capacitor cases, and shorted wires. The acquired readings are considered unreliable and therefore have not been treated as data. The other instruments, 1200-6 on pod B-1 and 1200-7 on pod B-3 show no evidence of mechanical damage. Therefore, there is no reason to reject the readings of these instruments on the grounds of spurious effects given by high g-loadings.

A dividend of this experiment is the acquisition of data on permanent damage suffered by individual electrical components due to nuclear radiation. It should be emphasized that the possibility of this type of damage was taken into consideration in the design of the experiment so that for proper recording it was necessary only that the passive components survive (see Figure 2.17).

Wherever measurements were possible, the capacitors which had been used (.01- μ f, 3-kv Dearborn 104-3N) were found to have maintained the rated capacity and insulating properties. The leakage current measured on all is less than 0.5 microampere. All resistors (1/4-watt carbon film) retained the original value of the resistance as well as their insulating properties. All photocells (FW 128 ITT) not mechanically damaged were operative. In pod B-2 there were indications that relays had been mechanically damaged so that the contact mechanism was jammed and/or the latching mechanism was inoperative. In all other cases the relays were in operating conditions. All batteries with the exception of the one on pod B-3 were found to be leaking and discharged. This is in most cases due to mechanical damage. In pod B-3 the batteries read 6.75 volts (nominal rating). The conclusion is that all passive components survived with no measurable effects, so that the measurements were presumably not affected by spurious effects due to the nuclear environment.

Damage presumably produced by nuclear radiation was observed in transistors. The performance of four semiconductors was recorded; namely, of the three diodes indicated in the diagram (Figure 2.17) CR-1, CR-2, CR-3 of the 1N645 type, and the germanium transistor VT-3, 80 volts, in the Victory DD8-1 high-voltage power supply.

In both instruments on pod B-2 all diodes except one which

was mechanically damaged were operative and showed a correct back resistance. The germanium VT-3 transistor in the high-voltage power supply in Instrument No. 1200-8 on pod B-2 showed a collector-to-emitter short. The power supply on Instrument No. 1200-4 (also on pod B-2) showed severe mechanical damage, and no measurement was performed on the transistor.

All diodes of Instrument No. 1200-6 in pod B-1 had failed and exhibited infinite resistance. The transistor VT-3 in the high-voltage power supply showed a shorted collector-to-emitter.

In pod B-3 all diodes of Instrument No. 1200-7 showed correct backward resistance, and the transistor VT-3 in the high-voltage power supply was operating correctly.

These measurements show that damage occurred in the semiconductors in the pod nearest to the burst (B-1). In the next pod (B-2) all the diodes were performing correctly, even though one germanium transistor VT-3 had failed. In the farthest pod (B-3) all diodes and the germanium transistor remained intact. It should be possible to correlate this data with radiation levels obtained by Projects 2.1 and 2.2. This correlation has not been attempted.

The data from pods B-1 and B-3 seem to be consistent with proper instrument performance and with the measurement of X-radiation. To fully determine whether the data are consistent with the expected X-ray fluxes at the location of the pods, additional laboratory calibrations to determine absolute response is required. These calibrations have not been performed.

3.2.10 Further Sources of X-ray Intensity Information. To aid further in calculation of X-ray intensities, two X-ray-irradiated areas on the aluminum retainer plate on the top of cluster 62 on pod B-1 were examined metallurgically (see Figure 3.67). The

irradiated areas were crescent shaped. These crescents were created by the clearance space between pistons and backplate. Progressive sections through each crescent were made to determine the variation in transformation depths from the widest part of the crescent to a narrow part. Measurements of material removed and resolidified melt are presented graphically in Figures 3.68 and 3.69 for these sections.

It should be noted that resolidified material was not present in some of the sections examined. This may be due to splashing of material from the exposed region. The remaining surface is believed to be the base of the melt in this exposed region. Figure 3.70 shows a photomicrograph of a typical section through one of the examined crescents.

X-ray-illuminated regions were also detected on the side of the indent recorder guide sleeve on pod B-1 (Figure 3.71). This aluminum surface was exposed to X-rays at a near-grazing angle of approximately 13 degrees. From a macroscopic examination of the exposed region, there was evidence of surface melt. This was confirmed from a microscopic examination, and the latter also revealed a measurable melt depth in the sections examined. Figure 3.72 shows a graphical representation of the abstracted data.

3.3 PRELIMINARY X-RAY AND THERMAL INPUT ANALYSES

3.3.1 X-ray Inputs. The attenuation of X-ray intensity by atmospheric absorption was calculated on the basis of an average atmospheric density between the pod and the burst. This average value was derived from data (provided by Dr. K. Champion, Project 9.1a) taken over Johnston Island up to 90-km altitude. The densities at the pods and the total mass between burst and pods are as follows:

<u>Pod</u>	<u>Density (gm/cm³)</u>	<u>Intervening mass (gm/cm²)</u>
B-1	1.47 x 10 ⁻⁶	0.147
B-2	1.49 x 10 ⁻⁶	0.209
B-3	1.56 x 10 ⁻⁶	0.320

The filtering property of the atmosphere and the inverse-square-law diminution determine the X-ray intensity received at each pod as a function of its range. Appendix J describes the techniques used to calculate the X-ray inputs. Figures 3.73, 3.74, and 3.75 show X-ray spectra transmitted to each pod as a function of weapon temperature. In all cases a blackbody source is assumed. The X-ray transmission and deposition calculations were carried out on an IBM 1620 computer. A brief discussion of the pertinent programs is presented in Appendix K.

The fraction f_R of the total X-ray yield transmitted to a range R is described by

$$f_R = \frac{I(R)4\pi R^2}{Y_{X-RAY}} = \int_{h\nu=0}^{\infty} b_{h\nu} e^{-\mu_{h\nu} \int_0^R \rho(r) dr} dh\nu \quad (3.2)$$

where the terms are described in Appendix J.

It follows that the ratio of intensities received at two ranges, R_1 and R_2 , is given by

$$\frac{I(R_1)}{I(R_2)} = \frac{f_{R_1}}{f_{R_2}} \cdot \frac{R_2^2}{R_1^2} \quad (3.3)$$

These transmission properties are presented in Tables 3.7 and 3.8.

The analyses carried out in this and following sections require repeated use of the bulk thermal properties of aluminum and steel.

For convenience these properties are presented in Table 3.9. The aluminum alloys used were 6061 and 5052. The bulk properties of 356 aluminum are actually presented in Table 3.9, but these are very close to those of 5052 and 6061 aluminum. In the calculation of X-ray absorption within the steel and aluminum alloys the mass absorption coefficients of pure iron and pure aluminum were used.

The analytic techniques employed to determine the X-ray intensity and source temperature are presented in detail in Appendix J. Coupling with the small thermal input, which follows the X-rays, is neglected. This neglect can be justified by consideration of the very small solid angle and the nature of the X-ray and thermal sources, i. e., the former is a point source and the latter source is of finite size. The aperture-focal length geometry associated with this data is such that the energy input to the sample from the finite source would be greatly diminished compared to the input from the point source. In addition, closure of the aperture by vapor blow-in would tend to increase the attenuation of thermal radiation compared to X-radiation because of the longer time scale. The importance of aperture closure is clearly demonstrated by a comparison of the data in the steel detectors in B-1 under the 1-mm, 3-mm, and 10-mm apertures. These data indicate that for apertures of 1- and 3-mm diameter vapor closure diminishes the energy input compared to the detector beneath the 10-mm aperture.

A lower bound on the input received at pod B-1 may be calculated using the crescent data described in Section 3.2.10. Based on 75 measurements, the melt depth is 41 microns with an error of ± 2 microns. This 2-micron error describes the accuracy to which the original surface of the sample can be measured. The standard deviation of the mean of the measured depths is much less than 2 microns. The large effective focal length to the crescent

and the sharpness of its edges provide evidence that a thermal source of any reasonable size would have deposited little energy at the crescent location. These data represent a lower bound, because the total amount of energy absorbed between the surface and the 41-micron depth must be equal to or larger than the amount of energy required to barely melt a 41-micron layer of aluminum. To calculate the upper curve in Figure 3. 77, each of the normalized deposition curves in Figure 3. 76 has been renormalized by equating the energy deposition between the surface and the 41-micron depth to the minimum amount required to melt 41 microns of aluminum. The critical minimum energy for incipient melting in the aluminum alloy was calculated from

$$\begin{aligned} E_{\text{solidus}} &= c T_{\text{solidus}} \\ &= 140 \text{ cal/gm} \end{aligned} \quad (3. 4)$$

where c is the specific heat averaged up to the solidus temperature T_{solidus} . The bulk material properties are presented in Table 3. 9. From the renormalization one obtains a curve of intensity versus source temperature. Any correction to account for thermal conduction will only increase the intensities; thus, it is a lower bound. The results are shown in Figure 3. 77. The deviations of the intensities based on the deviations of the mean melt depths are omitted on this figure; these deviations are approximately one percent.

An isotropic X-ray yield corresponding to each value of intensity may be calculated at a given weapon temperature using Equation 3. 5, i. e. ,

$$Y_{\text{X-ray}} = \frac{I(R) 4 \pi R^2}{f_R} \quad (3. 5)$$

where $I(R)$ is the incident integrated intensity calculated from the data at a given weapon temperature
kT

$Y_{X\text{-ray}}$ is the X-ray yield from a weapon radiating a temperature, kT , which would cause an intensity $I(R)$ at a range R

Figure 3. 77 also presents a lower bound of calculated yield as a function of weapon temperature .

Section 3. 2. 10 described an X-ray-illuminated area on the aluminum indent recorder guide sleeve. Using the fact that the surface just melted gives the same lower bound as the crescents. The actual melt depth measurements have not yet been used in an intensity calculation.

An upper bound calculation may be made using the thermal pinhole camera with a 3-mm aperture from pod B-2. No pearlite-martensite transition was found and there was no evidence of melting or material removal. The lack of a pearlite-martensite transition was not used to determine the upper bound, because it was felt that the transition temperature was not sufficiently well known at the heating and cooling rates existing on this sample (see also the discussion toward the end of this section). This gage must have seen the X-rays incident at B-2 plus at least a portion of the thermal. The lack of response, therefore, implies an upper bound. The normalized energy deposition at the surface of the steel detector on pod B-2 is given in Table 3. 10. One can now renormalize the deposition at the surface of the detector in a similar manner to that done for the aluminum sample below the surface and obtain two curves (one for yield and one for intensity). In this calculation the critical energy for the solidus is taken to be 240 cal/gm as given by Equation 3. 4. These two curves would not be valid upper

bounds because of the finite loss of heat through conduction. This effect is, of course, highest with good conductors and at the surface of the detector where the temperature gradient is greatest. Therefore, Equation J. 5 has been used to account for conduction effects. This has been done by calculating the X-ray mean free paths in steel (in pod B-2) at weapon temperatures of 0.50, 0.75, 1.00, and 1.50 kev. The mean free paths are then substituted into Equation J. 5 to determine the reduction in surface temperature due to conduction during deposition. The second term on the right-hand side of Equation J. 5 is the first order correction due to conduction. The mean free paths in steel at 0.50-, 0.75-, 1.00- and 1.50-kev temperatures are approximately 5, 5, 5, and 7 microns, respectively. These give increases in input intensity (over those obtained assuming no conduction) of 20%, 20%, 20%, and 15%, respectively. These corrections are incorporated into the results depicted in Figure 3.77. Table 3.8 is used to transfer the intensities to pod B-1. It can be seen from Figure 3.77 that the upper bound curves for steel complement the lower bound curves obtained from the aluminum. The intensity curve for the steel goes through a minimum at a temperature of about 1.5 kilovolts. This minimum results from the strong effect of the absorption edge in steel at 7 kilovolts. For weapon temperatures higher than one kilovolt, the upper bound for steel falls below the lower bound for aluminum. Therefore, the possibility of weapon temperatures above about 1.23 kilovolts may be ruled out within the limitations of the present analytical model. In addition, if the yield in the pod direction was its nominal value of 200 kilotons or lower, the calculated weapon temperature was between 0.62 and 1.23 kilovolts, and the intensity at B-1 was between 2.8 and 7.6 cal/cm². The bounds on incident integrated intensity received at B-1 are given in Table 3.11 as a function of weapon temperature. The low source temperature bound probably represents a realistic lower bound because of the rapid steepening of the curves at low temperatures. At the upper bound end the temperature will be quite sensitive to intensity.

The copper heat shield which was present between the pods and the source may have, of course, substantially decreased the yield in the direction of pods. Also, the nominal yield prediction may be in error. One of the principal assumptions of this model is that the source radiates as a single blackbody. It is possible that the weapon radiated X-rays at more than one blackbody temperature because of the heat shield. This effect of the heat shield has been estimated in Reference 23. In this calculation the heat shield was divided up into segments of one inch thickness. A radiation diffusion type analysis was performed within each segment. This resulted in a local blackbody source temperature describing each segment of the heat shield. These segments were then weighted according to their projected solid angles in the direction of the pods. A blackbody temperature curve close to 1 kilovolt was fitted to the integrated spectrum. The resultant spectrum was somewhat different from that of a blackbody.

The data used to derive Figure 3.77 and Table 3.11 represent only a small portion of the available X-ray information on the pods. A few of these other sources are described below.

An apparent contradiction was encountered when using the data corresponding to absence of martensite in the steel detector used in the above derivation. This calculation gave an upper bound which was lower than the lower bound obtained from the aluminum data on pod B-1 in the temperature range of interest. It is felt that this seeming contradiction is due to the extremely high heating and cooling rates and short dwell times encountered in this experiment. As was mentioned in Appendix I the assumed value of 722°C for the pearlite-martensite temperature is based on equilibrium heating. The conditions of this experiment are probably such that the transformation temperature may be much higher. Some laboratory calibration to measure this value using a laser as the energy source was attempted. The results

obtained to date were inconclusive because of experimental difficulties.

The absence of ablation in aluminum at B-2 was checked as an upper bound. This upper bound is higher than that derived above, and it is, therefore, consistent with the above argument.

The lead in the X-ray pinhole cameras on pods B-1 and B-2 is also a source of intensity information (see Section 3.2.8). The problem with the lead is in interpretation of the craters. The lead has melted certainly to the crater depth, but it has not been possible to distinguish a more realistic melt depth below the crater. This is probably due to the high purity of the lead which apparently precludes the retention of a visible melt line. Thus, an upper bound analysis has not yet been attempted with the lead. A lower bound estimate using the observation that the surface melted is not useful, since it is much lower than that obtained from the aluminum at B-1 due to its low threshold and high absorptivity.

3.3.2 Short-Time Thermal Radiation Inputs. The instruments analyzed to obtain estimates of the short-time thermal radiation inputs are the 10-mm thermal cameras on the three pods and other flush-mounted materials on pod B-3. The thermal camera consists of a 1019 steel sample situated directly below a 10-mm-diameter aperture (see Figure 2.9).

The 1019 steel detector on pod B-1 contains a circular image approximately 10 mm in diameter; a cross-sectional cut of the detector shows remnants of a non-uniform melt layer and also a non-uniform layer of pearlite that has been transformed into martensite. Figure 3.33 shows the data from the cross section. The deepest penetration of the martensite transformation is 150 microns.

The non-uniformity of the melt and martensite layers may be due to either non-uniform energy inputs at the surface of the

detector or three-dimensional conduction effects if the input time is sufficiently long. A non-uniform input may be caused by: (1) non-uniformity associated with the source of thermal radiation, and (2) non-uniform transmission and/or transport of radiation through the plane of the aperture due to partial vapor closure of the aperture. Thus, the interpretation of the non-uniformity of the transformations in the steel detectors beneath the apertures is not straightforward.

Estimates of the thermal radiation inputs to the central regions in the detectors can be made by utilizing the maximum depths of the transformations. To derive these estimates the X-ray and thermal radiation inputs are assumed to be decoupled, or more specifically, the transformations in the steel are assumed to be caused by the thermal radiation inputs and the X-ray inputs have been ignored. This assumption will be checked as results are derived. Also, the thermal radiation inputs have been assumed to be in the form of a rectangular wave in time, i. e., a constant input intensity I_0 , up to a time Δt and zero intensity thereafter.

The average maximum depth at which the P-M transition occurs (on the 10-mm thermal camera on pod B-1) is obtained by averaging seven depth measurements in the vicinity of the central region. These depths were chosen over a region where no definite decreasing trend in the P-M depth appeared. The lateral extent of this region is approximately 0.6 mm. The average P-M depth is 138 microns with a standard deviation (in a single measurement) of 9 microns. The presence of the thin melt layer is ignored in this preliminary analysis. Appendix J describes the techniques used to calculate the thermal inputs. Equation J.6 is used to calculate normalized temperature profiles corresponding to this depth. These profiles are presented in Figure 3.78. The bulk thermal properties of the 1019 steel and other materials that have been used in these and subsequent calculations are presented in Table 3.9. In all the calculations

an initial temperature of 20°C has been assumed. If the depth of the martensite layer is temperature limited (see Appendix J), then Equation J. 7 may be used in conjunction with Equation J. 8 to determine the energy input corresponding to each pulse duration. The results are shown in Figure 3. 79 where the critical temperature for martensite formation has been assumed to be 722°C . From this plot it can be seen that the energy input required to produce a P-M transition at a 138-micron depth is greater than 25 cal/cm^2 with pulse times greater than 10^{-4} second. For this detector the upper bound on the energy input is not specified by the critical cooling rate associated with martensite formation but is specified by the pod motion relative to the burst. It is of interest to note that for pulse durations less than 10^{-2} second the material at a depth of 138 microns is subjected to essentially a delta function input so that it cannot distinguish between different pulse times.

Another factor that may limit the depth of the martensite is the requirement that the temperature decline between 722°C and 500°C in a time equal to or less than 0.8 second. This may be checked by assuming that the martensite depth is cooling rate limited and by using the normalized temperature histories in Figure 3. 78 in conjunction with Equation J. 6. This calculation results in maximum temperatures at the 138-micron depth in excess of the melt temperature up to pulse durations of several seconds. Thus, the cooling rate may be a limiting factor in the steel samples only for very long pulse times (a remote possibility as will be shown later in this section). Also, if the cooling rate criterion was the limiting factor one would expect to see bainite in the vicinity of the P-M transition (see Appendix I). No bainite was observed in any of the steel samples.

The locus of points in Figure 3. 79 derived from the maximum martensite depth assumes that the critical temperature for martensite

formation is 722°C . For very short pulse times, however, the relaxation time for pearlite to austenite transition may be comparable to or less than the dwell time at a temperature of 722°C . Therefore, for these short pulses a higher temperature may be required to achieve the pearlite to austenite transition. Thus, the curve in Figure 3.79 derived from the martensite data and all subsequent curves derived from such data are lower bounds on the energy inputs required to transform pearlite into martensite to a given depth.

The maximum melt depth on the steel detector within the 10-mm aperture on B-1 is approximately 20 microns which is considerably in excess of the approximately 5 microns on the steel detector beneath the 1-mm aperture. Thus, it is reasonable to assume that the thermal radiation inputs to the steel detector under the 10-mm aperture caused melting. Using Equation 3.4 and the bulk thermal properties of 1019 steel in Table 3.9, the threshold for melting has been calculated for various pulse durations and is presented in Figure 3.79. A machine code that computes melt depths in materials subjected to surface heating has been used to perform a preliminary analysis of the Blue Gill data. This code is described in Appendix L. Using the lower bound intensities described by the martensite curve in Figure 3.79 for various pulse times, depths of melt have been computed in an attempt to fit the observed 20-micron melt depth. Vaporization of the steel surface has been neglected. Bulk thermal properties of the 1019 steel in both the solid and liquid state were averaged and used in the machine code. However, the lack of accurate data on liquid steel makes the derived results tentative. The calculated input pulse times leading to melt depths of approximately 20 microns were between 2×10^{-3} and 4×10^{-3} second. The reason for the range in pulse times is that the pulse time is somewhat sensitive to the range of assumed bulk thermal properties of the steel. The actual

pulse duration leading to melt at a 20-micron depth may be below the calculated range if surface vaporization occurs. These results are tentative, pending inclusion of vaporization in the code and more accurate determination of the bulk thermal properties (especially of the melt).

The maximum X-ray input to the steel sample on B-1 is 7.6 cal/cm^2 . The minimum energy input required to transform pearlite to martensite down to a depth of 138 microns is 25 cal/cm^2 . Thus, to a fairly good degree, the assumption of decoupling the X-ray and thermal radiation inputs has been justified.

Figure 3.39 shows the transformation depths on a cross section of the 1019 steel alloy in the 10-mm thermal camera on pod B-2. No melt is present on the sample surface. A non-uniform layer of martensite is present. The average maximum martensite depth from seven measurements is 105 microns with a standard deviation (in a single measurement) of 4 microns. The lateral extent over which these measurements were made is approximately 1.0 mm. This extent is small because of the non-uniformity of the data distribution. Figure 3.80 presents the normalized temperature profiles corresponding to a depth of 105 microns. The calculated energy inputs corresponding to a critical martensite temperature of 722°C are shown in Figure 3.81. The lower bound thermal radiation input is 17 cal/cm^2 with pulse times greater than 10^{-4} second. The cooling rate criterion is applicable only for pulse durations of several seconds; the pod motion apparently is the limiting factor for defining an upper bound on input time and energy.

The absence of resolidified melt on the steel sample from pod B-2 provides upper bound estimates on the energy inputs. This is accomplished by computing the threshold energy inputs for melting of steel corresponding to a range of pulse durations. Where melt is absent these threshold values are upper bound estimates on the

energy inputs. The locus of these upper bound energy inputs is also presented in Figure 3.81. The intersection of the curves at a time of 2×10^{-3} second is the minimum pulse time for a rectangular input that simultaneously describes the martensite data and lack of melt on the surface. The upper bound curve describing energy inputs compatible with absence of melt assumes that the solidus temperature of the 1019 steel alloy is 1490°C . Again, it is possible that the alloy subjected to short-time heating pulses may not begin to melt at the nominal solidus temperature but at a somewhat higher temperature. If this were true, the upper bound curve in Figure 3.81 would not be a true upper bound. However, it is felt that any increase in melt temperature due to heating pulses in the millisecond range would be small.

From Table 3.8 and Figure 3.77 the maximum X-ray input to pod B-2 is seen to be approximately 1.5 cal/cm^2 . This input is small compared to the minimum thermal radiation input from Figure 3.81 of 17 cal/cm^2 , thus justifying the decoupling of thermal and X-radiation inputs.

The cross-sectional data of the 1019 steel sample beneath a 10-mm aperture on pod B-3 is shown in Figure 3.40. In this sample, corrosion of the exposed surface has taken place. A somewhat non-uniform layer of pearlite transformed into martensite is present and has a maximum thickness considerably less than that on pod B-2. It has therefore been assumed that since no melt was present on the sample in pod B-2 it is reasonable that no melt was present in the sample on B-3.

The average maximum P-M depth is 53 microns with a standard deviation (in a single measurement) of 4 microns using 23 depth measurements. The lateral extent over which these measurements were taken

is about 2.2 millimeters. This flat portion of the distribution is considerably larger than the corresponding portion in the detectors on pods B-1 and B-2. Figure 3.82 displays the normalized temperature profiles corresponding to the 53-micron depth. Again, it is assumed that the critical temperature for martensite formation is at least 722°C leading to lower bound estimates of the energy input. The lack of melt as before affords upper bound estimates of the energy input. These estimates are presented in Figure 3.83. The intersection of the curves leads to a minimum energy input and pulse time of approximately 9 cal/cm^2 and $1/2$ millisecond, respectively. Again, the critical cooling rate for martensite formation is the limiting factor only for pulse times of the order of several seconds; the pod motion, however, leads to a lower estimate of the maximum pulse time.

From Table 3.8 and Figure 3.77 it can be seen that the maximum X-ray input to pod B-3 is approximately 0.3 cal/cm^2 . This is negligible compared to the minimum of 9 cal/cm^2 required to produce martensite at the 53-micron depth and again justifies the decoupling of X-ray and thermal radiation inputs.

A preliminary analysis has been performed using some of the experimental data on pod B-3 to draw more restrictive limits on the magnitude and duration of the short-time thermal radiation inputs than is afforded by Figure 3.83. Some spectral information can also be derived from this analysis. The data utilized were associated with the 1019 steel alloy beneath the 10-mm aperture, filters used in the cut-off filter spectral gages, and other materials that were flush mounted or nearly so.

The work with these specific data sources must be considered preliminary and subject to substantial modification after further analysis. The primary reason for this is that results are derived

by comparison of data from different heights above the backplate. These different heights correspond to different depths within the vapor covering the backplate. No estimate is yet possible of this effect.

This analysis also makes use of the assumption that a detector with a relatively high transformation threshold (i. e., high conductivity and high transformation temperature) within an aperture experiences the same maximum input as the same material in a flush configuration. The validity of this assumption was borne out by the equivalent transformation depths in the 10-mm aperture steel detector and its flush counterpart (Figures 3. 40 and 3. 41) (true for pod B-3 only). An upper bound based on this assumption is valid for a low-threshold detector when the data from a flush configuration only is used, since it would see more of the source than the recessed version. On the other hand, the sensitive (Bi - Sn) flush detector cannot be used to define a lower bound on the recessed detector input. These points can be seen by a comparison of Figures 3. 54 and 3. 56.

The specific data utilized to compute the characteristics of the short time thermal radiation input to pod B-3 are:

- (1) No melt of 1019 steel.
- (2) Melting of 1095 steel (piston material).
- (3) Martensite in 1019 steel to depth of 53 microns.
- (4) No melt of aluminum.
- (5) Melting of TiO_2 filter material behind the 3-mm aperture (ratio of aperture diameter to focal length is unity—the same as the steel detector behind the 10-mm aperture).
- (6) Melting of the tin foil in the flush copper long-time thermal gage to a depth of less than 0. 01 inch.

Figure 3.84 presents bound curves associated with the short-time thermal radiation input to pod B-3. The curves associated with no melt and appearance of martensite in 1019 steel are taken from Figure 3.83. The curves corresponding to the 1095 melt and the aluminum non-melt are transformation threshold curves; the former is lower bound, and the latter is upper bound. The surface melting of the TiO_2 filter also affords a lower bound estimate of the energy input in a particular wavelength region (ultraviolet regime). The upper bound corresponding to the melting of the tin foil in the flush-mounted long-time thermal gage is taken from Section 3.3.3. The curves in Figure 3.84 have been derived using bulk properties of the materials as shown in Table 3.9. These curves depict bounds on the absorbed energy inputs to the exposed materials. If it is assumed that the incident energy is ultraviolet radiation and also that the spectral absorptivity is unity, the curves also depict bounds on incident energy. If, on the other hand, we assume that the incident energy is visible radiation, then we must correct the curves in Figure 3.84 to account for surface reflection. Figure 3.85 presents the bounds on incident energy corrected for reflection in the visible. Table 3.9 presents average values for reflection in the visible for the various materials analyzed. Note that the assumption of inputs in the visible portion of the spectrum leads to larger values of integrated intensity and pulse duration. The shaded regions in Figures 3.84 and 3.85 indicate allowable combinations of incident intensity and pulse duration within the framework of each set of assumptions. The apparent overlap where the upper bound curve of aluminum (no melt) is below the allowed region may result from the relatively coarse nature of the present calculations or be an indication of the fact that visible radiation made up a portion of the input. The lower bound on the pulse time is insensitive to the assumption of reflectivity, since the intersection involves two curves associated

with the same material (corrections due to reflectivity do not alter the relative positions along the horizontal axis). The reflectivity correction does affect the intensities at the lower end of the shaded regions in Figures 3.84 and 3.85. Nevertheless, the assumption of ultraviolet radiation inputs (zero reflectivity) leads to strict lower bounds on incident intensity and pulse time. The same statement cannot be made with respect to upper bounds on the short time input intensity and pulse duration. These upper bounds are determined by the intersection of the 1095 steel curve and the long-time thermal gage curve from Section 3.3.3. This intersection is indeed sensitive to the magnitudes of the assumed reflectivities of copper and steel (in the visible), and it could be moved to a higher integrated intensity and longer pulse time. Therefore, the upper bound on the energy input and pulse time for the short-time thermal radiation input must be considered as tentative. From Figures 3.84 and 3.85 the bounds on incident integrated intensity $I_0 \Delta t$, and pulse time Δt , for the so-called short-time input are:

$$9 \leq I_0 \Delta t \lesssim 50 \text{ cal/cm}^2$$

$$0.5 \times 10^{-3} \leq \Delta t \lesssim 3.7 \times 10^{-3} \text{ sec}$$

3.3.3 Long-Time Thermal Radiation Inputs. The melt depths corresponding to the various metallic foils contained in the long-time thermal gages that have been analyzed are shown in Table 3.6. On pod B-3 no surface melt was observed on any of the heat sinks. On pod B-1 all of the directly exposed surfaces of the heat sinks melted presumably from a combination of X-ray and thermal inputs. In this analysis, surface melt and vaporization of the heat sink material is ignored, thus leading to estimates of absorbed energy that may be considerably less than the actual incident energy (even after correcting for reflectivity). Table 3.12

lists the assumed bulk thermal properties of the heat sink materials and the melt temperatures of the foils. Equation J. 6 has been used to compute normalized temperature histories at the specified depths corresponding to rectangular wave inputs of varying pulse durations. The maxima are then determined and used to calculate the required energy inputs to attain the foil melt temperatures at specified depths. The derived long-time energy inputs to the gages on pod B-1 are presented in Figure 3.86 for various pulse durations. The flush copper gages indicate a larger energy input than the flush steel gage. The explanation, presumably, lies in the relative ease of vaporizing steel compared to copper. Thus, if vaporization did occur, the steel heat sink would have lost more energy via vapor blow-off than the copper heat sink. Therefore, if we consider the derived inputs using the copper gages (and neglect reflectivity corrections), a lower bound estimate of the long-time energy input to the gages on pod B-1 may be specified as

$$I_0 \Delta t \geq 165 \text{ cal/cm}^2 \text{ for pod B-1}$$

No accurate estimate of pulse times associated with the flush gages on pod B-1 are available at present.

Figure 3.86 also shows the calculated energy inputs to the recessed gages on pod B-1. Since the copper heat sink absorbs more energy than the steel (because of its higher vaporization threshold), the intersection of the two curves affords lower bound estimates of the magnitude and duration of the energy inputs to the recessed gages. These estimates are

$$I_0 \Delta t \geq 37 \text{ cal/cm}^2$$

$$\Delta t \geq 3 \times 10^{-2} \text{ s c for pod B-1}$$

Figure 3.87 shows the calculated energy inputs to the flush and recessed gages on pod B-3. The curve corresponding to the tin foil melt depth in the flush-mounted copper gage is an upper bound on energy input, since the melt depth that was used was experimentally determined as an upper bound. Again, if corrections due to surface reflectivity are ignored, bounds on the inputs and pulse times associated with the flush gages may be derived. These are, using the same argument as above,

$$I_0 \Delta t \geq 72 \text{ cal/cm}^2$$

$$\Delta t \geq 1.6 \times 10^{-1} \text{ sec for pod B-3}$$

The datum, for the tin foil, for the input to the recessed steel gage in pod B-3 leads to lower bound estimates of the long-time thermal input and pulse time (if we utilize one of the curves for the flush-mounted gage). These estimates are

$$I_0 \Delta t \geq 24 \text{ cal/cm}^2$$

$$\Delta t \geq 1.4 \times 10^{-2} \text{ sec for pod B-3}$$

If much of the energy inputs to the long-time thermal gages were in the form of visible radiation, the derived inputs in Figures 3.86 and 3.87 should be corrected for reflectivity of the heat sink surfaces. At the present time no accurate estimates of the spectra for the long-time inputs are available. Therefore, these corrections have not been made in this preliminary analysis. The effect of surface reflectivity corrections would be to increase the lower bounds on the energy inputs and decrease the lower bound pulse times where they can be determined by curve intersections.

3.3.4 Spectrum of Thermal Radiation, Pod B-3. To determine the approximate spectrum of the energy inputs to pod B-3, two sets of data have been utilized. The first set of data is shown in Figure 3.84 and consists of bounds on energy absorbed by the various exposed materials. For the purpose of this report, we restrict ourselves to radiation in the vicinity above and below 4000 \AA . The incident spectrum has been crudely divided into two regions: visible and ultraviolet. The absorptivity of the materials in the ultraviolet is assumed to be unity, and the average absorptivities in the visible portion of the spectrum are listed in Tables 3.9 and 3.13. A pulse time of 10^{-3} second has been chosen as representative of a mixed visible and ultraviolet input (see Figures 3.84 and 3.85). The corresponding absorbed energies $I_{\circ} \Delta t$ as derived from Figure 3.84 in the ultraviolet (uv) and visible (vis) portions of the spectrum are

$$11.5 < I_{\circ} \Delta t [1.00 \text{ (uv)} + 0.45 \text{ (vis)}] \leq 13.4 \text{ cal/cm}^2, \text{ steels}$$

$$I_{\circ} \Delta t [1.00 \text{ (uv)} + 0.30 \text{ (vis)}] \leq 10.7 \text{ cal/cm}^2, \text{ copper}$$

In addition, the lack of melt on the aluminum sample gives:

$$I_{\circ} \Delta t [1.00 \text{ (uv)} + 0.10 \text{ (vis)}] \leq 11.1 \text{ cal/cm}^2, \text{ aluminum.}$$

The presence of melt on the TiO_2 filter behind the 3-mm aperture (where the ratio of aperture diameter to focal length is the same as the ratio for the steel sample behind the 10-mm aperture) leads to an additional bound, i. e.,

$$I_{\circ} \Delta t [1.00 \text{ (uv)}] > 5.1 \text{ cal/cm}^2, \text{ TiO}_2$$

The curves associated with these bounds are also shown in Figures 3.84 and 3.85.

The four sets of bounds on absorbed energy thus depicted overdetermine the solution for the magnitudes in the visible and ultraviolet. However, by taking appropriate combinations, maximum and minimum values of the fraction of the total incident energy in the visible may be determined. These fractions are indicative only of the so-called short-time thermal input and are:

$$0.09 \leq \text{fraction of incident energy in} \\ \text{visible } (\lambda > 4000 \text{ \AA}) \leq 0.78$$

A major potential source of error is the condition of the filter surfaces during the thermal pulse. Specifically, the following sequence of events might have occurred:

- (1) A small fraction of the thermal energy vaporizes material from the backplate in a very short time. Assuming the filter is transparent to this energy, it remains cold at its surface.
- (2) The refrasil vapor products condense on the surface of the filter as an opaque coating.

This sequence of events would lead to the erroneous conclusion that the radiation was not capable of penetrating the filter. Black condensate was observed in the interior of all of the instruments, although little was observed on the exposed filter surfaces after recovery.

3.3.5 Thermal Source Size. Estimates of thermal source size were derived from the transformation data on the thermal instruments. It should be mentioned at the outset that any derived source size is, of course, an effective one as defined by the intensity threshold of the detector, i. e., a more sensitive detector would record a larger source.

A qualitative comparison of the data from certain high-and low-

threshold instruments suggested that two distinctly different sources were responsible for the observations. A starting point is provided by the results obtained from the side flush detectors (steel) on the B-1 thermal pinhole camera. The orientation of these three detectors with respect to the burst is given in Figure 3.3. The detector which faced toward the burst recorded the data shown in Figure 3.38 (along the vertical center line), while the one whose surface was essentially in the burst-pod plane contained only a small transformed area on its upper edge (see Figure 3.35). This latter detector, by virtue of its orientation, must have seen about half of the source, yet it recorded no transformation on its face. Finally, the third detector, facing away from the burst, possessed no transformation whatever and could not have seen any part of a source less than 200 meters in diameter. The pattern of the data on these three detectors obviously points to the probability of exposure to an effective source of small dimensions. The fact that this data resulted from a thermal source rather than X-rays is shown by Figure 3.38. The gradual decrease to zero transformation depth could only have been caused by an intensity which decreased with penetration into the vapor on the backplate surface. Any X-ray effect would have been constant in transformation depth.

A further indication of the small effective source was apparent from the transformation data on the 1, 3, and 10-mm top detectors of the thermal pinhole camera. These data are shown in Figures 3.30 through 3.33. The 1-mm aperture data are believed to be entirely due to X-rays. This belief is based on the very small increase in P-M depth from the 1-mm to the 3-mm aperture detectors and calculations which indicate that the incident X-ray intensity could have produced the observed data. Since the directly visible X-ray beam, as seen by the 1-mm detector, illuminates the surface over a span of only about 0.3 mm (owing to the nominal 13° orientation angle), the

remaining portion (on either side) of the image (Figure 3.30) must have been created by X-ray penetration of the mica heat shield through the edges of the aperture. This means that the extremities of the 3-mm and 10-mm detector images must also be at least partially the result of X-ray shine-through rather than thermal radiation. Bearing this in mind, the small extent of the 3-mm and 10-mm images (Figures 3.31, 3.32 and 3.33), qualitatively points to a small effective thermal source. Equally important and indicative is the displacement of these same images from the aperture axis. It is clear that a larger source would have yielded a more centrally located as well as larger image.

These indications of a small effective source are in striking contrast to the data on low-threshold instruments which imply a large source. These data consist of melted areas in the Bi-Sn detectors of the reflective coating spectral gages as is shown in Figures 3.49, 3.50, and 3.52 through 3.55. It is apparent in all of these figures that the images are larger than the apertures and tend to be centered below them. Both of these characteristics qualitatively suggest a larger source than was responsible for the steel data.

Quantitative estimates of thermal source size were derived from the transformation data discussed above. The detector elements were cross-sectioned in the plane of the burst; the lateral extent of a transformation may then be used in a straightforward manner to calculate an apparent source size. The burst/instrument geometry on which the source calculations are based is illustrated in Figure 3.88. The angles α_1 and α_2 (and hence α_3) are determined from the location of the image with respect to the aperture.* The source diameter is then calculated

* If the source is sufficiently large and/or located centrally enough, the bottom edge of the aperture occludes the source on the left-hand side as well as on the right—see Figure 3.88.

from

$$\frac{D}{2} = R \sin \frac{\alpha_3}{2}$$

while the source orientation is given by

$$\theta = \frac{\alpha_3}{2} + \alpha_1 - 90^\circ$$

The apparent source sizes and orientations calculated using these relations are listed in Table 3.14. Each entry corresponds to a single detector in an instrument. In the case of the steel detectors, the image extent was taken as that of the P-M transformation at the surface. The span of the melted zone was used in the case of Bi-Sn detector elements. The quoted uncertainty ranges represent an estimate of the effect of errors in measurement and manufacturing tolerances in aperture size. The sensitivity of the data and the uncertain X-ray effect precluded more than an upper bound estimate in the case of steel detectors.

The estimates in Table 3.14 clearly show that the higher threshold of steel led to images of an appreciably smaller effective source than that corresponding to the images retained by the low-threshold Bi-Sn detectors. No source size information could be obtained from the steel detectors on pods B-2 and B-3, because the vapor, rather than the camera aperture, occluded the source.

The different Bi-Sn detectors on pod B-1, as shown in Table 3.14 recorded significantly different source sizes, evidently as a result of the difference in surface condition. The larger source recorded by the gold-black-coated surface was presumably due to the higher absorptivity of this surface. This is consistent with the fact that

significant energy existed in the visible portion of the spectrum where a gold black surface has a higher absorptivity than would the uncoated metal.

The Bi-Sn detectors on B-3 appear to have seen a somewhat smaller source than was viewed at B-1. This permits an estimate to be made of the spatial variation of the integrated intensity for the large source from a comparison of identical thermal gages on the two pods. The bismuth-tin detectors under 10-mm apertures without coatings were used for this purpose. The apparent source radii for these gages were 370 m at B-1 and 260 m at B-3. Since the detectors were identical, they must have identical thresholds; the intensities at the edges of the apparent images in each of the two detectors must, therefore, have been equal. The factor of four inverse-square law diminution of intensity from B-1 to B-3 means that the intensity at a radius of 260 m must have been a factor of four higher than at a radius of 370 m. This estimate has been made without consideration of aperture closure due to vapor blow-in. Since vapor closure is more predominant at B-1 than at B-3 (compare Figures 3.33 and 3.40), this effect would make the factor of four an upper bound.

An alternative explanation for the smaller source viewed at B-3 is that much of the spectrum was in the ultra violet which would be attenuated by the intervening atmosphere. In this case the above estimate of spatial variation would not be valid.

A few remarks are in order concerning the Bi-Sn data. The images are zones of resolidified melted material. As is particularly evident on pod B-1, molten detector material was moved around, probably by the vapor blowing in through the aperture. This may have promoted the development of an enlarged image. The X-ray energy deposited at pod B-1 could have had a similar effect. Bearing this in mind, the source orientation data in Table 3.14 cannot be regarded

as contradictions of the orientations derived earlier in this report. Vapor blow-in effects, for example, tend to center the image, since they are probably symmetric to the aperture axis. When α_2 is significantly smaller than α_1 the cosine law tends to create the same effect (see Figure 3.88). It is apparent that, in the case of a steel detector where no thick molten layer existed, the orientations in Table 3.14 agree reasonably well with the 12.1° to 13.1° range derived from the X-ray pinhole camera.

It is obvious from the thermal source size calculations that, owing to a threshold difference of about one order of magnitude, a small and a large source were photographed by the steel and Bi-Sn detectors, respectively. Since the large source may have radiated over a longer period of time than the small one, the intensity ratio at the edges of these two sources may be less than the ratio of thresholds (see Section 3.3.3).

TABLE 3.1

SUMMARY OF CONTROL PISTON DATA

Pod B-1

Piston No.	Piston Type	sm_p/A_h^*	d cm	Remarks
1160	G-1	38.83	no indent	
1161	G-1	39.73	no indent	
1162	G-1	39.96	no indent	
1179	G-2	61.41	no indent	
1180 ^{a***}	G-2	59.11	.0263	Indent size comparable to others in cluster.
1181 ^b	G-2	60.28	**	Indent size small compared to others in cluster.

Pod B-2

1163	G-1	37.93	no indent	
1164	G-1	38.24	no indent	
1165	G-1	38.36	no indent	
1182 ^c	G-2	60.91	**	Indent size comparable to others in cluster.
1183 ^d	G-2	58.91	.0374	Indent size comparable to others in cluster.
1184 ^e	G-2	60.52	.23	Extremely large indent compared to others in same cluster, probably due to water impact.

Pod B-3

1166 ^f	G-1	39.39	**	Indent size small compared to others in cluster.
1168	G-1	37.99	no indent	
1207	G-1	39.88	no indent	
1185	G-2	57.83	no indent	
1186	G-2	60.30	no indent	
1187 ^g	G-2	59.07	**	Indent size small compared to others in cluster.

*Units of sm_p/A_h are $\text{dyne}\cdot\text{sec}^2/\text{cm}^2$

**Severely distorted indent

***Superscript letters denote clusters in which these control pistons were located; the other pistons in these clusters are similarly identified in Table 3.2.

G-1 = Doubly-blind control

G-2 = Blind control

TABLE 3.2

SUMMARY OF IMPULSE DATA

Pod B-1

Piston No.	Piston [†] Type	Material	$\frac{sm_p}{A_h}$ *	d cm	Impulse**	Objec- tive****	Remarks
711	A-1	Refrasil	.35	.0756	2.39±0.10	1	
712A	A-2	"	.82	.0829	2.73±0.11	1	
713	A-3	"	3.42	.0952	3.49±0.16	1	Slightly Distorted Indent
729	A-1	Lead	.84	.0723	2.78±0.13	1	
730	A-2	"	1.58	.0709	2.78±0.11	1	
731	A-3	"	4.90	.0850	3.81±0.20	1	Double Indent
748	A-3	Micarta	3.25	.0975	3.57±0.15	2	
749	A-3	"	3.27	.0919	3.33±0.16	2	
758	A-3	Pyro-Graph- ite (perp.)	3.49	.0919	3.36±0.16	2	
759	A-3	"	3.43	.0898	3.30±0.16	2	
772	A-3	Pyro-Graph- ite (para.)	3.25	.0892	3.16±0.15	2	
773	A-3	"	3.35	.0950	3.07±0.16	2	
784	A-3	Steel	4.40	.0819	3.34±0.18	2	
785	A-3	"	4.35	.0838	3.44±0.18	2	
972	C-1	Refrasil	7.57	.0364	3.38±0.09	1	
973	C-2	"	34.11	.0497	5.29±0.15	1	10-g Ball Plunger Setting
985 ^{a****}	C-1	Lead	8.24	.0345	3.23±0.10	1	10-g Ball Plunger Setting
986 ^b	C-2	"	38.14	.0360	3.23±0.17	1	
1008	C-2	Copper	38.25	.0393	3.72±0.18	2	Slightly Distorted Indent
1009 ^b	C-2	"	38.75	.0518	5.99±0.29	2	
1016	C-2	Aluminum	36.07	-		2	10-g Ball Plunger Setting; Severely Distorted Indent
1017 ^b	C-2	"	37.97	.0518	5.83±0.28	2	
1026A ^b	D-1	Refrasil	88.82	.0466	9.84±0.27	1	
1033	D-1	Lead	88.83	.0476	10.52±0.29	1	
1068	D-1	Silver	89.31	.0441	9.20±0.27	2	
1070 ^b	D-1	"	89.93	.0462	9.96±0.27	2	
1041	D-1	Phenolic	83.62	.0448	9.41±0.27	2	
1042 ^b	D-1	"	85.00	.0458	9.71±0.27	2	
1053	D-1	Zinc	90.69	.0442	9.10±0.27	2	
1054 ^b	D-1	"	89.56	.0474	10.33±0.28	2	

TABLE 3.2 CONTINUED

Pod B-1

Piston No.	Piston [†] Type	Material	$\frac{sm}{p/A}^*$	d cm	Impulse**	Objec-**** tive	Remarks
1076 ^a	E-1	Refrasil		.0779	11.46±0.18 [#]	3	Collar
1085 ^a	E-1	Lead	192.5	.0178	<3.1	1	Read Below Threshold
1092 ^a	E-1	Fe-Devcon	193.4	no indent	<3.1	2	
1095 ^a	E-1	"	193.4	.0337	13.42±0.56		
1104 ^a	E-1	Teflon	193.2	.0309	11.06±0.61		
1106 ^a	E-1	"	201.5	.0379	17.01±0.68		
1122	F-1	Refrasil	.33	.0327	0.71±0.07	4	
1123	F-2	"	1.21	.0422	1.08±0.06	4	
1124	F-3	"	3.91	.0442	1.33±0.13	4	Double Indent
1136	F-1	Lead	0.91	.0358	0.98±0.10	4	
1135	F-2	"	1.72	-		4	Severely Distorted Indent
1139	F-3	"	5.72	.0453	1.75±0.17	4	Slightly Distorted Indent
715	A-1	Refrasil	.35	.0626	1.82±0.10	1	Slightly Distorted Indent
717	A-2	"	1.02	.0589	1.15±0.07	1	
716	A-3	"	3.26	.0715	2.43±0.14	1	Double Indent
736A	A-1	Lead	.71	.0540	1.59±0.05	1	
734	A-2	"	1.64	.0551	1.88±0.07	1	
733	A-3	"	5.21	.0652	2.69±0.17	1	Slightly Distorted Indent
751	A-3	Micarta	3.29	.0763	2.62±0.15	2	Anvil Found all the way up Barrel, Data Questionable
750	A-3	"	3.14	.0675	2.21±0.14	2	
760	A-3	Pyro-Graph- ite (perp.)	3.51	.0706	2.22±0.15	2	Slightly Distorted Indent
761	A-3	"	3.65	.0645	2.14±0.14	2	
777	A-3	Pyro-Graph- ite (para.)	3.30	.0691	2.34±0.14	2	Slightly Distorted Indent
775	A-3	"	3.71	.0709	2.44±0.15	2	Double Indent
788	A-3	Phenolic	3.18	.0724	2.35±0.14	2	
789	A-3	"	3.16	-		2	Severely Distorted Indent

TABLE 3.2 CONTINUED

Pod B-2

Piston No.	Piston ⁺ Type	Material	$\frac{sm_p}{A_h}^*$	d cm	Impulse ^{**}	Objec- ^{****} tive	Remarks
975	C-1	Refrasil	9.01	.0299	2.39±0.09	1	
977 ^c	C-2	"	39.79	.0336	2.58±0.16	1	10 - g Ball Plunger Setting
988 ^d	C-1	Lead	9.89	.0274	2.14±0.10	1	10 - g Ball Plunger Setting
987 ^e	C-2	"	38.69	.0282	1.99±0.13	1	
1011 ^c	C-2	Copper	38.11	.0387	3.55±0.18	2	Anvil 1/2" Past Key. Data appear to be consistent, however.
1010 ^e	C-2	"	40.21	.0349	2.93±0.16	2	
1019 ^c	C-2	Aluminum	38.45	.0312	2.31±0.17	2	10- g Ball Plunger Setting
1018 ^e	C-2	"	37.11	.0587	7.08±0.34	2	
1002 ^c	C-2	Steel	37.83	.0357	3.09±0.16	2	Anvil 1/4" Past Key. Data appear to be consistent, however.
1001 ^e	C-2	"	38.37	.0365	3.19±0.16	2	
1028A ^e	D-1	Refrasil	88.19	.0376	6.72±0.30	1	
1036 ^c	D-1	Lead	90.70	.0413	8.18±0.30	1	
1071 ^c	D-1	Silver	90.81	.0374	6.79±0.31	2	
1016A ^e	D-1	"	88.51	.0401	7.77±0.31	2	
1056 ^c	D-1	Zinc	88.09	.0406	7.88±0.29	2	
1055A ^e	D-1	"	86.22	.0846		2	Piston Found Resting on Anvil. Data Questionable
432 ^d	E-1	Lead	198.6	.0306	10.50±0.64	1	
1079 ^d	E-1	Refrasil		.0564	6.73± 0.14 [#]	4	Collar
1097 ^d	E-1	Fe-Devcon	241.2	no indent	<3.1	2	
1099 ^d	E-1	"	185.5	.0315	11.52±0.61	2	Double Indent
1110 ^d	E-1	Teflon	194.4	no indent	<3.1	2	
1111 ^d	E-1	"	201.2	.0412	19.59±0.78	2	
1128	F-1	Refrasil	.44	.0251	0.43±0.06	4	
1112A	F-2	"	1.22	.0231	0.37±0.07	4	Double Indent
1127	F-3	"	4.14	.0315	0.78±0.13	4	Double Indent
1145	F-1	Lead	.43	no indent	<.2	4	
1142	F-2	"	1.93	no indent	<.2	4	
1146	F-3	"	5.58	.0425	1.47±0.16	4	

TABLE 3.2 CONTINUED

Pod B-3

Piston No.	Piston ⁺ Type	Material	$\frac{sm_p}{A_h}$ *	d cm	Impulse **	Objec- tive ****	Remarks
718 ^f	A-1	Refrasil	.49	.0445	1.07±0.02	1	
719	A-2	"	.53	.0449	1.12±0.02	1	
714	A-3	"	3.40	.0493	1.44±0.03	1	Double Indent
735 ^f	A-1	Lead	.24	.0419	1.19±0.10	1	
737	A-2	"	1.54	.0392	1.09±0.07	1	
732	A-3	"	5.15	.0445	1.54±0.16	1	Double Indent
793	A-3	Copper	5.70	.0551	2.01±0.15	2	
794	A-3	"	4.47	.0485	1.66±0.15	2	Double Indent
763 ^f	A-3	Pyro-Graph- ite (perp.)	3.55	.0456	1.30±0.13	2	
762	A-3	"	3.41	.0476	1.39±0.13	2	Double Indent
774 ^f	A-3	Pyro-Graph- ite (para.)	3.32	.0523	1.59±0.13	2	
776	A-3	"	3.20	.0469	1.37±0.13	2	Double Indent
801	A-3	Aluminum	3.36	.0475	1.40±0.13	2	Slightly Distorted Indent
800	A-3	"	3.48	.0484	1.42±0.13	2	
976 ^f	C-1	Refrasil	8.82	.0188	1.05±0.09	1	
974	C-2	"	35.86	no indent	<1.6	1	10- g Ball Plunger Setting; Read Below Threshold
990	C-1	Lead	10.25	-		1	10- g Ball Plunger Setting; Severely Distorted Indent
989 ^g	C-2	"	36.57	.0216	0.93±0.16	1	
994	C-2	Micarta	33.84	.0250	1.50±0.13	2	
993 ^g	C-2	"	33.55	.0256	1.58±0.13	2	Double Indent
999	C-2	Steel	37.45	.0252	1.48±0.13	2	Double Indent
1000 ^g	C-2	Steel	36.92	.0215	0.87±0.16	2	Double Indent
1022	C-2	Zinc	37.89	-		2	10- g Ball Plunger Setting; Severely Distorted Indent
1023 ^g	C-2	"	34.37	-		2	Severely Distorted Indent
1029 ^g	D-1	Refrasil	88.42	-		1	Severely Distorted Indent
1034	D-1	Lead	91.61	.0315	3.24±0.34	1	

TABLE 3.2 CONTINUED

Pod B-3

Piston No.	Piston [†] Type	Material	sm_p/A_h^*	d cm	Impulse ^{**}	Objective ^{****}	Remarks
1072	D-1	Silver	90.12	.0331	5.22±0.32	2	
1060A ^g	D-1	"	89.30	-		2	Severely Distorted Indent
1046	D-1	Phenolic	88.92	.0319	4.71±0.33	2	
1045 ^g	D-1	"	88.58	.0246	1.68±0.71	2	
1086	E-1	Lead	187.7	.0296	9.60±0.69	1	
1078	E-1	Refrasil		.0298	2.02±0.18	4	Collar; Double Indent
1096	E-1	Fe-Devcon	192.0	.0313	11.00±0.61	2	
1098	E-1	"	192.0	.0316	11.18±0.58	2	
1108	E-1	Teflon	190.9	.0321	11.59±0.58	2	
1109	E-1	"	195.9	.0323	11.68±0.55	2	
1129 ^f	F-1	Refrasil	.60	.0221	0.32±0.06	4	
1126	F-2	"	1.12	.0239	0.38±0.07	4	Slightly Distorted Indent
1125	F-3	"	4.05	.0225	0.41±0.12	4	Double Indent
1143 ^f	F-1	Lead	.85	no indent	<.2	4	
1144	F-2	"	1.25	no indent	<.2	4	
1147	F-3	"	5.66	.0114	<.2	4	Read Below Threshold

* Units of sm_p/A_h are $\text{dyne-sec}^2/\text{cm}^2$

** Units of Impulse are $10^3 \text{ dyne-sec}/\text{cm}^2$

*** Superscript letters identify clusters in which control pistons made indents. The corresponding control pistons are similarly identified in Table 3.1

10^3 dyne-sec (no applicable area)

[Indicates matched piston pairs

**** Objective

- 1 = Time history
- 2 = Total impulse
- 3 = Backplate deflection velocity
- 4 = Pressure insensitive

+ Piston type notation is explained in Table 2.1

TABLE 3.3 QUALITY OF INDENTS, SHOT BLUE GILL

<u>Pod</u>	<u>Perfect Indents</u>	<u>Double Indents</u>	<u>Slightly Distorted</u>	<u>Severe Distortions</u>
B-1	40	2	3	3
B-2	36	5	4	3
B-3	29	10	2	7
Percent of Total	73.0%	11.8%	6.2%	9.0%

TABLE 3.4

BLUE GILL ABLATION DATA
(weight change in units of milligrams/cm²)

<u>Material</u>	<u>Data Source</u>	<u>Aborted Shot</u>	<u>Pod B-1</u>	<u>Pod B-2</u>	<u>Pod B-3</u>	
Refrasil-Phenolic	<u>Piston Sample Dimensions</u>					
		A-piston sample	-74 ± 5 to -112 ± 5	(2)	(4)	
		F-piston sample	-87 ± 4 to -148 ± 4	(1)	(4)	
		<u>Piston Sample Weights</u>				
		A-piston	+15 to +16 -1 to +3	-74 to -78	(2)	-30 to -31
		F-piston	-1 to 0 +5 to +6 -1 to 0	-105 to -117	(1)	-23 to -30 -43 to -48
		C-piston		(1)	(1)	-19 to -26
		D-piston		(1)	(1)	-21 to -36
		<u>Ablation-Condensation Gage Sample Weights</u>				
		1-mm aperture	+19	-91	(1)	-41
		3-mm aperture	+17	-94	(2)	-35
		5-mm aperture	+20	-62	-29	-35

TABLE 3.4 CONTINUED

<u>Material</u>	<u>Data Source</u>	<u>Aborted Shot</u>	<u>Pod B-1</u>	<u>Pod B-2</u>	<u>Pod B-3</u>
Refrasil- Phenolic	<u>Backplate Plug Weights</u>				
	A		-54	-46	+3
	B		-60	-48	+5
	C		-51	-44	-11
	D		-53	-52	+4
	E		-52	-42	-12
	F		-64	-41	-17
	G				-4
	H				-30
	I				-7
	<u>Ablation-Condensation Gage Sample Weights</u>				
	<u>5-mm aperture</u>				
Micarta	"	(3)	-125	(4)	-61
Black Phenolic	"	(3)	-90	(4)	-46
Iron-Devcon	"	+12	-248	-171	-106
Teflon	"	-1	(4)	(4)	-21
Pyrolytic Graphite (grain parallel)	"	+2	-12	(2)	-1

1. Not recovered
2. Mechanical damage
3. Not in experiment
4. Not yet examined

TABLE 3.5

CONDITION OF TOP FILTERS IN
CUT-OFF FILTER SPECTRAL GAGES

<u>POD B-1</u>			
Instrument No.	Filter Material	Aperture Size (mm)	Condition
14	Fused Quartz	1	No effect.
		3	Minor etching 3 mm across; hairline internal fracture.
		8	Several deep and long hairline fractures; front surface streaked milky blue color; micarta holder charred between filters; second filter has ingrained blackening.
		3	Minor etching; short deep fracture in second filter probably due to handling.
15	TiO ₂	1	Brown area 1 mm in span and some depth.
		3	Deep radial fractures, chipped out section at center; metallic (black) appearing center spot 3-mm diameter with short radial outward splash marks.
		8	Fractured deeply in coarse square grid; first surface has shallow metallic (black) surfaced crater surmounted off center by domed metallic (black) up-welling.
		3	Identical to Aperture 3 above.
16	MgF ₂	1	No Effect.
		3	Shattered into seven pie-shaped pieces; no apparent substantial etching.
		8	Deeply fractured; entire exposed area deeply etched.
		3	Several radial cracks; center area fragmented.
17	Al ₂ O ₃	1	Two side-by-side shallow parallel fractures about 1 mm long in center area at first surface; no apparent etching.

TABLE 3.5 CONTINUED

Instrument No.	Filter Material	POD B-1	
		Aperture Size (mm)	Condition
		3	Similar to above, but larger and more widely separated fractures; transparency unaffected.
		8	Shattered into small pieces; clear amber throughout exposed area with deeper amber colored perimeter.
		POD B-3	
14	Fused Quartz	1	No effect.
		3	Superficial etching of 1-mm spot.
14	Fused Quartz	8	Superficial etching of irregular 4-mm area; several small fractures; several front surface spalls.
		3	Etched ring 2-mm diameter.
15	TiO ₂	1	1/2-mm amber internal void; otherwise clear.
		3	Square fracture grid 3 mm diameter; bluish spot in center 1 mm diameter.
		8	Deeply fractured; metallic raised blisters—bluish transition zones into crystal.
		3	Same as Aperture 3 above plus four deep radial fractures to edge (see Figure 3.42).
16	MgF ₂	1	No effect.
		3	No effect.
		8	Deep fractures in fan pattern from one edge; no apparent surface deterioration.
		3	No effect.
17	Al ₂ O ₃	1	No effect.
		3	No effect.
		8	No effect.
		3	No effect

TABLE 3.6 FOIL MELT DEPTHS, LONG-TIME THERMAL GAGE

POD B-1

Steel Heat Sink

Lateral Position (in)	<u>Flush Geometry</u>			<u>Recessed Geometry</u>		
	Lead Foil (Quartz Filter) (in)	Tin Foil (in)	Gold Foil (in)	Lead Foil (Quartz Filter) (in)	Tin Foil (in)	Gold Foil (in)
0	0.081	0.128			0.032	
.025	0.076	0.122	Constant	Surface	0.033	Surface
.050	0.065	0.116	Depth	Melt	0.033	Melt
.075	0.065	0.117	of	Only	0.033	Only
.100	0.064	0.115	0.005		0.033	
.125	0.071	0.115			0.034	
.150	0.065	0.114			0.033	
.175	0.074	0.115			0.033	
.200	0.076	0.117			0.033	
.225	0.073	0.118				
.250	0.073	0.121				

POD B-1

Copper Heat Sink

Lateral Position (in)	<u>Flush Geometry</u>		<u>Recessed Geometry</u>	
	Lead Foil (Quartz Filter) (in)	Tin Foil (in)	Lead Foil (Quartz Filter) (in)	Tin Foil (in)
0	0.141	0.178		0.018
.025	0.131	0.178	Constant	0.017
.050	0.134	0.178	Depth	0.016
.075	0.112	0.177	of	0.016
.100	0.131	0.175	0.003	0.017
.125	0.147	0.177		0.015
.150	0.143	0.177		0.014
.175	0.139	0.164		0.015
.200	0.141	0.178		0.015
.225	0.178	0.177		0.016
.250	0.191	0.181		0.016

TABLE 3.6 CONTINUED

POD B-3

Steel Heat Sink

Lateral Position (in)	<u>Flush Geometry</u>			<u>Recessed Geometry</u>		
	Lead Foil (Quartz Filter) (in)	Tin Foil (in)	Gold Foil (in)	Lead Foil (Quartz Filter) (in)	Tin Foil (in)	Aluminum Foil (in)
0	0.041	0.054			0.022	
.025	0.041	0.053	Surface	Surface	0.022	No
.050	0.036	0.053	Appears	Melt	0.022	Apparent
.075	0.037	0.053	Not	Only	0.022	Melt
.100	0.035	0.053	To		0.022	Line
.125	0.036	0.052	Have		0.022	
.150	0.037	0.053	Melted		0.021	
.175	0.041	0.053			0.021	
.200	0.044	0.054			0.021	
.225	0.044	0.054			0.022	
.250		0.055			0.023	

POD B-3

Copper Heat Sink

<u>Flush Geometry</u>		<u>Recessed Geometry</u>	
Lead Foil (Quartz Filter) (in)	Tin Foil (in)	Lead Foil (Quartz Filter) (in)	Tin Foil (in)
Estimated	Estimated	Surface	Surface
to	to	appears	appears
be	be	not	not
0.004	0.010	to	to
		have	have
		melted	melted

TABLE 3.9

**BULK THERMAL PROPERTIES OF EXPOSED MATERIALS,
ANALYSIS OF SHORT-TIME AND X-RAY INPUTS
(References 24 and 25)**

Material	1019 Steel ²	1095 Steel	Aluminum	TiO ₂		
Average Thermal Conductivity ¹ (cal/cm sec°C)	0.088	0.088	0.081	0.57	0.57	0.010
Specific Heat ¹ (cal/g°C)	0.17	0.16		0.24	0.24	
Average Thermal Diffusivity ¹ (cm ² /sec)	0.073	0.073	0.069	0.846	0.846	0.011
Transformation Temperature (°C)	722°C (pearlite → austenite)	1492°C (melt)	1350°C (melt)	580°C (Solidus)	650°C (Liquidus)	1833°C (melt)
Latent Heat of Fusion (cal/g)		66		93	93	
Average Absorptivity in visible	0.45	0.45	0.45	0.10	0.10	-----

1. Conductivity, specific heat, and diffusivity have been averaged up to the transformation temperature except where noted.
2. Conductivity and diffusivity have been averaged up to the melt temperature for the analysis of the pearlite → austenite → martensite transformation.

TABLE 3.12

**BULK THERMAL PROPERTIES OF EXPOSED MATERIALS, ANALYSIS OF
LONG-TIME INPUT
(References 24 and 26)**

Material	Copper	1019 Steel	Tin	Lead
Average Thermal Conductivity ¹ (cal/cm sec °C)	0.94	0.12	----	----
Average Thermal Diffusivity ¹ (cm ² /sec)	1.10	0.13	----	----
Melt Temperature (°C)	----	----	232	327
Average Absorptivity in Visible Fraction	0.30	----	----	----

1. Conductivity and diffusivity for copper and steel have been averaged up to a temperature of 300°C.

TABLE 3.13 BULK THERMAL PROPERTIES OF EXPOSED MATERIALS,
ANALYSIS OF INPUT SPECTRUM

(References 15, 24 and 25)

Material	Bismuth-Tin Alloy ²		TiO ₂
Average Thermal Conductivity ¹ (cal/cm sec °C)	0.018	0.018	0.015
Average Thermal Diffusivity ¹ (cm ² /sec)	0.057	0.057	0.016
Transformation Temperature (°C)	139 (eutectic melt)	260 (Matrix melt)	642 (solid transformation)
Average Absorptivity in Visible Fraction	0.45	0.45	-----

1. Conductivity and diffusivity have been averaged up to the transformation temperature.
2. Density and specific heat of 10.0 g/cm³ and 0.031 cal/g°C, respectively, were also used.

TABLE 3.14 THERMAL SOURCE SIZE ESTIMATES

Pod B-1				
Instrument	Detector	Aperture Dia. (mm)	Source Size (m)	Source Orientation (degrees)
Thermal Pinhole Camera	1019 steel (slotted)	3	< 95	13 ± 1
"	1019 steel (unslotted)	3	< 75	12.5 ± 1
"	1019 steel	10	< 75	11 ± 1
Reflective Coating Spectral Gage	Bi-Sn (no coating)	10	730 ± 35	4.5 ± 2.5
"	Bi-Sn (gold black coating)	10	860 ± 40	0 ± 2.5
Pod B-3				
Reflective Coating Spectral Gage	Bi-Sn (no coating)	3	640 ± 40	0 ± 2.5
"	Bi-Sn (gold black coating)	3	730 ± 40	0 ± 2.5
"	Bi-Sn (no coating)	10	520 ± 40	0 ± 2.5
"	Bi-Sn (gold black coating)	10	520 ± 40	0 ± 2.5

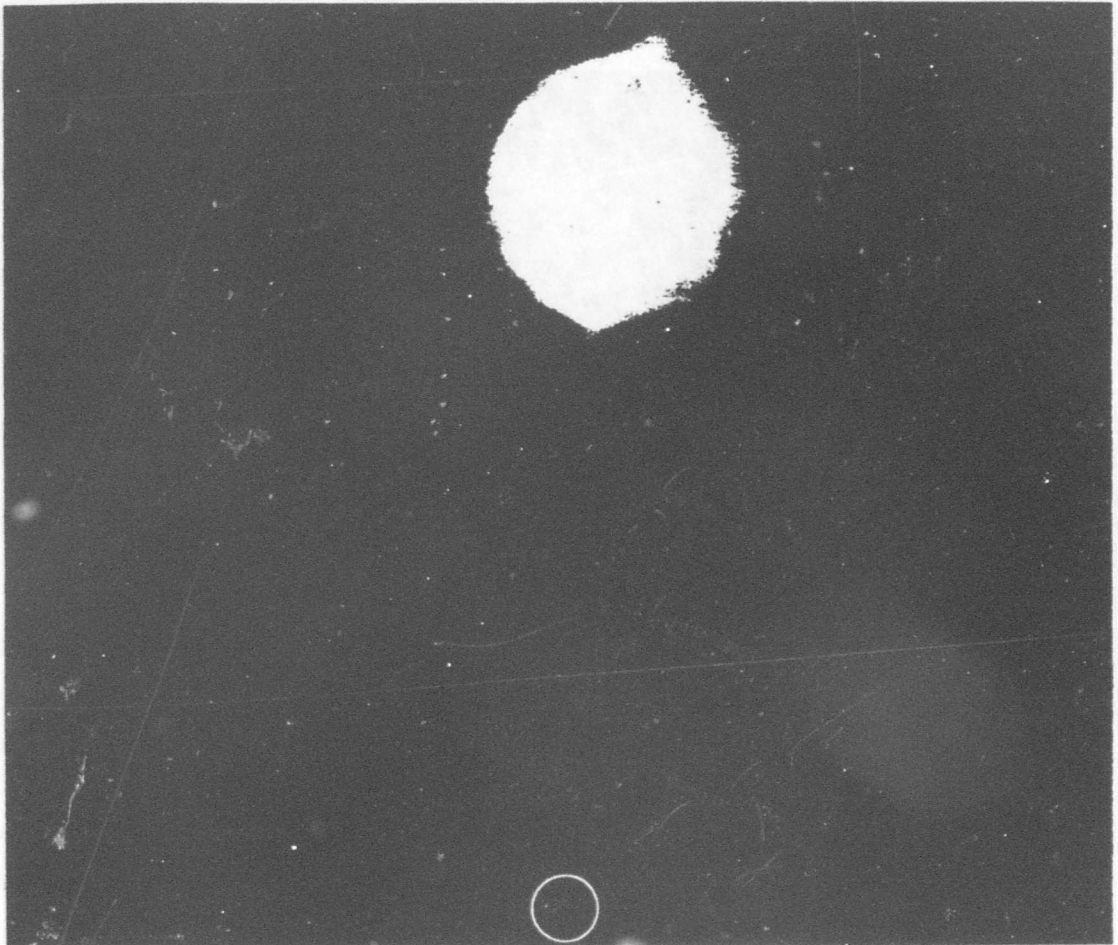


Figure 3.1 Blue Gill pod reentry. (ASE photo)

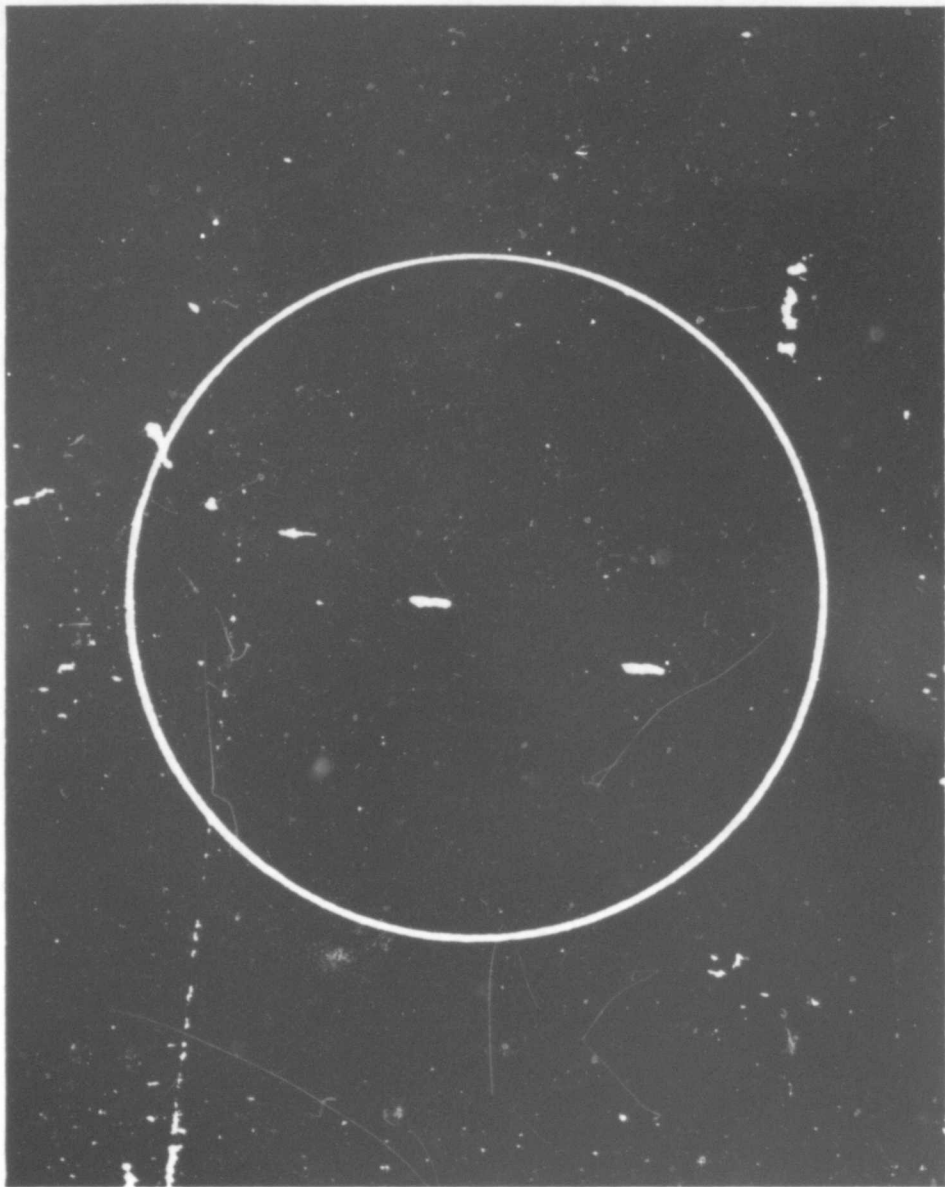
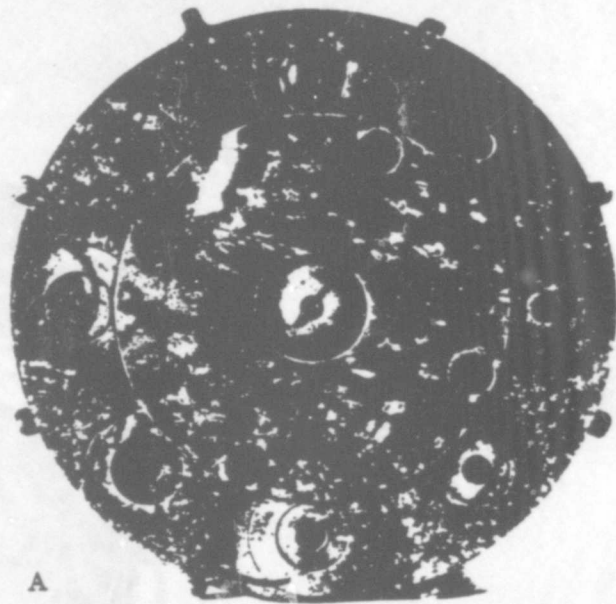


Figure 3.2 Blue Gill pod reentry (closeup).
(ASE photo)



A



B

Figure 3.6 Flow patterns on indent recorder cluster, Blue Gill Pod 1. (Photograph A, top of cluster; Photograph B, steel piston on.) (ASE photos)

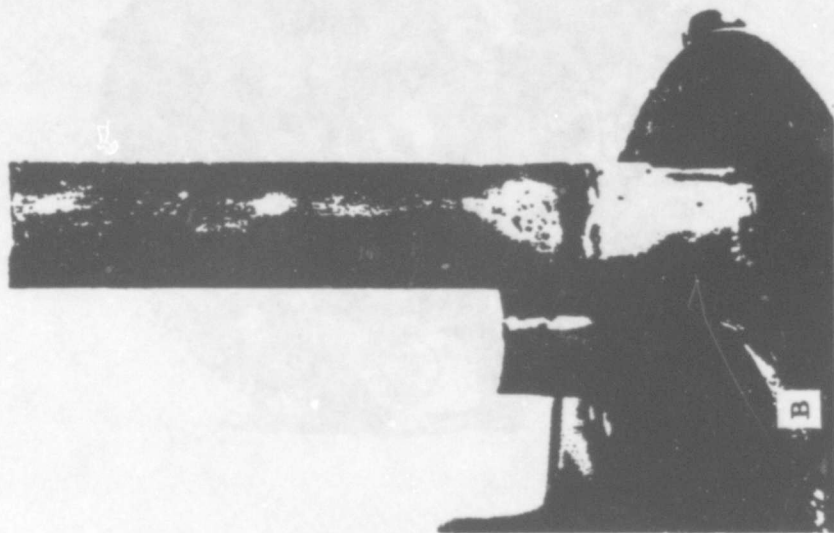
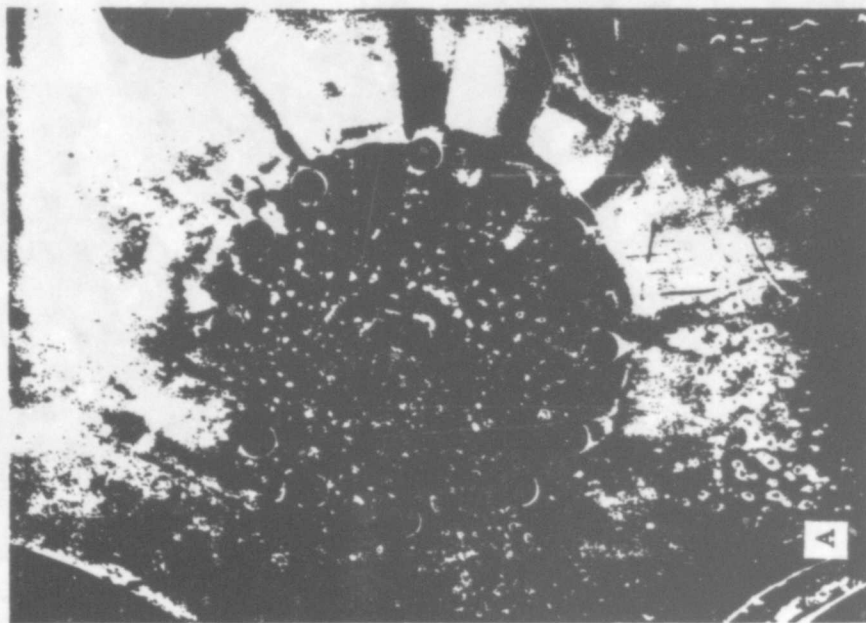
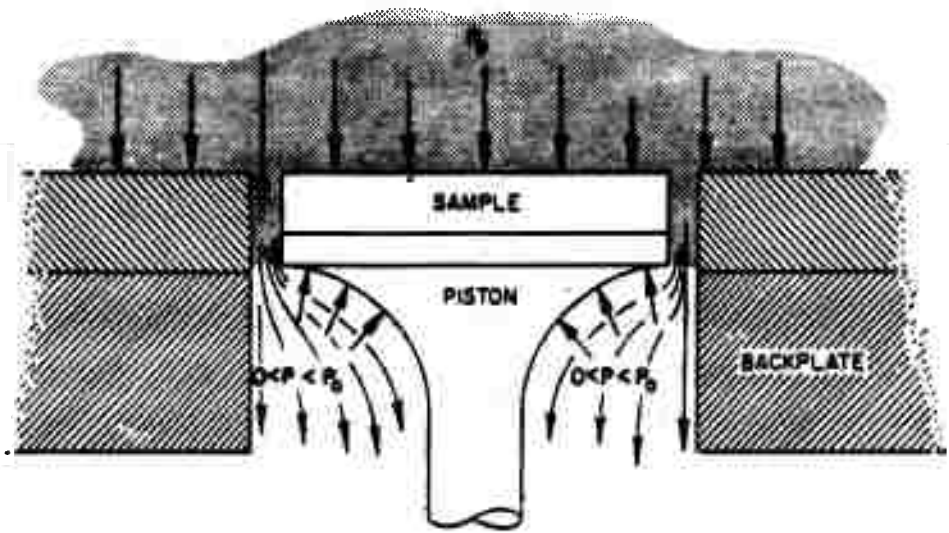
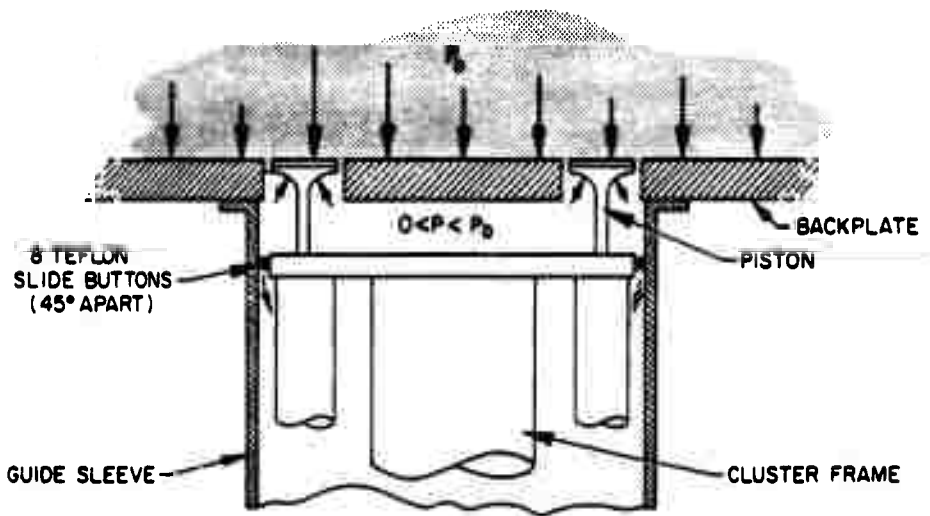


Figure 3.7 Gas flow patterns below backplate, Blue Gill Pod 1. (Photograph A, X-ray pinhole camera clearance apertures; Photograph B, D piston.) (ASE photos)

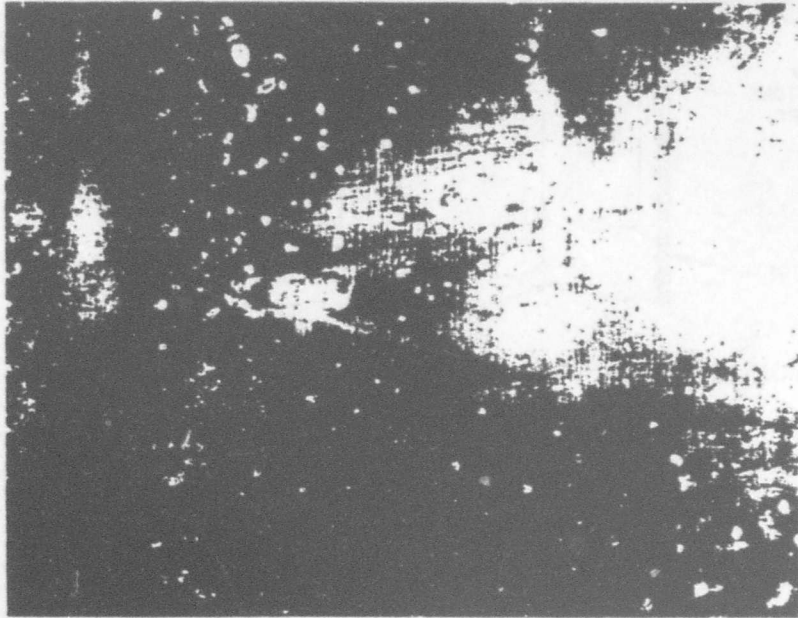


(a) LOCAL PRESSURE INFLUENCE

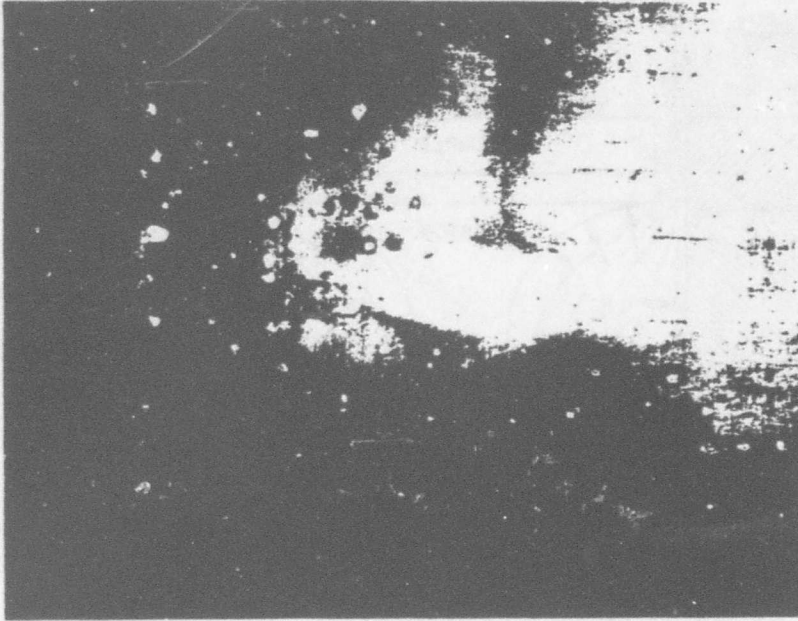


(b) VOLUME PRESSURE INFLUENCE

Figure 3.8 Possible back-pressure influences on piston measurements.



CLUSTER WITH A - PISTONS



CLUSTER WITH E - PISTONS

Figure 3.9 Indications of cluster motion, Blue Gill Pod 1. (ASE photos)

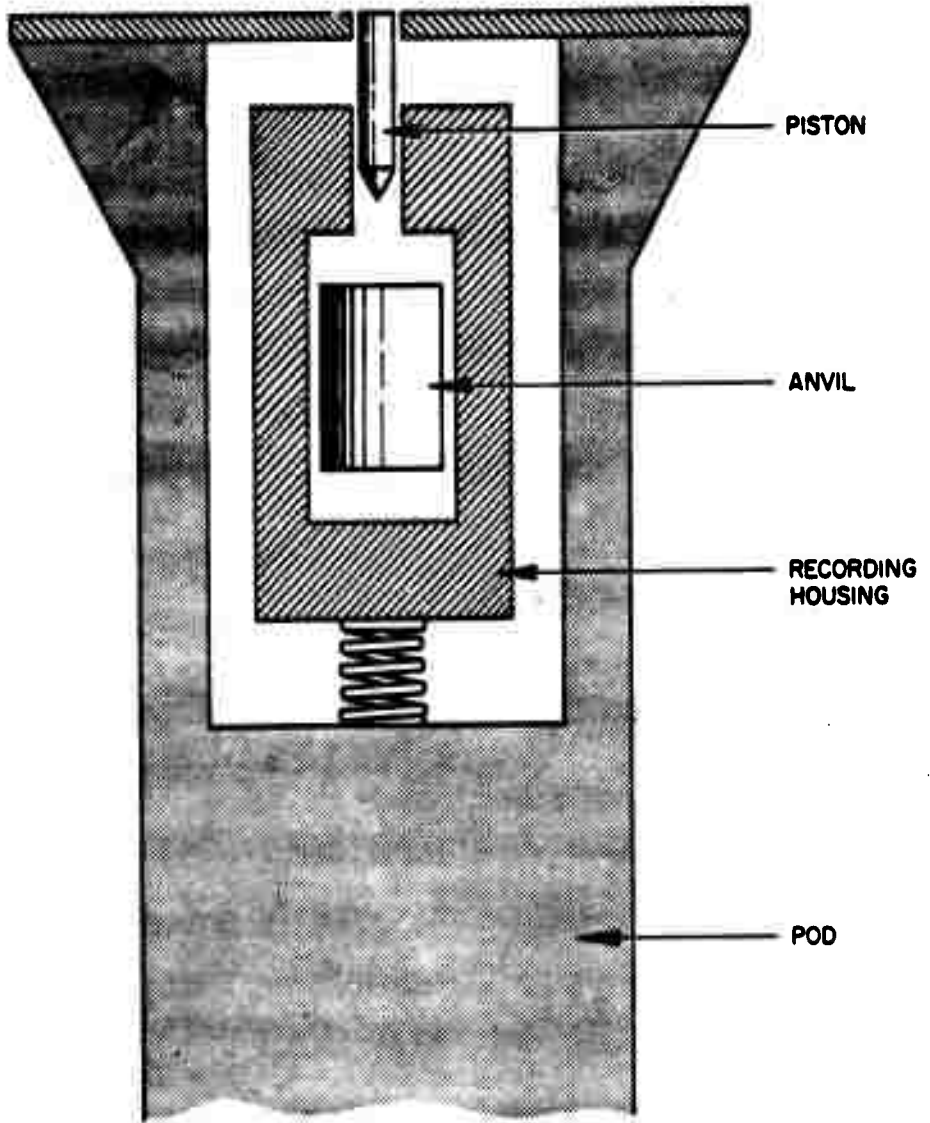
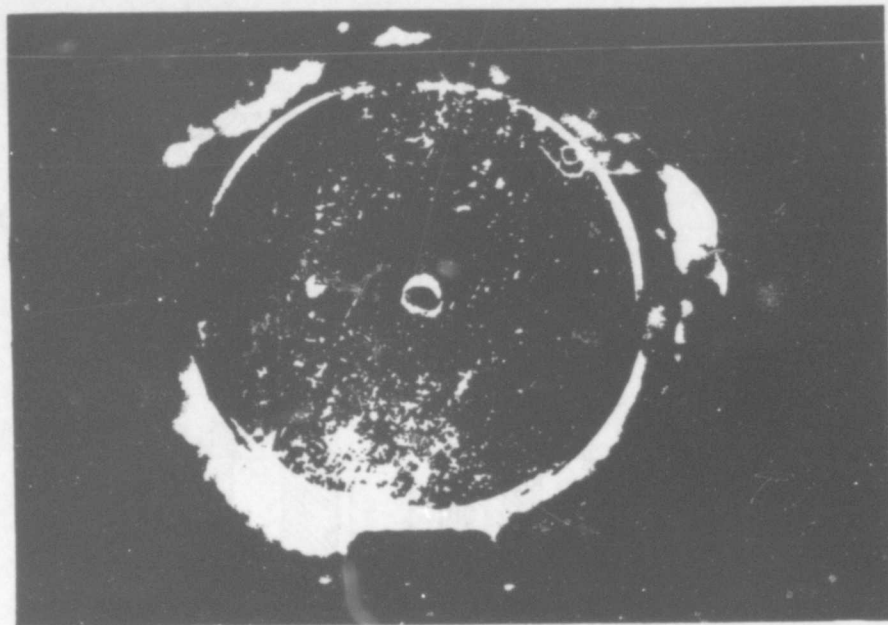
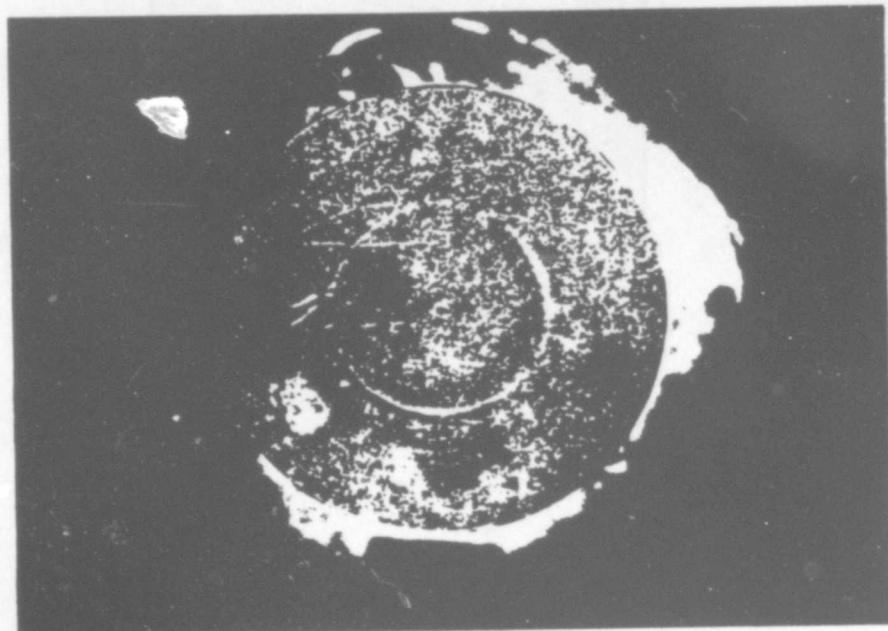


Figure 3.10 Schematic interaction of pod and indent recorder.



LARGE INDENT (no impact ring)



SMALL INDENT (impact ring)

Figure 3.11 Postshot condition of anvils, Blue Gill. (ASE photos)

D-PISTON DATA

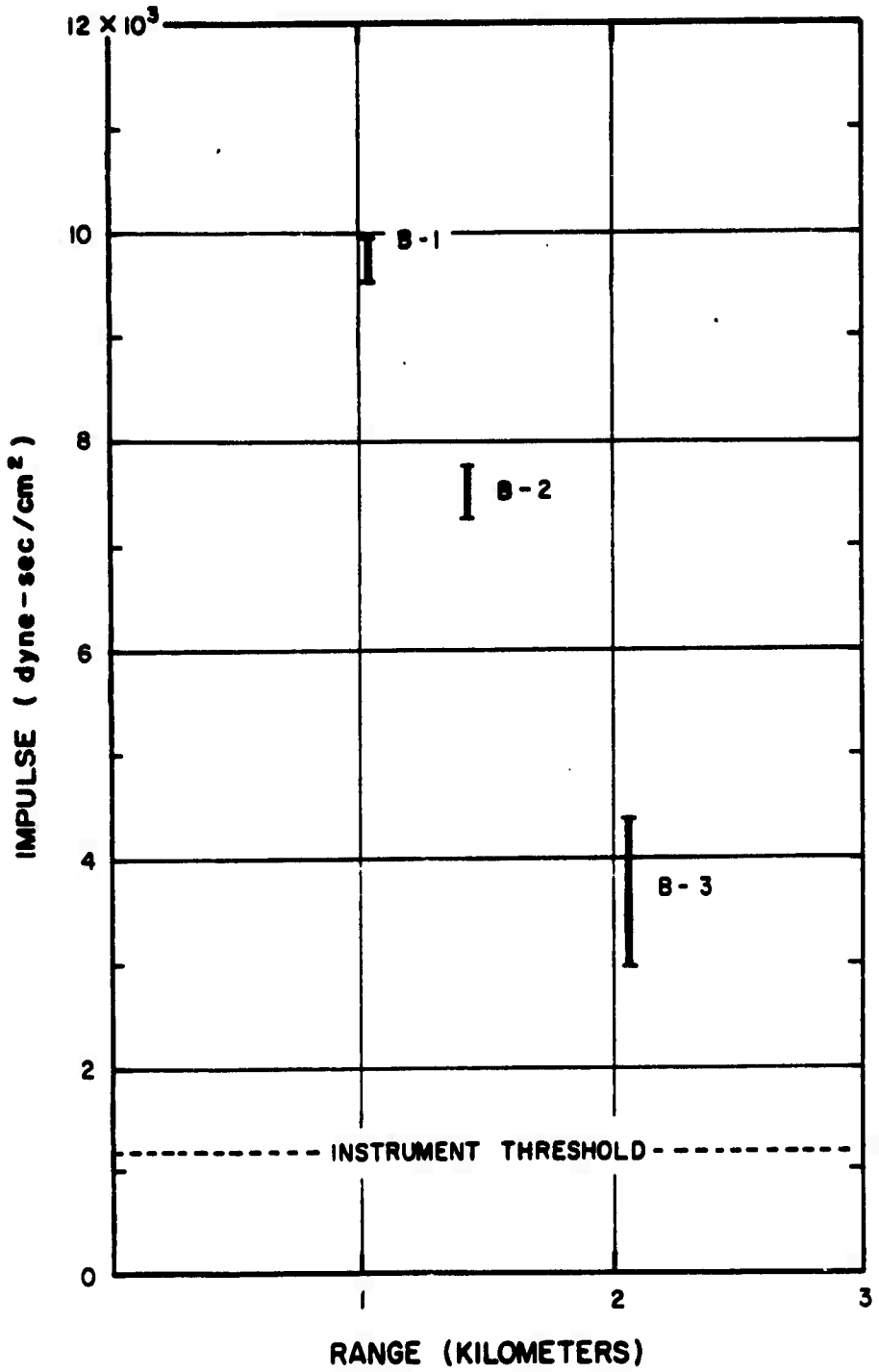


Figure 3.12 Variation of total impulse with pod-to-R/V range.

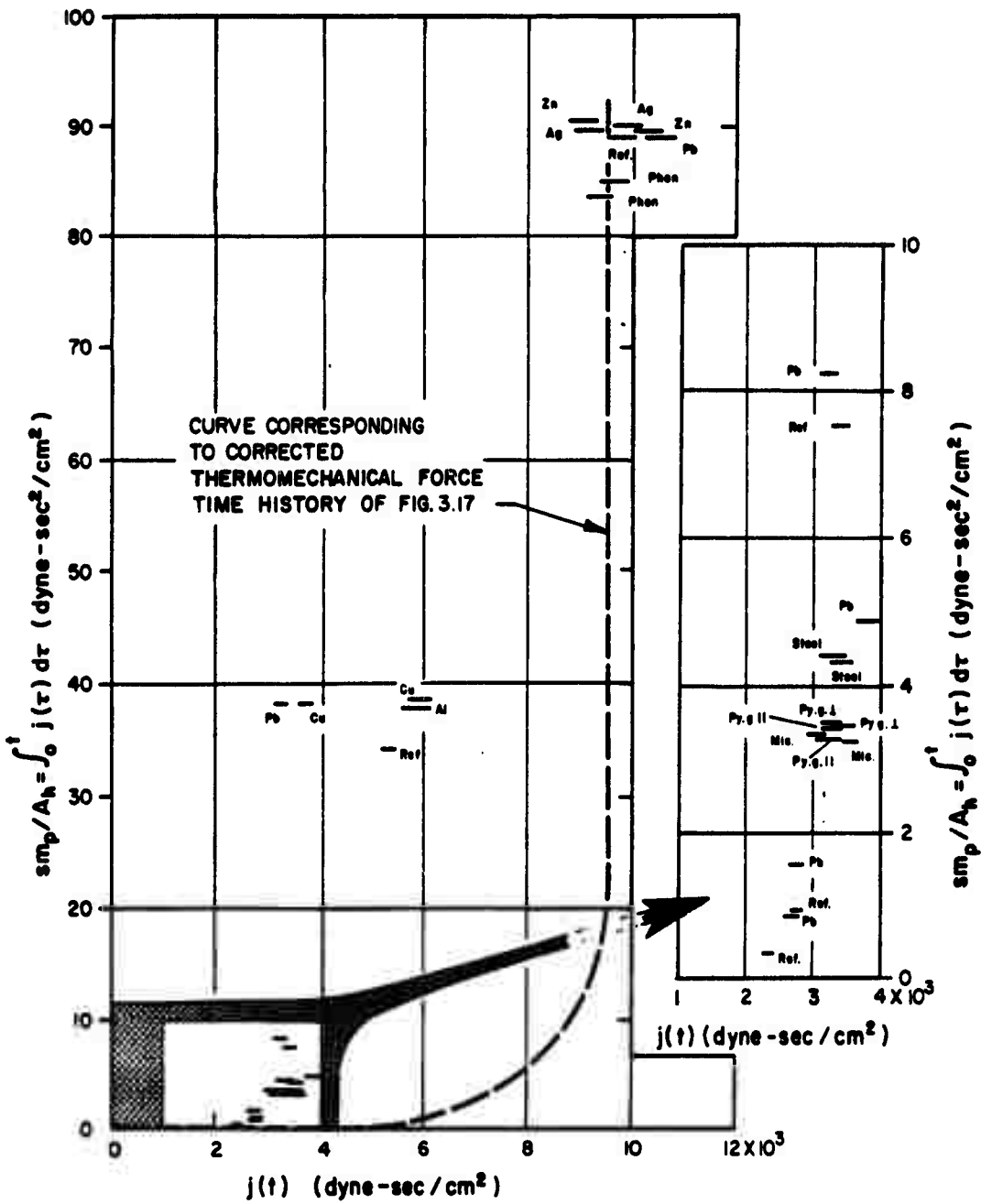


Figure 3.13 Integral of impulse versus impulse, Pod B-1.

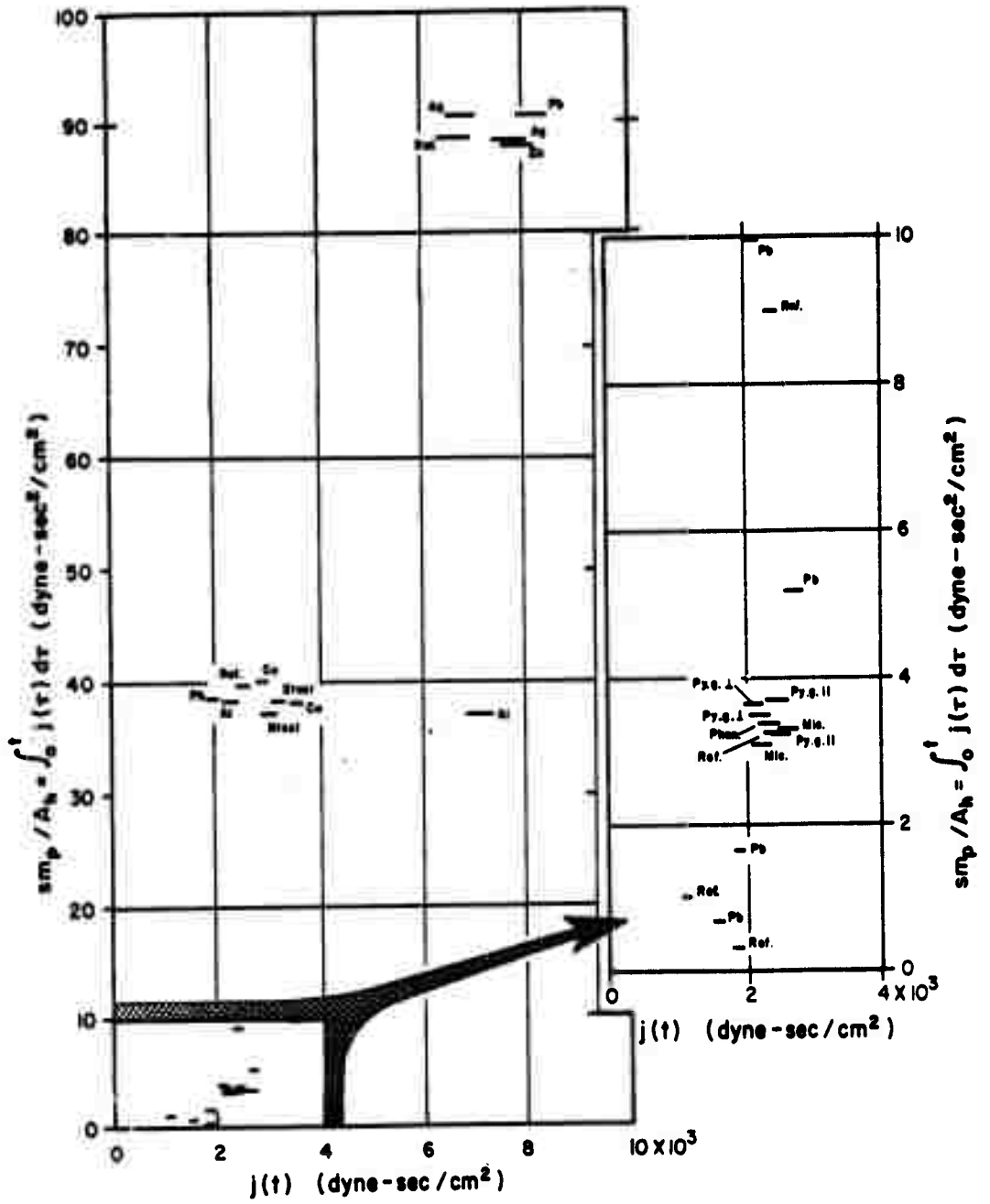


Figure 3.14 Integral of impulse versus impulse, Pod B-2.

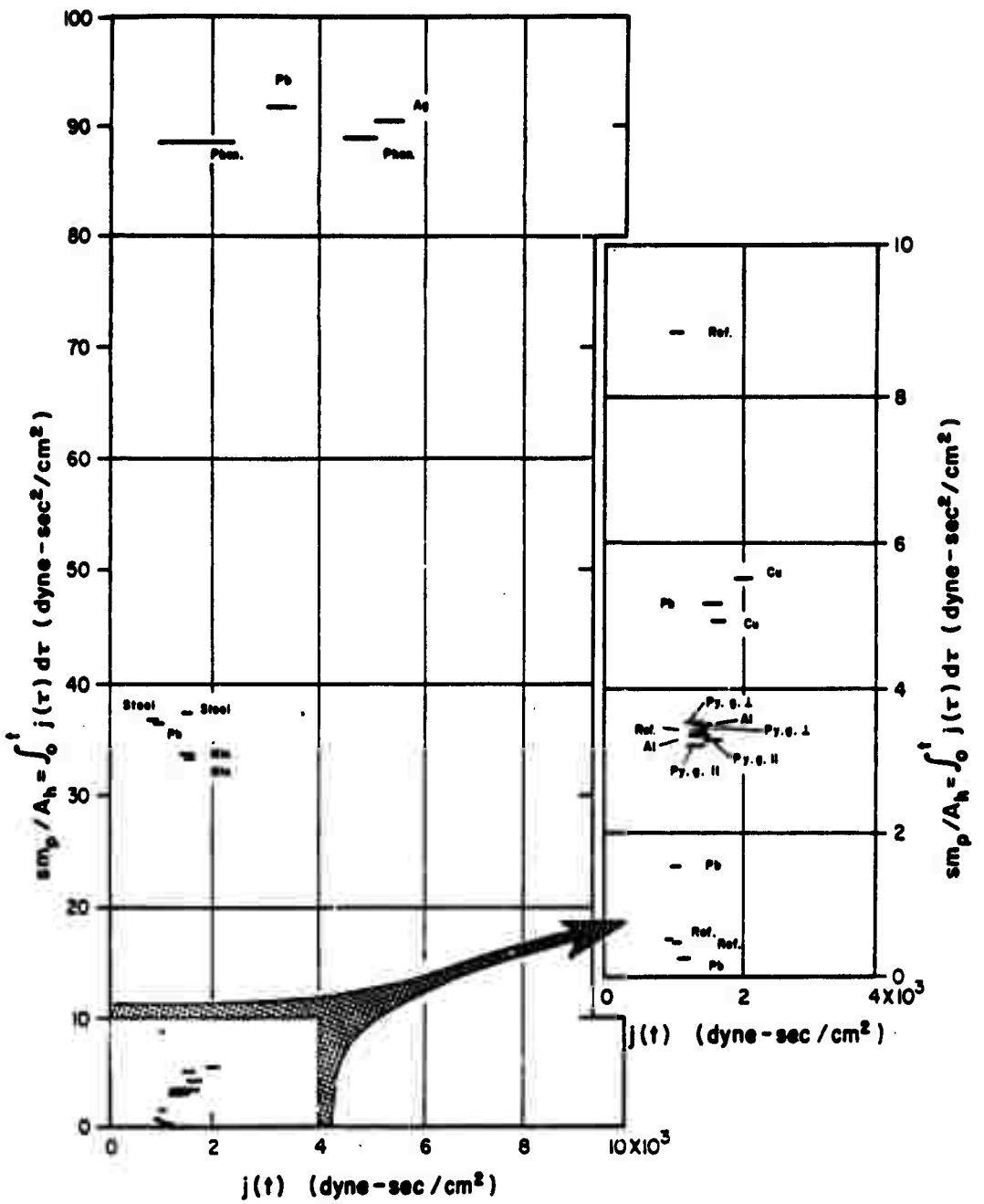


Figure 3.15 Integral of impulse versus impulse, Pod B-3.

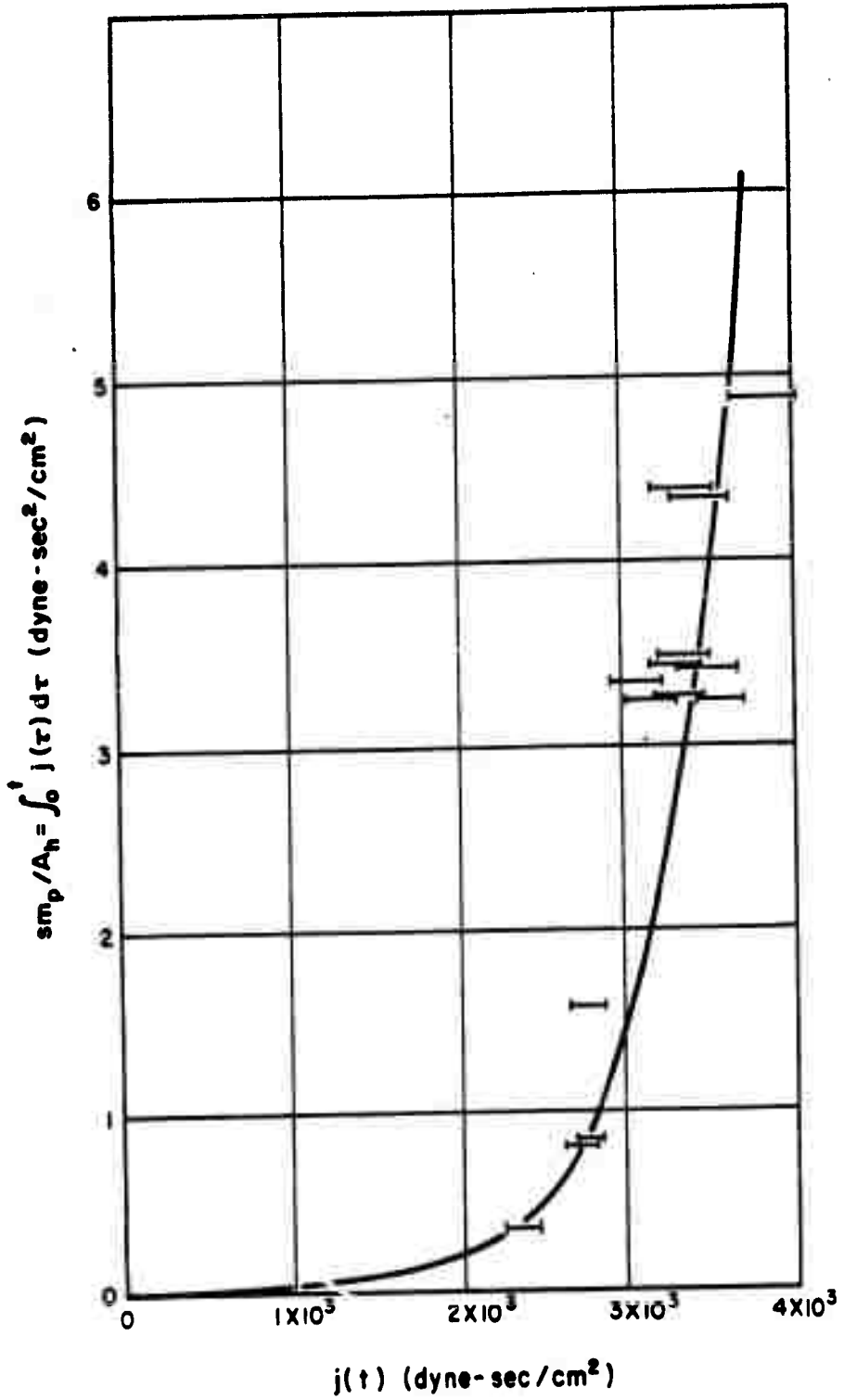


Figure 3.16 Integral of impulse versus impulse, Pod B-1, A-pistons.

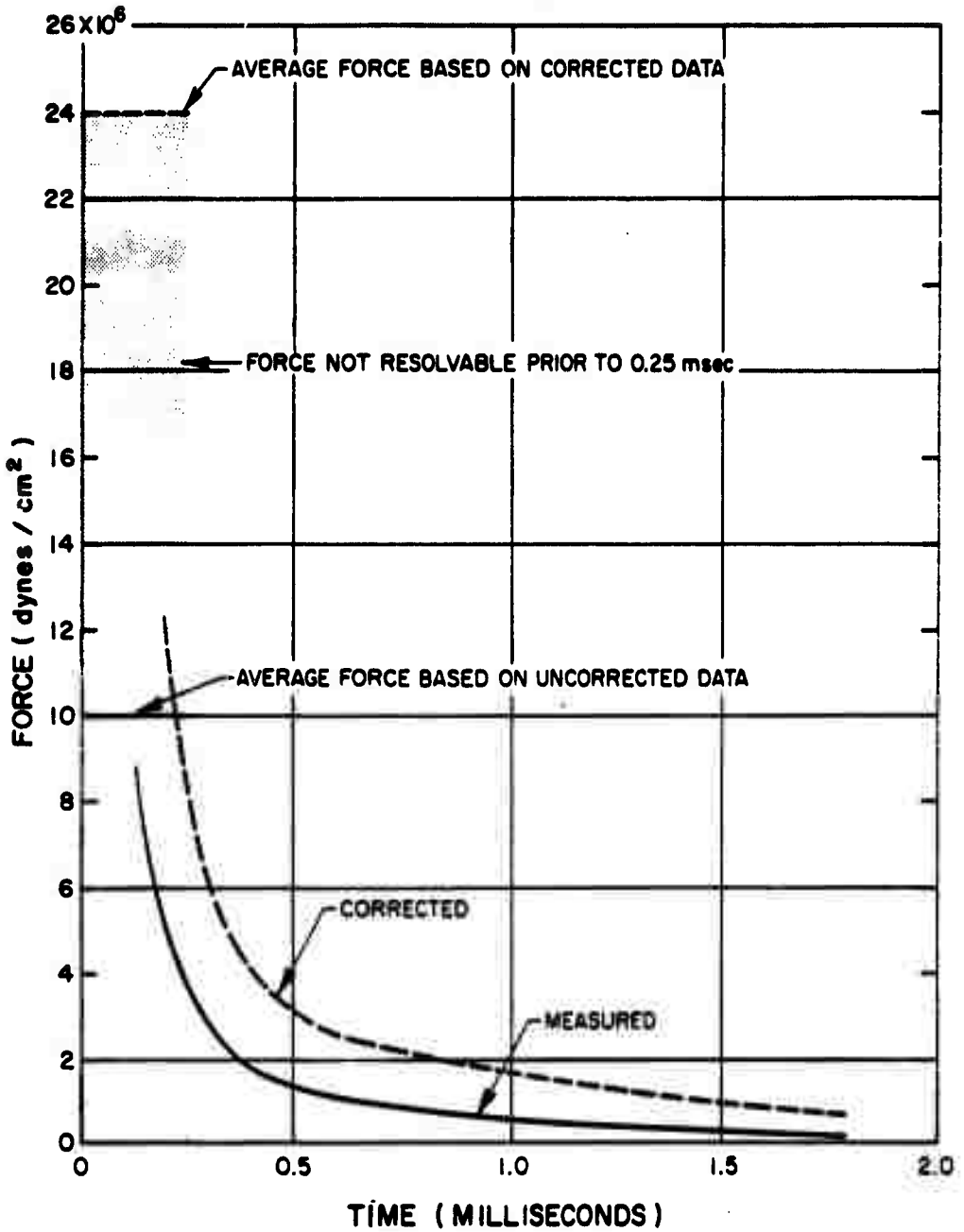


Figure 3.17 Force time history, Pod B-1.

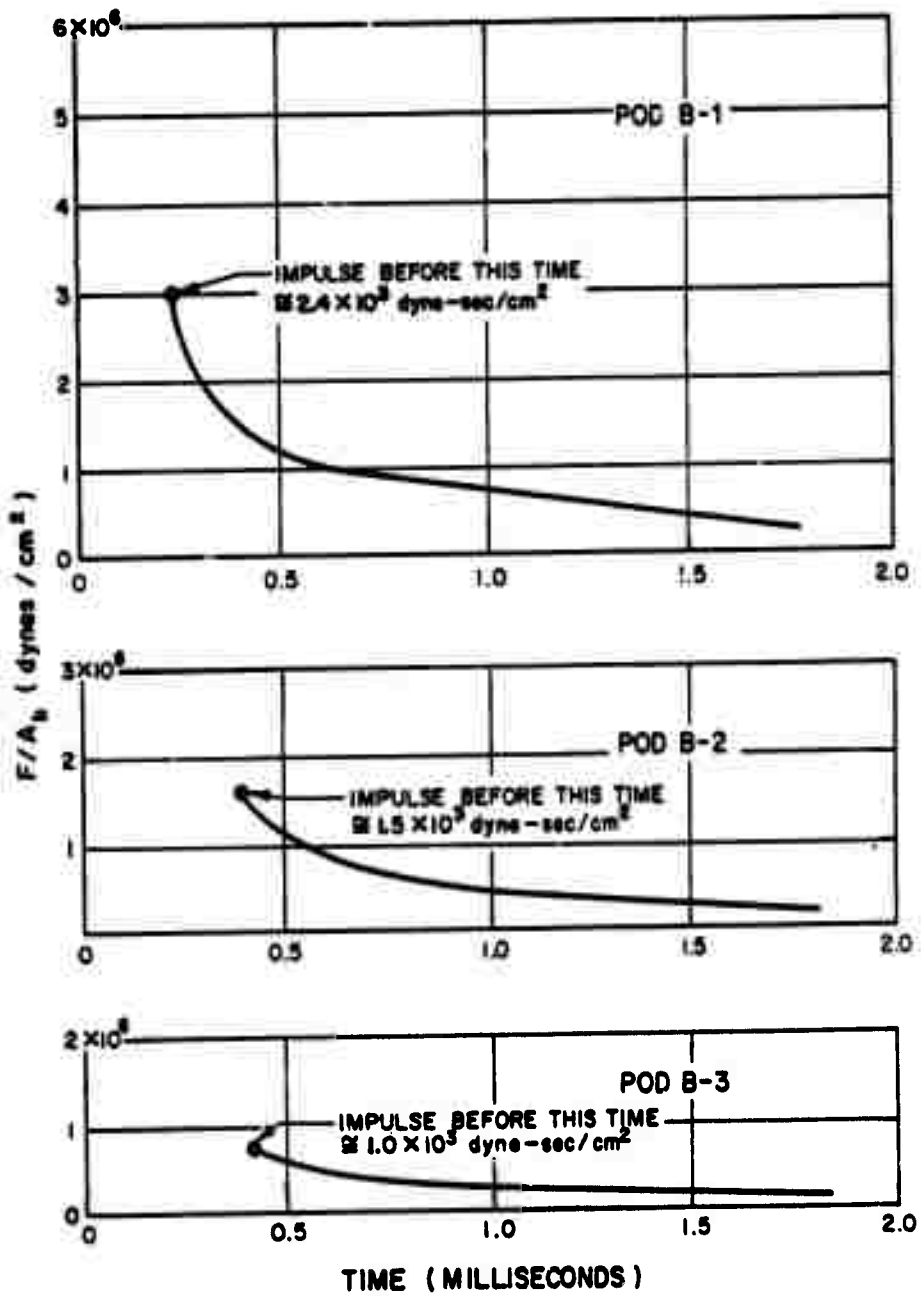
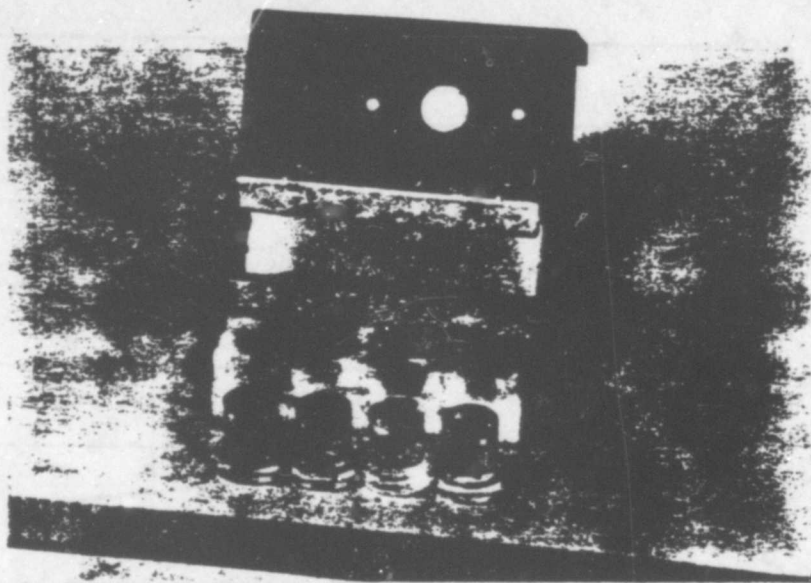
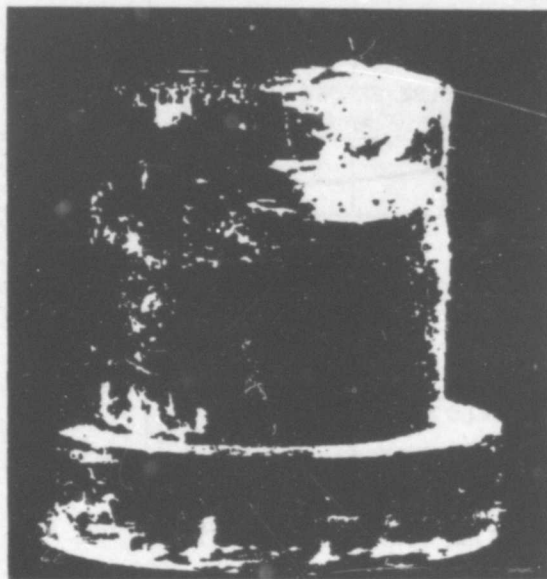


Figure 3.18 Uncorrected force time histories, A-pistons.



A. DISASSEMBLED GAGE



**B. DETECTOR UNDER
LARGE APERTURE**

**Figure 3.19 Postshot condition of spall gage, Pod B-1.
(ASE photos)**

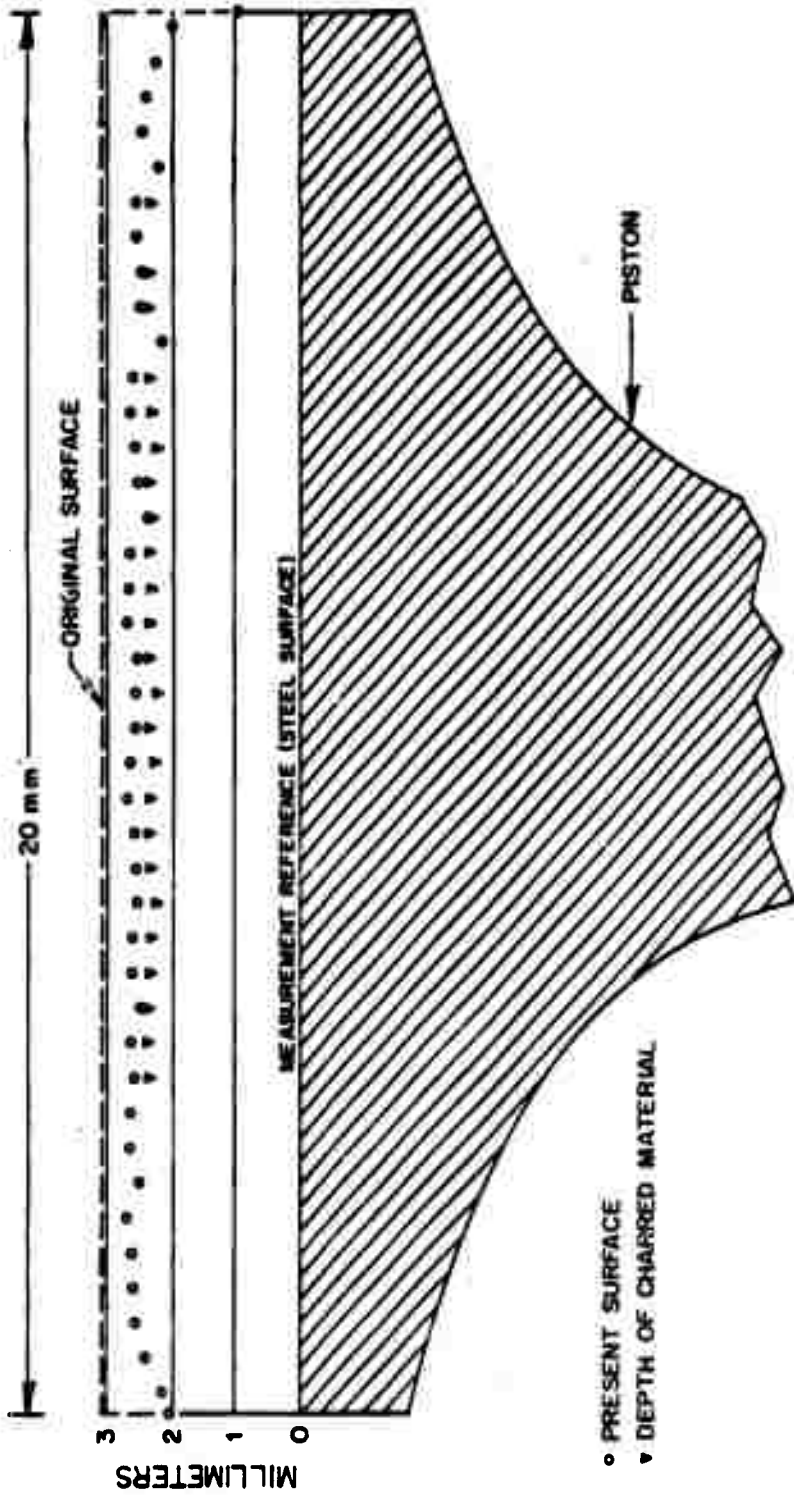


Figure 3.20 Ablation of refrasil-phenolic. A-piston sample.

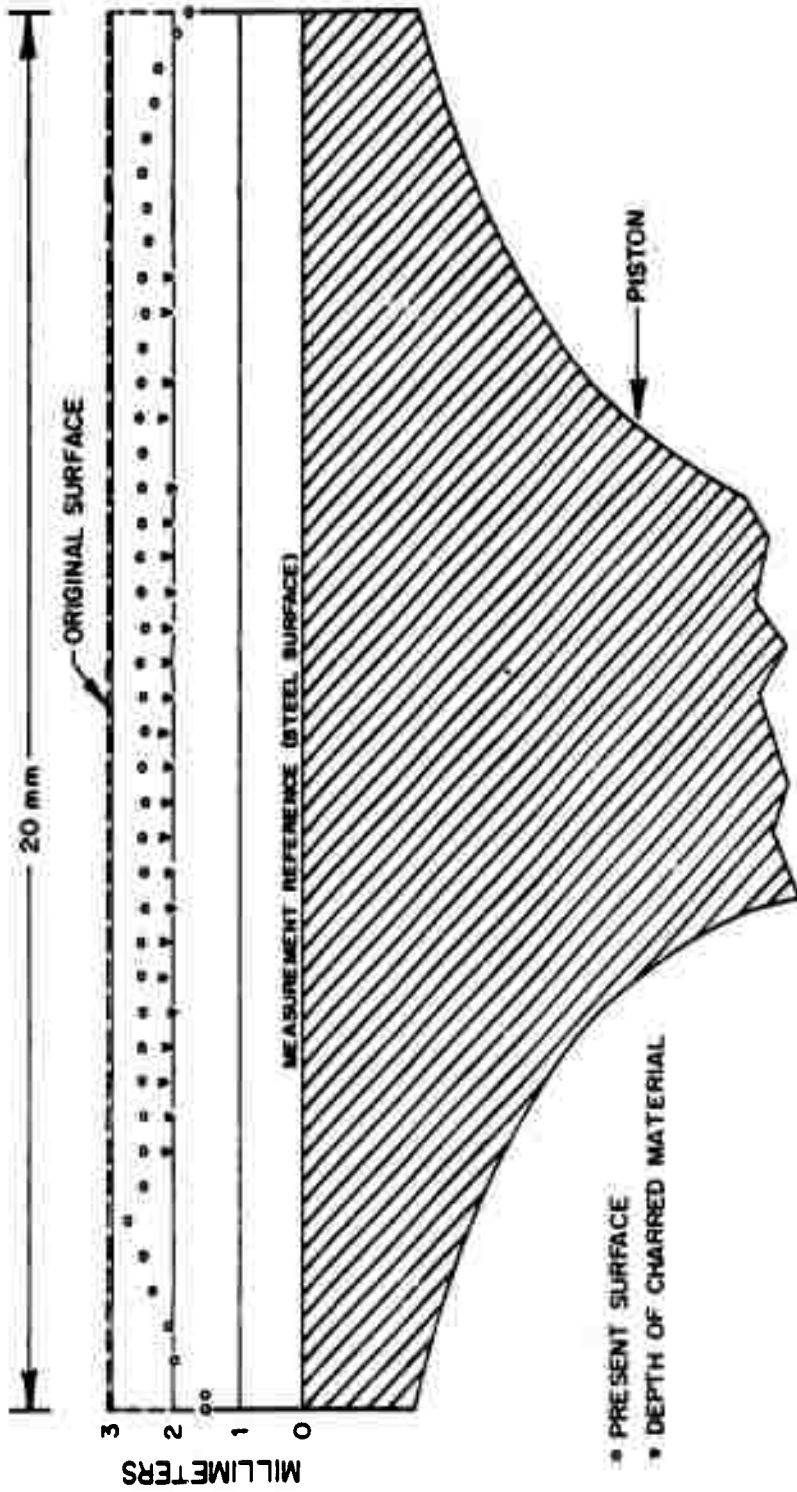
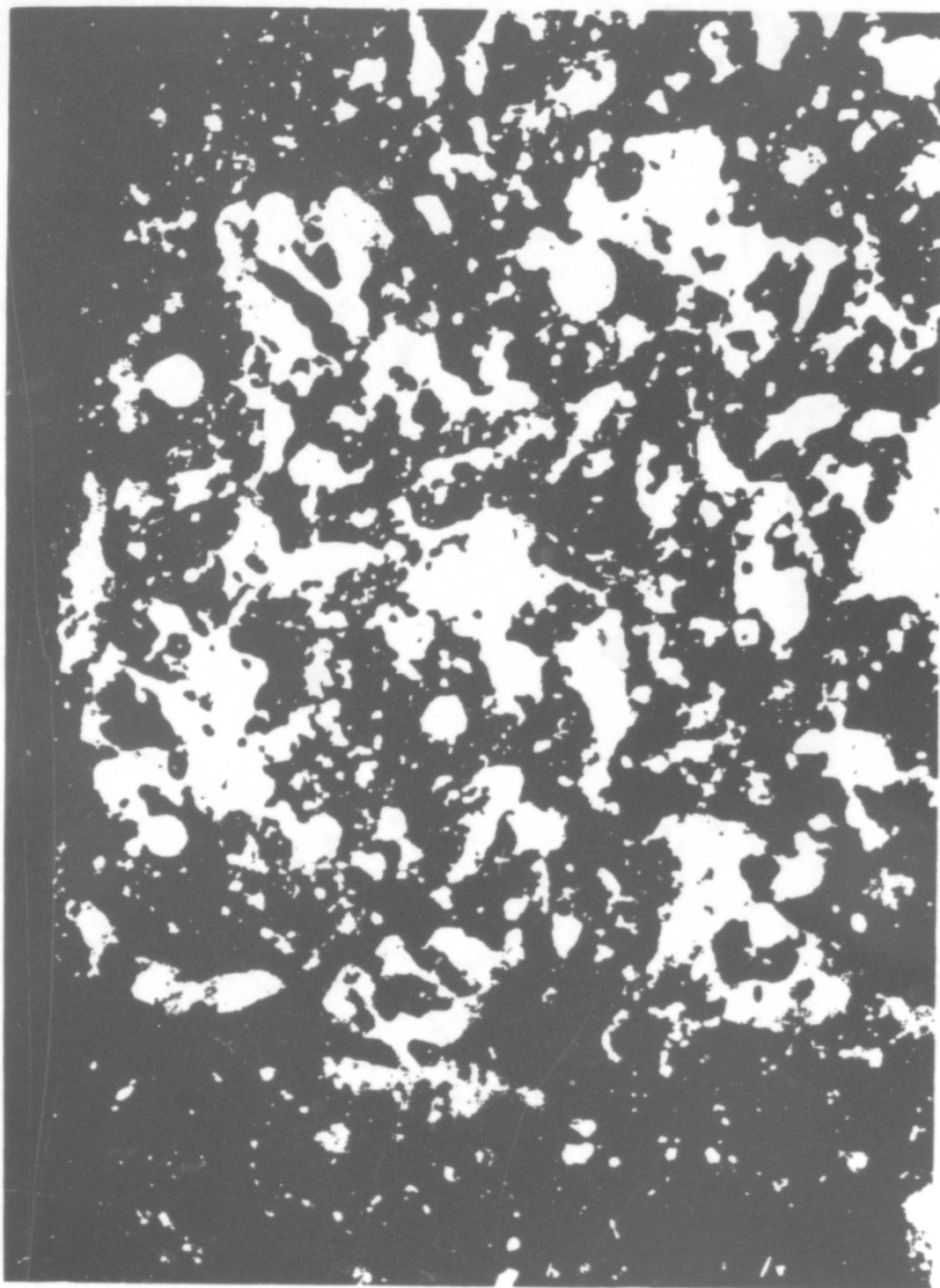


Figure 3.21 Ablation of reffrasil-phenolic, F-piston sample.



ORIGINAL PHOTO IN CCI.OP

Figure 3.22 Refrasil-phenolic before exposure.
(ASE photo)



ORIGINAL PHOTO IN COLOR

Figure 3.23 Exposed refrasil-phenolic, Pod B-1.
(ASE photo)

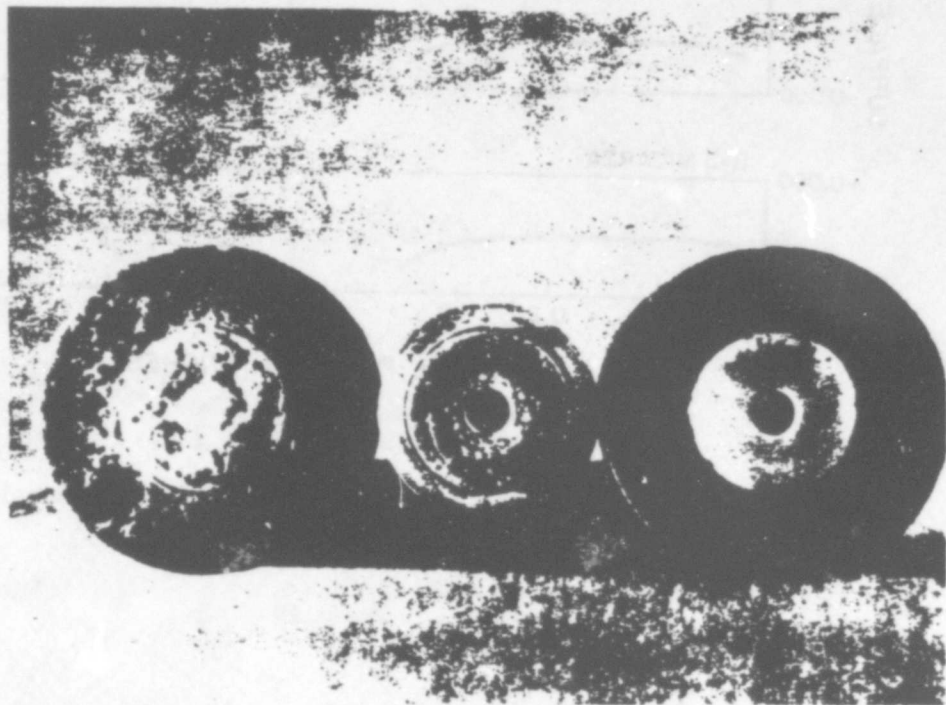
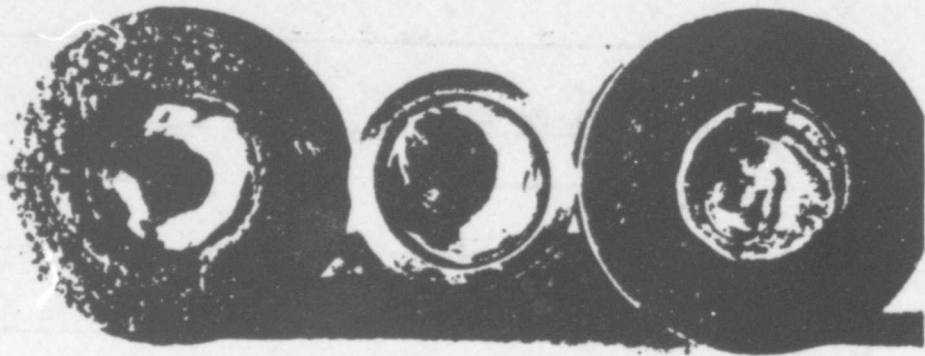


Figure 3.24 Postshot condition of ablation-condensation gages.
(ASE photos)

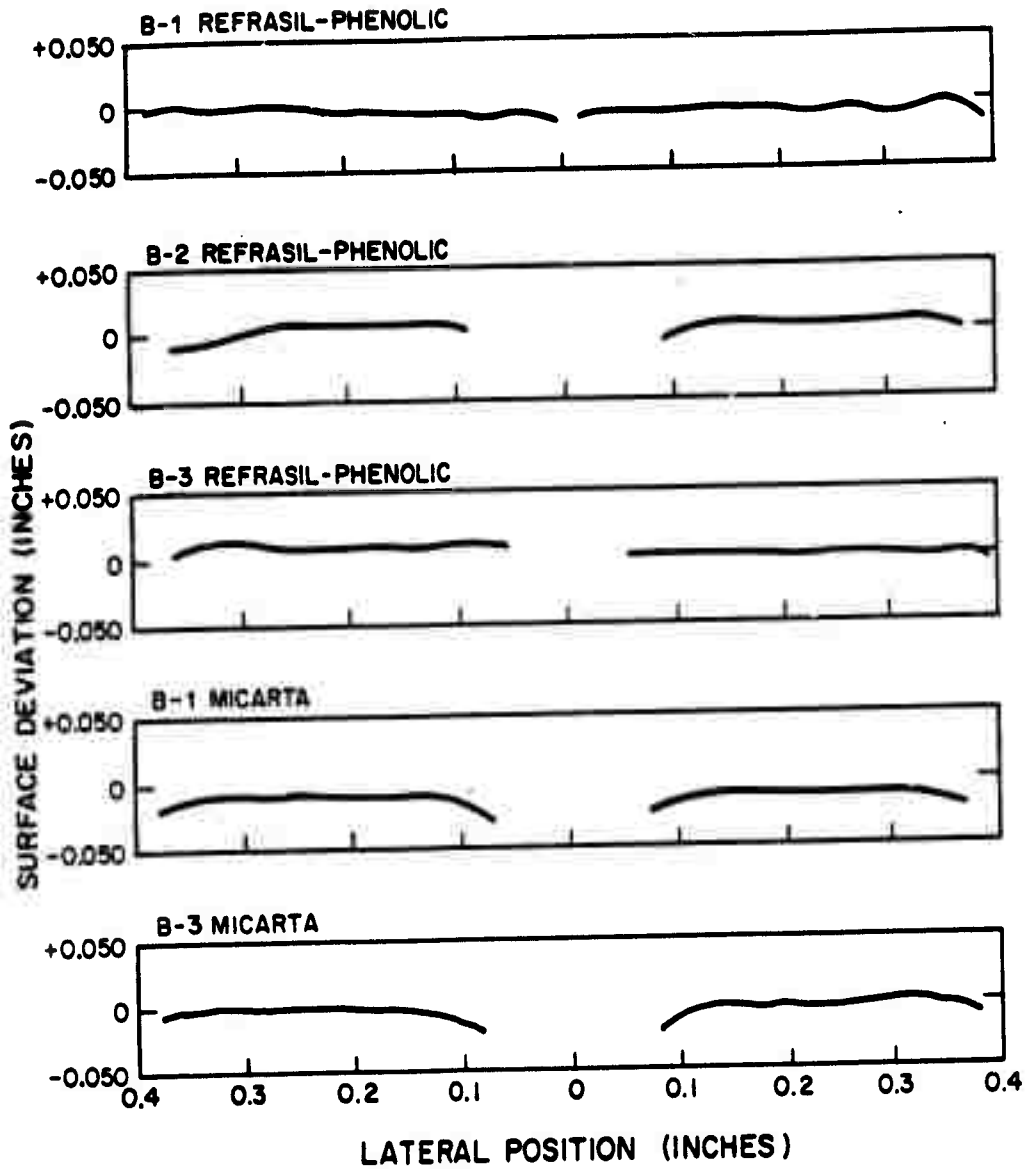


Figure 3.25 Surface profiles of Blue Gill ablation samples (refrasil-phenolic and micarta).

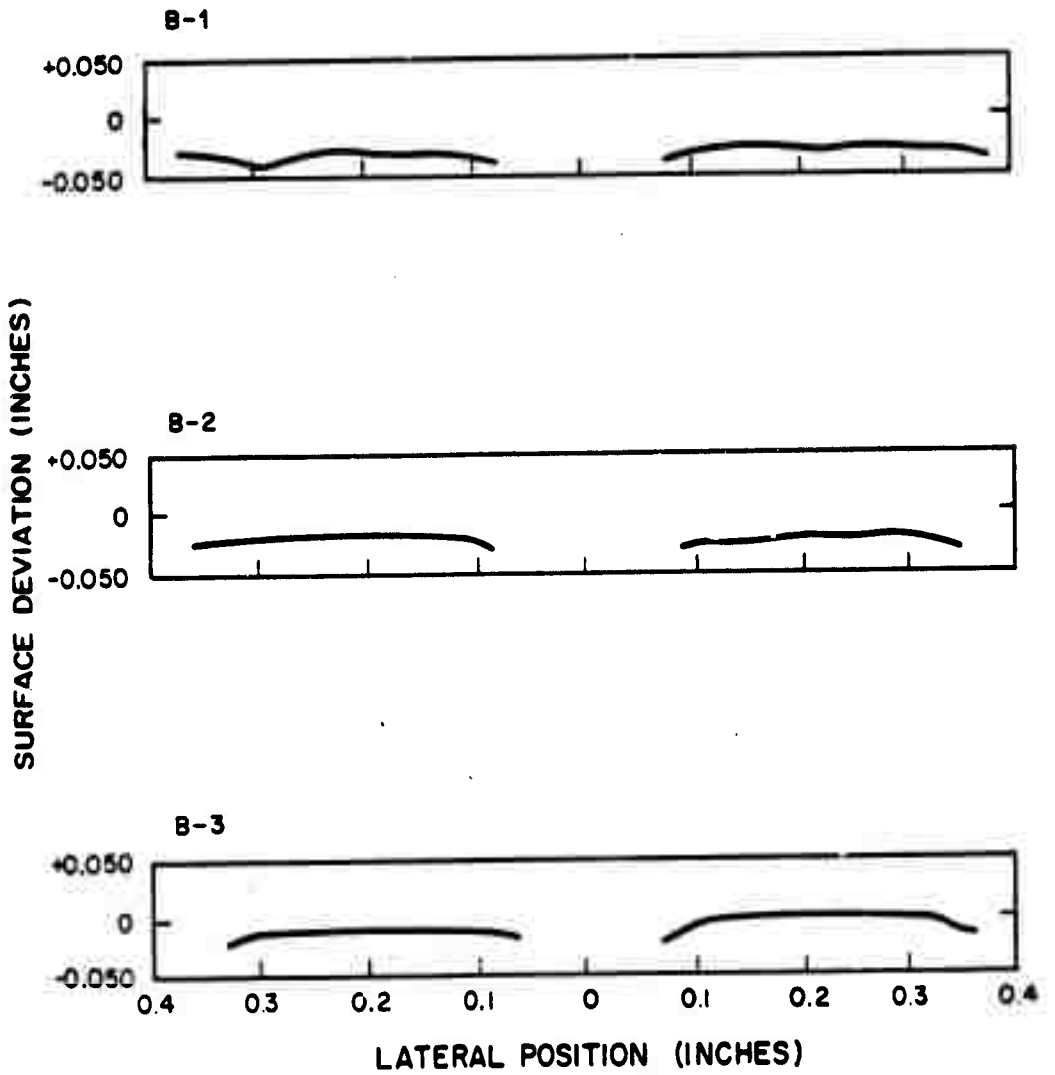


Figure 3.26 Surface profiles of Blue Gill ablation samples, iron devcon.

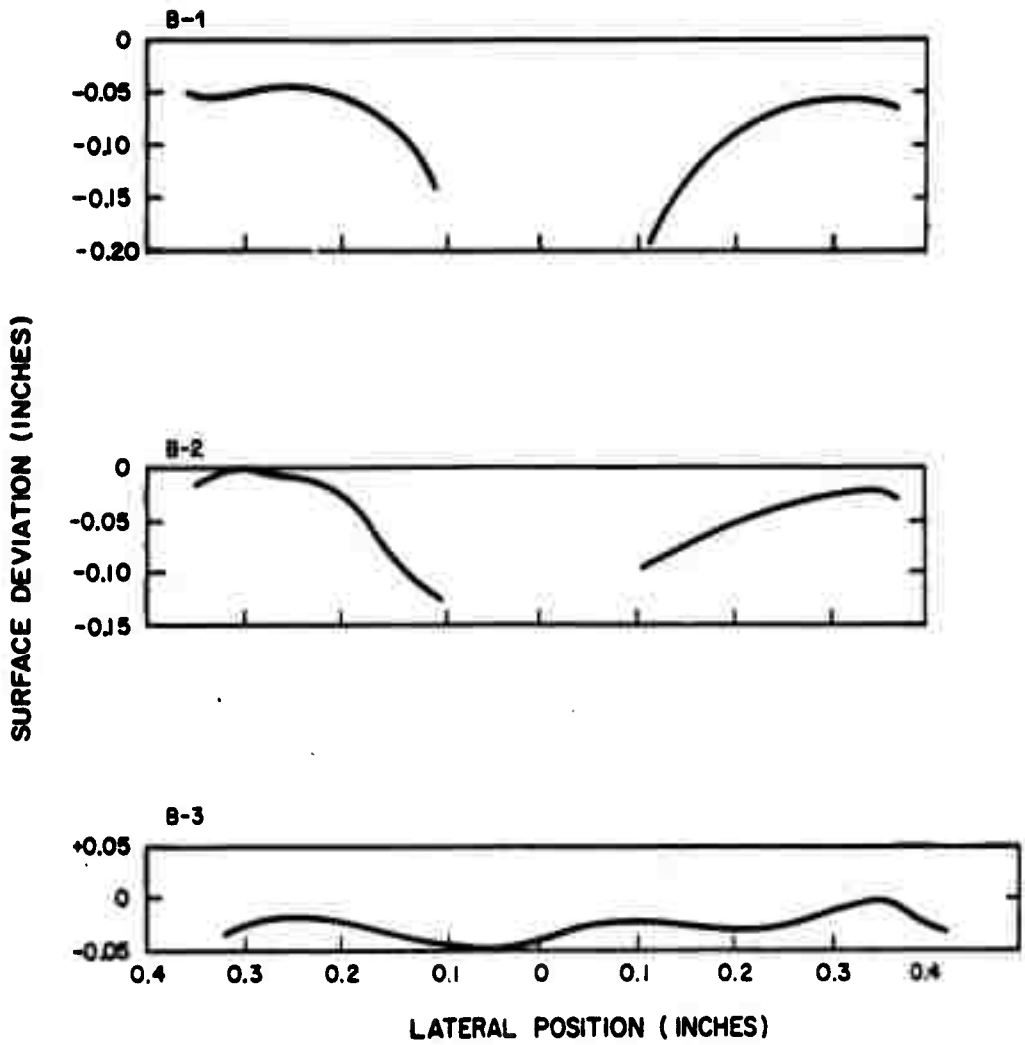


Figure 3.27 Surface profiles of Blue Gill ablation samples, lead.

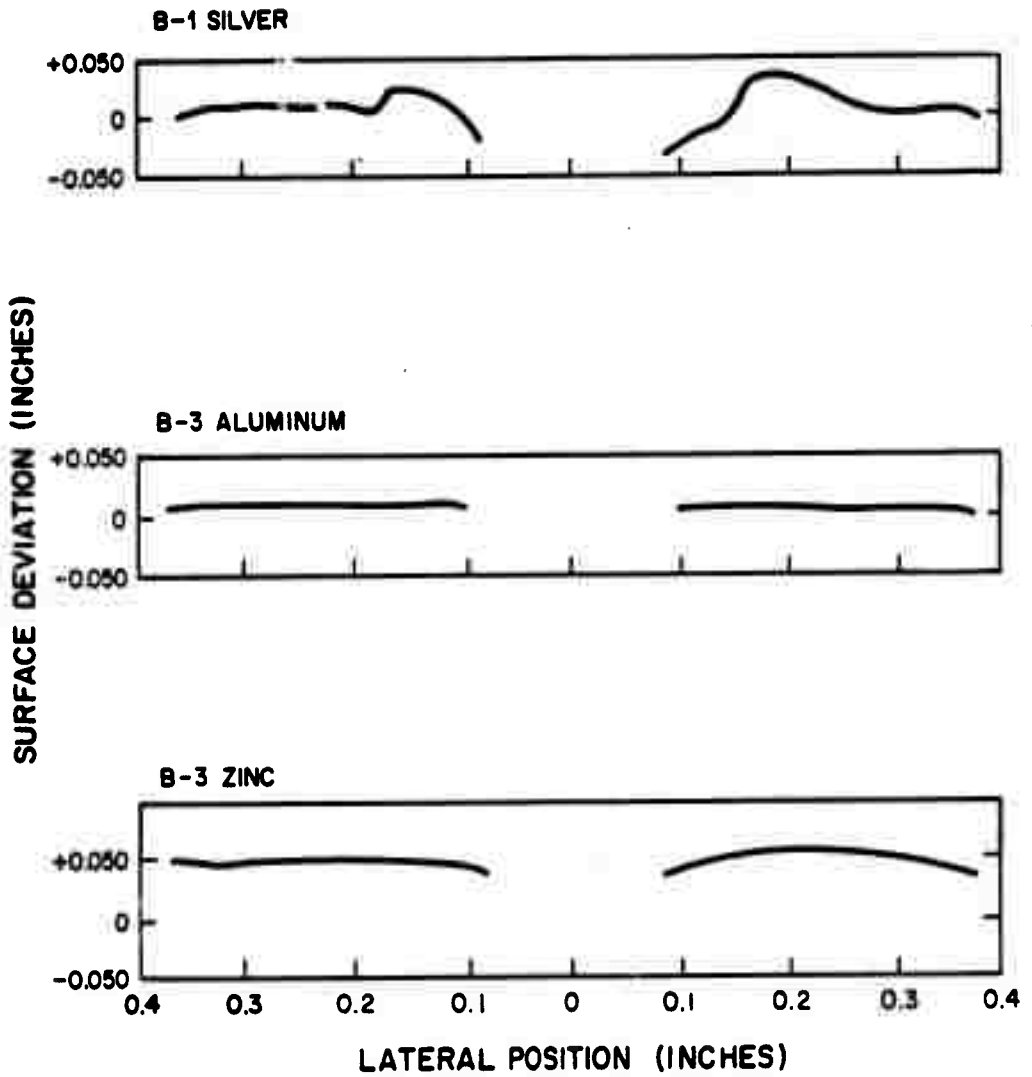
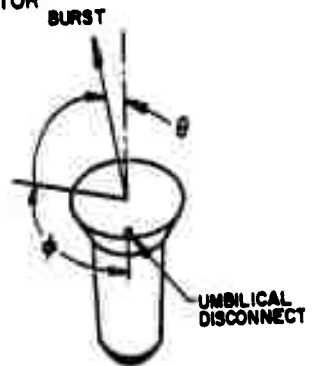
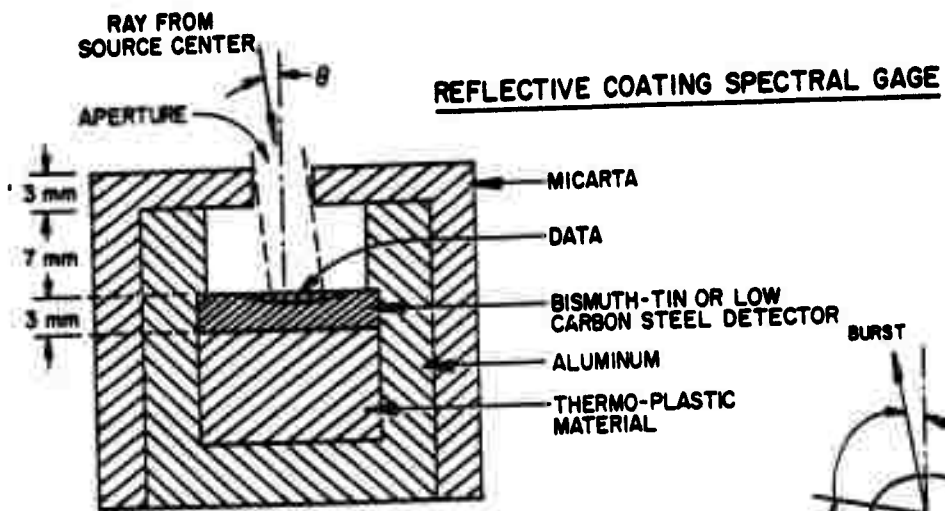
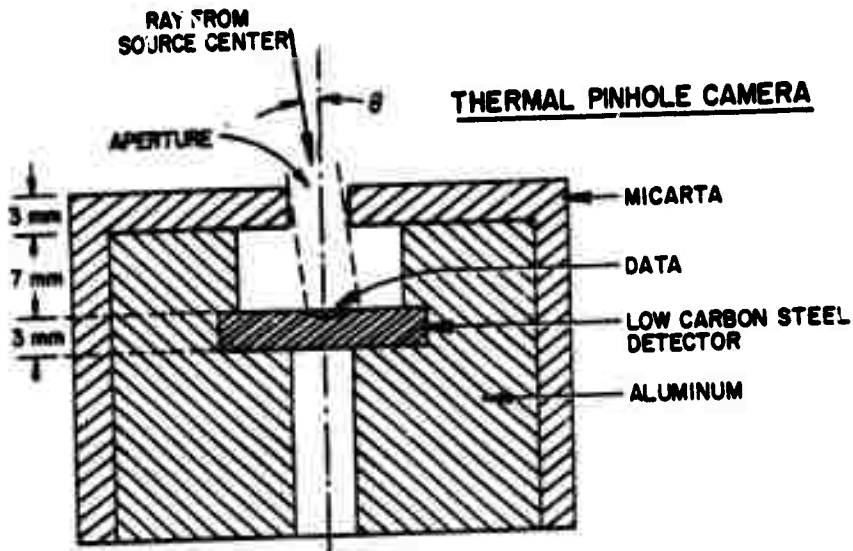


Figure 3.28 Surface profiles of Blue Gill ablation samples, silver, aluminum, and zinc.

ALL CROSS SECTIONS MADE IN PLANE OF BURST



POD NUMBER	NOMINAL ORIENTATION ANGLES	
	ELEVATION, θ	AZIMUTH, ϕ
B-1	12.1° TO 13.1°	306°
B-2	7.5° TO 8.7°	114°
B-3	3°	250°
K-1	3° TO 5°	100°

APERTURE DIAMETERS
1, 3, 10 mm

Figure 3.29 Location of metallurgical data in thermal instruments.

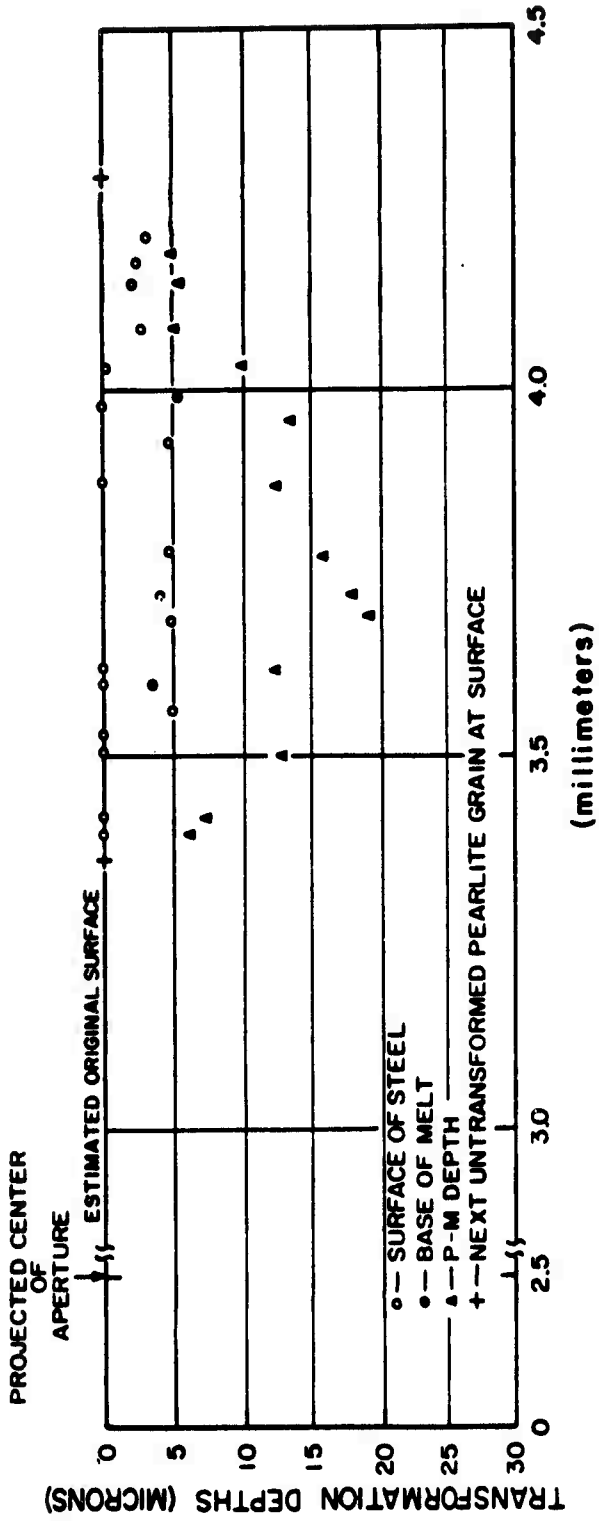


Figure 3.30 Transformation depths in thermal pinhole camera, top slotted steel gage, 1-mm aperture, Pod B-1.

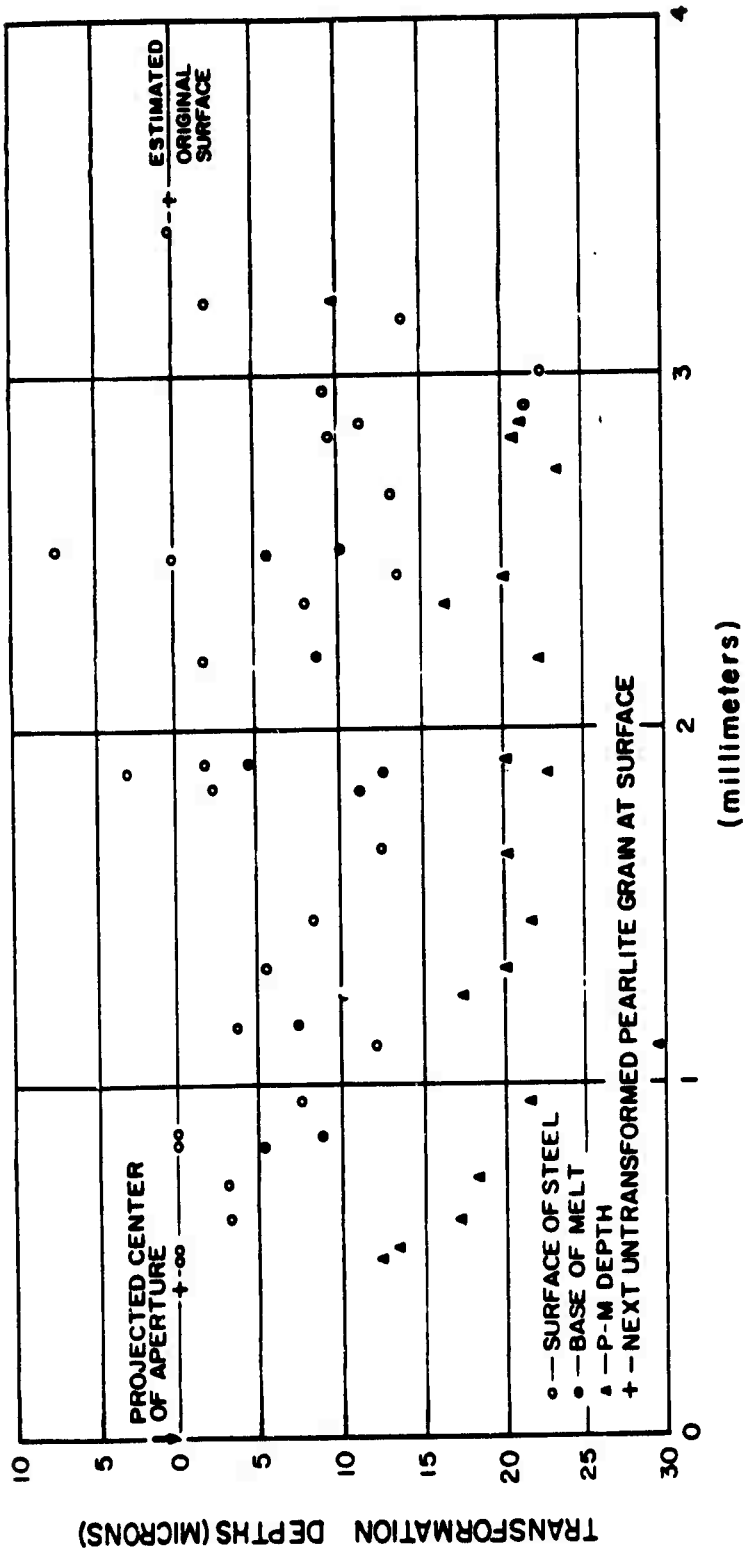


Figure 3.31 Transformation depths in thermal pinhole camera, top slotted steel gage, 3-mm aperture, Pod B-1.

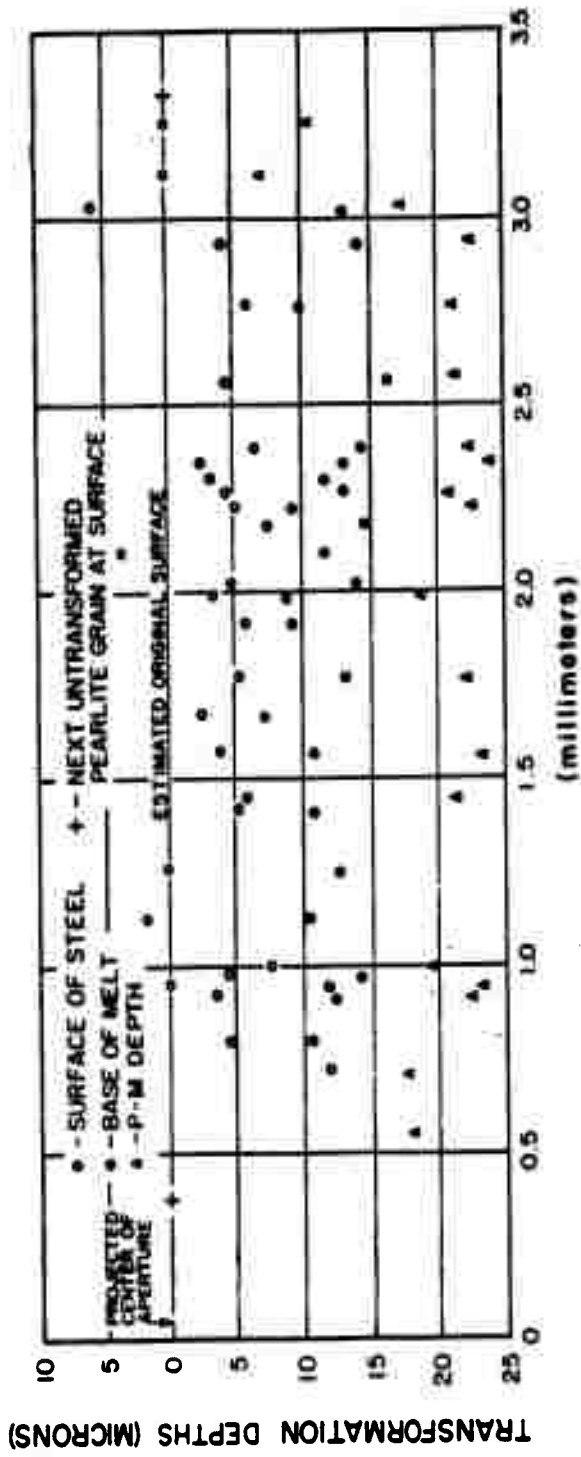


Figure 3.32 Transformation depths in thermal pinhole camera, top unslotted steel gage, 3-mm aperture, Pod B-1.

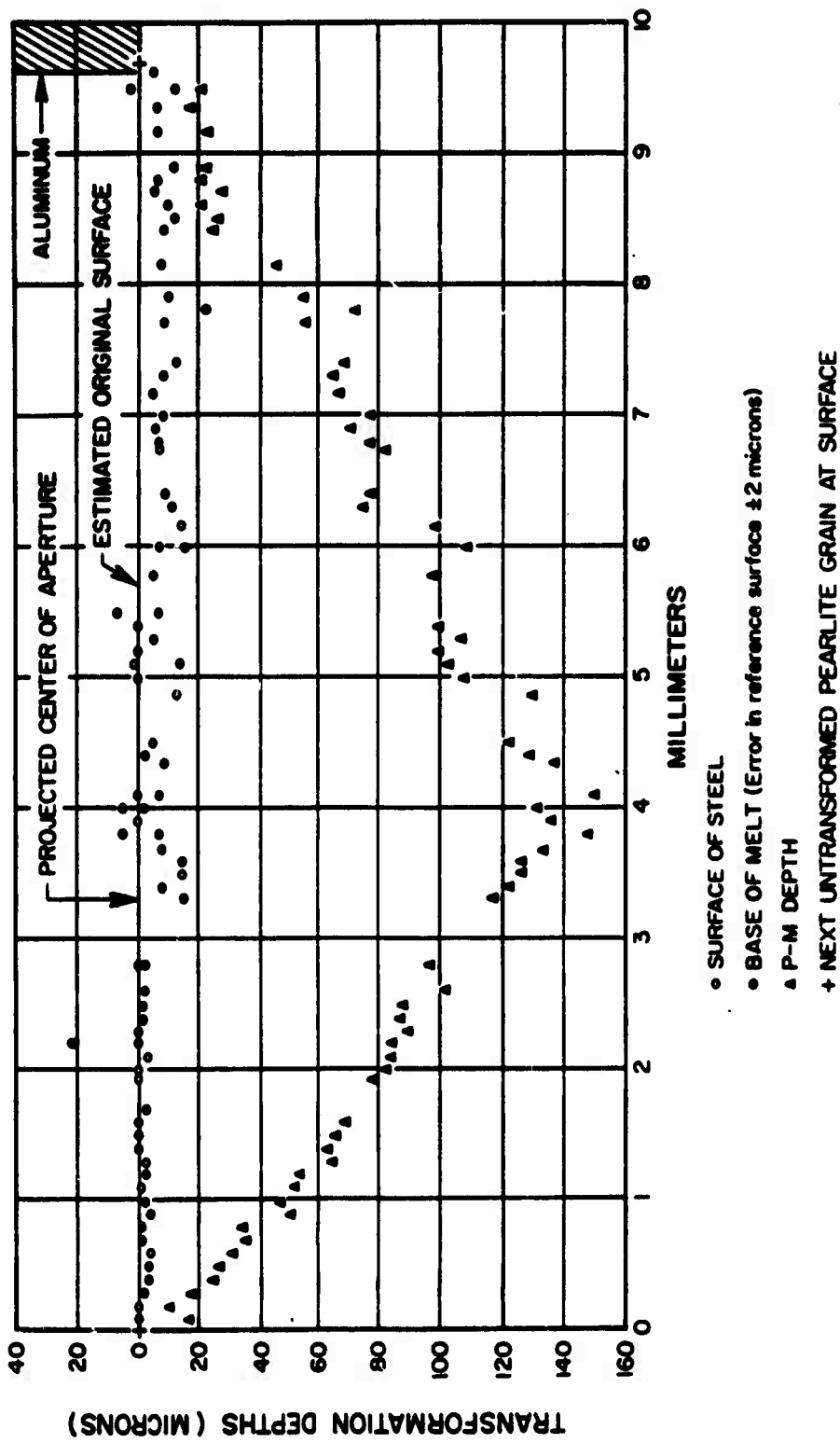


Figure 3.33 Transformation depths in thermal pinhole camera, top slotted steel gage, 10-mm aperture, Pod B-1.

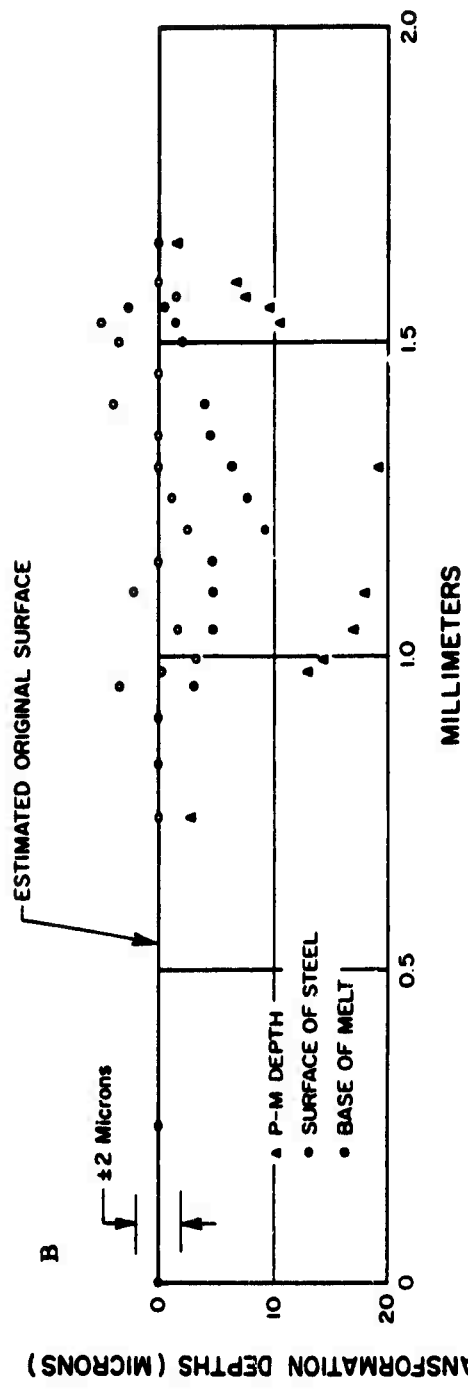
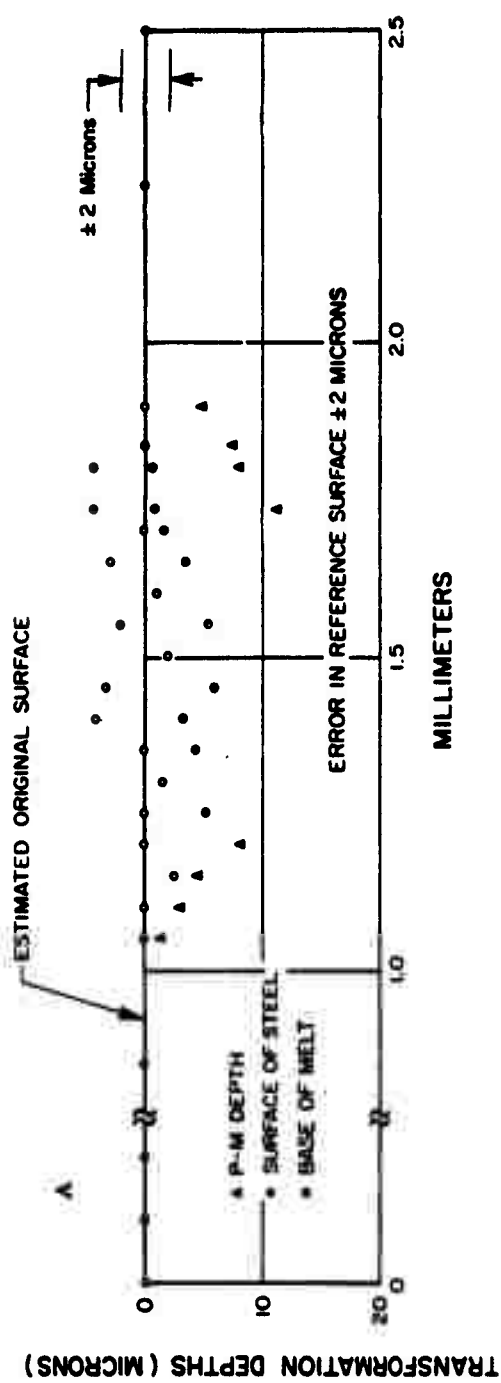
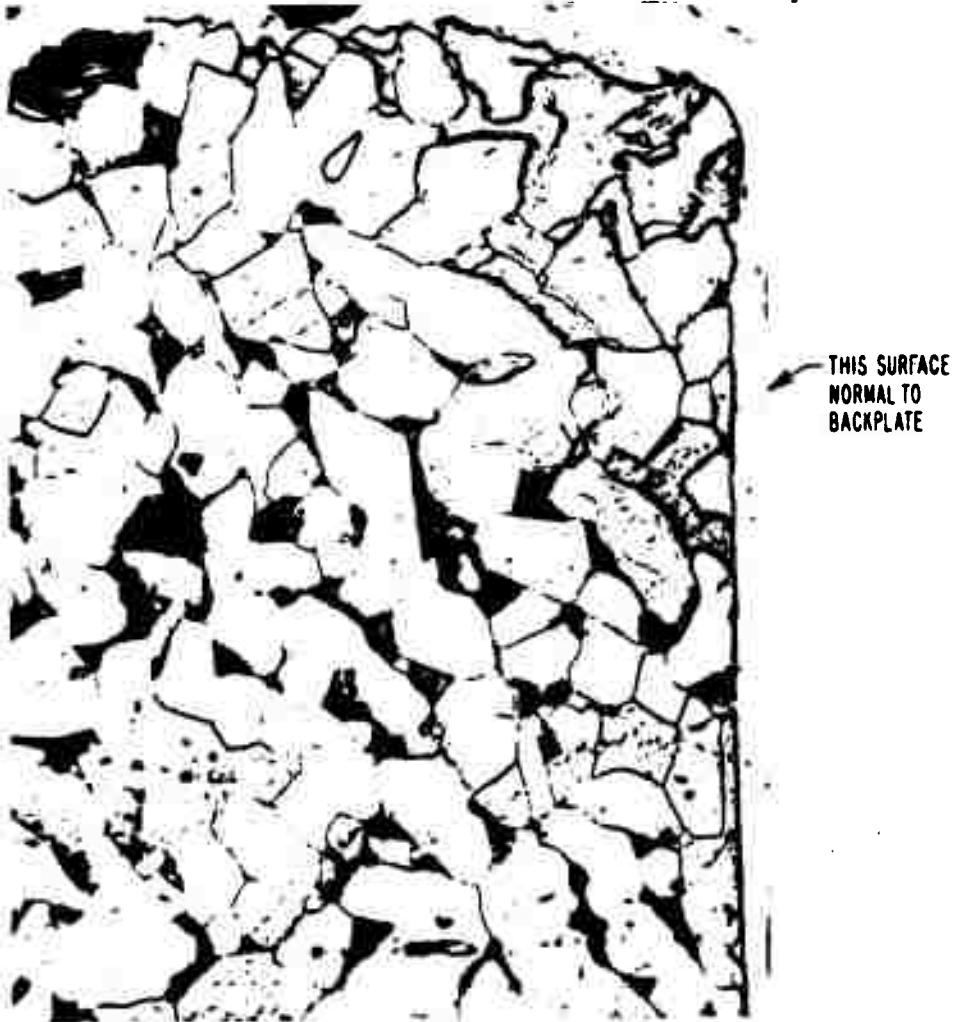


Figure 3.34 Transformation depths in thermal pinhole camera, top slotted steel gage, 1-mm aperture, Pod B-1.

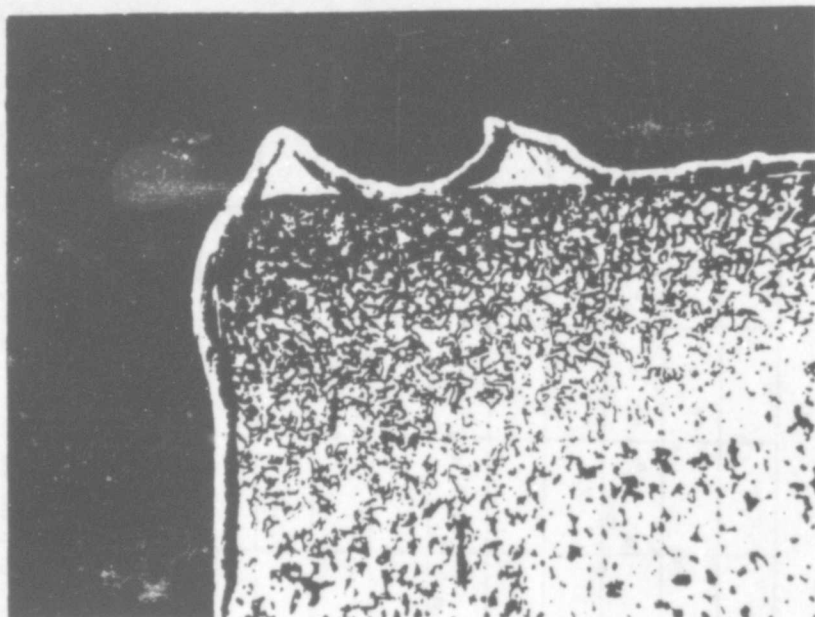
THERMAL PINHOLE CAMERA
SIDE FLUSH STEEL DETECTOR
BLUE GILL POD 1



MAGNIFICATION = 670X
ETCHANT = 1% NITAL

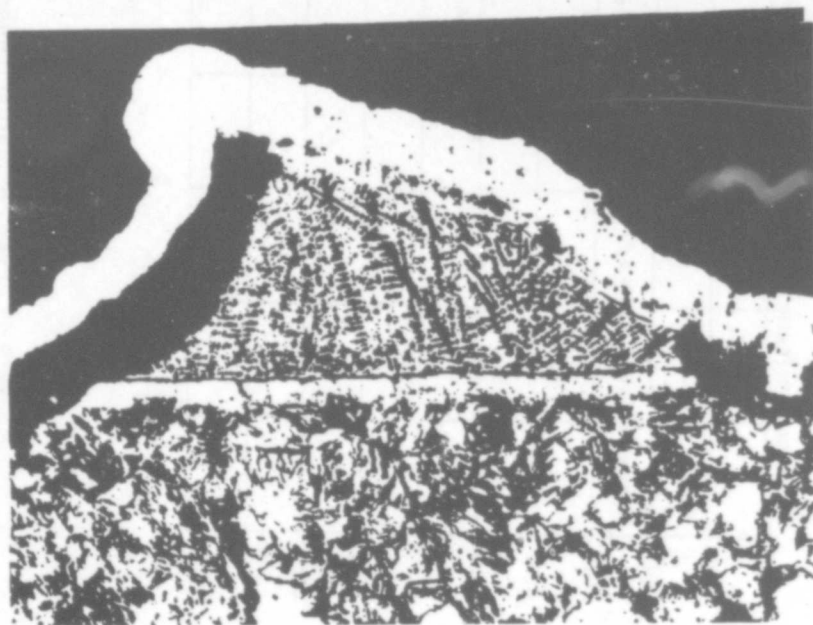
Figure 3.35 Photomicrograph of solid transformation.
(ASE photo)

POD B-1 THERMAL PINHOLE CAMERA



ETCHANT -
1% NITAL

MAGNIFICATION -
125 X



ETCHANT -
1% NITAL

MAGNIFICATION -
600 X

Figure 3.36 Photomicrographs showing transformations on top flush steel gage. (ASE photos)

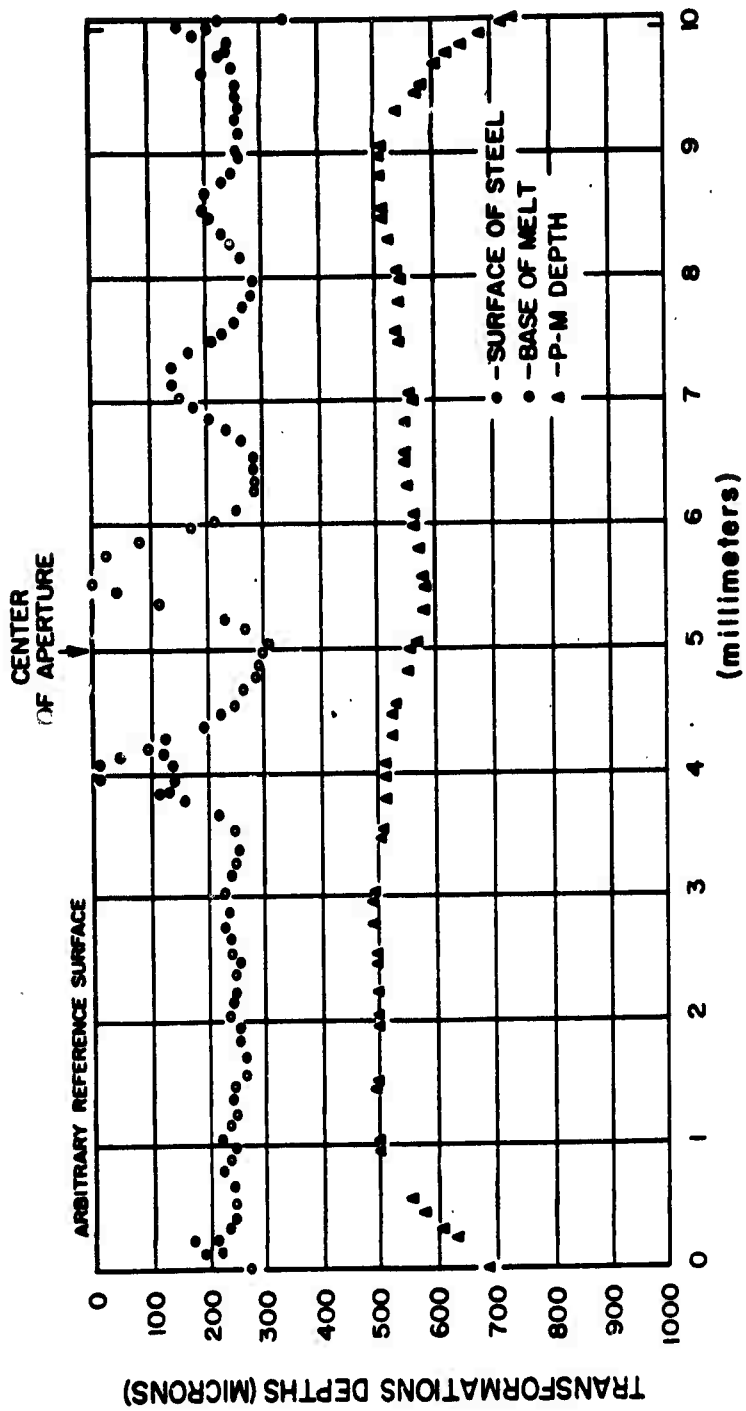


Figure 3.37 Transformation depths in thermal pinhole camera, top flush steel gage, Pod B-1.

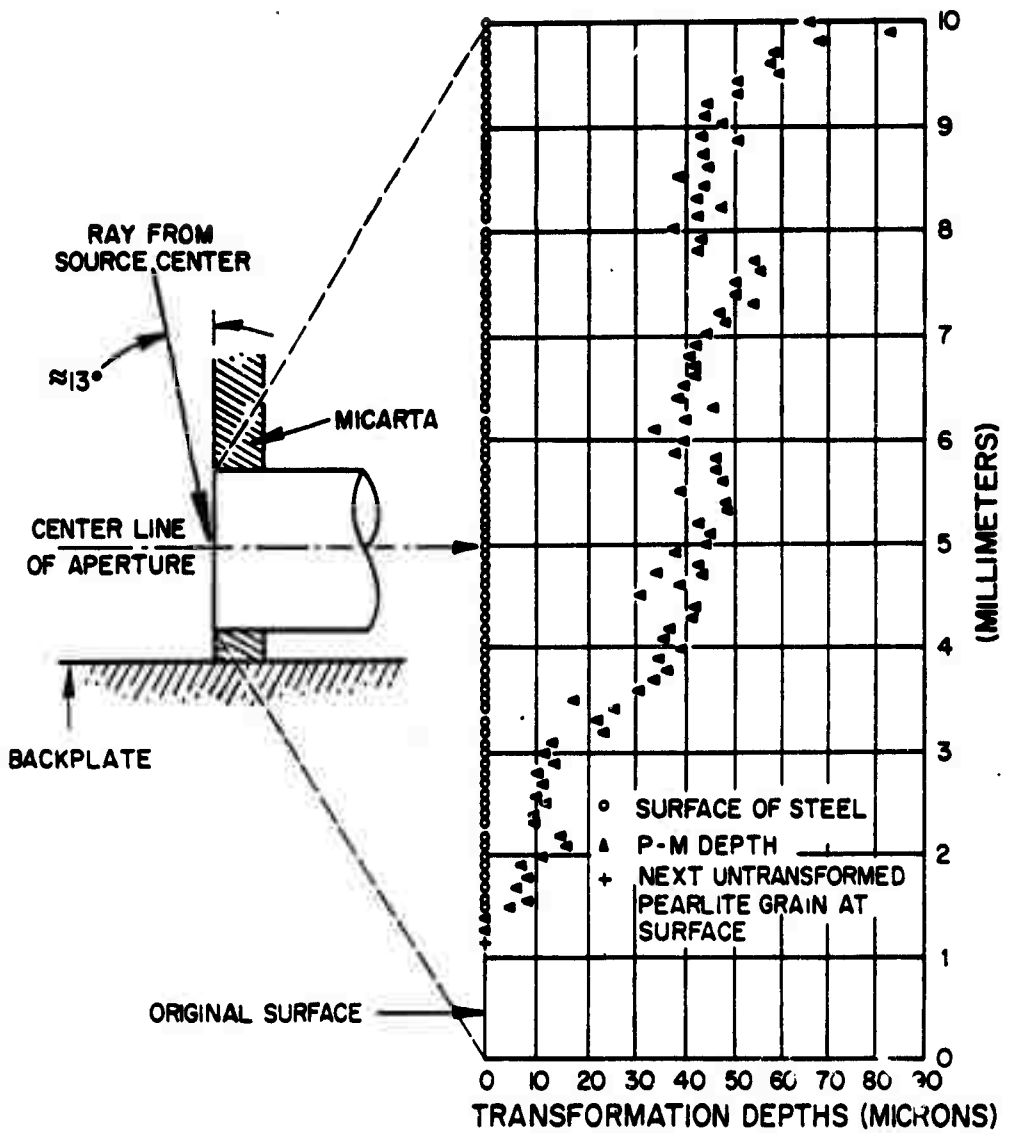


Figure 3.38 Transformation depths in thermal pinhole camera, side flush steel gage, Pod B-1.

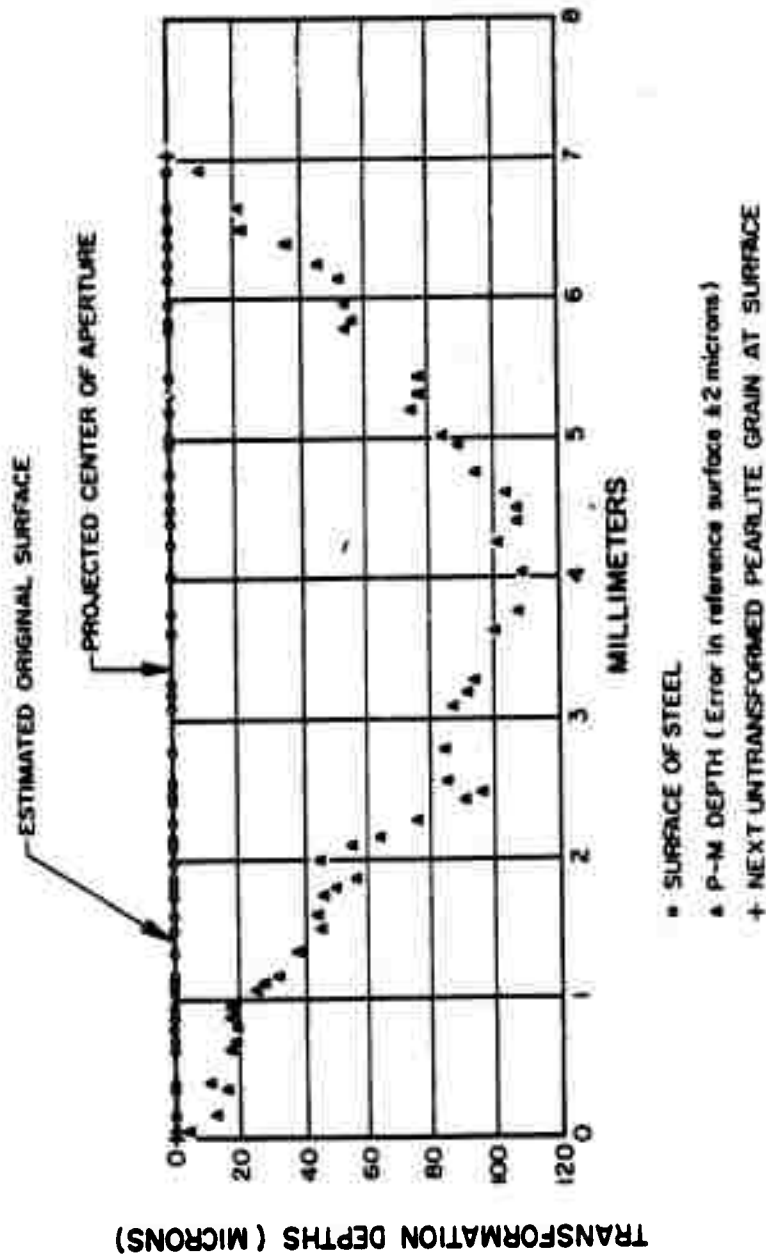


Figure 3.39 Transformation depths in thermal pinhole camera, top slotted steel gage, 10-mm aperture, Pod B-2.

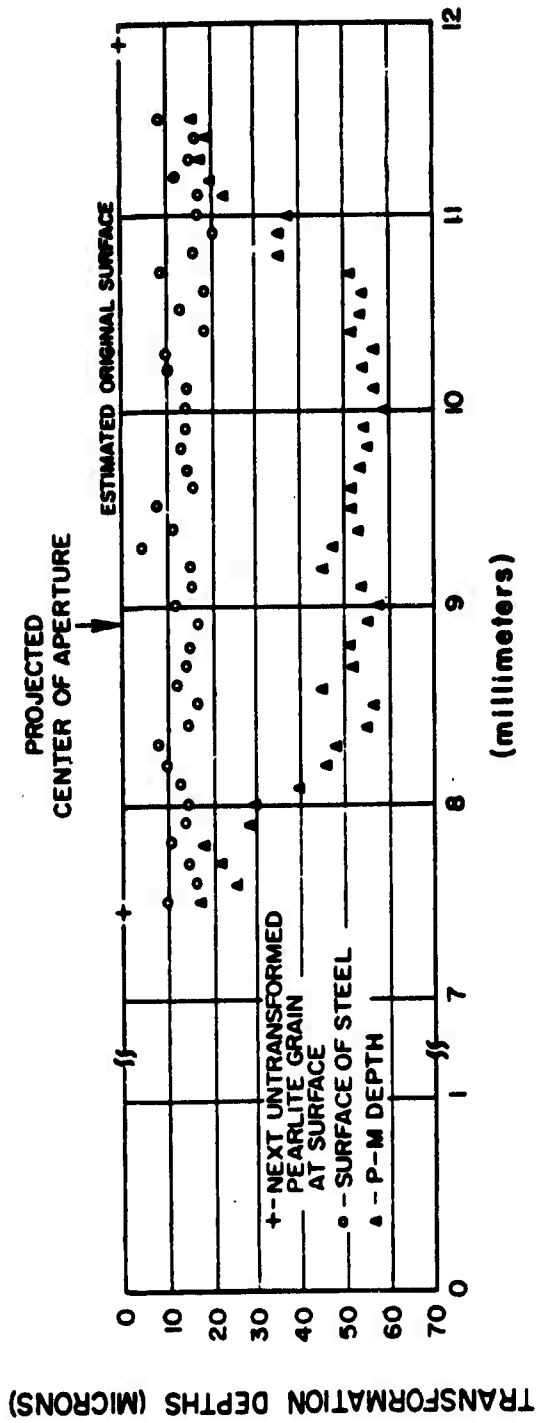


Figure 3.40 Transformation depths in thermal pinhole camera, top slotted steel gage, 10-mm aperture, Pod B-3.

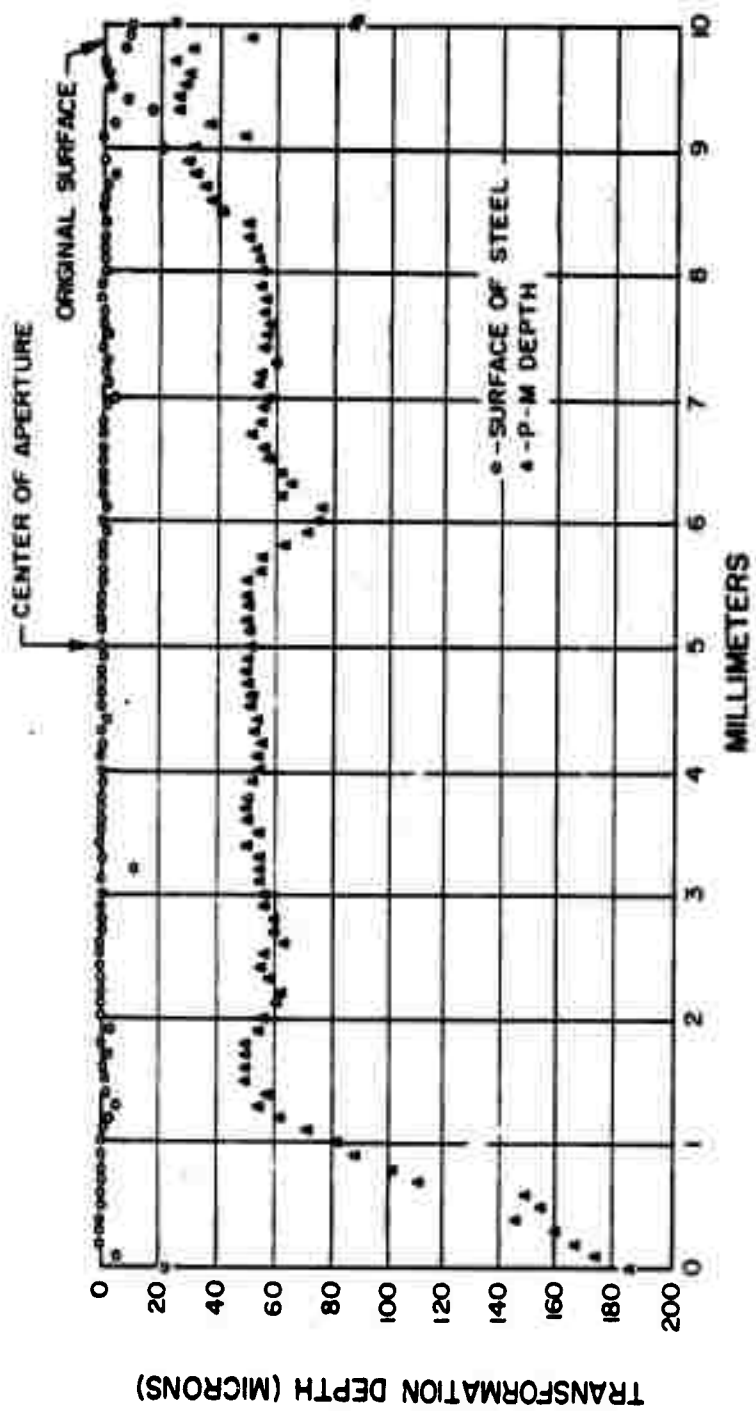


Figure 3.41 Transformation depths in thermal pinhole camera, top flush steel gage, Pod B-3.

3 mm APERTURE
POD B-3

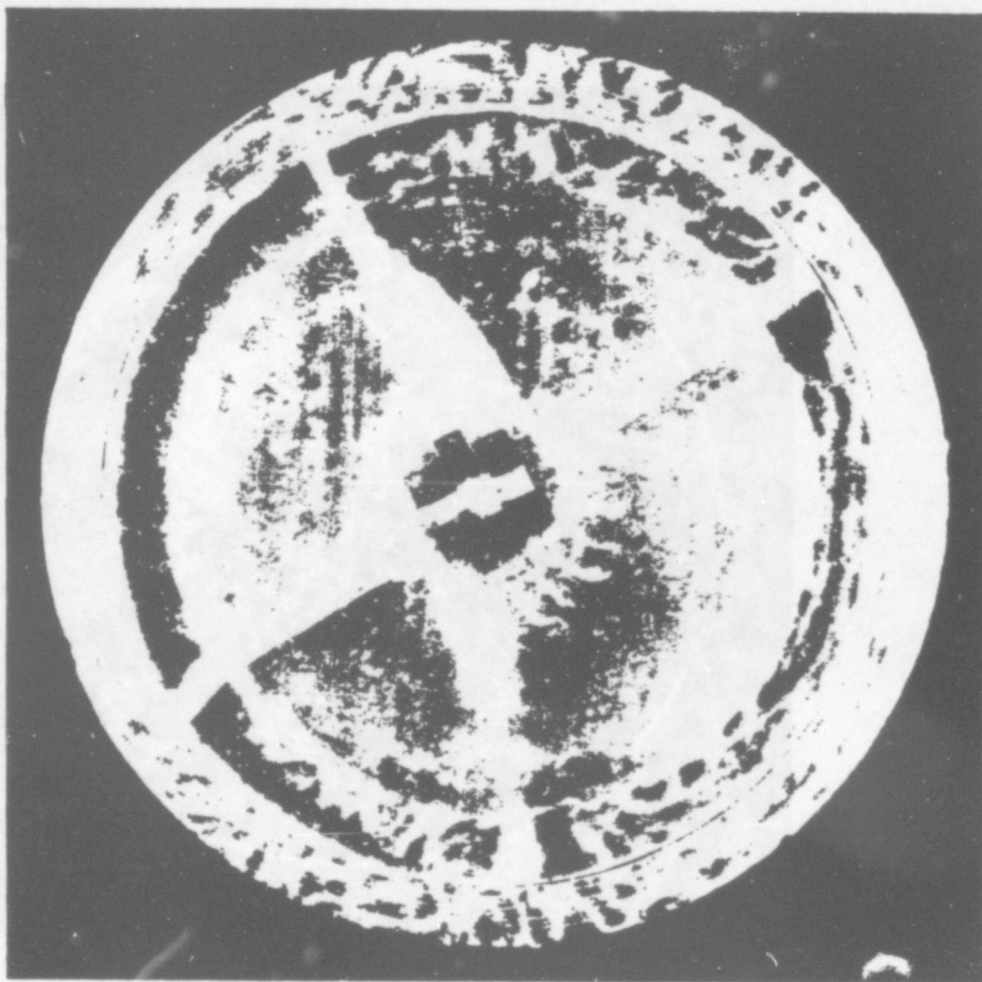


Figure 3.42 Postshot condition of TiO₂ filter. (ASE photo)

FUSED QUARTZ FILTER
BLUE GILL POD 1

MAGNIFICATION = 11 X

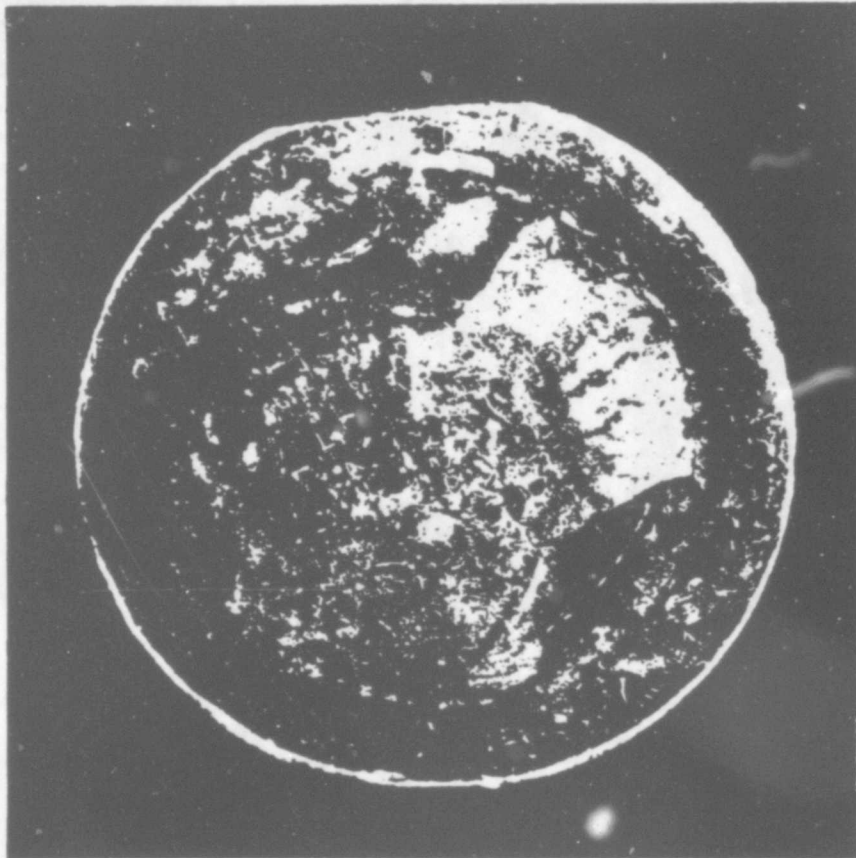


Figure 3.43 Surface of bismuth-tin detector in cutoff filter spectral gage. (ASE photo)

1020 STEEL DETECTOR
SILVER COATING
BLUE GILL POD 1

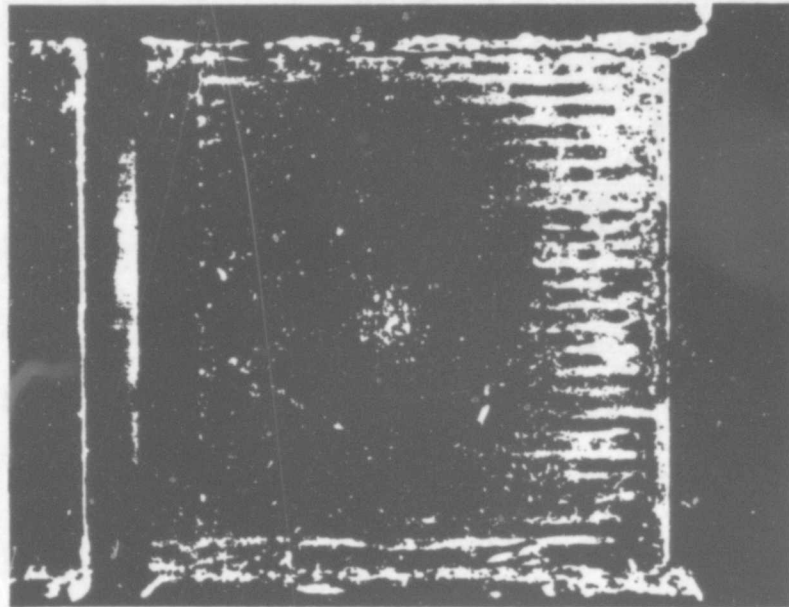
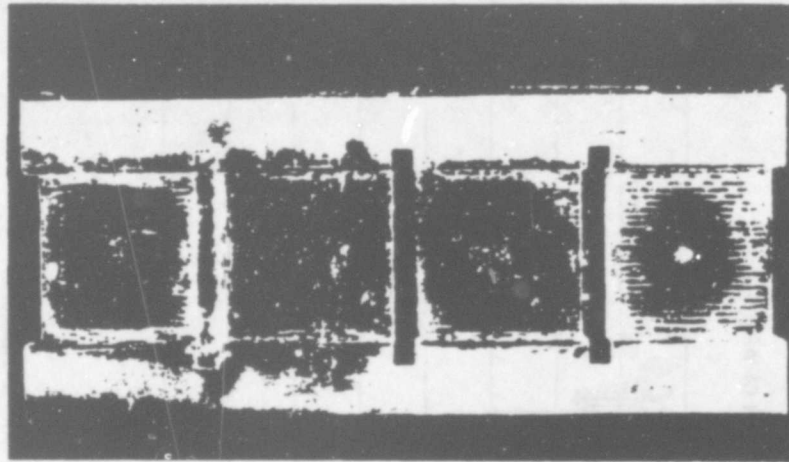


Figure 3.44 X-ray shine-through in reflective coating spectral gage. (ASE photos)

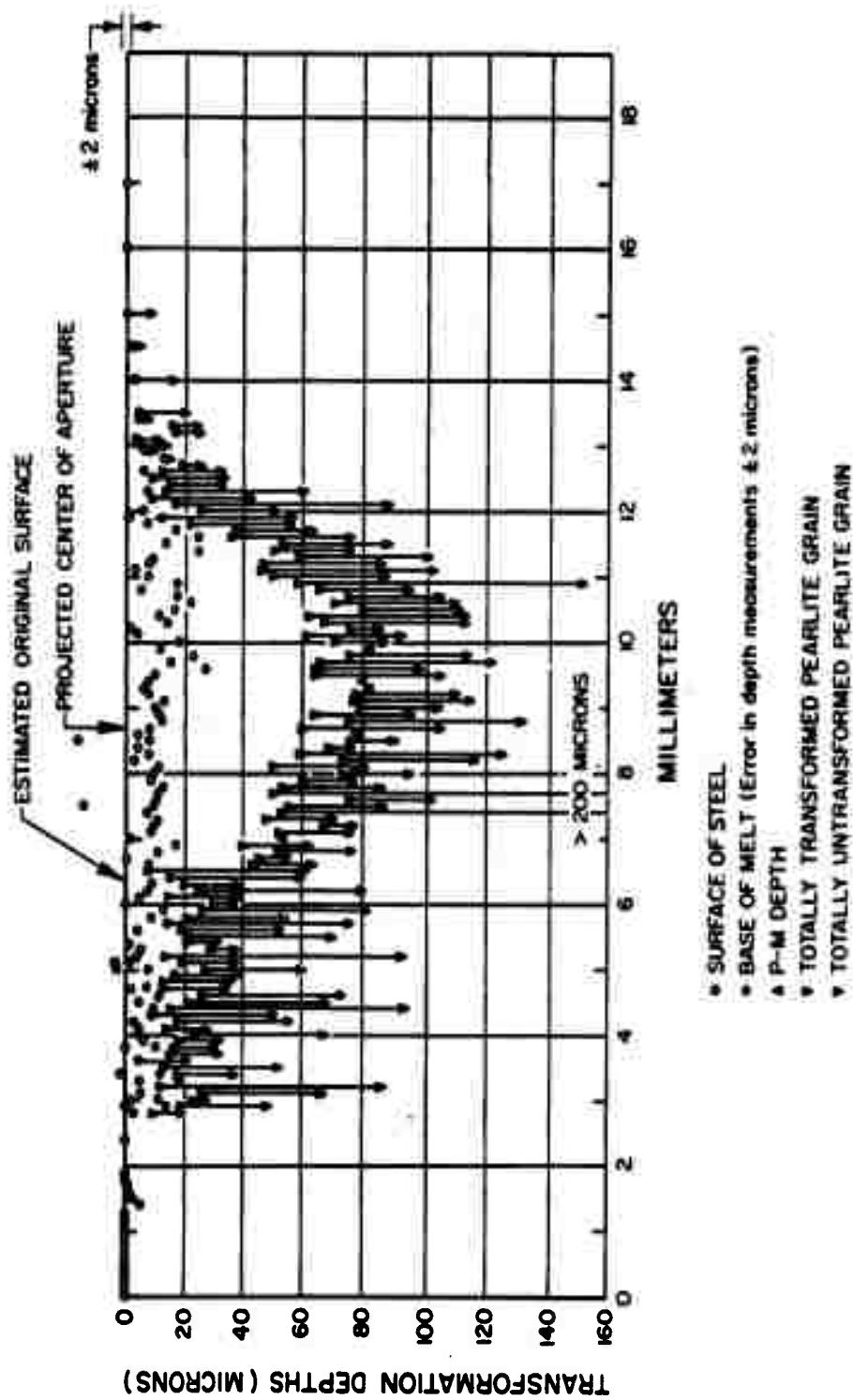
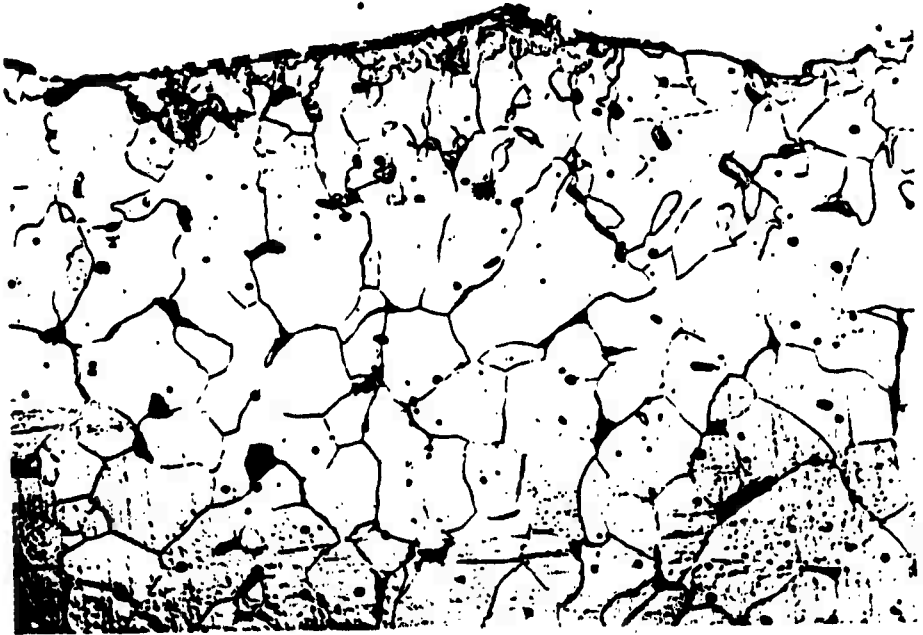


Figure 3.45 Transformation depths in reflective coating spectral gage, steel, no coating, 10-mm aperture, Pod B-1.

UNCOATED STEEL DETECTOR
10 mm APERTURE
BLUE GILL POD 1



MAGNIFICATION = 570X
ETCHANT = 1% NITAL

Figure 3.46 Photomicrograph of transformations in reflective coating spectral gage. (ASE photo)

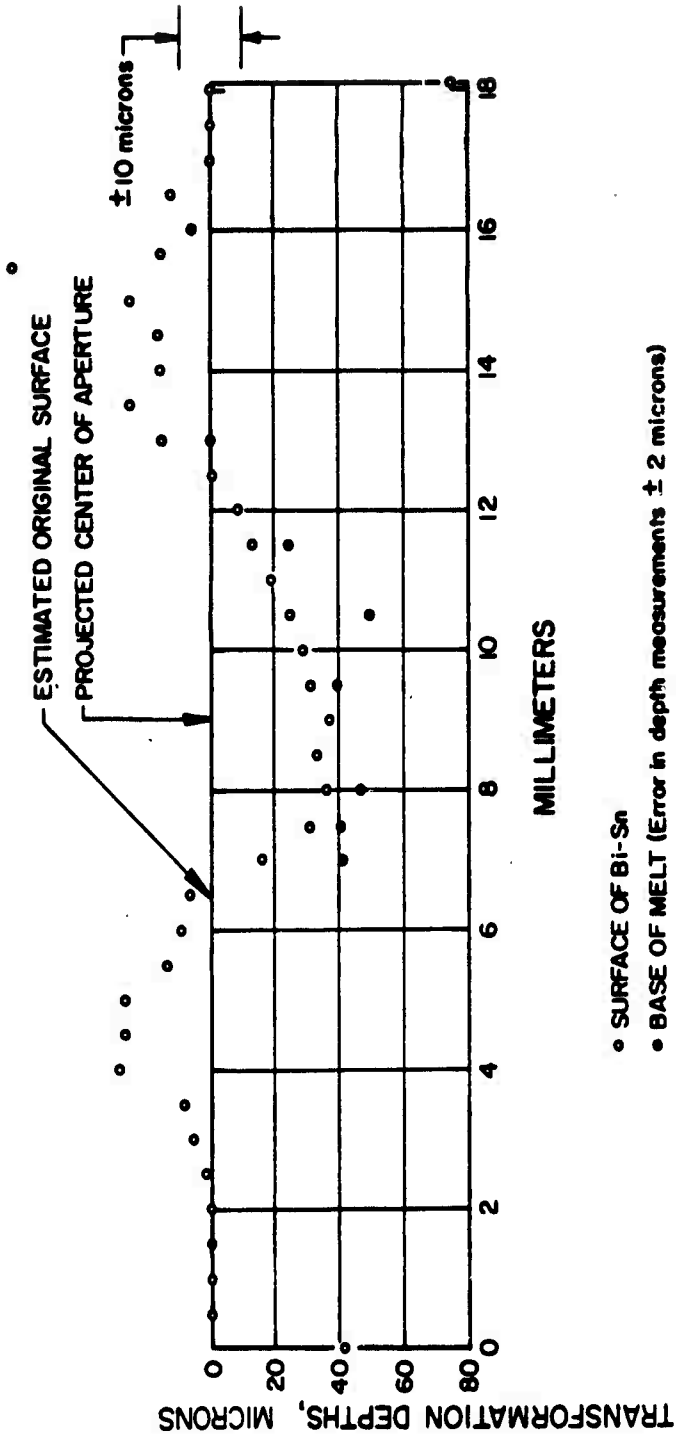


Figure 3.47 Transformation depths in reflective coating spectral gage, Bi-Sn, no coating, 3-mm aperture, Pod B-1.

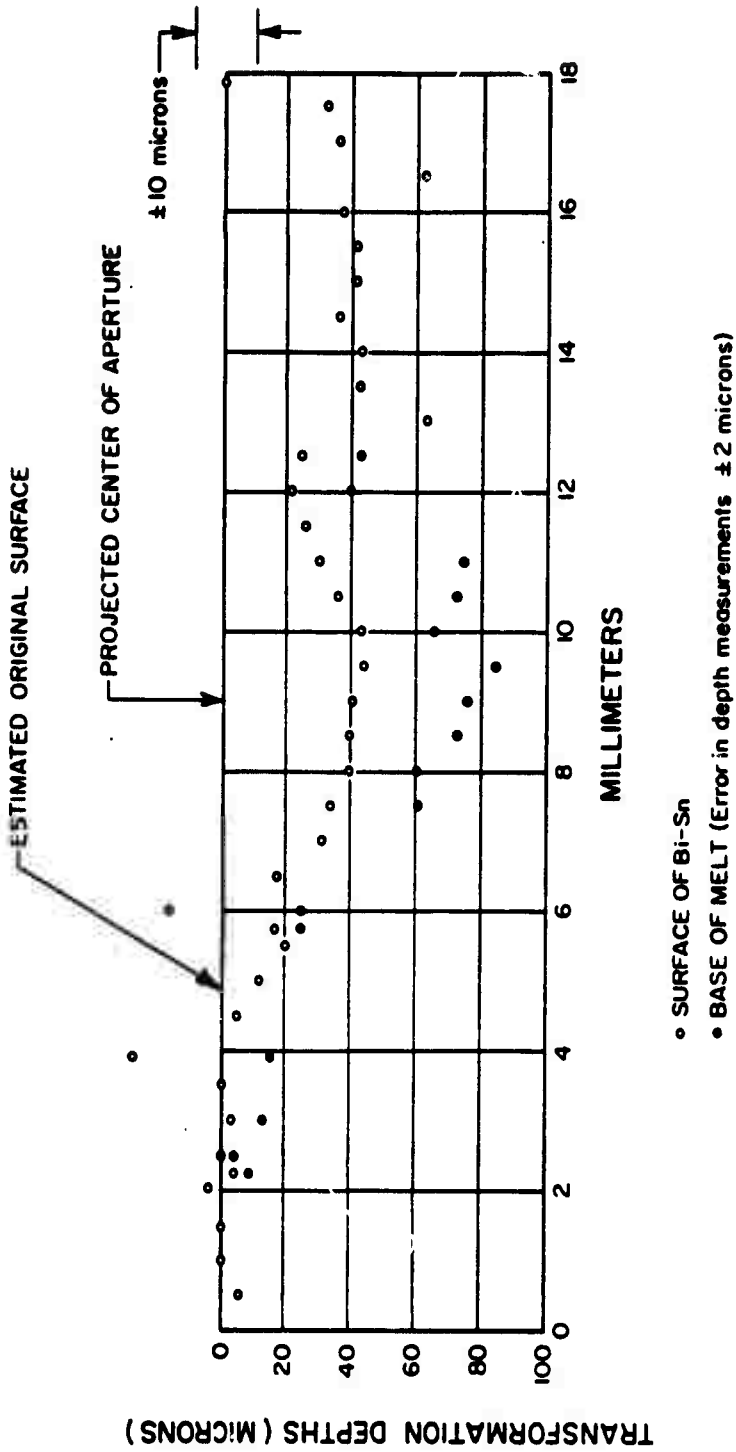


Figure 3.48 Transformation depths in reflective coating spectral gage, Bi-Sn, gold black, 3-mm aperture, Pod B-1.

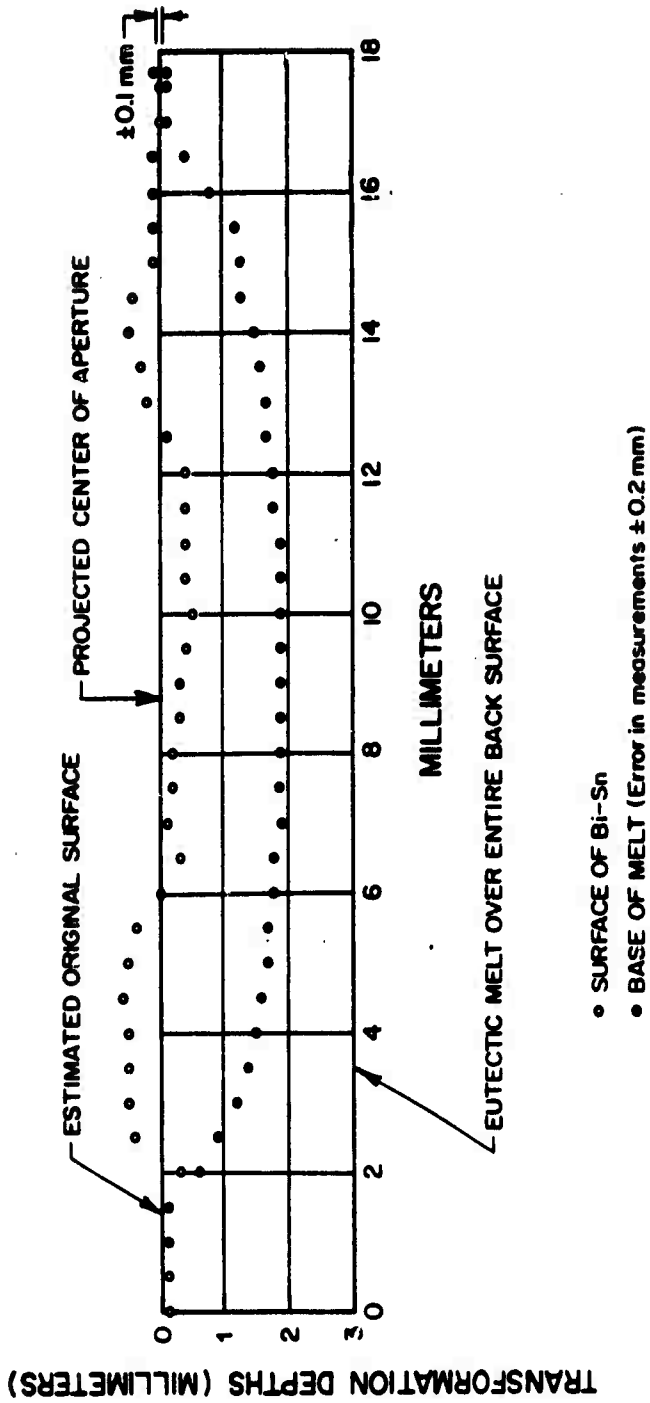


Figure 3.49 Transformation depths in reflective coating spectral gage, Bi-Sn, no coating, 10-mm aperture, Pod B-1.

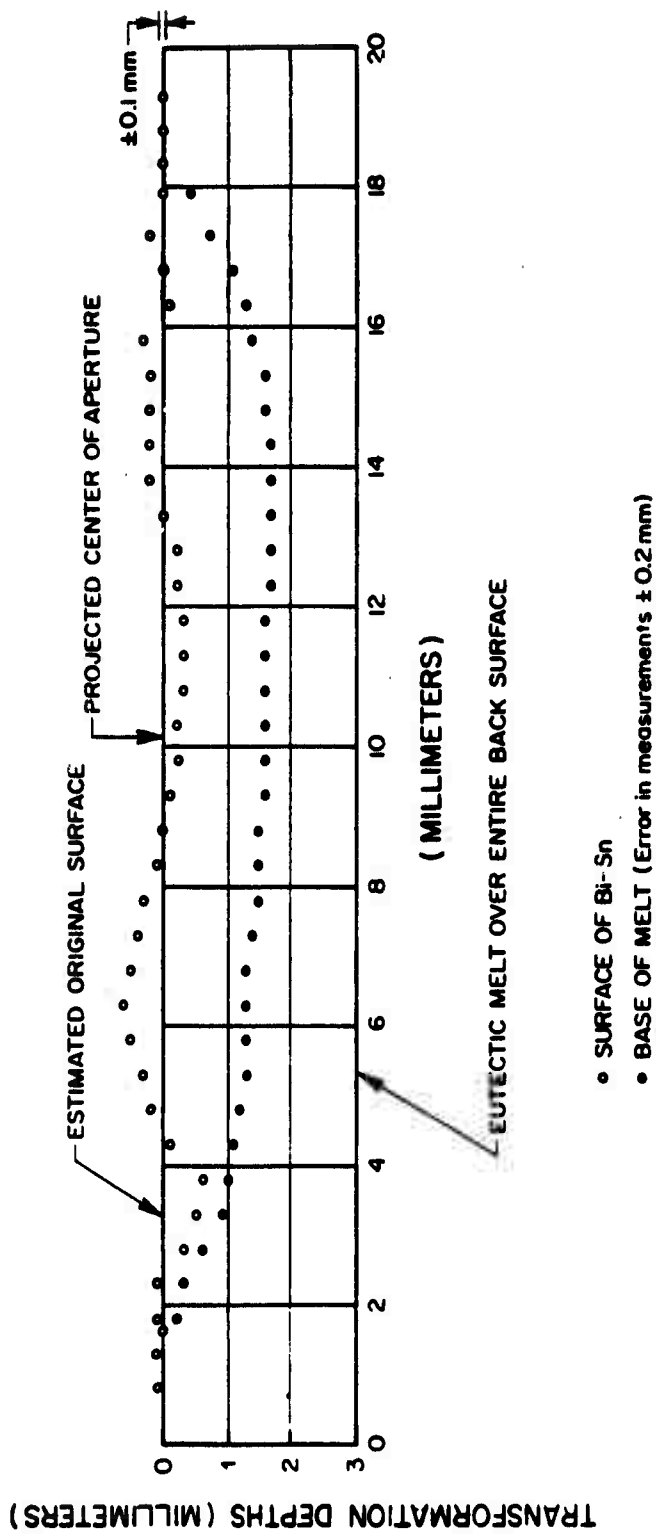


Figure 3.50 Transformation depths in reflective coating spectral gage, Bi-Sn, gold black, 10-mm aperture, Pod B-1.

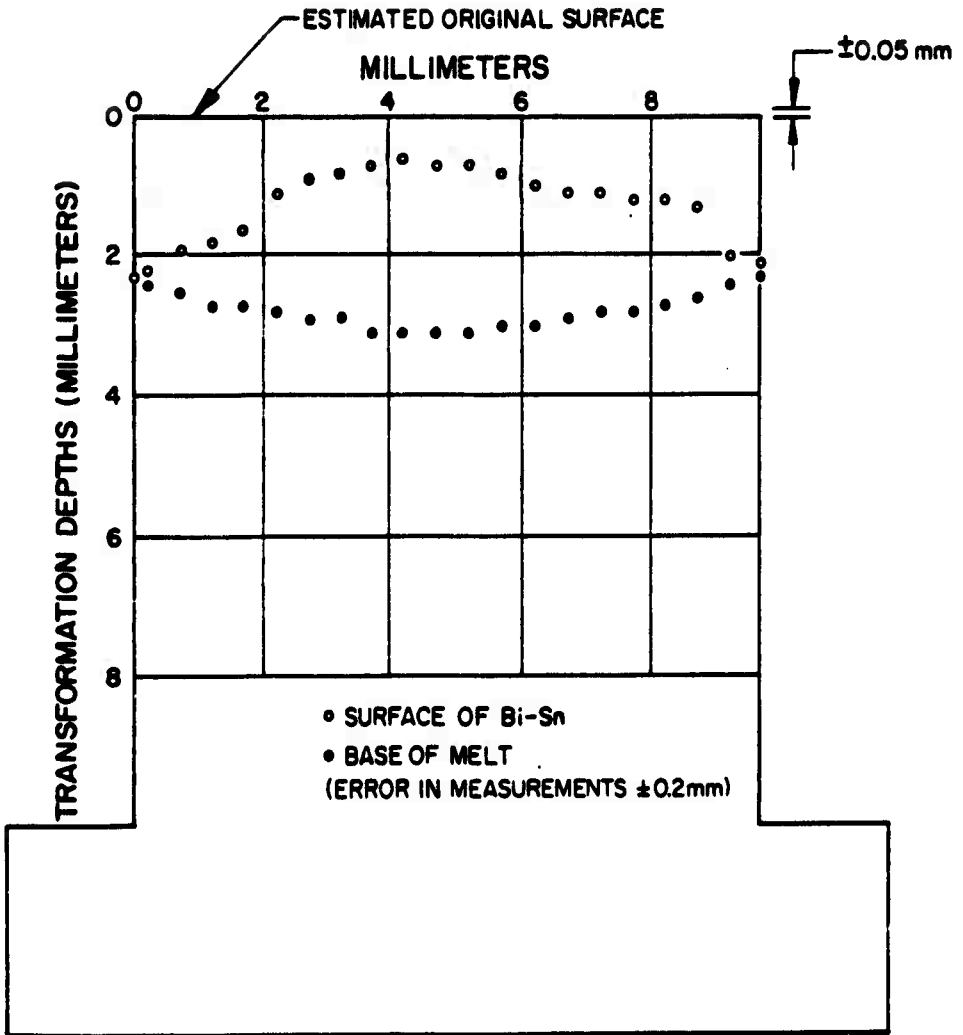


Figure 3.51 Transformation depths in reflective coating spectral gage, Bi-Sn, no coating, flush, Pod B-1.

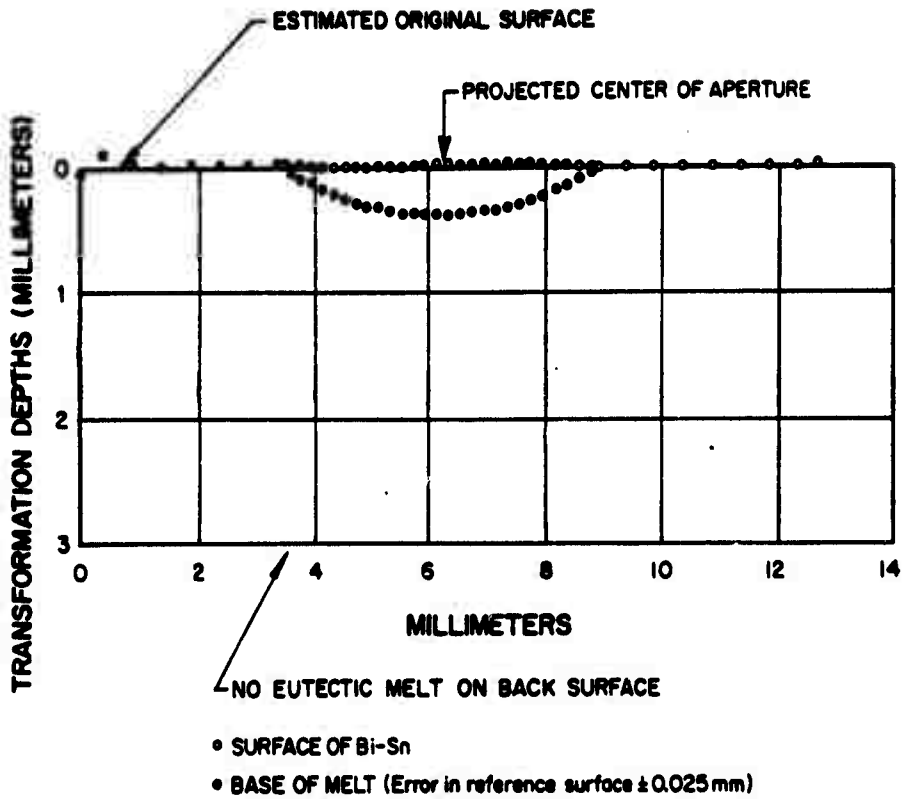


Figure 3.52 Transformation depths in reflective coating spectral gage, Bi-Sn, no coating, 3-mm aperture, Pod B-3.

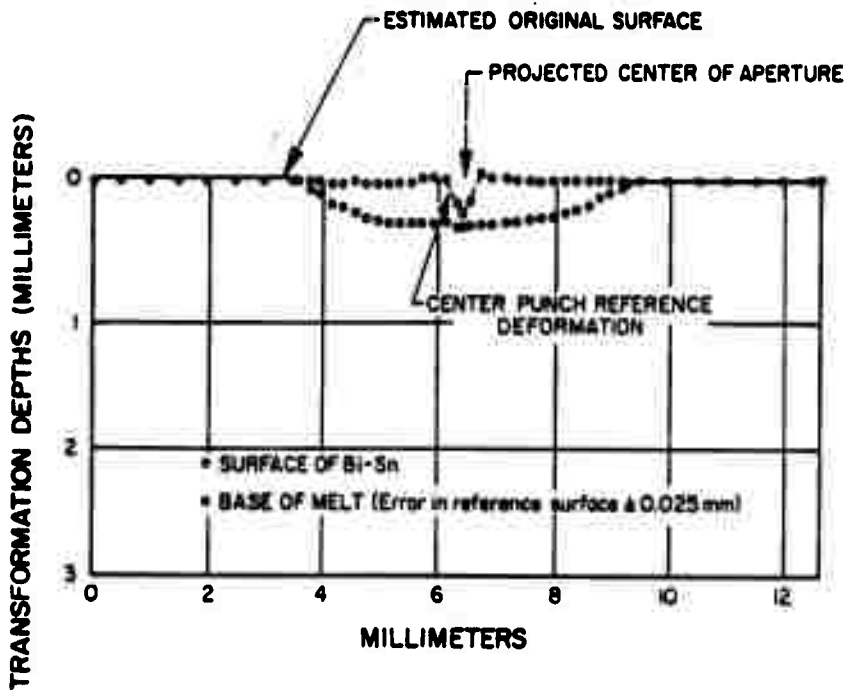


Figure 3.53 Transformation depths in reflective coating spectral gage, Bi-Sn, gold black, 3-mm aperture, Pod B-3.

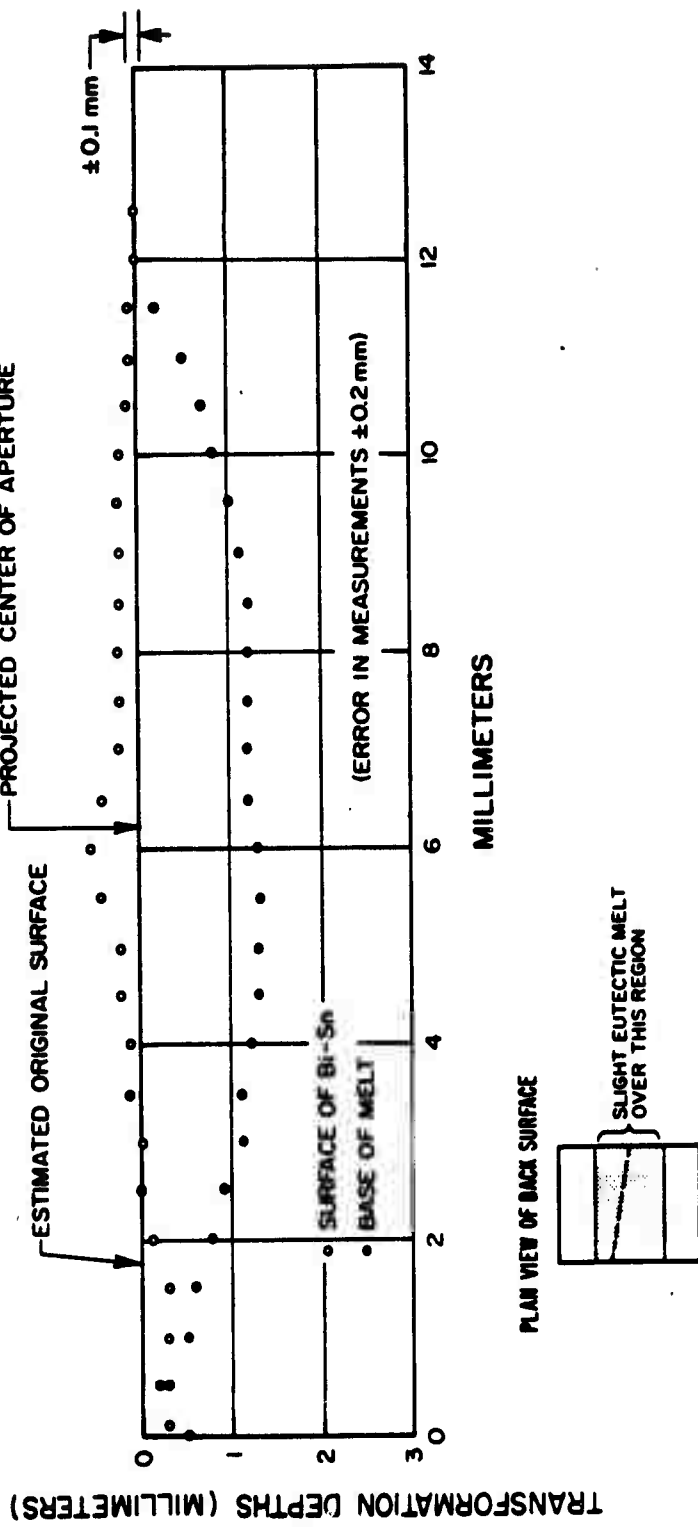


Figure 3.54 Transformation depths in reflective coating spectral gage, Bi-Sn, no coating, 10-mm aperture, Pod B-3.

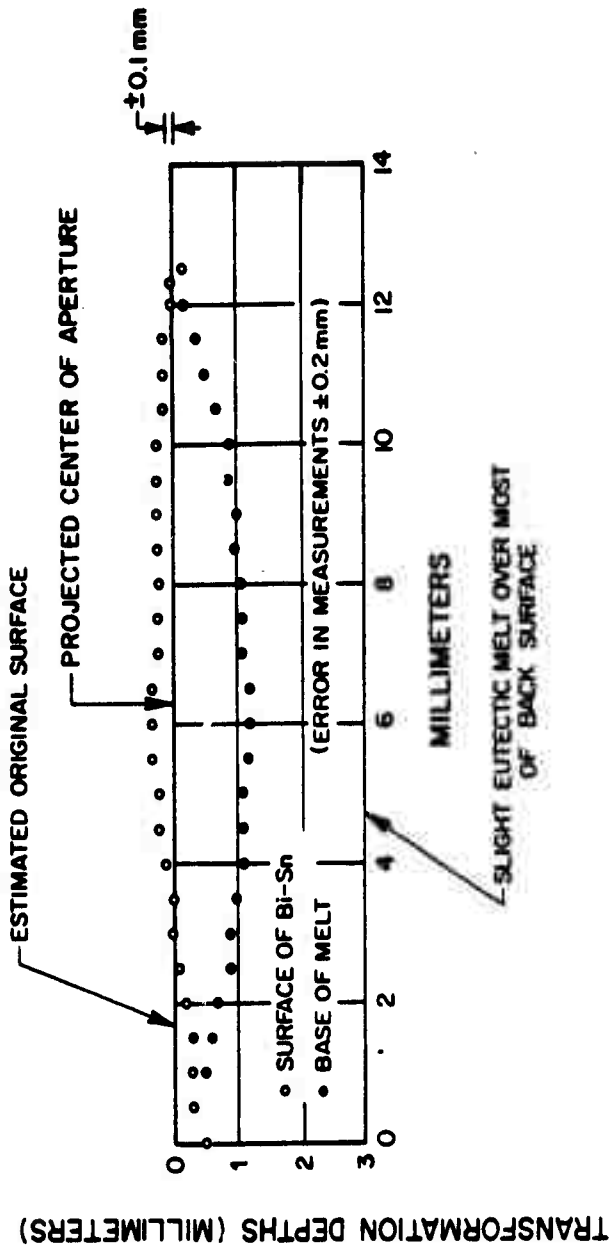


Figure 3.55 Transformation depths in reflective coating spectral gage, Bi-Sn, gold black, 10-mm aperture, Pod B-3.

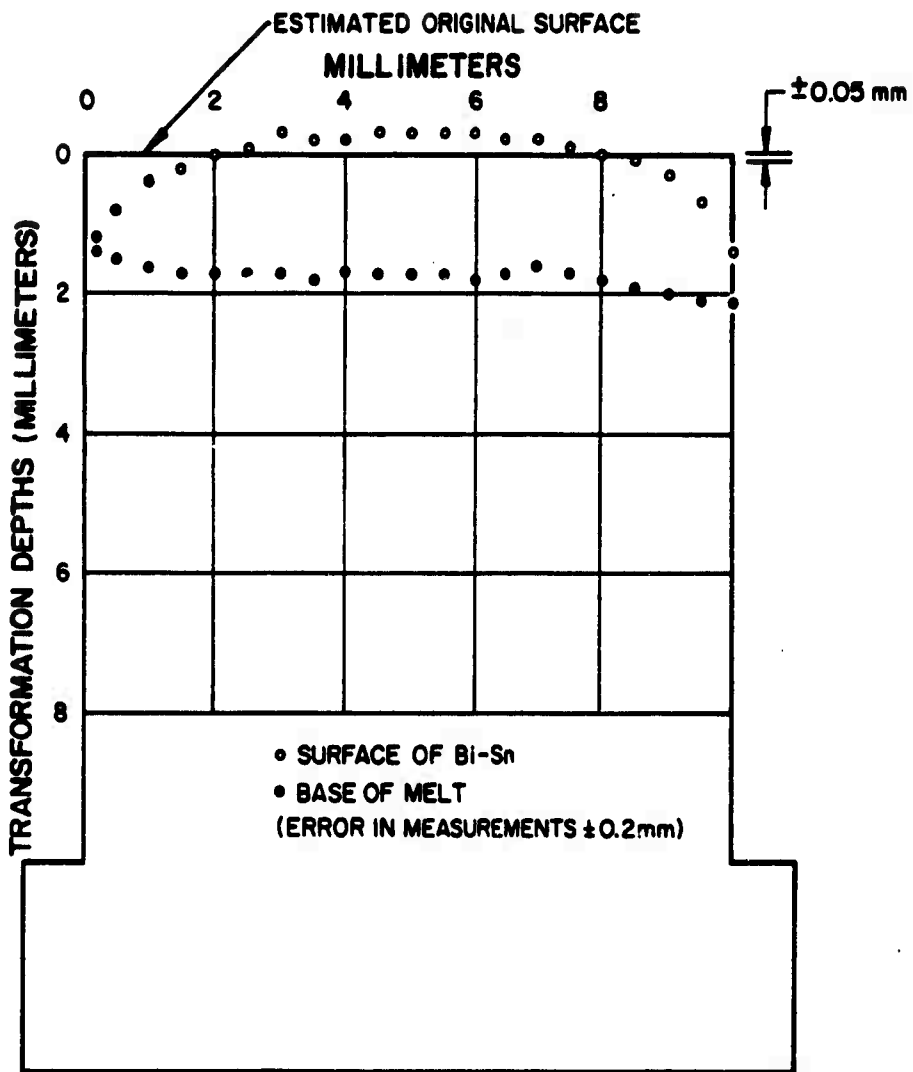
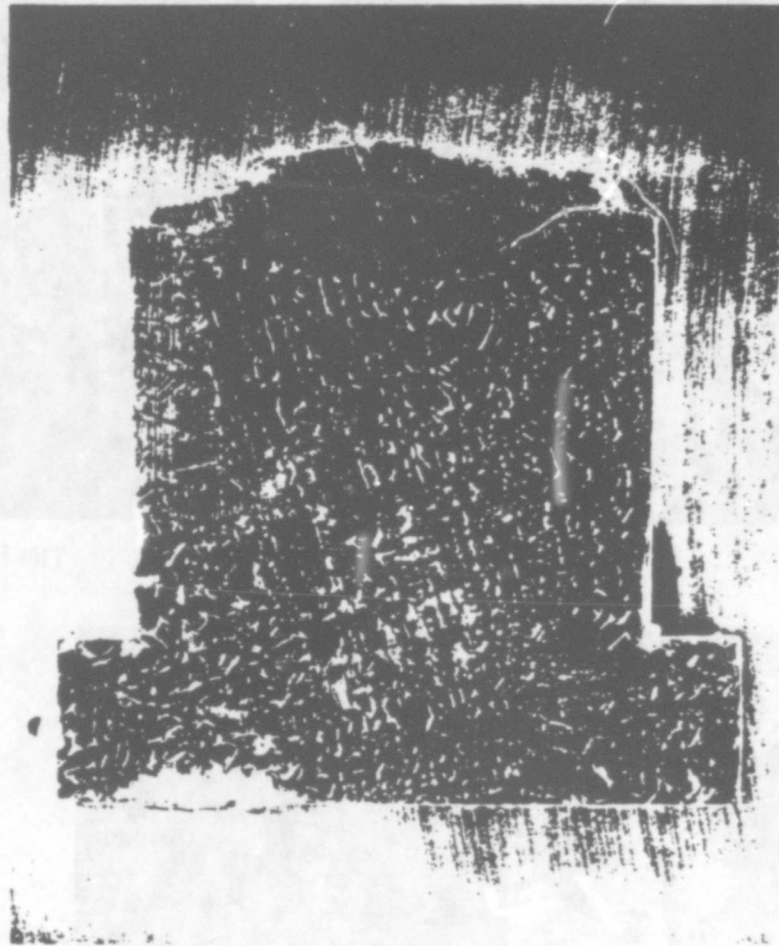


Figure 3.56 Transformation depths in reflective coating spectral gage, Bi-Sn, no coating, flush, Pod B-3.

REFLECTIVE COATING FLUSH GAGE
BLUE GILL POD 1



MAGNIFICATION = 7.5X

ETCHANT (ELECTROLYTIC SOLUTION)

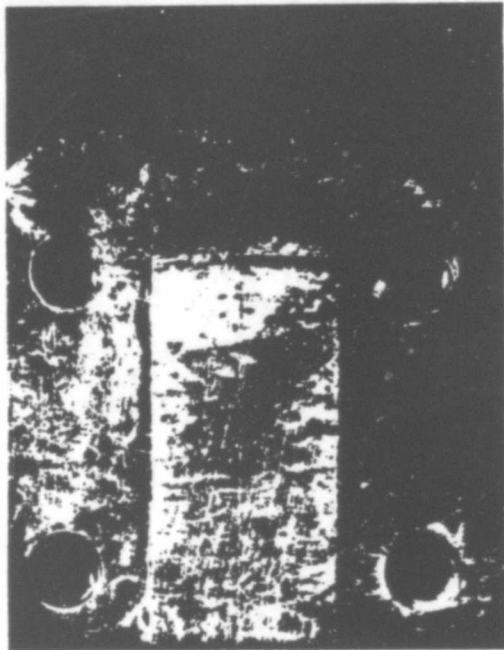
100 ml H_3PO_4

100 ml Ethyl Alcohol

30 ml HCl

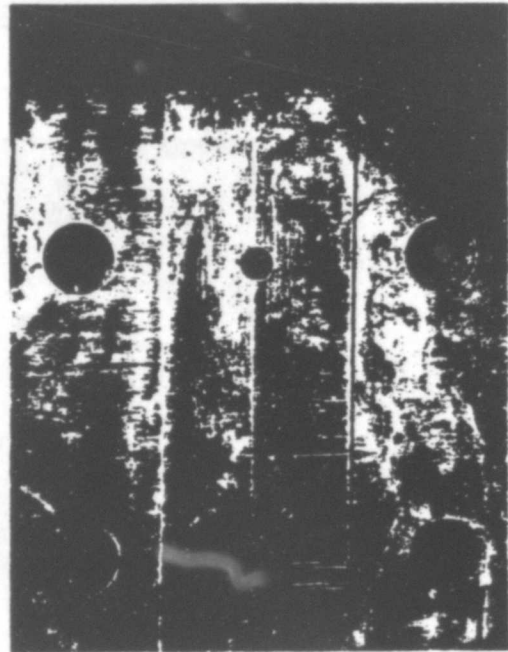
Figure 3.57 Depth of melt in bismuth-tin detector.
(ASE photo)

COPPER HEAT SINK — POD B-1

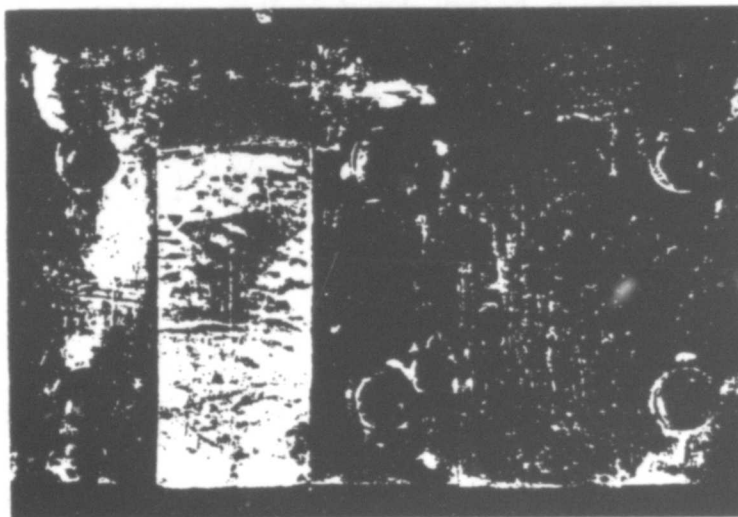


TIN FOIL

STEEL HEAT SINK — POD B-3



TIN FOIL

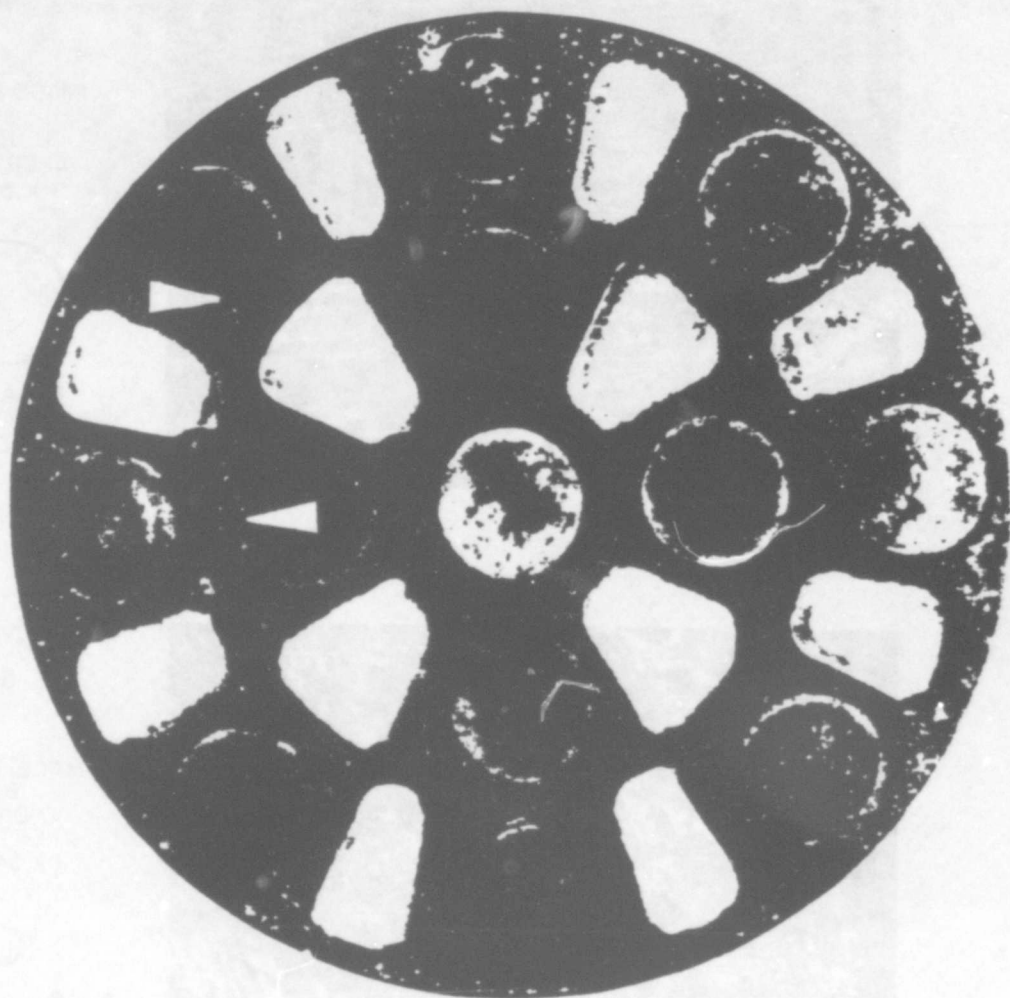


TIN FOIL

LEAD FOIL

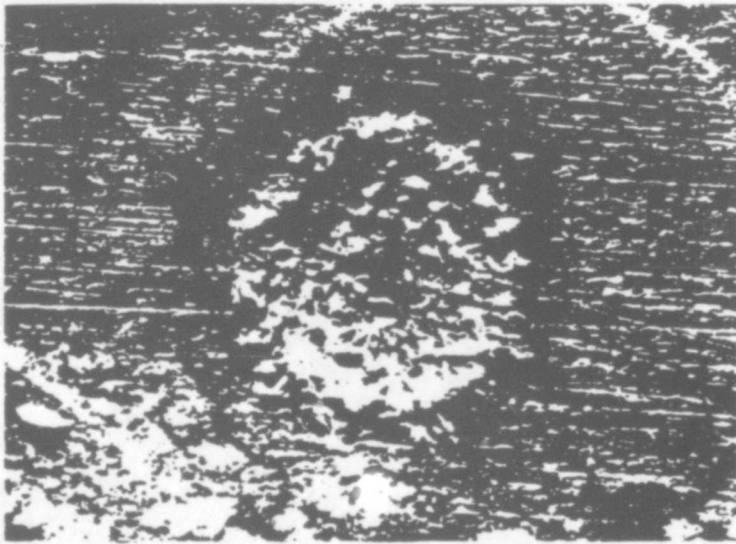
COPPER
HEAT SINK
POD B-1

Figure 3.58 Response of long-time thermal gage.
(ASE photos)



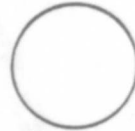
▲ ARROWS INDICATE LOCATION
OF PHOTOMICROGRAPHS OF FIG 3 60

Figure 3.59 X-ray pinhole camera film plate, Blue Gill Pod 1.
(ASE photo)

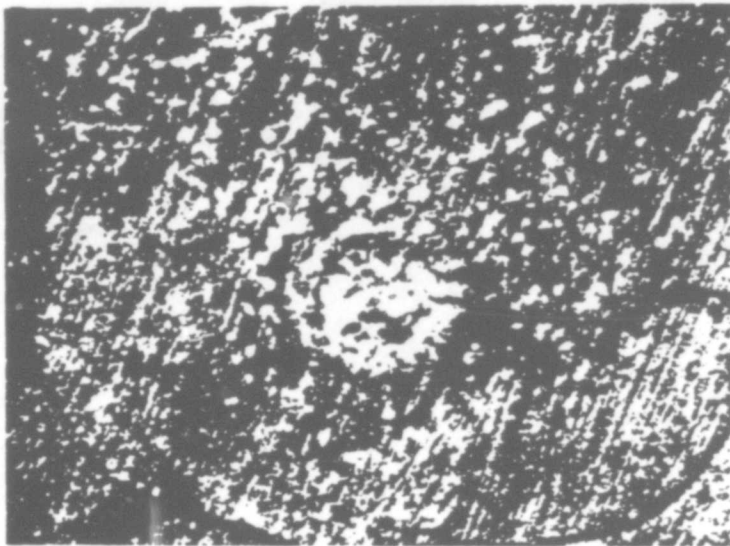


A

IMAGE FORMED
BY
0.033 cm
APERTURE
(X 54.8)



RELATIVE
APERTURE
SIZE



B

IMAGE FORMED
BY
0.010 cm
APERTURE
(X 54.8)



RELATIVE
APERTURE
SIZE

Figure 3.60 X-ray pinhole camera images, Blue Gill Pod 1.
(ASE photos)

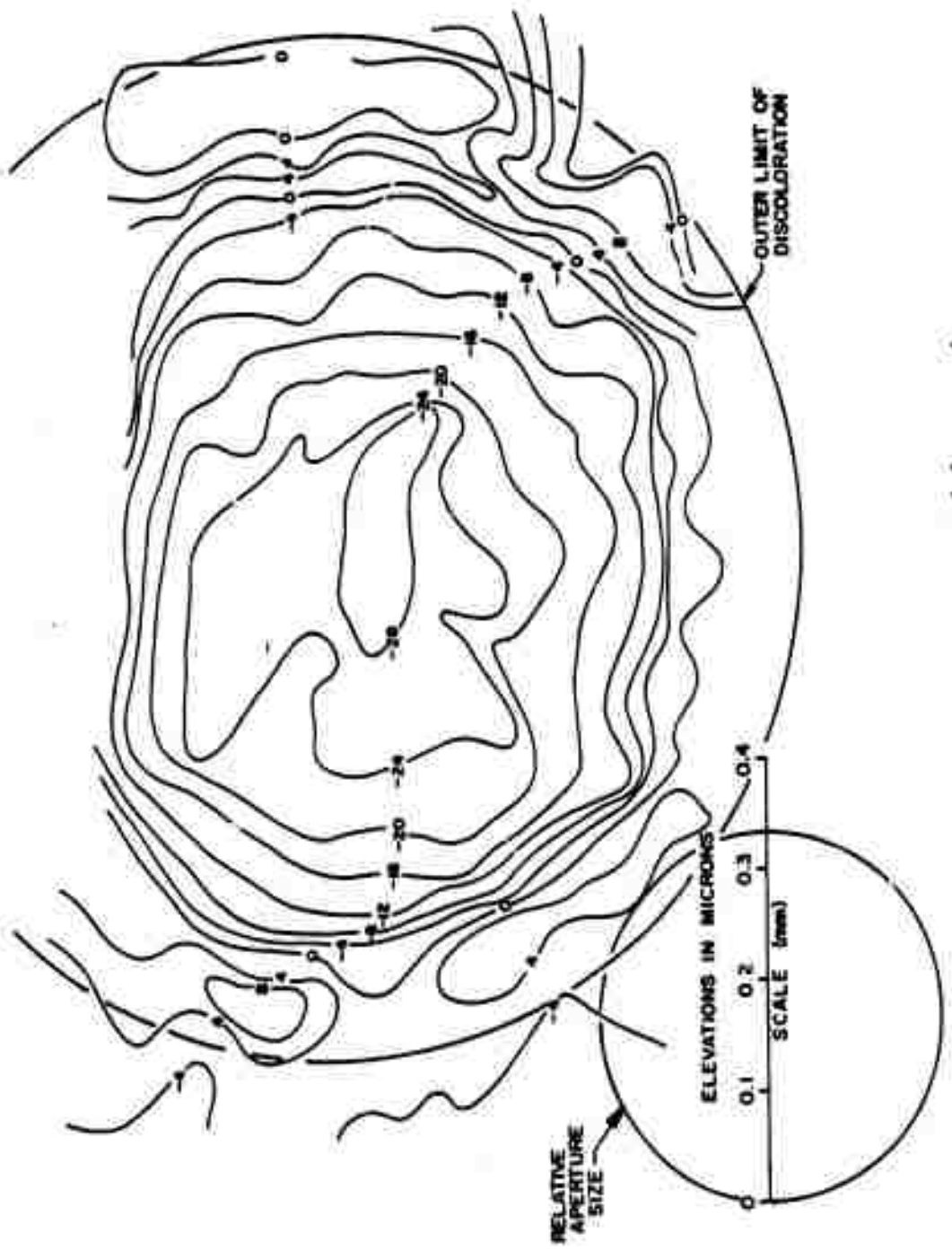


Figure 3.61 Contour map of X-ray pinhole camera image. Blue Gill Pod 1, 0.033-cm pinhole.

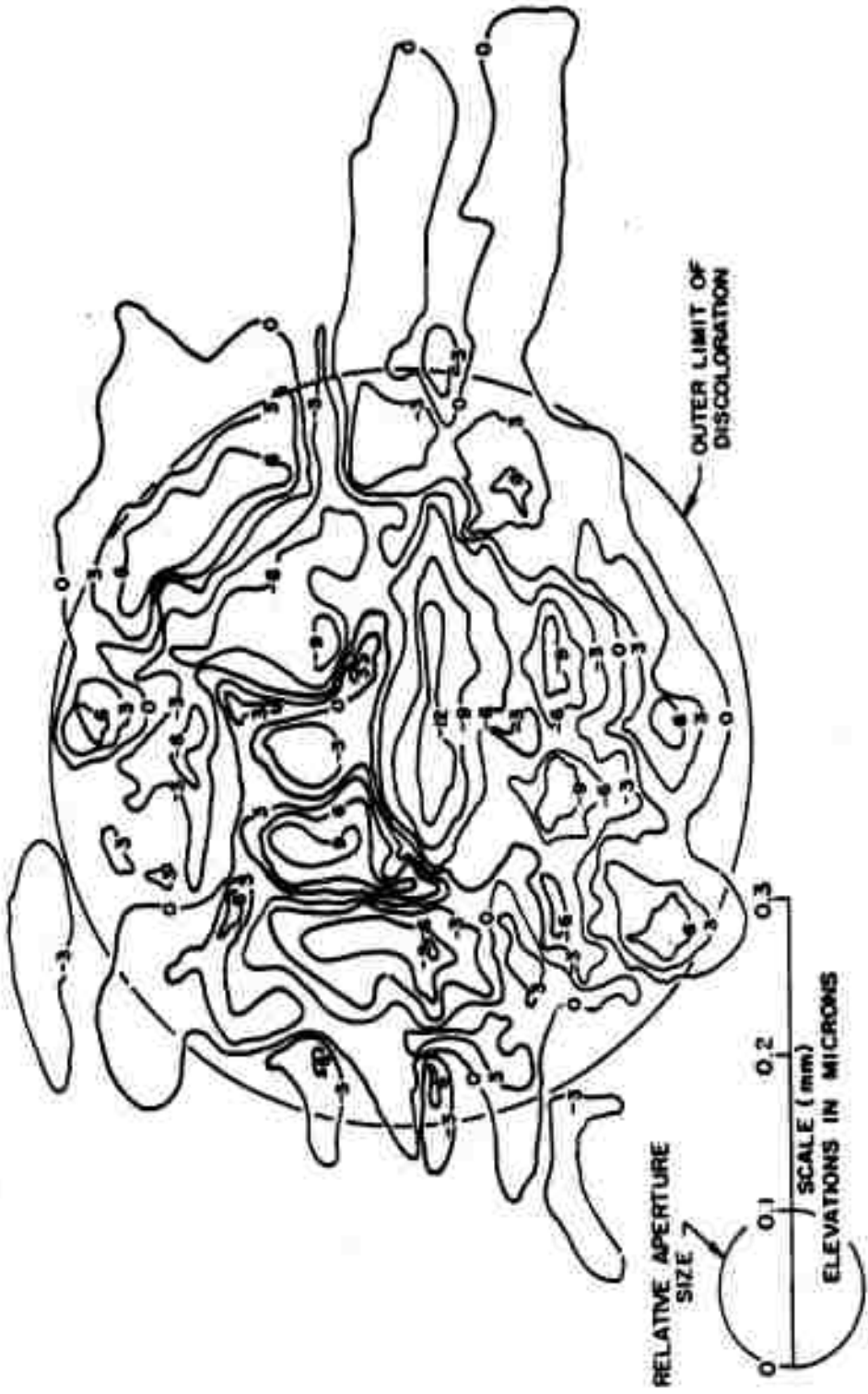


Figure 3.62 Contour map of X-ray pinhole camera image, Blue Gill Pod 1, 0.010-cm pinhole.

NOTE: SYMBOLS REPRESENT TRAVERSES AT VARIOUS ARBITRARY ORIENTATIONS

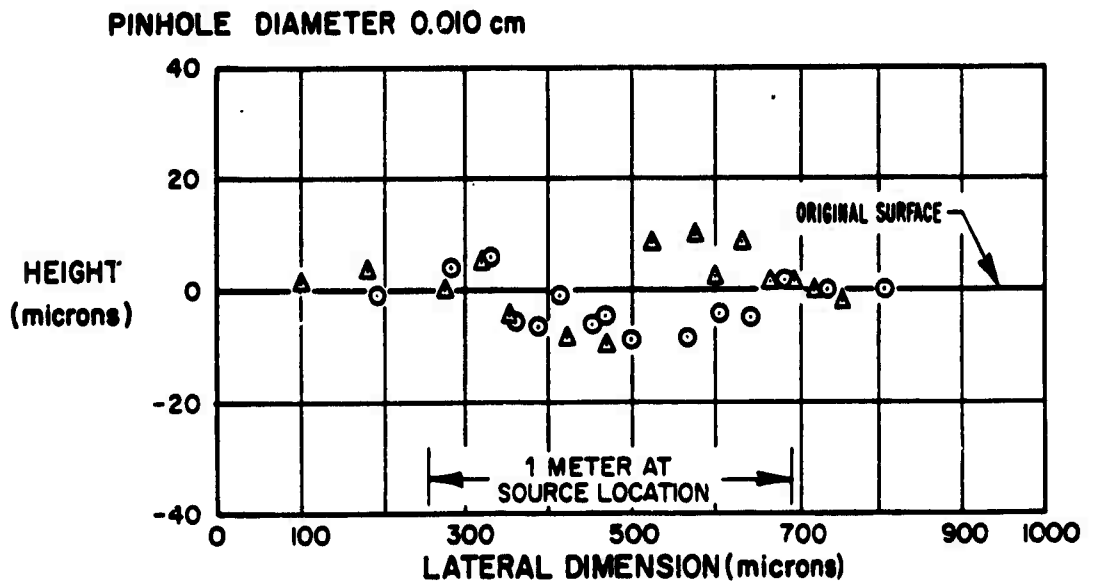
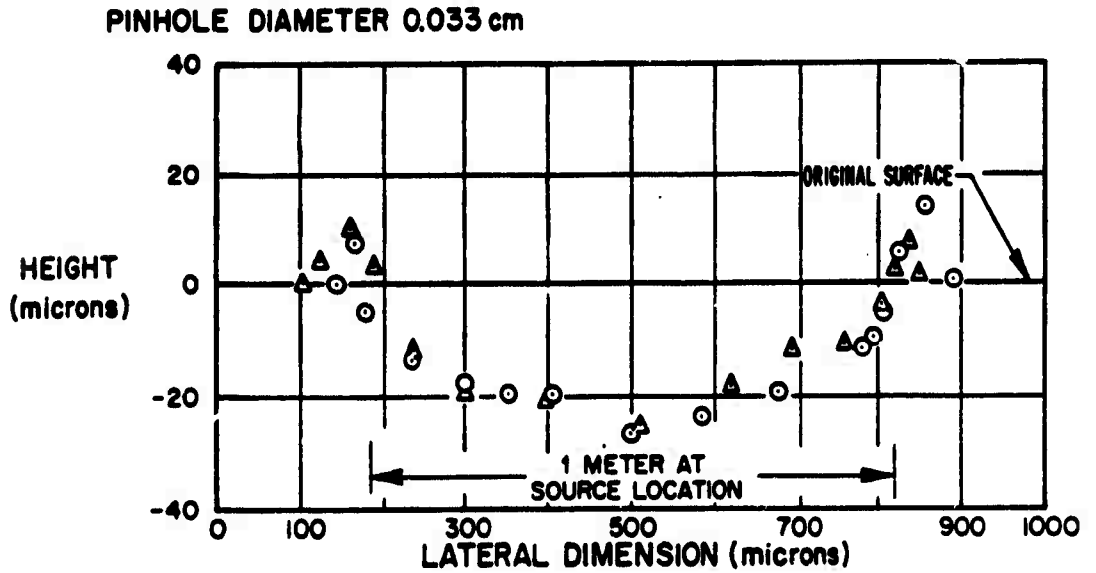
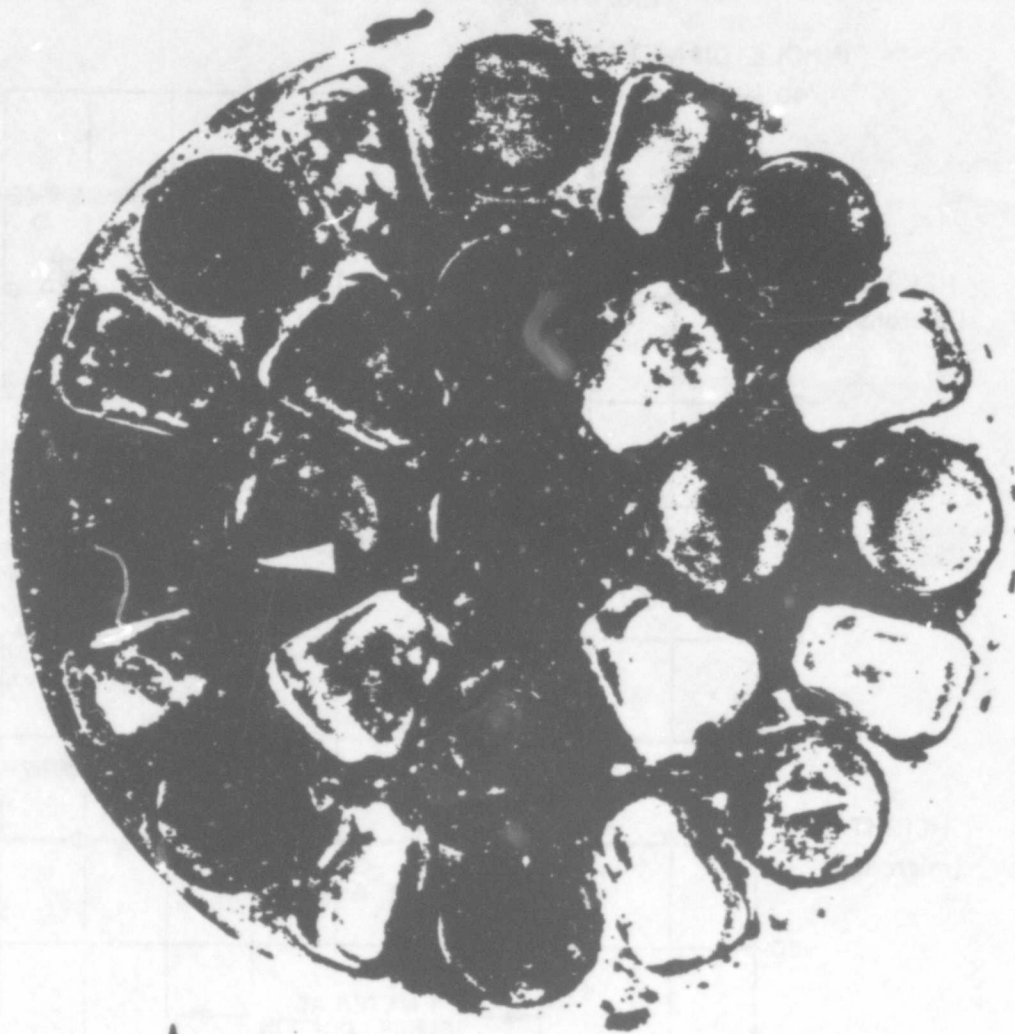
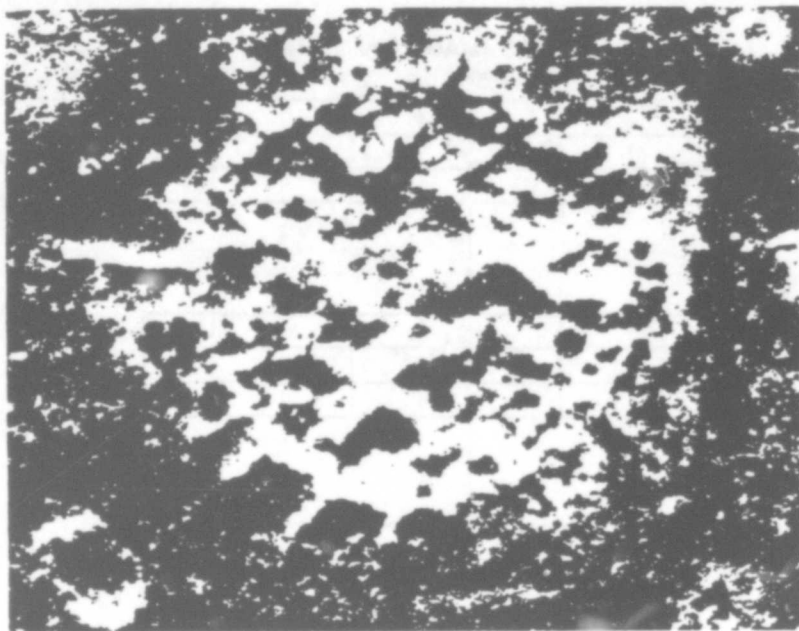


Figure 3.63 Cross section of images in X-ray pinhole camera, Blue Gill Pod 1.

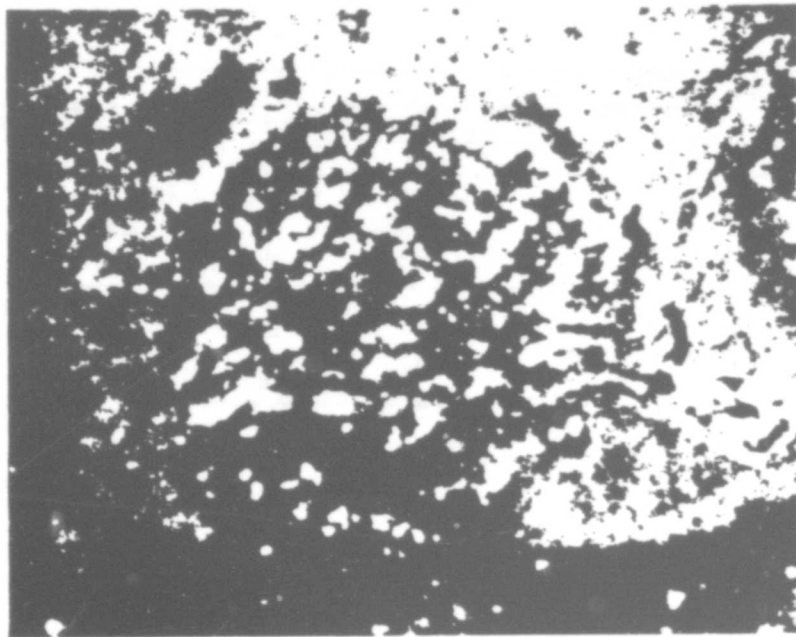


▲ ARROWS INDICATE LOCATION
OF PHOTOMICROGRAPHS OF FIG 3.65

Figure 3.64 X-ray pinhole camera film plate, Blue Gill Pod 2.
(ASE photo)



a.



b.



Figure 3.65 X-ray pinhole camera images, Blue Gill Pod 2.
(ASE photos)

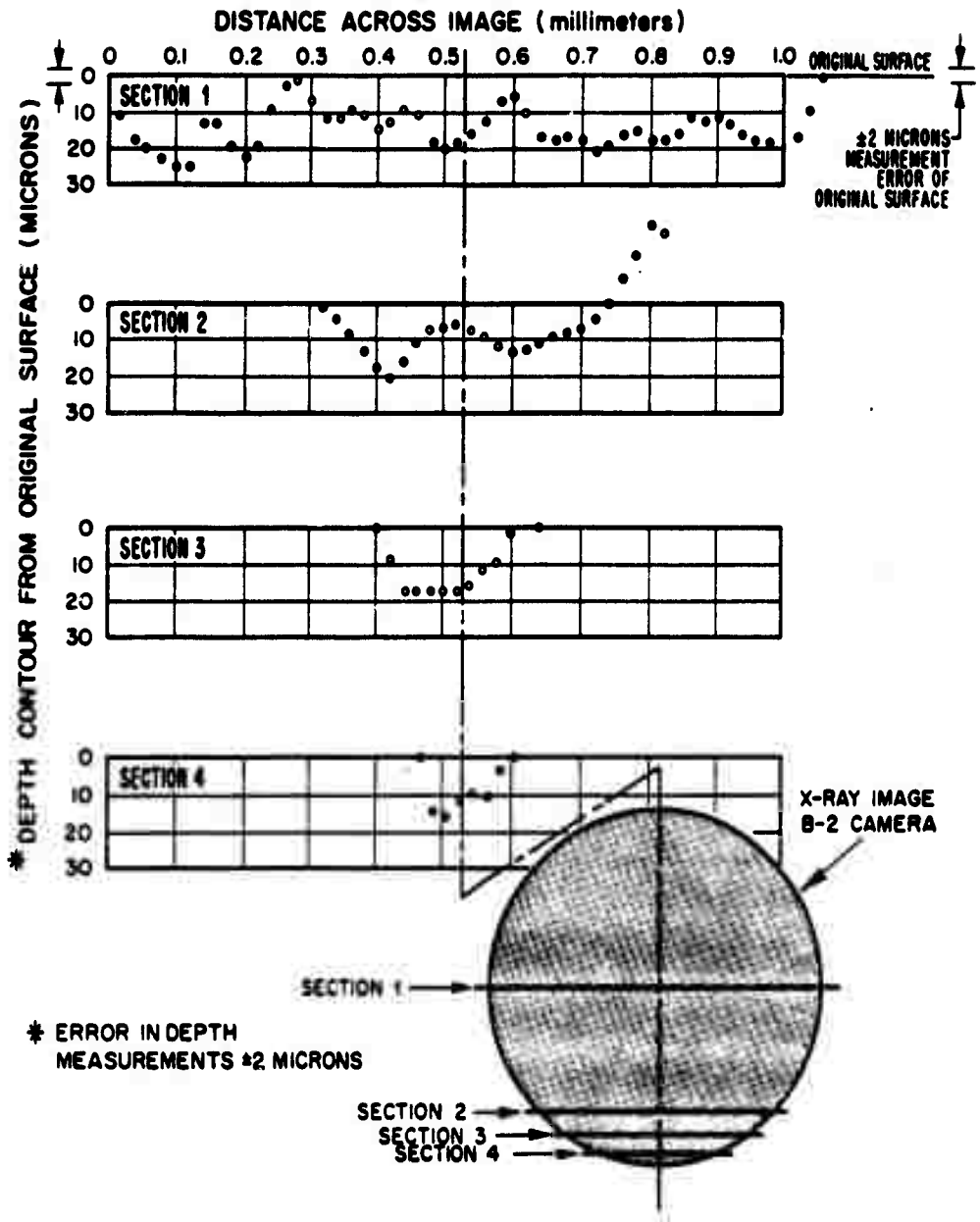


Figure 3.66 Cross section of crater in film plate on X-ray pinhole camera, Blue Gill Pod 2, lead.

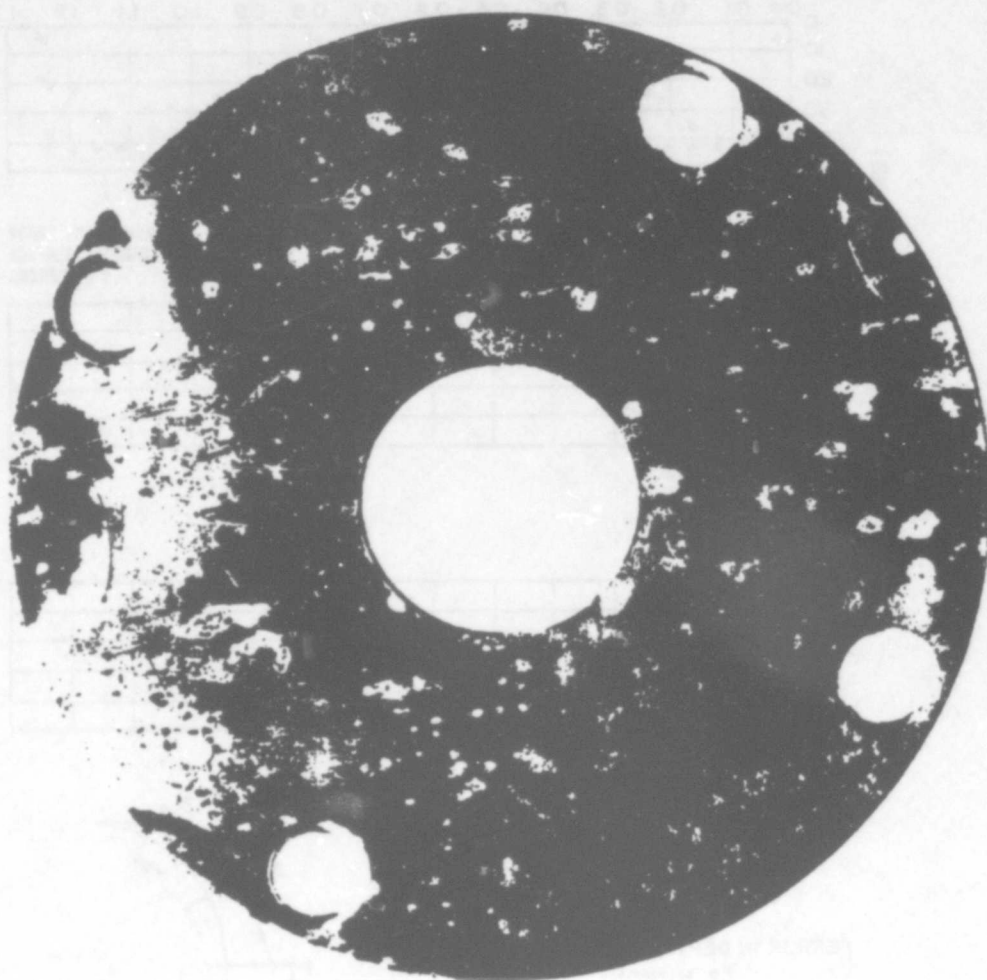


Figure 3.67 Photograph showing X-ray-illuminated areas on aluminum, Blue Gill Pod 1, Cluster 62. (ASE photo)

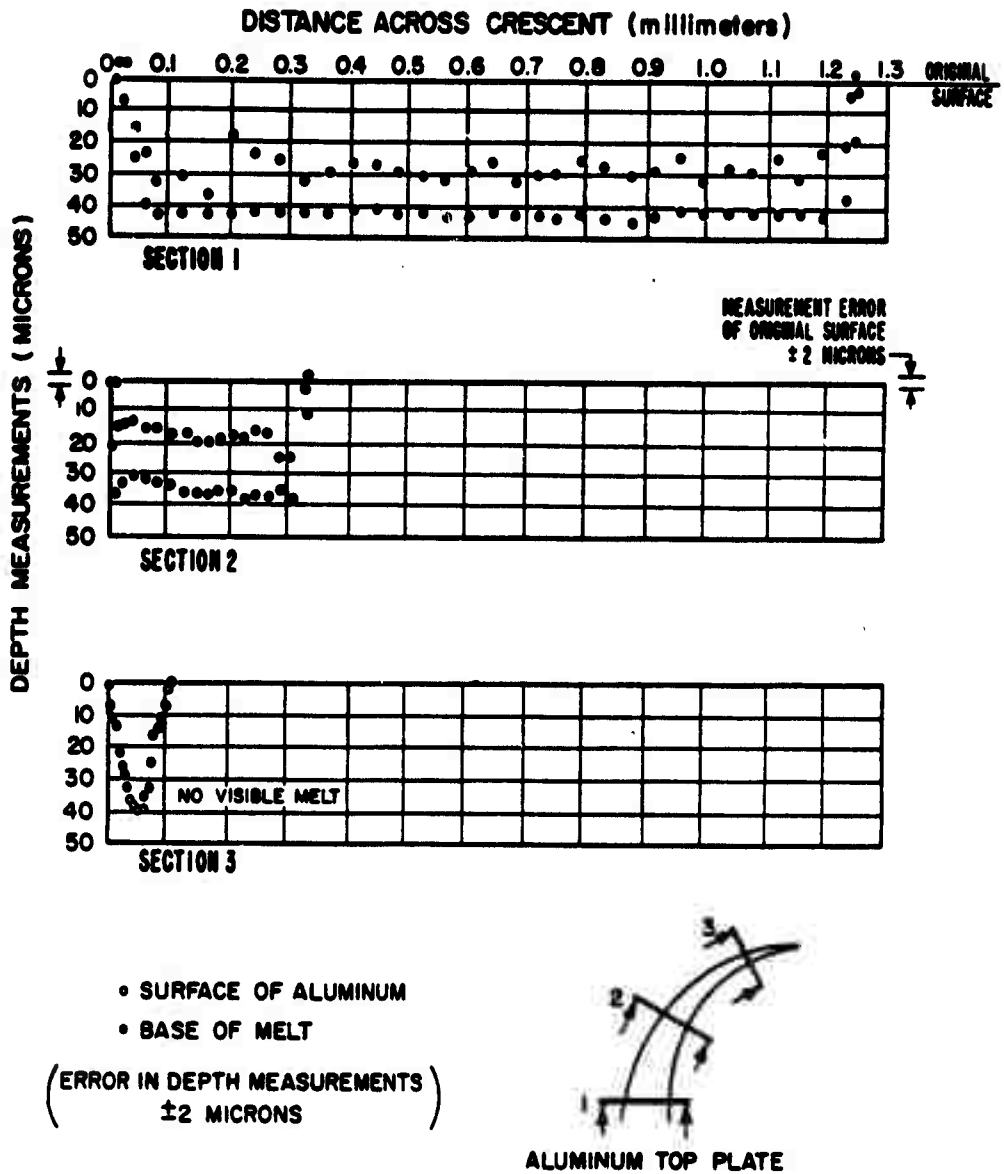


Figure 3.68 X-ray effects on aluminum, Pod B-1, Cluster 62, Crescent 1.

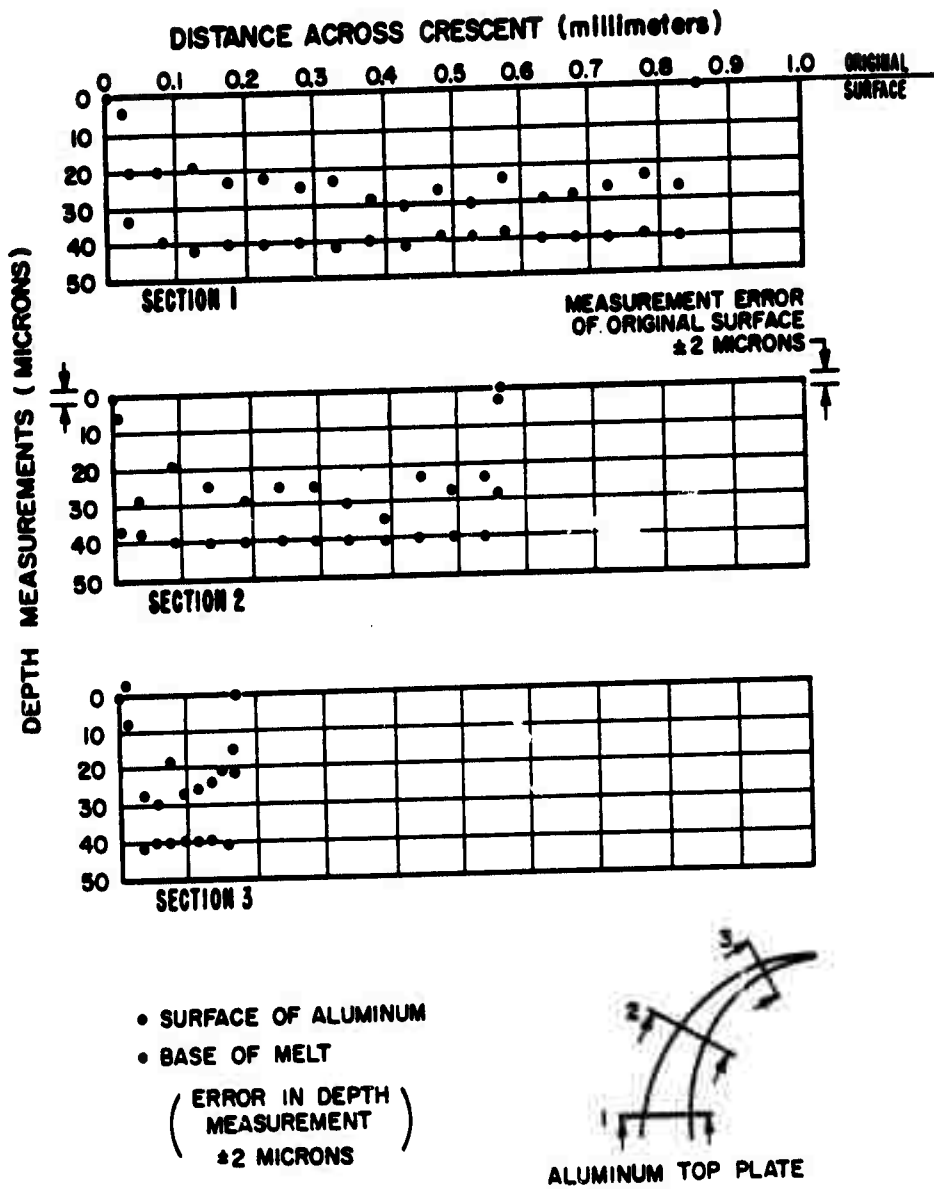
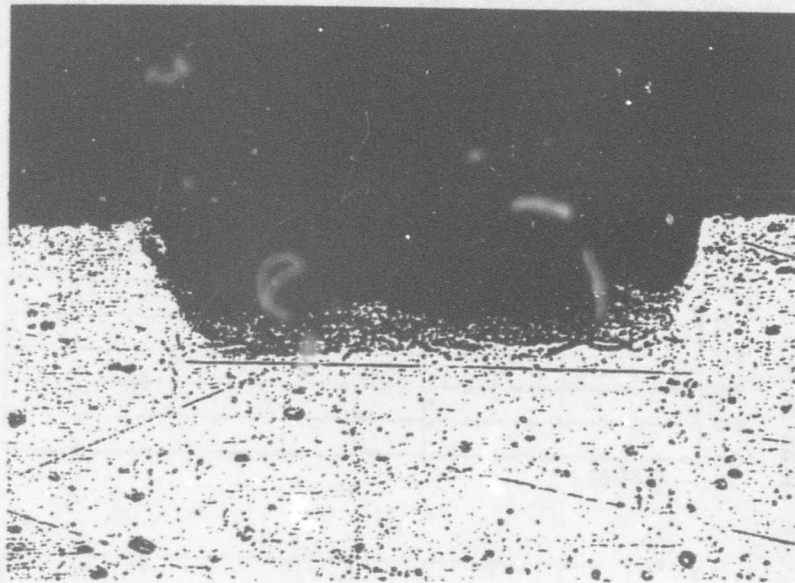


Figure 3.69 X-ray effects on aluminum, Pod B-1, Cluster 62, Crescent 2.



ETCHANT = AMMONIUM OXALATE AND AMMONIUM
HYDROXIDE SOLUTION

MAGNIFICATION = 500 X

Figure 3.70 Photomicrograph showing melt in aluminum, Pod
B-1, Cluster 62. (ASE photo)

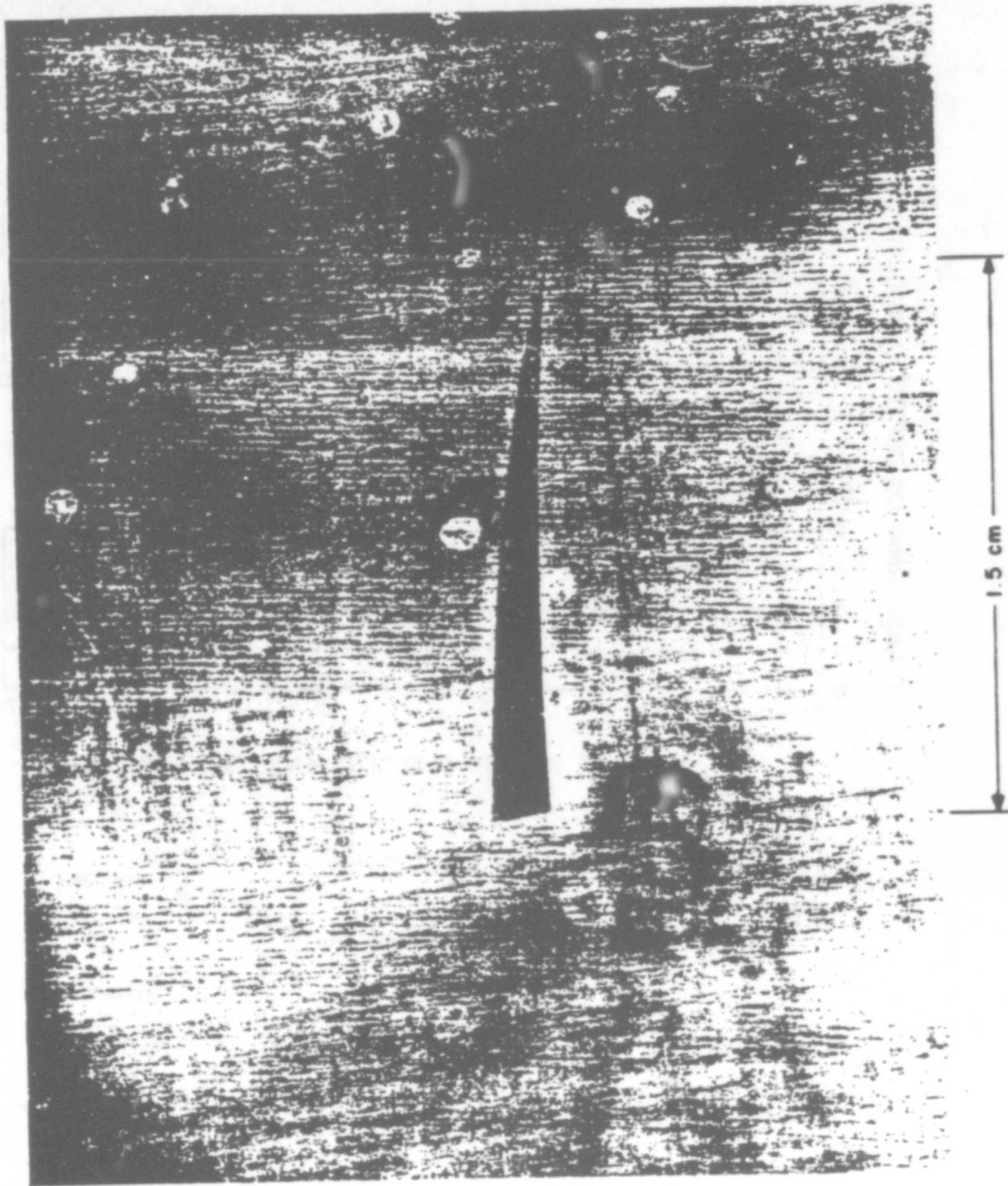
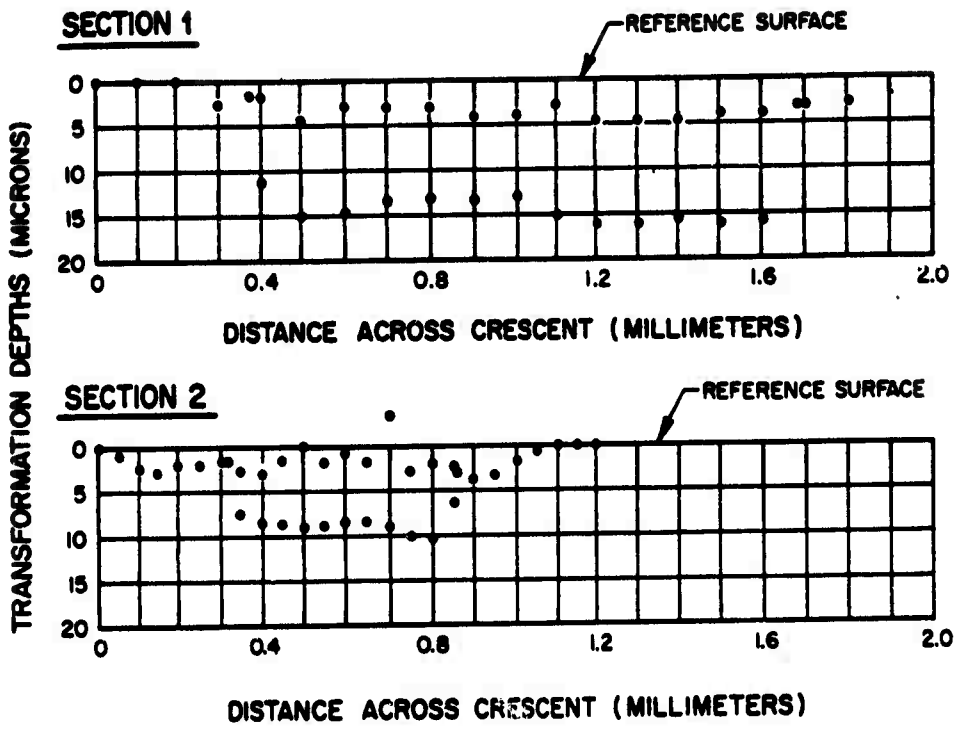


Figure 3.71 X-ray-illuminated area on inner surface of aluminum guide sleeve, Pod B-1. (ASE photo)



- SURFACE OF ALUMINUM
 - BASE OF MELT
- (ERROR IN DEPTH MEASUREMENTS ± 2 MICRONS)

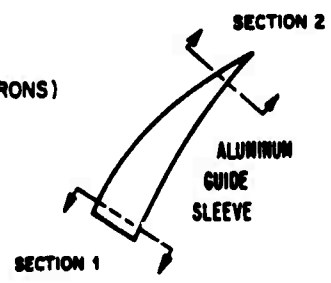


Figure 3.72 X-ray effects on aluminum guide sleeve, Pod B-1, Cluster 57.

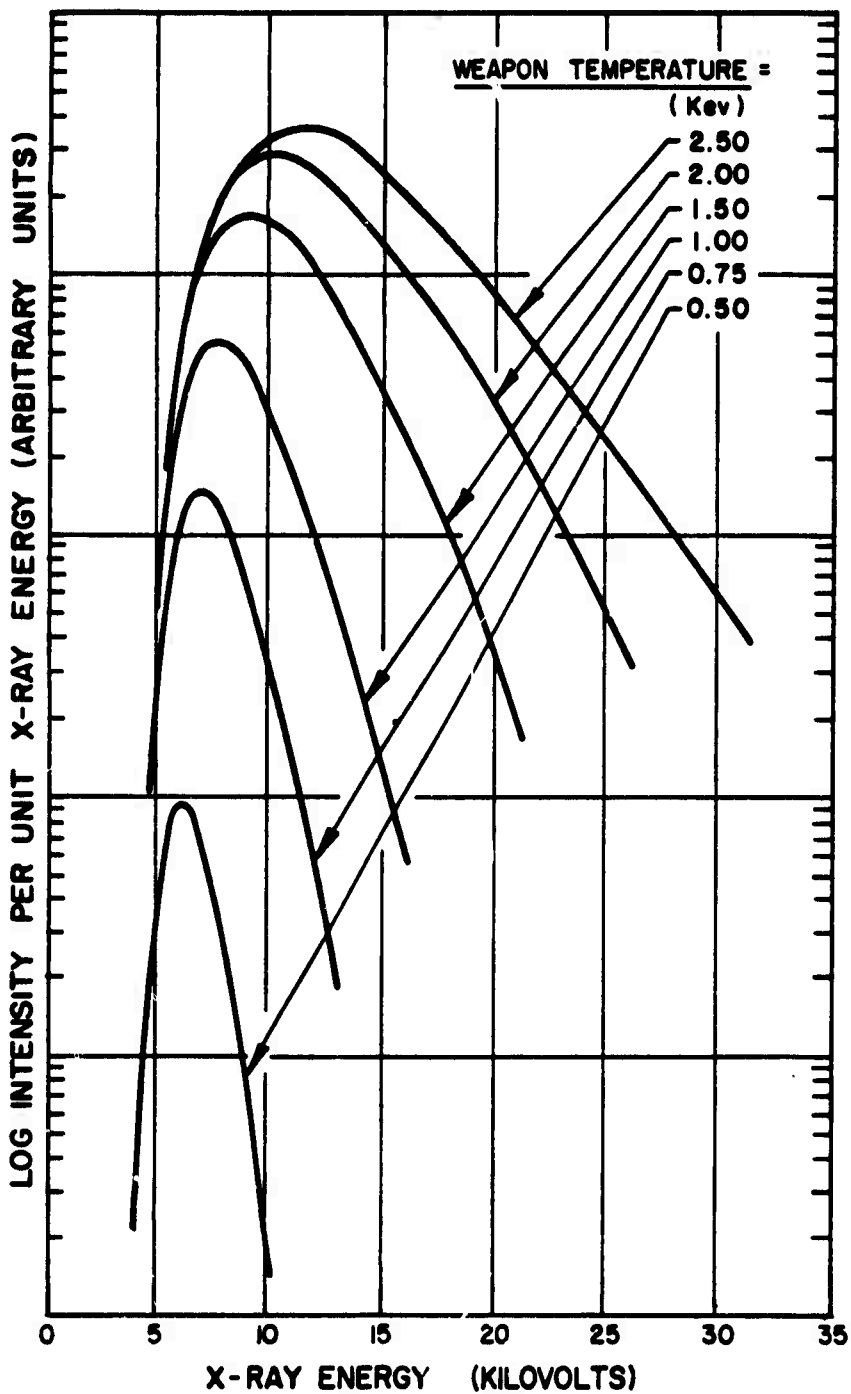


Figure 3.73 Transmission spectra at B-1.

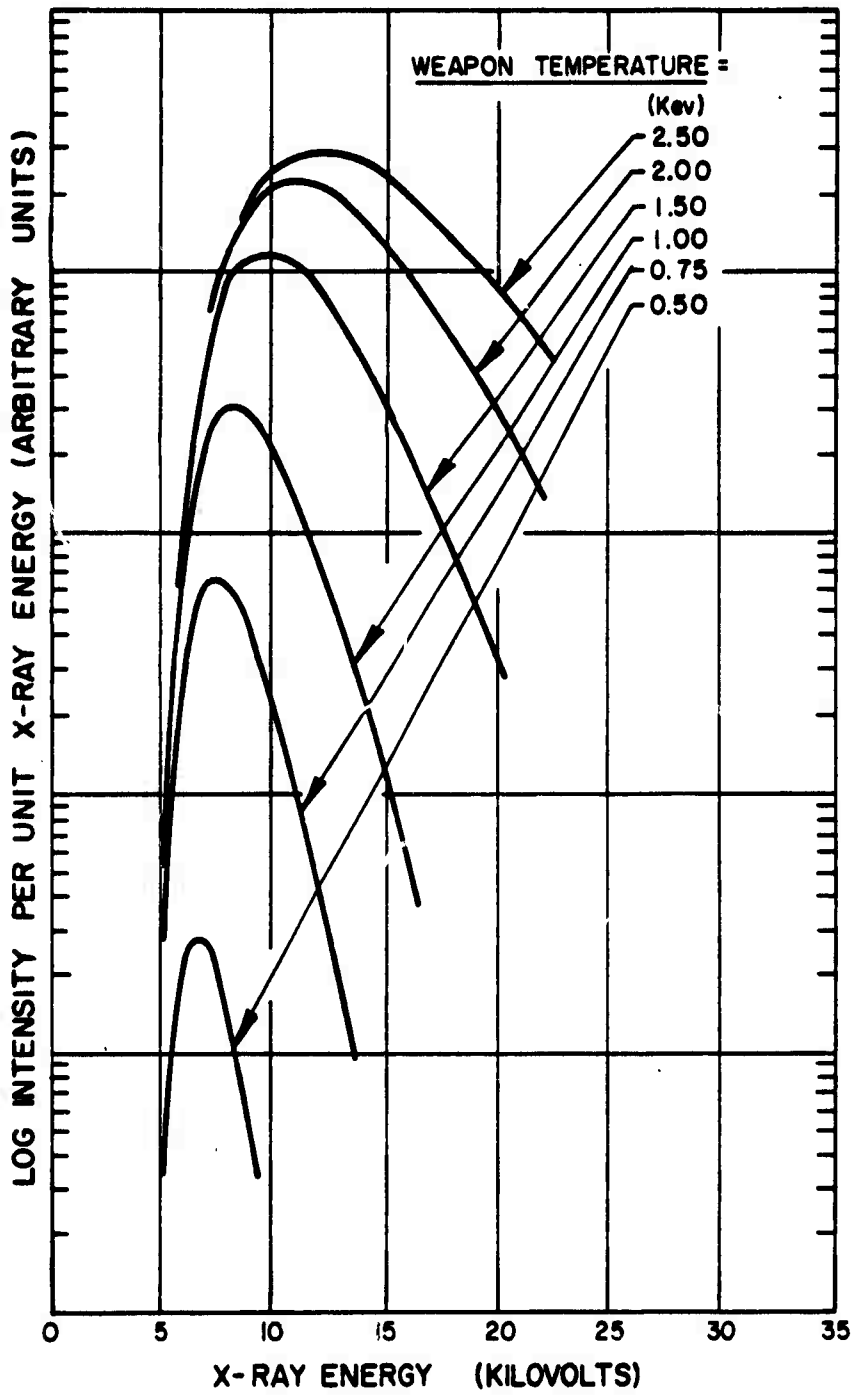


Figure 3.74 Transmission spectra at B-2.

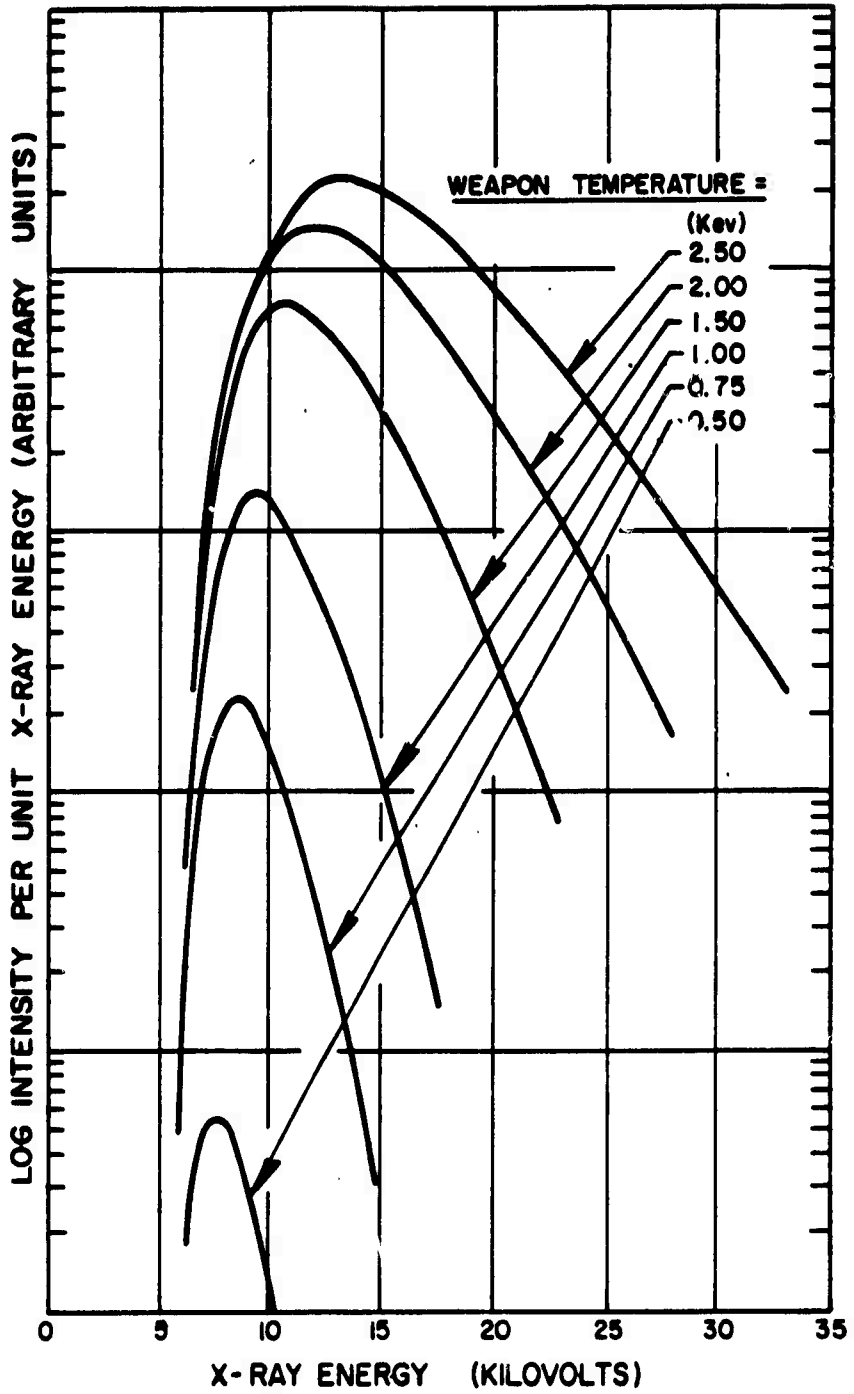


Figure 3.75 Transmission spectra at B-3.

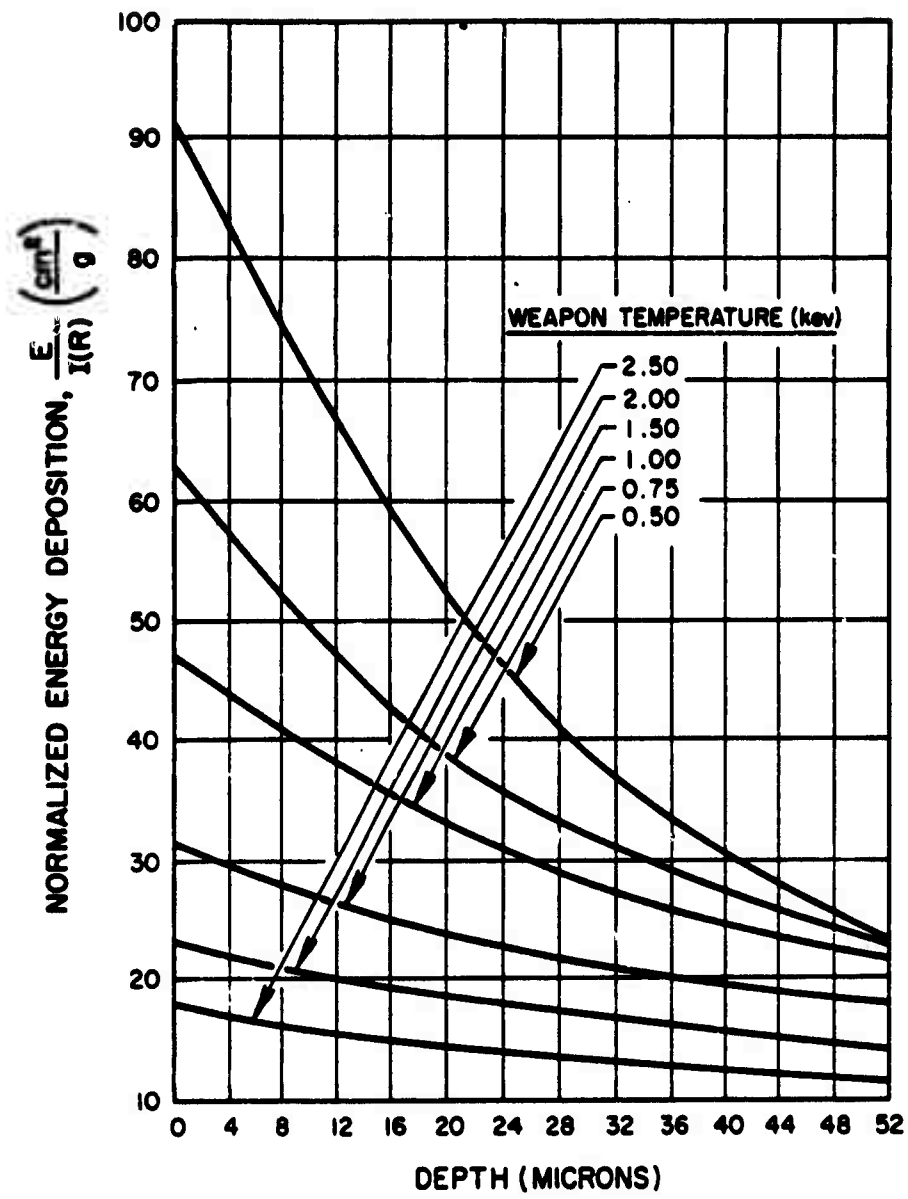


Figure 3.76 Normalized X-ray energy deposition in aluminum at B-1.

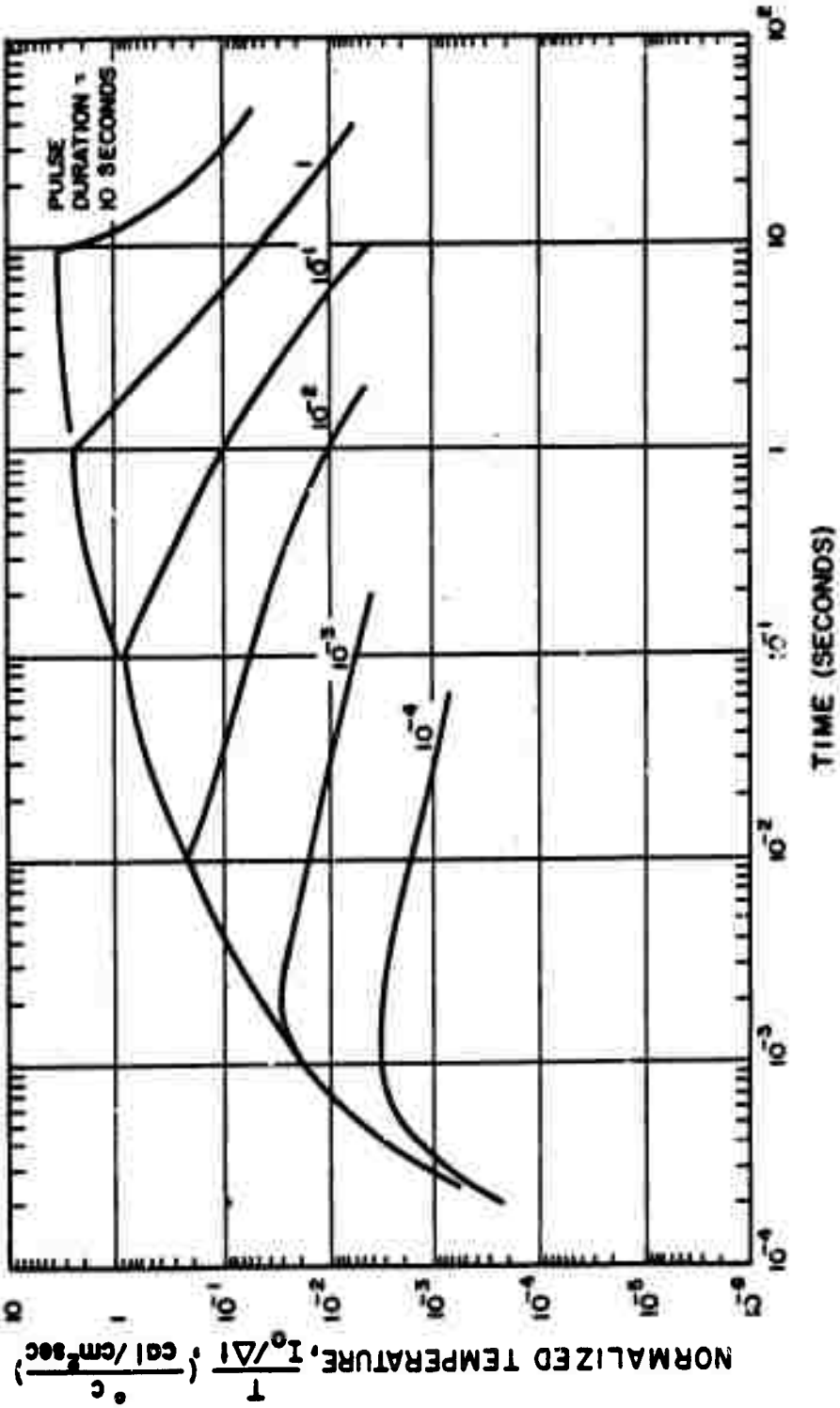


Figure 3.78 Time-temperature profiles at 138-μ depth in 1019 steel.

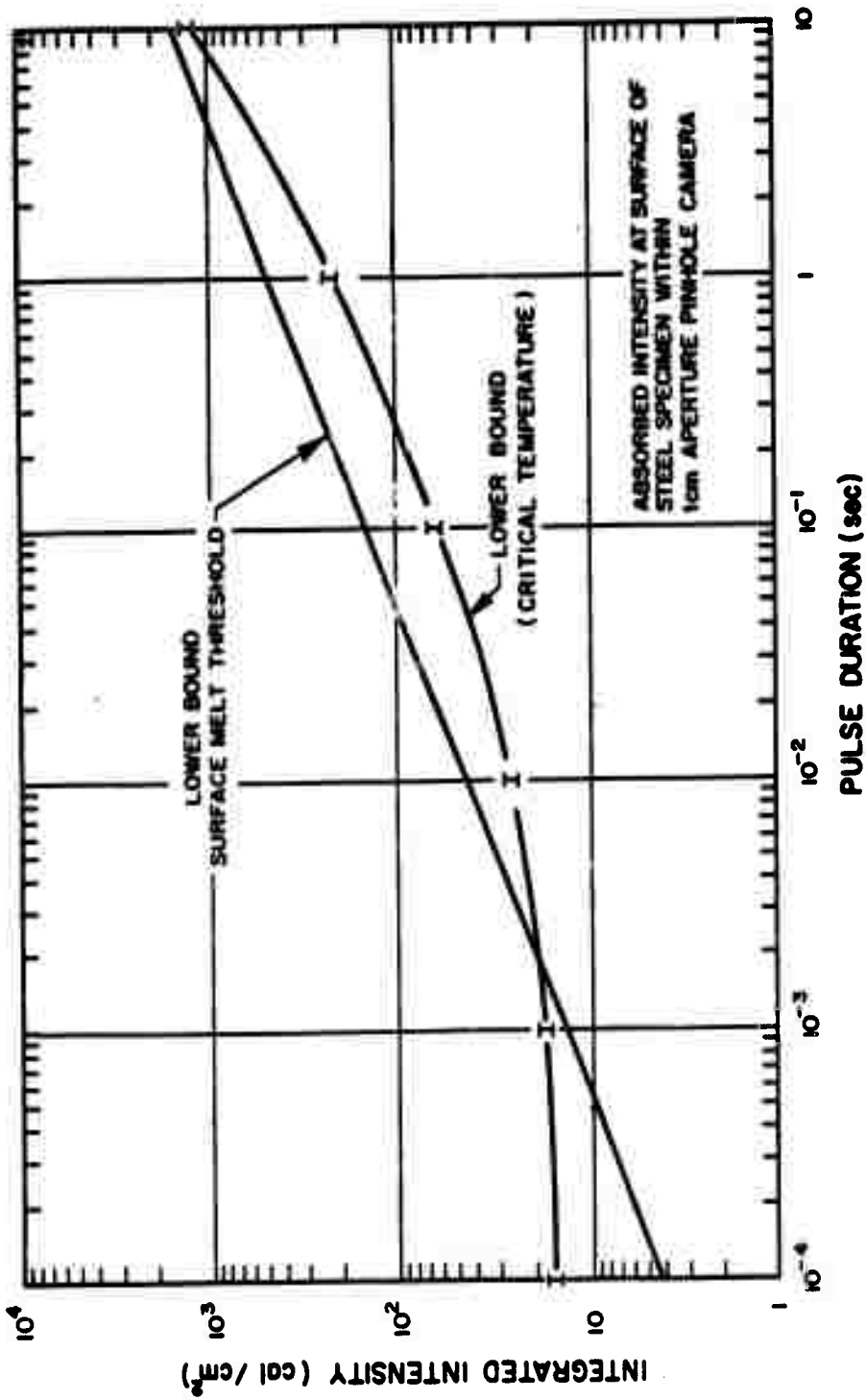


Figure 3.79 Calculated thermal radiation input to B-1 instrument, based on martensite formation at 138- μ depth, rectangular wave input.

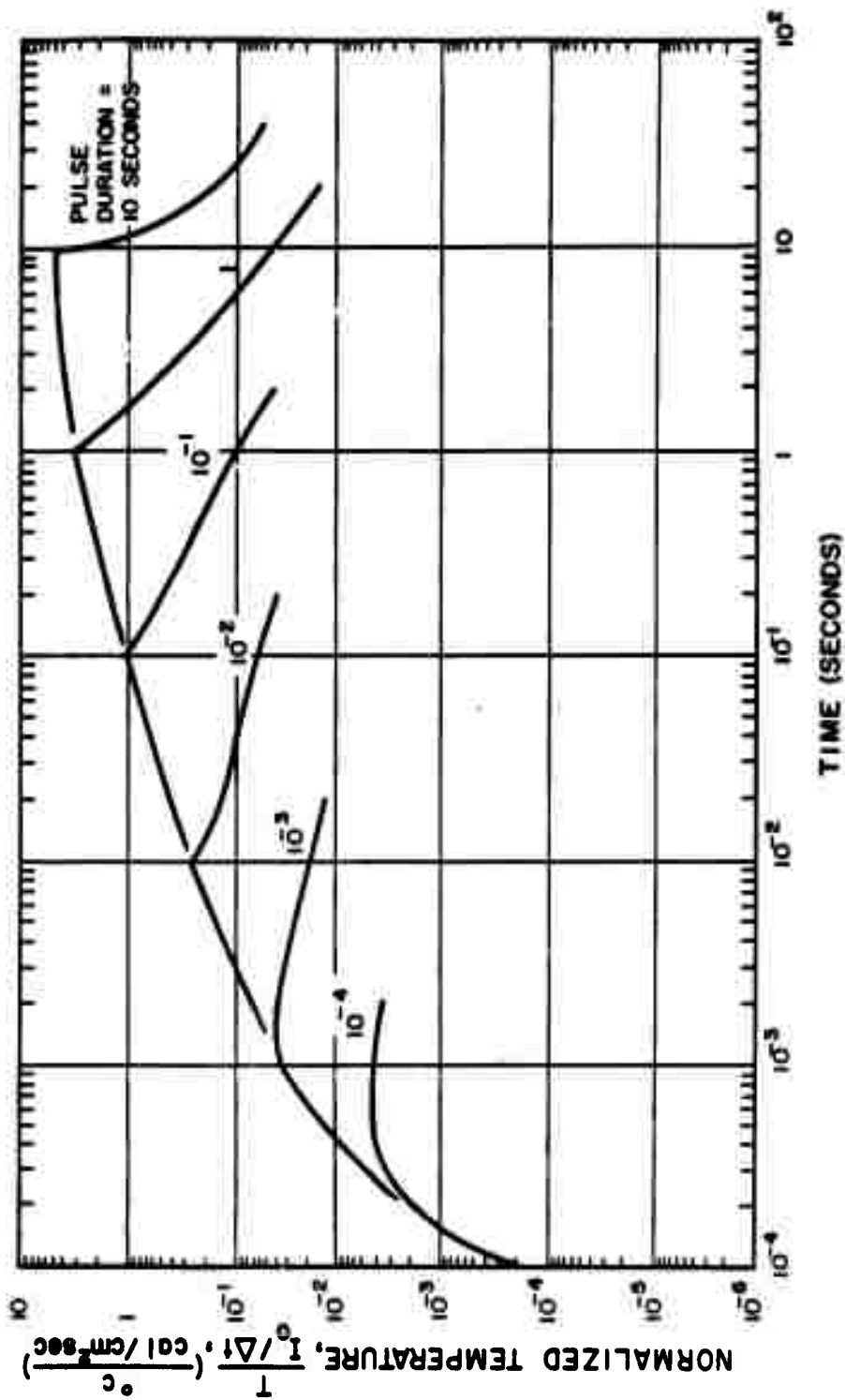


Figure 3.80 Time-temperature profiles at $105\text{-}\mu$ depth in 1019 steel.

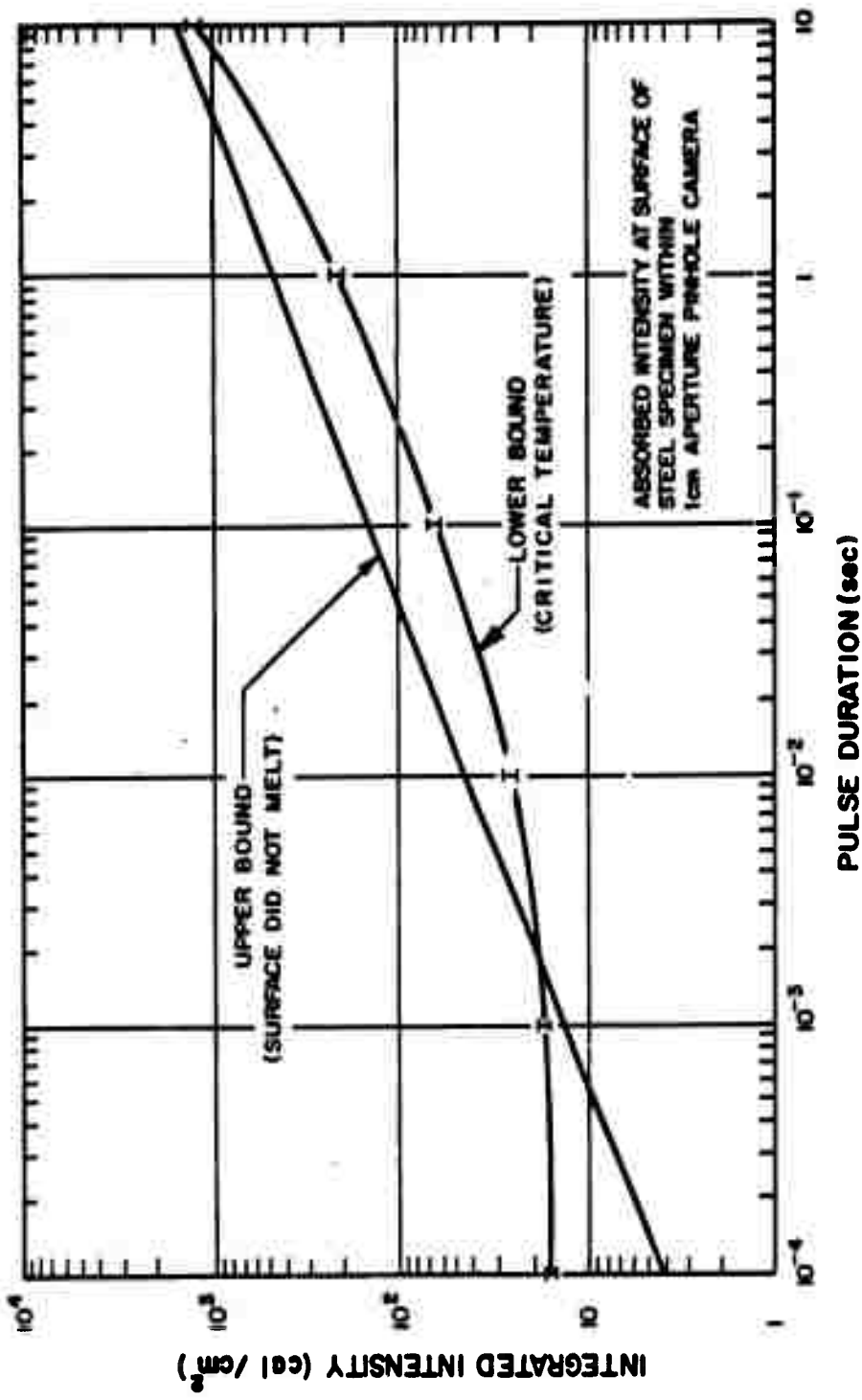


Figure 3.81 Calculated thermal radiation input to B-1 instrument, based on martensite formation at 105- μ depth, rectangular wave input.

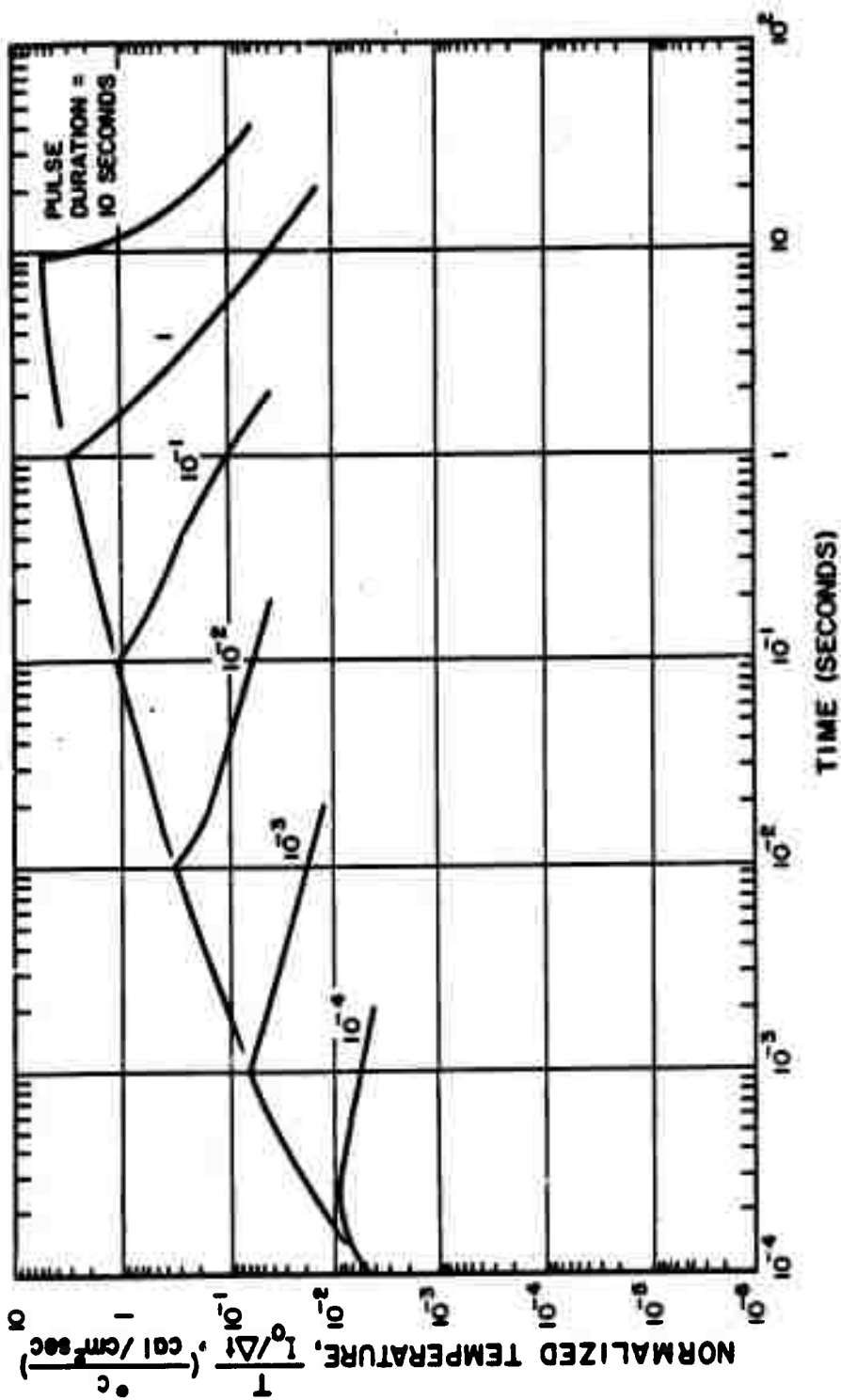


Figure 3.82 Time-temperature profiles at 53-μ depth in 1019 steel.

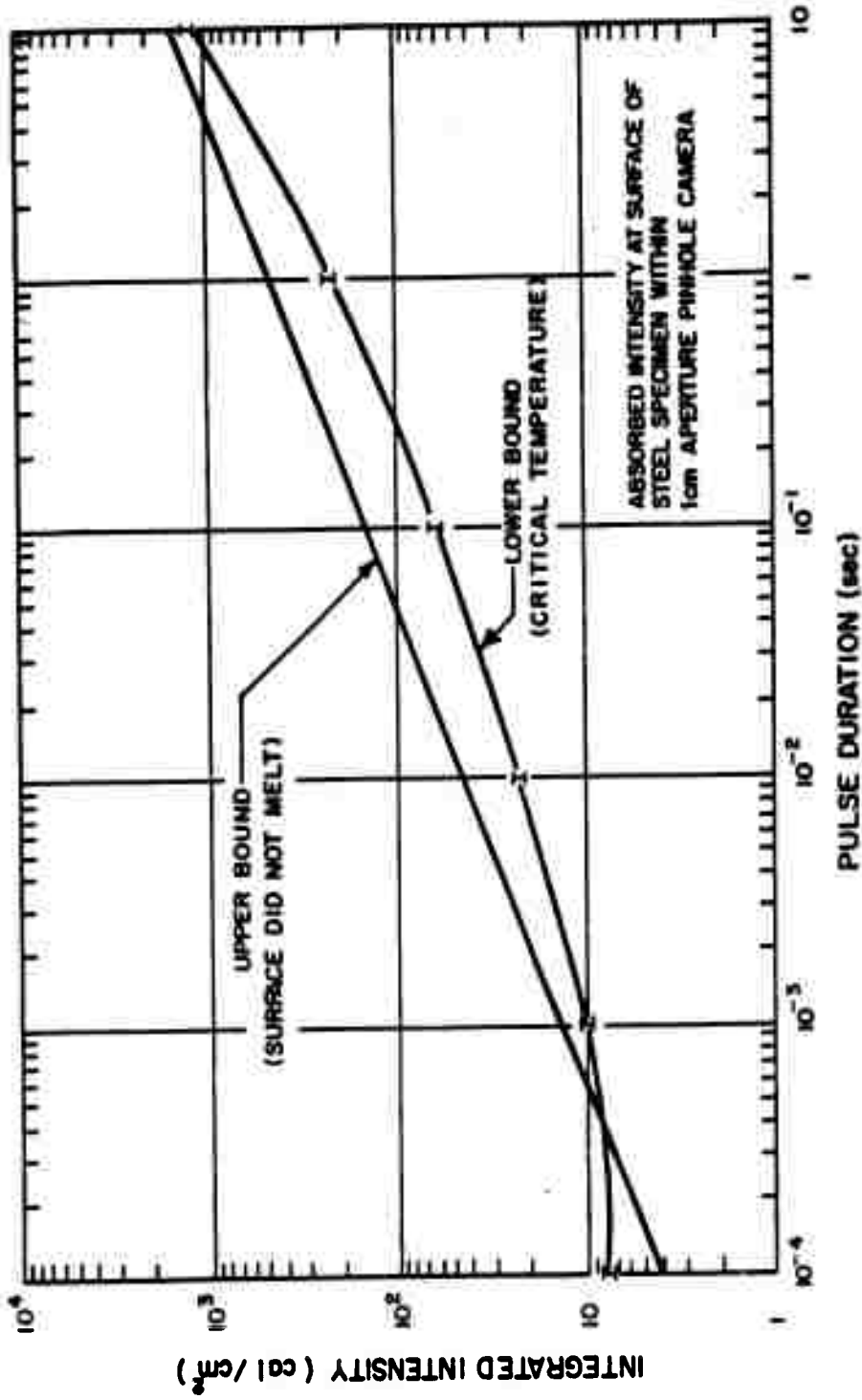


Figure 3.83 Calculated thermal radiation input to B-3 instrument, based on martensite formation at 53- μ depth, rectangular wave input.

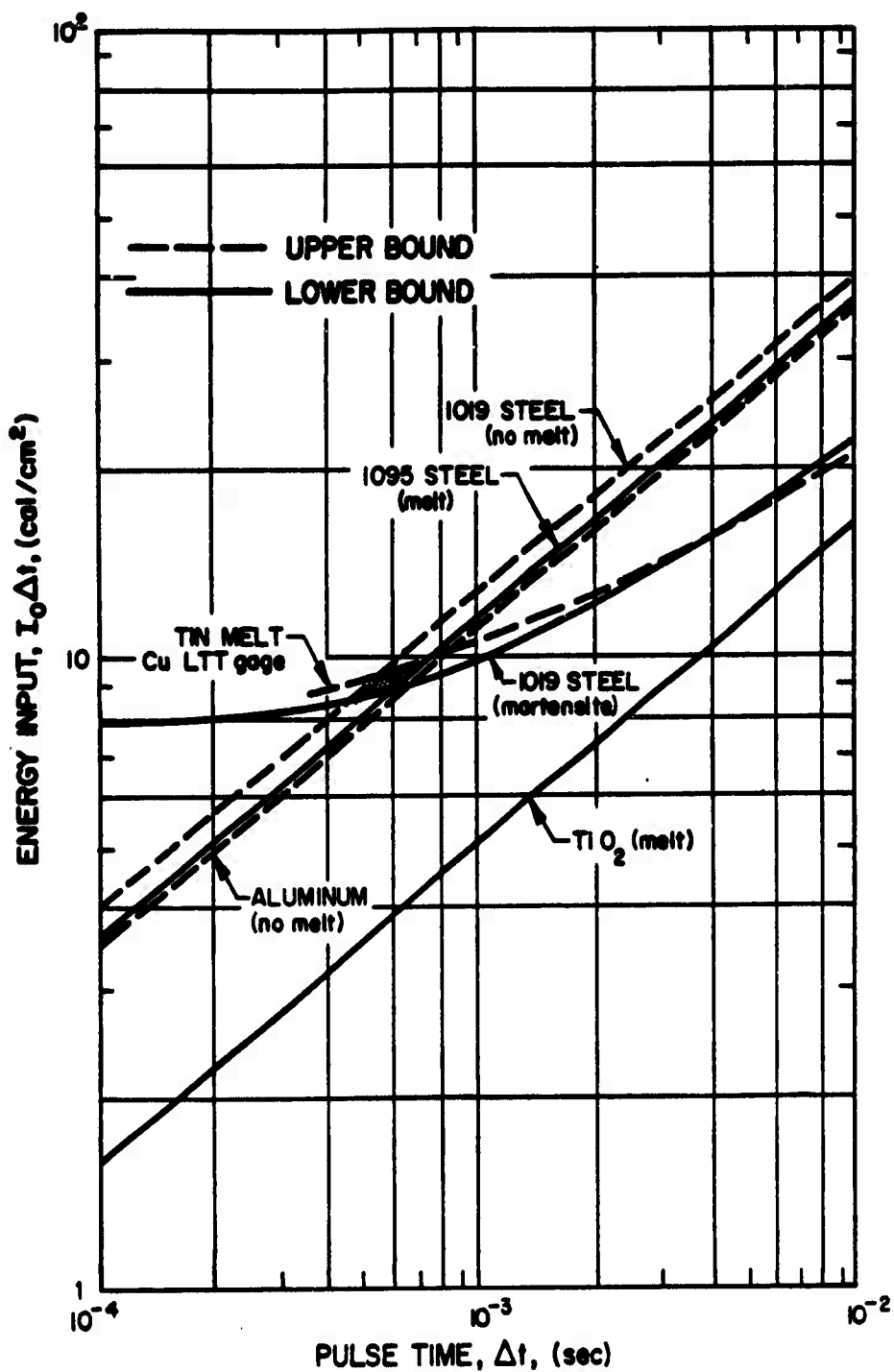


Figure 3.84 Calculated bounds on absorbed energy in Pod B-3 instruments, short-time input.

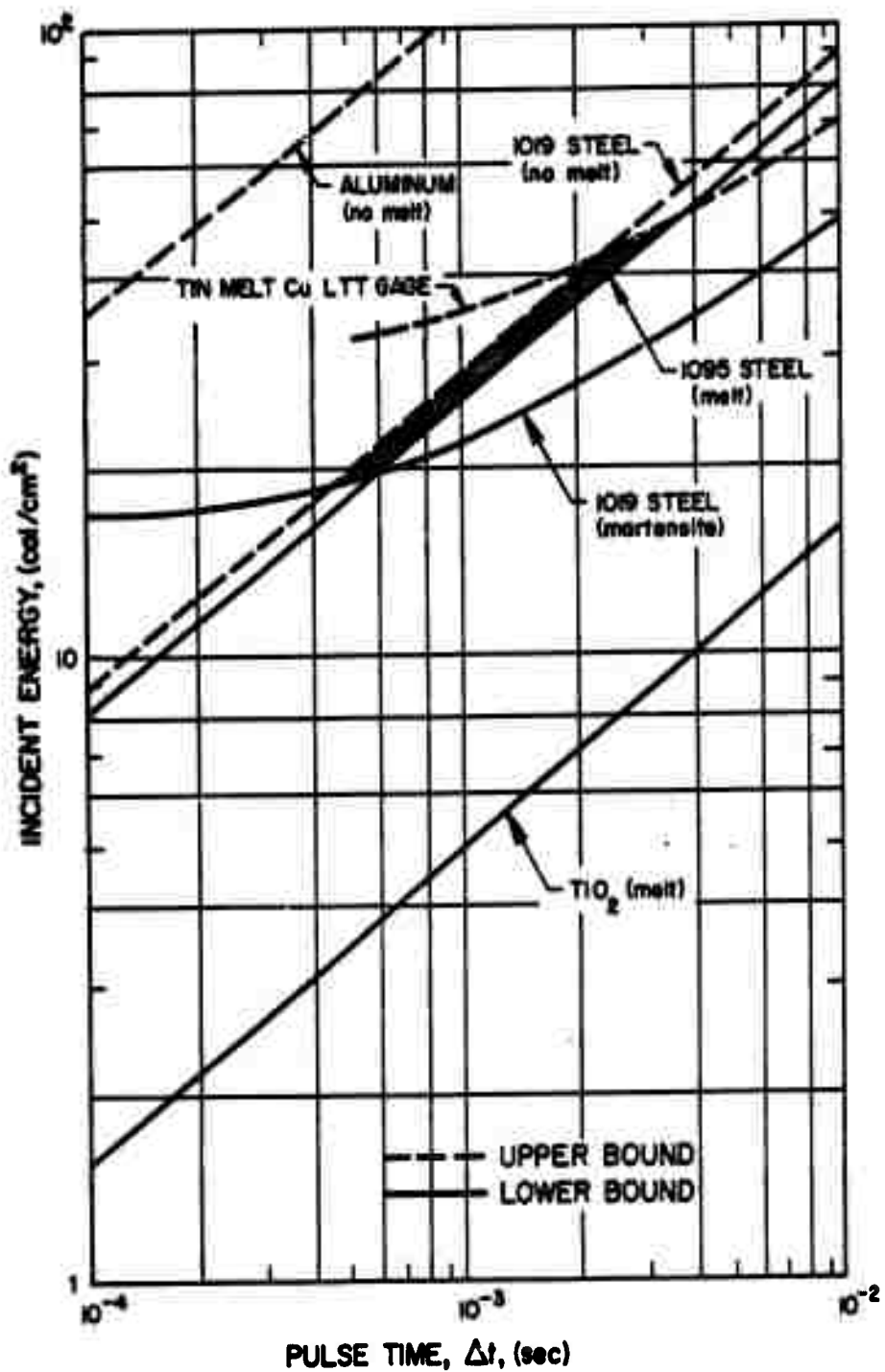


Figure 3.85 Calculated bounds on incident energy, assuming input is visible radiation, short-time input, Pod B-3.

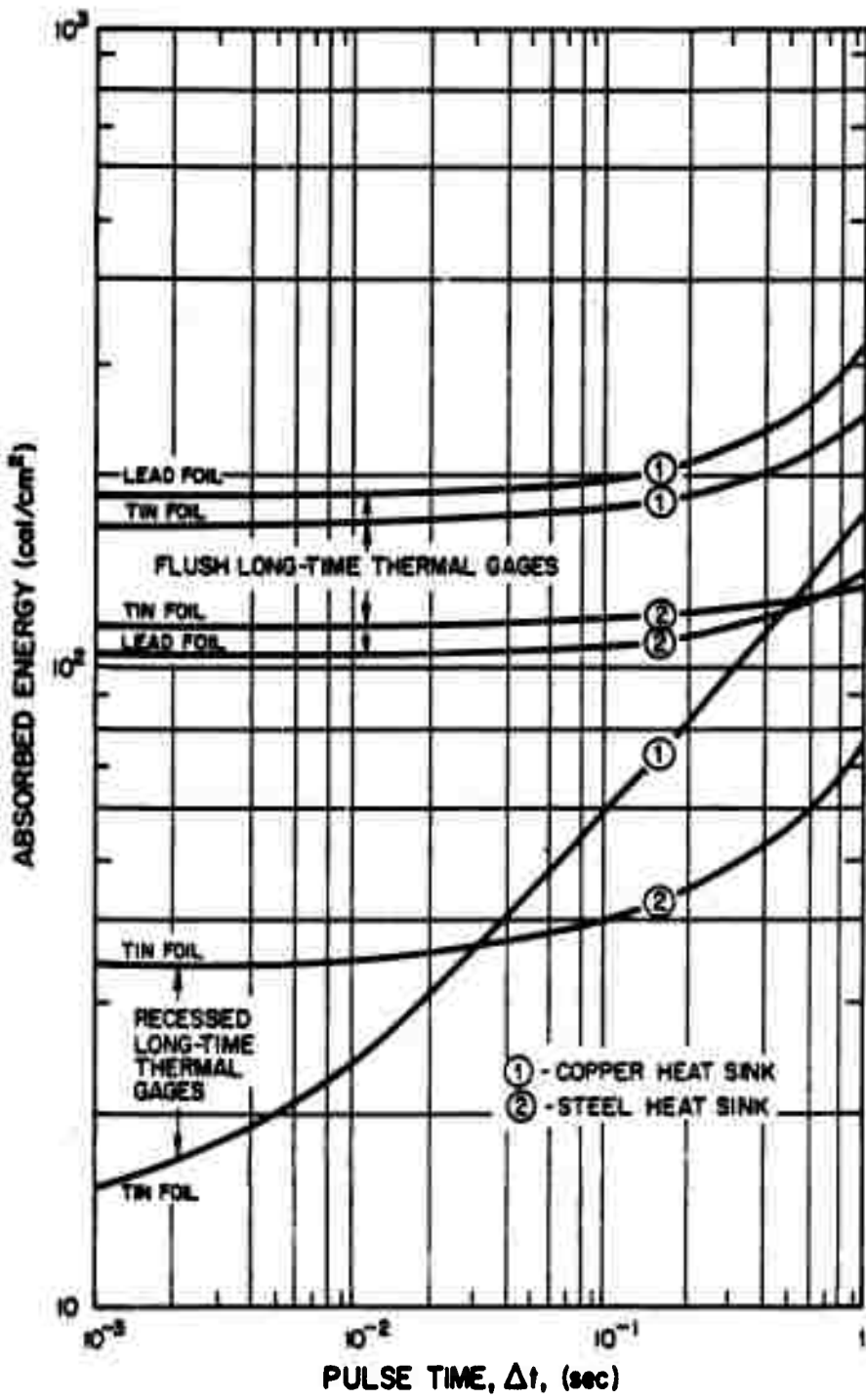


Figure 3.86 Calculated energies absorbed by long-time thermal gages, Pod B-1.

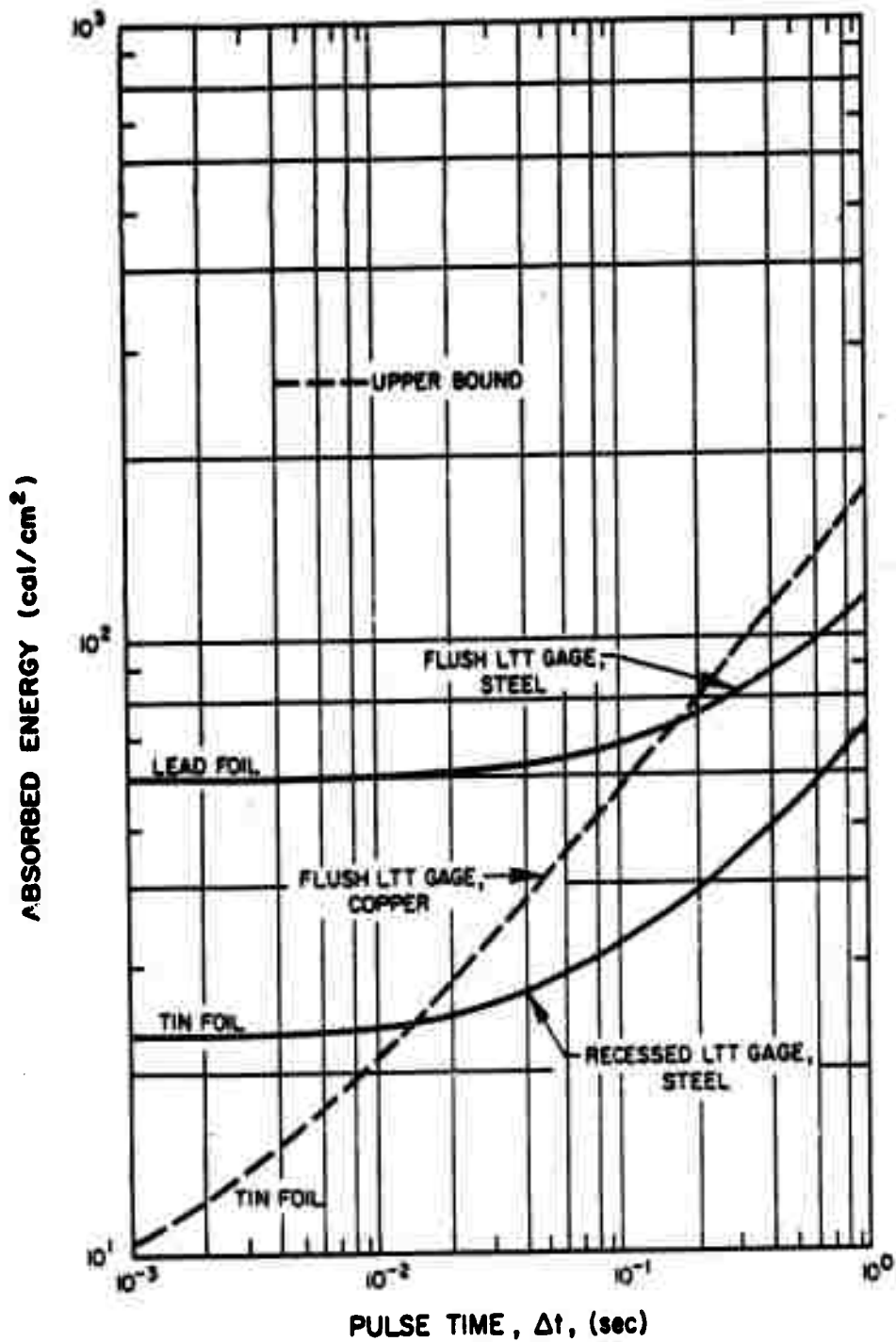


Figure 3.87 Calculated energies absorbed by long-time thermal gages, Pod B-3.

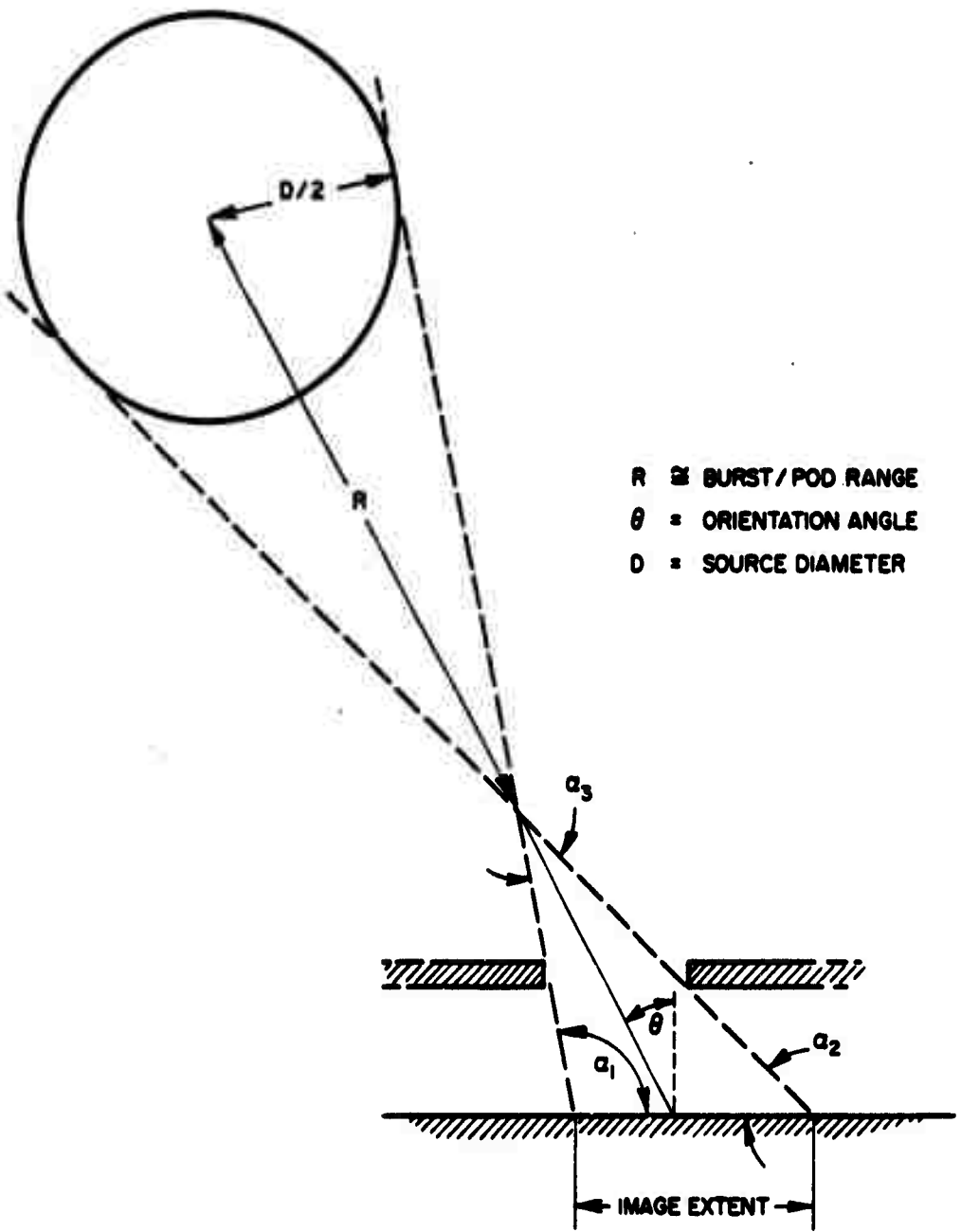


Figure 3.88 Thermal source/camera image geometry.

CHAPTER 4

SUMMARY AND DISCUSSION

The following table is presented to serve as a guide to figures and tables which contain information of general interest.

<u>Subject</u>	<u>Figure No.</u>	<u>Table No.</u>
X-ray source size	3. 63	
X-ray intensity.....	3. 77	3. 11
Thermal source size	4. 2.....	3. 14
	4. 3	
Short-time thermal intensity.....	3. 79	
	3. 81	
	3. 83	
	3. 84	
Long-time thermal intensity.....	3. 86	
	3. 87	
Short-time thermal spectrum.....	3. 84	
	3. 85	
	3. 88	
Abiation		3. 4
Thermomechanical impulse (total).....	3. 12.....	3. 2
	4. 4	
Thermomechanical impulse (time history).....	3. 17.....	3. 2
	3. 18	
Thermomechanical vulnerability of Mark 3 R/V....	4. 6	
Thermomechanical vulnerability of Mark 4 R/V....	4. 7	

4.1 INPUT MEASUREMENTS

4.1.1 X-Ray Inputs. The X-ray pinhole cameras on both pods B-1 and B-2 yielded readings. At B-1 two true images were recorded, whereas on B-2 the detector was affected but true images were not formed because the apertures were too large to behave as pinholes. The image sizes at B-1 correspond to a source approximately one meter in diameter (see Figure 3.63). If the five-foot diameter of the copper heat shield had been the source, it would have formed an image about 1/3 greater; this difference would be readily discernible. The heat shield was to be oriented in a downward position which would interpose it between the weapon and the pods. There is no evidence in the data to indicate that there was a high intensity halo, which might be expected if the source had been visible beyond the heat shield. The apparent source diameter of one meter is shown to scale on the schematic view of the R/V in Figure 4.1. It is interesting to note that the X-ray source measured with the King Fish pinhole camera had approximately the same size despite the absence of a heat shield.

The weapon radiating temperature is shown in Figure 3.77 to be within the bounds of 0.62 and 1.23 kev with a corresponding range of intensity at pod B-1 of

The effectiveness of the heat shield as an absorber of X-rays seems to be consistent with a model which treats the heat shield as a secondary source. these

measurements of a small source appear to confirm the feasibility of an X-ray shield oriented toward the earth and intercepting only a small fraction of the weapon yield.

The photocell X-ray detector has not been calibrated. On pods B-1 and B-3 the qualitative results appear consistent with proper operation. On pod B-2 mechanical damage nullified all recordings. Since this pod had the control instrument to measure the background, the readings of the instruments on the other two pods may never yield meaningful results.

A dividend of this instrument is data on radiation damage to semi-conductors. Transistors and diodes suffered permanent damage on pod B-1. On pod B-2 the diodes appeared to have survived, but the transistors were damaged. The interpretation of the condition of the elements in pod B-2 is somewhat ambiguous because of mechanical damage to the instruments. All elements in pod B-3 were capable of operating correctly after the event.

In all cases passive components (capacitors, resistors, photocells, relays) survived without any damage, which could be ascribed to the nuclear environment. The design of the instruments was such that only passive components were required to operate in the burst environment.

4.1.2 Thermal Inputs. It has been brought out that the Blue Gill experiment apparently took place in an environment composed of the vapor products from the refrasil-phenolic backplate. All instruments reacted to a weapon input which was modified by this vapor. The thermal instruments, and other incidental sources of thermal data on the pods, were generally at varying distances above the backplate. The available evidence shows that the thermal intensity increased with distance above the backplate. The vapor layer is believed to be responsible for the variation. This phenomenon is borne out, for example, by the variation in transformation depth in the sideways-viewing steel detector (Figure 3.38). The same trend is apparent in the data on the ablation of refrasil-phenolic. In

Table 3.4 it can be seen that the ablation was generally lowest on A-pistons and the backplate. Next in order both in distance above the backplate and in degree of ablation are the ablation-condensation gage samples. The maximum ablation was recorded on the F-pistons, which were the most distant from the backplate. The scatter is too large, however, to permit quantitative use of this ablation data.

The preliminary analysis of thermal inputs has not yet taken into account the apparently significant variation of observed effects with distance above the backplate. Some of the derived results are based on a comparison of instruments immersed at different depths in this vapor. These comparisons may not be valid without accounting for the different vapor depths. The results presented herein are, therefore, suspect to a degree impossible to ascertain without further analysis. It is clear that the intensity actually incident on the backplate has not been measured in this experiment. This limitation must be borne in mind, particularly when reading this section. The effect on thermal source size is not expected to be significant; on the other hand, the effect on thermal intensity results may be large.

The Thermal Source The thermal source as measured by the steel detectors in the various thermal pinhole cameras is less than 100 meters in diameter (see Section 3.3.5 and Table 3.14).

The recording thresholds for these two materials differ by about one order of magnitude. The two observations are depicted schematically on Figure 4.2 along with the theoretical source derived in Chapter 1. Figure 4.3 depicts the placement of the pods with respect to the two apparent thermal sources. The flattening of the sphere at the bottom is a qualitative depiction of what might be the effect of the heat shield on the fireball.

The interpretation of the two apparent thermal sources can only amount to conjecture at this time because of the limited amount of analysis that has been done. One tempting hypothesis is that there are indeed two distinct sources; an inner fireball created by the expanding debris and an outer fireball due to the X-ray deposition in the atmosphere. There is no evidence to indicate that even the closest pod was ever immersed in the fireball. In addition, the inner fireball might be expected to be of higher density at the center than at its periphery for the times and distances of interest. Thermal radiation from the inner fireball would depend on the emissivity of the gas which would be greater at the center. It is, therefore, not obvious that the observed thermal source size would be as large as the edge of the debris cloud. In the context of this discussion the effective source is defined by the threshold sensitivity of the detector.

Another hypothesis which has been offered to explain the small high-intensity source is that the radiation was bremsstrahlung X-rays from debris electrons.

A calculation has been performed which indicated that the data do not offer support to this hypothesis. The X-ray deposition in steel was calculated for the B-3 position; a similar calculation was performed at the B-1 position where the steel was shielded by 3 mm of micarta. These calculations assumed several Planckian and flat distributions

The calculated energy deposition curves at B-1 were always above those at B-3. This result contradicts the observation that there was a transformation in a directly exposed steel detector in

B-3 and no transformation in the steel detectors under 3 mm of micarta in B-1. This result must be considered tentative because it is conceivable that there exist spectra which can transpose the deposition curves.

Presumably, a high X-ray temperature weapon without a heat shield could produce a much larger fireball and a concomitant higher thermomechanical kill radius through engulfment of the target. This statement, however, depends upon the yield of the weapon, the burst altitude, and the postulated hardness of the target.

The data have not been analyzed with the viewpoint of establishing any sequence to the sources. For example, with the absence of this information the two sources can be hypothesized to occur simultaneously with the inner source visible within the large outer source. Alternatively, they could be an early and a late view of the same source. Presumably, the source would continue to radiate as it grows, with the later radiation being emitted slowly at lower intensity. This intensity would not be detected by the high-threshold instruments in this experiment nor would it contribute appreciably to the impulse.

Thermal Intensity. The intensity and pulse duration of the short-time thermal radiation input were determined from the 10-mm aperture thermal pinhole cameras on all three pods and from flush-mounted materials on pod B-3. The results based on a pearlite-martensite transition temperature of 722°C must be considered tentative because of the probability that this value is substantially higher for the very short time inputs of this experiment. In all computational procedures a rectangular pulse shape was used,

The maximum transition depth in the B-1 camera gave a

minimum energy input of 25 cal/cm^2 .

An upper bound on time and a realistic upper bound on intensity are not yet available.

A more complete analysis of the intensity and pulse duration was possible on pod B-3 within the scope of the present effort because of the absence of complications due to material melt. The sources of data were: no melt of 1019 steel, melt of 1095 steel, a finite martensite depth in 1019 steel, no melt of aluminum, melting of TiO_2 filter material, and melt of tin foil sensor in copper long-time thermal gage. The bounds from these data are 9 to 50 cal/cm^2 for incident energy

If a pulse duration of 10^{-3} sec is arbitrarily chosen as representative of the ultra-violet and visible, a tentative estimate of spectrum would place between 0.1 and 0.8 of the incident energy in the visible part of the spectrum.

The long-time thermal gages are capable of detecting the integrated thermal input out to long times because of the inherent sensitivity of the sensor foils. On pod B-1 the lower bound to the absorbed intensity in a flush gage is 165 cal/cm^2 ; no time duration estimate is presently available. Lower bound estimates for the intensity absorbed and the duration from the recessed long-time gages in B-1 are 37 cal/cm^2 . The recessed gage has a view angle 1/10 of the flush gage. A superficial comparison of the flush and recessed gages indicates

that the latter saw about 1/5 of the long-duration source.

The lower bound estimates for the flush long-time gages in B-3 are 72 cal/cm^2 for absorbed intensity and 0.16 sec for pulse duration. The recessed gages recorded a lower bound intensity of 24 cal/cm^2 A comparison of the recessed gages in B-1 and B-3 (37 and 24 cal/cm^2 , respectively) is consistent in that the gage on the latter apparently saw more of the source.

Another noteworthy check on consistency of measurements is a comparison of the flush long-time gages on pods B-1 and B-3. When the lower bound value of 165 cal/cm^2 (absorbed) is modified for an absorptivity value of 0.3 for copper, the incident intensity is 550 cal/cm^2 . In the case of pod B-3 the modification has to be made in both copper and steel (absorptivity = 0.45), because the bound is obtained from an intersection (Figure 3.87). This modification moves the intersection to approximately 140 cal/cm^2 . Since the pod ranges from the burst differ by a factor of two, the comparison of 550 and 140 cal/cm^2 is just about that predicted by the inverse square law.

4.2 RESPONSE MEASUREMENTS

4.2.1 Thermomechanical Response. The most evident feature of the impulse measurements on Blue Gill is the absence of a significant variation that could be attributed to sample material. In addition, this impulse extended over a relatively long time ($t \lesssim 1 \text{ msec}$). These results indicate that the impulse-recording instruments responded to more than the X-ray input. Additional indication that the X-ray impulse must have been small is furnished by the King Fish impulse data wherein an intensity greater by more than an order of magnitude generated an impulse only 20% of that measured on Blue Gill Pod 1. Also worthy of mention in this regard is the fact that, while the impulse

on B-3 was 40% of that on B-1, the B-3 X-ray intensity was at most 7% of the B-1 level ($< 0.3 \text{ cal/cm}^2$ at B-3). The existence of a thermomechanical effect at this altitude and for the pod ranges was, therefore, unambiguously demonstrated. Furthermore, the loading must have been characteristic of the backplate covering material—refrasil-phenolic.

The measured total impulses at pods B-1, B-2, and B-3 were, respectively, $(9.7 \pm 0.2) \times 10^3$, $(7.5 \pm 0.3) \times 10^3$, and $(3.7 \pm 0.7) \times 10^3$ dyne-sec/cm² based on D-piston readings. These values are plotted vs. range in Figure 4.4 along with the theoretical estimates derived in Chapter 2. At short ranges the predicted impulse is higher than measured. This disagreement may be at least partially due to the fact that the pods were never immersed in the effective fireball. Another modifying influence is the energy attenuation due to the vaporized pod material. It can also be seen that the drop-off in impulse with increasing range is much slower than predicted. Thus, although the measured and predicted impulses are, in general, not in serious disagreement over the ranges in question, one must seriously question whether the model used to predict these impulses is correct. It is conceivable that the impulses on Figure 4.4 could increase almost discontinuously at the point where immersion occurs.

The total impulse by itself is not sufficiently descriptive of the thermomechanical loading to a vehicle, because the loading can have a duration which is not necessarily much shorter than the characteristic response time of missile structures. The loading pulse shape must, therefore, be taken into account in the evaluation of structural vulnerability. By contrast, X-ray-induced loadings are always substantially shorter than structural response times so that the loading in this regard can be considered truly impulsive in nature. In this experiment most of the impulse was delivered in about 1/4 msec,

with concomitant average loads over this time at the 1-km range of between 10 and 24 sea-level atmospheres. The peak values can, of course, be much higher. The unidirectional nature of the loads was indicated by the behavior of essentially seismic components of the indent recorders. This result is consistent with the thermal source data which places the pods outside the apparent source. The pods had a ratio of mass to back plate area of about 50 gm/cm^2 so that 10 sea-level atmospheres corresponds to a rigid body acceleration of about 200 g's. The impulse data show that pod B-1 received an incremental velocity of almost 200 cm/sec.

It should be noted that an extrapolation of Figure 4.4 to the range of pod K-1 of Shot King Fish * indicates that the thermomechanical impulse and the X-ray impulse are very comparable in magnitude.

The pod B-1 backplate has been examined in an effort to find evidence of permanent deformation. The evidence has been inconclusive, and certainly any deformation present cannot be put into quantitative terms. The evidence does indicate, however, that the pod B-1 backplate was different from the pod B-3 backplate and an unused backplate. The differences were qualitatively consistent with expected burst-induced behavior. The backplates were designed by General Dynamics/Astronautics to a pressure criterion of 500 psi.

The short duration of the initial impulse spike together with the short-time thermal evidence indicate that only a very small initial portion of the total energy reached the pod. The rest of the energy probably then interacted with the material already vaporized and did not reach the surface of the pod. A specification of this energy incident on the vapor shield has not yet been made.

* For a description of the Project 8A.3 participation in Shot King Fish, see Part 2 of this report.

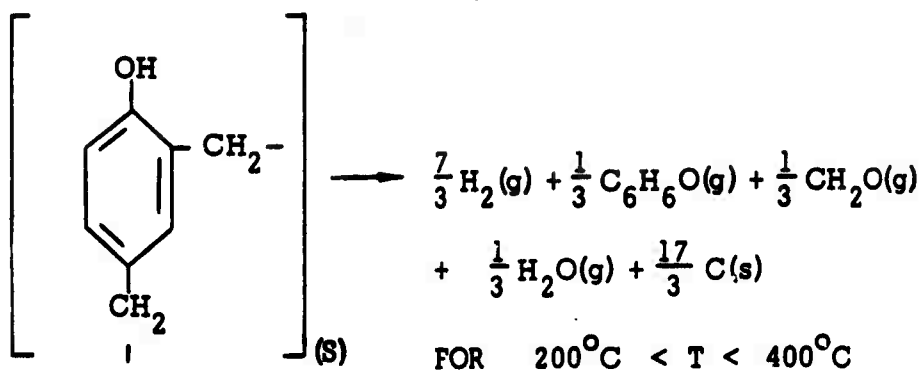
4.2.2 Ablation Response. The evidence on the pods demonstrates that the experiment took place in a reffrasil-phenolic vapor environment. The ablation of reffrasil-phenolic is, therefore, the only directly applicable ablation data. The data for similar materials (e. g., micarta, black phenolic) are significant in that their behavior qualitatively confirms the behavior of reffrasil-phenolic. This similarity in behavior is probably due to the fact that the vapor they would create is not drastically different from that created by reffrasil-phenolic.

At pod B-1 the ablation of reffrasil-phenolic was less than 0.1 gm/cm^2 . The ablation at pod B-3 was approximately one-half this amount. Ablation of this material, therefore, cannot in itself, be considered a significant damage mechanism. Judging from the small amount of energy which penetrated to the instruments on the backplate, the vaporizing reffrasil-phenolic is an effective radiation shield making its ablation a self-limiting phenomenon.

At first glance, the small amount of energy measured in the short-time thermal pulse and the low ablation seem inconsistent with the large impulse. However, the energy incident on the vapor can contribute appreciably to the impulse, even if this energy does not reach the pod surface in the form of radiation (Reference 14). From the expression

$$KE = \frac{I^2}{2 M}$$

where KE is the kinetic energy in the blowoff, it can be seen that about 20 cal/cm^2 could be sufficient for an impulse of $10^4 \text{ dyne-sec/cm}^2$ if the effective heat of ablation were close to zero. It is possible to hypothesize an ablation scheme for reffrasil-phenolic which results in a negative heat of ablation. This reaction is as follows:



In the required temperature range, the heat of ablation is

$$H_{400^\circ\text{C}} - H_{25^\circ\text{C}} = -524 \text{ cal/g}$$

For this decomposition scheme to occur, the energy must be deposited at a rate above that available through conduction. A possible method by which thermal radiation could be deposited rapidly in depth is illustrated in Figure 4.5. The glass fibers act somewhat as light pipes to conduct the radiation within the material. Also, the phenolic itself is somewhat translucent which may permit deep and rapid penetration of the thermal energy. If this were the reaction, it had to occur very early, because eventually the environment, at least locally, reached temperatures much above 400°C as demonstrated by the fact that pyrolytic graphite ablated. The X-ray flux was too low to ablate appreciable carbon so that the thermal pulse must have caused this ablation of pyrolytic graphite. This very early time is consistent with the impulse data, which showed that most of the impulse was delivered in times less than $1/2$ msec.

Any derivation of the effective heat of ablation is very sensitive not only to the time history of the thermal input but also to the ablation history. It is possible to hypothesize an ablation history which gives

heats of ablation which are qualitatively different from that given by the above decomposition scheme. As discussed previously, the energy incident on the refrasil-phenolic backplate was apparently not measured directly in this experiment. The 10-mm pinhole camera (B-1) gave an absorbed energy of about 25 cal/cm^2 in the short-time pulse. This value can be considered an upper bound to that reaching the backplate. The 3-mm camera was affected by the vapor to the extent that it just barely reacted to the thermal. This observation is based on the fact that the 3-mm camera achieved about 4 or 5 microns deeper transition than did the 1-mm camera. A crude value for the input to the 3-mm camera, considering that it takes about 7 cal/cm^2 to transform the surface, might then be 10 cal/cm^2 . The long-time thermal instruments absorbed on the order of 200 cal/cm^2 . One might then suppose that $10/200$ of the ablation occurred during the short-time pulse. Since the total ablation was about 0.06 gm/cm^2 , the short-time ablation would then be $\frac{10}{200} \times 0.06 = 3 \times 10^{-3} \text{ gm/cm}^2$. The corresponding heat of ablation would be about 3000 cal/gm which is reasonable for this situation. The thermal input to the vapor would be about 400 cal/cm^2 in this situation which again does not seem unreasonable in view of the fact that $\text{Yield}/4 \pi R^2 = 1600 \text{ cal/cm}^2$.

4.3 APPLIED BLUE GILL RESULTS

Figures 4.6 and 4.7 (a replotting of Figure 3.12) show measured total impulse as a function of range for the three Blue Gill pods. On Figure 4.6 are spotted values for different levels of damaging impulse for the Mark 3 re-entry vehicle; Figure 4.7 presents similar data for the Mark 4. These impulses were obtained from References 16 and 17, which summarize experimental results of R/V's subjected to HE loadings to simulate the response to X-radiation. Much of the damage of these tests was in the nature of material failure because of the shock characteristic of HE loading.

An attempt was made in Figures 4.6 and 4.7, however, to pick structural deformation type failure mechanisms which should not be highly sensitive to the duration of the loading. Within the limitation of applying these damage criteria to the thermomechanical situation, it can be seen that the Blue Gill experiment encompassed the range at which United States R/V's can be expected to suffer serious damage. This observation is strengthened by the fact that the pod B-1 back-plate may have experienced threshold permanent damage.

It is perhaps not premature to perform HE tests of current U. S. nose cones covering a range of loads consistent with the total impulse of Figure 3.12 and the time history presented in Section 3.2.1 to assess their vulnerability to the thermomechanical force environment. Such testing was done for GD/A by SRI to implement the design of the Blue Gill pods. The pods were designed to withstand an impulse of about 3.5×10^4 dyne-sec/cm² delivered in one millisecond. These pods, however, were considerably more rugged than conventional R/V's because they were purposely reinforced for the experiment. Figure 4.8 depicts the placement of the Blue Gill results for a kill criterion of 10^4 dyne-sec/cm² in relation to ranges for other damage mechanisms. This experiment has demonstrated that there may be no gap in the vulnerability picture between predominantly low altitude and high altitude effects.

It must be cautioned that the impulse values referred to in this section can be considered at this time to apply only to a vehicle covered with refrasil-phenolic. This material on the closest pod ablated less than 0.1 gm/cm². Ablation of this material in a thermomechanical environment is, by itself, not a significant damage mechanism. The refrasil-phenolic coating obviously was a very effective inhibitor of ablation. Whether or not other materials behave

* Stanford Research Institute

the same way is unknown at this time. It cannot be stated at this time that other materials would experience either greater or less impulse.

4.4 CONCLUSIONS

1. The existence of a significant thermomechanical loading has been demonstrated. Thus, there may be no gap in the vulnerability picture in the intermediate altitude region.

2. The measured thermomechanical loading is of sufficient magnitude to cause structural damage to present generation re-entry vehicles.

3. Observed material ablation on all three Blue Gill pods was small.

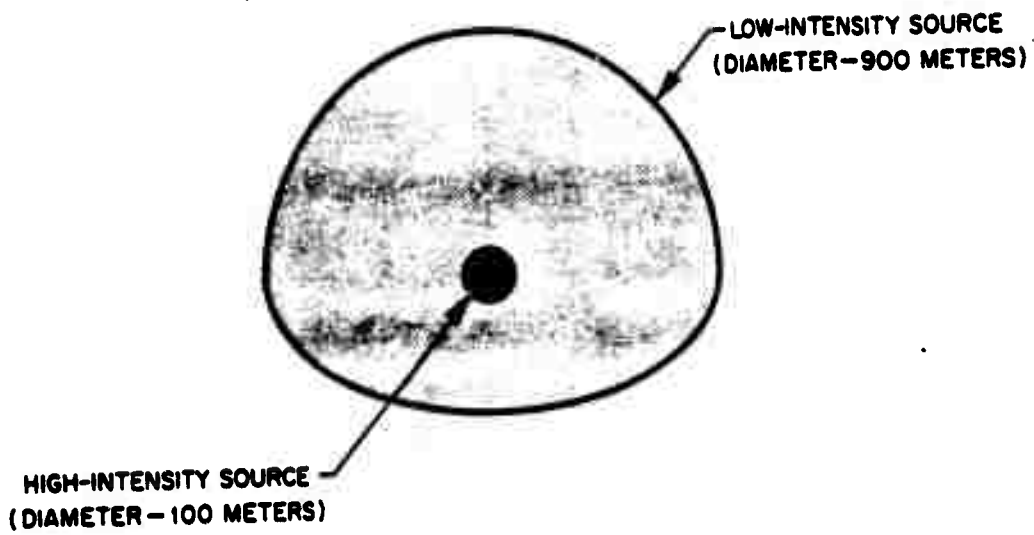
4. Two apparent thermal sources were measured; one was a small high-intensity source, while the other was much larger and of lower intensity.*

5. None of the pods was engulfed by the isothermal sphere.

6. The copper heat shield on the Blue Gill R/V substantially affected the X-ray and thermal environments of the pods.

7. The X-ray source size was smaller than the heat shield.

*Subsequent to the submission of this report, certain ambiguities have become apparent in the data relating to the size and importance of the small source. Later analysis of these data may, therefore, necessitate revision of the tentative results presented in this text.



POD B-1 

POD B-2 

POD B-3 

Figure 4.3 Blue Gill fireball geometry.

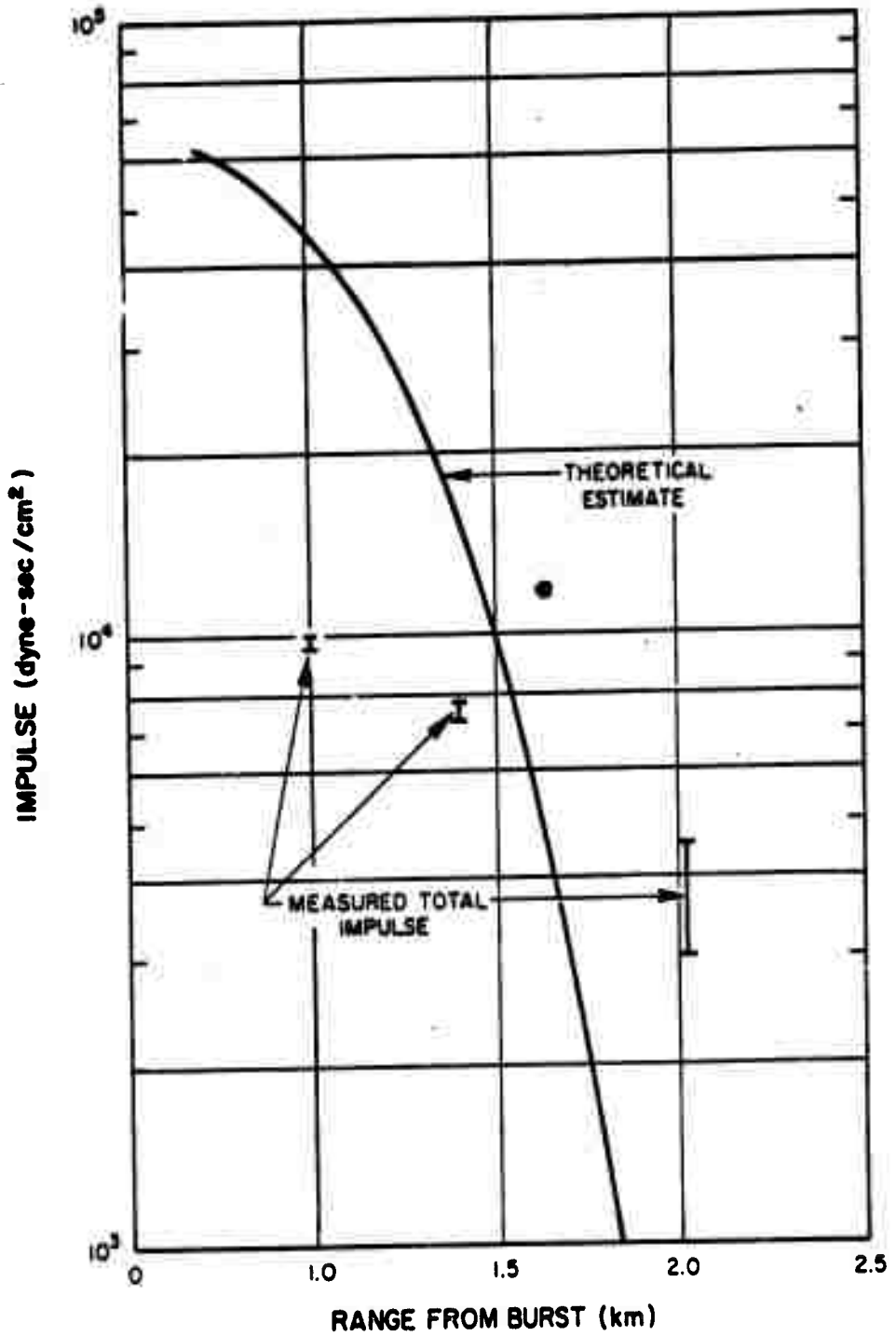


Figure 4.4 Comparison of estimated and measured impulses.

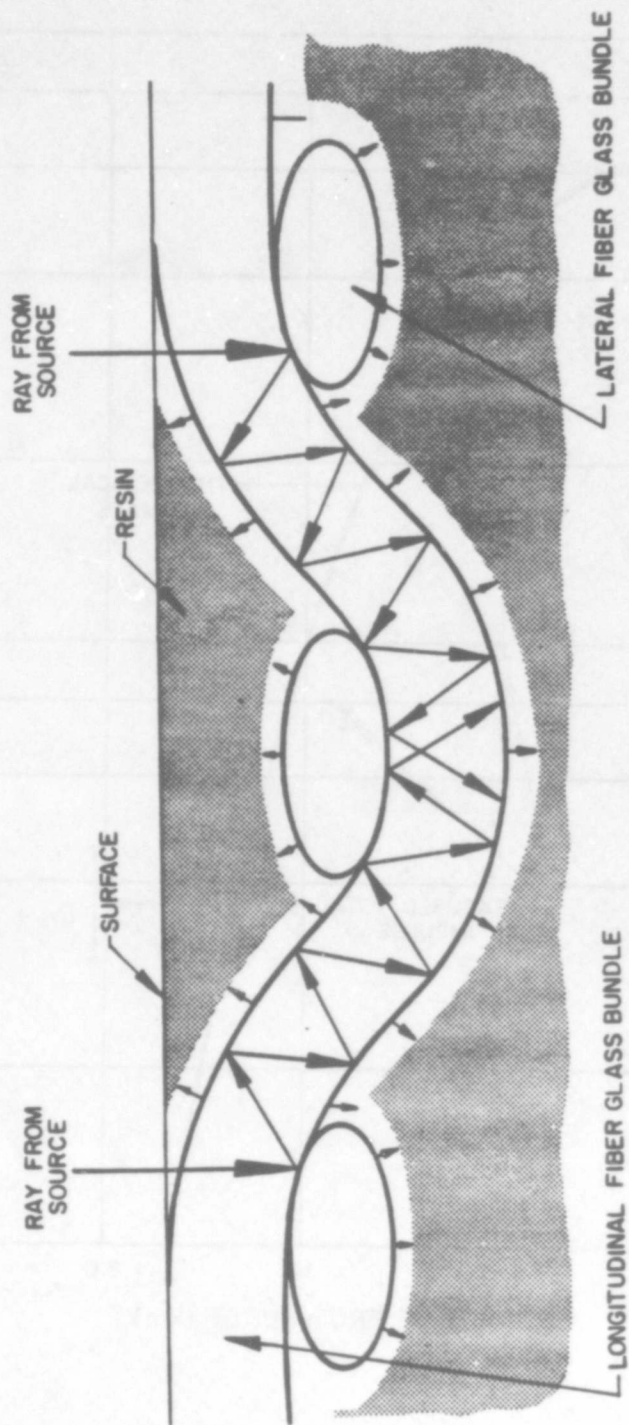


Figure 4.5 Mechanism for fast absorption of energy in refrasil-phenolic.

Part 2

SHOT KING FISH

CHAPTER 5

INTRODUCTION

Shot King Fish of Fish Bowl

probably represents a regime of transition between X-ray effects and X-ray-plus-debris effects in regard to weapon phenomenology and effects. Project 8A.3 participation in the event, therefore, was a logical sequel to participation in Blue Gill, which is reported in Part 1. Moreover, many of the instruments used in Blue Gill are applicable or readily adaptable to the King Fish conditions. Descriptions of these instruments are available in Part 1 and are not repeated herein. Instruments specially designed for the King Fish experiment are described in this part.

During the data reduction, the Shot Blue Gill instruments received the greater emphasis. Consequently, it has not yet been possible to examine all King Fish instruments except in a superficial manner. The data reduction for Shot King Fish must then be considered to be incomplete at this time.

5.1 OBJECTIVES

The general objective of the Project 8A.3 participation in Shot King Fish of Fish Bowl was to measure the structurally significant effects of a high-altitude nuclear detonation. The

specific objectives of the experiment were to:

1. Measure the total impulse due to interaction of the weapon energy with materials of selected properties.
2. Attempt to measure the impulse due to X-radiation alone.
3. Attempt to measure the impulse due to forms of energy other than X-rays.
4. Measure the time history of the total loading.
5. Measure the ablation characteristics of materials of selected properties.
6. Measure the total impulse to and the ablation characteristics of a variety of re-entry vehicle heat shield materials.
7. Investigate the following characteristics of the X-ray source:
 - spatial distribution
 - spectrum
 - total flux
8. Investigate the following characteristics at the test vehicle surface of any other (thermal/debris) source:
 - spatial distribution
 - variation of flux with time
 - total flux
9. Perform sufficient control measurements to separate unequivocally the effects due to X-radiation and to the thermal/debris energy sources.

5.2 TECHNICAL DISCUSSION

At altitudes above about 75 km the predominant missile

structural kill mechanism is expected to be the impulsive reaction to X-radiation blowoff. Shot Star Fish of Fish Bowl, which occurred at about 400-km altitude, and Shot Marshmallow of Operation Ncugat, which occurred underground provided certain definitive data on the effectiveness of X-radiation in structural vulnerability.

When a typical nuclear device is detonated at vacuum altitudes, approximately 70 per cent of the energy is expected to be radiated away from the weapon in the form of soft X-radiation (a typical temperature of about 1 kev). This leaves a large fraction of the energy which must be accounted for in other ways. At least 25 per cent of the total energy is, therefore, expected to remain with the expanding debris cloud. This energy will interact with the ambient atmosphere in ways which depend strongly on altitude. In any case, this energy must eventually manifest itself on any surface in its path. At low altitudes, where the mean free path of the debris is small compared to the range to a target, this energy distributes itself in the fireball radiation and in hydrodynamic shock.

At vacuum or near-vacuum altitudes this debris will suffer little energy loss on diffusion and will impinge directly on any surface in its path. This debris can interact with the surface and create an impulse through two mechanisms. First, its own momentum will be transferred by collision to the surface. If it is assumed that 10^8 cm/sec is a typical debris velocity, the momentum of the debris at a range of 1.9 km would be about 2×10^2 dyne-sec/cm².

This is small compared to structurally significant impulse values. The second mechanism can conceivably be much more effective. This considers the debris merely as a source of energy.

For the above conditions the energy remaining with the debris is of the order of 100 cal/cm^2 at the target surface. It is obvious that this amount of energy if utilized efficiently could cause considerable material blowoff.

In the intermediate region, where the debris mean free path is large compared to vehicle dimensions but small with respect to the burst-to-target range, the situation is more complicated. In this region the energy impingement may represent a combination of direct debris impingement, hydrodynamic shock, and debris-induced thermal radiation.

Observations from Shot Star Fish give a debris velocity range of 0.5×10^8 to 10^9 cm/sec. At a distance of about 2 km the arrival times of the debris would then range from 0.2 to 4 milliseconds. The arrival time for the debris-induced thermal flux will probably also fall within this range. These times correspond closely to the times for which the Shot Blue Gill instrumentation was designed. From the response time standpoint, therefore, the Blue Gill instrumentation was suitable for use in King Fish.

A

qualitative measure of atmospheric interactions with debris is probably afforded by the number of bomb masses represented by the ambient atmosphere in a sphere with a radius equal to the range from burst to pod.

There is, therefore, probably a qualitative difference in the energy flux at the pod at these two altitudes. It was uncertain prior to the shot whether the energy flux (aside from X-rays) would be characterized more by debris or

by thermal radiation. The expectation was that it would tend toward the latter, where the thermal radiation issues from the intervening ambient atmosphere which has been energized partially by absorbed X-radiation but mostly by interaction with the debris. In this report the energy in the ambiguous regime is referred to as debris/thermal energy.

CHAPTER 6

PROCEDURE AND INSTRUMENTATION

6.1 PLANNED TEST OPERATIONS

The planned operational procedures for the King Fish event were much the same as those described in Chapter 2. For the King Fish event, however,

the predicted impact point was 70 kilometers down range. Three pods were again carried aloft by a Thor IRBM, but for this event Project 8A.3 was responsible for instrumenting only one of these, pod K-1. Pods K-2 and K-3 were instrumented by DASA and Allied Research Associates, Inc. (ARA) and were essentially a repeat of the event Star Fish pod experiments. However, one Project 8A.3 indent recorder cluster was included on each of the DASA/ARA pods. This cluster was identical to one of the six clusters on Pod K-1.

The Shot King Fish device was the same as that used for Blue Gill except that the R/V did not have a heat shield.

6.1.1 Pod Positioning. The pod ejection mechanism for the King Fish event was somewhat different from that used for the Blue Gill event. To achieve separation at burst time, each pod was released a different time before vernier engine cut-off. The difference in velocities between the pods and the warhead was to be such that the pods would be at the following nominal ranges:

Pod K-1.....1.9 kilometers

- Pod K-2.....2.4 kilometers
- Pod K-3.....3.3 kilometers

6.1.2 Beryllium Facility. Since all pods had considerable amounts of beryllium as part of the instrumentation on the back-plate, it had to be assumed that the recovered pods would be contaminated with beryllium. Although the original beryllium was in clean solid pieces, it was considered probable that vaporization of the metal by the burst and subsequent condensation would leave a recondensed beryllium deposit on the instrument and pod surfaces. To protect personnel from beryllium poisoning during the disassembly of pods, a small field laboratory facility was constructed. One chamber of this facility was, in essence, a low-speed wind tunnel which provided a continuous controlled air flow past the working station. Another chamber provided a hood and sink for safe disassembly and cleaning of instruments. The exhaust air was filtered before discharge to the atmosphere. Personnel were also required to wear protective clothing and air masks.

6.1.3 Recovery and Radiation Protection. The recovery operations described in Chapter 2 were also used for the King Fish event. The hot cell facility was utilized for radiation protection to personnel.

6.2 INSTRUMENTATION

Many of the instruments used in King Fish were adaptations of those used in the Blue Gill event, or in many cases they used the same basic gage body (box car or thermal pinhole camera body). In this section the entire array of instruments is described with emphasis on the instruments and concepts which differ from those of the Blue Gill experiment.

As noted previously, the objective in this experiment was to gain some understanding of the interaction with materials of the structurally significant energies which are distinct from X-radiation. In order to achieve this objective it is, of course, necessary to measure also the effects due to X-radiation. An actual physical separation was attempted by the use of mechanical hatches which would be actuated by the X-radiation.

6.2.1 Indent Recorder Clusters. The basic indent recorder for the King Fish event was the same as that used in Shot Blue Gill. There were six indent recorder clusters in pod K-1 and one each on pods K-2 and K-3. The K-2 and K-3 clusters were identical to one of the clusters on pod K-1.

About half of the data pistons (out of a total of 42) were designed to measure total impulse. These were mainly D, K, and L-2 type pistons (see Fig. 6.1). A group of six A, C, and D type pistons was included to achieve some information on time history of the impulse. If, indeed, the debris/thermal energy does manifest itself in times of the order of milliseconds, an array of pistons with different response times would give some indication of the time variation of the resultant loading. If they all read the same, it could be deduced that the loading was all due to X-rays. Because of its sensitivity at low fluxes (due to low heat of ablation), lead was used as the sample material for the time history measurements. The remainder of channels on pod K-1 was made up of special-purpose indent recorder configurations which made use of the L-1 type piston. These will be described further on in this section.

The sample materials for Shot King Fish were selected to have specific properties which could provide some insight into the response of materials to the weapon environment. These

materials are listed below along with the pistons on which they were mounted.

<u>Material</u>	<u>Piston Types</u>	
	<u>Pod K-1</u>	<u>Pod K-2*</u>
Refrasil-Phenolic	K	
Lead	A, C, D, K, L	K
Pyrolytic Graphite (grain perpendicular)	K	K
Pyrolytic Graphite (grain parallel)	K, L	K
Micarta	K	
1020 Steel	L	
Phenolic	K	K
Aluminum	L	
Beryllium	L	
Copper	L	
Zinc	C	
Teflon	K	K
Oblique tape-wound refrasil	K	
Tape-wound Phenolic	K	
Avcoat 19	K	
Rad 58-B	K	
Glass-Filled Phenolic	K	

Pyrolytic graphite was again used because of its unique property of having widely different conductivities in its two orientations while maintaining constant all other material properties. The high conductivity orientation provides (in conjunction with copper) an experiment on the effect of heat of ablation. A measure of

*Pod K-3 material assignments were the same as those of pod K-2; pod K-3 was not recovered.

the effect of heat-to-vaporize while maintaining atomic number constant is afforded by a comparison of copper and zinc. Some insight into the degradation of plastic was to be provided by phenolic and teflon samples. One series of pistons was devoted to the measurement of total impulse to an array of re-entry vehicle materials.

Seven L-1 type pistons were designed to view the burst through beryllium windows. The beryllium window configuration is illustrated in Figure 6.2. The beryllium windows were intended to admit a portion of the X-radiation but physically prevent the admission of non-penetrating forms of energy. The sample materials were lead, copper, and carbon. The lead was used to achieve high sensitivity in case the bomb were to be so cool that the beryllium windows would be relatively opaque. The copper was used because of its high conductivity.* The carbon was used to ensure sufficient dynamic range in case the flux were much higher than expected. Two thicknesses of beryllium window were used—2 mm and 3 mm. These thicknesses were a compromise between strength and transparency. The high X-ray transparency and strength of beryllium make it an excellent window material and offset the handling complications created by the dangerous nature of some beryllium compounds.

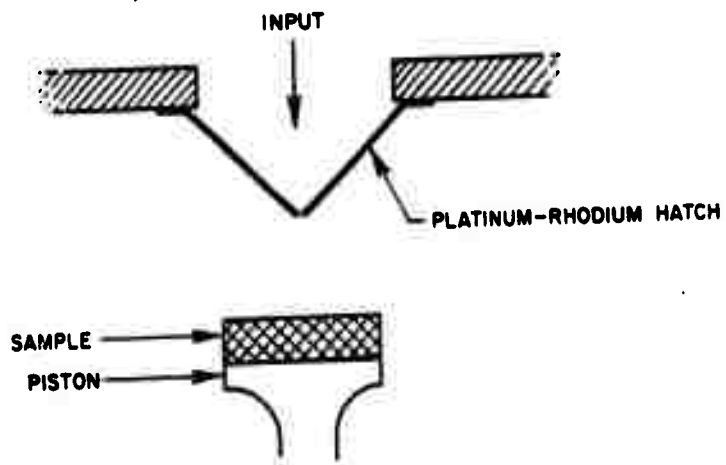
In order to prevent or at least to minimize the effect of a beryllium window striking a piston in case of severe bulkhead deformation, the cluster was set lower within the pod. A bellows was fitted between the cluster and the bulkhead to minimize

* High conductivity was expected to be a significant parameter for input energy fluxes (thermal/debris) having a duration of the order of milliseconds. Readings on high-conductivity materials exposed under beryllium windows were in the nature of control experiments to be compared to readings from the same material exposed to the total energy flux.

contamination of the pod interior by beryllium vapor. This configuration is illustrated in Figure 6.2. These bellows were very flexible in compression, a feature which served to retain the inertial isolation inherent in the unmodified cluster installation.

One of the seven pistons under the beryllium windows also had a blow-away hatch which could be activated by X-rays which penetrated the beryllium. This piston was designed to serve as a control. For this control to work perfectly, the hatch should be blown aside beneath an intact beryllium window and the anvil should bear no indent. These conditions would show first that X-rays alone can indeed actuate the hatch and, second, that the window protects the piston from subsequent energy inputs.

The action of this hatch can be visualized by means of the following sketch.



The hatch absorbs the X-radiation, and the resultant impulse accelerates the hatch in a direction normal to its surface. The hatch is placed so that such a trajectory will miss the detector.

It does not matter whether or not it will hinge about the bend line. After the hatch is removed, the detector is exposed to respond to any later energy fluxes. The hatch was fabricated from 3-mil-thick platinum-rhodium alloy. If it is assumed that the impulse to the platinum-rhodium is 10^3 dyne-sec/cm² under the anticipated flux (a relatively low value), the velocity of the hatch will be approximately 7×10^3 cm/sec. If one centimeter approximates the required trajectory length, the piston will be exposed in a time of the order of 10^{-4} sec. This time is sufficiently short so that essentially all the debris/thermal energy should be incident on the piston.

Four of these hatches were used (over L-1 pistons) in an attempt to acquire directly any debris/thermal impulse to lead, copper, or carbon. With the exception of the hatch replacing the beryllium window, the piston-bellows configuration was identical (see Figure 6.3). The hatch-piston-bellows configuration, aside from maintaining geometrical similitude with the beryllium window configuration, provided a means of catching and preserving the hatch for later examination.

In order to measure the total impulse to the same materials under similar geometrical conditions, four other L-1 pistons with the same materials (lead, copper, and carbon plus a duplicate lead) were recessed within the bellows but with neither beryllium windows nor hatches. The open, hatch, and beryllium window configurations should permit a separation of the loading into causal components.

6.2.2 Spall Gages. Three spall gages were included in the surface instrument array. One of these gages was identical to that used in Blue Gill (see Figure 2.7 in Part 1 of this report). This gage was expected to respond to a very

low X-ray flux, i. e., a few cal/cm². The two other gages were intended to obtain some direct information on the possible spalling behavior of typical structural materials. Both used the typical box car body configuration. Figure 6.4 illustrates the gage with metallic samples. The samples are flat rectangular pieces; they are backed up by a block of foam so that the top surfaces are coplanar. The samples in these gages are listed below.

<u>Material</u>	<u>Thickness</u>
1020 Steel	0.125, 0.075
Aluminum	0.100, 0.040
O. T. W. R.	0.380, 0.250, 0.190, 0.125

The metal thicknesses were chosen to supplement the thickness spectrum of the structural gages, which could also act as spall gages (see Section 6.2.9). The oblique tape-wound refrasil samples were selected to obtain some insight into the spall behavior of composite materials.

6.2.3 Ablation-Condensation Gage. The ablation-condensation gages used in Shot King Fish were identical to those used in Blue Gill. Again, the same materials were used for samples as on the pistons (except for beryllium). The total array of twenty-two instruments is listed below.

<u>Sample Material</u>	<u>Entrance Aperture (dia in mm)</u>
Lead	5
Pyrolytic graphite, parallel	5
Pyrolytic graphite, perpendicular	5
Copper	1, 5
1020 steel	1, 3, 5
Aluminum	5

<u>Sample Material</u>	<u>Entrance Aperture (dia in mm)</u>
Zinc	5
Teflon	5
Iron Devcon	5
Linen-filled phenolic	5
Refrasil-Phenolic (bulkhead cover material)	1, 3, 5
Oblique tape-wound refrasil	5
Tape-wound nylon phenolic	5
Avcoat 19	5
Rad 58-B	5
Glass-filled phenolic	5
Micarta	5

6.2.4 Thermal/Debris Pinhole Camera. The thermal pinhole camera used in Blue Gill was modified for King Fish by the addition in some gages of an X-ray opaque hatch within the top aperture. This hatch (Figure 6.5) was intended to be blown aside by the X-ray impulse, thus exposing the detector to subsequent energy fluxes. The detectors under these X-ray opaque hatches were designed to measure only the characteristics of the thermal/debris source. Other top aperture detectors, without hatches, were intended to record metallurgically the total intensity and spatial distribution of both the X-ray and the thermal/debris source.

The sideways-facing detector elements would not see the burst except at large pod misorientation. They could conceivably see a very late large source, but the flux from a source of this size would be expected to be below the recording threshold of the detectors. If the debris/thermal energy flux is of sufficient intensity, however, the material vaporized off the bulkhead itself might become a secondary thermal source. The sideways-

viewing ports, therefore, could measure the radiation from the vapor comprising this secondary source. In order to identify the origin of this source by its spectral characteristics, the function of the reflective coating spectral gage was incorporated in some instruments by using various coatings on the exposed surfaces of the detector elements.

The complete array of thirteen cameras is listed below:

Aperture Size (mm)	Hatch	Detector in Side Ports
1	No	Plain
3	Yes	Plain
10	No	Plain
1	Yes	Ag Plated
3	No	Ag Plated
10	Yes	Ag Plated
1	No	Au Plated
3	Yes	Au Plated
10	No	Au Plated
1	Yes	Al Plated
3	No	Al Plated
10	Yes	Al Plated
3 at 45°	Yes	Plain

All detectors were of 1020 steel, and they were all slotted in a manner similar to the Blue Gill thermal pinhole camera. The hatches were made from 3-mil-thick platinum-rhodium alloy sheet.

6.2.5 X-Ray Intensity Gage. Two X-ray intensity gages were included on the instrument array. These two gages are illustrated in Figures 6.6 and 6.7. They are the same in function

and aperture geometry; they differ only in the detector element. One gage uses a stack of mylar film in which each alternate sheet in the stack is coated with a vacuum-deposited layer of gold. This gold layer is less than 1000 \AA thick; the coated mylar sheets are one mil thick; the clear interleaves are one-half mil thick. The other gage uses a stack of seven disks of polystyrene in which fine metal particles are dispersed. The metals used are zinc, tungsten, copper, and bismuth. The approximate particle diameter is 50 microns, and a concentration of about $1000 \text{ particles/cm}^3$ was sought in the fabrication. The particles which were used had as a requirement that they be irregular in shape. This irregularity aids in distinguishing with a microscope whether or not the particle has been melted by the absorbed X-radiation. The four metals provide a wide range of melting temperatures.

Both gages operate on the same principle, i. e., the incident X-ray flux intensity can be derived from the depth at which phase changes occurred in the gold layer or in the metal particles.

Two aperture sizes were used. Three of the apertures were 5 mm in diameter; one was 2 mm in diameter. Beryllium windows were located under the two 5-mm apertures in the center. These windows were 2 and 3 mm in thickness to conform to the thickness of the windows above the indent recorder pistons. Information should thus be available from these instruments on the intensity and spectrum of the flux penetrating to the piston sample. The aperture array in the mica heat shield was overlaid with a 3-mil-thick mask of platinum-rhodium alloy. The apertures in this mask were slightly smaller than the nominal 5-and 2-mm diameters in the mica heat shield. The objective

of this mask was to provide an aperture with minimal edge fuzziness. Therefore, if the X-ray pinhole camera (Section 6.2.8) were to malfunction, it might still be possible to achieve some information on the spatial extent of the X-ray source through analysis of the penumbral region created by this sharp edge in the aperture. A sharp edge will also eliminate any confusion in the edge region because of X-ray transmission through the micarta.

6.2.6 Pinhole Closure Gage. The pinhole closure gage is illustrated in Figure 6.8. The detector element is identical to the film stack X-ray intensity gage of Section 6.2.5. The aperture is a long slot tapered from zero width at one end to approximately 3 mm at the other. The aperture is formed by gold foil which is the material used for the pinhole plate of the X-ray pinhole cameras used in Shots Blue Gill and King Fish (Section 6.2.8 below). It was also used by ASE for the pinholes of Project 823 in Shot Marshmallow of Operation Nougat (Reference 27). Preliminary observations from this shot indicate that the pinholes may have closed before all of the X-ray energy was emitted from the source. In Shots Blue Gill and King Fish the pinhole diameters required for any useful resolution were all much smaller than 1 mm. The pinhole closure gage was, therefore, devised to obtain some information on the possible choking off of the pinholes by the vaporized material surrounding the pinhole. This choking off of the slot during the burst can also be a measure of the velocity of the vapor. The tapered slot in the gage is in effect a pinhole or aperture of continuously varying size.

6.2.7 Long-Time Thermal Gages. The complete array of four long-time thermal gages which were used in each pod in Shot Blue Gill were also used in pod K-1 of Shot King Fish. These gages were identical in every respect to those described in Section 2.3.7 of Part 1 of this report.

6.2.8 X-Ray Pinhole Camera. Figure 6.9 illustrates the X-ray pinhole camera used on pod K-1. Two cameras were used, one with a nominal focal length of 12 inches and the other with a nominal focal length of 4 inches. The pinhole sizes were the same for both cameras. A total of 13 pinholes were used in each camera. The center pinhole was 2 mm in diameter; this size is too large to provide any resolution of the X-ray source, but it could conceivably create an image of the debris/thermal source if this source is large with respect to the X-ray source but small with respect to the range to the pod. In addition, it would assure that some X-ray flux would get through to the film plate in case of very severe pinhole closure through vapor blow-in. The nominal diameter of the twelve pinholes around the periphery of the pinhole plate were 0.003, 0.008, 0.012, and 0.035 cm. The smallest pinhole with a one-foot focal length will resolve about one-tenth of the diameter of the X-ray source if it is assumed that this source is about 2 meters in diameter. The films for the two cameras are identical except in lateral dimension. These films are comprised of a stack of 1-mil-thick mylar leaves coated with less than 1000 Å of vacuum-deposited gold interleaved with 1/2-mil clear mylar sheets. The total stack thickness is about 1/2 inch.

In addition to the possibility of obtaining a photograph of the weapon in its own radiation, an assumed Planckian weapon temperature can be determined by an analysis of image from two cameras having identical pinhole diameters but different magnifications (focal length). For this case the intensities incident on the film planes differ only by the ratio of the squares of the pinhole-to-film plane distances (a constant). The energy density necessary to cause an observed effect in the film stacks is assumed to be the same for identical effects. The ratio of the calculated

relative energy densities at the maximum depth of occurrence of the effect in the two film stacks then has a fixed value which, in turn, defines a unique Planckian temperature for the incident radiation (Reference 27).

6.2.9 Membrane Structure Gages. Several structures in the form of membranes were included in the instrumentation for King fish. The purpose of these gages was to explore failure in a simple structural element under purely impulsive loads. Hopefully, the results would provide some insight into the mode of failure and establish the validity of analytic methods.

The two materials used for the membranes were 1020 steel and 1100-0 aluminum alloy; all were in their softest condition to provide a maximum elongation before rupture. Five steel membranes and two aluminum alloy membranes were included. Thicknesses of the membranes were chosen so that under the range of loadings expected some degree of plastic deformation would be observed among the samples. The thicknesses were 0.010, 0.020, 0.030, 0.050, and 0.075 inch for the 1020 steel membranes and 0.020 and 0.050 inch for the 1100-0 aluminum alloy membranes. The diameter of the membranes was 1.050 inches for all gages. All aluminum alloy samples were covered with a 2-mil-thick foil of lead to ensure that a significant input could be obtained without an unreasonably large amount of ablation. In addition, lead foil was put on the 0.020-inch-thick steel membrane, thus providing a direct comparison between the response of aluminum and steel membranes.

The membranes were mounted in a gage having the same general outward appearance as the thermal pinhole camera. Details of this gage are shown in Figure 6.10. Support for the membranes was provided by a massive aluminum gage body that was constructed in one piece so that for practical purposes

it may be considered rigid. The membranes themselves were made in such a way that a heavy ring of material was left at the edge. This ring was fitted very closely over the gage body and then pinned in place. This manner of mounting provided the membranes with a fixed, clamped edge. The entire gage except for the active area of the membrane was shielded from the burst by a micarta cover.

6.2.10 Instrument Installation. As with the Blue Gill pods, all indent recorder clusters in pod K-1 were mounted on bridges which spanned the space between the inner and outer structural cylinders. These bridges were placed about 12 inches below the surface of the bulkhead. After mounting, the indent recorders were secured to the pod structure by steel lanyards.

The single indent recorders in pods K-2 and K-3 were mounted within heavy aluminum cylinders. These cylinders were inserted through the bulkhead and attached thereto.

The aperture plates of the pinhole cameras were attached to the underside of the bulkhead. The film plates were mounted within the pod from brackets attached to the pod aft structure. The attachment of the external instruments to the bulkhead was identical to that done in Blue Gill. In King Fish, however, there were 52 of these bulkhead-mounted instruments instead of 40. The arrangement of the instruments on the bulkhead for pod K-1 is shown in Figure 6.11.

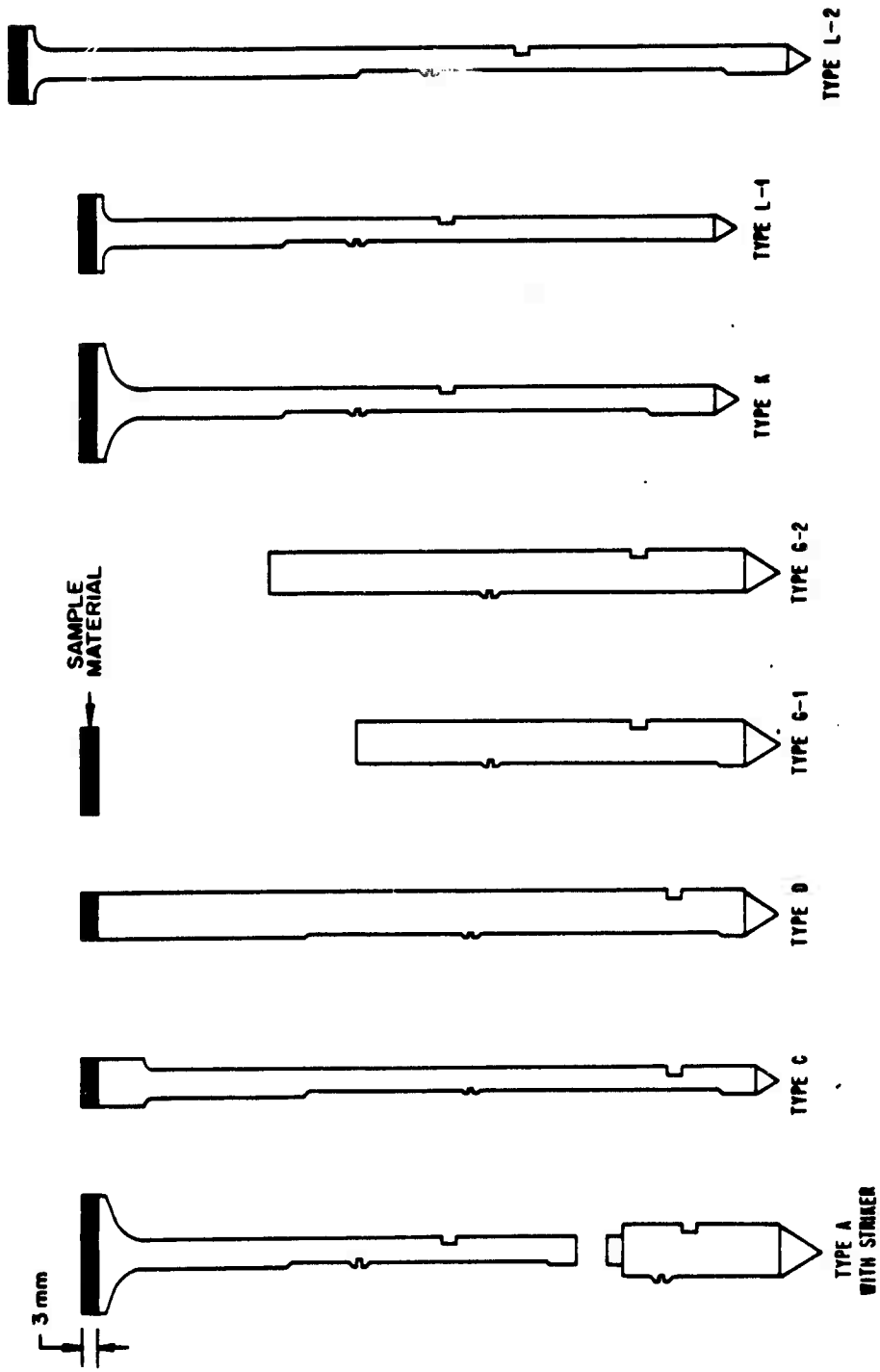


Figure 6.1 Indent recorder pistons, Shot King Fish.

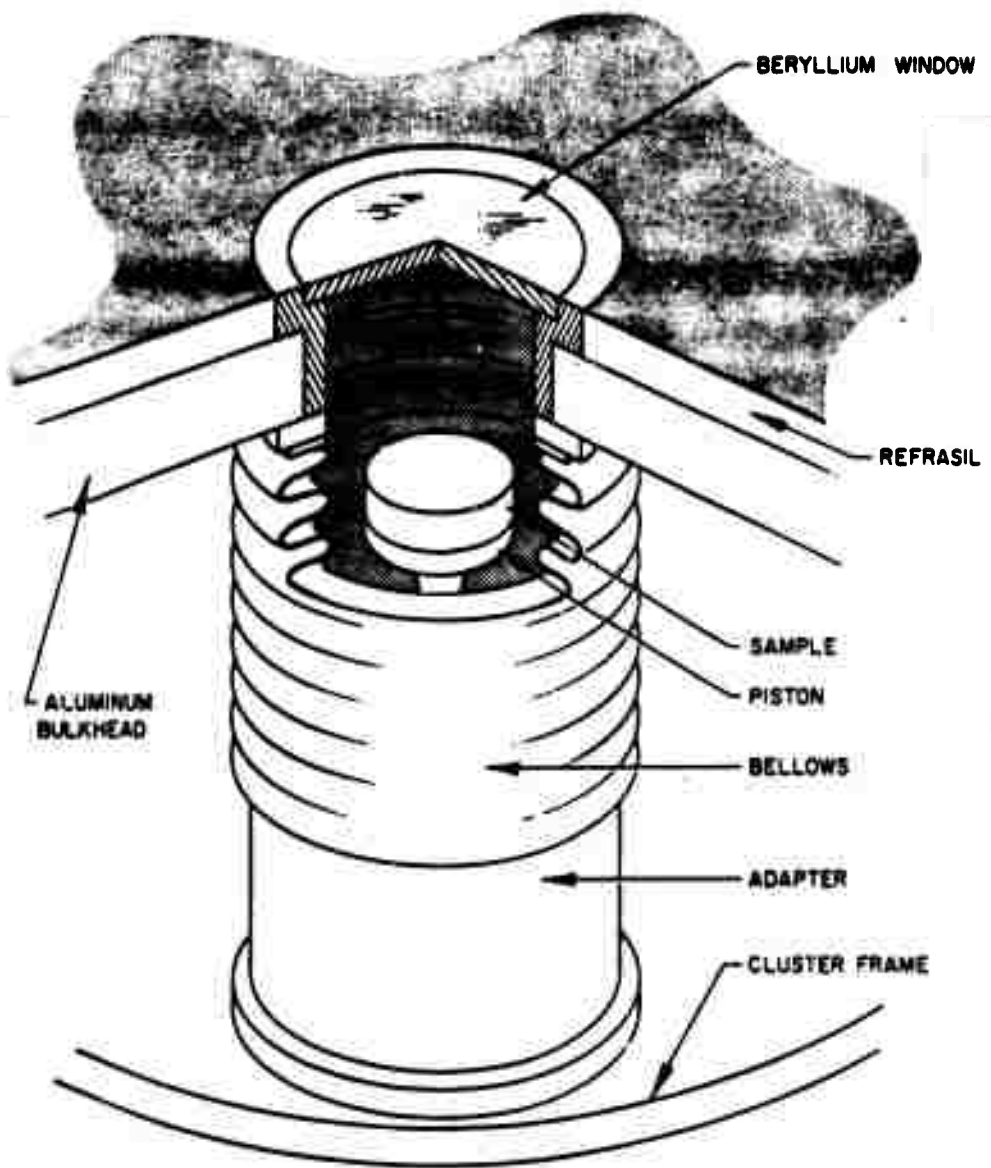


Figure 6.2 Indent recorder piston beryllium window configuration.

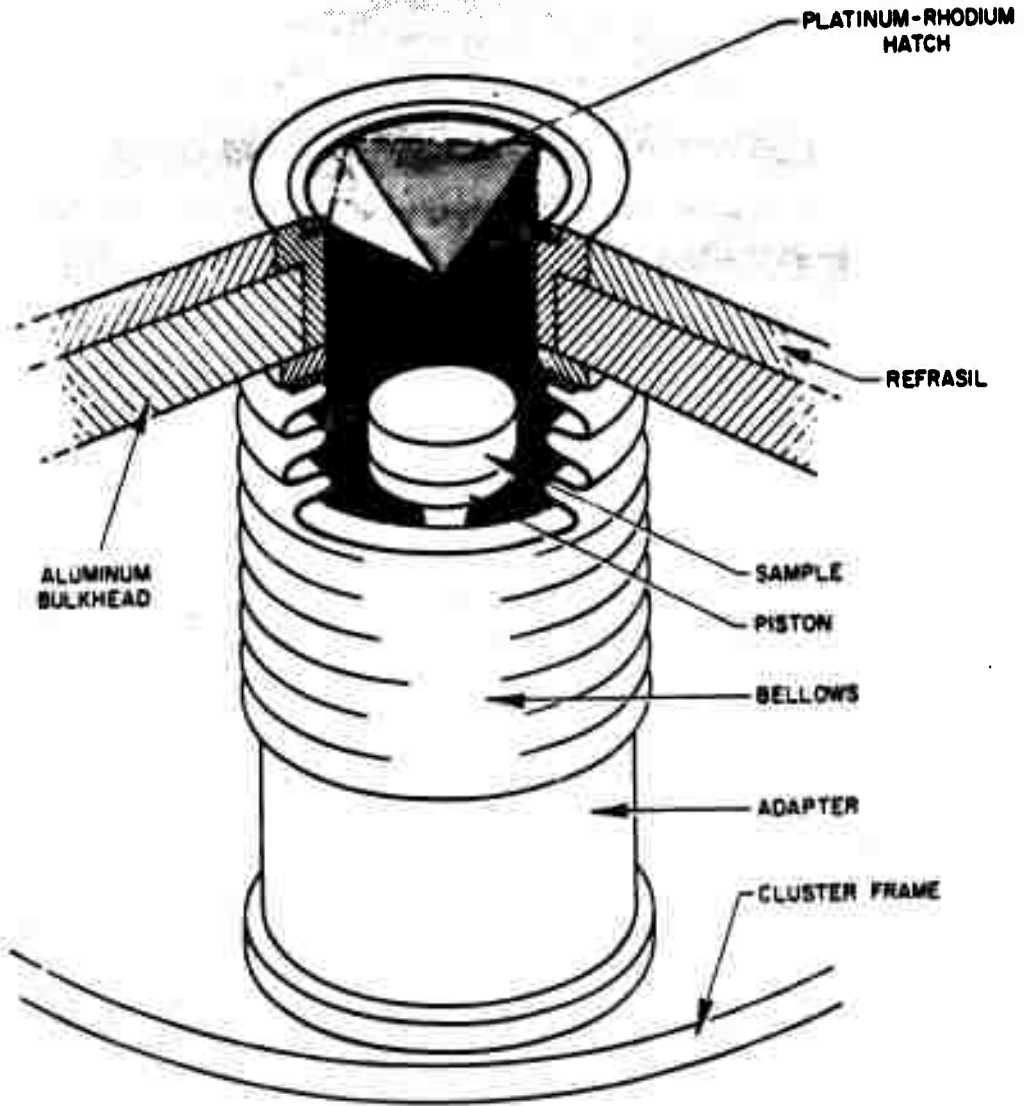


Figure 6.3 Indent recorder piston hatch configuration.

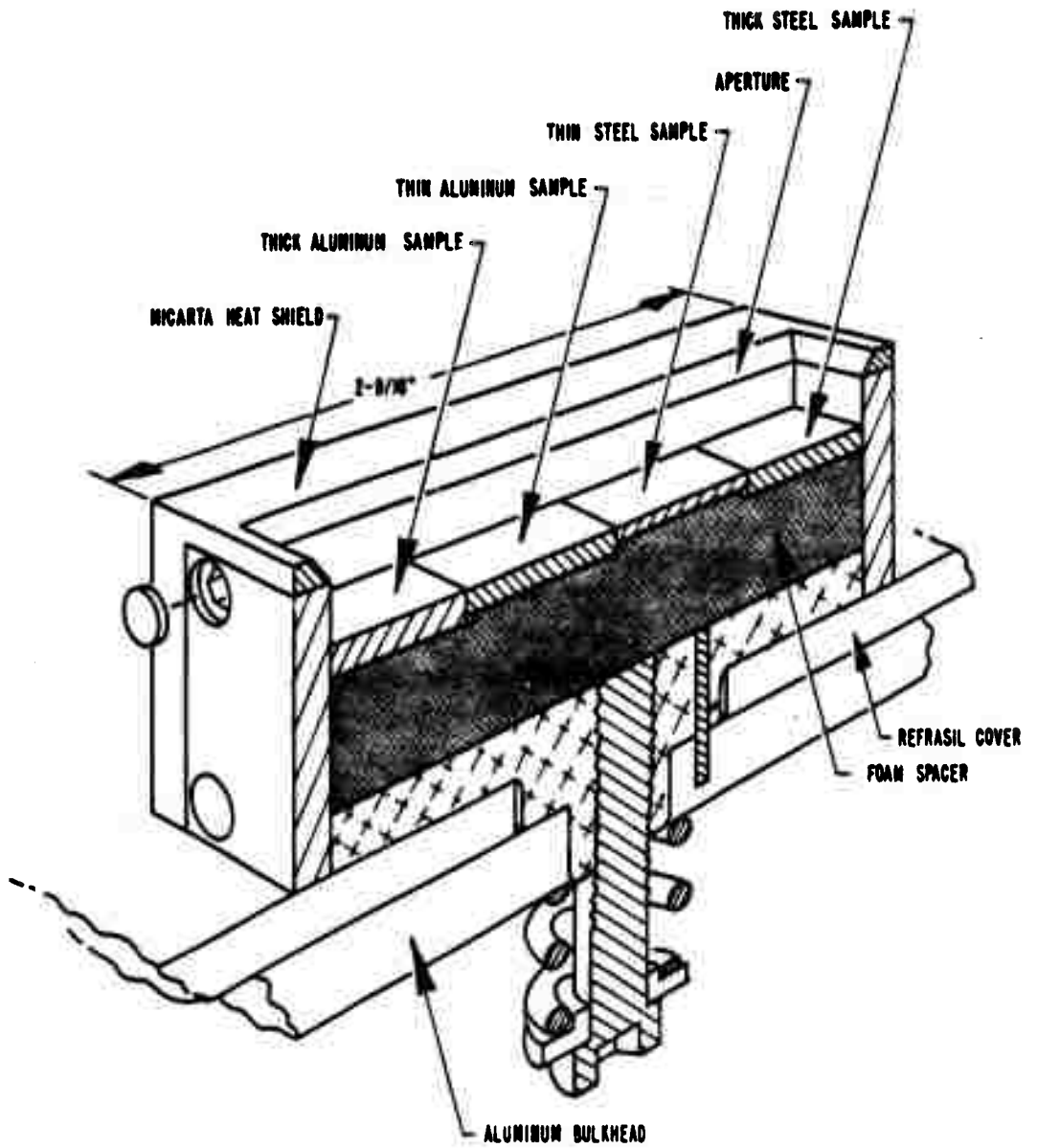


Figure 6.4 Spall gage, metallic samples.

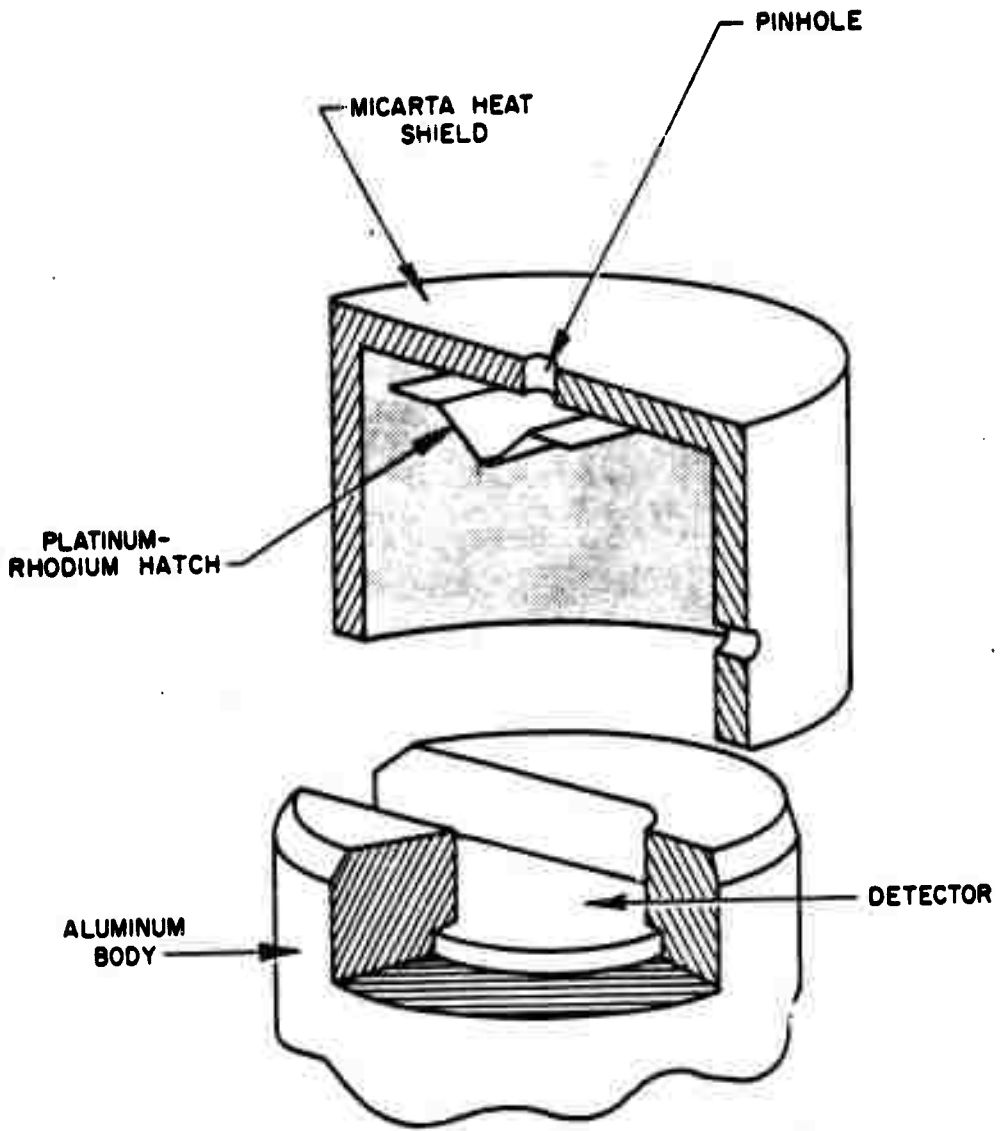


Figure 6.5 Debris/thermal pinhole camera hatch configuration.

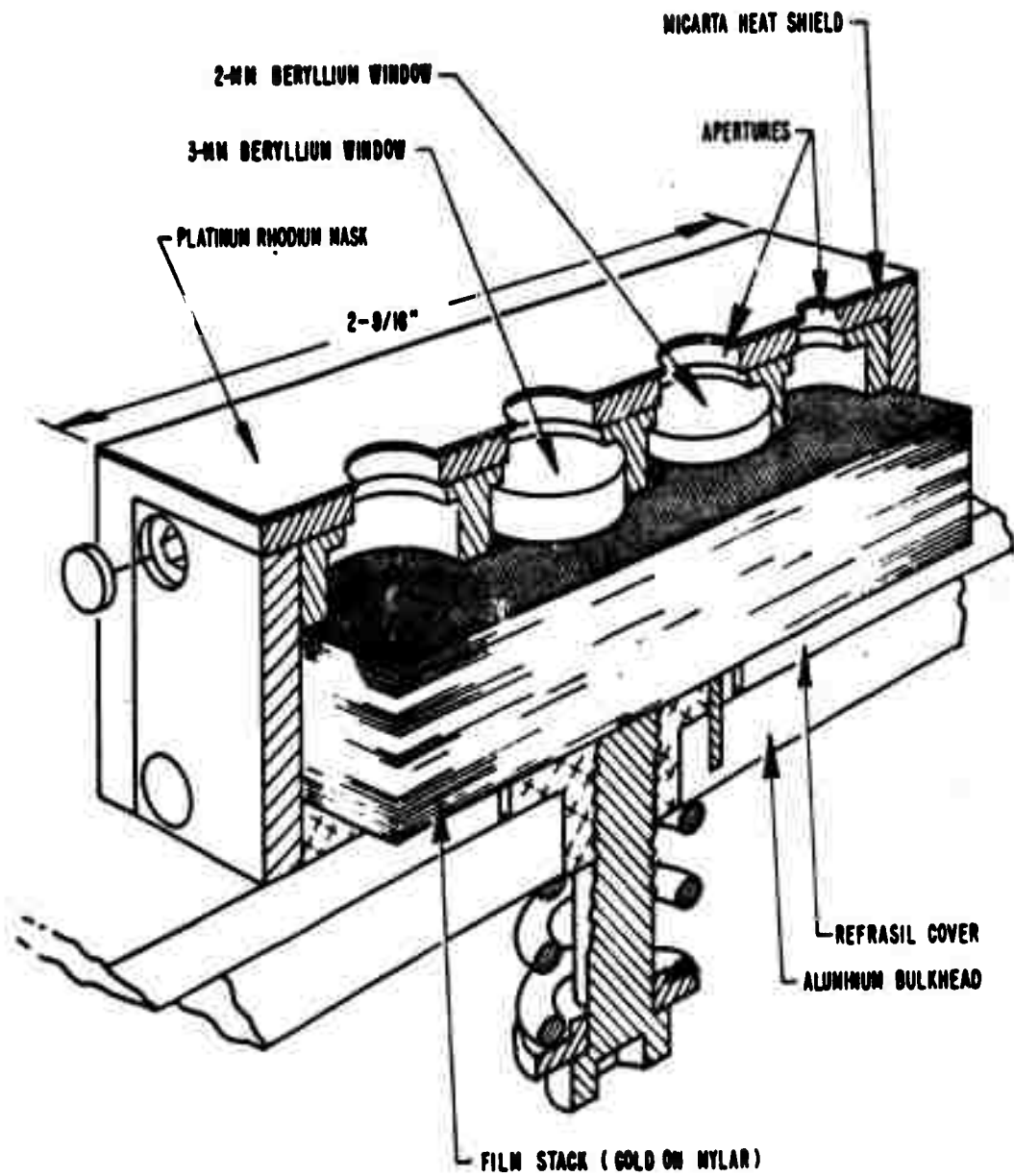


Figure 6.6 X-ray intensity gage, film stack.

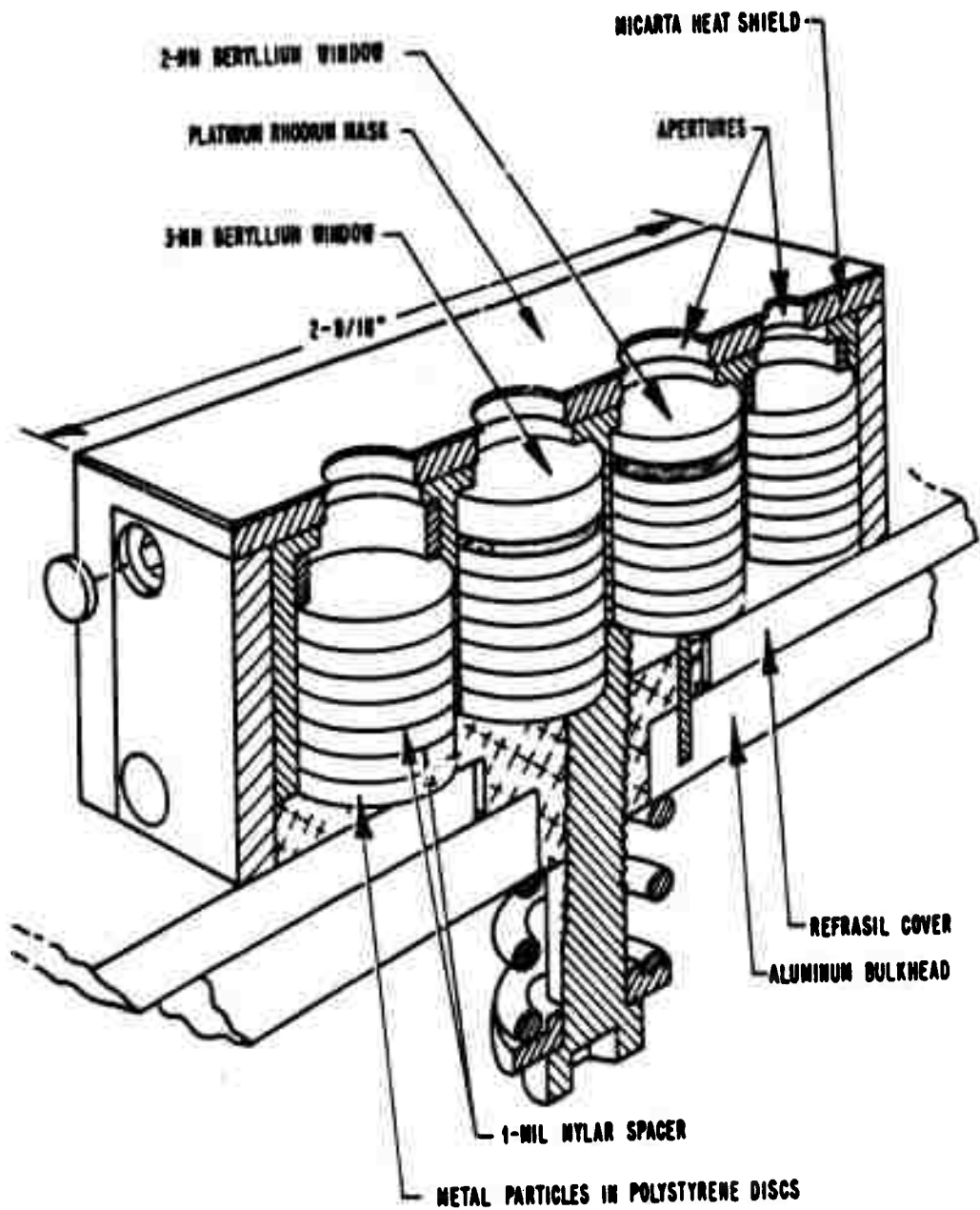


Figure 6.7 X-ray intensity gage, particle suspension.

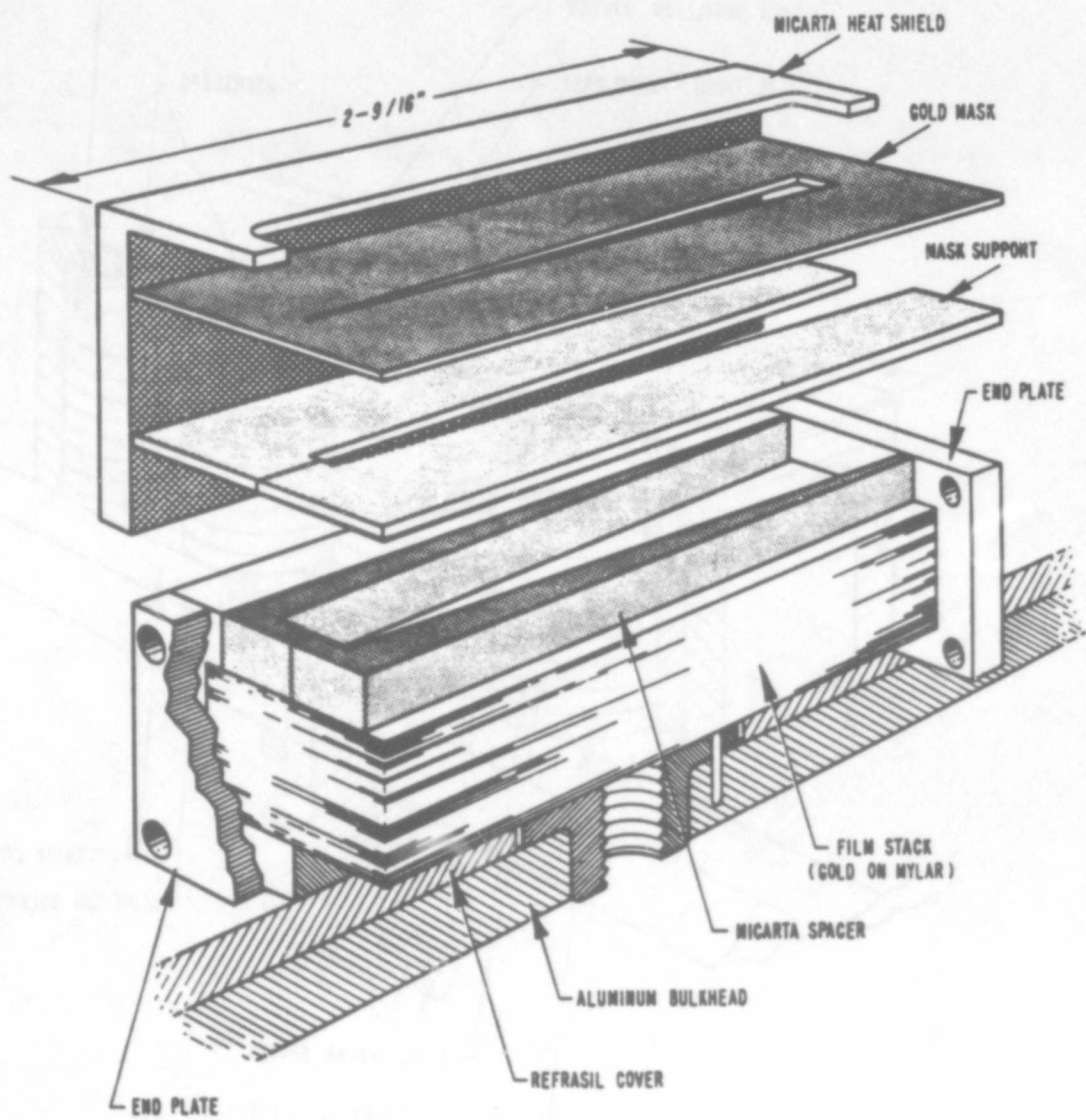
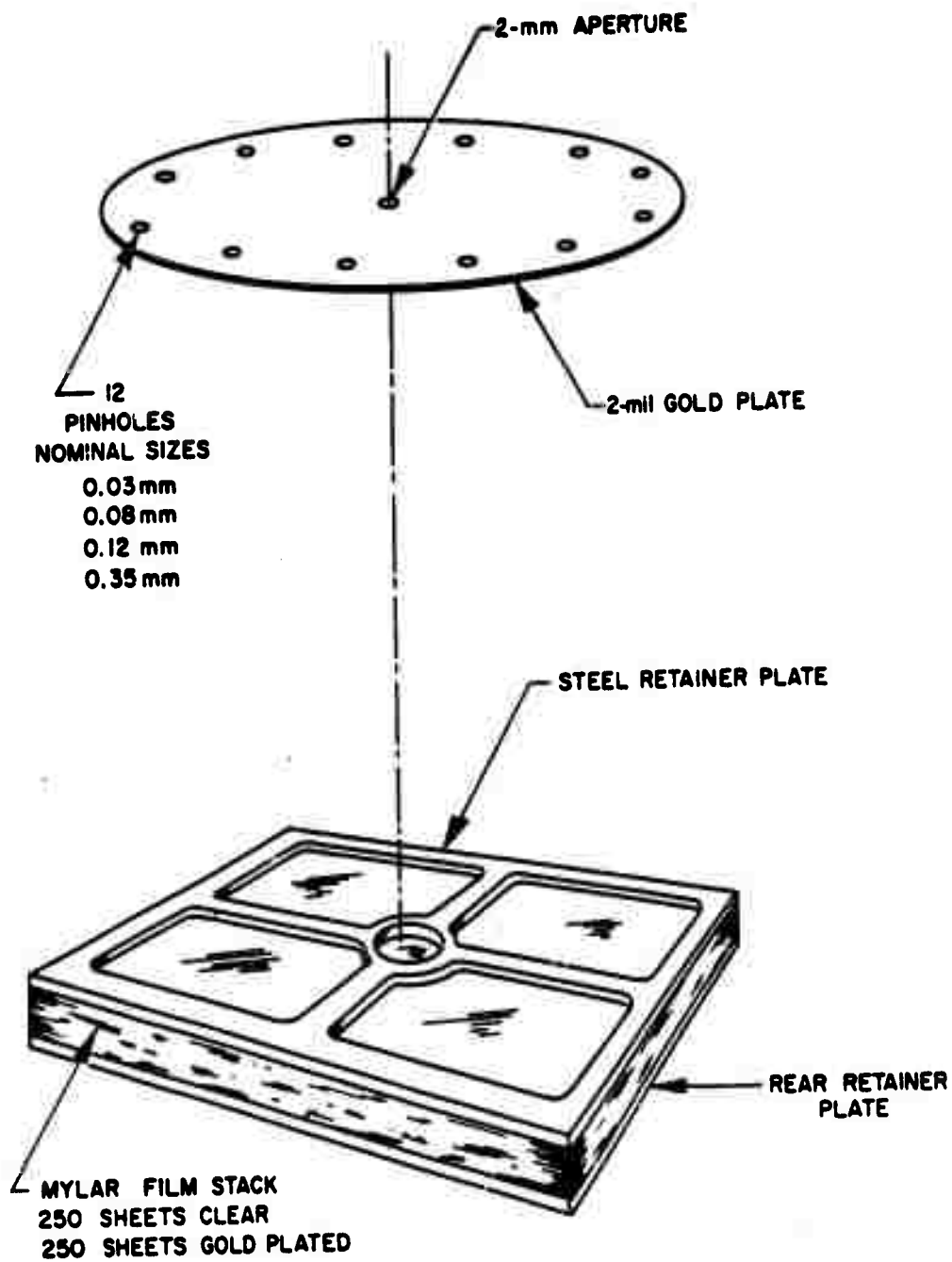
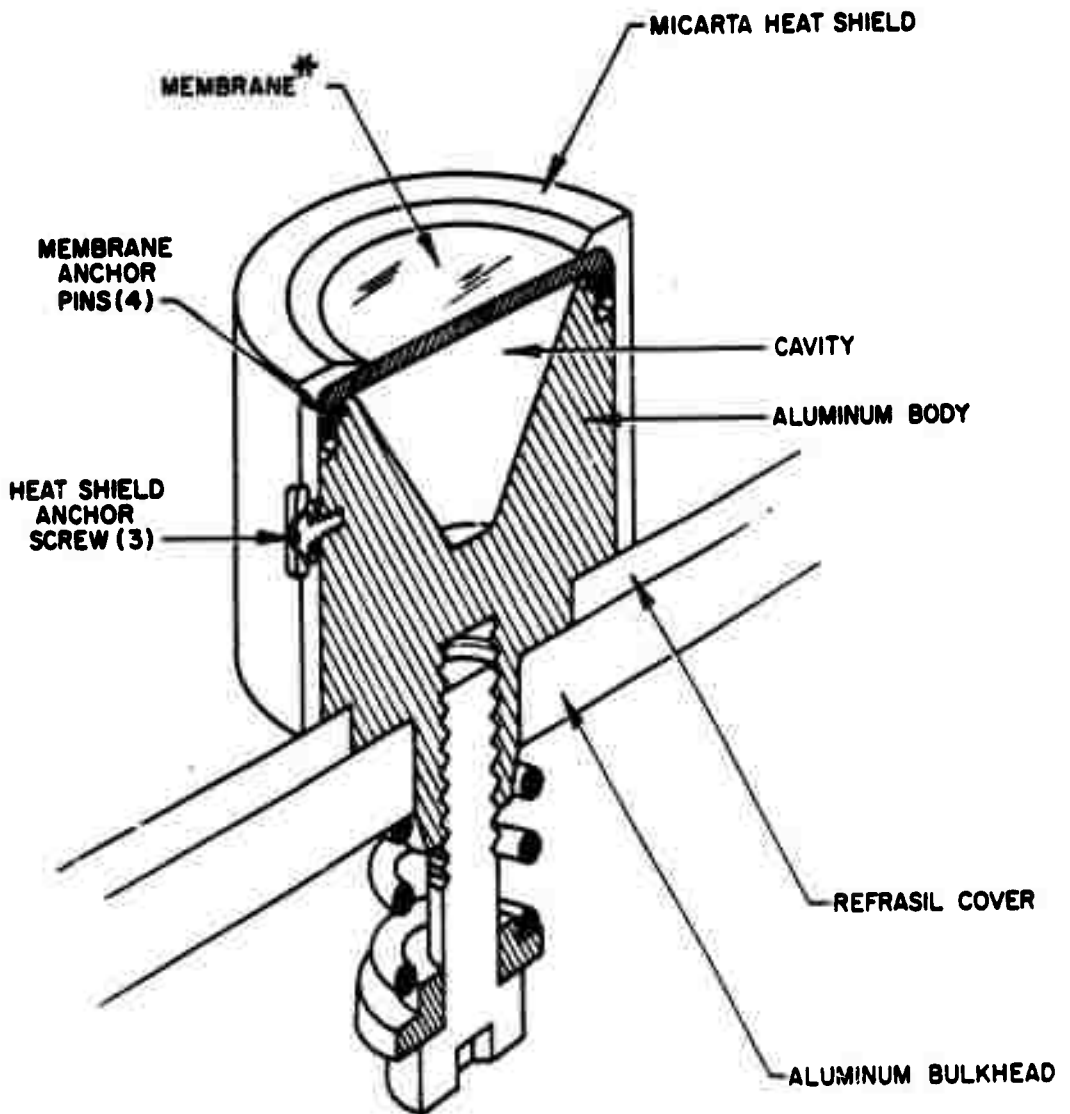


Figure 6.8 Aperture closure gage.



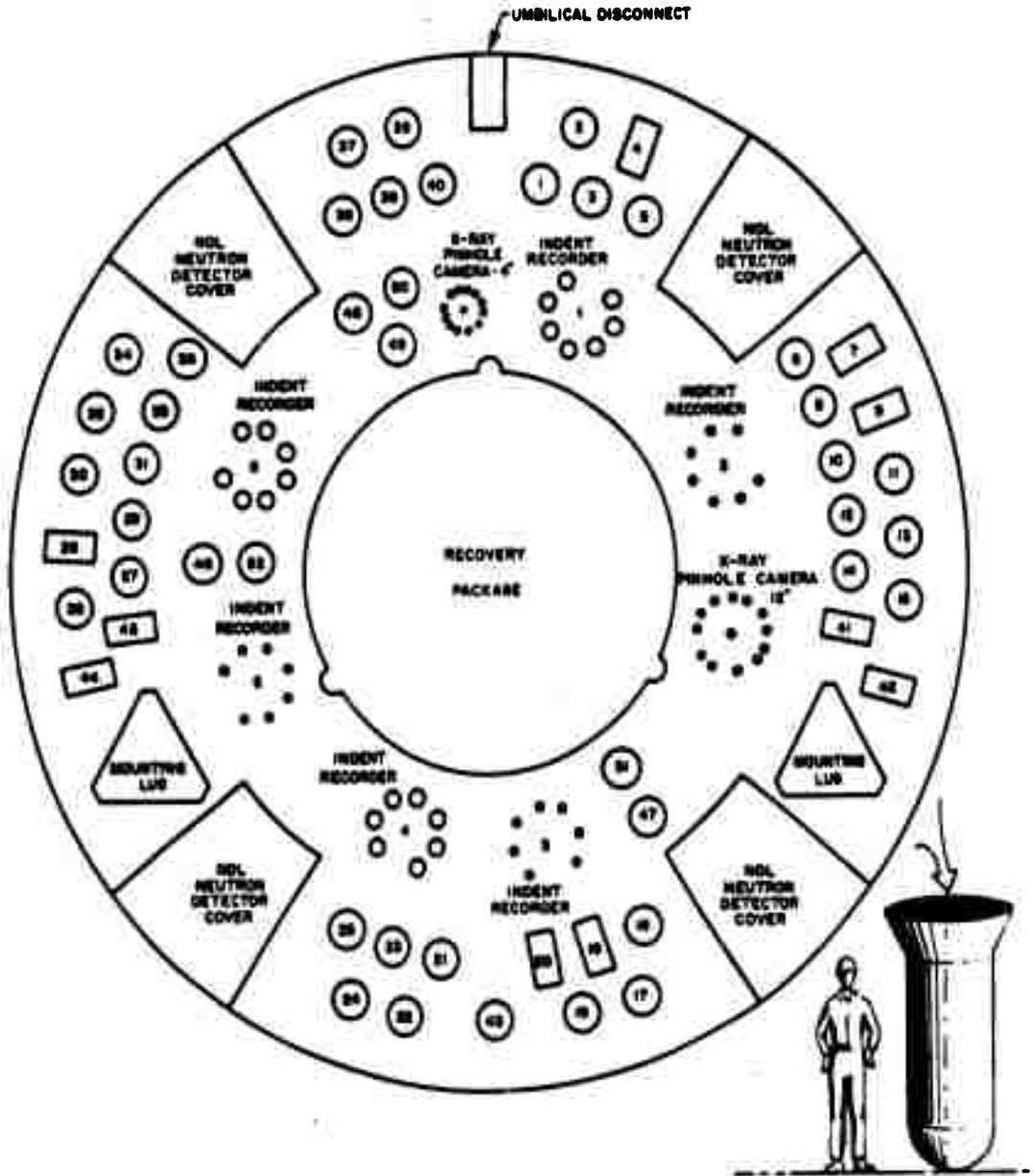
NOMINAL FOCAL LENGTHS — 4" & 12"
 FILM STACK DIMENSIONS — 4-1/2" X 4-1/2" & 6" X 6"

Figure 6.9 X-ray pinhole camera.



* ALUMINUM — 0.020"† & 0.050"† (1100-0 SOFT)
 STEEL — 0.010", 0.020"†, 0.030", 0.050" & 0.075"
 (1020 FULLY ANNEALED)
 † 2-mil LEAD FOIL ON SURFACE

Figure 6.10 Structural gage.



- THERMAL / DEBRIS PINHOLE CAMERA ("TURRET GAGE") _____ 1,2,11,21,26,30,32,34,37,39,40,47,51
 STRUCTURAL GAGES (MODIFIED "TURRET") _____ 13,15,17,19,22,24,43
 X-RAY INTENSITY DETECTORS ("BOXCAR GAGE") _____ 4,7,9
 SPALL DETECTOR ("BOXCAR GAGE") _____ 28,42,44
 LONGTIME THERMAL DETECTOR - RECESSED ("BOXCAR GAGE") _____ 41,45
 LONGTIME THERMAL DETECTOR - FLUSH ("BOXCAR GAGE") _____ 18,20
 ABLATION CONDENSATION GAGE _____ 3,5,6,8,10,12,14,16,23,25,27,29,31,33,35,38,39,46,48,49,50,52

Figure 6.11 Instrument array, King Fish Pod 1.

CHAPTER 7

EXPERIMENTAL RESULTS

7.1 OPERATIONAL RESULTS

Event King Fish occurred at 0210 hours on 1 November 1962. Preliminary tracking data indicate that the Thor warhead and pod trajectories were nominal.

Pods K-1 and K-2 were recovered; however, pod K-3 was not found. Neither recovered pod was located until after dawn. The flashing lamp and Sarah beacon systems failed to operate. The sea dye dispensers did function and aided search aircraft in locating each pod. Helicopters were utilized to retrieve and return both pods to the Johnston Island recovery area. Pod K-1 was picked up by the nylon loop provided in the recovery package. Pod K-2 had to be retrieved using a modified cargo net because of a recovery system malfunction.

It appears that the recovery system in both pods K-2 and K-3 did not function correctly. Pod K-2 sustained severe damage at water impact. Only the nose portion of the K-3 pod was recovered. The K-3 recovery system was known to have a malfunctioning time delay switch that could not be replaced or repaired in time for the event.

Pod K-1 re-entered normally, and the parachute deployment system functioned as planned. This pod was recovered in excellent

mechanical condition. The pod forebody and bulkhead were blackened. The blackening on the bulkhead, however, was very superficial, and a washing for the purpose of decontamination removed much of the blackening. The pod-to-missile attachment fittings (the DACO fittings^{*}) had created sharp shadows on the adjacent refrasil-phenolic. These shadows indicated an excellent orientation as noted below. The refrasil-phenolic cover was missing from the bulkhead over the NDL neutron detectors^{**} and one very small area adjacent to one of the DACO fittings. Elsewhere, the refrasil-phenolic was intact, except that it was detached from the aluminum over most of its area. Removal of the bulkhead and indent recorders was straightforward. Later during routine handling of the backplate, the entire refrasil-phenolic cover came off in one piece. Over most of its area the failure seemed to be in the glue line, although several thin patches of fiber from the refrasil-phenolic remained adhering to the aluminum.

As stated before, pod K-2 sustained severe damage upon water impact. The nose section of this pod was completely sheared off. The backplate, the Allied Research Associates, Inc. (ARA) instrumentation and the NDL neutron packages were also sheared off and lost. The ASD/ASE indent recorder cluster and the NDL gamma packages were recovered intact. (ASD, Aeronautical Systems Division.)

Both pods were radioactive upon recovery. No accurate activity level measurements were made by this project; however, the surface activity on the K-1 pod backplate was approximately 1.3 roentgen per hour at eight hours after the event as measured by other projects. A 0.4-roentgen-per-hour reading was taken two inches from the K-2 pod aft end about six hours after the event. The beryllium facility was utilized during the disassembly of the K-1 pod and

*Douglas Aircraft Company

**Nuclear Defense Laboratory

instruments. Respirators and protective clothing were worn by personnel.

Pod and warhead positions at burst time as obtained from Cubic Corporation (Cubic Corporation messages of 18 and 19 April 1963) are as follows:

<u>Object</u>	<u>Slant Range (ft)</u>
R/V	
Pod K-1	8, 149
Pod K-2	12, 576

Preliminary pod orientation information was obtained for the K-1 pod by examining the X-ray shadows etched in the bulkhead. This preliminary orientation was then refined by using the images on the X-ray pinhole camera plate (see Section 7. 2. 8). The only FDL/ASE instrument on pod K-2 was one indent recorder cluster. Orientation information on this pod was obtained from areas etched on the cluster frame by X-rays shining through the gap between piston and backplate. The following table summarizes the orientation information for the two pods where θ is the angle between the normal to the backplate and the line between the pod and burst, and ϕ is the azimuth angle measured clockwise from the umbilical disconnect. This latter angle can be considered accurate only within several degrees.

<u>Pod</u>	<u>θ</u>	<u>ϕ</u>
K-1	3 to 5 ^o	100 ^o
K-2	8 to 10 ^o	230 ^o

7.2 INSTRUMENT PERFORMANCE

The sections which follow summarize the laboratory examination of the instruments and of other aspects of the pod which are pertinent to the objectives of the program. A summary of the King

Fish data reduction status is pictorially represented in Figure 7.1. This figure shows the locations of the individual instruments on the pod backplate. It also includes notations where applicable of the apparent quality of the data extracted from the instruments. The notation "Effect Observed" signifies that the reading (e.g., on control indent recorder anvils) cannot be evaluated as to quality without consideration of other instruments. It is also used with detectors which show an external effect but have not yet been opened to extract quantitative information. "Improper Operation" denotes an instrument failure, generally through excessive corrosion. "Redundant Channel" indicates a detector which has not been examined because it would provide no information not already available from identical instruments. Instruments which have not yet been examined are denoted by "No Data Yet."

7.2.1 Indent Recorder Clusters. All of the recovered indent recorders were in good condition. No evidence was found to indicate improper operation of the instruments. The darkening of the top of the clusters and guide sleeves was much less intense than that observed in Shot Blue Gill. This suggests that less vapor flowed around the pistons and into the King Fish pod.

Most of the King Fish piston samples were not recovered. The tally is given by the table below.

<u>Material</u>	<u>Pod K-1</u>		<u>Pod K-2</u>	
	<u>Installed</u>	<u>Recovered</u>	<u>Installed</u>	<u>Recovered</u>
Refrasil-phenolic	1	delaminated		
Pyrolytic Graphite (grain parallel)	6	3	2	2
Pyrolytic Graphite (grain perpendicular)	2	1	2	1

Recovered Samples (Continued)

<u>Material</u>	<u>Pod K-1</u>		<u>Pod K-2</u>	
	<u>Installed</u>	<u>Recovered</u>	<u>Installed</u>	<u>Recovered</u>
Lead	14	5	1	0
Copper	4	3		
Teflon	1	1	1	1
Phenolic	1	0	1	0

In addition, the following samples were installed on pod K-1 and none were recovered: Aluminum (2), Beryllium (2), 1020 steel (2), Zinc (1), OTWR (1), TWNP (1), Avcoat 19 (1), Rad 58B (1), Glass-filled phenolic (1), Micarta (1). The number in parentheses indicates the number installed. It should be pointed out that all of the parallel grain graphite samples recovered on pod K-1 were exposed to the burst behind beryllium windows. In addition, all of the copper and lead samples recovered were either behind beryllium windows or X-ray hatches. The recovered metal samples, which were not directly exposed to the burst, showed only surface melt at most. The area around pistons which carried metal samples that were directly exposed (and not recovered) revealed very little melted sample residue. This is consistent with the absence of an intense thermal source. Since there is no indication to show that poor conductors survived any better than good conductors, the failure of the glue joint was probably not thermally induced. It is more likely that the sample was dislodged by failure of the glue joint under the X-ray shock loading.

Many of the cluster tops had stippled ring-shaped areas underneath the pistons. These areas were exposed to X-rays which passed through the gap between piston heads and bulkhead. Measurements of the positions of the rings confirm the orientation

estimates presented in Section 7.1. Figure 7.2 presents a photograph of the top of an indent recorder cluster on which the X-ray impingement areas are prominent.

One control piston was included in each of the indent recorder clusters in the King Fish experiment. Three singly blind (type G-2) and three doubly blind pistons (type G-1) comprised the controls on pod K-1; the cluster on pod K-2 contained a singly blind piston. As shown in Table 7.1, two of the doubly blind and one of the singly blind pistons in the K-1 pod did not make an indent. The singly blind piston in the K-2 pod did make an indent in its anvil. The conclusions which can be drawn from the control pistons in the King Fish experiment are similar to those reached in the Blue Gill experiment. The doubly blind pistons indicate that the indent recorder functioned in the intended manner, although the evidence is less strong in the case of the King Fish shot, since only three doubly-blind pistons were used. The singly blind pistons do not present strong evidence to the contrary.

Of the pistons on the K-1 pod which were used for time history measurements or total impulse to various material samples, about 75 per cent recorded indents. These impulse data are presented in Table 7.1. No modification of the data to account for loss of samples has been made. No indents were made by pistons located behind hatches or beryllium windows. Only two readings were obtained by pistons in this part of the experiment. These were pistons which, while maintaining geometric similarity to the pistons in the hatch-window experiment, had no hatches or windows above them. Two of the beryllium windows were in place after recovery and appeared to be undamaged. All of the hatches were either deflected into an open position or missing, indicating that the hatches functioned as designed.

The time history data, in which lead was the sample material, are plotted in Figure 7.3 in the form required for time history studies—that of impulse integral vs. impulse. Examination of these data reveals that most of the points follow a consistent trend, i. e., slower responding pistons must measure an impulse equal to or greater than the impulse levels measured by faster responding pistons. The K-piston, however, measured somewhat less than the impulse measured by the A-1, A-2, A-3, and C-1 pistons. The L-1 pistons are not directly comparable because they were recessed beneath the backplate.

It is believed that the K-piston malfunctioned. On the basis of response characteristics (indicated by sm_p/A_h) the K-piston should have responded in about one-third the time that the D-piston did. In the experiment, however, the measured impulses showed the minimum response time of the K-piston to be about 21 milliseconds and the D-piston to be about 20 milliseconds. Since both pistons responded in about the same time interval, both should have been subjected to the same burst-induced loading before making indents. The fact that the K-piston recorded such a low impulse level compared to the D-piston in spite of this equal exposure time indicates some adverse influence on the K-piston performance.

One possibility is that backpressure under the mushroom head of the K-piston (see Figure 3.8) reduced the loading sensed by the piston in the same manner as the Blue Gill pistons were affected (see Section 3.2.1). The surfaces beneath the pod K-1 backplate showed signs of gas flow comparable to the darkened surfaces of the B-3 pod which was at comparable range. It is possible, therefore, that enough vapor may have flowed beneath

*Piston designations refer to different response characteristics (Table 7.1).

the pod K-1 backplate to influence the response of the K-piston to a significant extent.

It is also possible that the low reading of the K-piston in the time history experiment was the result of mechanical malfunction. Unfortunately, there is no way of confirming this hypothesis. The validity of the data point obtained by the lead-sample K-piston is considered questionable at this time and has been omitted from any time history considerations.

The form that the remaining time history data (i. e., A-1, A-2, A-3, C-1, C-2, and D-piston) take in Figure 7.3 does not permit a straightforward time history analysis to be made, since essentially only two impulse levels are defined with no intervening data to describe the evolution of the loadings. These data, however, do permit some time information on the King Fish loading to be gathered from a consideration of individual piston response characteristics.

The four data points obtained by the A-1, A-2, A-3, and C-1 pistons represent the same impulse level with very little scatter. This result indicates that the impulse was delivered to these pistons within a time earlier than the time at which the fastest piston responded. At the impulse level measured, the fastest piston (A-1) responded in approximately 3×10^{-4} second. This means the load application occurred in a time less than 3×10^{-4} second. The response time of the slowest piston in that group (C-1) is a measure of the length of time over which no additional load was applied. This time is approximately 5×10^{-3} second.

The apparent additional loading which caused the upper impulse level described by the C-2 and D-pistons had to occur

after the C-1 piston made its reading, since this piston measured only the lower level of impulse. This later loading, however, had to occur before the C-2 piston could have struck its anvil as the result only of the early loading. Otherwise, the C-2 piston would not have sensed the later loading. The second load pulse, therefore, had to occur after 5×10^{-3} second (C-1 piston response time to the early loading), but this loading had to begin before 20×10^{-3} second (C-2 piston response time to the early loading alone). The fact that the D-piston recorded a slightly higher impulse than did the C-2 piston indicates that the second loading mechanism had not been completed by the time the C-2 piston read. These data are summarized in Figure 7.4.

An immediate possibility which comes to mind for these results is that the large-headed pistons were affected by back pressure in the same manner as that hypothesized for Shot Blue Gill. As mentioned above, this alternative must be considered since the amount of data is limited.

Alternatively, if the data of Figure 7.4 were to be believed, they imply a flux of significant energy at times long after the X-radiation is over. These data cannot, of course, be considered valid until there is some confirmation or, at the least, no contradiction from other data. The first source of confirmatory information would be the pistons under hatches. As noted previously, the hatches appear to have functioned as designed. One would, therefore, expect that the pistons under hatches would have recorded impulse values commensurate with the increment between the early and late impulses of Figure 7.4.

These pistons, however, recorded zero impulse. There are several possibilities which can nevertheless explain these zero

readings. If the late loading were characterized largely by vapor pressure akin to a thermomechanical loading, the pistons below hatches could have been insensitive, since equalization about their heads would have been very rapid. It must be recalled that these pistons were recessed within a soft bellows (Figure 6.3) so that the effective plenum below the head was quite small with a concomitant very short pressure-equalization time constant. The shank area of these pistons, which would be the only pressure-sensitive portion, is about one-seventh of the head area. The incremental impulse being sought is about 2×10^3 dyne-sec/cm². The corresponding loading would be less than 0.3×10^3 dyne-sec/cm². By reference to Appendix D it can be seen that this loading is below the threshold value for these pistons.

Another possibility is concerned with the dynamic response of the pod-cluster-anvil/piston system. Let it be assumed that the late loading did not commence much before 20 milliseconds. In this time the incremental rigid body motion of the pod relative to the seismically mounted indent recorder clusters is about 0.8 cm, and local motions at the backplate could be somewhat larger. It is conceivable, therefore, that the cluster may have bottomed out the soft bellows, and the abrupt stopping of cluster motion relative to the pod could have invalidated all readings on that cluster.

At this time, therefore, it cannot be concluded that the indent recorder channels under hatches either confirm or contradict the possibility of a second loading.

Other data which would confirm, at the least, the possibility of late loading would be non-X-ray energy measurements. This type of data should have been available in the most unambiguous

manner from the debris/thermal pinhole camera with hatches. Most of these hatches appear to have functioned as designed, but there was no indication in the detectors of metallurgical transformation. The threshold energy flux to create transformation in the detector for a 10-millisecond pulse is about 20 cal/cm^2 . Another source of this type of confirmatory data is the sections of long-time thermal gages which were under the quartz filter. Any reading on these would indicate that there existed significant radiation in the wavelength regime above 2000 \AA . These gages have been examined, and there is no indication of significant energy absorption. The quartz filters, however, were severely fractured and crazed by the X-ray pulse which would make them relatively opaque to visible light. The lack of transformation under them, therefore, is not positive proof that there were no later radiant inputs. If the late-energy source were hydrodynamic rather than thermal, there would be no readings on the thermal instruments. In this case, however, the indent recorder pistons should all read values greater than the increment between early and late loadings (approximately $2 \times 10^3 \text{ dyne-sec/cm}^2$). There are, however, many zero impulse readings, which there is no reason to disbelieve at this time.

In summary, then, the division of the impulse into early and late components is preliminary, and the data must presently be regarded as inconclusive.

7.2.2 Spall Gages. All three spall gages were recovered in excellent mechanical condition. The gage incorporating steel and aluminum samples showed ablation of the samples consistent with ablation measured on other instruments and exposed surfaces. There was no externally visible evidence of spalling. The oblique-tape-wound refrasil showed only superficial charring with no evidence of mechanical damage.

The spall gage incorporating the lucite cylinders is illustrated in Figure 7.5 . The top photograph shows the disassembled instrument. The lead foil was missing over all cylinders. The bottom photograph on Figure 7.5 is a close-up of the cylinder under the largest aperture, which was the only cylinder showing any signs of fracture. The fracturing occurred in two main areas. The easily visible area is nearly parallel to the bottom surface of the cylinder with four radial fractures perpendicular to this surface. The other fracture area is generally conical in shape, emanating from the re-entrant corner of the shoulder and progressing downward toward but not connecting with the first fracture.

The fracture parallel to the bottom surface varies from 1.2 to 2.3 mm in distance from this surface. The relation for order-of-magnitude estimation of the pulse duration was given in Section 2.3.2 for lucite as:

$$\Delta t = \frac{d}{2.7 \times 10^5} \text{ seconds}$$

where d is the perpendicular distance in centimeters from a free shock-reflecting surface to the fracture. For this fracture, then, the apparent pulse duration is approximately 0.5 microsecond.

7.2.3 Ablation-Condensation Gages. As noted previously the Blue Gill experiment received the primary effort during the data reduction program. The ablation values presented in this section, therefore, do not represent all the data which could eventually be extracted from the King Fish instruments. At present, ablation information is only available for samples which could be easily removed from the instrument body. Because of the generally small

degree of ablation, any damage during sample removal can create large uncertainties. In the King Fish experiment the ablation values do, of course, have more direct applicability than in Blue Gill, because the influence of the surround is much smaller due to the short duration of the X-ray input.

All of the ablation-condensation gages on pod K-1 were recovered. The majority of the gages had suffered no mechanical damage, although several had lost the portion of the micarta heat shield over the steel sample retainer.

Appearance of the Sample Material. All the samples were examined on disassembly of the gages at the test site. The samples were then washed, dried, and packed for shipment. The cleaning solution for all samples was a 1% solution of Oakite 202. The cleaning procedure seemed to remove the salt deposits and did not otherwise change the appearance of the samples.

Two of the nose cone materials, Avcoat 19 and Rad 58B, had disintegrated almost completely, leaving only a segment of the threaded portion. Figure 7.6 illustrates the before and after appearance of Avcoat 19. The composite plastic materials, i. e., glass-filled phenolic, linen-filled black phenolic, micarta, tape-wound nylon phenolic, and oblique tape-wound refrasil were generally charred to varying degrees but otherwise appeared to have suffered very little ablative or mechanical damage. The uniformity of the surfaces is apparent from the profiles presented in Figure 7.7. The refrasil-phenolic samples had the same lightly charred character as the bulkhead. The face of the iron-devcon sample was uniformly rusty. The teflon samples remained white but seemed to be etched. The pyrolytic graphites showed essentially no surface change but disintegrated upon instrument disassembly.

The metal samples generally had stippled surfaces. No substantial resolidified splash was apparent. Except for light corrosion, the 1020 steel samples were in excellent condition. Copper appeared virtually unaffected. The surface of the aluminum was strongly stippled. Zinc did not appear to have lost material, although it had the grey appearance characteristic of corrosion. The lead sample had radial splash lines, but it did not appear to have suffered much material removal.

The general appearance of the King Fish samples was qualitatively different from the Blue Gill samples. In pod B-1 the samples showed evidence of having been heated severely. In pod K-1, while some evidence of heating could be seen such as charring of the refrasil-phenolic, the samples appeared more to have been etched. Even the charred samples appeared different from their equivalents in pod B-1. The charred areas were brownish on pod K-1— not black as on pod B-1— and the fibers in the refrasil-phenolic did not appear to have melted as they did in the Blue Gill samples. This difference can be seen by a comparison of Figure 7. 8 and Figures 3. 22 and 3. 23 for the backplate material.

Changes in Dimensions and Weight. The King Fish samples were weighed and measured prior to the event. Errors and uncertainties in the values of ablation arise from non-uniform response over the sample surface, sea water immersion, and the effects of ambient moisture.

The measured weight changes per unit area of refrasil-phenolic, micarta, black phenolic, iron-devcon, and teflon samples are listed in Table 7. 2. The uncertainties in the weight changes caused by measurement precision, atmospheric moisture, and sea salt absorption are assumed to be the same as in Blue Gill,

i. e., $\pm 15 \text{ mg/cm}^2$ for refrasil-phenolic and micarta, $\pm 20 \text{ mg/cm}^2$ for black phenolic, $\pm 10 \text{ mg/cm}^2$ for iron-devcon, and $\pm 2 \text{ mg/cm}^2$ for teflon.

No data on ablation for the metal samples are available at this time. In contrast to the Blue Gill experiments, almost all the metal samples adhered to the gage body. Only the aluminum samples could be freed easily.

Condensed Products. The platinum-rhodium liners and end caps were removed from the gages at the test site several days after recovery and their appearance recorded. In general, the liners and end caps had the appearance of the liners and end caps in the Blue Gill experiment. Rusting of the gage body had occurred, and many of the liners seemed to have deposits of rusty sea salt on them.

Most of the King Fish liners were found to have long elliptical patterns on them, an inch or so in length and a quarter-inch or so in width at the widest part. These patterns are undoubtedly the areas illuminated by the X-rays through the entrance aperture. No particularly striking deposits were found in the condensation chamber except for the large deposit of white oxide under the aluminum sample.

7.2.4 Debris/Thermal Pinhole Cameras. All cameras were recovered with only minor damage; this damage is considered to be burst-induced. All of the damage was in the micarta covers over the top aperture chamber, many of which had been partially punched out, leaving a large irregular hole. In one case this micarta had jammed into the cavity and had remained wedged therein. The magnitude of the lateral displacement of stippled areas visible within apertures was consistent with other orientation clues on the bulkhead and instruments.

By external observation it appeared that at least some of

the hatches had performed as designed. Some hatches had disappeared with the punched-out portion of the micarta cover. In one case with a large aperture, the cover was intact, and one element of the hatch was plastered against the end of the chamber. The detector element was exposed over essentially its entire surface. In another case, the hatch was severely deformed and crushed, but its present position was such that the detector was not exposed. Several of the gages with small apertures were intact, and the performance of the hatches could not be ascertained without disassembly.

None of the debris/thermal pinhole cameras had any discernible surface images or shadows on side-viewing ports. A metallurgical examination was performed on some of the detectors in those instruments in order to estimate any radiative inputs. All detectors were of nominal 1020 steel. See Appendix H for a detailed discussion of metallurgical evaluation and measurement errors.

A visual examination of the detectors behind 10-mm and 1-mm unhatched apertures revealed that the surfaces had melted. A cross-sectional examination through the exposed regions confirmed the existence of this melt and also revealed a solid-state transformation beneath the melt layer. Because of the orientation of the cut with respect to the slots in the detector, only a small unaffected portion of the surface remained as a reference for the depth measurements in the 10-mm aperture gage. The maximum error in the depth measurements for this gage is, therefore, estimated to be ± 4 microns because of the difficulty in establishing the reference surface. A graphical presentation of the depths of material removed, resolidified melt and solid state transformation for the detectors within the 10-mm and 1-mm

apertures are presented in Figures 7.9 and 7.10 , respectively. Figure I.4 shows a photomicrograph taken along a typical cross-section of the detector beneath the 10-mm aperture. Figure 7.11 is a photograph showing the orientation for metallurgical sectioning of the 1-mm aperture steel detector.

Two hatched gages behind 10-mm apertures and one hatched gage behind a 3-mm aperture were also examined. A macroscopic examination of the detector surfaces showed no evidence of melt. A cross-section through the predicted illuminated region revealed neither melt nor solid state transformation in any of these three gages.

One sideways-viewing detector was examined. This was within a 10-mm aperture in the most favorable orientation to view the burst region. There was no surface evidence of any transformations. This lack of transformation was confirmed by metallographic examination of the cross section.

7.2.5 X-ray Intensity Gages The platinum-rhodium mask over the apertures was missing on both gages; its shadow, however, was prominent. The gage body was otherwise in excellent condition. The beryllium windows were strongly stippled.

A preliminary examination of the particle suspension stacks has been made, and appreciable data in the form of transformed and/or exploded metallic particles are present in some of the disks. These transformations occurred even under the 3-mm beryllium window. These data have been compared in a cursory manner to those associated with the particle suspensions utilized in the Marshmallow underground test (Reference 27). This comparison has indicated

that many of the qualitative effects are similar and that some are different. A detailed analysis of the King Fish particle suspension devices has not yet been performed.

7.2.6 Pinhole Closure Gage. The gold mask which formed the tapered slot and the top area of the micarta cover was missing. There appeared to be a blackened depression through the center area of the film stack. Qualitatively, the depth of this depression appears to vary along the slot with the deeper areas being beneath the wide end of the slot. No further examination of this instrument has yet been made.

7.2.7 Long-Time Thermal Gage. All of the King Fish (pod K-1) long-time thermal gages were recovered and appeared to be unaffected except for rust on the steel heat sinks. Disassembly in the field was limited to removal of the heat sinks from the gages.

Macroscopic examination of the exposed portions of the copper and steel heat sinks revealed that all surfaces which directly viewed the burst had melted. Shadows on the surfaces due to pod misalignment with the burst direction were prominent on the recessed gages. Only those heat sinks recessed beneath quartz filters possessed unmelted surfaces. The quartz filters were severely crazed with prominent fracture lines. The coating of soot deposited on these filters was about the same as that of Blue Gill pod B-3. In shot King Fish, however, the crazed condition of the filters, presumably a result of X-rays, may have reduced their transmission characteristics prior to any subsequent radiative inputs.

The aluminum and polystyrene foils failed in the same manner as in shot Blue Gill (see Section 3.2.7). Therefore, no data from these foils are included herein.

The data obtained from the lead, tin and gold foils were reasonably good but in some cases obscured by corrosion. Table 7.3 summarizes the observations noted in a detailed examination of the foils. The numerical results presented are estimated to be in error by not more than ± 0.002 in. In cases where foil material is noted as missing, it is difficult to tell whether or not it melted to that depth.

The King Fish long-time thermocouple appears, in general, to have functioned as designed. The data are not as clear as was the case in shot Blue Gill; this may be due to the preponderance of X-rays rather than relatively long duration thermal radiation in the input pulse.

7.2.8 X-Ray Pinhole Camera. The King Fish X-ray pinhole camera is schematically illustrated in Figure 6.9. The two cameras differed only in spacing of pinholes and slightly in film plate geometry. Figure 7.12 illustrates schematically the emplacement of the cameras in the pod. Both cameras were recovered in excellent mechanical condition. The orientation was such that the images associated with all pinholes fell on the film stack. The film stacks have not yet been disassembled. The work to the present time has been limited to an external examination of the stacks. Figure 7.13 illustrates the location of images that have been found on the 11.5-inch camera. The figure numbers refer to the photomicrographs of Figures 7.14, 7.15, and 7.16 which follow. The background on the photomicrographs is gold, the crater is apparently formed by melted mylar, and the irregular dark halo surrounding the crater is clear mylar from which the gold has disappeared. It should be noted that the orientation of the images is preserved throughout the photomicrographs. The images on these photomicrographs are typically 0.035 cm in diameter. This dimension is not large enough so that any of the apertures can be

considered a true pinhole. In the case of a finite size pinhole a dimension at the source location is related to a dimension on the image very closely by the relation

$$D \cong \frac{R}{f} (i - d)$$

where:

- D is a dimension at the source location
- R is the range to the source from the pinhole
- f is the focal length of the camera
- i is a dimension on the image
- d is the pinhole diameter

The one-meter scale length depicted on Figure 7.14 is derived from this relation using the range to the burst as 8,149 feet.

Figure 7.17 depicts the location of images found on the four-inch camera. Figure 7.18 shows photomicrographs of the images associated with a large and small aperture.

Several general observations on the performance of the cameras in Shots Blue Gill and King Fish may be made:

1. Low carbon steel presents a severe rust problem after immersion in sea water, making the location of very small images extremely difficult. A high polish (as was done with some other Blue Gill and King Fish instruments) may help to alleviate the rust problem. Corrosion of aluminum also presents severe problems in finding and examining small images.
2. With many-leaved film stacks, it is preferable not to have a closed container for the camera. This conclusion is based on a comparison of the Blue Gill and King Fish film stacks. In Blue Gill

if any images had fallen on mylar, severe problems would have been encountered in finding and interpreting them because of dried salt deposits. The comparatively cleaner appearance of the King Fish film stacks is possibly due to the fact that the sea water could drain off easily.

3. Lead is a suitable detector for very low flux levels. Some characteristic dimension of the source is easily obtainable in lead, but any details of the source structure may be difficult to derive.

4. Gold-covered mylar is a feasible and probably sensitive detector element for X-ray pinhole cameras. It is not clear yet, however, that much detail of the source can be derived because of the lack of distinctive transformations. From cursory examination of the stacks it appears that the most that can be said is that the gold deposit either is or is not intact.

5. Pinhole sizes as small as 0.003-cm diameter in gold foil are feasible at the flux levels available in Shot King Fish at the closest pod location. The effect of pinhole closure is unknown at this time, but sufficient energy did get through to cause visible transformation in the gold/mylar film plate.

7.2.9 Membrane Structure Gages. The set of membrane structure gages appears to have responded very well, with a spectrum of results obtained. At the extremes, one membrane ruptured, and one exhibited no permanent deformation, while varying degrees of plastic behavior are observed in the gages between these extremes. Photographs of the deformed gages are shown in Figures 7.19 and 7.20. The thinner (0.020 inch) aluminum alloy membrane deformed to a deep dish shape and ruptured at the edge restraint for half of its circumference. Of

the remaining membranes, all but the thickest (0.075 inch) steel sample exhibited some degree of permanent plastic deformation. The final shapes of the deformed membranes are illustrated in Figure 7.21 where the curvature at the restraint should be noted.

The degree of plastic deformation suffered by each of the gages may be shown by measuring the average radial plastic strain for each membrane. Average radial plastic strain is a good indication of the degree of permanent strain, and it is readily obtained by comparing the original and deformed length of a diameter. By assuming that the deformed shapes of the membranes can be approximated by cosine curves, the plastic strain may be expressed as:

$$\epsilon = \frac{\pi^2}{4} \left(\frac{\delta}{d} \right)^2 \quad (7.1)$$

where $\frac{\delta}{d}$ is the ratio of center deflection to the membrane diameter. The table below uses Equation 7.1 to indicate the average radial plastic strain.

Membrane	Average Radial Plastic Strain In/In
0.020" Al	$< 6 \times 10^{-1}$
0.050" Al	8.6×10^{-3}
0.010" Steel	5.8×10^{-2}
0.020" Steel	2.6×10^{-2}
0.030" Steel	2.5×10^{-3}
0.050" Steel	8.6×10^{-5}
0.075" Steel	0

Energy dissipated plastically is proportional to the plastic strain, and energy dissipated elastically is proportional to half the elastic strain at yield. Since the elastic strain at yield for the materials involved is approximately 10^{-3} , it can be seen from the table that:

1. Both of the aluminum membranes and the 0.010- and 0.020-inch steel membranes dissipated essentially all the absorbed energy by plastic deformation.

2. The 0.075- and 0.050-inch steel membranes had all or nearly all energy dissipated elastically.

It is interesting to see to what extent the behavior of the membranes might be predicted by analytical methods. Mathematically, rigorous analyses were performed by Witmer, et al (Reference 28) at the Aeroelastic and Structures Research Laboratory of the Massachusetts Institute of Technology. These analyses lumped the membrane into twenty masses from the center to the restraint, with the thickness broken into four layers. The governing differential equations were made into difference equations and were solved for failure mode shape for given impulsive loads. Two calculations were performed for the 0.050-inch aluminum membrane subjected to an impulse of 10^3 dyne-sec/cm² — one using a perfectly plastic stress-strain curve with a constant plastic stress, and the other using a realistic stress-strain curve taking strain hardening into account. This value of impulse was selected for the computational procedures since it matches the theoretical and experimental maximum deformations. The fact that this value is very close to that measured with the indent recorders for steel and different from the measured lead impulse (the aluminum membranes were covered with lead foil) by about a factor of two cannot be considered significant at this time. The maximum deformation is primarily dependent on the magnitude of the yield stress on the stress-strain curve, whereas the deformed shape is dependent on the shape of the stress-strain curve. The primary interest in this investigation was in determination of the failure mode shape. The results of these analyses are shown in Figure 7.22 where they are compared with the actual deformed shape of the membrane. The

experiment and the strain-hardening theory give almost identical deformed shapes. The most significant area where the two theories differ is at the support. In this area the curvatures may differ by an order of magnitude. The perfectly plastic theory which predicts the sharper curvature may, therefore, be overly conservative in predicting failure. The importance of being able to describe mode shape, and especially edge curvature, is confirmed by the fact that the thinner aluminum membrane failed at the edge.

An estimate of the maximum deformation of membranes, which agrees with the more elaborate theories used above to within less than 10%, can be obtained by the use of a very simple analysis assuming:

1. All energy was dissipated by plastic deformation.
2. Strain was uniform over the membrane and is given by Equation 7.1.
3. The plastic stress was uniform and independent of strain rate.

The resulting deformation from this analysis may be expressed as:

$$\delta = \frac{J d}{\pi t \sqrt{\rho \sigma}} \quad (7.2)$$

where:

- | | |
|----------|---|
| J | is the applied impulse, dyne-sec/cm ² |
| t | is the thickness of the membrane, cm |
| d | is the diameter of the membrane, cm |
| ρ | is the density of the membrane material, gm/cm ³ |
| σ | is the plastic (or yield) stress, dynes/cm ² |

As noted above, no conclusions can be drawn yet on the suitability of the theory to predict maximum deformation. The well-behaved response of the membranes indicates, however, that the maximum deformation and failure can probably be predicted closely if accurate material strength properties are available. This behavior also suggests that membranes and other simple structural elements can be used as impulse measuring devices. They must, of course, be calibrated in the laboratory.

Three conclusions can be drawn from these tests:

1. Simple structural elements can be expected to fail under X-ray impulse loadings in accordance with present structural models.
2. Prediction of rupture of membranes requires use of a theory that properly describes the deflected mode shape.
3. Membranes of the type used in this experiment can, with proper calibration, be used as impulse-measuring instruments.

Other interesting observations were made in addition to the structural effects described above. These effects have received no more than superficial observation to the present time, since further investigation would involve procedures that might destroy information useful for the structural analysis of these gages.

One observation was that the gages with steel membranes without the lead foil cover exhibited a distinct flowing of the molten surface along radial lines toward the center of the membranes. Solidified drops of material were apparent at the center of the membrane where these flow lines converged. Another observation was that the rear surface of the 0.050-inch-thick aluminum alloy membrane exhibited several blisters in the material, none of which had broken through. For the present time, these blisters have been ascribed to incipient spalling.

7.2.10 Additional X-Ray Intensity Data. Some useful intensity data for pod K-1 was obtained from a cross-section through a crescent on the aluminum top retainer plate of an indent recorder (Figure 7.2). The crescent resulted from exposure to X-rays passing through an annular opening between the piston head and the backplate. A metallurgical examination through the crescent revealed that the exposed material melted, splashed, and resolidified. Depth measurements were made from the original unaffected surface. Figure 7.23 is a graphical representation of the depths to which material was removed and resolidified.

An X-ray exposed area was also found on the side of an aluminum indent recorder guide sleeve (Figure 7.24). This area was exposed through the clearance opening between a piston and the backplate in the same way as the crescent. The guide sleeve wall was situated perpendicular to the backplate, and this area was, therefore, exposed at a near-grazing angle of about 4° . From a microscopic examination through the irradiated area, there was evidence of melt. Depth of melt measurements were made, and these data are presented graphically in Figure 7.25.

7.3 X-RAY INPUT ANALYSIS

In Shot King Fish the X-radiation should provide the predominant input because of the low atmospheric density. The phenomenology and response are, therefore, qualitatively different than in Blue Gill. In fact, there has not yet been found any evidence of an intense early thermal radiation input from this shot. That is, no variable-depth temperature profiles similar to those found in the thermal pinhole cameras from Shot Blue Gill were found. Therefore, no thermal analysis is carried out in the following sections. There is, nonetheless, the possibility of a significant heat input to the King Fish pod either from direct impingement of weapon debris or from the re-radiation of air

heated by the debris. The debris thermal input is not analyzed herein because at present there exist only upper bound data (i. e. , no observable effects with the exception of some charring in X-ray shadow regions). For the present then, the X-ray input is assumed to be decoupled from any debris input. No check of the validity of this assumption is presently available.

X-Ray Transmission to Pod K-1.

There were several sources of X-ray intensity data on the pod. These are analyzed individually below and then combined to provide the best presently available estimate of intensity. Specific instruments designed to provide this information are described in Chapter 6, and the post-test appearance has been discussed previously in Chapter 7. The data from these instruments has not yet been reduced.

Directly Exposed Aluminum. The crescent described in Section 7. 2. 10 is used in this analysis. An upper bound similar to that derived for Blue Gill (see Section 3. 3. 1) can be determined using the maximum

melt depth. The average value of this maximum melt depth was calculated from 82 measurements in the uniform region (i. e., not including the edges of the image).

(see Figure 7.23). Figure 7.27 shows normalized X-ray energy deposition in this aluminum sample. Application of Equation 3.4 to the values shown in Table 3.9 gives a critical melt energy of 140 cal/gm.

These results are plotted in Figure 7.28.

It should be pointed out that the curves of Figure 7.28 have a steep slope in the vicinity of the nominal yield, so that a small change in X-ray yield implies a relatively large change in intensity. On the other hand, in this same vicinity, weapon temperature is relatively insensitive to a change in nominal yield.

A lower bound on intensity may be obtained by using the fact that the aluminum surface melted, but this value is too low to be of interest. This is because the absorption of the low energy portion of the X-ray spectrum results in a steep energy gradient at the surface of the aluminum (see Figure 7.27). Furthermore, even the fact that the aluminum melted on the guide sleeve (Section 7.2.10) does not give a better lower bound. This is so because surface X-ray absorption can be shown to be independent of the incidence angle of the X-rays. Bragg reflection effects are neglected.

Aluminum Behind Beryllium Window. The aluminum indent recorder cluster behind a 3-mm beryllium window (see Figure 6.2) exhibited X-ray-etched crescents similar to, but shallower than, the

crescents found on indent recorders without windows. A calculation analogous to that described above was carried out for the surface of the aluminum. This time a lower bound may be obtained, since the surface of the aluminum must have reached at least its solidus temperature. The lower bound includes the effect of thermal conduction during energy deposition as given by Equation J. 5. The results are depicted in Figure 7.28, where this lower bound on effective yield and intensity is plotted as a function of X-ray source temperature.

It can be seen from the figure that this lower bound lies extremely close to and just below the upper bound

There is no intersection over the range of source temperatures shown. Although the intensity is closely defined for a given temperature, the data yield no bounds on source temperature. The table below gives the intensity at the pod and weapon temperature for a few values of the X-ray yield.

Platinum. The liners in the ablation-condensation gages were made from a platinum-rhodium alloy. These liners were exposed to the X-rays at a near-grazing incidence angle of 4° . The surface within the exposed area was melted and a portion may have been vaporized. This material was not cross sectioned. A lower bound calculation was made, however, using the fact that the surface melted. This bound is much less than the lower bound calculated from the aluminum data, since the deposition in platinum-rhodium is rather steep at the surface (because of a high atomic number) and since it has a rather low melt threshold (70 cal/gm). A cross sectioning and upper bound analysis might prove more useful. This has not yet been done.

Table 7.1

SUMMARY OF IMPULSE DATA

Pod K-1

Piston No.	Piston ⁺ Type	Material	$\frac{sm}{p \cdot A \cdot h}^*$	d cm	Impulse**	Remarks
1210 ^{a***}	G-1		39.94	no indent		
1208	G-1		40.77	.0147		Indent size comparable to others in cluster.
1209	G-1		40.50	no indent		
607 ^b	G-2		60.46	.0242		Indent size comparable to others in cluster.
610 ^c	G-2		60.97	.0179		Indent size comparable to others in cluster.
609	G-2		60.60	no indent		
741 ^c	A-1	Lead	.52	.0500	1.90 \pm 0.08	
742 ^c	A-2	"	1.68	.0464	1.80 \pm 0.07	
743 ^c	A-3	"	5.19	.0143	1.84 \pm 0.16	Double Indent
317 ^c	C-1	"	8.99	.0171	1.87 \pm 0.10	
318 ^c	C-2	"	37.87	.0253	3.54 \pm 0.13	
1037 ^c	D-1	"	91.78	.0157	4.6	
323 ^c	C-2	Zinc	36.81	.0200	2.52 \pm 0.18	
1483 ^a	L-1	Lead	40.56	no indent	<.3	3-mm Beryllium Window
1482 ^a	L-1	"	40.88	no indent	<.3	2-mm Beryllium Window
1481 ^a	L-1	"	40.38	---		Hatch plus 2-mm Beryllium Window; Severely Distorted indent
1480	L-1	"	40.26	.0199	1.2	
1486	L-1	"	40.68	.0058	0.5	Slightly Distorted Indent
1484	L-1	"	40.28	no indent	<.3	Hatch
1485	L-1	"	33.41	no indent	<.3	Hatch
1499 ^a	L-1	Pyro-Graph-ite (para.)	39.59	---		3-mm Beryllium Window Severely Distorted Indent
1498 ^a	L-1	"	30.19	no indent	<.2	2-mm Beryllium Window
1502	L-1	"	30.35	no indent	<.2	
1503	L-1	"	30.76	no indent	<.2	Hatch

Table 7.1 CONTINUED

Pod K-1

Piston No.	Piston ⁺ Type	Material	$\frac{sm_p}{A_h}$ *	d cm	Impulse**	Remarks
1511 ^a	L-1	Copper	37.46	no indent	<.3	2-mm Beryllium Window
1510 ^a	L-1	"	37.24	no indent	<.3	3-mm Beryllium Window
1512	L-1	"	37.65	.0205	1.1	
1509	L-1	"	37.33	no indent	<.3	Hatch
1519	L-2	1020 Steel	42.27	.0183	1.1	
1521	L-2	"	41.38	.0154	0.9	
1529	L-2	Beryllium	35.20	no indent	<.2	
1528	L-2	"	35.75	no indent	<.2	
1535	L-2	Aluminum	36.52	.0103	0.6	
1533	L-2	"	34.93	no indent	<.2	
1405 ^b	K	Pyro-Graph-ite (perp.)	15.58	no indent	<.1	
1407 ^b	K	"	15.97	.0164	0.4	Double Indent
1426 ^b	K	Pyro-Graph-ite (para.)	16.34	no indent	<.1	
1418 ^b	K	"	15.99	.0206	0.5	
1431 ^b	K	Phenolic	15.41	.0665	3.04±0.40	
1441 ^b	K	Lead	25.63	.0298	1.23±0.07	Double Indent
1450 ^b	K	Teflon	16.14	.0334	0.97±0.09	Slightly Distorted Indent
1458	K-2	Refrasil-phen.	15.19	.0389	1.19±0.12	
1461	K-2	O. T. W. R.	15.11	.0433	1.42±0.17	
1464	K-2	T.W. Nylon Phenolic	14.82	.0322	0.87±0.08	
1467	K-2	Avcoat 19	14.68	.0811	4.13±0.43	
1470	K-2	Rad 58-B	14.68	.0442	1.45±0.17	
1474	K-2	Glass-Filled Phenolic	15.28	.0530	2.06±0.27	
1476	K-2	Micarta	14.79	.0666	3.00±0.40	

Table 7.1 CONTINUED

Pod K-2

Piston No.	Piston Type ⁺	Material	sm_p/A_h^*	d cm	Impulse**	Remarks
608 ^d	G-2		62.40	.0475	Double Indent;	Indent size larger than others in cluster.
1402 ^d	K	Pyro-Graphite (perp.)	15.71	---		Severely Distorted Indent
1406 ^d	K	"	16.06	no indent	<.1	
1417 ^d	K	Pyro-Graphite (para.)	16.06	no indent	<.1	
1428 ^d	K	"	16.03	no indent	<.1	
1432 ^d	K	Phenolic	15.15	.0269	0.69±0.06	Slightly Distorted Indent
1442 ^d	K	Lead	26.17	.0232	0.9	
1451 ^d	K	Teflon	16.12	no indent	<.1	

*Units of sm_p/A_h are $\text{dyne-sec}^2/\text{cm}^2$

**Units of Impulse are $10^3 \text{dyne-sec}/\text{cm}^2$

***Superscript letters denote clusters in which the control pistons made indents; pistons common to a cluster are identified by the same letter

G-1 = Doubly blind control

G-2 = Blind Control

+ = Piston Type notation is explained in Table 2.1 and Section 6.2.1; 5-mm-thick samples were used only on K-2 pistons

TABLE 7.2

MEASURED WEIGHT LOSSES OF KING FISH ABLATION SAMPLES

Sample Materials	Weight Loss (mg/cm^2)
Refrasil-phenolic	
1 mm	40.1
3 mm	58.5
5 mm	45 *
Micarta	91.0
Black Phenolic	65.3
Iron Devcon	25.8
Teflon	56.4
Pyrographite (perpendicular)	fractured during disassembly
Pyrographite (parallel)	fractured during disassembly
Rad 58B	severely fractured
Avcoat 19	severely fractured

* unreliable measurement due to edge chipping

TABLE 7.3 LONG-TIME THERMAL GAGE DATA, POD K-1

Steel Heat Sink

Flush Geometry

Observations

Lead Foil
(Quartz Filter)

Melt depth estimated as several thousandths of an inch.

Tin Foil

Melt depth of about 0.010 in.

Gold Foil

Surface melt only.

Recessed Geometry

Lead Foil
(Quartz Filter)

Surface appears to have barely melted (unclear).

Tin Foil

Melt depth of about 0.008 in.

Copper Heat Sink

Flush Geometry

Lead Foil
(Quartz Filter)

Material missing to a depth of several thousandths of an inch. Corroded.

Tin Foil

Material missing to a depth of about 0.015 in. Corroded.

Recessed Geometry

Lead Foil
(Quartz Filter)

Surface appears to have barely melted.

Tin Foil

Material missing to a depth of 0.008 in. Corroded.



Figure 7.2 Postshot condition of Indent Recorder Cluster 80.
(ASE photo)

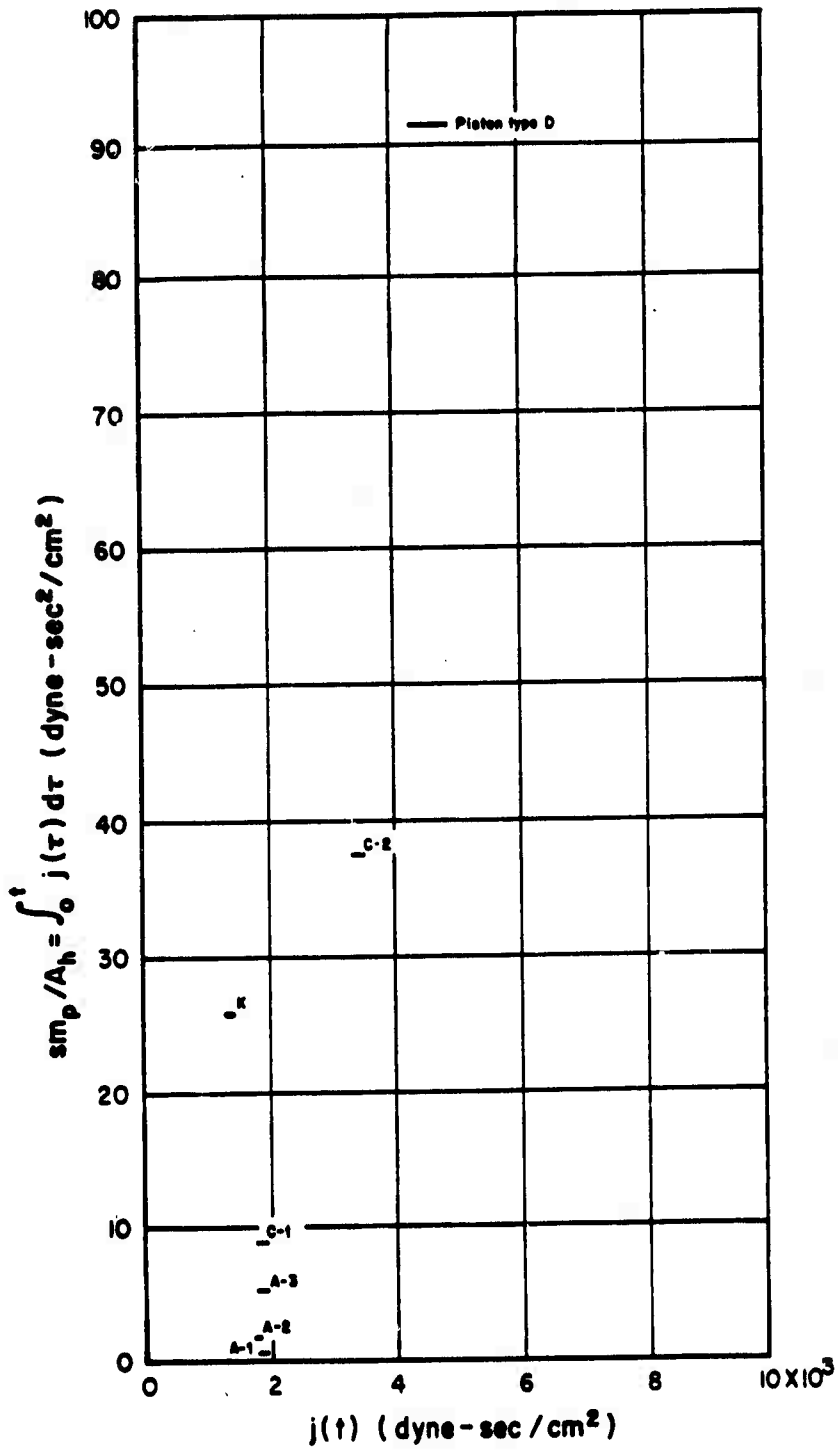


Figure 7.3 Integral of impulse versus impulse, Pod K-1, lead.

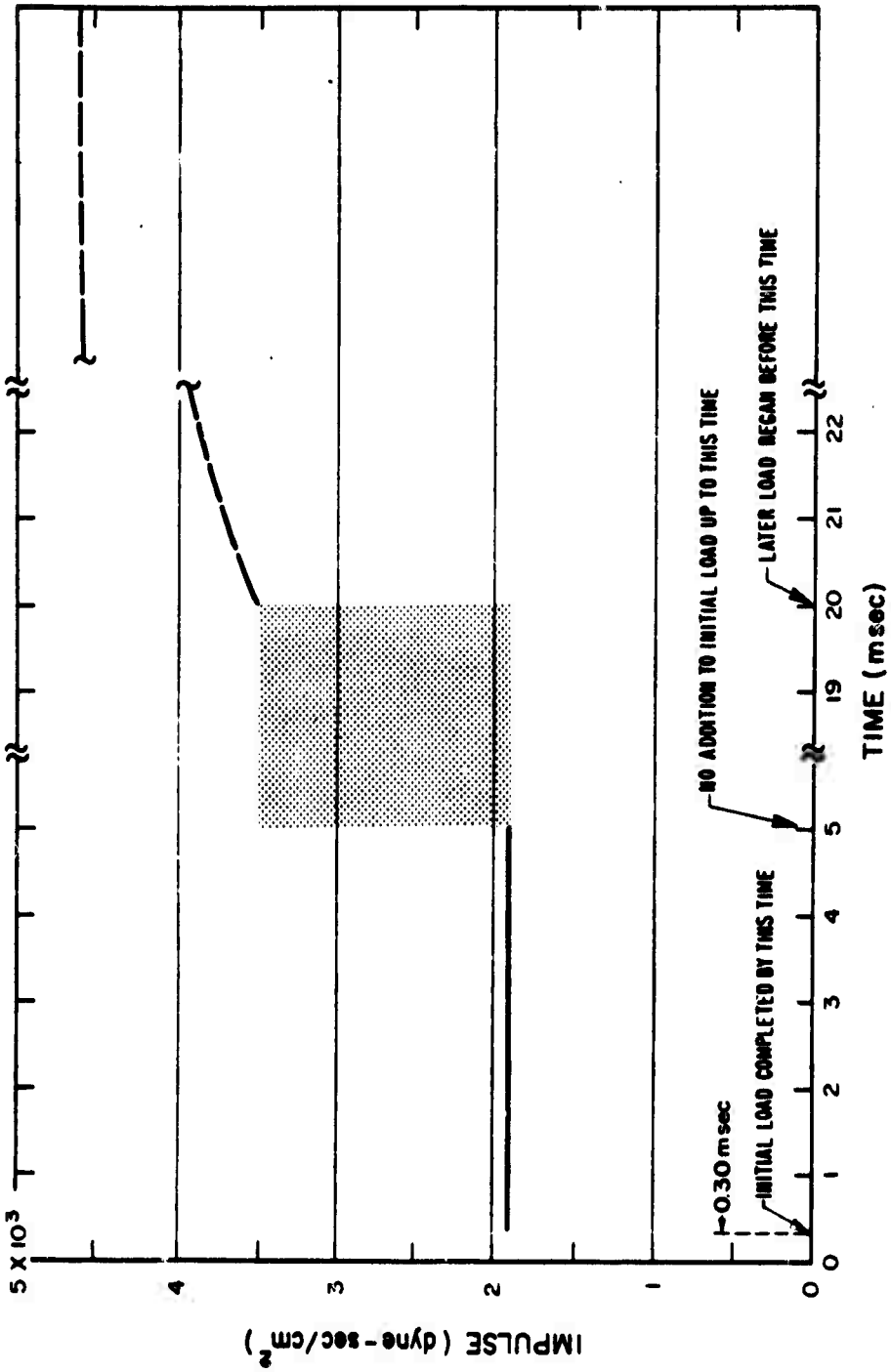
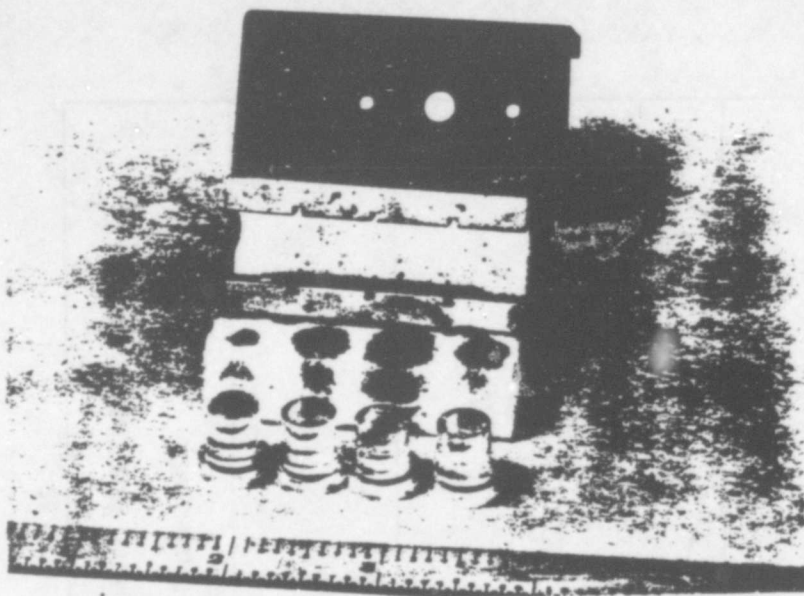


Figure 7.4 Loading time data, King Fish Pod 1; lead.

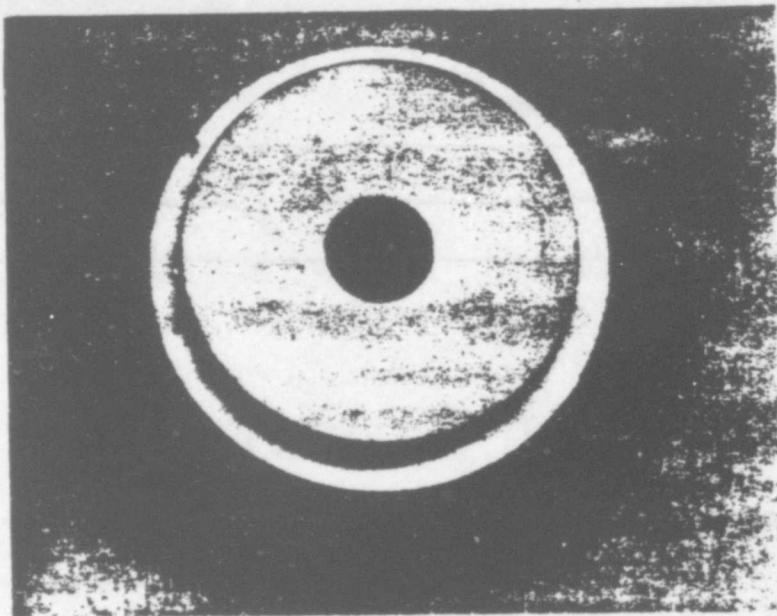


A. DISASSEMBLED GAGE

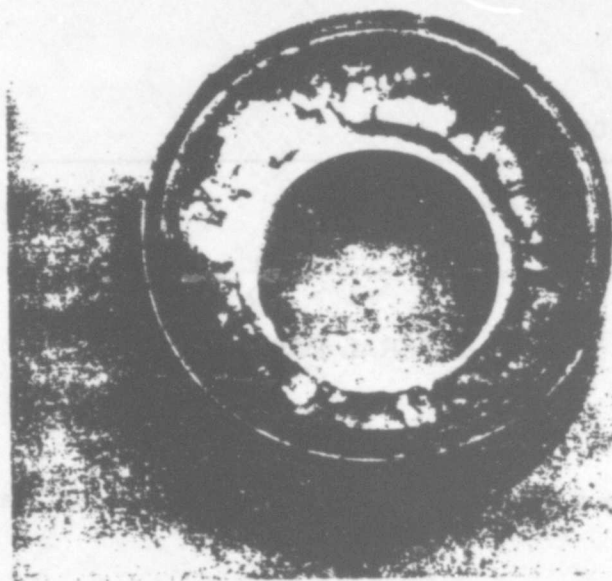


B. DETECTOR UNDER
LARGE APERTURE

Figure 7.5 Postshot condition of spall gage, Pod K-1. (ASE photos)



BEFORE



AFTER

Figure 7.6 Ablation-condensation gage reer*
Avcoat 19, King Fish. (ASE photos)

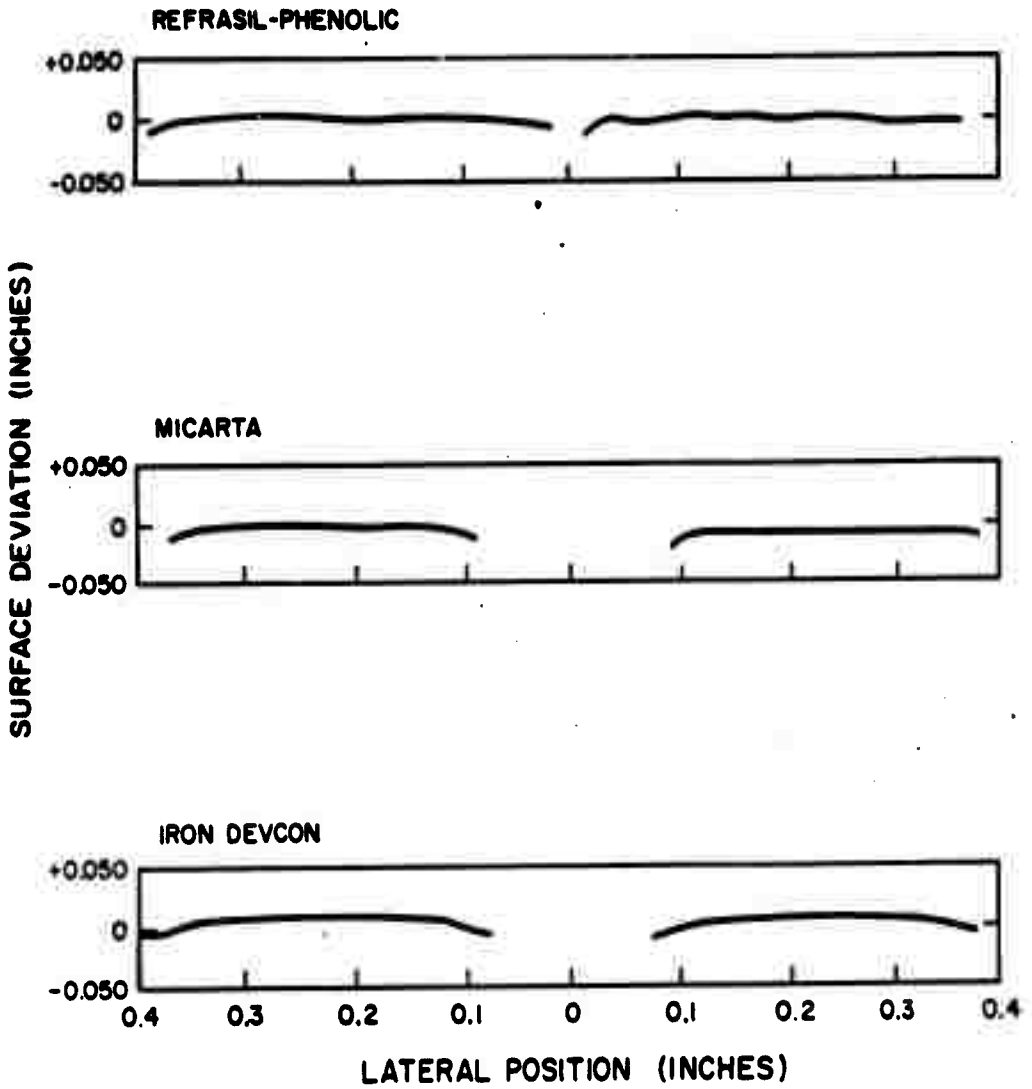


Figure 7.7 Surface profiles of King Fish ablation samples.



Figure 7.8 Postshot condition of refrasil-phenolic,
King Fish Pod 1. (ASE photo)

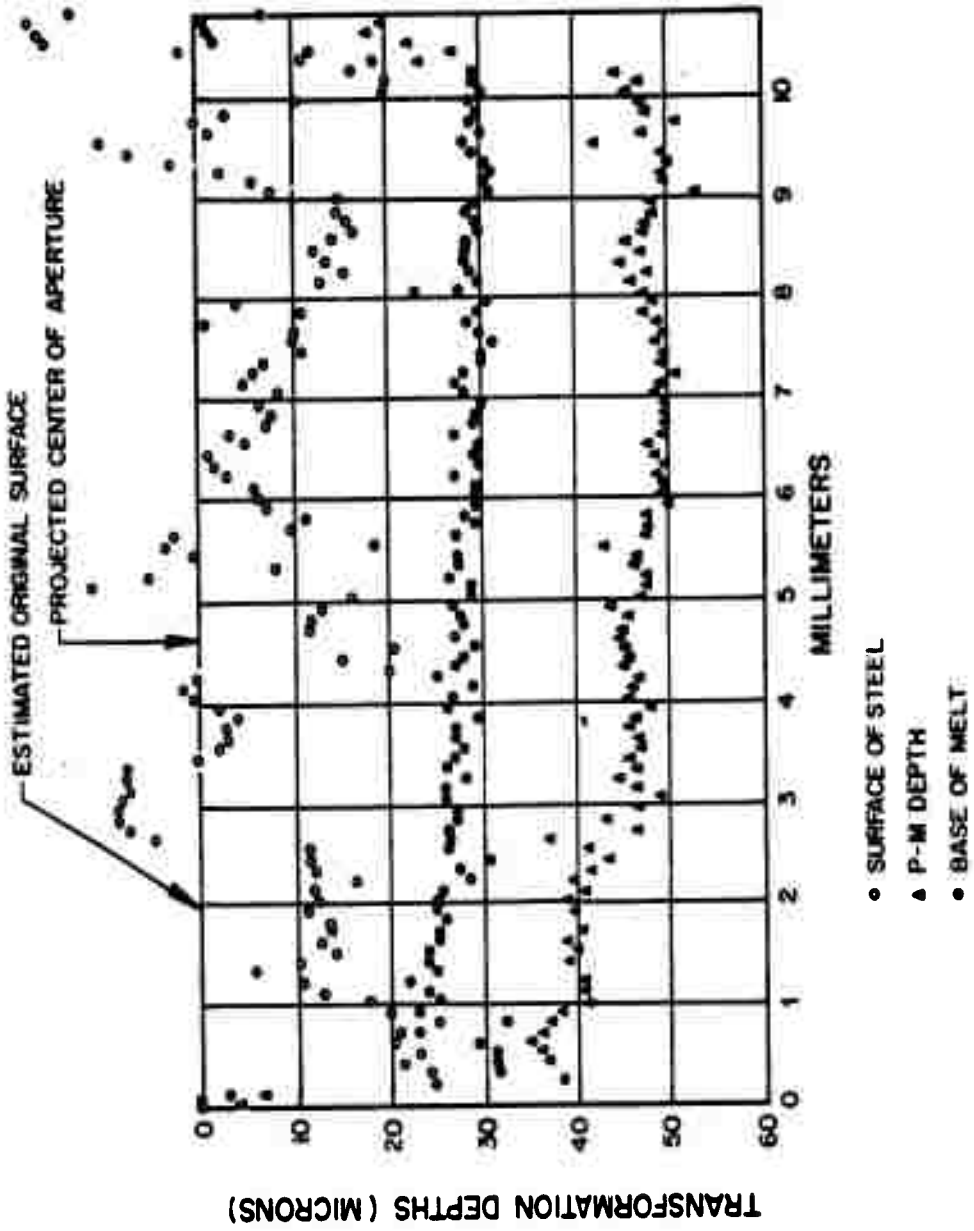


Figure 7.9 Transformation depths in thermal pinhole camera, top-slotted steel gage, 10-mm aperture, without hatch, Pod K-1.

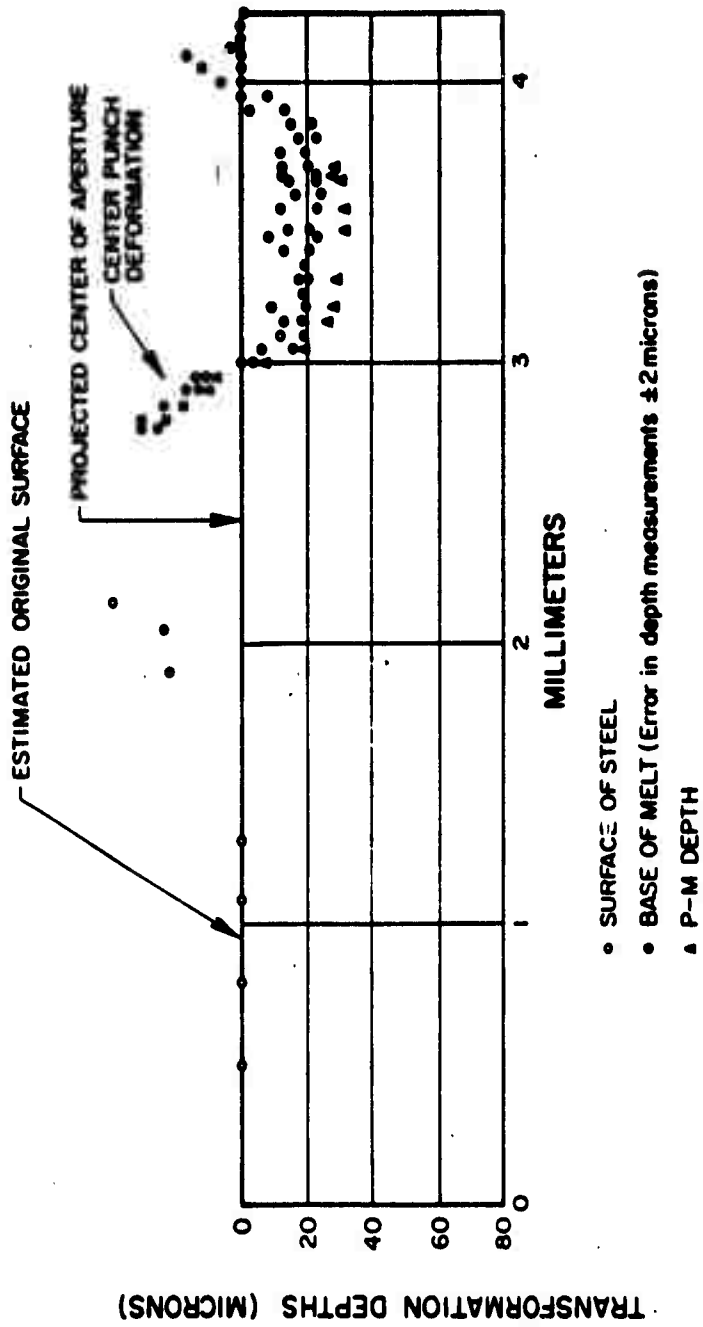
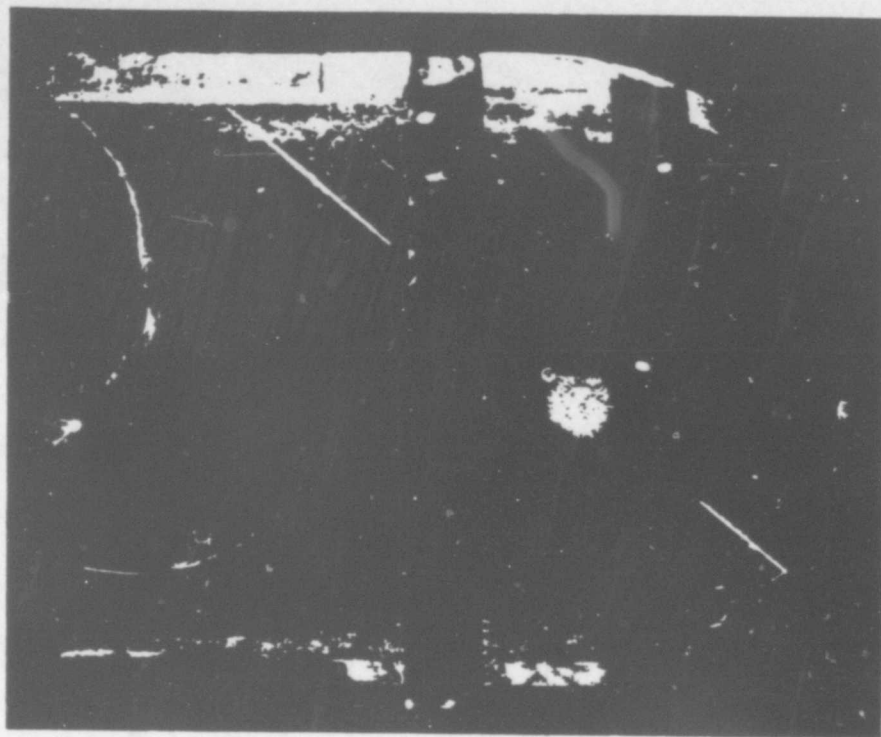


Figure 7.10 Transformation depths in thermal pinhole camera, top-slotted steel gage, 1-mm aperture, without hatch, Pod K-1.



MAGNIFICATION = 6X

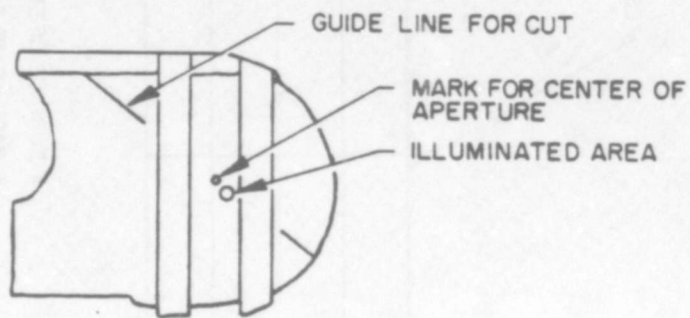


Figure 7.11 Cross-sectioning orientation for thermal pinhole camera, 1020 steel detector, Pod K-1. (ASE photo)

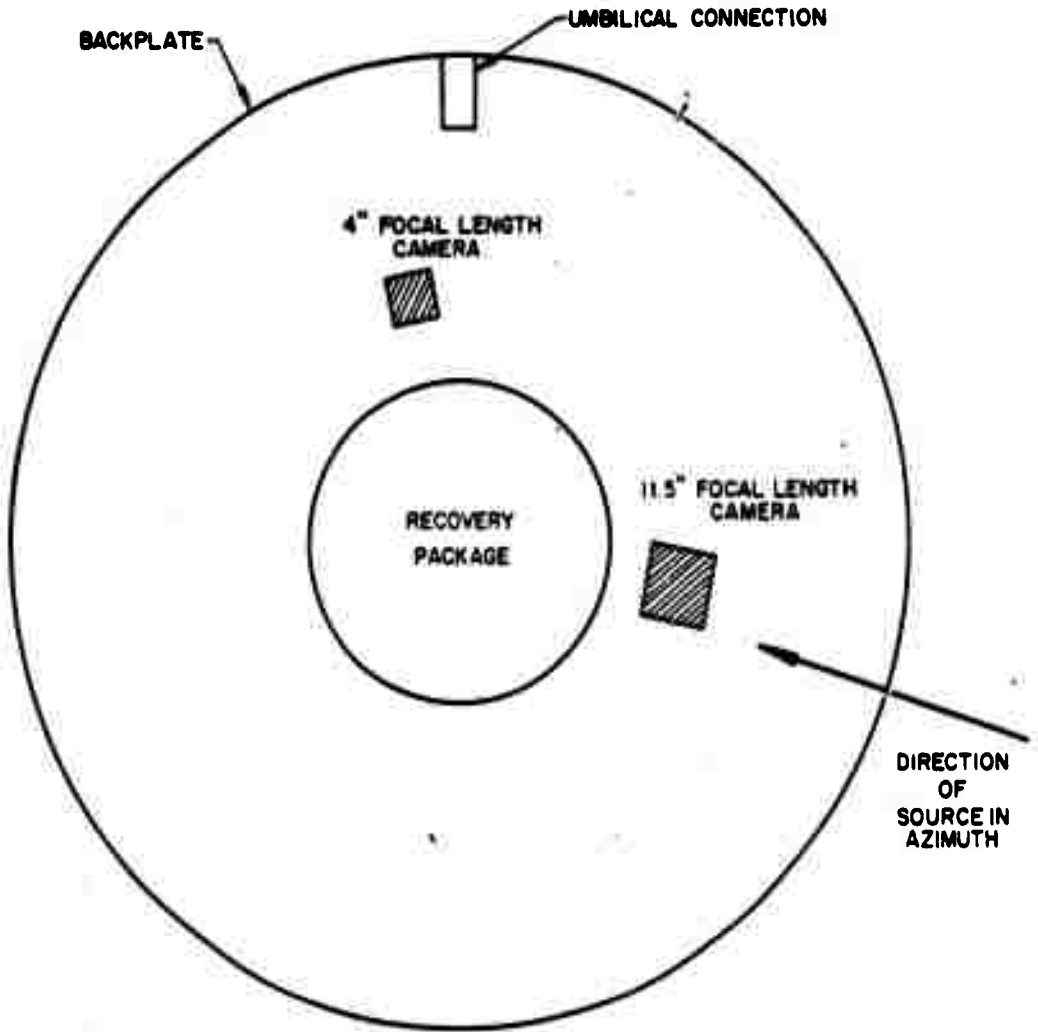


Figure 7.12 Orientation and location of pinhole camera with respect to Pod K-1.

ILLUSTRATING APERTURE AND IMAGE ORIENTATION (FULL SIZE)

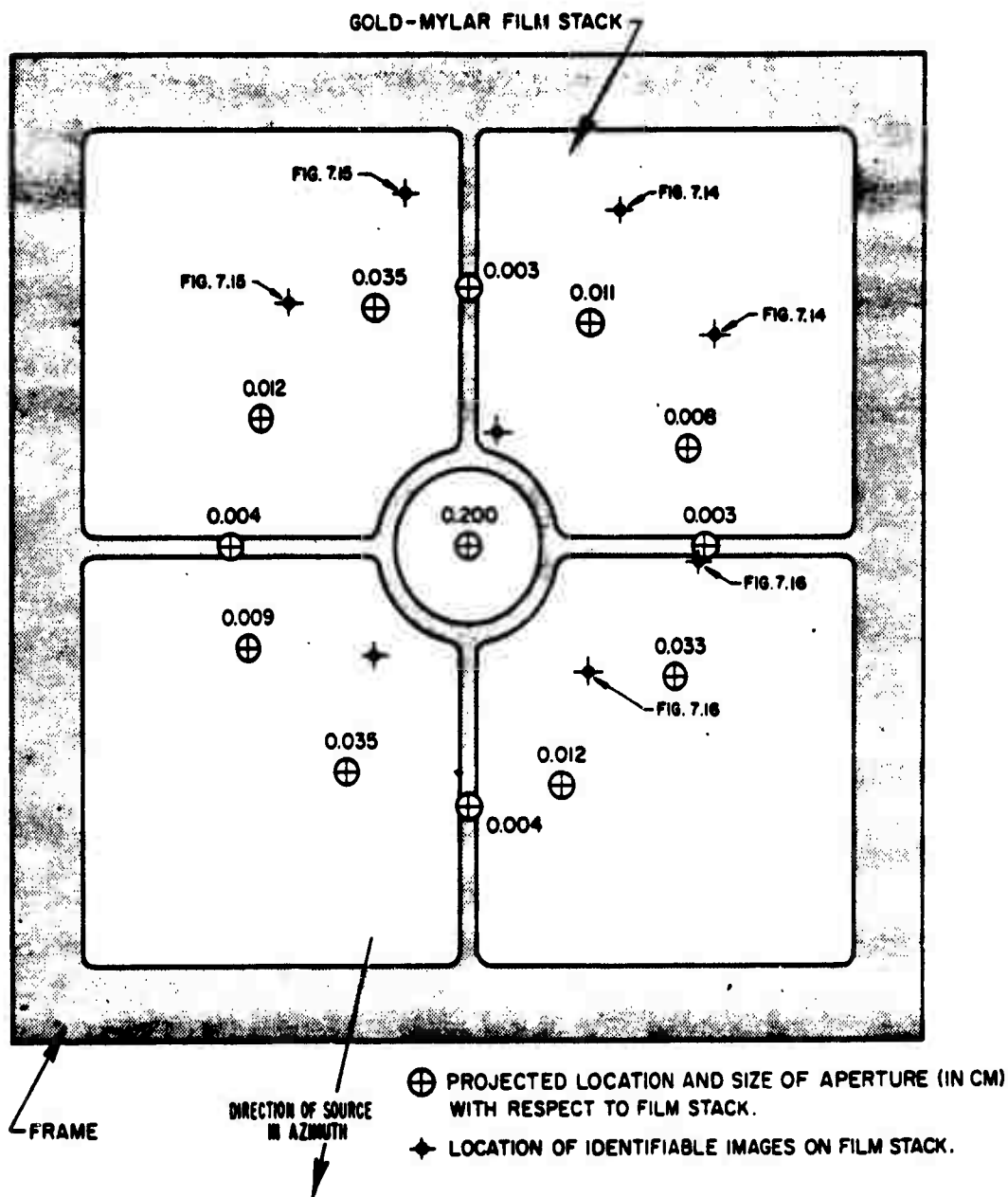


Figure 7.13 11.5-inch-focal-length X-ray pinhole camera film stack.

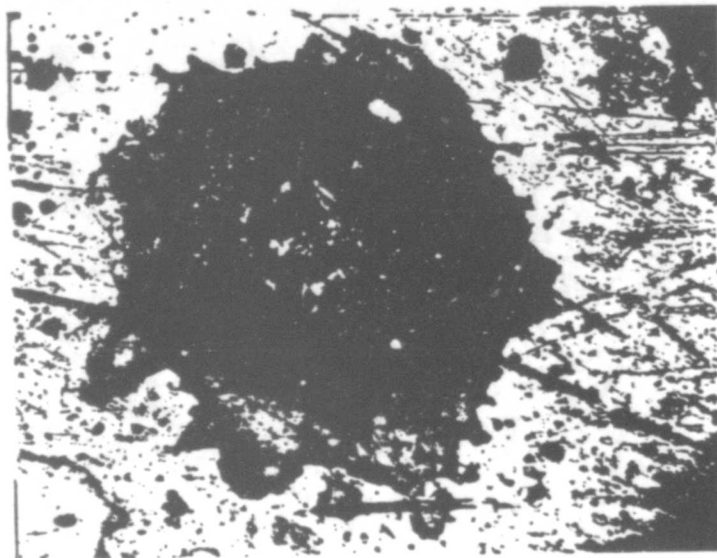
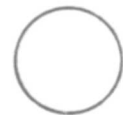


IMAGE FORMED
BY
.011 cm
APERTURE
(X144)



RELATIVE
APERTURE
SIZE

DIRECTION TO
SOURCE IN
AZIMUTH

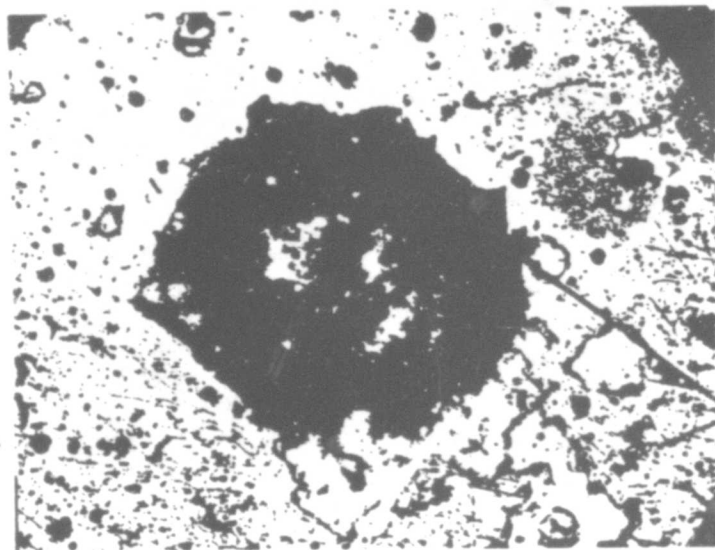


IMAGE FORMED
BY
.008 cm
APERTURE
(X144)



RELATIVE
APERTURE
SIZE

Figure 7.14 11.5-inch-focal-length X-ray pinhole camera images, 0.011- and 0.008-cm apertures, King Fish. (ASE photos)

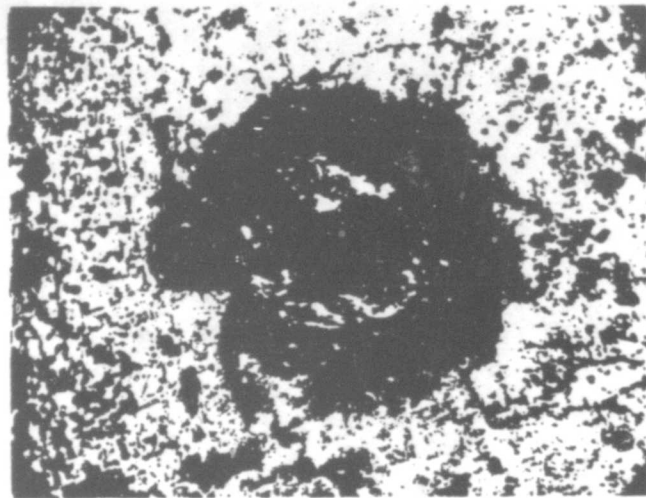
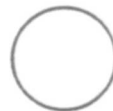


IMAGE FORMED
BY
.012 cm
APERTURE
(X144)



RELATIVE
APERTURE
SIZE

DIRECTION TO
SOURCE IN
AZIMUTH

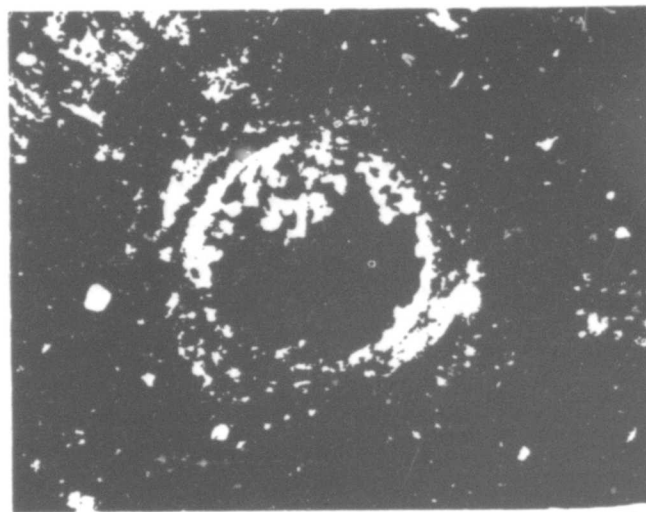


IMAGE FORMED
BY
0.035 cm
APERTURE
(X144)



RELATIVE
APERTURE
SIZE

Figure 7.15 11.5-inch-focal-length X-ray pinhole camera images, 0.012- and 0.035-cm apertures, King Fish. (ASE photos)

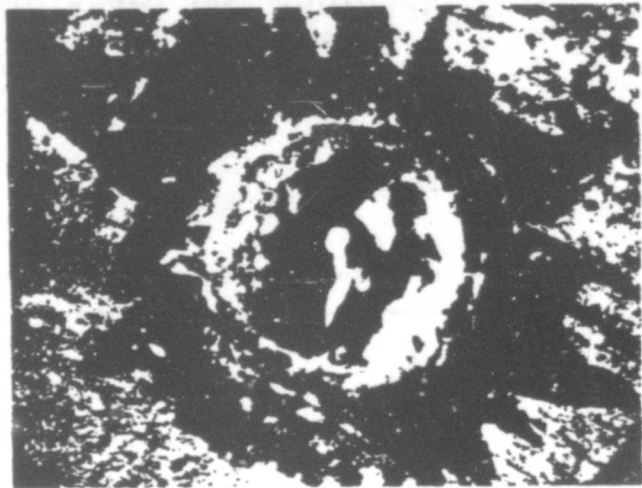


IMAGE FORMED
BY
0.033 cm
APERTURE
(X144)



RELATIVE
APERTURE
SIZE

DIRECTION TO
SOURCE IN
AZIMUTH

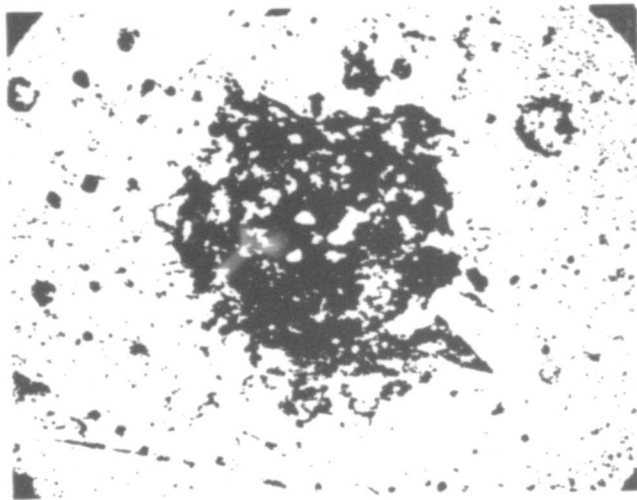
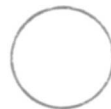


IMAGE FORMED
BY
0.012 cm
APERTURE
(X144)



RELATIVE
APERTURE
SIZE

Figure 7.16 11.5-focal-length X-ray pinhole camera images,
0.033- and 0.012-cm apertures, King Fish. (ASE photos)

ILLUSTRATING APERTURE AND IMAGE ORIENTATION (FULL SIZE)

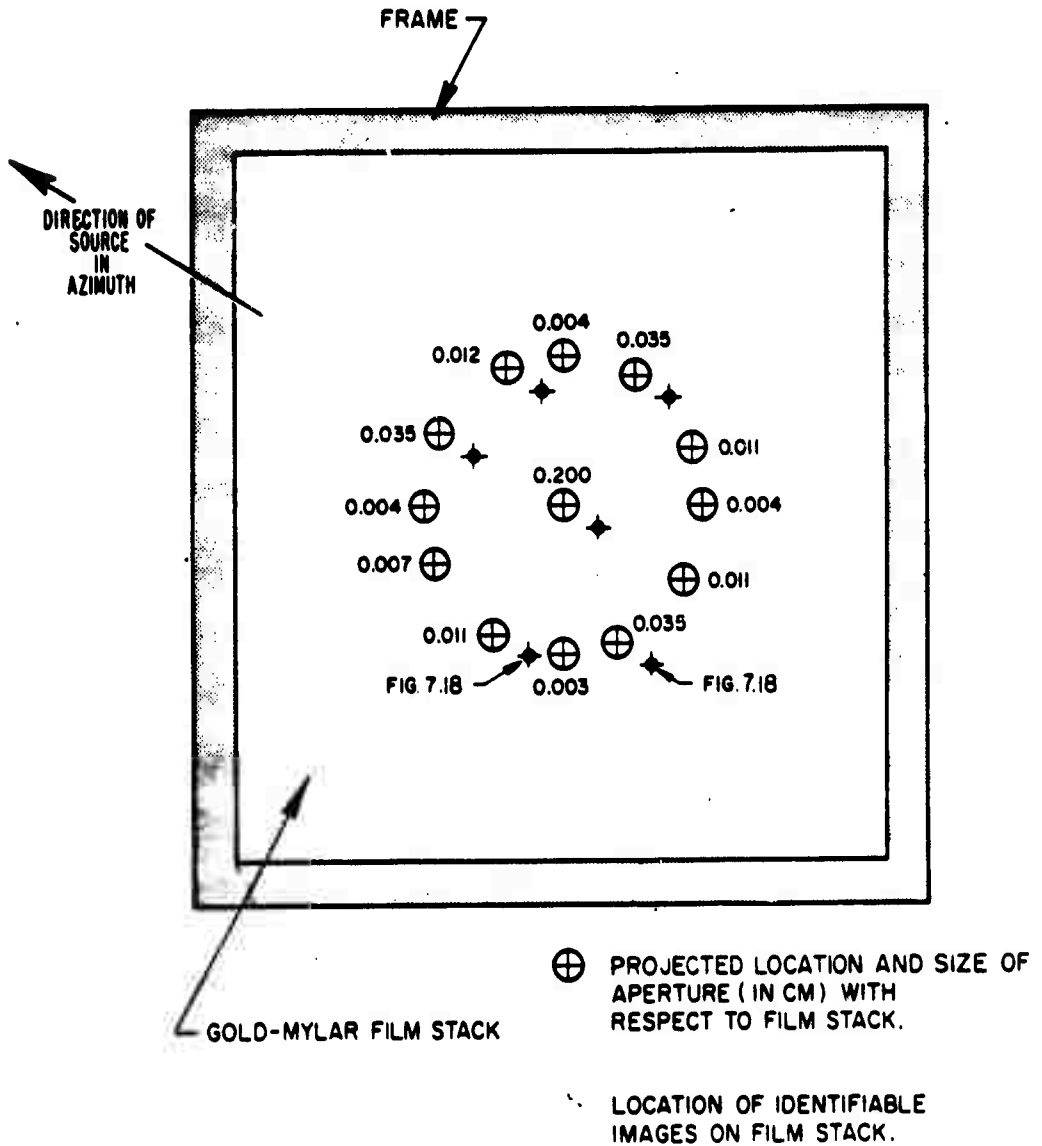


Figure 7.17 4-inch focal-length X-ray pinhole camera film stack.

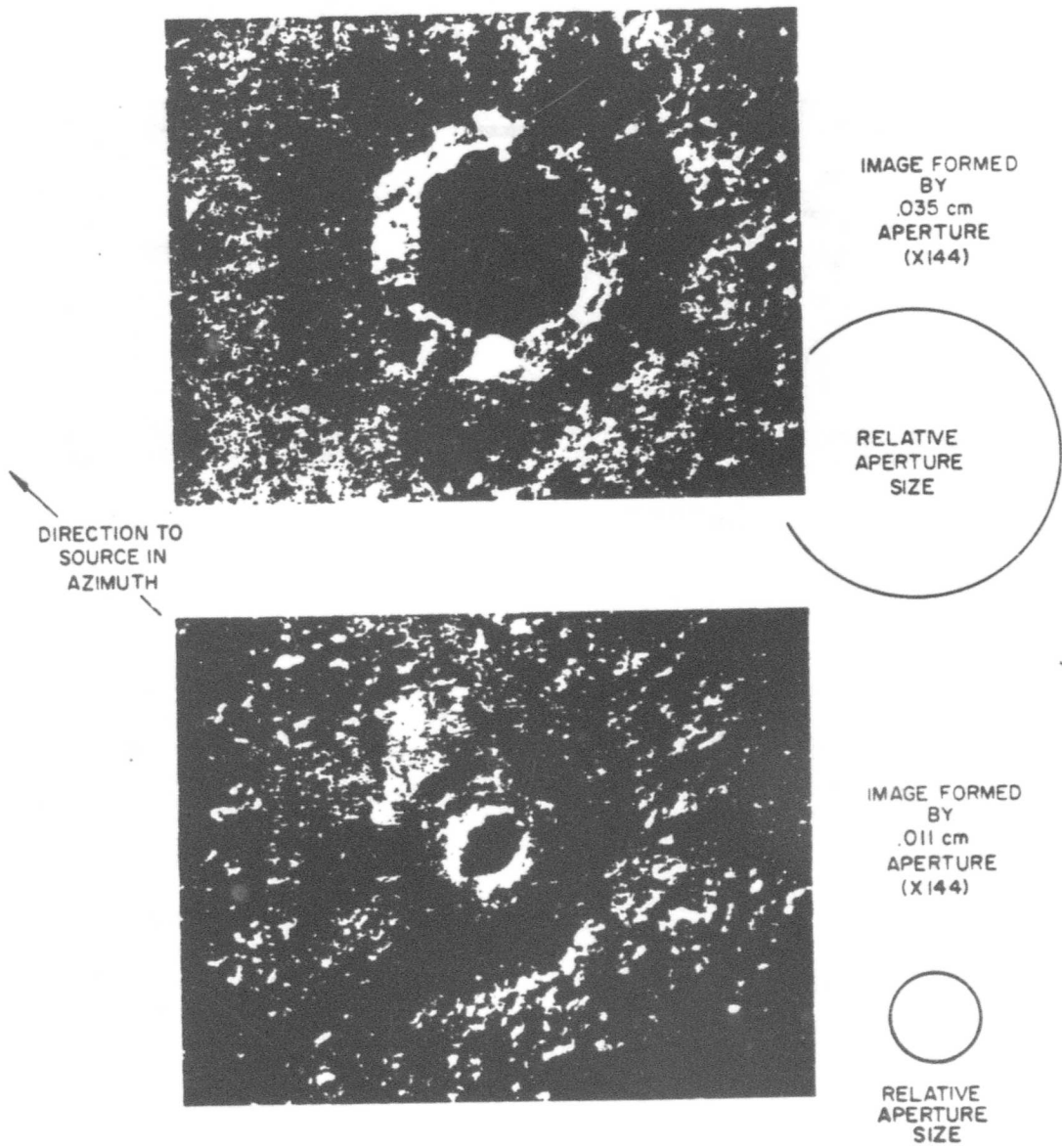
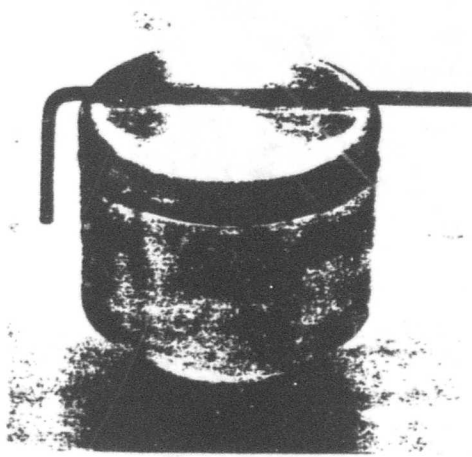
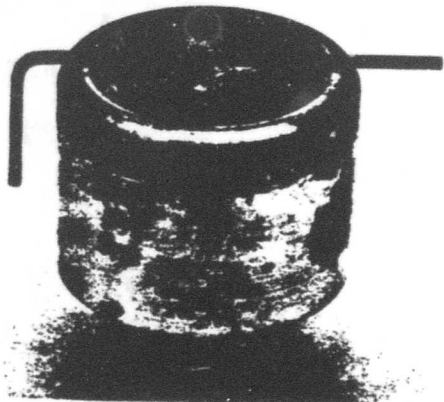


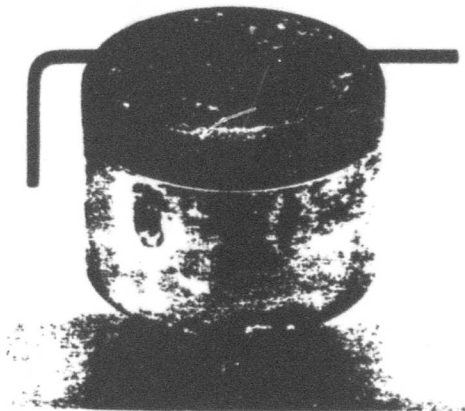
Figure 7.18 4-inch-focal-length X-ray pinhole camera images, King Fish. (ASE photos)



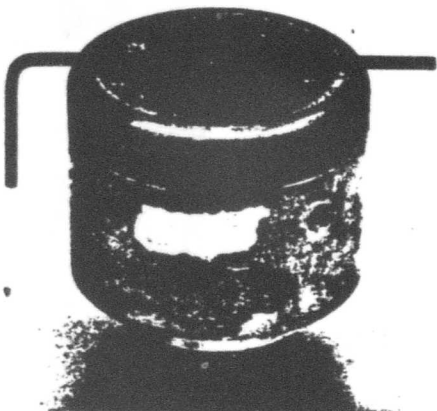
BEFORE



.010" AFTER

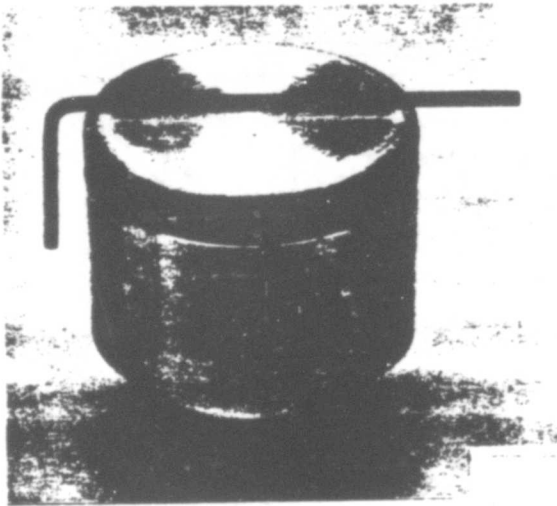


.020" AFTER



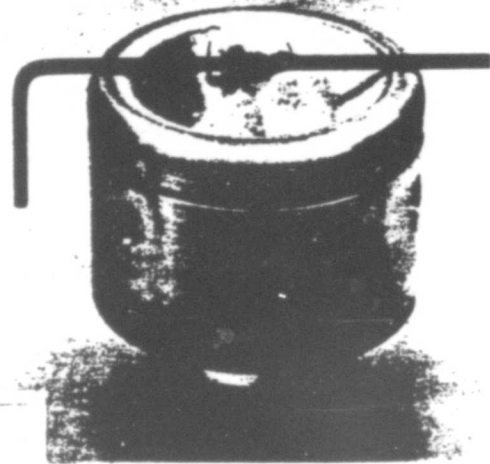
.030" AFTER

Figure 7.19 Structural gages, steel, King Fish. (ASE photos)



BEFORE

.020" AFTER



.050" AFTER

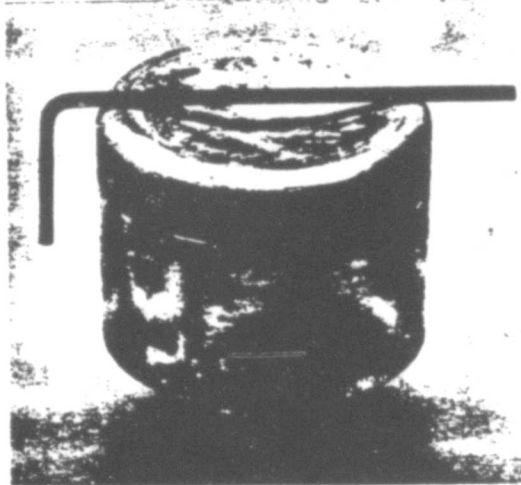


Figure 7.20 Structural gages, aluminum, King Fish. (ASE photos)

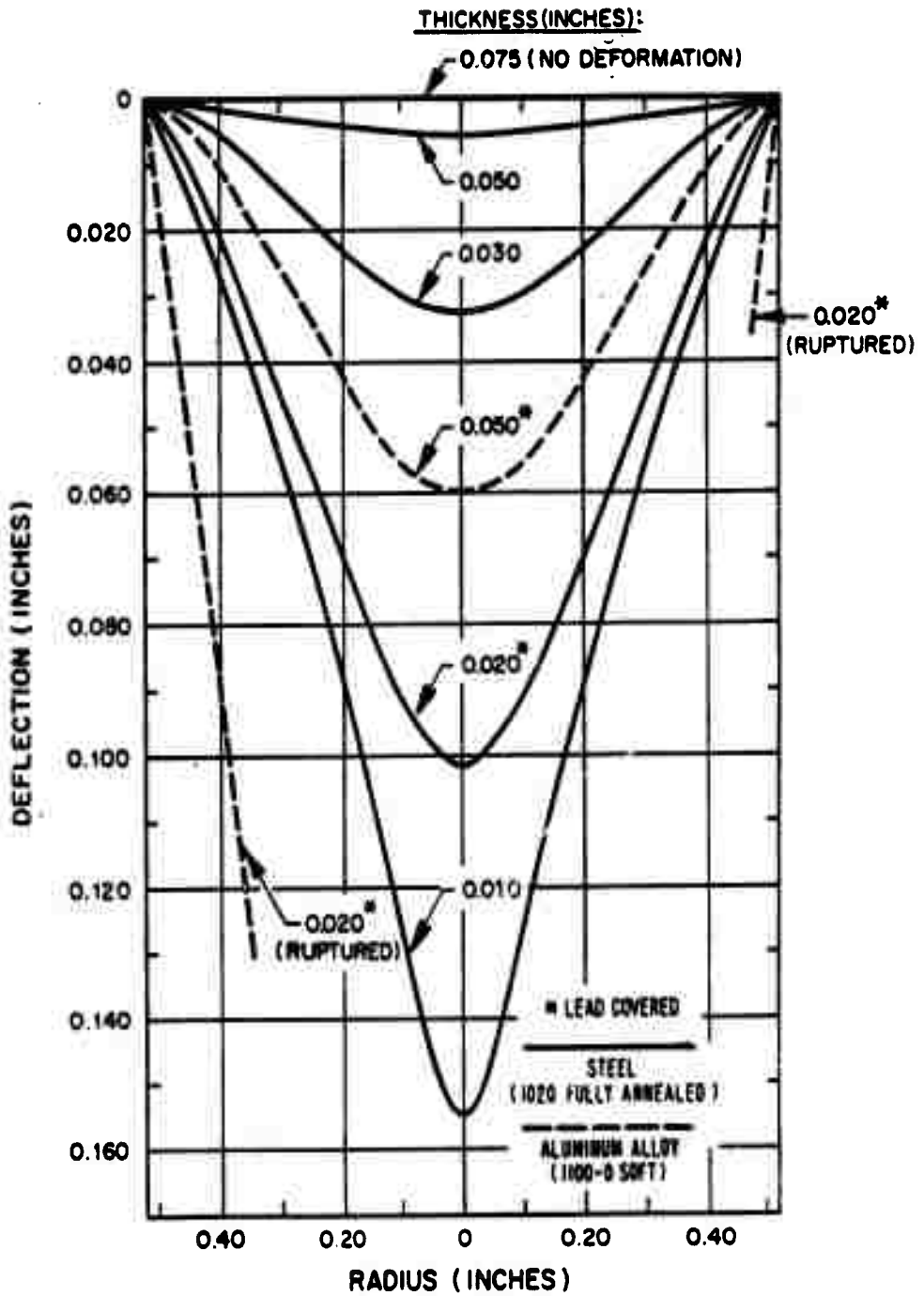


Figure 7.21 Deflected shapes of membrane structural gages.

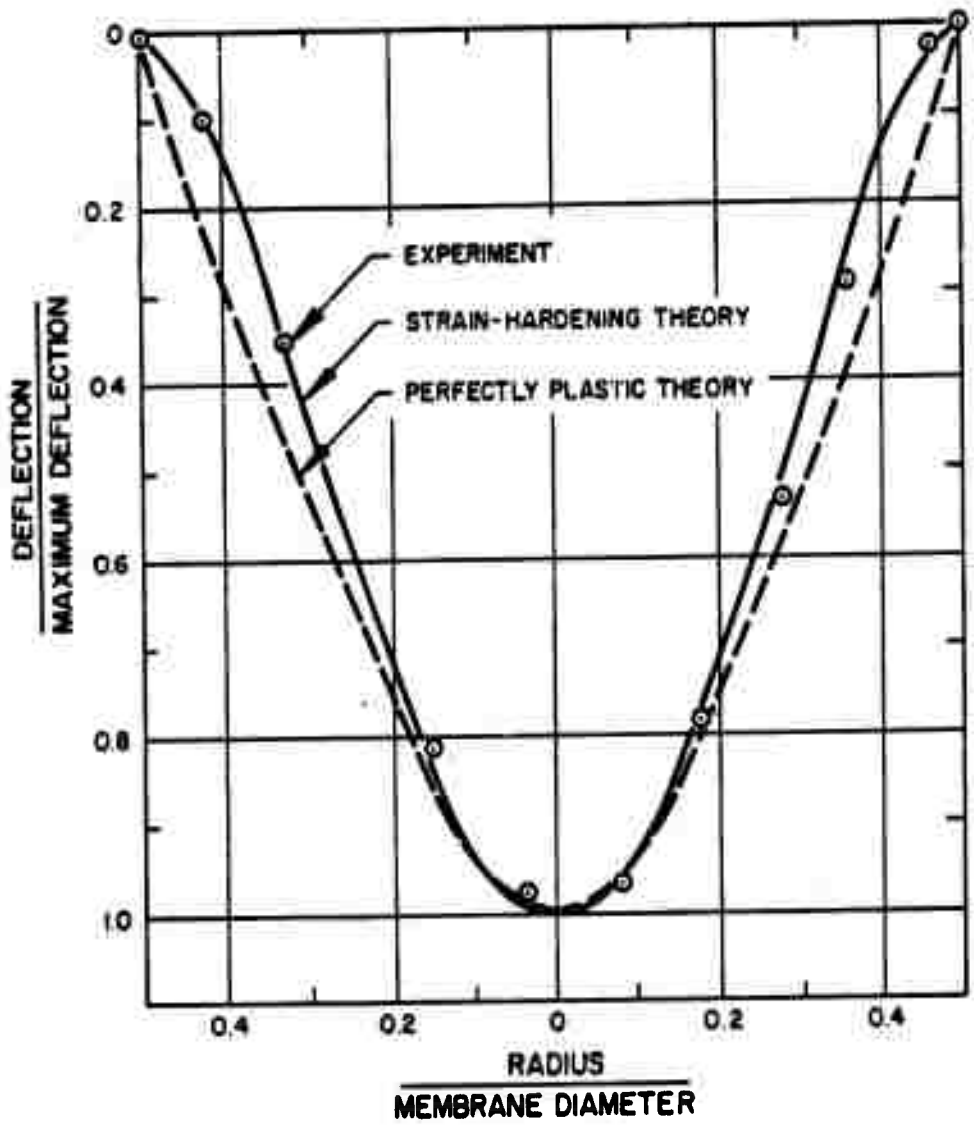


Figure 7.22 Deflection mode of membrane structural gage, 0.050-inch aluminum, King Fish.

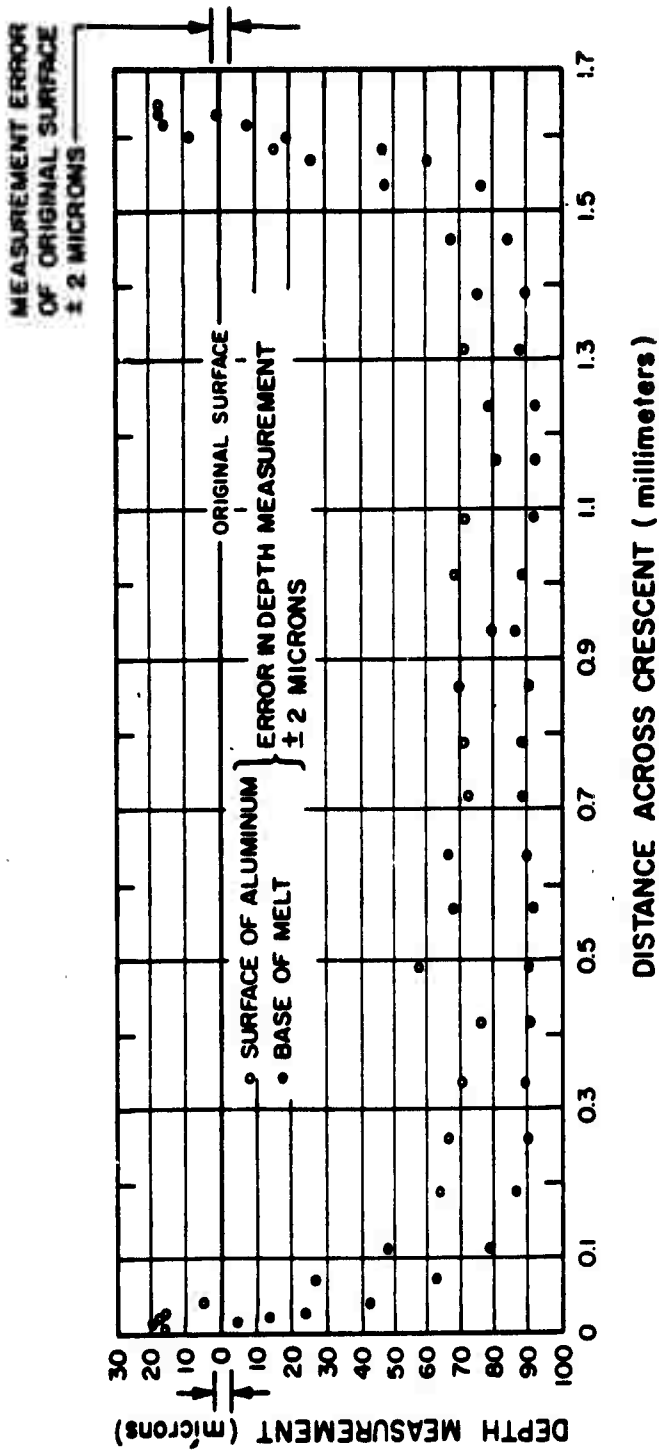


Figure 7.23 X-ray effects on aluminum, Cluster 80, Pod K-1.

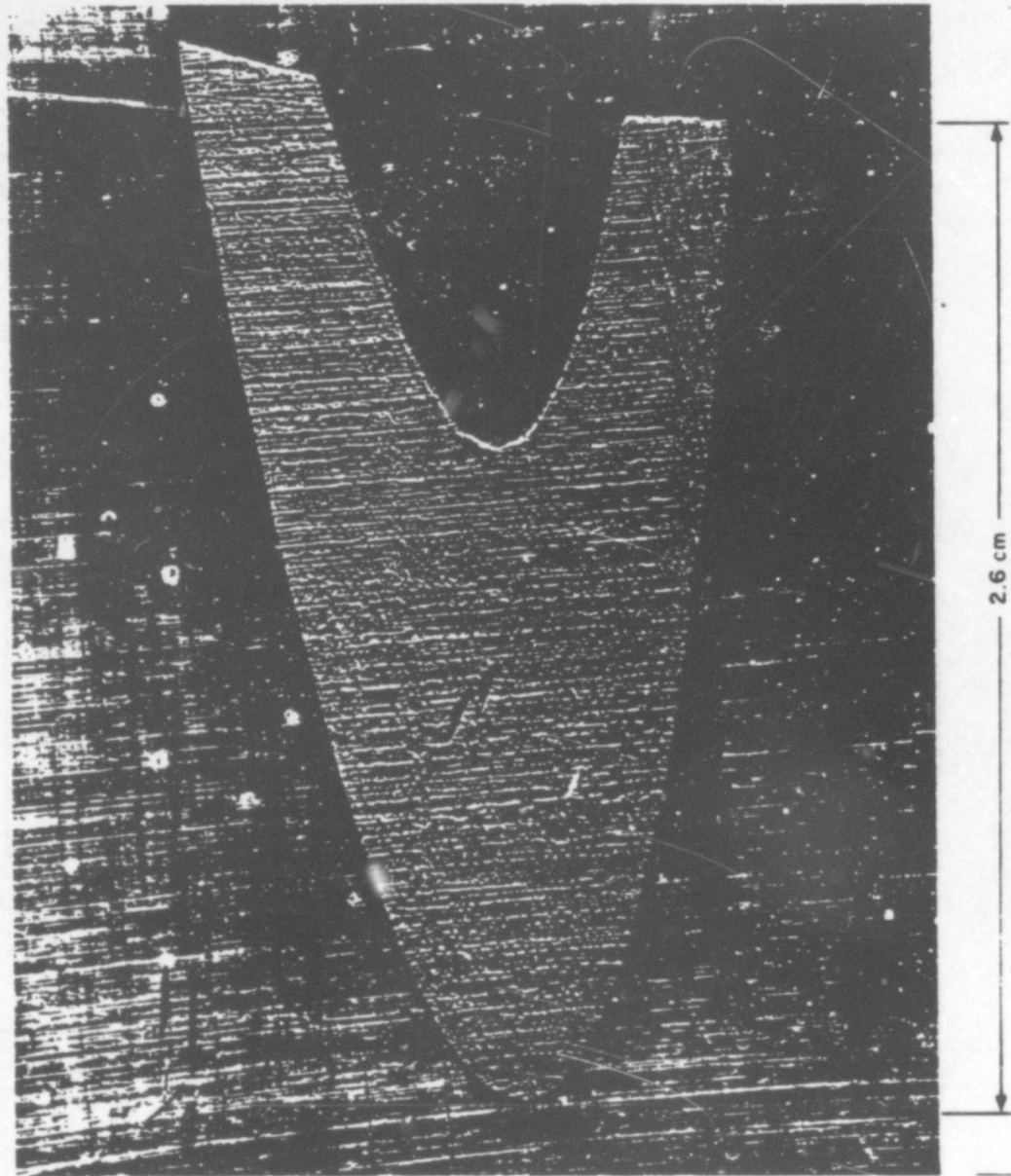


Figure 7.24 X-ray-illuminated area on inner surface of aluminum guide sleeve, Pod K-1. (ASE photo)

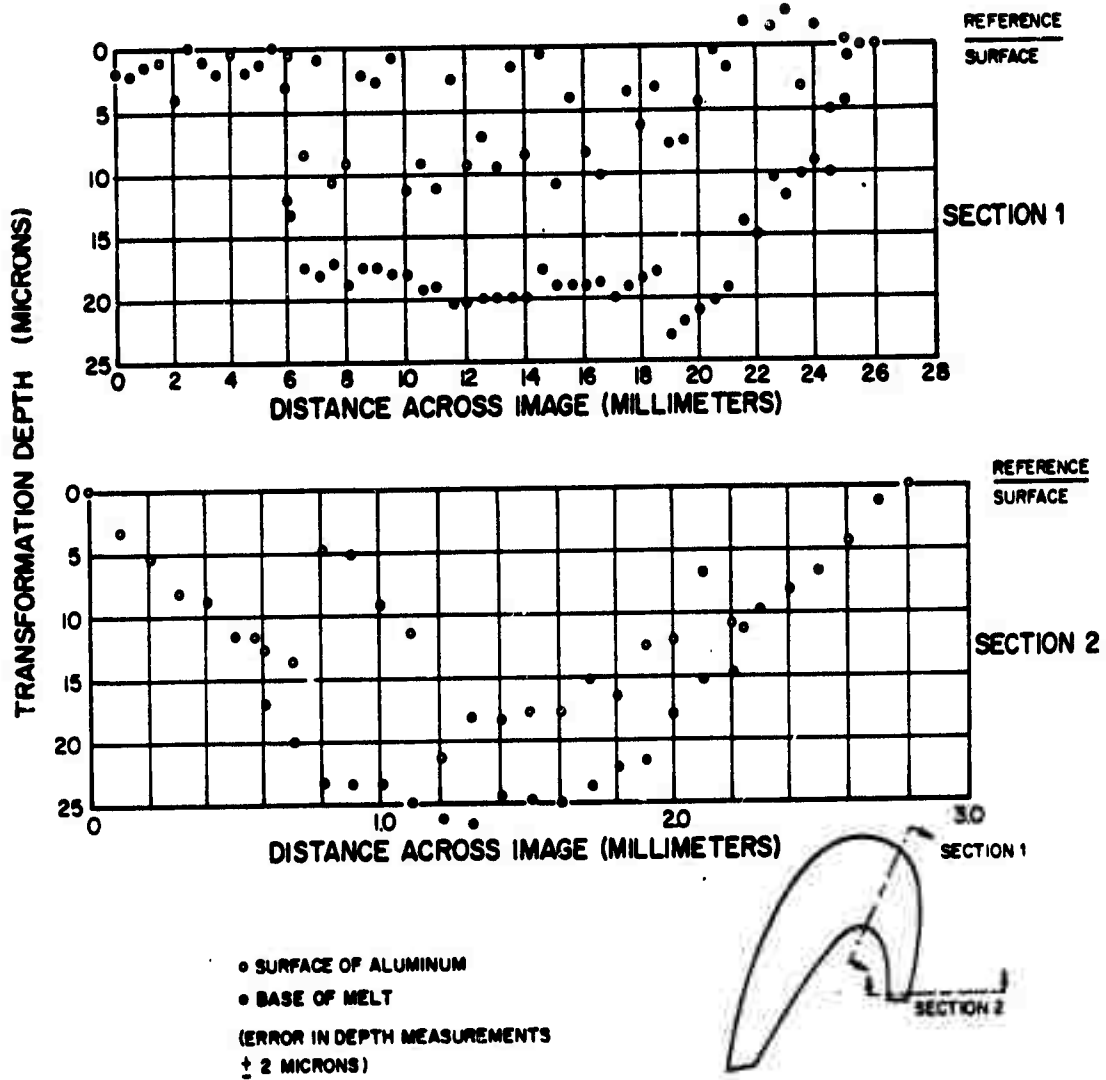


Figure 7.25 X-ray effects on aluminum guide sleeve, Cluster 80, Pod K-1.

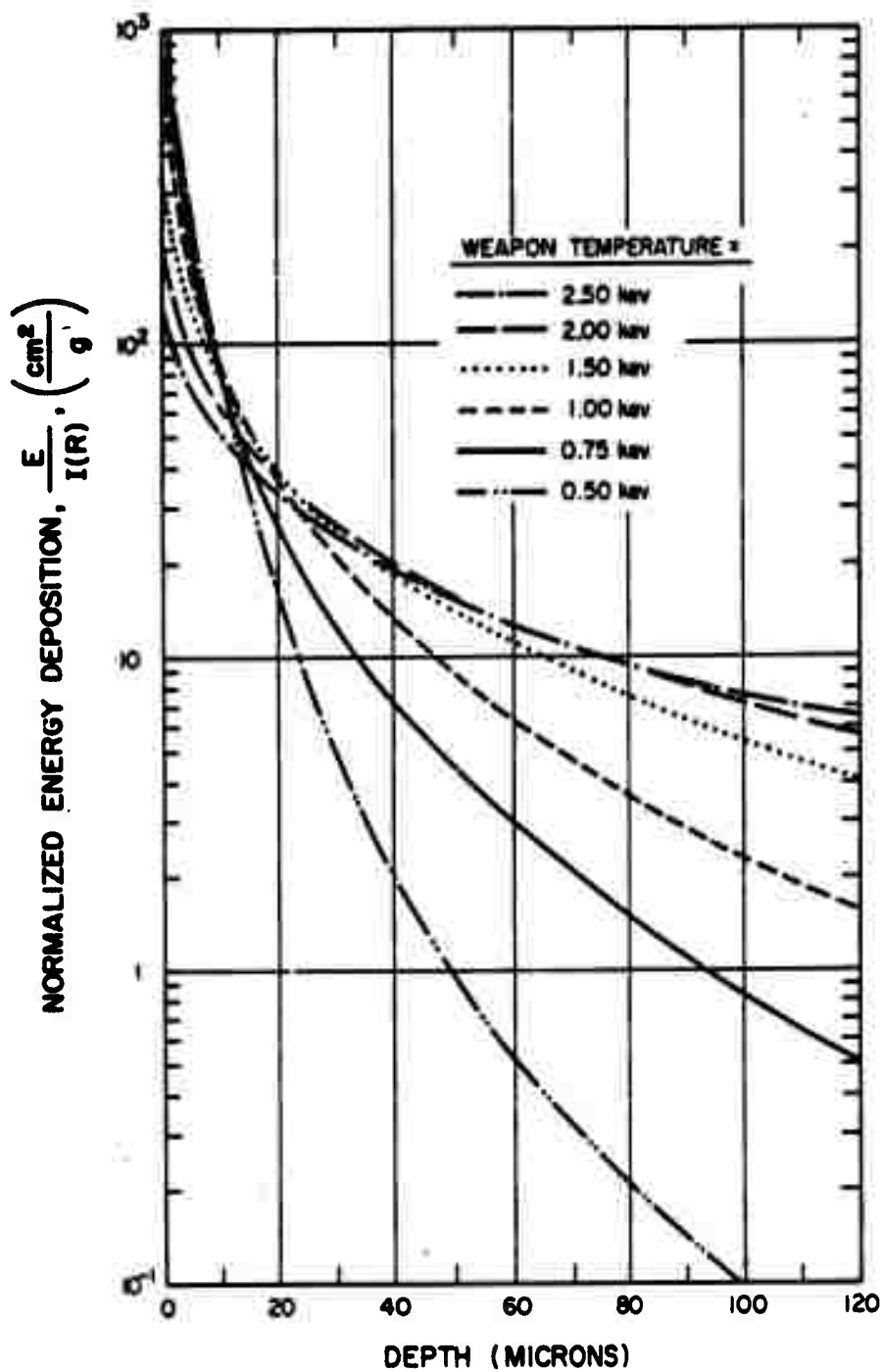
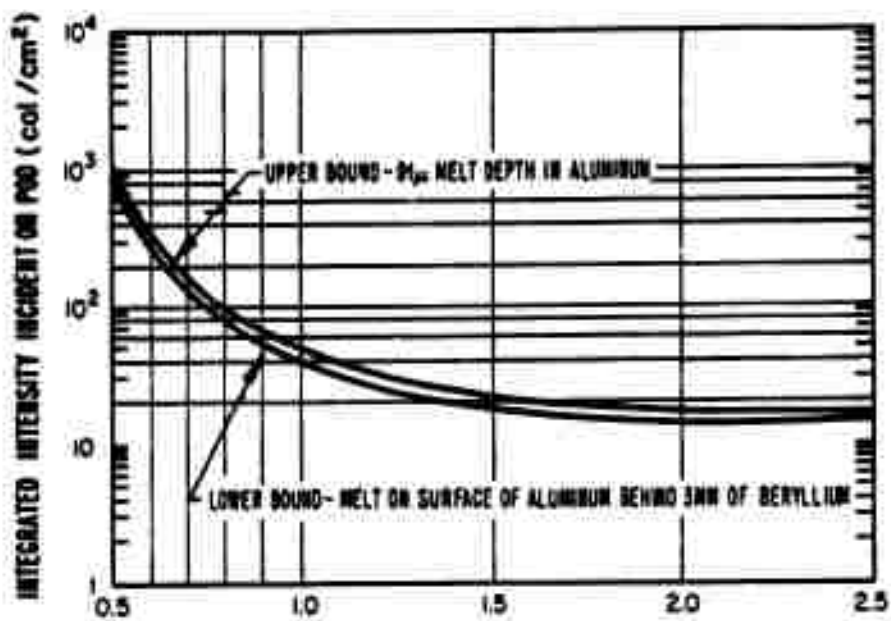


Figure 7.27 Normalized X-ray energy deposition in aluminum at Pod K-1.



CHAPTER 8

SUMMARY AND DISCUSSION

As noted previously, the data from Shot King Fish have not yet been reduced to the same extent as in Shot Blue Gill. The results, therefore, must be considered preliminary and somewhat incomplete.

Several images of the source were obtained in X-ray pinhole cameras. These images have not yet been examined in detail. They do, however, consistently correspond to a source about 1 meter in diameter. This diameter agrees with the X-ray source size measured in Blue Gill. The presence or absence of a heat shield, therefore, does not appear to affect source size, as viewed in the direction of the shield.

The instruments specifically designed to measure X-ray intensity have not yet been examined in detail. Estimates of intensity and source temperature have, however, been made from the response of various metals which were exposed to the burst. The specific material which provided the best data was aluminum, both directly exposed and behind a 3-mm-thick beryllium window. With these two data the intensity is closely bounded as a function of weapon temperature. At present no bounds on temperature are available from the data.

No definite statement can be made on the relative nominal X-ray source temperatures for Shots King Fish and Blue Gill. Two factors are of importance. First, the presence of the heat shield between the weapon and pods in Shot Blue Gill and its absence in Shot King Fish would tend to reduce the source temperature in the former compared to the latter (or perhaps raise it, if the shield did not act as a secondary emitter)

The effects of these two factors make a detailed analysis necessary to determine the relative source temperatures of the two weapons.

An attempt was made to compare the King Fish and Star Fish intensities, utilizing an exchange of metallurgical samples with Allied Research Associates, Inc. This comparison has not yielded conclusive results as yet.

Some of the measured impulses in units of 10^3 dyne-sec/cm² on pod K-1 (2.5 km) and pod K-2 (3.8 km) are as follows:

	<u>Pod K-1</u>	<u>Pod K-2</u>
Refrasil-Phenolic	1.2	
Oblique tape-wound refrasil	1.4	
Tape-wound nylon phenolic	0.9	
Tetlon	1.0	< 0.2 *

	<u>Pod K-1</u>	<u>Pod K-2</u>
Phenolic	3.0	0.7
Avcoat 19	4.1	
Rad 58-B	1.4	
Glass-filled phenolic	2.1	
Micarta	3.0	
Pyrolytic graphite (perpendicular grain)	< 0.2*	0.2*
Pyrolytic graphite (parallel grain)	< 0.2*	< 0.2*
Lead	1.2 to 4.6	0.9
Aluminum	0.6	
1020 Steel	1.0	
Beryllium	< 0.2*	
Copper	1.1	

*Instrument threshold level

In contrast to Blue Gill, there were definite differences in impulse among the materials. No adjustment has been made in the data for possible effects of the loss of samples.

The indent recorder is incapable of resolving the short times associated with X-ray loadings. A set of time-history pistons similar to those used in Blue Gill with lead samples was included to check the possibility of a debris/thermal loading of long duration. This set of pistons apparently recorded a time history (Figure 7.4) with an initial fast rise that could not be resolved and a doubling of the impulse somewhere between 5 and 20 msec. There has not yet been found any other data on the pod to corroborate this late loading. Such corroboration could have come, for example, from the pistons below hatches or the steel thermal detectors behind hatches .

Such corroboration was not obtained from the pistons beneath hatches, since none of these recorded any impulse. The pistons behind beryllium windows recorded no impulses either. The pistons below hatches and windows were recessed within a relatively small volume bellows, however, so that any pressure within the piston chamber would have quickly equalized about the piston heads. Consequently, these pistons would have been extremely insensitive. For example, a thermomechanical impulse less than 2×10^3 dyne-sec/cm² would not be measurable below the hatches because of this effect. In retrospect, the use of the bellows was not conducive to the measurement of a thermomechanical impulse.

The steel detectors behind hatches in the debris/thermal pinhole cameras measured no energy input to corroborate the impulse time history. No strong conclusion can be drawn from this, since the same type of gage on pod B-3 with a 3-mm aperture but without a hatch also showed no effect. From other instruments, however, it was apparent that pod B-3 did receive appreciable thermal radiation. Thus, the question of whether a thermal input existed in King Fish remains unanswered.

The ablation of materials was generally too small to be of direct structural significance. The two noteworthy exceptions are Avcoat 19 and Rad 58-B where the relatively large material loss appeared to be the result of some form of mechanical fragmentation rather than chemical decomposition or vaporization.

A comparison of the ablation data on pod B-3 and pod K-1 is of some interest, since they were at nearly the same ranges. It is rather striking that certain materials (e. g. , iron devcon) on

exposure to thermal radiation lose approximately four times more mass than they do on exposure to X-rays, whereas other materials (such as teflon) lose nearly three times more mass due to X-radiation. Thus, an understanding of the differences in response phenomenology may be critical to the determination of the vulnerability of missiles to X-rays and to thermal radiation. It is also interesting to note that the kinetic energy of the blowoff for reffrasil-phenolic as obtained from the expression

$$KE = \frac{J^2}{2M}$$

is only about 0.3 cal/cm^2 ($J = 10^3 \text{ dyne-sec/cm}^2$, $M = 0.05 \text{ gm/cm}^2$) compared to an input energy which is of the order of 100 cal/cm^2 . Thus, the heat of ablation must have been the order of 2000 cal/gm . This value is in reasonable agreement with the decomposition scheme for Blue Gill where it is assumed that the ablation occurs along the same schedule as the thermal input (see Section 4.2.2).

Both plastic deformation and failure were observed on steel membranes and on lead-covered aluminum membranes. The deformed shapes correlated extremely well with theoretical treatments which included strain hardening.